Computational study of the structure-function relationship of Kir3 channels and applications to the design of light-gated Kir3 channels

Zlatomir Todorov

THÈSE

Pour obtenir le grade de

DOCTEUR DE LA COMMUNAUTE UNIVERSITE GRENOBLE ALPES

Spécialité : **Biologie Structurale et Nanobiologie**

Arrêté ministériel : 25 mai 2016

Présentée par

Zlatomir TODOROV

Thèse dirigée par **Michel VIVAUDOU**

préparée au sein du **Laboratoire Institut de Biologie Structurale** dans **l'École Doctorale Chimie et Sciences du Vivant**

Étude computationnelle de la relation structure-fonction des canaux Kir3 et application dans la conception de canaux Kir3 sensibles à la lumière

Computational study of the structure-function relationship of Kir3 channels and applications to the design of light-gated Kir3 channels

Thèse soutenue publiquement le **18 novembre 2019**,
devant le jury composé de :

Monsieur Michel VIVAUDOU
CEA, Institut de biologie structurale, Membre

Madame Cécile Breyton
Directeur de Recherche, Institut de biologie structurale, Président, Membre

Madame Lucie Delemotte
Professeur assistant, Department of Applied Physics KTH Royal Institute of Technology, Rapporteur

Monsieur Thibaud Jean-Baptiste
Directeur de Recherche, IBMM UMR 5247, Rapporteur

Monsieur Pierre Charnet
Directeur de Recherche, IBMM UMR 5247, Membre

Monsieur François Dehez
Chargé de Recherche, Université de Lorraine, Faculté des Sciences et Technologies , Membre

Acknowledgements

First of all, I express my greater gratitude to Dr. Michel Vivaudou who accepted me in his team, for his advice and valuable help during the completion of this work. I particularly want to thank all members of the ruling comity of the Label ICST for funding my fellowship and for granting me financing for the extra fourth year of fellowship during which I was able to obtain most of the results which are described in the manuscript. My great gratitude is addressed to Dr. François Dehez who paved the way for me through our collaboration to acquire expertise in molecular-dynamics simulations and to obtain results by advising me and granting me access to the high-level computers in the LPCT in Nancy. I thank all the members of my team in the IBS for their kindness, friendship and warm scientific discussions. Namely I thank Ana-Sophia Olivera, Jean Revilloud et Laura Lemel for having given me a hand during some overwhelming work days. I address my special thanks to Dr. Christophe Moreau who taught me to work with the electrophysiological setups and shared many hints on how to master the lab work. I am also very grateful to Dr. Christophe Moreau because he revived my interest for an article which in the end became one of the main bibliographic references that I used to build my modeling project. I thank Prof. Emad Tajkhorshid from University of Urbana-Champaign for answering many of my questions about a specific topic on the analysis of simulated trajectories, this discussion helped me to adapt a method that Prof. Tajkhorshid's team published for the analysis module I use to survey the allosteric signal over time in the contact network extracted from the simulated trajectories. I also thank Prof. Benoit Roux who reviewed part of my work and the analysis I had at some point and greatly advised me on how to continue in the scope of future publication of my results. Many thanks to Dr. Jacques Neyton et Dr. Jean-Luc Pellequer from IBS, with whom I had lots of very fruitful discussions about experimental techniques, data analysis and the biophysics of proteins and channels in particular. I thank everyone else who have supported me and motivated me to give my best for this doctoral thesis. I particularly thank my dear wife who has provided me the greatest moral support during this very challenging period for me. Last but not least, I thank the members of the jury for accepting to review my dissertation.

Abstract

This doctoral thesis focuses on a family of transmembrane proteins expressed as tetrameric assemblies which function as selective potassium ion channels – the potassium inward rectifier member 3 (Kir3). In the sub-family, four genes coding Kir3 proteins are present in mammals, namely, members Kir3.1-4. The activity and tissue-specific expression of Kir3 channels greatly vary with subunit composition. Kir3 channels are activated by direct simultaneous interactions with G-protein beta-gamma dimers (Gβγ) released from G-protein heterotrimers of the $G_{(i/o)}$ class, PIP_2 lipids from the inner membrane leaflet and intracellular Na^+ ions. These channels mediate hyperpolarizing potassium currents at membrane potentials close to E_K, thus they are critical for development and health as they play an important role in decreasing cell excitability in different tissues. Disease conditions have been linked to misregulation of wild-type Kir3 channels or mutations of their genes.

Starting from an X-ray crystallographic model, our goal was to obtain trajectories demonstrating simulated molecular dynamics of the wild-type Kir3.2 channel. We optimized a computational protocol using a set of brute-force simulations where different combinations of Kir3 activators were implemented. We observed the Kir3.2 channel transitioning between different conformational and conductive states – successfully reproducing dynamic features reported in the literature. We discovered novel functional lipid-protein interaction sites potentially involved in a negative-auto-feedback mechanism intrinsic to the Kir3.2 channel. Interestingly, this prediction is backed by previously published X-ray crystallography data not exploited in this scope. Detailed analysis of the trajectories provided description of novel allosteric pathways linking the channel gates and the ligand interaction sites. In addition, based on the observed dynamics of the wild-type channel, we proposed molecular mechanisms for several experimentally-characterized pathologic mutants.

In parallel to the computational project, we attempted to engineer light-gated Kir3 channels. This work was aided by homology models which guided the selection of positions satisfying an arbitrary set of criteria for cysteine mutagenesis. The presence of reduced cysteines is required for the labeling of the proteins expressed into the membrane of *Xenopus laevis* oocytes with the photoswitchable tethered ligands (PTL) we used. Among the twenty screened cysteine mutants, one construct showed a mild photo-blocking phenotype. Further engineering greatly improved this phenotype, yielding the first light-activated Kir3.4 homotetrameric channel.

We believe that our simulation procedure is particularly suited for the investigation of various Kir3 assemblies of interest. An additional perspective for our models is to be used for the rational design of compounds targeting a specific conformation of Kir3.2 channel in the absence of experimentally obtained fully open/closed and transition-states conformations. Lastly, the developed photo-blocked Kir3.4 homotetramer could find applications in synthetic biology as a light-enabled diode. Alternatively, this mutant could be knocked-in *in vivo* – it should remain silent upon PTL-labeling in the resting-state, and provide information on the physiological role of the increase of Kir3 mediated currents when activated by ultra-violet light.

Résumé

Cette thèse de doctorat porte sur une famille de protéines transmembranaires exprimées sous forme de tétramères qui fonctionnent en tant que canaux ioniques sélectifs pour le potassium - le membre 3 des canaux potassiques à rectification entrante (Kir3). Quatre gènes codant pour les protéines Kir3 sont présents chez les mammifères dans la sous-famille, à savoir les membres Kir3.1-4. L'activité et l'expression tissulaire varient fortement en fonction des sous-unités constituant les canaux Kir3. Ces canaux sont activés par des interactions simultanées et directes avec des dimères bêta-gamma de la protéine G (Gβγ) libérés par les hétérotrimères de la protéine G de la classe $G_{(i/o)}$, des lipides PIP_2 du feuillet interne de la membrane et des ions Na^+ intracellulaires. Ces canaux permettent la genèse d'un courant potassique hyperpolarisant à des potentiels membranaires proches de l'E_K. Ils jouent un rôle important dans la régulation de l'excitabilité cellulaire dans différents tissus. Des maladies ont été associées à une mauvaise régulation des canaux Kir3 de type sauvage ou à des mutations de leurs gènes.

Un de mes objectifs a été de caractériser la dynamique conformationnelle sous-jacente à la fonction du canal Kir3.2 en utilisant la dynamique moléculaire. En partant de modèles obtenus par cristallographie aux rayons X, au lieu d'utiliser Gβγ pour ouvrir le canal dans nos simulations nous avons cherché à établir la stoichiométrie d'un ensemble de petites molécules connues pour l'activation de Kir3.2. Ainsi, dans une série de trajectoires où différentes combinaisons de partenaires étaient modélisées, le canal Kir3.2 a traversé différents états conformationnels et conducteurs – tout en reproduisant des caractéristiques décrites dans la littérature. Cette approche a amené à la découverte de nouveaux sites d'interaction lipide-protéine, potentiellement impliqués dans un mécanisme de rétroaction négative intrinsèque au canal Kir3.2. Cette prédiction est corroborée par des données de cristallographie aux rayons X publiées antérieurement et non exploitées dans ce contexte. L'analyse des trajectoires a également montré de nouvelles voies allostériques reliant les sites d'interaction du ligand aux portes du canal. De plus, sur la base de la dynamique du canal de type sauvage, nous avons proposé des mécanismes moléculaires pour plusieurs mutants pathologiques caractérisés expérimentalement.

Parallèlement au projet théorique, j'ai travaillé à l'élaboration de canaux Kir3 sensibles à la lumière pour l'optogénétique. L'utilisation de modèles par homologie a guidé la sélection de résidus du canal qui ont été mutés en cystéine. La présence de cystéines réduites est nécessaire pour le marquage des protéines exprimées dans la membrane des ovocytes de *Xenopus laevis* avec les ligands photosensibles que nous avons utilisés. Parmi les vingt mutants cystéines criblées, l'un d'entre eux a montré un phénotype modéré de photo-activation. Ce phénotype a pu être considérablement amélioré par une mutation additionnelle, nous permettant d'obtenir le premier canal Kir3 constitutivement inactif et activable par la lumière.

La procédure de simulation éprouvée dans ce travail est particulièrement adaptée à l'étude de divers canaux Kir3 d'intérêt. Une perspective pour nos modèles serait leur utilisation dans la conception de composés visant des conformations spécifiques du canal Kir3.2 en l'absence de données expérimentales sur les états d'ouverture et de fermeture complètes. Enfin, le canal Kir3.4 photosensible pourrait trouver des applications en biologie synthétique en tant que diode contrôlée par la lumière. En outre, ce mutant pourrait être inoculé *in vivo* – il devrait rester silencieux après marquage et fournir des informations sur le rôle physiologique de l'augmentation des courants médiés par canaux Kir3 lorsqu'il est activé par la lumière ultraviolette.

CONTENTS

1 Ion channels and Kir general 1

1.1 The cell, the cell's membrane, ion channels and the membrane potential 1

1.2 Physiological role of Kir family members 2

1.2.1 Kir1 2

1.2.2 Kir2 3

1.2.3 Kir3 3

1.2.4 Kir4 3

1.2.5 Kir5 4

1.2.6 Kir6 4

1.2.7 Kir7 4

1.3 Structural overview of Kir channels 4

1.3.1 Selectivity filter 5

1.3.2 Transmembrane domain 5

1.3.3 Cytoplasmic domain 6

1.4 Motivation and scientific objectives 7

1.4.1 What is the niche in the scientific field for these doctoral thesis projects? 7

1.4.2 Scientific objectives 8

2 Kir3: Literature review 9

2.1 Overview of the Kir3 sub-family members 9

2.2 Activation of Kir3 by G heterotrimeric proteins in the physiological and cellular contexts . 11

2.3 Molecular mechanism of G heterotrimer activation of Kir3 12

2.3.1 Evidence of the Gα-Kir3 contacts *in cellulo* and *in vitro* 12

2.3.2 The Gβγ-Kir3 interaction 14

2.4 Activation of Kir3 by PIP_2 and Na^+ in the cellular contexts 17

2.5 PIP_2 is the primary activating co-factor controlling the HBC gate of Kir3 18

2.6 Opening of the G-loop gate of Kir3 by canonical activators 21

2.6.1 The role of PIP_2 in the gating of the G-loop gate 21

2.6.2 The role of Gβγ and the reorganization of the Kir3.2 channel in response to activating R201A mutation 21

2.7 Evidence of gating mechanism at the selectivity filter of Kir3 22

2.8 Activation of Kir3 by alcohol 23

2.9 Influence of cholesterol on Kir3 24

2.9.1 Cholesterol and effects on members of the Kir channels family 24

2.9.2 Effect of cholesterol on Kir3 25

2.10 Rectification 26

2.11 Pharmacology 26

2.12 Pathology 27
3 Background to study area 27
4 Methodology 29
4.1 Homology modeling 29
4.2 Molecular dynamics simulations 30
4.2.1 What is Molecular dynamics simulation and why I used it? 30
4.2.2 Software used to generate and analyze the MD trajectories 31
4.2.3 Assembly of the simulation box: generic example 33
4.2.4 Precision on the nomenclature of the subunits of Kir3.2 homotetramer 35
4.2.5 Remark about the measurement of the opening of the pore of the Kir3.2 channel 35
4.3 Molecular biology 36
4.4 Electrophysiology 36
4.4.1 Handling of *Xenopus laevis* oocytes 36
4.4.2 Microinjection of *Xenopus laevis* oocytes 36
4.4.3 TEVC recording 37
5 In silico activation of Kir3.2: Results and discussion 39
5.1 Building the simulation box 39
5.1.1 Starting atomic coordinates for Kir3 39
5.1.2 Protonation state of titratable groups of Kir3.2 40
5.1.3 Modeling all atom PIP_2 42
5.1.4 Modeling alcohol ligands in putative binding pocket in Kir3.2 43
5.1.5 Solvation of the Kir3.2 model 44
5.2 Optimization of the simulation protocol 45
5.2.1 Simulation protocol retained for investigating the dynamical control of the Kir3.2 gates 47
5.3 MD Kir3.2 in presence of propanol and Na^+ 50
5.3.1 K^+ transport 50
5.3.2 Conformation of the K^+ permeation pathway 53
5.4 MD Kir3.2 in presence of PIP_2, propanol and Na^+ 79
5.4.1 K^+ transport in the selectivity filter 80
5.4.2 Conformational changes involving the HBC and G-loop gates 84
5.5 MD Kir3.2 in presence of PIP_2 interacting with two protein sites, propanol and Na^+ 92
5.5.1 Modeling of additional PIP_2 interacting with the slide helix of mmKir3.2 92
5.5.2 Conformational changes towards open pore and associated increased K^+ transport 95
5.6 MD Kir3.2 in presence of PIP_2 interacting with three protein sites, propanol and Na^+ 97
5.6.1 Modification of the simulation protocol: saturation of all PIP_2 interaction sites 97
5.6.2 Overview of the K^+ transport along the pore 98
5.6.3 Conformational changes which affected the gates of the mmKir3.2 101

5.7 MD Kir3.2 in absence of any specific ligands 106
5.7.1 Overview of K^+ transport along the pore 107
5.7.2 Conformational changes which affected the gates of mmKir3.2 109
5.8 MD Kir3.2 in presence of Gβγ dimers, PIP_2 and Na^+ 118
5.8.1 Conformational changes of the selectivity filter, the HBC and the G-loop gates, and associated K^+ transport 118
5.8.2 Novel interpretation of the R201A activating mutation 122
5.9 Conclusion and perspectives for application and future research 128
6 Design of light-gated Kir3 channels: Results and discussion 135
6.1 Selection of positions for cysteine mutagenesis 136
6.2 Functional tests of cysteine mutants 138
6.2.1 Cysteine mutations in wild-type Kir3.1 and Kir3.4 141
6.2.2 Cysteine mutations in homomeric Kir3.1(F137S) and Kir3.4(S143T) channels 142
6.3 Testing the PTL-induced light-sensitivity 144
6.4 Optimization of Kir3.4(E159C) 147
6.5 Conclusion and perspectives for application and future research 150
7 Bibliography 152
8 Annex 169
8.1 Figure legends 169
8.2 Simulation 0 172
8.3 Simulation I 175
8.4 Simulation II 187
8.5 Simulation III 199
8.6 Simulation IV 214
8.7 Simulation V 229
8.8 Simulation VI 238
8.9 Simulation VII 253
8.10 Simulation VIII 268
8.11 Simulation IX 277

List of Tables:

Table 1: Predicted pK_a shifts of titratable sidechain groups in the mmKir3.2 homotetramer from PDB:4KFM._____ 41
Table 2: Molecular constituents of the simulation boxes in each test condition when the number of PIP_2 was varied, and the simulation protocol of the applied constraints used to prevent ligands from diffusing away from protein._____ 48
Table 3: Normalized current changes induced by illumination with λ=380 nm and λ=500 nm of oocytes expressing various CYS mutant Kir3 channels labeled with the indicated PTLs._____ 145

List of Figures:

Figure 1: Available crystal structures of mouse Kir3.2 channel containing intact transmembrane and truncated cytoplasmic domains. 6

Figure 2: Interactions of PIP_2 4'- and 5'-phosphates with mouse Kir3.2 channel observed in the crystal structure PDB:4KFM. 42

Figure 3: The alcohol binding pocket in Kir2.1 and in Kir3.2 is located at the inter-subunit interface involving the N_{ter} and the βD-βE strands of one subunit and the βL-βM strands of the adjacent subunit. 44

Figure 4: Simulated binding of alcohol in the hydrophobic binding pocket of mouse Kir3.2. 49

Figure 5: The pre-open Kir3.2 closes to K^+ impermeable state in absence of PIP_2. 52

Figure 6: Closure of the selectivity filter of Kir3.2 in Simulation I. 54

Figure 7: Closed conformation of the transmembrane vestibule of Kir3.2 in absence of PIP_2. 55

Figure 8: Evolution of the curvature of selected secondary structures in mouse Kir3.2 during simulation in absence of PIP2. 59

Figure 9: Topology of subset of secondary structures in Kir3.2. 60

Figure 10: Conformational changes in the transmembrane helix bundle and in the pore helix in mouse Kir3.2. during simulated channel closure. 61

Figure 11: Rotamer states of the sidechain of residue E152 in mouse Kir3.2 observed by molecular dynamics simulation. 63

Figure 12: Timeseries of dihedral angles χ_1 and χ_2 of residue E152 of mouse Kir3.2 molecular dynamics simulation. 65

Figure 13: Atomic contacts monitored in the region of the selectivity filter of mouse Kir3.2 molecular dynamics simulation. 66

Figure 14: Diagrams of the instantaneous correlations between couples of interatomic distances collected in the region of the selectivity filter of mouse Kir3.2 during molecular dynamics simulation. 67

Figure 15: Profile of the pore lumen showing closure of mouse Kir3.2 in two molecular dynamic simulations. 71

Figure 16: Correlation of the conformation of the sidechain of I155, and the width of the central K^+-binding site in the selectivity filter of mouse Kir3.2 from molecular dynamics simulation. 73

Figure 17: Different conformation of the G-loop gate of moue Kir3.2 from molecular dynamics simulation in absence of PIP_2. 77

Figure 18: Conformation of the G-loop gate of mouse Kir3.2 during the coordination of a single K^+ observed when the HBC gate of the channel is closed during molecular dynamics simulation in absence of PIP_2. 78

Figure 19: The pre-open mouse Kir3.2 in presence of PIP_2 modeled into the crystallographic binding sites (equivalent to PDB:4KFM), adopted alternative conformations of the TM vestibule during molecular dynamics simulation of two atomic-replica systems. 81

Figure 20: Displacement of superimposed β-sheets upon opening of the G-loop gate and the hydrophobic network connecting the $G_{\beta\gamma}$ binding site with the cytosolic gate represented in one subunit of mouse Kir3.2 during molecular dynamics simulation. 87

Figure 21: Displacement of superimposed β-sheets upon opening of the G-loop gate and the hydrogen-bonding network connecting the $G_{\beta\gamma}$ binding site with the cytosolic gate represented in one subunit of mouse Kir3.2 during molecular dynamics simulation. 89

Figure 22: Core of a hydrophobic network inside the cytoplasmic domain controlling the G-loop gate of mouse Kir3.2; from two molecular dynamics simulations of systems evolved to closed and open G-loop gate states. 91

Figure 23 : Electrostatic contribution of mouse Kir3.2 to an all-atom simulation box and location of a putative secondary PIP_2 interaction site on the channel. 93

Figure 24: The pre-open Kir3.2 in presence of PIP_2 modeled into the crystallographic binding site and along the slide helix, adopted similar con-formations of the TM vestibule during molecular dynamics simulation of two atomic-replica systems. 96

Figure 25: The pre-open Kir3.2 in presence of PIP_2 modeled into the crystallographic binding site, near the N_{ter} and along the slide helix, adopted similar conformations of the TM vestibule during molecular dynamic simulation of two atomic-replica systems. 99

Figure 26: Pocket between adjacent βH-βI loops of mouse Kir3.2 with high K^+ affinity observed during molecular dynamics simulation. 100

Figure 27: The blotting of the slide helix to the inner membrane layer allows the opening of the βH-Iβ loop in the same subunit mouse Kir3.2 during molecular dynamics simulation. 101

Figure 28: Change of the predominant atom types lining the lumen of the G-loop gate in Kir channels as the gate adopts more extended conformations during molecular dynamics simulation and from observation of crystallographic models. 103

Figure 29: Modular organization of the inter-subunit interface in the βD-βE/βL-βM loops cleft-region of activated mouse Kir3.2 during molecular dynamics simulation. 105

Figure 30: When molecular dynamics were simulated of the pre-open mouse Kir3.2 in absence of any ligands, the channel evolved rapidly into a closed state. 107

Figure 31: Water and K^+ distribution along the pore observed during molecular dynamics simulation of mouse Kir3.2 in absence of specific ligands. 108

Figure 32: Subset of differing contacts in the βD-βE/βL-βM cleft-region of mouse Kir3.2, from molecular dynamic simulation of systems with varied ligand compositions. 111

Figure 33: Molecular dynamics simulations of mouse Kir3.2 in presence of a variable number of ligands, suggest the existence of two allosteric pathways controlling the G-loop gate from within the βD-βE/βL-βM cleft region. 114

Figure 34: Timeseries of inter-atomic distances from a molecular dynamics simulation of mouse Kir3.2 in absence of any ligands. 117

Figure 35: The HBC and the G-loop gates of the pre-open mouse Kir3.2 stabilized by Gβγ, PIP_2 and Na^+, opened during molecular dynamic simulation. 119

Figure 36: Alternative conformations of the distal N_{ter} of mouse Kir3.2 correlate with bending of the apex of the βH-βI loop in the same channel subunits; results from unrestrained molecular dynamics simulation of the mouse Kir3.2 channel interacting with Gβγ dimers, Na^+ and PIP_2 molecules. 121

Figure 37: Subsets from difference and composite electronic-density maps of PDB:3SYQ (Whorton and MacKinnon, Cell, 2011) showing electron densities not accounted for in the final model near K64. 124

Figure 38: Putative mechanism of activation of the HBC and the G-loop gates of mouse Kir3.2, derived from results of molecular dynamic simulations, crystallographic models and whole cell recordings. 126

Figure 39: Histograms and the associated free energy profiles of the minimal radii of the HBC and the G-loop gates, obtained by MD simulation of mmKir3.2. 133

Figure 40: Photoisomerizable tethered ligands (PTLs) used in the project. 135

Figure 41: Model of Kir3.2 serving as reference to choose position for engineered cysteine mutations in Kir3.1. 137

Figure 42: Most Kir3 cysteine mutants were expressed and functional. 139

Figure 43: Functional testing in Xenopus oocytes of heterotetrameric Kir3.1/Kir3.4 channels with cysteine mutations in one subunit. 140

Figure 44: Functional testing in Xenopus oocytes of cysteine mutants implemented in the turret region of the Kir3.1 subunit in the heterotetrameric Kir3.1/Kir3.4 channel. 142

Figure 45: Functional tests in Xenopus oocytes of Kir3.1S and Kir3.4T with mutations to cysteine mutants in the TM helix bundle. 143

Figure 46: The extracellular entrance of the selectivity filter of Kir3 is “guarded” by bulky sidechains. 148

Figure 47: The mutant Kir3.4T(F154G, E159C) labeled with MAQ displays a solid block by 500-nm light, which is relieved by 380-nm light. 149

1 ION CHANNELS AND KIR GENERAL

1.1 THE CELL, THE CELL'S MEMBRANE, ION CHANNELS AND THE MEMBRANE POTENTIAL

This doctoral thesis is focused on a particular family of proteins expressed as tetrameric assemblies which function as selective potassium ion channels – the potassium inward rectifier member 3 (Kir3), a subclass in the family of potassium inward rectifier (Kir) proteins. The projects presented in the manuscript aimed to describe and manipulate the biophysical properties of the Kir3 ion channels.

In the context of living organisms, ion channels are macromolecular entities which cross a biological membrane with at least two transmembrane segments and potentially by formation of multimeric assemblies. These proteins delimit water-filled transmembrane pores which are selective for specific ionic species and have specific gating properties. The transmembrane segments of eukaryotic ion channels are predominantly α-helices. They possess a "Selectivity filter" which designates the tertiary or quaternary structural elements conferring the ability to discriminate the permeant ion species between all monoatomic ions in solution in the cytosol or the extracellular medium. The structural elements which impede the passive transmembrane transport of permeant ions are called the "gates" of the channel. The phenomenon of closure of channel gates is called "gating". It is mainly operated through conformational changes leading to the split of the water column along the ion permeation pathway. The ion channels are classified by their ion selectivity and mode of activation – two characteristics which distinguish the ion channels from the porin proteins which also allow water and ions to cross the biological membranes by passive diffusion. However, generally, porins are not selective, are constitutively open and allow large molecules to cross. From a structural point of view channels sharing the same activation mechanisms often have similar domains. For instance, the voltage-gated channels have similar voltage-sensing domains. A major difference in the structural organization of these channels is that the Ca^{2+} and Na^{+} voltage-gated channels are single proteins, while the K^{+} channels are tetramers. However, they all have the same number of trans-membrane helices which place the selectivity filter assembled by four pore loops at similar near-extracellular locations. Furthermore, channels with different activation modes but which are specific for the same ionic species also share common structural elements. For instance, the selectivity filter and the water-filled transmembrane domain are homologous in all potassium cannels.

All living cells need to exchange nutrients, molecular waste and electrolytes with their environment. In addition to being expressed at the plasma membrane, ion channels are also found in the membrane of organelles. The ions transported by channels are charge carriers and serve to modulate membrane potential. Some ions like Ca^{2+}, Mg^{2+}, Na^{+}, are also used as intracellular messengers, being ligands or co-factors for various physiological processes. Na^{+}, K^{+} and Cl^{-} have the highest concentrations of all monoatomic ionic species. In physiological conditions, there are strong concentration gradients of these three ionic species across phospholipidic bilayers. Maintenance of these gradients is essential for life and requires large cellular energy expenditures. The combination of gradients of some ions and selective membrane permeability for these ions, a transmembrane potential V_m is created.

A mathematical expression of the membrane potential is provided by the Goldman-Hodgkin-Katz voltage equation. This equation, which takes into account the permeability of the membrane for each ion species and their concentrations on both sides of the membrane, yields the equilibrium electrical potential expected across the membrane. Thus, the value of the transmembrane potential depends on the distribution and permeability of the major ionic species. Because the distribution is maintained relatively constant by the cell using active transporters such as the Na/K ATPase, changes of V_m are triggered by changes in permeability of the membrane for each one of the main ionic species, i.e., changes in gating of the ion channels present in the membrane.

Excitable cells, such as neurons and muscle cells, use a stereotyped voltage pattern, the action potential, as a signal to transmit information fast and reliably along the cell and from cell to cell. The action potential results from the successive opening of voltage-gated Na^+ or Ca^{2+} channels (depolarization phase) and voltage-gated K^+ channels (repolarization phase). Kir channels are not voltage-gated and serve to regulate the triggering of action potentials, and to some extent their shape. In the early stages of the depolarization due to cation influx into the cell, outward flow of K^+ through Kir channels can increase the voltage threshold for activation of the Na^+-voltage gated channels. Once Na^+ channels open, their conductance dominates the setting of V_m. Later on, during the repolarization phase, once the V_m returns to negative values, the Kir channels participate in the repolarization of the membrane and the clamping of V_m to the reversal potential for K^+.

Structurally, all potassium channels share a commonly folded transmembrane-pore domain. The selectivity filter has astonishing conservation of the primary sequence across the entire superfamily – a fact which helped for the genome-wide identification of sequences encoding proteins implicated in K^+ selective transport.

Kir channels are studied by various experimental and theoretical means, but, as with all ion channels, the dominant technique employed to decipher the properties of Kir is the electrophysiological recording of the currents mediated by K^+ ions. The name "inward rectifier" refers to the observations that Kir channels conduct significantly more inward current than outward current. The underlying mechanism is that Kir channel are blocked by intracellular factors (Mg^{2+}, polyamines) which are pushed into the Kir pore and block it when $V_m > E_K$. From an evolutionary perspective, the inward K^+ conductance of Kir could have been developed to favor K^+ uptake, a role played in the kidney by Kir1.1 which is the first identified member of the Kir family (see section 1.2.1). The Kir channels are interesting and important because of their crucial physiological role, as well as their implication in numerous pathological processes, a fact that justifies the interest of the research community for these complex biological machines.

1.2 Physiological role of Kir family members

This section is largely based on the extensive reviews by Wei and colleagues (Wei 2005) and by Hibino and colleagues (Hibino et al. 2010). The phylogenic three of the Kir family has two central branches. The smallest branch traces the early divergence of Kir1 and the group containing Kir7 and Kir4. The larger branch of the thee is subdivided in two groups, a group including Kir5 and Kir2 members and a group including Kir3 and Kir6 members. Kir channels mediate hyperpolarizing potassium currents at membrane potentials close to E_K. At potentials more positive than E_K, currents supported by Kir channels have the particularity to be silenced by a rectification phenomenon which relies on intracellular factors such as Mg^{2+} and polyamines binding inside the Kir pore. The rectification phenomenon makes it difficult to study Kir channels in conditions where potassium currents are outward. Thus, most often, Kir channels are functionally characterized using data describing the inward flux of K^+ recorded in cells natively expressing Kir channels, either in native cell types or in heterologous expressing systems. Recordings of outward flux using experimental setups where the rectification factors are missing/removed are also possible, such as the reconstitution of purified Kir channels in artificial lipidic bilayers.

The first inward rectifiers to be cloned were Kir1.1 and Kir2.1. The family of K^+ Inward Rectifier (Kir) in mammalians regroups seven members named from Kir1 to Kir7. Few blockers are known to directly affect the Kir family. These channels are blocked by Ba^{2+} and Cs^+. Kir2 and Kir6 channels are weakly blocked by tetraethylammonium (TEA) and 4-aminopyridine (4-AP), whereas tertiapin Q is a Kir3 and Kir1.1 specific blocker.

1.2.1 Kir1

This sub-family has a single member, Kir1.1, with six identified splice variants (Kir1.1a-f) which can form homo- and heteromeric assemblies as a means to vary the conductive properties of the

channels. Kir1 channels are found in the kidney where Kir1.1a and Kir1.1c excretes K^+ in the distal renal tubules, while Kir1.1b in the thick ascending limb of loop of Henle is involved in K^+ recycling. These channels are constitutively active under normal physiological condition, while they remain sensitive to intracellular acidosis which causes their closure.

1.2.2 Kir2

The subfamily consists of four members Kir2.1-4. Kir2.1 plays a role in the excitability of brain and hearth tissues, skeletal muscles and macrophage cells. Kir2.1 forms heteromeric channels with Kir2.2, Kir2.4 and Kir4.1 subunit. Kir2.1 channels are constitutively active in resting physiological conditions when they are activated by interactions with PIP_2 and phosphorylation by protein kinase A (PKA), and Kir2.1 channels are primarily gated by the intracellular polyamine charge upon depolarization of the cell, but also by their activity is decreased by phosphorylation by tyrosine kinase or indirectly decreased by inhibition of the PKA. The Kir2.2 subunits can heteromerize with Kir2.1 and Kir2.3 counterparts, the tissue distribution follows that of Kir2.1 and Kir2.3. Kir2.3 channels are activated by intracellular and extracellular alkalization and requires simultaneous PIP_2 interactions – the acidification of the environment caused the channels to gate. The activation of Kir2.4 is also mediated by alkalization of the medium while intracellular Na^+ and acidification of the medium inhibits the channels.

Kir2 channels are called classical Kir channels, because they are constitutively active in the resting cell and they exhibit very strong rectification. The current through these channels is called I_{K1} in the heart Purkinje fibers, ventricular and atrial tissues, and is associated with channels composed of subunits Kir2.1, Kir2.2 and Kir2.3 (Hibino et al. 2010). Although the exact composition of heart channels is not completely understood, it is likely that the major part of I_{K1} is carried by the Kir2.1/Kir2.2 heterotetramers and that all Kir2 channels *in vivo* contain the Kir2.1 as a mandatory element. I_{K1} is a background K^+ current. Like all Kir currents, at potentials more negative than E_K, it is inward and linearly related to voltage. At potentials more positive than E_K, it is outward and decreases with voltage when the cell gets more depolarized. Kir2 channels are constitutively active in the resting cell. During the action potential of ventricular myocytes, I_{K1} is blocked by the rectification phenomenon during the depolarization phase (phase 0 and phase 1). It then starts to develop again during the plateau phase (phase 2) and it dominates the cell conductance, shaping most strongly the phase of repolarization (phase) 3 and the resting state (phase 4). Pharmacological compounds blocking the cardiac Kir2 are chloroquine and quinidine.

1.2.3 Kir3

The subfamily consists of four members Kir3.1-4. These channels are activated by PIP_2, Na^+ (except Kir3.1 subunits) and G protein βγ subunits. The inhibition of the Kir3 channels involve indirect depletion of the Gβγ subunits by Gα and the phosphorylation by protein kinase C. The voltage dependent bock by intracellular polyamines is also a major factor for decrease of the Kir3 conductance. Kir3.1 does not function as homomer but it partners with the other three sub-family members in tissue specific manner. The Kir3.1 subunit is found in brain and heart tissues. Four splice variants with tissue specific distributions are reported for the Kir3.2 proteins. Kir3.2a forms functional homotetramers in the brain, Kir3.2b is found ubiquitously in a variety of tissues. Kir3.2c forms heterotetramers with Kir3.1 in the brain. Homotetrameric Kir3.2d is involved in gametogenesis in testis. Kir3.2 can also heteromerizes with Kir3.3 and Kir3.4. Kir3.3 is often found to follow the distribution of Kir3.1 and Kir3.2, and Kir3.4 is primarily expressed in the heart. More detailed information about the Kir3 sub-family is provided in chapter 2.

1.2.4 Kir4

This subfamily is composed of two members Kir4.1 and Kir4.2. Historically, these members were part of the Kir1 sub-family, respectively members Kir1.2 and Kir1.3 but their nomenclature was adjusted to follow the molecular phylogeny. These channels are constitutively open and are stimulated by addition of intracellular ATP, probably acting to increase the pool of PIP_2 in the inner leaflet of the

membrane. The regulation of Kir4 channels is voltage-dependent and is made effective by rectification co-factors, i.e., intracellular Mg^{2+} and polyamines. Kir4.1 heterotetramerizes with Kir4.2, Kir5.1 and Kir2.1. It is expressed in glial cells surrounding synapses and blood vessels in the brain, retina, ear and kidney. The Kir4.2 channels are sensitive to intracellular acidification. Two splice variants are identified as expressed in kidney, pancreas, liver, lung and testis.

1.2.5 Kir5

A single member constitutes this sub-family. Kir5.1 is only found in heteromeric channels with Kir4.1 or Kir4.2. Kir5.1-containing channels are pH-sensitive and are inhibited by intracellular acidification and phosphorylation by PKA. These channels are expressed in convoluted tubule cells in kidney, pancreatic acinar and ductal cells, thyroid gland, retina, year, spleen, adrenal glands, liver, testis, various regions in the brain.

1.2.6 Kir6

The two members of this family are Kir6.1 and Kir6.2. The functional Kir6 channels are obligatory octameric assemblies of four Kir6 and four sulfonylurea receptor (SUR) subunits, a complex called the ATP-sensitive K^+ channel (K_{ATP}). The activity of the K_{ATP} channel is controlled by the Kir6 and the SUR constituents independently. The Kir6 pore is inhibited by intracellular ATP, while the SUR subunits bind ADP causing Kir6 activation through an allosteric mechanism. In vascular smooth muscle, Kir6.1 subunits are associated with SUR2B and are involved in the regulation of the vascular tone. In native tissues the Kir6.2 subunits are found to interact with all SUR members (SUR1, SUR2A-B). These channels are expressed in pancreatic β-cells, heart, skeletal muscle and brain.

1.2.7 Kir7

Kir7.1 is the sole member of this sub-family. It has been known as Kir1.4 but, recently, like the Kir4 members, it was removed from the Kir1 sub-family and reassigned to a new Kir7 sub-family. These channels are activated at hyperpolarizing conditions (V_m < -130 mV). They are expressed in Purkinje cells in the cerebellum, pyramidal cells in the hippocampus, choroid plexus, retinal pigment epithelium, small intestine, stomach, prostate, lung and testis.

1.3 STRUCTURAL OVERVIEW OF KIR CHANNELS

The transmembrane pore assembled by proteins of the Kir family is constituted by four Kir subunits. This tetrameric pore domain can involve either subunits of the same sub-type, i.e., a homotetramer, or subunits of different sub-types, i.e., a heterotetramer. As described in the previous subsection some Kir channels like the Kir6 channels, required other proteins as mandatory structural partners. In the case of the Kir3 channels, the formation of a permeant complexes with G-heterotrimeric proteins have been proposed (see section 2). The overall secondary, tertiary and quaternary folds of just the transmembrane pore-domain of Kir channels are conserved, with only slight variations of the polypeptide length in the highly flexible N-terminal polypeptide sequence (N_{ter}), C-terminal polypeptide sequence (C_{ter}) and in the small extracellular domains – called the turret which forms a small extracellular vestibule. The N_{ter} and the C_{ter} of the Kir subunits are intracellular. The peptide sequence of the N_{ter} domain is approximately 90 amino acids long. The available experimental structural models have shown that it is overlaid on the C_{ter} domain which contains about 200 amino acids. The cytosolic N_{ter} and the C_{ter} contribute the cytoplasmic channel domain (CTCD). In many studies the CTCD of the Kir channels has been successfully expressed from a concatemer cDNA and, as the subsequent X-ray crystallography experiments have shown, the isolated CTCD on its own can be refolded to resemble the conformations in the full-length channels. Such constructs are often investigated by nuclear magnetic resonance (NMR) spectroscopy because the size of the CTCD matches the technical limits of this method and the NMR spectroscopy allows to decipher various dynamical/interaction properties of the domain. The remaining part of the channel constitutes the transmembrane domain (TMD). Kir TMD has eight transmembrane α-helices (two per subunit) which delimit a water-filled transmembrane vestibule (TMV). The α-helices of the TMV are arranged in a

clockwise twisted bundle, with two layers. The four TM1 are positioned as the outer helices predominantly contacting the membrane, and the four TM2 are positioned as the inner helices predominantly contacting the water filled TMV. When viewed along the plane of the membrane, the TM bundle resembles a 'funnel' with its narrow end pointed towards the cytosol. The polypeptide linking each TM1-TM2 of a Kir subunit historically has been called the "pore-loop". Since the first 3D structures of K^+ channels (Doyle et al. 1998), it is clear that the pore-loop is constituted by the turret-loop which exits from the plane of the membrane and reenters inside the TMV helix bundle with the formation of a four-turn α-helix called the pore-helix. The pore-helix is oriented 45° to the normal of the membrane and reaches nearly half the depth of the TMV. The quartet of pore-helices of the channel accomplishes the segregation of water inside the TMV. The selectivity filter of the Kir channels is stabilized along the principal axe of symmetry by the pore-helices and the a β-beta strand connecting the pore-loop to the TM2. The pore-helices, the selectivity filter and the terminal β-strand of the pore-loop constitute a massive (water-free) protein plug on top of the TM helix bundle. The structure of the TMD of the Kir channels is common to all TMDs of channels of the VIC family, while the structural properties of the Kir CTCD are unique to this family. Both the TMD and the CTCD host functional elements called 'gates' which are the effectors of the arrest of the K^+ transport through the Kir pore – the selectivity filter has also been proposed to possess gating properties.

More details on the structure and the dynamics of the TMD and the CTCD can be found in the section dedicated for the state-of-the-art knowledge on the Kir3 channels and the chapters 5 and 6 where I expose and discuss the results of the projects.

1.3.1 Selectivity filter

The specificity of K^+ transport through the pore is mediated by a quaternary structure called the Selectivity Filter (SF). The particular polypeptide motif T-X-G-Y(F)-G of the selectivity filter is a common signature in all potassium channels (Heginbotham et al. 1994). Historically, the identification of this motive allowed the sorting of Kir channel genes and their subsequent cloning from the newly available genomes (Glaaser and Slesinger 2015). The second particularity of the amino acid arrangement in the SF is that the process of ion selection occurs directly at the level of the backbone carbonyls of each amino acid involved in the assembly (Doyle et al. 1998). In fact, the carbonyls of each of the four subunits are turned towards each other along the potassium permeation pathway, providing a narrow and oxygen lined passage at each level of the filter (Figure 1C) (Whorton and MacKinnon 2013). The crystal structures show five potassium binding sites named S0 to S4 starting at the extracellular entrance of the pore. As reviewed elsewhere, molecular simulations showed that the selectivity filter at room temperature would experience angstrom-scale fluctuations and still remain selective for K^+ over Na^+, thus identifying dynamic and electrostatic factors as responsible for predominant K^+ occupation of the SF over other cations (Roux 2005).

Recently it has been admitted that the selectivity filter also possesses gating properties. It was demonstrated that the conformation of the SF in the KcsA channel is governed by interactions with the transmembrane helices (Heer et al. 2017; Xu, Bhate, and McDermott 2017) and the water from the extracellular bulk interacting with the protein (Raghuraman et al. 2014). The dynamics of these interactions cause the filter to oscillate between conformations of larger (activated state) and reduced opening of the permeation pathway (closed and inactivated states) (Xu, Bhate, and McDermott 2017; Tilegenova, Cortes, and Cuello 2017; Mitchell and Leibler 2018). Beyond the purely geometrical dynamics, the changes in the conformations of the filter also leads to modulations of the binding affinity towards the permeating K^+ ions, thus employing the energetics of the interactions of K^+ and the carbonyl oxygens for additional factor for the gating properties of the filter (Heer et al. 2017; Medovoy, Perozo, and Roux 2016).

1.3.2 Transmembrane domain

Another common feature within the potassium channels superfamily is the transmembrane domain (TMD) which delimits a water filled inner vestibule. The transmembrane (TM) vestibule has a variable

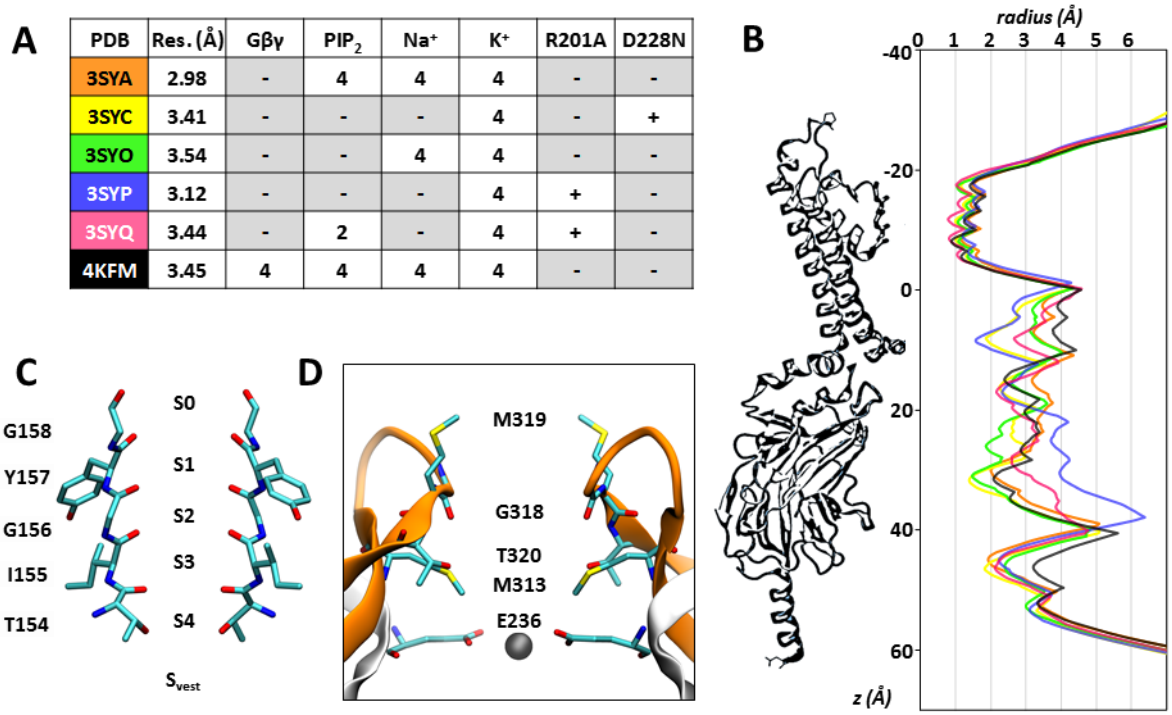

Figure 1: Available crystal structures of mouse Kir3.2 channel containing intact transmembrane and truncated cytoplasmic domains. (A) List of co-crystalized ligands and engineered functional mutations (see text for literature references). (B) Pore profile of the K+ permeation pathway of all atom models (hydrogen included) based on the crystal structures in panel A. Individual profiles are colored according to the color-code in the first column of panel A; all profiles are aligned at the selectivity filter. On the left is represented water-mark of part of the pore from PDB:4KFM. (C) Topology of the K+ binding sites in the selectivity filter of mmKir3.2 from PDB:4KFM. (D) Residues of the G-loop gate lining the K+ permeation pathway and the residue E236 coordinating one K+ crystalized in the PDB:4KFM. The representations in panel C and D use only two subunits from PDB:4KFM

volume which depends on the extent of the opening of the hydrophobic gate of the vestibule, called the helix bundle crossing (HBC) (Doyle et al. 1998; Shrivastava and Bahar 2006). Several hydrophobic residues in the inner helix (TM2) face the water inside the TM vestibule (TMV). In the Kir family, the HBC gating function is attributed to a conserved phenylalanine near the carboxyl-terminus of TM2 and to a I/V residue in Kir3 located in the helix turn prior to the conserved phenylalanine (T. Jin et al. 2002; Haider et al. 2007). The mechanism of hydrophobic gating allows the water column along the pore to be dynamically discontinued, it consists of a dewetting phenomenon which propagates over a longer distance compared to the simple van der Waals constriction of the vestibule. It depends on a combination of parameters such as: the polarity of the involved protein sidechains, the change in diameter of the opening, and the electric potential between both sides of the constriction (Aryal, Sansom, and Tucker 2015).

1.3.3 Cytoplasmic domain

The large cytoplasmic channel domain (CTCD) of Kir channels is unique structural feature among the potassium channels super-family and accounts for about 2/3 of the polypeptide sequence. CTCD is constituted by the N-terminal polypeptide sequence (N_{ter}) prior to the first transmembrane helix (TM1) and the C-terminal polypeptide sequence (C_{ter}) emerging after the second transmembrane helix (TM2). The CTCD of Kir channels harbors the sites where most of the regulation of the channels is possible, it includes phosphorylation sites, pH sensing domains, ligand and protein binding sites (Hibino et al. 2010). The cytoplasmic gate of the Kir channel is called the G-loop gate, it is constituted by four loops named G loops and provided by each one of the subunits in the tetramer. This gate is located just below the plane of the inner membrane leaflet and upon closure isolates the inner vestibule from the cytosol. Our models showed that, if both the HBC and the G-loop gate are simultaneously closed a small water filled volume remains in between, thus upon closure the G-loop gate does not extend the dewetting of the vestibule produced by the closure of the HBC gate.

The cytoplasmic channel domain (CTCD) of Kir channels hosts most of the regulatory sites of these channels. Hence, it accounts for most of the differences between each member inside of the Kir family. This domain represents half of the mass of the pore of Kir channel. Most of the Kir family members are constitutively open and are sensitive to pH variations (Kir1, Kir2, Kir4, Kir5, Kir7). Auxiliary pH sensitivity has been recently identified in Kir3. The Kir3 and Kir6 channels depends on other subunit types for their physiological function, and these regulations are also mediated by interactions with the CTCD. Interestingly, on a multisequence alignment, the sites specific for each Kir channel modulation appears as degenerated sequence signals in the same columns of the alignment. The CTCD also contains sites for interaction with the rectification co-factor, the polyamines. These sites are conserved in sequence and structure, whereas variations of the involved amino acids can be traced back to the intrinsic potency of rectification of the different Kir channels (Pegan et al. 2005; Janice L Robertson, Palmer, and Roux 2008; J. L. Robertson, Palmer, and Roux 2012).

1.4 MOTIVATION AND SCIENTIFIC OBJECTIVES

1.4.1 What is the niche in the scientific field for these doctoral thesis projects?

The research field dealing Kir channels is very active in adequation with the major physiological importance of this class of K^+ transporters. It is generally admitted that the description of molecular function and the underlying mechanisms are easily transposable among members of the Kir family. This is particularly true in the case of the highly-conserved primary PIP_2 binding site which all Kir proteins contain at the C-terminus of the second transmembrane helix (TM2), and also in the case of the almost identical sequence of the selectivity filter. However, the obvious conservation of major structural and functional characteristics among the super-family members is not suited to explain the detailed sequence-function differences observed between members of the same sub-family. For instance, the Kir3.1 channel is the only Kir member which contains a phenylalanine (F137) at a position where all other members possess a serine residue. The simple consideration of the presence of F137 in Kir3.1 is not sufficient to explain the fact that homotetramers of this protein are not electrically active and that the exchange of F137 for a serine converts the non-conductive homotetramers of Kir3.1 to conductive ones (Chan et al. 1996; Vivaudou et al. 1997).

While functional studies are ordinarily employed to investigate the properties at the phenotypical level, they are not very suited to provide detailed knowledge about phenomena occurring on the sub-macromolecular level where complex-allosteric relations govern the dynamics of the molecular function of the proteins. For the study of potassium channels, it is common practice to identify residues important for channel function with screening-like strategies, often employing site directed mutagenesis and functional characterization by electrophysiological recordings as a means to provide rapid identification of important actors. However, the subsequent characterization of the molecular role of these newly discovered actors requires them to be studied by more advanced biochemical/biophysical spectroscopic techniques. Among these, several technologies can currently access the molecular dynamics at an atomic resolution. To name several of such techniques: X-ray free electron laser (XFEL) crystallography, Nuclear Magnetic Resonance (NMR) spectroscopy, Infrared (IR) spectroscopy, Raman spectroscopy and Electron paramagnetic resonance (EPR) spectroscopy. However, the most classical molecular structure investigating technique, X-ray crystallography, lacks the ability to access the transition dynamics of the studied system, mostly providing a single image of preliminary prepared samples representative of limit conformations of the protein. The greater drawback of all these techniques is that they require to manipulate and to image purified proteins, furthermore, some of the techniques are limited on the size of the studied macromolecules.

This very brief overview of the applications and limits of the existing advanced biophysical methodologies is sufficient to explain why we did not intend to use any of them to study Kir3 channels. While the Kir3 channel on its own is a large macromolecule, its complex with the G-protein

activators make the size of the system even more difficult to be manipulated and studied with the above-mentioned techniques. Moreover, the overall 3D structure of the Kir3/G-protein complex was resolved recently and is less of an interesting matter for further research. However, with the advance of the current theoretical and computational abilities, the simulation of the molecular dynamics of macromolecular systems is a very relevant alternative to the practically complex experiments.

The simulation of molecular dynamics has been used for a very long time in the research field of Kir channels and Kir3 in particular. Nevertheless, previous studies were limited by the availability of relevant starting structures, for instance, the non-existent experimental models of an open state of Kir2 required such a conformation to be modeled by homology from the conformation of activated mutant channels (J. Li et al. 2015a). Another consequent issue with the simulation of the dynamics of the macromolecules is that the simulated timescales are very short compared to the native dynamics of the proteins in general. Thus, in such a study, the computational-experimenter will often have the tendency to speed-up the events by applying unphysiological conditions to the system, i.e. high temperature or external forces, thus risking driving the system away from its native behavior. In the end, the setting of molecular dynamics simulation assays requires a big deal of experimental knowledge about the system of interest – a requirement which closes a full loop between the theoretical and experimental research techniques.

At the time when we began working on this project, little was known about the detailed molecular dynamics of the Kir3 family, the majority of the information was provided by studies conducted with other members of the potassium channels superfamily or with mutant or chimeric Kir3 proteins. Thus, it was important to take advantage of the recent theoretical development and the availability of experimental models of the complete wild-type Kir3/G-protein complex in order to investigate the molecular dynamics of the activation and inactivation of Kir3 channels. Our strategy was to produce a consequent amount of data representative of the molecular function of Kir3 channels and to describe the molecular function of the channel as profoundly as we could on the basis of these results, while aiming at to remain in adequation with already published experimental data preferably describing wild-type Kir3 systems. The allosteric interplay between parts of Kir3 channels ought to be first reproduced by simulation of molecular dynamics of wild-type Kir3 members, where the expected result was to obtain measures of microscopic events which could be linked to quantities provided by macroscopic experimentations such as the functional characterization of the channels by electrophysiological recordings. Initially, we focused our efforts on the production and analyses of data with the wild-type Kir3.2 in order to establish theoretical protocols producing relevant results which would be applied as a baseline for further investigation of other Kir3 channels. More about our scientific objectives is said in the next section.

1.4.2 Scientific objectives

The main objective of this doctoral thesis is to acquire additional fundamental knowledge about the molecular function of various wild-type, mutant and engineered Kir3 channels. Thus, our first goal is to provide the community with a set of trajectories demonstrating the molecular dynamics of wild-type Kir3 channel(s) which should contain the information about the molecular function of Kir3 channels on an atomic scale. Nevertheless, the production of the intended trajectories is not straight forward and despite the availability of the necessary computational tools, it requires the development and the optimization of a computational protocol which would allow to observe the channel in different conformations representative of stages of its physiological function. Primarily, we have to restrain our operations to simulations of the wild-type Kir3.2 channel for which high-quality experimental structural models are available. We intend to study models of the wild-type Kir3.2 until having enough confidence that the computational protocol is capable of reproducing the channel function when starting the simulation from experimentally determined conformations. Fortunately, the reference experimental data to which our simulations will be compared already exists. Validation of this part of the project will serve as a baseline for simulations of Kir3 constructs for which no experimental structural models are available and which require to be modeled by

homology prior to molecular dynamics simulation. In particular, we would like to investigate the molecular role of specific mutations which modify the phenotype of Kir3 channels, namely, the activating-mutation F137S in homotetrameric Kir3.1 channels and its positional equivalent S143T in Kir3.4 homotetramers. However, we decided to postpone the simulation of models of the modified channels until we successfully establish the baseline simulations methodology.

We believe that analysis of the trajectories describing wild-type channels would allow for better understanding and interpretation of the vast amount of published functional data experimentally measured by macroscopic scale experiments. Furthermore, if our strategy is fruitful, and indeed produces a molecular movie of Kir3 function, there is a likelihood of additional positive outcomes such as predicting novel properties and molecular actors engaged in the operation of Kir3 channels.

In parallel to the theoretical project, I performed experimentation to the design light-sensitive Kir3 channels. It implied the experimental application of well-established protocols for molecular biology and electrophysiology to study light-sensitive phenotypes of Kir3 channels labeled with a photoswitchable tethered ligands (PTLs). Since the labeling of the channels with the tether ligands requires the presence of reduced cysteine residues, we performed limited cysteine-scanning of the Kir3 proteins to identify suitable positions which enable reversible modification of phenotype of the PTL-labeled Kir3 channel(s) upon light illumination triggering the isomerization of the tether.

This development has fundamental and applied research relevance. First, it could reveal the functional importance of individual residues and parts of the channels. Second, such an opto-pharmacological/genetic tool has potential applications in synthetic biology and in *in-vitro*, *in-vivo* experiments where the light-sensitive Kir3 could be used as a "light-sensitive diode" controlling the potassium permeability of a lipid membrane. The most obvious application of these engineered Kir3 channels would be as tools to study the physiological role of native Kir3 channels. The light-sensitive Kir3 channels could be expressed in native tissues, in parallel to endogenous wild-type Kir3 channels. It would then be possible to selectively modulate specific channels with light and observe the physiological consequences.

The following chapter (2) of the manuscript presents an extended overview of the current understanding of the function of Kir3 channels. In chapter 3, I describe the current projects with respect to the state-of-the-art. The next chapter (4) describes the tools and techniques used. The following two chapters (5 and 6) describe the results of the two projects conducted during my thesis. Since the workflow of these projects was not linear and not completely predictable, in chapters 5 and 6 I adopted a 'Results and Discussion' format of reporting to better transmit the logical continuity of the various choices made to meet the goals of the projects. The last sub-section of both chapters 5 and 6 is a synthetic overview of the work and includes perspectives to pursue the projects and to exploit the already obtained results. The last chapter (7) of the manuscript lists the bibliographic references cited in the text. Finally, a series of annex sections containing figures describing part of the analysis of the raw data of the project Kir3 MD are attached to the manuscript. These annexes are organized as separate sections individually related to each one of the simulated systems presented in chapter 5. The annex sections have common nomenclature which is presented at the beginning of the Annexes chapter.

2 KIR3: LITERATURE REVIEW

2.1 OVERVIEW OF THE KIR3 SUB-FAMILY MEMBERS

Four genes coding Kir3 proteins are present in mammals, namely, for the sub-family members Kir3.1-4, the respective gene codes are KCNJ3, KCNJ6, KCNJ9, KCNJ5. Historically, the most frequently use aliases of the Kir3.1-4 proteins were the GIRK1-4 (standing for: G protein-coupled inwardly-rectifying potassium channel), but other name can also be encountered throughout the literature:

KGA for Kir3.1; BIR1, KATP-2, KCNJ7, KPLBS, for Kir3.2; CIR, KATP1, LQT3 for Kir3.4. In humans, different isoforms of the subunits are identified only for Kir3.1: isoforms 1-4. The Kir3 members have tissue specific expression patterns, thus (levels ≥1 RPKM) (Fagerberg et al. 2014): Kir3.1 is found in adrenal, brain, colon, duodenum, heart, kidney, liver, prostate, small intestine; Kir3.2 is found in the brain; Kir3.3 is found in the brain; Kir3.4 is found in adrenal, brain, gall bladder, heart, kidney, lung, lymph node, pancreas, placenta, spleen, stomach, urinary bladder. Kir3 family comprises channels that are activated by the direct interaction with G-protein beta-gamma dimers (Gβγ) released from G-protein heterotrimers of the $G_{(i/o)}$ class. The G-protein activation is dependent on activation of the appropriate (requires G-proteins of the $G_{(i/o)}$ class) G-protein coupled receptors (GPCR). However, this is only one bit of the activation pathway of Kir3 channels. As all Kir channels (Hansen 2015), the activation of Kir3 requires interactions with PIP_2 from the intracellular leaflet of the membrane – thus, the channels are regulated by parameters of the PIP_2 metabolism. For instance, the ATP-dependent phosphorylation of PI(4/5)P to PI(4,5)P_2 by specific phosphatidyl inositol (PI) kinases has a positive effect on Kir3 activity, while hydrolysis of PIP_2 by phospholipase C (PLC) inhibit the Kir3 channels. Kir3 channels are also sensitive to intracellular Na^+, whose intracellular concentration rises when sodium channels are activated during action potentials. The cytosolic influx of Na^+ increases the open probability of Kir3 channels. The resulting outflow of K^+ through the Kir3 channels tends to counterbalance the initial depolarization caused by cytosolic Na^+ influx. Kir3 channels are also regulated by protein kinases.

The first Kir3 channel to be recorded and later cloned was the channel conducting the cardiac acetylcholine potassium current (I_{Ach}) (Sakmann, Noma, and Trautwein 1983; Diomedes E Logothetis et al. 1987). Shortly after, the first Kir3 channel was recorded in brain tissues (Miyake, Christie, and North 1989). The cardiac heterotetramer expressed in atrial cells was characterized as sustaining a 40 pS conductance and a mean open time of 1 ms. The closures of the channel are of variable duration (1 and 100 ms), giving the name “trains of bursts” to the distinct periods of activity of the channel (Hibino et al. 2010). The first cloned cDNA, Kir3.1, was obtained from rat heart and brain in 1993 (Dascal et al. 1993; Kubo et al. 1993). The KCNJ3 gene coding for four isoforms (1, 2, 3, 4) of the Kir3.1 protein is highly expressed with value of reads per kilobase per million (RPKM) superior to 1, in the brain, heart, kidney, duodenum, small intestine, prostate, gall bladder, liver, adrenal gland and colon (Fagerberg et al. 2014). Kir3.2 and Kir3.3 were both cloned from mouse brain shortly after Kir3.1 (Lesage et al. 1994). The KCNG6 gene coding for three isoforms (A, B, C) of the Kir3.2 protein and the KCNG9 gene coding for a single isoform of the Kir3.3 protein are highly expressed in the brain only (Fagerberg et al. 2014). For the first time, the Kir3.4 protein was shown to coimmunoprecipitate with the Kir3.1 protein and then cloned from rat atrial tissue (Krapivinsky et al. 1995). The KCNJ5 gene coding for a single isoform of the Kir3.4 protein is expressed in adrenal glands, spleen, placenta, lungs, heart, pancreas, kidney, stomach, gall bladder, urinary bladder, brain and other (Fagerberg et al. 2014).

Functional Kir3 channel assemblies can either be homotetramers in the case of Kir3.2 and Kir3.4, or heterotetramers such as Kir3.1/Kir3.2, Kir3.1/Kir3.3 and Kir3.1/Kir3.4, Kir3.2/Kir3.2 (Hibino et al. 2010). Numerous studies investigated factors that are simultaneously required for the activation of Kir3 channels, thus the requirement for the simultaneous presence of Gβγ dimers, Na^+ and PIP_2 was identified (Sui, Petit-Jacques, and Logothetis 1998). The PIP_2, Gβγ dimers and Na^+ bind to the CTCD by interacting simultaneously with the short N_{ter} domain and different regions in the large C_{ter} domain of the Kir3 channels, these interaction sites are now observable in the recent crystal structure: PDB:4KFM (Whorton and MacKinnon 2013). Later on, it was demonstrated that the PIP_2 and the Gβγ are mandatory cofactors for the activation and that the Na^+ is an optional positive modulator (Wang, Whorton, and MacKinnon 2014).

The Kir3.1 protein cannot properly maturate and traffic to the plasma membrane unless it is partnered with other types of Kir3 subunits (Zylbergold et al. 2014). Interestingly, an activating single point mutation was identified in the pore region Kir3.1 F137S. The expression of homomeric channels

with this mutation allows the whole-cell recording of stronger currents than the wild-type (Chan et al. 1996; Vivaudou et al. 1997). Nevertheless, this activating mutation of Kir3.1 does not seem to rescue the intracellular distribution of the Kir3.1 homomers in favor of a better expression at the plasma membrane. Thus, the recorded conductance is probably due to an increase of the open probability of the mutant channel, which, like its wild-type counterpart, reaches the plasma membrane by flaws in the cell trafficking metabolism. Authors also showed that modification at the equivalent position in the Kir3.4 S143T greatly enhances the open probability of the channels when stimulated by Gβγ.

The dependence of the Kir3.1 subunit on other subunit types for export to the plasma membrane can be attributed to the lack of endoplasmic reticulum (ER) export signal on this subunit. In contrast such signatures are identified in mmKir3.2 [D20-Q-D-V-E-S-P-V30] and in Kir3.4 [N10-Q-D-M-E-I-G-V17]. The Kir3.3 subunit also lacks the ER export signature. Furthermore, this subunit contains a signal [350Y-W-S-353I] targeting the Kir3.3 homomeric channels directly to lysosomes, without being delivered at the membrane (Hibino et al. 2010). Much more has been discovered on the Kir3 turnover in the native cellular environment but this information is out of scope with the topic of this manuscript and will not be further discussed, for more details see reviews by Hibino *et al*. in 2010, Lujan *et al*. in 2015 (Hibino et al. 2010; Luján and Aguado 2015).

2.2 *Activation of Kir3 by G heterotrimeric proteins in the physiological and cellular contexts*

A hallmark of the Kir3 subfamily is its specific activation by the Gβγ dimers. In brief, the signaling pathway consists of the ligand binding to the GPCR, which leads to the exchange GDP/GTP bound to the Gα subunit of the G protein, and to the dissociation of the heterotrimeric complex in $G\alpha^{GTP}$ monomer and Gβγ (Pfaffinger et al. 1985; Diomedes E Logothetis et al. 1987; Gilman 1987). It was demonstrated that the Gβγ dimers activating Kir3 are released after activation of GPCR coupled to pertussis-toxin sensitive $G\alpha_{i/o}$ proteins (Pfaffinger et al. 1985; North et al. 1987). For instance, in atrial myocytes, the result of acetylcholine stimulation of the muscarinic receptor (m2R) leads to the release of free Gβγ which binds to the cardiac Kir3.1/Kir3.4 channel, causing an increase of the recorded burst frequency (Ivanova-Nikolova and Breitwieser 1997). Among the five $G\beta_{1\text{-}5}$ subtypes, when coupled to Gγ, only $G\beta_5$ is not capable of activating the Kir3 channels (Mirshahi et al. 2002). The consequence of the binding of Gβγ to Kir3 is to increase channel affinity for PIP_2, since, in excised patches from Xenopus oocytes expressing Kir3, the completely run-down channels are not sensitive to addition of Gβγ but are activated by addition of PIP_2 (Huang, Feng, and Hilgemann 1998). I would like to comment on this reference that the interpretation of the results was made without taking into account the fact that the PIP_2 is constantly hydrolyzed and thus, the run-down of the channel could be due to the insufficient amount of PIP_2 in the patches.

It was demonstrated that the initial Gβγ-Kir3.1 contacts will govern the fate of the channels towards maturation or degradation (Zylbergold et al. 2014). By manipulating the abundance of different members of the Gβ and the Gγ families, authors identified the $G\beta_1\gamma_2$ dimer as a potent partner protecting the Kir3.1 channel from degradation and helping the channel to reach the plasma membrane. These findings suggest that the specificity of the initial Gβγ-Kir3 interactions can also serve to control the Kir3 abundance, the turnover of the Kir3 channels and the subunit composition of the Kir3 channels found in the plasma membrane.

The interplay between the $G\alpha^{GDP}$ subunit and the Gβγ dimer is implicated in the regulation of Kir3 channels. The $G\alpha^{GDP}$ binds Gβγ in a reconstituted membrane environment with K_d 6-9 nM (Sarvazyan, Remmers, and Neubig 1998). The control of the cardiac Kir3.1/3.4 channels by different Gα and Gβγ subtypes was accessed by perfusion of purified G proteins on excised patches of rat atrial cells (Wickman et al. 1994). Authors reported K_{act} depending on the Gβγ subtype to be 3-30 nM, and the IC_{50} of the $G\alpha_{i3}$-induced silencing of the K^+ current was measured at 10 nM. In excised patches from

Xenopus oocytes and in atrial myocytes, authors reported the $G\alpha_{s1}$ subunits as potent inhibitors of Kir3 activated by $G\beta_1\gamma_2$ dimers, thus pointing to the specificity of the coupling between G proteins and Kir3 (Schreibmayer et al. 1996).

An interesting issue such as the ratio between the basal (I_{basal}) and the evoked (I_{evoked}) currents was addressed by Kahanovitch and coworkers (Kahanovitch et al. 2014). Authors pointed to the fact that heterologously expressed Kir3.1 containing channels in intact Xenopus oocytes or mammalian cells exhibit significant levels of I_{basal} and as a consequence, the activation by Gβγ provokes only a moderate I_{evoked}. On the contrary, Kir3.2 homotetramers expressed in the same condition only have a small I_{basal} and respond vigorously to the Gβγ stimulus. The difference between I_{basal} of the Kir3.1 containing channels and the Kir3.2 homotetramers relies on the dependence on Gβγ. In the case of Kir3.1, the Gβγ-dependence of I_{basal} is very strong and consequently, the further increase of the Gβγ concentration upon receptor activation has a very limited effect on the channel. On the other hand, it appeared that the I_{basal} of Kir3.2 channel is Gβγ-independent. Thus, upon receptor stimulation the channel response to free Gβγ is more pronounced compared to the response of the Kir3.1-containing channels. Authors have measured a 3-fold increase of the Gβγ expression at the plasma membrane when the tested cells were expressing Kir3.1/Kir3.2 channels. No change of levels of Gα at the plasma membrane was detected and the Kir3.2 channels did not have an effect on the plasma membrane levels of Gα or Gβγ. It was already suggested that the apparent recruitment of Gβγ to the Kir3.1 containing channel relies on the distal C_{ter} of Kir3.1 (Chen et al. 1995). Unfortunately, this part of the channel has never been observed in any of the available crystal structures. In the Kahanovitch study, the deletion of the distal C_{ter} of Kir3 abolished the recruitment of Gβγ. Thus, the peculiar role of the Kir3.1 distal C_{ter} was confirmed, and although it does not bind the Gβγ by itself, it is the factor for the enhancement of I_{basal} of the native heterotetramers. The inverse relation between the amplitude of I_{basal} and I_{evoked} was further investigated and experimental data was finally fitted by a novel mathematical model in order to identify the stoichiometry of the recruitment of G heterotrimeric constituents to the Kir3 channel (Yakubovich et al. 2015). Authors suggested that the levels of I_{basal} is highly dependent on the $G\alpha_{i/o}$ subunits available to the channel, thus the I_{basal} ratio to the I_{evoked} is directly proportional to the limited quantity of $G\alpha_{i/o}$ in the native neuronal culture cells, and also in the heterologous expression systems: HEK cells and Xenopus oocytes. The authors' model identified that three or four Gβγ bound to the Kir3.1/Kir3.2 channel, whereas at most two $G\alpha_{i/o}$ are available per channel. According to the authors, the fine-tuned stoichiometry of the G heterotetramer constituents and the Kir3 channel would be responsible for the control of the basal activity and the magnitude of the neurotransmitter-induced response of the Kir3 channels, thus being very important for physiological phenomena such as neuronal excitability, bistability of neuronal networks, neuronal plasticity, dendritic integration, atrial arrhythmia and remodeling, where Kir3 channels play a role.

2.3 Molecular mechanism of G heterotrimer activation of Kir3

2.3.1 Evidence of the Gα-Kir3 contacts in cellulo and in vitro

The Gα subunits of the G-heterotrimeric proteins are not part of the canonical ensemble of Kir3.2 activators. Nevertheless, it has been demonstrated that the presence of Gα subunits and even a potential macromolecular complex between the Kir3 and the Gα subunits could be responsible for the potency of the Kir3 activation in recording made with native tissues and in reconstituted and heterologous expression systems. Thus, an overview of the implication of the Gα subunits on the electrical activity of the Kir3 channels is an important part of the literature review of the manuscript.

The specificity of the Gα proteins involved in the Kir3 activation was attributed to the selectivity of C_{ter} of Kir3 for the class of Gα, and to the Gαβγ-Kir3 complex existing prior to the receptor activation (Clancy et al. 2005). An even larger ternary complex between GPCR- Gαβγ-Kir3 was proposed in the scope of the results of bioluminescence resonance energy transfer (BRET) experiments with

luciferase-labelled channel subunits as the donor and the fluorophore-labeled G protein subunits as the receptor of bioluminescent emission (Rebois et al. 2006). Authors reported that an energy transfer signal was obtained by a membrane-permeable agonist, corresponding to the activation of G proteins before they were transported to the cell membrane, thus suggesting the early ternary complex.

Another team investigated the action of Gα on Kir3 channels by controlling the levels of Gα in Xenopus oocytes. Authors proposed that the Gα not only inhibits the basal current of the Kir3 channels by acting as a Gβγ scavenger, but also that Gα keeps the channel into a closed basal state allowing the channel to conduct stronger ligand-induced currents (Varon et al. 2002). The second line of thought is supported by an observed correlation between the channel density and the amount of $G\alpha_i$ that is needed to inhibit the basal current, while at the same time the Gβγ dose-response curve is not shifting in response to an increased number of scavenging events. These reports demonstrated that the affinity of $G\alpha^{GDP}$ for Gβγ is higher than the affinity of the Kir3 for the Gβγ, thus $G\alpha_i$ serves as an effective inhibitor of the basal currents of Kir3 channels and allows it to ensure high signal to noise ratio upon activation.

Coimmunoprecipitation of Kir3 cytoplasmic domains and derived peptides with G proteins were used to identify a set of six amino acids that are responsible for the selectivity of the class of Gα proteins binding the Kir3 channels (Clancy et al. 2005). Namely these residues in the mmKir3.2 are: G318, C321, A323, I328, T329 and S330. As one can notice in the crystal structure of the mmKir3.2-Gβγ-PIP_2 complex (PDB:4KFM), the last three of the above-mentioned residues are potentially accessible for binding a membrane-anchored Gα subunit on the surface of the channel CTCD. Authors observed that the mutation of these residues to the analogous residues in the Kir2.1 completely abolished the coimmunoprecipitation of the $G\alpha_{i/o}$ monomers and the $G\alpha_{i/o}\beta\gamma$ heterotrimers with the mmKir3.2 CTDC. Experiments with immunofluorescence in mammalian cell lines also demonstrated that the Gαβγ heterotrimer is associated to Kir3 channels prior to the signal transduction by the stimulated receptor (Rebois et al. 2006). Furthermore, authors observed that upon activation of the channel, there was evidence of the rearrangement of the G protein heterotrimer, but the Gα remained associated to the channel since the level of energy transfer between the channel and G proteins remained unchanged. These observations are consistent with the model of ternary complex proposed by Clancy and coworkers, and authors supported their hypothesis by experimental evidence where such rearrangements were observed in experiments involving crosslinked G proteins and FRET measurement of fluorophore-tagged G heterotrimeric proteins in HEK cells (Clancy et al. 2005; F. Yi, Denker, and Neer 1991; Bunemann, Frank, and Lohse 2003). Biochemical studies have shown that the interactions between Kir3.2 and Gβγ are stronger than those between Kir3.2 and Gα and that the complex $G\alpha^{GDP}\beta\gamma$ is promoted by Gβγ heterodimer. Thus authors suggest that, in the complex, Gα is bound to the channel via Gβγ, and a similar conclusion was made concerning the $G\alpha^{GDP}\beta\gamma$ interaction with the truncated CTCD of Kir3.1 (Berlin et al. 2011; Kahanovitch et al. 2014). Interestingly, by varying the location of the fluorescent tag on the Gα subunit, authors were able to manipulate various properties of the recorded current: the levels of inhibition of basal currents, the ratio of the receptor-evoked current and the speed of reaching the maximal current. This data suggested that the Gα possibly have a dual role on the Kir3. Firstly, it regulates the basal current by scavenging free Gβγ and secondly, it controls the speed of activation of the channel by the rate at which the Gβγ are released. Yet in 2012, Mase and colleagues published a NMR based study where spectral measures showed direct binding modes between $G\alpha^{GTP}$ and Kir3.1 CTCD (Mase et al. 2012). Contrary to all other information discussed above, authors observed the interaction site of one GTP-bound Gα to be located simultaneously at the distal-C_{ter} alpha helices of two Kir3.1 subunits, involving residues at position 355 to 386 (eq. mmKir3.2 366 to 392). According to the generated model, the α2/α3 helical domain encompassing the GTPase activity of the Gα interacts with one Kir3.1 subunit and the helical domain of Gα interacts with an adjacent Kir3.1 subunit. Because the predicted position of the Gα N_{ter} is 3.5 nm away from the inner leaflet of the membrane, in order to

account for the membrane-anchoring modification of Gα *in vivo*, authors suggested that the long α helix of $G\alpha^{GTP}$ should be unstructured for this binding mode to be plausible. This hypothesis is strengthened by the 4.2 nm length of the α helix (residues 5 to 33) of $G\alpha_{i1}$ observed in the crystal structure PDB:1AGR, where the G protein is activated by AlF^{4-} and is seen in a presumably GTP-activated transition state (Tesmer et al. 1997).

Nevertheless, as of today, the canonical role of the free $G\alpha^{GDP}$ is accepted to be limited to the scavenging of Gβγ. This behavior has recently been demonstrated in minimalistic experimental conditions using planar lipid bilayers incorporating engineered *Mus musculus* Kir3.2 (mmKir3.2) channels pre-activated by Gβγ and perfused with soluble $G\alpha^{GDP}$ subunits (Wang, Whorton, and MacKinnon 2014). The $G\alpha^{GDP}$ closed the channels, while the $G\alpha^{GTP\gamma S}$ did not have any effect on the recorded currents neither in the activating sense nor in the inhibiting sense, thus authors did not find evidence to support a direct interaction between Gα and Kir3.

A detailed thermodynamic mechanism of the Gβγ activation of Kir3.2 was provided by summarizing already known structural and functional characteristics of the interaction and activation phenomena, and combined with recordings of the reconstituted channel in artificial membranes upon activation by purified Gβγ (Wang et al. 2016). Authors were able to fit the kinetics observed experimentally and the dose-dependent behavior of the Gβγ activation, to a thermodynamic mathematical model including 25 states where all possible combinations are considered for the occupation of the four Gβγ and the four Na^+ binding sites. Authors concluded that the binding of Gβγ to the Kir3.2 is cooperative and that four Gβγ are needed to bind in order to increase the open probability of the Kir3.2 channel. Mechanistically, the first Gβγ dimer binds to the CTCD of the channel and the binding energy is used to initiate a rigid body rotation of the TMD involving all four channel subunits. This concerted rotation also changes the conformation of the CTCD in such a manner that the binding affinity of the CTCD for Gβγ becomes 37-times higher than the affinity for the first Gβγ dimer. Thus, the estimated affinities are 1.9 mM for the first Gβγ binding and 50 µM for all four Gβγ. Finally, according to the authors, the rotation of the helical TMD extends the diameter of the HBC gate and in presence of PIP_2, the channel can be open.

2.3.2 The Gβγ-Kir3 interaction

Several residues have been pointed out as important in Gβγ-Kir3 coupling. For instance, two residues in Kir3.4, the H64 and L268 (eq. mmKir3.2: H69 and L273) were reported as critical to mediate the activation by Gβγ and it was proposed that these residues are directly in contact with the G protein (He, Yan, Zhangţ, et al. 2002). However, these residues are not directly interacting with the Gβγ, as it can be observed in the crystal structure PDB:4KFM (Whorton and MacKinnon 2013). The reason which designated the H64 as important is that its mutation H64F in Kir3.4 resulted in the loss of basal currents and of Gβγ sensitivity of the channel. Later on, the H69 was linked to the Na^+ sensitivity of the channel by establishing a ionic bond with D228 in the absence of Na^+ (Inanobe et al. 2010). When mutated to glutamine, the residue renders the Kir3.2 homomers more active in presence of PIP_2 and the channels sensitivity to Na^+ was reduced 10-fold compared to the wild-type. It is clear that the phenotype obtained by both mutations on the equivalent histidine in mmKir3.2 H69N and in Kir3.4 H64F resulted from the ability of the mutated residues to establish hydrogen bonds with their environment. In the case of the phenylalanine mutation, which is equivalent to the native position in Kir2 and preserved the geometry of the side chain of the wildtype histidine, the hydrogen-bonding through the phenylalanine side chain is impossible. In contrast, upon Na^+ binding, the glutamine most probably substituted itself in some or all of the interactions that are in place with the wild-type histidine, thus increasing the affinity of the channel for PIP_2 similar to the wild-type histidine. Finally, these observations seem insufficient to conclude on the interaction between the Kir3.4 H64 and the Gβγ dimers. The second proposed interaction between the Kir3.4 L268 and the Gβγ can also be refuted by the observed conformation of this residue in the PDB:4KFM. In fact, the Kir3.2 L273 residue is buried deep inside the CTCD and it is not intuitive to imagine a conformational change that will allow L273 to contact the Gβγ. Mutations of L273 residues seem to induce conformational

defects that alter some of the functionalities of the channel, implying that the L273 residue is implicated in the transduction of the conformational changes upon binding of Gβγ.

The next residue which was proposed to directly interact with Gβγ is located in the βL-βM loop of Kir3.4 the L339 (eq. mmKir3.2 L344) (He et al. 1999). When mutated to the equivalent glutamate in Kir2.1, the basal activity of the Kir3.4 homomers was abolished and the channel became insensitive to Gβγ. By inspecting the Kir3.2-Gβγ crystal structure one notices that the L339 residue is directly interacting with the Gβγ via van der Waals interactions. However, it is not clear why and how the L339E will "repel" the Gβγ, since no other negatively charged residue can be observed nearby in the Gβγ-Kir3.2 complex. It is a pure speculation for the moment but it is possible that the mutation L339E stabilizes the βL-βM loop in interaction with the positive cluster KRK of the N_{ter} of Kir3.2, thus hindering the binding of Gβγ to the channel. Thus, the interaction between Gβγ and the channel CTCD could be rendered inefficient to produce the splitting of the βL-βM loop and the βD-βE loop and impeding the opening of the cytoplasmic gate of the channel observed by comparison of the available crystal structures. This possibility is discussed later in the manuscript in the scope of observations in the computational model where numerous interactions are observed between the N_{ter} and the βD-βE βL-βM loops.

In fact, the above mentioned separation of the βL-βM and the βD-βE loops was described in 2007 by Nishida and coworkers, from the crystal structure of a chimeric channel composed of the Kir3.1 CTDC and the KirBac1.3 TMD (PDB:2QKS) (Nishida et al. 2007). Surprisingly, two different conformations of the channel were caught in a single crystal diffracting at 2.2 Å. One had approximately a 10 Å opening of the G loop, thus classifying the gate as being in an open state. The configuration of the G-loop gate was correlated to the rigid-body motion of the CTCD and the rearrangement in loop structures in the CTCD. In the structure with the extended G loop, the entire CTCD moves towards the TMD by 3.4 Å, and, in parallel, the βL-βM loop moves towards the membrane by ~30° in comparison to the structure with the constricted G loop. Later on, another team used these observations in a computational study where rigid body docking of the Gβγ dimers on the crystal structures of the chimeric Kir3.1-KirBac1.3 channel was performed (Mahajan et al. 2013). The interaction between Kir3.1 F243, Kir3.1 L333 and Gβ L55 was found among the best scoring docking models and was confirmed to be crucial for the G protein activation of Kir3.1 and the Kir3.1/Kir3.4 channels by mutagenesis and electrophysiology.

An NMR study by Yokogawa and colleagues investigated the binding interface between Gβγ and Kir3.1 CTD (Yokogawa et al. 2011). Authors used isothermal titration microcalorimetry (ITC) to measure the dissociation constant of the complex to be 250 µM and the stoichiometry of the complex was fitted to one Gβγ heterodimer per Kir3.1 monomer. This affinity is 4-times higher than the measured 1 mM affinity of $G\alpha_{i1}$ for the Kir3.1 CTCD (Mase et al. 2012). The experimentally observed low ratio of complexed Gβγ-Kir3.1 was attributed to the fact that non-prenylated Gβγ were used in this experiment. Thus, in solution the correct orientation of the G proteins with respect to the Kir3 CTDC is less likely to take place than in the naturally occurring membrane delimited diffusion process. The K_{act} of Gβγ-Kir3 in membrane delimited conditions was measured to be 3-30 nM depending on the Gβ subtype (Wickman et al. 1994). Yokogawa and colleagues used transferred cross-saturation experiments (TCS) to identify residues of Kir3.1 interacting Gβγ. These residues are, using mouse Kir3.2 numbering and residue types instead of Kir3.1: in the βD-βE loop K247, Q248, T249, E251, G252, E253, F254 and I255, in the βL-βM loop E331, L344, E345, F348, E350, D352, E361. Authors also used chemical shift perturbation (CSP) experiments to investigate the Gβγ-Kir3.1 interaction. In addition to the residues identified by TCS, the equivalent Kir3.2 residues identified by CSP were: in the N_{ter} R57, Y58, V59, D62, G63, N66, in the βG-βH coil K301, in the βL-βM loop I328, T329, S330, G347, Y349, Y353, N354, S355, E338, T339. Authors examined the structural motifs of Gβγ-Kir3 and the Gα-Gβγ interaction sites and uncovered a significant similarity. In both cases the region binding the Gβγ contains a hydrophobic region flanked by two acidic regions. On the Kir3.1 the hydrophobic surface consists of F243, L244 and P245 in βE strand (eq. mmKir3.2 F254, I255,

P256), and P329 and I331 in βL strand (eq. mmKir3.2 P340, L342), while the acidic regions are represented by E242 and E334 (eq. mmKir3.2 E253, E345). According to this data, the binding of the Gβγ to Kir3 CTCD would cause rearrangement in the channel to allow the hydrophobic surface and the flanking acidic regions to interact properly with the signal transducing protein. Yokogawa and coworkers also inferred the propagation of the conformational changes in the Kir3.1 CTCD caused by the binding of Gβγ. Authors reported significant CSP signal for Kir3.1 G307 and M308 in the G-loop (eq. mmKir3.2 G318, M319), suggesting rearrangement in the G-loop gate upon Gβγ binding. This data was correlated with the inter- and intra-subunit interactions between the G-loop and the adjacent slide helix, TM2 and C-linker, observed in the crystal structure of a chimera between the TMD of bacterial KirBac3.1 and the CTCD of Kir3.1 (PDB:2QKS) (Nishida et al. 2007). The interactions, using mmKir3.2 numbering, are: between slide helix and G-loop F83-A316, T84-A316, between TM2/C-linker and G-loop V193-A316, Q197-A316, S196-T317, S196-M319, Q197-M319, P198-V314, P198-C321, between slide helix and βC-βD loop T84-H233, between C-linker and βC-βD loop K199-R230. These interactions are based on a 4 Å distance-threshold in the crystal structure. They show the proximity between secondary structures which are involved in the conformational change detected in the NMR experiments when Gβγ binds the Kir3 CTDC (Yokogawa et al. 2011).

The crystal structure of the mouse Kir3.2 in complex with Gβγ has elegantly confirmed the set of residues unique to the Kir3 family involved in the complex between the channel and the signal transducing G protein (Whorton and MacKinnon 2013). As pointed by the authors, in mmKir3.2 these residues are: Q248 and F254 in the βD-βE loop and L342, S/T343 and L344 in the βL-βM loop. Residues observed in the crystal structure which were identified by mutagenesis of the G protein and which decrease the activation of Kir3.1/Kir3.4 by Gβγ include: Gβ K89 interacting with mmKir3.2 E345, and Gβ W99 and Q75 interacting with mmKir3.2 Q248. The first of these interactions involves the part of the βL-βM loop which is closest to the membrane, while the second interaction involves the βD-βE loop. These are consistent with the described mechanism implying the separation of the βD-βE loop from the βL-βM loop (Mahajan et al. 2013; Diomedes E. Logothetis et al. 2015) and the NMR detected interfaces between Gα and Gβγ, and between Gβγ and Kir3. Despite the fact that the exact position of the residues described in both studies is not exactly the same, the concerned regions are equivalent in Kir3.1, Kir3.2 and Kir3.4 and both studies indicate position at ±2 residues of distance. On the other hand, more residues identified by mutagenesis as disrupting the activation of the channel by Gβγ are not seen to contact the Kir3.2 in the crystal structure. For instance, when present, the dominant mutant Gβγ W332A, which did not activate the channel, also prevented the wild-type Gβγ of activating the Kir3.1/Kir3.2 channels in HEK cells (Zhao et al. 2006). It was speculated that the Gβ W322 would bind the αA helix of the C_{ter} of Kir3.1, because the β adrenergic receptor kinase (bark) sequence of Kir3.1 is located immediately after the αA helix and the bark sequence in other proteins binding the Gβγ sequence is observed to interact with the Gβ W322 (Chen et al. 1995; Nishida and MacKinnon 2002). In fact, the bark sequence (Kir3.1 N378, E381, R382) has no equivalent in the Kir3.2 at the suggested position. This may be at least partially the reason why Kahanovitch and colleagues observed that the distal C_{ter} of Kir3.1 containing channels (but not the Kir3.2 homotetramers) recruit the Gβγ (Kahanovitch et al. 2014).

Finally, it is still unclear if in the macromolecular complex preassembled around the resting Kir3 any Gα subunits are present. Furthermore, the Kir3-Gβγ interaction in the resting state Kir3 is also subject to controversial reports (Yakubovich et al. 2015). In order to simplify the test conditions and also the interpretations of the results of molecular dynamics of Kir3 channels, we decided to naively assume that the Kir3 channel can be activated in presence of Na^+, PIP_2 and Gβγ, and that the removal of these partners will cause the channels to gate and this inactivation would be a sufficient model to compare the activated and the inactivated/closed states of the channel (for further details of the modeling strategy see chapter 4 and chapter 5).

2.4 Activation of Kir3 by PIP_2 and Na^+ in the cellular contexts

PIP_2 is one of the phosphorylated forms of phosphatidyl inositol (PI). PI contains two fatty acid chains, a polyunsaturated 20-carbon chain and a saturated 18-carbon chain. The type of PIP_2 interacting with Kir3 channels is phosphorylated at positions 4' and 5' and requires consecutive phosphorylation of PI by specific series of phosphorylation/dephosphorylation reactions operated by different phosphatidylinositol kinases (PIK) (Diomedes E. Logothetis et al. 2015; D E Logothetis et al. 2015). The PIP_2 pool in the membrane is depleted by activation of phospholipase C (PLC) which is activated by the Gq class of G-proteins. Both, the replenishment and the depletion of PIP2 in the membrane exert influence on Kir3 activity. For instance, acetylcholine (ACh) activation of m2 receptors has positive effect on Kir3 activity while ACh activation of m1 or m3 receptors enhances PLC activity, causing a time-delayed negative effect on the Kir3 activity. Increase of the intracellular Na^+ concentration results in positive modulation of the Kir3 channels.

The cooperativity of the binding of the Gβγ dimers and Na^+ has recently been quantified in experiments using reconstituted Kir3.2 (Wang et al. 2016). Thus, in the context of the Kir3 activation mechanism, Na^+ was found to stabilize the open state of the channel in direct proportion to its occupancy of the four Na^+ binding sites on the Kir3.2 channel. Using an equilibrium mathematical model, authors fitted the titration measurements and concluded that the binding of four Na^+ to the channel increased Gβγ binding affinity by 6-fold. Authors pointed to the physiological relevance of this positive modulation of K^+ currents through Kir3. In fact, upon depolarization of the neuronal cell, the intracellular Na^+ concentration increases via influx of Na^+ through voltage-gated Na^+ channels, thus amplifying Kir3 activation significantly even at low Gβγ concentrations.

The fact that the Kir3.4 subunit forms functional homotetrameric channels whereas the Kir3.1 subunit forms nonfunctional homotetramers has recently been exploited in the HEK cells (Touhara, Wang, and Mackinnon 2016). Authors demonstrated that in the cardiac Kir3 channel, the Kir3.1 subunit is responsible for the potentiation of the activation of the heterotetramer. Authors observed that the sequence of Kir3.1 corresponding to the Na^+ binding site in Kir3.2 and Kir3.4 does not bind Na^+ but mimic the conformation of a Na^+-occupied site. Thus, Kir3.1-containing channels are in a state of enhanced affinity for Gβγ and for PIP_2 even in low Na^+. It was demonstrated that the overexpression of wild-type Kir3.4 homomers in atrial myocytes is able to produce Na^+-activated and Gβγ-independent inward currents, thus showing for the first time the activation of Kir3 in a G-protein independent manner (Mintert et al. 2007). The presence of the Na^+ binding site in the Kir3.2 and Kir3.4 allows these channels to function as homotetramers, whereas the Kir3.1 cannot be expressed as a highly pre-activated homotetramer because of the maturation hindrance (Zylbergold et al. 2014).

A model of the molecular mechanism of gating of the Kir3 channel was provided by a study of crystallographic structures of the CTCD of the mouse Kir3.2 and by functionally characterized native and mutant full-length mouse Kir3.2 channels by patch-clamp recordings (Inanobe et al. 2010). In this model, the channel first binds the Na^+ and the Gβγ dimers in order to adopt a conformation in which it has higher affinity for PIP_2. However, this hypothesis has already been proposed in another study where the effect of the transposition of two residues from Kir2 to Kir3.2 was investigated. Namely, Kir3.4 I229L and K237Q increased the interaction between PIP_2 and channel, yielding the development of maximum current by the application of PIP_2 alone. At the same time, authors showed that these mutations did not impede Gβγ binding, despite the fact that the application of purified G proteins had only a minor activation effect (Zhang et al. 1999). Inanobe and coworkers observed that in the crystal structures, in absence of Gβγ and Na^+, the D228 in the βC-βD loop interacts with H69 of the βA strand and Y353 of the βM strand. This observation strongly supports the hypothesis of a rotation of the sidechain of D228 involving a conformational change of the βC-βD loop upon the opening of the channel. Furthermore, the existence of this interaction is supported by the increase of the PIP_2-induced current observed when the interaction between the N_{ter} and the βC-βD loop was eliminated by D228N or H69N/C mutations. Interestingly, authors observed that the

channel remained sensitive to Na^+, suggesting that the disruption of the interaction between the N_{ter} and the βC-βD loop is not the only effect of the Na^+ binding. The remaining Na^+ sensitivity is probably due to factors contained in the TMD and the sliding helix. It can be argued that the Na^+-induced difference in the crystal structures is off-site because it may be influenced by a reorganization of the protein in response to the heavy truncation performed for the crystallization of the CTCDs. The site H64 in Kir3.4 (eq. mmKir3.2 H69) was reported to play a role in the Gβγ sensitivity of the Kir3 (He, Yan, Zhangţ, et al. 2002). Taken together these observations concerning the same histidine residue suggest a potential dual control of this hot spot involving interactions between the βM strand, the N_{ter} and the βC-βD loop.

2.5 *PIP_2 IS THE PRIMARY ACTIVATING CO-FACTOR CONTROLLING THE HBC GATE OF KIR3*

The first model of the gating of Kir3 was provided by Sui and coworkers (1998), it consists in a two-gated model where one functional component of the channel is activated by Gβγ and Na^+ and the other functional gate is opened by the loading of PIP_2 on the channel (Sui, Petit-Jacques, and Logothetis 1998). Authors observed that the two functional elements can be activated independently of the sequential order of activation, but both are required for the opening of the channel.

The conformational changes occurring when Kir is gated were quantified by FRET experiments with tagged Kir3.1/Kir3.4. (Riven et al. 2003) and lately, by comparison of newly resolved crystal structures of the full-length mouse Kir3.2 (Whorton and MacKinnon 2011, 2013). Both studies inferred that upon opening, the channel seen from the extracellular side experiences a counter-clockwise rotation of about 8°-10° of the CTCD in respect to the TMD. This “twist to open” conformational change appears to be correlated with the opening of individual gates. It was modeled as the second slowest collective motion predicted by normal mode analysis of elastic network models of different potassium channel crystal structures (Shrivastava and Bahar 2006). A crucial event of the twist-to-open mechanism occurring in the TMD is the bending of the TM2 around a conserved glycine residue. This mechanism was suggested by observations in crystal structures of MthK and KcsA potassium channels (Jiang et al. 2002) and was further investigated by proline scanning of the TM2 (Sadja et al. 2001; B. A. Yi et al. 2001). In crystal structures presumably showing the open state of four potassium channels, the bending of TM2 was quantified and authors found that the largest difference between the open and the closed states is observed at the residue (eq. mmKir3.2 L179) immediately preceding the conserved glycine (eq. mmKir3.2 G180) (Rosenhouse-Dantsker and Logothetis 2006). Proline scanning of the TM2 of Kir3 confirmed this position by recording the maximal constitutive activity among the different mutated channels. Moreover, authors reported that the opening of the channels requires the substitution to proline to be located before the central glycine. This last observation is intuitive from the perspective that the HBC gate is located on the helix turns following the identified hinge residue. Thus, if the proline kink is implemented after the HBC gate, it is reasonable to expect that the proline-induced kink will have no effect on the conformation of the gate.

In order to allow transport of hydrated K^+, it is expected that the G-loop and the HBC gates should both and simultaneously adopt an opening of more than 9 Å. As of today, a set of crystal structures provides an insight on the conformation of the engineered mouse Kir3.2 channel in presence of different partners (Whorton and MacKinnon 2011; Wang, Whorton, and MacKinnon 2014). In the crystal structures PDB:3SYA of the Kir3.2 homomer in presence of PIP_2 and Na^+, the HBC gate is open to 10 Å, and the G-loop gate to 8 Å (Whorton and MacKinnon 2011). This conformation suggests that a hydrated K^+ can pass the inner helix gate but not the G-loop gate. In PDB:4KFM, Kir3.2 is in presence of PIP_2, Na^+ and $G_{\beta\gamma}$ dimers, the HBC gate is open at 9.5 Å and the G-loop gate at 7.3 Å (Whorton and MacKinnon 2013). Although Kir3.2 is put in contact with all the partners required to promote the opening of the channel, the pore is even less dilated than in the absence of the $G_{\beta\gamma}$. Thus, the pore is qualified as being in a pre-opened state. The model of the gating of Kir3 inferred

from a set of full-length Kir3.2 crystal structures implies that PIP_2 lipids regulate the HBC gate, because the inner helix gate is wider in presence of PIP_2 and Na^+, 8.6 Å compared to 8.3 Å observed with Na^+ alone. The large opening of the HBC gate is observed to be 10 Å, but in this case Kir3.2 has the mutation R201A which causes a rearrangement of the CTCD. We therefore chose not to consider these findings in the discussion on the wild-type Kir3.2 channel. In more details, the 1'-phosphate of the PIP_2 interacts with the "inner helix" (TM2) at residue K194, close to F192, the effector of the hydrophobic gating. The same 1' phosphate group also interacts with R92 and K90 of the "outer helix" (TM1). At the level of the C_{ter} of TM2, the binding of PIP_2 promotes the formation of the "tether helix" (or C-linker). This event in turn helps to bring the TMD closer to the CTCD by ~6 Å (Whorton and MacKinnon 2011, 2013). The same observations were made in the case of the Kir2.2 homotetramer (Hansen, Tao, and MacKinnon 2011). The formation of the "tether helix" is possible via the interactions of K199 and K200 with the 5' phosphate of the PIP_2 as suggested by (Hille et al. 2015). Inspection of the crystal structures of Kir3 seems to confirm this hypothesis as all sidechains of the positive residues in the C-linker are resolved only in presence of the PIP_2 analogue, suggesting a stabilizing effect of the PIP_2-C-linker interactions. For instance, the PIP_2-Kir2.2 interaction is sufficient to activate the channel (Rohacs et al. 2003). In other crystal structures with and without PIP_2, the observed overall effect of PIP_2 binding is the "pooling" of the CTDC towards the TMD by 6 Å, the extension of the HBC gate, and a conformational change of the G-loop gate. The observed PIP_2-Kir interaction is not equivalent in Kir3.2 and Kir2.2. In presence of PIP_2 and Na^+, Kir3.2 exhibits only a minor change compared to the structure with Na^+ alone and the conformational change of the HBC and the G-loop gates is smaller compared to the change observed in the case of Kir2.2.

Inspection of the crystal structures seems to confirm the hypothesis of strengthening of the PIP_2-Kir3.2 interactions upon binding of the cofactors Na^+ and $G_{\beta\gamma}$. Indeed, all sidechains of the positive residues in the C-linker are resolved only in presence of the PIP_2 analogue. An exception concerns the PDB:3SYQ (Whorton and MacKinnon 2011), where the pore is observed in a C:2 symmetric configuration. There are two different conformations of the C-linker depending on whether there is a co-crystalized PIP_2 analogue in proximity to the C-linkers of individuals subunits. In the subunits where the PIP_2 analogue is absent, the helix is partially unfolded starting at Q197 and the sidechain of this residue contacts the carbonyl of the backbone of A316. This inter-subunit interaction is observed only in PDB:3SYQ. It is likely to be present because of the extended conformation of the G-loop containing the A316 residue allowing the interaction with Q197 of the adjacent subunit. This is potentially an interesting observation which could indicate an inter-subunit cooperation in the stabilization of the open state of the G-loop gate. In the remaining two subunits, Q197 interacts with the 5'-phosphate of the PIP_2 analogue and/or with K194 of the same subunit, and the same is observed in PDB:4KFM and PDB:3SYA. Another peculiarity of Q197 arises from the fact that, in the constitutively active Kir2 channels, its equivalent are K/R residues. Thus, it is possible that the increased number of interactions proximal to the HBC gate with PIP_2 in Kir2 could be contributing to the higher open probability of this channel in contrast to Kir3. This speculation is strengthened by the fact that the C-linker is separated by a proline-induced kink, where two positive residues in Kir2 are on the side of the HBC gate and two positive residues are on the side below the kink. Furthermore, as discussed later, in 2017 Lacin and coworkers showed that among the four conserved positive residues in the C-linker of the Kir family, the most distant residue from the HBC, Kir3.2 K200, is not essential for the activation of this channel.

The above model is in accordance with a variety of functional data from wild-type and mutant channels, describing the region where PIP_2 directly binds on Kir channels, or other distant sites whose mutation has an effect on the apparent affinity of the channel for PIP_2. For instance, the perfusion with soluble PIP_2 of excised inside-out patches containing Kir2.1 or Kir7.1 greatly increased currents, demonstrating that the levels of PIP_2 in the excised membrane patches are insufficient to activate these constitutively open channels (Rohacs et al. 2003). Conversely, activation of PLC or application of antibodies depleting PIP_2 from the patches decreased currents (Du et al. 2004). In contrast,

application of PIP_2 is capable of reverting PLC/PKC inhibition of the channels (Sohn et al. 2007). Interestingly, it was demonstrated that it is possible to confer PIP_2 affinity to a naturally PIP_2-insensitive invertebrate Kir channel by inserting the TM1 and C-linker positive residues associated with PIP_2 sensitivity in vertebrates Kir (Tang et al. 2015). The primordial PIP_2-Kir3 interactions for the activation of the channel is further demonstrated by the I229L mutation in Kir3.4 (Kir3.2 I234) which allows the Kir3.4 homotetramer to be activated in presence of PIP_2 alone (Zhang et al. 1999). The mutation R201A in Kir3.2 has a similar effect of increasing the basal currents (Whorton and MacKinnon 2011). Moreover, R201A is in the same region as I229L, suggesting a similarity of the induced conformational change.

A new cause-effect model has been published recently, explaining the PIP_2-induced conformational change in the Kir3.2 homomer. This model describing PIP_2-channel interactions is the most detailed to date and is derived of molecular dynamics simulations of wild-type and mutant Kir3.2 channels in presence of PIP_2. Lacin and colleagues demonstrated that one of the positive residues conserved in the PIP_2 binding site of different members of the Kir family is not essential for the PIP_2 induced activation of the Kir3.2 (Lacin et al. 2017). The substitution K200Y yielded a significant increase in the basal currents compared to the wild type. According to the authors, the 20-fold increase of the basal currents and the recorded inefficiency of alcohol stimulation are descriptors of constitutively activated channels. This position is always occupied by K/R in the mammalian Kir family. However, authors showed that a bulky hydrophobic phenylalanine yields a basal current density similar to a wild-type lysine, but application of methyl-pentane-diol decreased the currents in a similar fashion as with the constitutively open ROMK1 channel. Moreover, the conservative mutation to arginine resulted in the reduction of basal currents, and was also less effective than the wild-type or the non-conservative mutations to polar residues. In MD simulations of the wild-type protein, the authors observed a downward movement of the K200 sidechain which is mediated by interaction with E203, leading the PIP_2 5'-phosphate to disengage K194 in favor of interactions with K64. This change in interaction partners of the PIP_2 was correlated with the observed decrease of opening of the HBC gate. Interestingly, for the first time authors observed the partial activation of Kir3.2 reconstituted into liposomes by the $PI_{(5)}P$ which also confirms the critical role of the interactions between the 5'-phosphate of the PIP_2 and the channel. Authors concluded that absence of interaction between K200Y and E203 causes PIP_2 to interact strongly with residues K194 and K199. To our knowledge, these are the only reported Kir3 mutations involving residues directly interacting with the PIP_2 and increasing the recorded currents.

Significantly, the study of Glaaser and colleagues showed that the PIP_2 is sufficient to activate the native Kir3.2 channel (Glaaser and Slesinger 2017). Authors reconstituted the purified mouse Kir3.2 into liposomes containing 1-palmitoyl-2-oleoyl-sn-glycero-3-phosphoethanolamine (POPE) and 1-palmitoyl-2-oleoyl-sn-glycero- 3-phospho-(1'-rac-glycerol) (POPG) at a 3:1 ratio and 1 % PIP_2 in the test condition. The Kir3.2 activity was assessed by monitoring the K^+ flux using fluorescence-based assay where a pH-sensitive dye 9-Amino-6-chloro-2-methoxyacridine (ACMA) is the reporter for the displacement of K^+ from the interior of the liposomes upon activation of the channels (Whorton and MacKinnon 2013). In presence of cytoplasmic Na^+ and 1% PIP_2, the channel exhibited a significant dose-dependent activation compared to the PIP_2 free condition, the same activation profile was observed upon application with soluble short-tail C_8-PIP_2.

The PIP_2 biding site in Kir3 channels is located at the triple interface between the membrane and two adjacent channel subunits. There are four such sites on a Kir3 channel which have been mapped earlier by modification of the protein sequence and can be now observed in a variety of experimentally derived 3D structural models. The PIP_2 biding site involves a cluster of positively charged residues and unspecific H-bonding contacts provided by exposure of the protein backbone at turns between successive α-helices – one located in the middle of the slide helix and the other at the slide helix-TM1 junction. Figure 2 depicts the PIP_2 binding site observed in recent crystallographic

model. The PIP_2 molecule interacts with K194, K199 and K200 of the TM2 and K64 in the N_{ter} domain. Other ionic interactions involve residues K90, W91 and R92 from TM1 (not depicted).

The Na^+ binding site is *per se* absent in the Kir3.1 subunit. In Kir3.2 and Kir3.4 it has been mapped to an aspartate residue at position D228 in mmKir3.2 and D223 in hsKir3.4. Several crystal structures show that Na^+ in fact interacts with a set of carbonyl oxygens and the single carboxyl group of D228.

2.6 *Opening of the G-loop gate of Kir3 by canonical activators*

2.6.1 The role of PIP_2 in the gating of the G-loop gate

Evidence for a link between G-loop and PIP_2 binding has been provided by molecular dynamics simulation studies where authors investigated the effect of the presence of PIP_2 in the binding site at TM2 in a Kir3.1 chimeric channel (X. Y. Meng et al. 2012a). The Kir3.1 chimera was constructed from the TMD of bacterial Kir3.1 (KirBac3.1) and the CTCD of mouse Kir3.1. Once reconstructed in planar lipid bilayers, the channel exhibited the expected PIP_2-dependence but did not require Gβγ for activation. Authors reported a PIP_2-driven transition of the N_{ter} and the C-linker which appeared to stabilize the βC-βD loop and consequently the G-loop gate in an open conformation. This description is indeed very interesting and is completely reproduced by the set of simulations that I performed (see section 5). However, it is unclear whether PIP_2 suffices to open the G-loop gate in native Kir3 channels. On the other hand, if not the entire process, at least some of the causality relationships described by the authors could be attributed to PIP_2 and, most probably, one should expect that PIP_2 modifies the conformation of the C-linker by direct interaction, and in turn the G-loop gate which directly interacts with the C-linker.

2.6.2 The role of Gβγ and the reorganization of the Kir3.2 channel in response to activating R201A mutation

In which way the allosteric effect propagates from the $G_{\beta\gamma}$ binding site to the gates of the channel remains unclear. Today the best experimental pieces of evidence are provided by the crystallographic structure of Kir3.2-$G_{\beta\gamma}$. Unfortunately the channel conformation in the crystal structure is characterized as a "pre-open" state with insufficiently dilated HBC and G-loop gates to conduct hydrated K^+ (Whorton and MacKinnon 2013). Furthermore, the only open state of Kir3.2 is observed only partially with the Kir3.2-R201A activating mutant in presence of PIP_2 (PDB:3SYQ). In fact, the opening has symmetry of C:2 instead of C:4, which is caused by the binding of PIP_2 molecules to only two diametrically opposed subunits of the channel. Nevertheless, the mutant R201A is proposed to induce conformational changes similar to those induced by $G_{\beta\gamma}$ binding to the channel. Whorton and MacKinnon described these by comparing the displacement of the backbone of the R201A mutant with respect to the wild-type apo-structure (Whorton and MacKinnon 2011). An important remark on this comparison should be made here. The so called wild-type apo-state is in fact the conformation of the Kir3.2 pore observed in presence of Na^+ (PDB:3SYO). As discussed above, the binding of Na^+ has non-negligible effects on Kir3.2, thus it is not completely true that the R201A conformational change is compared to the Kir3.2 wild-type without ligands, rather the comparison is made between the Na^+-bound state and the R201A-Na^+-bound states. Nevertheless, these are the most detailed experimental observations available and their authors proposed that the observed conformational changes are similar to those induced by $G_{\beta\gamma}$ binding, because the rearrangement of the CTCD under the R201A mutation are propagated from the C-linker to the βL-βM and the βD-βE loops which are shown to interact with G proteins (Whorton and MacKinnon 2011).

In more details, R201A-induced conformational changes begin with a twist of the βC-βD loop. It is observed as the rotation of Kir3.2 H233 from radially extended away from the principal axe of symmetry of the channel, to a state where the sidechain of H233 is placed in the void left by the missing sidechain atoms of the R201A mutation. It is noticeable that in both cases the Kir3.2 D228 in the βC-βD loop has the same orientation, i. e. pointing towards the C-linker. D228 in the wild-type interacts with R201, while in subunits Kir3.2-R201A with bound PIP_2 the ionic interaction is satisfied

by the H233, which is one of the nearest positive residues. Another positive residue near D228 is R230. This residue in the wild-type structure interacts with D81 from the sliding helix. The R230-D81 interaction is also observed in Kir3.2-R201A in both subunits lacking PIP_2 molecules. However, in the Kir3.2-R201A structure, the subunits with bound PIP_2 also display the twist of the βC-βD loop and the displacement of the H233. In this case, the R230 is not resolved probably because its interaction with D81 is sterically hindered by the sidechain of H233 which is displaced to interact with D228. In consequence, this event is potentially linked to the nearby destabilization of the sliding helix, i.e., the sliding helix is not resolved before position 82 in subunits of PDB:3SYQ where PIP_2 is modeled. Furthermore, by comparison of Kir3.2-R201A without PIP_2 (PDB:3SYP) and Kir3.2-R201A with bound PIP_2 (PDB:3SYQ), one notices that the sliding helix is more destabilized in the subunits where the PIP_2 is bound, than in the Kir3.2 wild-type structures without PIP_2 (PDB:3SYO) where the sliding helix is partially missing, and in the wild-type Kir3.2 in presence of PIP_2 (PDB:3SYA) where all the backbone atoms and most of the sidechains of the sliding helix are resolved. Next, reorganization of the CTDC caused by the Kir3.2 R201A mutation is propagated in two directions. The first one concerns the G-loop adjacent to the βC-βD loop where the H233 is displaced in response to PIP_2 binding. In this case, the βC-βD loop twists and moves away from the principal axis of symmetry, in fact one can observe that this displacement is followed by the adjacent G loop. Thus, in the subunits with bound PIP_2, the G-loop is in more expanded conformation than in the subunits without PIP_2. The G-loop is reorganized by the diaphragm-like rotation of sidechains of M313 and M319 clearing the K^+ permeation pathway of these hydrophobic residues. The net result is that the minimum observed diameter of the G-loop is increased to 10 Å compared to the 6 Å of the wild-type structure. Interestingly, in this conformation, surface of the G-loop gate is lined by the carbonyl oxygens of G318 and the sidechain hydroxyl group of T320 (Whorton and MacKinnon 2011). The second direction of propagation of the CTDC reorganization from R201A mutation is oriented towards the βD-βE loop and the βL-βM loop. In this case all β-strands of the CTDC move away from the principal axis of symmetry of the channel following the described motion of the βD-βD loop. Authors of the 3SYP structure point to residues V67, Y58, L257 and V276 as experiencing the strongest change in respect to the wild-type structure, as pointed by the RMSD analysis of the backbone heavy atoms and the first carbon of the sidechains. An important change is observed in the βF-βG loop containing the residue L273. This buried residue was initially thought as directly contacting the $G_{\beta\gamma}$ (He, Yan, Zhangţ, et al. 2002). In fact, in the Kir3.2-R201A structure, the βF-βG loop is approached by the βD strand as a result of the twist of the βC-βD loop. This reinforced contact between β-strands involves the L273 residue, thus authors propose that the actual role of L273 could be to transmit the conformational change from the G protein binding site towards the G-loop gate. At the same time, in the Kir3.2-R201A crystal structure, V276 in the apex of the βF-βG loop is getting closer to V67. In this conformation, one can also observe the approach of Y58 and C66 to V276, and the resulting minor twist at G60 of the backbone of the N_{ter} towards the βD-βE loop of the adjacent subunit.

2.7 Evidence of gating mechanism at the selectivity filter of Kir3

Equivalent to Kir3.2 E150: the KiR3.1(E141Q)/Kir3.4(E147Q) mutant has approximately one order of magnitude longer burst duration (10 vs 100 ms) and open duration (1 vs 10 ms) compared to wild-type heterotetramer (Alagem, Yesylevskyy, and Reuveny 2003).

In recent years a series of reports suggested that the dynamics of the selectivity filter of K^+ channels and KcsA in particular (Bernèche and Roux 2005) would contribute to the gating properties of the K^+ channel. The most prominent evidence came from the bacterial KcsA channel, where the E71A mutant is not capable of C-inactivation (Cordero-Morales et al. 2006). In Kir3 channels the mutation at the equivalent position to KcsA E71, the Kir3.4 E145Q causes the Kir3.1/Kir3.4(E145Q) channels to lose inward rectification (Dibb et al. 2003). The Kir3.4 residue R155 flanking the selectivity filter (equivalent to mmKir3.2 R160) has been identified as involved in the phenomenon of K^+-activation which consists of an increase of the conductance after a “first” K^+ contact has been established

(Claydon et al. 2004). Furthermore, The Kir3.1(E141Q)/Kir3.4(E147Q) mutant channel (equivalent to mmKir3.2 E152 positions) has approximately one order of magnitude longer burst duration (10 vs 100 ms) and open duration (1 vs 10 ms) than the wild-type heterotetramer (Alagem, Yesylevskyy, and Reuveny 2003). In Kir3.2, mutations of E152 to D, T, V, Q, A, H, G, S, I residues (listed in decreasing order in respect to the potentiation effect) all increased the open probability of the channel, as the current amplitudes ranged from 171% to 15,740% of those recorded for the wild-type channel (B. A. Yi et al. 2001). However, among these mutations, only E152D/Q/S/I preserved the selectivity to K^+ over Na^+. These reports suggested that the C-type inactivation is also present in the Kir3 channels. Furthermore, a recent study on KcsA demonstrated that the TM1-pore helix interface transmits conformational changes to the selectivity filter, thus mediating the change of binding affinity of the selectivity filter for K^+ (Heer et al. 2017). The latter interface in KcsA channels is at the equivalent position of Kir3.2 E152 residue, thus suggesting potential conservation of the gating properties of the selectivity filter in different K^+ channels including the Kir3 family.

2.8 *Activation of Kir3 by alcohol*

Initially, Kir3.2 activation by short monovalent alcohols was reported in experiments with Xenopus oocytes (Kobayashi et al. 1999; Lewohl et al. 1999). A direct interaction between the alcohol and the channel was suggested because there was no correlation between the change in lipid solubility, which is a function of the alcohol size, and the recorded currents. Furthermore, using a chimera between Kir3.2 and Kir2.1, a region of 43 amino acids in the CTCD was identified as critical for the alcohol sensitivity of Kir3.2 (Lewohl et al. 1999). Kir3.2 activation by acute extracellular application of monovalent alcohols follows a pattern of increasing effect depending on the size of the alcohol and this activation is independent of the amount of available G proteins (Kobayashi et al. 1999). Going from methanol to butanol, the greatest activation observed was with propanol. All alcohols except butanol activate the channel at concentrations from 0.1 to 200 mM. Butanol, up to a maximal concentration of 30 mM, also activated Kir3.2 in a dose-dependent manner. In contrast, 0.1 to 30 mM pentanol dose-dependently inhibited the outward currents (Kobayashi et al. 1999). The pattern of alcohol activation observed with Kir3.1/Kir3.4 is slightly different from that of Kir3.2. First, the maximum activation is approximately 2-times lower than what is observed with Kir3.2 over the same concentration range of 0.1 to 200 mM of methanol, ethanol and propanol. Moreover, the effect on Kir3.1/Kir3.4 of these three molecules had almost the same amplitude for equivalent concentrations, whereas the effect observed with Kir3.2 increases with the size of the alcohol. The inhibition pattern for Kir3.1/Kir3.4 channels started with the application of 0.1 to 30 mM of butanol and the channel was inhibited to a greater extent by 30 mM of pentanol. These discrepancies of the alcohol-induced effect on both channels suggested differences at the level of the binding pockets for alcohol between the brain and the heart channels. The alcohol binding pocket of Kir3.2 and of the Kir3.4 S143T mutant (Kir3.4*) was mapped by site mutagenesis guided by PDB:2GIX, i.e., the crystal structure of the Kir2.1 CTCD in complex with 2-methyl-2,4-pentanediol (MPD) (Pegan et al. 2006; Aryal et al. 2009). In whole-cell patch-clamp experiments with HEK-293T cells the MPD alcohol activated Kir3.2 to an intermediate extent compared to other monovalent alcohols, ethanol < MPD < pentanol for concentrations from 10 to 300mM. This effect was independent of the G protein activation of the channel. Residues involved in hydrophobic interactions in the MPD-Kir2.1 crystal structure were mapped to the Kir3.2 Y58, I244, L257, L342 and Y349, and residues involved in hydrogen-bonding interactions were mapped to Kir3.2 P256 and F254. Thus, the hydrophobic binding pocket appeared to be conserved between both channels. Authors found a correlation between the complementarity of the fit of the alcohol inside the binding pocket and the potency of the alcohol-induced activation. A series of mutations of residues in the putative alcohol binding pocket identified L257 as important for alcohol sensitivity for Gβγ. The substitution L275W abolished alcohol response and the sensitivity for Gβγ. Furthermore, authors used a Kir3.2 mutant highly sensitive to PIP_2 to access the rate of inhibition by MPD of a constitutively open Kir3. The results indicated that the hydrophobic binding pocket is not implicated in MPD inhibition. Rather the inhibition was mapped to the selectivity filter,

since the Kir3.2 S148T mutant showed an increase in the IC_{50} of the MPD as inhibitor. This conclusion is not completely convincing since the Kir3.2 S148T produces channels with higher activity, thus the increase in the IC_{50} of MPD inhibition can be seen as the result of a requirement to consume more alcohol to inhibit the more active channel.

Another study further demonstrated the role of the relationship between the size and the hydrophobicity within the alcohol binding pocket of Kir3.2 for the alcohol activation of the channel (Bodhinathan and Slesinger 2013). Authors tagged the alcohol binding pocket with methanethiosulfonate (MTS) containing compounds, thus manipulating the available volume of the pocket for soluble alcohols. Upon MTS modification of Kir3.2 L257C, small alcohols like ethanol and propanol, but not the bulkier MPD, could still activate the channel. These observations in correlation with the computation of the volumes of the pocket and of different alcohols suggested that the pocket has an effective volume of 312 $Å^3$ and that it can accommodate two ethanol (263 $Å^3$) or two propanol (290 $Å^3$) molecules at the same time.

In the scope of the above description of the Gβγ-Kir3.2 interaction site (see related paragraph), a parallel with the binding pocket of alcohol was drawn by Bodhinathan and Slesinger in 2013. Authors suggested that Gβ L55 engages into the alcohol binding pocket and activates the channel in a similar manner as the MTS-alcohol modification of Kir3.2 L257C (Bodhinathan and Slesinger 2013). While the hypothesis suggests that the pathways of activation by the G proteins and by the alcohol both converge to the same sensory region on the Kir3 channel, it is not completely clear whether the allosteric mechanism leading to channel activation is the same for both co-factors. At the moment, there is no crystal structure of the full-length Kir3 channel in complex with alcohol molecules which would allow comparison with the conformational changes caused by Gβγ binding. Nevertheless, this hypothesis was assumed to be correct in our work. Observations on the alcohol-Kir3.2 are provided in the results and discussed later.

Until very recently it was unclear whether the observed alcohol activation arose from a synergetic effect with another activating partner from the complex cellular environment, or simply by alcohol disturbance of the cell membrane. This uncertainty was addressed by Glaaser and colleagues in a minimalistic-environment *in vitro* experiment (Glaaser and Slesinger 2017). As described previously in the case of the PIP_2 activation of Kir3.2, authors reconstituted purified Kir3.2 into a lipid bilayer and used fluorescence-based assay to monitor channel activity. Ethanol or propanol require PIP_2 for activation of the channel. Propanol is more potent than ethanol, as both ligands are active starting at 10 mM and no apparent saturation of the activation is observed up to 200 mM. Moreover, authors showed that compounds modifying the elasticity of the membrane have no effect on Kir3.2 activity, thus ruling out that a membrane disturbance caused by the alcohol induces Kir3.2 activation.

2.9 *Influence of cholesterol on Kir3*

2.9.1 Cholesterol and effects on members of the Kir channels family

The most represented sterol in the plasma membrane is cholesterol with up to 45 mol%. Changes in cholesterol modify the physical properties of the membrane. Cholesterol has an effect on a variety of integral membrane proteins, including a direct effect on Kir channels *in vitro*, *in cellulo* and *in vivo* (Levitan 2009; Bukiya and Rosenhouse-Dantsker 2015). Interestingly, depending on the Kir sub-family, the observed cholesterol influence is different. For example, an increase in membrane cholesterol inhibits the whole-cell current of the constitutively open Kir2 channel but has no effect on the single channel properties, suggesting that cholesterol decreases the number of active channels by directly interacting with the protein (D'Avanzo et al. 2011). Cholesterol significantly inhibits Kir1.1 and Kir6.2, has no effect on Kir4, and activates Kir3.4 channels (Rosenhouse-Dantsker et al. 2010).

A series of reports suggested that the PIP_2 and cholesterol sensitivity of the channels are interconnected. Primarily, the Kir2.1 region comprising βD and βE strands from L222 to N251 (eq. mmKir3.2 I234 and N263) was identified as intervening in the cholesterol sensitivity of the channel (Epshtein et al. 2009). The mutation L222I decreases cholesterol inhibition of Kir2.1, suggesting that this residue which is exposed to the membrane directly interacts with cholesterol. The N251 residue is implicated in the constriction of the cytoplasmic vestibule. Later on, it was shown that the same molecular switch regulates the PIP_2 induced hydrogen-bonding network which propagates to the G-loop gate (Rosenhouse-Dantsker et al. 2012). Moreover, two studies using computational docking and mutagenesis identified the transmembrane inter-subunit interface as a second region implicated in the cholesterol sensitivity of Kir2.1 (Rosenhouse-Dantsker et al. 2013; Fürst et al. 2014). Namely, the residues in Kir2.1 whose mutation impair the cholesterol sensitivity are: L69, A70, V77, L85, V93, S95, I166, V167, I171, I175, M183. In the crystal structures, all these residues are located near the region where PIP_2 is observed bound to Kir2 and Kir3 channels, and as suggested by the large number of hydrophobic residues listed above, upon binding cholesterol could be stabilized via numerous van der Waals interactions. The proposed mechanism of the cholesterol-induced locking of the pore conformation into a persistent inactive state is that cholesterol induces a conformational change competing with the bending of the TM2 required for the opening of the HBC gate (see above) (Rosenhouse-Dantsker et al. 2013).

2.9.2 Effect of cholesterol on Kir3

Despite the opposite phenotypes of Kir2 and Kir3.4 towards cholesterol, authors reported that a mutation in the βC- βD loop, Kir3.4 I229L, impairs cholesterol sensitivity similarly to the equivalent mutation in Kir2.1, suggesting a common hotspot for cholesterol sensitivity in these two channels. *In vivo* observations showed that in atrial myocytes of rabbits treated with a high cholesterol diet, the currents mediated by Kir3 channels increased (Deng et al. 2012). In the same report, using a heterologous expression system, authors found that cholesterol activation is dependent on the Kir3.4 subunit because Kir3.1 F137S homomers were inhibited by the cholesterol enrichment in the *Xenopus* oocyte. When authors depleted the PIP_2, the run-down of the Kir3.4 S134T tetramers in presence of cholesterol was significantly slower than in the absence of cholesterol. However, it was concluded that this effect was not produced by the strengthening of the interaction between the PIP_2 and the channel because the currents of the mutant D233N were not sensitive to cholesterol nor to the depletion of PIP_2. Authors also demonstrated that the mechanism of cholesterol activation is Gβγ independent because the co-expression in Xenopus oocytes of Gβγ scavengers did not affect the cholesterol-induced activation of Kir3.4 homomers. Furthermore, it was shown that cholesterol exerts its potentiating effect on Kir3 channels not by modifying unitary conductance properties but by increasing the open probability of the channel (Bukiya et al. 2015). Cholesterol and PIP_2 enhance the open probability of Kir3.4 containing channels in a synergetic manner, as shown by recording reconstituted Kir3 channels in artificial lipid bilayers (Bukiya and Rosenhouse-Dantsker 2017). The residues whose mutation eliminated the cholesterol sensitivity of Kir3.4 form a hydrophobic pocket in the center of the TMD at the interface of two channel subunits, namely: M95L, L169V, V170F, I173V, V178I (eq. mmKir3.2 M100, L174, I175, V178, V183) (Figure 5A in (Bukiya and Rosenhouse-Dantsker 2017)). Thus, authors were able to distinguish different binding sites for cholesterol and PIP_2 in Kir3.4 and these sites are topologically similar to those observed in Kir2. Cholesterol at a molar ratio of at least 5 % has the same effect on Kir3.2 and Kir3.4, as shown by tests on reconstituted channels in liposomes containing 1 % PIP_2, whereas cholesterol by itself is not sufficient to activate Kir3.2 (Glaaser and Slesinger 2017). In 5 % cholesterol, authors measured a 2-fold increase from 25 μM to 12 μM of the Kir3.2 apparent affinity for PIP_2, showing the enhancement of PIP_2-channel interactions upon cholesterol binding. It was also demonstrated that activation of Kir3.2 by alcohol and by cholesterol are independent, although they require PIP_2.These observations led to a conclusion which is the contrary to the one made by Deng and colleagues that the cholesterol-induced activation of the Kir3.4 channel is not mediated by enhancement of the PIP_2-channel interactions (Deng et al. 2012).

2.10 RECTIFICATION

The rectification of Kir3 channels relies on the presence of intracellular co-factors such as Mg^{2+} and polyamines. A study using NMR have mapped the site in the Kir3 CTCD where polyamines could reside in a resting (non-blocking) state (Osawa et al. 2009). The authors have obtained evidence that two spermine molecules ($C_{12}N_4H_{28}^{4+}$) can be accommodated in pockets build from two adjacent subunits. The pocket as mapped on the cytoplasmic domain formed only by Kir3.1 subunits is located approximately 17 Å below the G-loop gate and contains the same set of residues X_i and X_{i+1} in both adjacent subunits *i* and *i+1* – In the Kir3.1 subunit these residues are: Q227, F255, D260, Q261. The mmKir3.2 equivalent residues are: S238, Y266, D271, R272. A modification of the above list can be made by observation of multiple sequence alignment where one can notice that the mmKir3.2 E270 appears as local substitution for the R272 residue in the context of interaction with positively charges partners. Such an adjustment of the polyamine biding residues is somehow relevant especially when considering the correspondences between different sub-family members. For instance, Kir2.1 D255 maps to Kir3.1 S256 and to mmKir3.2 Y267, while having full equivalents in the rest of the Kir3 sub-family – the Kir3.3 D233 and the Kir3.4 D262. Indeed Kir2.1 D255 has been identified in molecular modeling study along with residues E244 and D259 (J. L. Robertson, Palmer, and Roux 2012). The latter residues are of particular interest for this project because their position-equivalents in mmKir3.2 – residues E236, Y167 and D271, appeared to be responsible for the increased K+ concentration in the cytoplasmic vestibule of the simulated mmKir3.2 (see section 5). After the release of the polyamines from the resting-state pockets these molecules travel into the transmembrane vestibule of the channel under the influence of the outward-directed driving force for positive molecules – condition which occurs once the V_m approaches 0 mV (during depolarization of the cell). Then, the polyamines have been shown to be able to reach the selectivity filter in phenomenon called 'deep site' binding. This hypothesis has been derived from studies involving the Kir2.1 channel which possesses an aspartate in the middle of the TM2 (D172) (Kurata et al. 2013). It is believed that this aspartate is also involved in the Mg^{2+} mediated rectification. The D172 residue would be suitably located in order to stabilize the stretch of polyamine between the S4 site of the selectivity filter and the D172. Thus, has been proposed an explanation to the relation between the length of the polyamines and the potency of the observed rectification (John, Xie, and Weiss 2004). Interestingly, in the Kir3 sub-family only Kir3.1 has an equivalent to Kir2.1 D172 – residue D173. This is a potential evidence of the differential specialization of the Kir3.1 subunit as providing key Kir properties to the heterotetrameric Kir3 channels (Dibb et al. 2003). While mutation of Kir3.1 D173Q did not appeared as crucial for the inward rectification the mutations around the selectivity filter of Kir3 channels causes the polyamines to permeate through the selectivity filter.

2.11 PHARMACOLOGY

Here I propose a non-exhaustive list of references concerning natural substances and pharmacological agents that target directly the pore of the Kir3 channel. This list is short because specific modulators of Kir3 in particular, and Kir channels in general, are extremely scarce.

Monovalent alcohols are natural substance which activate Kir3 channels (see section 2.8). The honey bee venom extracted peptide tertiapin and its air-oxidation protected variant tertiapin-Q have been the first discovered Kir3 inhibitors (W. Jin and Lu 1998). The local anesthetic bupivacaine has been proposed to compete for the PIP2 binding site thus inhibiting the Kir3 channels (W. Zhou et al. 2001). Recently has been identified the interaction site for the hydrogen sulfide inhibition of Kir3 – it is at the conserved cysteine residue N_{ter} of Kir3 channels (Ha et al. 2018).

To date very few pharmacological agents have been developed to activate directly the Kir3 channels, among those are the naringin flavonoid glucoside (Yow et al. 2011) and the ML297 compound which has anxiolytic properties (Ramos-Hunter et al. 2013). Interestingly, the action of ML279 requires the presence of Kri3.1 subunits with intact F137 and D173 residues. The lead scanning around ML279 have proven fruitful for identification of selective inhibitors of Kir3.1 containing channels (Wen et al.

2013). More recently ML279 have been evolved into VLOGO soluble opto-pharmacological tool (Trads et al. 2017). Recently a selective Kir3.1/Kir3.2 activator have been derived from ML297 (Wen et al. 2014). Another recently identified Kir3 modulator is the N-(2-methoxyphenyl) benzenesulfonamide (Walsh et al. 2017), which have some structural similarity to the VLOGO compound.

2.12 PATHOLOGY

Several pathological mutations have been isolated from patients. Some of them are listed here. Kir3.2 L171R which increases the monovalent cationic conductance (Horvath et al. 2018), is associated with the Severe Hyperkinetic Movement Disorder. Also in Kir3.2, T152del and G154S increase the monovalent cationic conductance (Masotti et al. 2015). The associated condition is the Keppen-Lubinsky Syndrome. Several mutations were isolated in Kir3.4 proteins: G151R, T158A, L168R, G151E, I157S (Choi et al. 2011; Mulatero et al. 2012; Charmandari et al. 2012). These mutations increase Na^+ permeation through the channel and are associated with the Familial Hyperaldosteronism Type III. Additional Kir3.4 mutations resulting in the same pathological condition are R52H, E246K, E282Q. They decrease the inward rectification of the channel. Finally, a condition called Long QT syndrome involves the Kir3.4 G387R mutation, which decreases the K^+ conductance of the channels.

Further pathological implications of the Kir3 channels involve the wild-type channel implication in various physiological and pathological processes. For instance, alcohol and drugs addiction has been discussed to be partially mediated through mechanisms involving the Kir3 channels in the brain. Kir3 has been also proposed as implicated in epilepsy, Down's syndrome, Parkinson's disease (Lüscher and Slesinger 2010; de Velasco, McCall, and Wickman 2015; Mayfield, Blednov, and Harris 2015; Tipps and Buck 2015; Rifkin, Moss, and Slesinger 2017).

To date no pathological mutation involving the direct PIP_2-Kir3.2 has been identified, and the citations above are just a small fraction of reports emphasizing the modulatory nature of the PIP_2-Kir3 interactions which depends on the reorganization of the protein. On the other hand, PIP_2-channel interactions are targets for pharmacological agents and protein regulators such as protein kinases and indirectly by phospholipases.

From the above listing it is easy to understand the motivation to study Kir3 cannels beyond the scope of a fundamental research topic.

3 BACKGROUND TO STUDY AREA

The effort provided by the community researching the Kir family of potassium channels have generated a tremendous amount of functional data. In recent years the accumulation of knowledge about this protein-family expanded even faster by taking advantage of the newly available partial and complete experimental structural models. Despite the recent advances in the domain there are still many pending questions and unverified hypothesis around the Kir proteins.

Probably the most important scientific advance around the Kir3 channels in the last decade has been the unveiling of a set of crystallographic structures of the Kir3.2 homotetramer. The advantage of these complete molecular systems is that the gating machinery and the ligand interaction-sites can be observed intact and most probably having the right geometry, in comparison with the artificial structural rearrangements occurring in the earlier structural models obtained from truncated proteins and chimeric assemblies. These experimental models allow for detailed perception of the macro-molecules. However, the level of detail they allow is only of static nature, hence limiting the understanding of the dynamics in complex molecular machinery underlying the physiological function of Kir channels. In fact, the crystallographic models represent only distant "moments" of the

fate of the Kir3 system in action. In order to describe its dynamics, one has to make hypothesis based on series of interpretations of static images, rather than establishing a robust thesis based upon the causality observed in sequential mechanistic relations. Importantly, the recent improvement of the computational techniques and the hardware enables access to the complex dynamics of the macromolecules at relatively small cost.

Our project was made possible by the recent publication of a very complete crystallographic model of Kir3.2 partnered with the full set of physiological partners: four Gβγ dimers, four PIP_2 analog molecules, four Na^+ ions and a file of K^+ ions in the selectivity filter. The channel conformation in this crystallographic model is qualified as pre-open/pre-activated because the channel gates are not fully open as expected for the permeation of hydrated K^+ ions. The rest of the full-pore models include less complete ligand sets (Figure 1A). Using these crystallographic models one can now benefit from the high sequence identity between the Kir3 members and be confident to perform homology modeling out of the "shadow-zone" for any Kir3 homo- and heterotetramers, and every Kir3 mutant channels. However, there is a small portion of the Kir3.2 structure which still remains unknown, the first 52 N_{ter} and last 45 C_{ter} residues.

This structural data makes it possible to start extensive modeling of the molecular dynamics of the Kir3 channels – especially as the meso-scale simulations of biological macromolecules become cheaper due to modern computational tools and hardware. Vast number of theoretical techniques have been developed for the speeding-up of the conformational sampling and other for the analysis of the massive loads of data generated by the simulation of the molecular dynamics. A large number of methods now allow to compute quantities which are directly comparable to experimentally recorded spectra, thus giving the opportunity to align theory and experiments, and to use the computed trajectories of molecular dynamics as a molecular movie in order to observe with atomic-scale details the molecular phenomena of the systems.

Our main interest in this project is to exactly reproduce the molecular-dynamics "movie" of different Kir3 channels in order to provide high-resolution description of the molecular function of the channels. Our objective is to explain the molecular function of the native Kir3 channels and the role of several functionally important mutations – for instance, the single-point activating mutations Kir3(F137S) and Kir3.4(S143T). We believe that our approach would be equally successful to reproduce the molecular dynamics of any other Kir3 channel of interest. This work has relevance predominantly as fundamental research. Nevertheless, the atomic-scale dynamic data which was obtained during the work on the current doctoral thesis, could be readily employed to guide pharmacological development and protein-engineering about the Kir3.2 homotetrameric channel.

A second facet of the doctoral project consists of the protein-engineering of a light-sensitive Kir3 channel. This side project mainly consisted of the cysteine scanning of suitable positions for the labeling of Kir3 channels with a photoswitchable tethers ligands (PTL) which would allow to generate reversible photo-sensitive phenotypes. All the technological development employed in this project have been made available by previous efforts of the community. Our main challenge was to manually perform the screening protocol until identification of a positive hit among the screened positions. The development of photo-sensitive Kir3 channels is important because they could be used as tools to decipher the physiological role of these proteins in the different organs of vertebrates. This work could also find applications in synthetic biology development, and the functional interpretation of the photo-sensitive phenotypes could in theory reveal new aspects of the molecular function of the Kir3 channels.

4 METHODOLOGY

4.1 HOMOLOGY MODELING

Homology modeling was used to build all atom models of the proteins of interest in both projects. The software I used was MODELLER version 9.13 (Sali and Blundell 1993). In these models, only missing heavy atoms of the protein were generated and very few optimization options were applied, because of further minimization of the proteins during the MD simulation. Optimization options included: the degree of optimization by the variable target function method was set to *automodel.library_schedule.slow* and the number of steps *automodel.max_var_iter* was set to 500, *automodel.md_level.slow* setting the degree of use of simulated annealing (SA), the optimization was set to loop maximum 5 times (*automodel.repeat_optimisation*) unless it reached a maximum of the objective functions of 10^6 (*automodel.max molpdf*).

In order to guide the choice of the positions for cysteine mutagenesis, I produced homology models of the Kir3 constructs available in our laboratory. These constructs correspond to human Kir3.1 and Kir3.4 proteins. Additional models were made for the constructs containing mutations promoting the homomer activity of Kir3.1(F137S) and Kir3.4(S143T) (Chan et al. 1996; Vivaudou et al. 1997). These models used mmKir3.2 residues in the range 55 to 380.

Homology modeling was also used to prepare the Kir3.2 channel for MD simulation. The crystallographic model (PDB:4KFM) used as template represents quantitatively well the engineered functional Kir3.2 channel, which polypeptide consists of the native residues K52 to E380. One of the advantages to model the polypeptide of mmKir3.2 from PDB:4KFM is that the crystallographic model contains information about all backbone atoms of residues in the range I55 to N382. On the other hand, in order to model the alcohol binding pocket, I had to *de novo* model the residues KRK in the range 52 to 54. I chose to use PDB:2GIX as a template for the missing residues (Pegan et al. 2006). In this crystal structure, a MPD alcohol was co-crystalized in Kir2.1 near the residues equivalent to the putative binding pocket of Kir3.2 (Aryal et al. 2009). The modeling process was broken into two stages, because the template protein is a concatemer of the N_{ter} and the cytosolic C_{ter} domain of Kir2.1, thus in respect to the native adjacency of the N_{ter} and the C_{ter} in the Kir channels, the template mixes elements from two subunits into one polypeptide. Thus, the use of the template would require a trickier input alignment for the parametrization of MODELLER. I bypassed the use of MODELLER for the backbone generation step. To do so, I wrote a Python script which aligned each N_{ter} sequence (residues < 64 in mmKir3.2 numbering) between the CTCD of Kir2.1 (PDB:2GIX) and Kir3.2 (PDB:4KFM), and then simply copied the backbone from Kir2.1 to Kir3.2 for the missing K52, R53 and K54 residues. The script also copied all sidechain heavy atoms of the template which have equivalents into the Kir3.2 sequence, for instance: Kir2.1:S41:CB was copied into mmKir3.2:K52:CB and Kir2.1:H42:CB:CG was copied into mmKir3.2:R53:CB:CG. The subsequent modeling of all heavy atoms of the mmKir3.2 including the KRK sequence was made by MODELLER as described above. In the following sections of the manuscript I will refer to this construct including the residues K52 to N382 simply as mmKir3.2, it was used in the MD simulation setups.

I also modeled all atom $G_{\beta\gamma}$ dimers straight from the crystallographic models in PDB:4KFM, these constructs bound to the mmKir3.2 were also used in MD simulations. The positions of the all-atom $G_{\beta\gamma}$ in the complex with the channel were simply those from the crystallographic model PDB:4KFM. The G_{γ} monomer poses a terminal cysteine geranyl-geranyl modification which eventually reduces the degrees of freedom for the orientation of the $G_{\beta\gamma}$ dimer by anchoring it to the inner leaflet of the membrane. The topology and the forcefield parameters of this modification were taken from the standard library distributed in the CHARMM-BUILDER-GUI (Jo, Kim, and Im 2007; Jo et al. 2008; J. Lee et al. 2016).

4.2 MOLECULAR DYNAMICS SIMULATIONS

4.2.1 What is Molecular dynamics simulation and why I used it?

Molecular dynamics (MD) simulations are used as a computational microscope to provide insight on the nanoscale dynamic events occurring in the system. The classical MD simulations are called brute-force simulations, this methodology produces molecular "movies" which has the advantage to be rather intuitive in respect to their interpretation. However, its major disadvantage is that it requires considerable work to parametrize the force field able to precisely reproduce empirical data about the simulated system, furthermore the MD simulations require very intensive computational effort in order to produce sufficiently long trajectories where one could expect to properly sample the dynamic events of interest. Consequently, this method does not allow an efficient exploration of the ensemble of conformational states of complex systems at equilibrium i. e. the microscopic conformational events underlying the function of biological systems. Currently, the timescale of the exploration of large biological macromolecules are limited to the low-microsecond range, even when using very powerful supercomputers – thus not compatible with the timescales of hundreds of microseconds to seconds representative of the large conformational changes involved in the biological events that one often wants to model. Nevertheless, in this project, I used only classical MD simulations in order to preserve atomic details in the K^+ permeation through the channel and the ligand-protein interactions.

The MD simulation procedure consists in the iterative resolution of the instantaneous forces ($\boldsymbol{F}$) acting on each atom ($\boldsymbol{i}$) in the system with initial coordinates ($\boldsymbol{r}$), and the integration of these forces over time ($\boldsymbol{t}$). The instantaneous forces are derived from the potential energy U, which accounts for all molecular interactions involving the current atom $\boldsymbol{r_i}$:

$$F_{ri} = -\nabla U_{r_i} \quad r_i \text{ for } i = 1, 2, \dots, N$$

Using Newton's second law, new coordinates for the particle can be computed for an ulterior timestep:

$$F_i = m_i a_i = m_i \frac{(d^2 r_i)}{dt^2} \quad i = 1, 2, 3, \dots, N$$

The result of the iteration of these steps (forces computation, integration, generation of new coordinates) is called a MD *trajectory*, consisting of lists of coordinates and velocities for each atom obtained at successive timesteps.

The term U is derived from two input parameters, one is the set of instantaneous coordinates of each particle in the system, and the other describes the specific molecular interactions. The second parameter is called the force field, it contains information describing various aspects of the bonded and nonbonded interactions between particles. The force fields include: topology terms such as bond-lengths, angles between three bound particles and dihedral angles involving four consecutive covalently bound particles; interaction terms such as bond and angle vibration potentials, electrostatic and van der Waals interactions. The calculation of the potential energy function requires also parameters for the targeted temperature and the pressure at which the system will be studied. Thus, another expression can be written describing the MD as a stochastic process driven by the absolute temperature:

$$\begin{cases} dq_t = M^{-1} p_t dt \\ dp_t = -\nabla(q_t) dt - \gamma M^{-1} p_t dt + \sqrt{2\gamma\beta^{-1}} dW_t \end{cases}$$

The stochastic process $(q_t, p_t)_{t \geq 0}$ take values in R^d. The expression of q_t is equivalent to the notation of Newton's second law above, where $\boldsymbol{M}$ is the mass matrix and the rest expresses the gradient of potential energy function. The second expression contains terms for the interaction potentials $\boldsymbol{\nabla(q_t)}$, the friction given by the damping parameter $\boldsymbol{\gamma > 0}$, both stored into the forcefield. The last term

describes the Brownian motion $\boldsymbol{W}$ where the noise level of the thermal agitation is controlled by the inverse temperature $\boldsymbol{\beta}$.

While the targeted temperature and pressure are easily decided for each simulation, it is very complicated to parametrize the force fields. In general, they are tuned to reproduce experimental thermodynamic quantities for each specific interaction they describe. In the case when no experimental measure is available or accessible, the parameters are derived from Quantum-Mechanics (QM) calculations. More details on the theory of MD simulations can be found in textbooks, please see for example the introduction to the subject matter Frenkel and Smit (Frenkel and Smit 2002), and by Vlugt and colleagues (Vlugt et al. 2009).

4.2.2 Software used to generate and analyze the MD trajectories

4.2.2.1 Force field and simulation

Trajectories were generated using NAMD (Phillips et al. 2005). Visualization of the trajectories were made using VMD (Humphrey, Dalke, and Schulten 1996). Trajectory analysis was made by VMD inbuild modules, inhouse scripts were written in TCL run by VMD, and other Python scripts using the ProDy library (Bakan, Meireles, and Bahar 2011), and several standard libraries as SciPy, Numpy, Matplotlib.

Another very important piece of technology is the force field describing the molecular interaction between the constituents of the simulation box. I used an unmodified version of *CHARMM-36-July-2016* forcefield (Yin and MacKerell 1998; Vanommeslaeghe et al. 2009), which official distribution included parameters for every molecule type that I modeled in the simulations presented hereafter.

4.2.2.2 External electric field as driving force for K^+

I used an external electric field to induce an electrostatic drop along the axis normal to the membrane, thus providing driving force for the K^+ to permeate the mmKir3.2 pore. The validity of this approach for simulation of membrane potential is described elsewhere (Gumbart et al. 2012). Other methods exist for simulation of membrane potential in membrane simulations they were not used (but were tested) because of the need to restart the systems periodically (see below). like the double membrane setup where two water compartments are isolated by two lipid bilayers (Kutzner et al. 2011), the other alternative method is the one starting with a standard setup of the simulation box with one membrane this time the box dimensions are largely increased by a vacuum slab along the axe normal to the membrane (Delemotte et al. 2008). Both methods, thus allow to set a chemical gradient using alternative ion concentration in either isolated water compartments, the driving force in this case is purely chemical gradient and the bias is applied only to ions in solution while the method I used apply a bias on every atom in the simulation box. However, the chemical gradient with the described methods is often represented by a number only few ions differing between the compartments thus as soon as one ion transits from one side to the other the simulated membrane potential is decreased and the simulation have to be restarted with restored chemical gradient.

The activation of the external electric field is a NAMD standard feature (parameter: ***eField on***), it also requires to set the magnitude and the direction of the force (parameter: ***eForce x y z***) acting on all atoms of the system which was scaled by NAMD force constant $\boldsymbol{n} = 0.0434$ and the length of the cartesian axe $\boldsymbol{L}$ (Å) on along which the electric field is applied will develop the desired voltage $\boldsymbol{V}$ $(Volts)$:

$$eForce = \frac{V}{nL}$$

The desired magnitude of the potential drop is developed via the periodic boundary conditions between two equivalent points found in two adjacent periodic images of the system. For a system with length of the $\boldsymbol{z}$ axe $\boldsymbol{L_z}$ and applied constant electric field along this axe $\boldsymbol{E}$, the equation for the applied potential is:

$$V = EL_z$$

It follows that the profile of the electrostatic potential $\boldsymbol{\Phi}$ along the entire simulation box is an additive function, consisting of the reaction potential $\boldsymbol{R}$ measured in each point of the simulation box and the applied external electric field $\boldsymbol{E}$ (Gumbart et al. 2012). Thus, the voltage drop is conserved between equivalent points and the electrostatic profile can be displayed along one simulation box:

$$\Phi = R + V$$

In the following chapters, the representations of the profile of the electrostatic potential of the systems are obtained by the computation of $\boldsymbol{R}$ by VMD plugin PME, and by the subsequent handling of this data by personal Python scripts.

The list of software used during this work is not exhaustive. In the following chapters and in future publications, the proper citations will be made as data analysis using more proprietary software are shown.

4.2.2.3 Conformational changes

The evolution of the conformational changes of the protein in different simulations was followed by routine metrics: distances between groups of atoms, evolution of three-point and dihedral angles, root mean square deviation (RMSD), root mean square fluctuation (RMSF) and normal mode analysis by cartesian PCA.

A nonstandard metric that I adopted to evaluate the conformation is the probability of information transfer between nodes of the contacts matrix of the protein during the simulation. In other words, it measures the correlated motion of couples of nonbonded atoms (two Cα for instance) subjects to a distance threshold – if the measured correlation is high, it means that there is an information transfer along the edge connecting the two atoms modeled as vertices in an unoriented graph. Following this methodology, the set of instantaneous contact-networks for each frame of a MD trajectory is used to group the analyzed atoms into communities which shares concerted dynamical properties. This subdivision of the macromolecule allows to identify regions of the molecule which could be referred to as domains with specific functions. This metric has been used to describe the allosterically related conformational changes resulting from the binding of tRNA to the glutamyl-tRNA synthetase (Sethi et al. 2009). In brief, the method first filters couples of Cα atoms that remain close within a threshold distance $\check{\boldsymbol{l}}$, during a time period $\check{\boldsymbol{t}}$ of the simulation. Then, a pairwise correlation matrix $\boldsymbol{C_{ij}}$ is computed using the 3D deviation of each Cα from its average location $\Delta \boldsymbol{r_i}(\boldsymbol{t}) = \boldsymbol{r_i}(\boldsymbol{t}) - \langle \boldsymbol{r_i}(\boldsymbol{t}) \rangle$, where $\boldsymbol{r_i}(\boldsymbol{t})$ is the instantaneous cartesian coordinates of the i^{th} atom:

$$C_{ij} = \frac{\langle \Delta\vec{r_i}(t) \cdot \Delta\vec{r_j}(t) \rangle}{\left(\langle \Delta\vec{r_i}(t)^2 \rangle \, \langle \Delta\vec{r_j}(t)^2 \rangle \right)^{\frac{1}{2}}}$$

The resulting correlation matrix can be used to represent the information flow in the structure as a network where the nodes correspond to individual Cα atoms which passed the filtering step ($\check{\boldsymbol{l}} \cup \check{\boldsymbol{t}}$), and the length of the edges will correspond to $\boldsymbol{C_{ij}}$ directly or to its logarithmic transform:

$$d_{ij} = -log\left(\left|C_{ij}\right|\right)$$

The $\boldsymbol{C_{ij}}$ computation is made by the package *Carma* (Glykos 2006) and the VMD plugin *Network View* was developed to read the $\boldsymbol{C_{ij}}$ matrix, and allows for the exploration of the network via the use of TCL scripting. Moreover, the package *Carma* can be used to cluster nodes in communities by their proximity and by their mutual contacts. The splitting of the network in communities can be used to compare different simulation conditions if they induce change in the protein packing and concerted motions of neighbor residues.

To use this method for detection of the conformational changes in the protein in the same simulation, I split the simulation into bins of 75 ns ($\boldsymbol{b_{t=75\,ns}}$). This bin-length has been chosen because in our trajectories the protein starts to experience important conformational changes after approximately 40 ns of unrestrained simulation, and since the first bin comprises the equilibration run of 45 ns, I decided to set the bin length to 75 ns. The rational guiding this decision was to admit that the protein will behave mostly same during the first 75 ns all simulations irrespective of the constituents of the simulation boxes, thus allowing to discretize the signal describing the conformational changes during the next periods. The same separation in bins was used to compare bins from different simulations where the simulation conditions were equivalent or were varied. Also, I used $\check{\boldsymbol{l}} = 4.5$ Å, $\check{\boldsymbol{t}} = 75\%$ in all analysis.

When comparing couples of bins ($\boldsymbol{b_n}, \boldsymbol{b_m}$), I contrasted both correlation matrices by subtraction of the submatrices $\boldsymbol{C_{ij}^{h}}$, containing entries corresponding to separated protein subunits in the tetramer $\boldsymbol{h}$: $\{A, B, C, D\}$:

$$D_{ij}^{h_n h_m} = C_{ij}^{h_n} - C_{ij}^{h_m}$$

Note that in the above expression the terms $\boldsymbol{h}$ are not exponents but are simply index values for combinatorial notation and increments slower than the $\boldsymbol{ij}$ indexes. The resulting matrix thus contained values in the range $\boldsymbol{d_{ij}^{h_n h_m}}$: $\{-1, 1\}$, where values close to 0 resulted from input values which were almost identical in both matrices. At this point there were sixteen $\boldsymbol{D_{ij}^{h_n h_m}}$ matrices resulting from the *all vs. all* subtraction. The entries among $\boldsymbol{D_{ij}^{h_n h_m}}$ matrices were standardized, meaning that the binary encoded edges in all networks were set to *true* if the contacts between two Cα were observed in at least one $\boldsymbol{D_{ij}^{h_n h_m}}$. The subtraction step allowed the reduction of the number of non-zero entries in either $\boldsymbol{C_{ij}}$ from approximately 10^4 to less than 10^3. Next, I scored the importance of individual contacts $C\alpha_i C\alpha_j$ in the conformational change by performing dimensionality reduction using principal component analysis (PCA). To do so, I flattened the $\boldsymbol{D_{ij}^{h_n h_m}}$ matrices in one-dimensional lists $\boldsymbol{L_{ij}^{h_n h_m}}$, which were the inputs for PCA. Then, the loadings of each $C\alpha_i C\alpha_j$ in each principal component (PC_p) quantified the contribution of these contacts to the conformational difference between two protein subunits. The results of these comparisons were written into 2D arrays understandable by the VMD plugin Network View and have been used for visual interpretation and cross-referencing with bibliography.

4.2.3 Assembly of the simulation box: generic example

After the starting coordinates for the simulation were chosen, the next step was to prepare the all-atom simulation setup. The homology model of mmKir3.2 including residues in the range K52 to N382 described before was the starting point for all simulations where the channel was simulated without Gβγ dimers. The following subsections will briefly present the steps followed in the assembly of the simulation box.

4.2.3.1 Protonation of protein titratable groups

The very important parametrization of the charges of the titratable groups of the protein is meant to set the constituents of the macromolecule into a charged state equivalent to the one they should have at the targeted pH. Since most of the amino acids have theoretical pKa values well above or below the physiological pH=7, it is tempting to predict that their protonation state should simply be set to its default value while in solution at pH 7. On the other hand, residues as histidine and glutamate often experience pKa shifts in the vicinity of pH 7. The protonation of histidine is very often neutral. The choice has to be made between protonation of Nε or Nζ, this can be easily resolved by visually inspecting the hydrogen bond propensity of their environment. Nevertheless, histidine as it is the case with glutamate can be subject to a pKa shift which is influenced by their environment, this situation is more complicated, and it cannot be detected by eye. It appears that

such pKa shifts are detected when comparing the crystallographic models of both protein complexes vs. the protomers and the bound vs. unbound forms of ligand-protein complexes, as reviewed elsewhere (Onufriev and Alexov 2013). Different algorithms are available nowadays to automatically analyze the structure of interest and to predict the protonation state of each titratable group in the protein. The core of some methods relies on the Poisson-Boltzmann linear equation which provides a value of the cumulative columbic interactions in each point in space of the studied protein. Thus, simulated titration curves can be computed, leading to the prediction of the protonation state of each residue. Other techniques, such as PropKa (Olsson et al. 2011; Søndergaard et al. 2011) are knowledge-based using sets of empirical rules. A simple way to obtain such a prediction is to supply the conformation of the protein of interest to an online server which automatically handles the computation for the desired parameter set: H++ server (Gordon et al. 2005), PropKa. The disadvantage of this technique is that the result absolutely depends on the conformation of the starting structure – adding further uncertainty to the overall lack of precision these techniques. Another strategy is to locally update the conformations of the protein around each titratable residue in order to reduce the potential energy, for instance the ROSIE server provides such repacking routine (Kilambi and Gray 2012; Lyskov et al. 2013).

To decide of the charged state of each residue in the homology model of mmKir3.2 I used both software cited above. However, the position of the proton on neutral histidine required visual inspection of the packing around the residues in order to privilege the formation of hydrogen bonds.

The protonation setup for several residues that required decision making is further described in a dedicated paragraph in the results chapter (see section 5.1.2 and Table 1).

4.2.3.2 Solvation of the protein in membrane and water

The easiest way for water solvation is to use the functionality of VMD. It is an automatic method which consists in the replication of a small volume of an equilibrated water bulk along the three cartesian coordinate axes of the newly generated simulation box. Next, all water molecules detected to sterically clash with any of the non-water atoms are removed. However, this technique is not suitable to efficiently fill the channel's transmembrane vestibule. The orientation of the water confined in the TM vestibule (TMV) is expected to be different from the one water adopts in a bulk solution, mainly due to the presence of hydrophobic and hydrophilic surfaces which control the entropy of the solvent. Thus, I used the program *SOLVATE* (Grubmüller and Groll 2013), which has the advantage to generate disordered water in the vicinity of the solute and then to further locally minimize the positions of all water molecules, thus providing a fluid water model around the solute.

The next step was to place the protein into the lipid bilayer model of the cytoplasmic membrane. Here again one can use the automation provided by VMD, but I have chosen to take advantage of available molten membrane models. I used a bilayer of pure POPC, which was equilibrated while enforcing a cylindrical pore with radius of 22 Å in the center, such patches are available on the CHARMM-GUI website [*http://www.charmm-gui.org/?doc=archive&lib=lipid_pore*] (Jo, Kim, and Im 2007; Jo et al. 2008). This bilayer patch was aligned with the region of the protein spanning from W91 to I116 in the TM1, and P167 to I195 in the TM2, as predicted by the OPM database (Lomize et al. 2012). After a minimization in vacuum of the protein-membrane system, I performed visual and manual corrections to remove all lipid fragments inserted into rings of amino acids (these last modifications required additional minimization step).

Then, I merged the information about the solvated protein and the protein inserted into the lipid bilayer and I removed all water molecules in the interface between the lipids and the protein. At this point, the protein in the membrane-protein assembly was surrounded by a thin layer of fluid water and the interior of the pore was also filled, this atomic ensemble was further solvated by the VMD solvate-plugin and the salinity of the system was set to 600 mM KCl also using VMD ionize-plugin. Special care was taken to avoid chlorine and extra potassium ions to be present into the TMV. Thus,

the TMV and the selectivity filter of the channel contained only K^+ ions in the positions found in the crystallographic model PDB:4KFM.

Until now I have described the assembly of the system where mmKir3.2 was modeled without any ligands. For the subsequent addition of PIP_2, POPG, Na^+ and propanol, I proceeded accordingly to the scheme described in Table 1. PIP_2 was generated at three different sites by mutation of POPC lipids. These sites are described in the chapter presenting the results of the project. The Na^+ and the propanol were simply generated inside their respective binding pockets and the subsequent minimization of the all-atom system took care of the steric clashes. Moreover, in order to simulate the concentration of Na^+ and propanol indicated in Table 1, I placed extra molecules at random positions in the bulk distant at least 20 Å from the protein.

4.2.4 Precision on the nomenclature of the subunits of Kir3.2 homotetramer

The homotetramer of Kir3.2 has four undistinguishable subunits, unfortunately the observed in our MD trajectories behavior of these subunits was never four-fold symmetric, thus we decided to adopt special nomenclature to designate each subunit. The subunits were name P1, P2, P3, P4 with subunit P1 being equivalent to the chain A in PDB:4KFM (Whorton and MacKinnon 2013), then viewed from extracellular side P2 is the diametrically opposed subunit to P1, while P3 is adjacent to P1 in the clockwise order and P4 is adjacent to P1 in the counterclockwise order. Furthermore, in our figures subunits P1-P4 are always colored with the same coloring scheme: P1 (red), P2 (blue), P3 (grey), P4 (green). This coloring scheme is always respected unless specified otherwise.

Additional nomenclature is used to refer to the subunits in the clockwise order. Thus, for example if the reference subunit is P1, we name subunit P1 "SELF" or "S". Then P3 is called "NEXT" or "N", P2 is called "OPPOSIT" or "O", and P4 is called "previous" or "P". The same "S-N-O-P" nomenclature is applied to each subunit P1-P4 when each of these subunits is regarded as reference subunits for analysis purposes. For example, when comparing the timeseries of interatomic distances (*d*) in each one of the subunits, the distance involving atoms *i* and *j* in subunit P1 will be referred as *SELF:i~SELF:j* and the corresponding distances in subunit P2 will be referred to as *OPPOSITE:i~OPPOSITE:j*.

4.2.5 Remark about the measurement of the opening of the pore of the Kir3.2 channel

Per se, one of the computational tools that was used in this project to describe the protein dynamics has a major drawback. The HOLE software (Smart et al. 1996) provided us with means to compare the topology of the pore of the Kir3.2 among the different atomic setups that we have simulated. While the results obtained from the software are meaningful in the perspective of a relative comparison of the bottleneck between two simulations, these results do not correspond to the actual diameter of the opening at certain point along the K+ permeation pathway. The disagreement between the measure of the HOLE software and the actual situation of K+ permeation observed in each simulation arises from the methodology of the software. In fact, HOLE scans the pore with a rigid sphere which radius is modified as to place the largest sphere at each position along the permeation pathway. On the first place, this methodology is very sensitive to the values of the vdW radii used to model each atom type – in our case we used the AMBER forcefield parameters as default in HOLE. Next, the representation of the pore profile with stacked hard-spheres is far for the reality on one hand, of the asymmetric evolution of the pore elements (in the tetramer), and on the other it does not takes into account the partial dehydration of the K^+ solvent shell which is possible (phenomenon experimentally described for the K^+ and selectivity filter interactions) and which was observed in our simulations. These, three biases result in the final impression that on the plots of pore profiles none of the pores observed in the set of nine simulations presented hereafter was not large enough to accommodate a K^+ ion or to allow a hydrated K^+ ion to permeate. Thus, these pore profiles should be regarded only in the scope of comparison between the profiles measured in similar conditions, and not at all as proof/suggestion of the width of the opening of particular gate – a concept which is inherited from the symmetry observed in crystallographic models and a paradigm

irrelevant in the case of our unrestrained dynamic modeling which is sole driven by the simulated thermostat.

4.3 MOLECULAR BIOLOGY

Initially, Kir3 cDNA was sub-cloned by two successive PCR reactions into the dual-expression pXoom vector. The pXoom vector was developed for high expression of RNA-derived proteins in Xenopus oocytes (Jespersen et al. 2002). The vector is suitable for in-vitro transcription of mRNA using the T7 or the SP6 promoters. The mRNA produced is optimized for oocyte expression as it contains untranslated 5' and 3' of the highly-expressed globin gene. The pXoom vector also contains a promoter for expression in mammalian cells under the CMV promoter. Two resistance genes allow for the selection of transfected cells: (*neoR-GFP*) neomycin resistance of eukaryotic cells with fused green fluorescent protein (*GFP*), (*kanaR*) kanamycin resistance of bacteria.

The human Kir3.1 and the human Kir3.4 cDNAs were extracted from previously available constructs sub-cloned in pGH3 vectors. All cysteine mutations were introduced by PCR (*QuikChange Lightning Site-Directed Mutagenesis Kit #210519*, Agilent Technologies) using directed single site mutagenesis oligonucleotides containing cysteine codon GTG. Oligonucleotides were synthetized by the company GeneWiz, Grenoble. *E. coli* XL10-Gold ultra-competent cells (*#200314*, Agilent) were transformed in liquid LB-broth and plated on the same medium supplemented with agarose (compounds from Sigma-Aldrich). The integrity of the mutated coding sequences was accessed by Sanger sequencing (company GeneWiz, Grenoble). All mutated Kir3 genes were transcribed *in vitro* (*SP6/T7 Transcription Kit*, Thermo Fisher) and mRNAs were stored at -80°C in sterile polypropylene Eppendorf® tubes (*#T9661*, Sigma-Aldrich).

4.4 ELECTROPHYSIOLOGY

4.4.1 Handling of Xenopus laevis oocytes

Oocytes were available from two sources, enabling the use of two batches of oocytes per week. Each Monday ovary lobes were collected from animals sold by CRB Xénopes and maintained in the CEA animal facilities close to our institute. Each Wednesday ovary lobes were received from a commercial seller (CRB Xénopes, Université de Rennes 1, France). Electrophysiological tests were usually performed 1 to 4 days after reception of ovary lobes.

Ovary lobes were stored in *buffer A*: 88 mM NaCl, 1 mM KCl, 2.4 mM NaHCO3, 0.82 mM MgSO4, 16 mM NaOH-HEPES (pH 7.4) (prepared *in situ* from dry compounds from Sigma-Aldrich). Digestion of the conjunctive tissue of the ovary lobes was performed by three successive baths (40 min.) of *collagenase A* [20mM] (*#C-9891*, Sigma-Aldrich) in *buffer A*. Isolated oocytes were incubated in *buffer A+B*: *buffer A + 0.3 mM Ca (NO3)2, 0.41 mM CaCl2* (prepared *in situ* from dry compounds from Sigma-Aldrich), which usually was protected by penicillin-streptomycin-gentamycin: 100 U/ml penicillin, 100 µg/ml streptomycin, 100 µg/ml gentamycin (*#P4333* and *#G1264*, Sigma-Aldrich) to prevent bacterial and fungal contaminations.

4.4.2 Microinjection of Xenopus laevis oocytes

Manual microinjection of mixture of mRNAs was used to express Kir3 channels of interest in the *Xenopus* oocytes. The activation of Kir3 in *Xenopus* oocytes was induced by the activation of heterologous expressed G-protein coupled receptors (GPCR). I used human M2 or delta-opioid receptors subcloned into pXoom, prepared by other members of the team following the same protocols as described above.

Each oocyte received 50 nL of mRNA mixture, containing the needed amount of mRNA stock solution diluted into demineralized water. The injections were performed with a manual microinjector (*NanoJect2*, Drumond®) mounted with glass pipets filled with the mRNA mixture and using mineral

oil (Sigma-Aldrich) as hermetic insulator for the injector piston. The thick-wall borosilicate glass capillaries (BF100-50-7.5, Sutter Instruments Co.) were broken into two needle-like tips using micropipette puller apparatus (Model P-97, Sutter Instruments Co.), and then manually cut with sterilized surgical tweezers to obtain an injection tip with an outside diameter of about 12-20 µm, verified under a monocular microscope with a ruler grid in the objective.

The variability of the quality of the *in vitro* prepared mRNAs required the adjustment of the amounts of mRNA injected in each oocyte. In order to record whole-cell currents >1 µA 24 to 48 hours after the injection, each oocyte received: 0.5 or 5 ng of Kir3 mRNA and 2.5 ng of mRNA of GPCR in the case of homomeric Kir3 channels; 0.25 or 2.5 ng of each Kir3 mRNA and 2.5 of mRNA of GPCR in the case of heteromeric Kir3. In addition, in some periods from 2015 to 2018 the *buffer A+B+peni-strep-gen* where oocytes were incubating after microinjection with mRNA was supplemented by 20 mM KCl. This was done in order to reduce intracellular K^+ depletion due to the important basal activity of the Kir3 channels. As a result, the mortality of the injected oocytes was reduced and no negative effect was observed on the Kir3 expression levels (data not shown). Oocytes were usually not recorded after more than 72 hours of expression because the physical quality of the cells was severely degraded, suggesting high levels of expression of the heterologous constructs.

4.4.3 TEVC recording

The two-electrode voltage-clamping (TEVC) recordings were made with a manual setup equipped with the *Digidata 1440A* digitizer from Axon Instruments®, an amplifier *GeneClamp 500B* from Axon Instruments® and an eight-channel perfusion system with a manually operated controller from AutoMate Scientific®. For opto-genetics recordings of the *Xenopus* oocytes, this setup was mounted with a two-channel LED light source from CAIRN Research, both LEDs (380nm and 500nm) have an input power consumption of 1 Watt. The effective illumination power on the oocyte was not measured because the hardware setup requires the repositioning of the light source before each experimentation and the level of the bath solution was also variable.

In most cases the TEVC recording protocol consisted of the repeated application of "sweeps" where the membrane potential was clamped stage-wise at different potentials. A sweep lasting 5 sec was constituted by the suite: 0 mV, -50 mV, 0 mV, +50 mV, 0 mV; a representative recording of the obtained current profile is shown in Figure 42C. The protocol started with a measurement in *low K^+* buffer. This step allowed to establish the zero-level of the K^+ current of each oocyte. If the oocyte had currents in the *low K^+* buffer above 0.5 µA it was rejected, because of the relatively high non-specific currents (the oocyte at rest is expected to not have significant ion permeability). The *low K^+* buffer (named ND96) contained: 91 mM NaCl, 2 mM KCl, 1.8 mM CaCl2, 1 mM MgCl2, 0.3 mM niflumic acid, 5 mM NaOH-HEPES (pH 7.4). Then the buffer was changed to *high K^+* containing: 91 mM KCl, 1.8 mM CaCl2, 1 mM MgCl2, 0.3 mM niflumic acid, 5 mM KOH–HEPES (pH 7.4). In these conditions the magnitude of recorded current increased due to the K^+ transport from the extracellular medium to the cytosol ($I_{K_{ctrl}}$). In the case of equimolar K^+ concentration in and out of the cell, the driving force for potassium is provided by the electrical gradient set by voltage-clamping electronics. The GPCR-induced activation ($I_{K_{act}}$) of Kir3 was accessed in *high K^+* buffer. After measuring the activation, a brief period of washing in pure high K^+ buffer preceded the final addition of 3 mM of Ba^{2+}. The non-specific K^+ channel blocker was used to measure the zero-level of Ba^{2+}-sensitive K^+ current (I_{K_0}).

4.4.3.1 Photoswitching compounds

Several photosensitive tethered ligands (PTLs) have been tested. All tested compounds share a common chemical composition except for the terminal group which determines their specificity. These compounds encompass three functional chemical groups synthetized in a linear fashion: maleimide, azobenzene and a specific purpose radical. The three functional groups are spaced by amide groups used to adjust the length of the compounds. Here I will describe one of the PTLs named MAQ for: maleimide, azobenzene, quaternary ammonium. The MAQ was designed and successfully used to obtain the photo-blocking of the K^+ Shaker channel (Banghart et al. 2004) and

the same function has since been transposed to other K^+ channels (Fortin et al. 2011). The terminal maleimide moiety can spontaneously react at pH 6.5-7.5 with the sulfhydryl group of reduced cysteine to irreversibly form a thioether linkage. The azobenzene group placed in the center of the molecule confers to the PTL its reversible photoswitching properties. The azobenzene moiety has a tendency to relax to its trans state in the dark, nevertheless (I was told by an expert that) one should expect a mixture of isomer states in the MAQ stock solution – approximately 40% cis and 60% trans. The MAQ trans-state isomer is achieved upon illumination with a green light of 500 nm, while the cis-state isomer is the major population upon near-ultraviolet light illumination ~380 nm. The terminal quaternary ammonium is mounted with ethyl chains, its function is to block the K^+ channel block by targeting the outer vestibule of the selectivity filter. This design was inspired by the well-known observation of the blocking of various K^+ channels by soluble tetraethyl-ammonium (TEA). The block is achieved because of the electrostatic attraction of the positive TEA by the selectivity filter. The TEA remains stuck to one side of the filter because of the sterically incompatibility with the K^+ permeation pathway, thus competing with the K^+ permeation. The other PTLs that were tested have the following compositions: maleimide-amide-azobenzene (MAP), maleimide-amide-azobenzene-amide-NH_3 (MAC), maleimide-amide-azobenzene-amide-SO_3^- (MAS), maleimide-CH_2-amide-azobenzene-amide-SO_3^- (MEAS), maleimide-CH_2-amide-azobenzene-amide-$N(CH_2CH_3)_3^+$ (MEAQ). The exact absorption spectrum of different azobenzene containing molecules varies with the geometry and the atomic composition of the molecule. Thus, the wavelengths cited above are those of the MAQ tether. The absorption spectra of the other PTLs are somehow similar according to our collaborator.

4.4.3.2 Data analysis

The analysis of the recording traces was automated by the use of *eeTECV* and *eeSTAT* software developed by our team (Vivaudou et al. 2017). The software are *Excel* macros and they also automate the graphing of the statistics of individual recordings and of the ensemble of experiments. In the dedicated chapter, the quantity of interest reported in the bar charts is the classically monitored normalized mean effect of the activation $\bar{\boldsymbol{N}}$ and its standard error of the mean $\boldsymbol{\sigma_{\bar{N}}}$. It summarizes by simple averaging among all equivalent recordings $\boldsymbol{n}$, the comparisons of the normalized currents before activation ($\hat{\boldsymbol{I}}_{\boldsymbol{K_{ctrl}}}$) and after activation ($\hat{\boldsymbol{I}}_{\boldsymbol{K_{act}}}$):

$$\hat{I}_{K_{ctrl}} = I_{K_{ctrl}} - I_{K_0}$$

$$\hat{I}_{K_{act}} = I_{K_{act}} - I_{K_0}$$

$$N_i = \frac{\hat{I}_{K_{ctrl}}(i)}{\hat{I}_{K_{act}}(i)}, \text{ for } i: \{1, n\}$$

$$\bar{N} = \frac{1}{n}\sum_{i=1}^{n} N_i$$

$$\sigma_{\bar{N}} = \frac{s}{\sqrt{n}}$$

$$s = \sqrt{\frac{1}{n-1}\sum_{i=1}^{n}(N_i - \bar{N})^2}, \text{ with } n > 1$$

where $\boldsymbol{s}$ is the corrected sample standard deviation. The estimator $\boldsymbol{\sigma_{\bar{N}}}$ should not be confused with confidence intervals, it only indicates the precision of the estimation of the population mean given the data.

In the experiments using the light source, a comparison was made between the currents recorded at 380 nm vs. 500 nm obtained in the same testing conditions ($I_{K_{ctrl}}$ or $I_{K_{act}}$). These experimental conditions will be denoted as the exponents in addition to the code names of the photosensitive ligands. For instance, $\bar{\boldsymbol{N}}_{\boldsymbol{K_{ctrl}}}^{\boldsymbol{MAQ:380}}$ denotes the average effect of activation of the currents induced by

the 380 nm vs. the 500 nm light, recorded while the oocytes labeled with the MAQ tether were perfused with the control buffer. In the same way if the code name of the PTL is not present, it indicates that the oocytes were light treated but not soaked into PTL containing solution prior to the recording.

5 *IN SILICO ACTIVATION OF KIR3.2: RESULTS AND DISCUSSION*

Two possible main strategies can be used to activate the Kir3 and of course a combination of both is also possible. The first consists in applying external forces acting on parts or on the whole channel in order to produce conformational disturbances leading to the change of the opening of the channel. The second possibility would be to model interaction with pharmacological activators, thus mimicking naturally occurring processes. In respect with the first possibility, a large amount of work had already been made by the community studying Kir channels before I started to work on this project. Recently, the conformational transition from closed to open state of the Kir2.1 channel has been simulated (J. Li et al. 2015b). Authors used targeted molecular dynamics protocol where an external force was acting on specific parts of the channel in order to reduce the RMSD between the starting and the targeted conformation. Thus, they showed that the folding of the C-linker in α-helix is a transition step before the opening of the channel. The other hotspots of the channel where force was set to action were the slide helix and part of the N_{ter} of the channel. The steering of these two parts of the channel revealed itself to be sufficient to change the conformation from the closed to the open state. Nevertheless, in my view this procedure has several flaws despite the fact that the hotspots on which the external force was set to act are consistent with many other reports and they are undoubtably correct. The first problem with the targeted protocol is the very strong assumption of the opened conformation of the channel and in particular the conformations of the C-linker and the slide helix. These two structures are poorly to not resolved in the targeted templates, thus requiring *de novo* modeling a procedure which is subject to very large uncertainty. Precisely, the templates of the closed state of Kir2.2 channel (PDB:3JYC) and the partially opened state of the Kir3.2 (PDB:3SYQ) lack the slide helix, and this second template is only two-fold symmetric in respect to the opening of the G-loop gate. Furthermore, the applied external force used to drive the dynamics were set to 500kcal/mol/Å^2 which appears to be so strong that one may expect to obtain any type of fold regardless of the existing energetic barrier in the conformational landscape of the folded wild-type protein. Thus, I did not find arguments convincing enough to use this type of methodologies in order to simulate the open state of the Kir3 channels. Especially since for the moment there is no consensus on the conformation of the open state and any wide opening of the gates may be considered as such. This is why I chose to simulate the Kir3 channels in presence of a combination of ligands which are experimentally confirmed as sufficient to induce the opened state of the channel.

I will proceed with a brief description of the assembly process of the simulated all-atom setups and then I will present my observations in detail for each simulation experiment.

5.1 *BUILDING THE SIMULATION BOX*

5.1.1 *Starting atomic coordinates for Kir3*

The input coordinates for the Kir3 channel were taken from the PDB:4KFM (Whorton and MacKinnon 2013). This crystal structure contains an engineered mouse Kir3.2 homotetramer in presence of four Gβγ dimers of the heterotrimeric guanine nucleotide-binding protein (G-protein), four short-tail C_8-PIP_2 (dioctanoyl, L-α-Phosphatidyl-D-myo-inositol 4,5-diphosphate), four Na^+ ions, five K^+ ions and four detergent molecules DDM (n-Dodecyl β-D-maltoside), surprisingly no water molecules are present in the crystallographic model. The wild-type sequence of the mouse Kir3.2 (mKir3.2) used in the assay contains residues 50 to 380, the N-terminus is flanked by M-A peptide and the C-terminus is flanked by S-N-S-L-E-V-L-F-Q peptide (residual from an EcoRI cloning site and the PreScission

recognition sequence (Feng et al. 2010)). In contrast to other structures of Kir3, this crystal structure has the advantage to display continuous peptide main chain in all Kir3.2 subunits, and only the K50, R51, K52 of the wild-type sequence were not resolved. Furthermore, few sidechains are partially or completely missing and those in residues are predominantly on the protein-water interface. Thus, this input coordinates required only a minor effort of *de novo* modeling made by the topology generator program PSFGEN of the NAMD suite.

5.1.2 Protonation state of titratable groups of Kir3.2

To decide of the protonation state of titratable groups in the protein I used three programs: H++ server (Gordon et al. 2005), ROSIE server (Kilambi and Gray 2012; Lyskov et al. 2013) and PropKa 3.0 standalone program (Olsson et al. 2011). These programs use continuum electrostatic models to compute and statistical mechanics to accept or reject the ionization state of titratable groups interacting with their local environment, thus predicting the pKas as the midpoint of the simulated titration curve. Whereas, H++ and PropKa run the calculation on the rigid input protein, whereas the ROSIE procedure was set to use local repacking around titratable sidechains before the pKa prediction. The results obtained by the different methods are listed in Table 1. An important point about the analyzed structure is that the crystallization conditions comprise a pH of 5.8 and a salinity of 600 mM NaK tartrate, thus both histidine reported in Table 1 should be protonated in the crystallized state, the same conclusion could also apply to the acidic residues in the table. Thus, the calculation of the simulated titration curves is biased by the conformation adopted by these putatively protonated residues and the task of deciding which of these protonated states would be preserved at pH 7.0 become trickier. The pKa shift of a titratable group of amino acid is admitted to be significant if it is larger than 1 pKa unit in respect to the control value of pKa in solution (Onufriev and Alexov 2013).

The first residue in this list is the H68 which was the only residue in the ROSIE output predicted with a pKa shift increased above 7.0. The proximity of the H68:HE2 atom to the V67:O suggested that this histidine could be a donor of hydrogen bond to its neighbor. The second interaction detected by ROSIE could have been a cation-π interaction involving the protonated state H68:HD2 which confers a net positive charge to the histidine sidechain, with the π system of the F348 sidechain. Nevertheless, this second interaction was not included in the generated topologies reported here as I have considered the possibility of the existing protonated state due to the low pH during the crystallization process. Moreover, I did not encounter any reference on the pH sensitivity of this residue in Kir3 and it would require to further combine alternative ionization setups in order to investigate if this residue is involved in a pH sensing phenomenon.

The residue H125 has been pointed by both software with an increased pKa shift, only H++ server output a value past the 7.0 mark. This detection of the increase of the pKa of H125 is in accordance with the experimental report of the pH sensor properties of the residue. It has been showed that the presence of a histidine at this position in Kir3.1 H117 and Kir3.4 H120 causes the inactivation of the channels at pH 8.0 and it activates the currents by 70% and 30% respectively at pH 6.2 (Mao et al. 2002). Despite the fact that I do not know of experimental reports concerning pH sensitivity of H125, in the latest version of the topology setup I set the protonated state of H125 to double protonated. The initial simulations did not include the positively charged H125 because there were only one sharply increased pKa value reported by H++, my opinion on this matter changed after I read the article of Mao *et al*.

The G150 residue has also been detected with significant pKa shift. The equivalent of this residue E71 in KcsA channels is admitted to be protonated because in crystal structures it is seen to interact with another glutamate E80 at the C_{ter} of the selectivity filter and this interaction is linked to the C-type deactivation of the selectivity filter of KcsA (Bernèche and Roux 2002; Cordero-Morales et al. 2011). In the KcsA, the E71 participates in a grouped interaction involving also W67 - E80 - R89, none of these residues has equivalent residues providing the same interaction network in the Kir3.2 protein.

In details, the KcsA W67 aligns with mmKir3.2 L164, the KcsA E80 has as counterpart mmKir3.2 Y159 and the KcsA R89 does not match the mmKir3.2 G169. Furthermore, in crystal structures of mmKir3.2 obtained at pH 5.8, the sidechain of E150 is close to the sidechain of R160 and the backbone nitrogen of G158. Considering these contacts, there is only one possibility of a hydrogen-bonding configuration which is such that the R160 and G158 are donors and E150 is the acceptor of the hydrogen bonds. Thus, I have adopted the hypothesis of the charged state of the E150 in all topology setups.

The residue E152 has been predicted with large pKa shift by both procedures which have evaluated the rigid body of the crystal structure in contrast to the conserved titration midpoint accessed by ROSIE after local repacking procedure. Here again it is likely that the conformation of this residue in the crystal structure is influenced by the crystallographic conditions of low pH. After inspection of the unmodified crystallographic model, I have noticed the hydrophobic environment of E152. The only residue prone to partner with the carboxylate group of E152 is T105, and it is less likely that this interaction will involve the carboxylate group in its charged state. It is a well-established fact that the ionization state of the glutamate residues shifts to neutral when the carboxylate function of the sidechain is located into a hydrophobic environment. Observations of such pKa shifts suggest the reversible nature of a mechanism implied in the molecular function of dynamic proteins, this is a rather common phenomenon and has been reviewed on the basis of comparison of large sets of crystal structures in the work of Onufriev and Alexov (Onufriev and Alexov 2013). I rationally admitted the existence of the protonated state of E152 and have implemented it in the topology of the starting models. After I produced some MD trajectories, I noticed the dynamic behavior of the E152 sidechain, this brought me to further investigate the ionization state of this residue and I will describe my findings later in a dedicated subsection of this chapter.

The residues E236 and D271 have also been predicted with large pKa shifts by the procedures

Table 1: Predicted pK_a shifts of titratable sidechain groups in the mmKir3.2 homotetramer from PDB:4KFM. Three programs were used in parallel for accessing the ionization state of all titratable groups in the protein in 600mM KCl solution. Residues with predicted pK_a shifts increasing above 7.0 are listed in rows and the predicted pK_a values are displayed in the 4th-5th-6th columns: (cyan) predicted pK_a shift ≥ 7.0, (orange) $|\Delta pK_a| > 1.0$ and predicted $pK_a \geq 7.0$. The 7th column states the CHARMM residue name adopted in the simulated topology, and the rational for this choice is resumed in the 8th column.

PDB:4KFM		pKa of aminoacide in solution	PropKa	H++	ROSIE	Choice of protonation state (CHARMM nomenclature)	Purpose
Residue name	Residue number		pK	pK	pK		
HIS	68	6.5	5.7	6.2	7.1	HSE, not protonated	HIS:68:HE2 and VAL:67:O are within range of hydrogen bond nteraction.
HIS	125	6.5	6.8	8.0	6.9	HSP, protonated	Kir3.4 H120 is identified as proton sensor (Mao. 2002)
GLU	150	4.5	7.0	4.6	3.7	GLU, not protonated	Visually interacting with R160
GLU	152	4.5	7.9	8.3	4.4	GLUP, protonated	Tested in both states, GLUP state was retained
GLU	236	4.5	10.7	12	4.9	GLU, not protonated	Topologically close to spermine binding site in mmKir3.1 Q227 (Osawa. 2009)
ASP	271	3.8	7.7	5.0	3.6	ASP, not protonated	Equivalent to spermine binding site in mmKir3.1 D260 (Osawa. 2009)

evaluating the titration in a rigid body protein. Contrary to the E152, the sidechains of E236 and the D271 are observed forming two consecutive belts lining the ion permeation pathway into the aqueous vestibule in the CTCD of the channel. Here once again I assumed that the crystallographic conditions helped for the actual protonation of the carboxylate group of these residues which allowed them to come close to each other as observed in the crystal structure. The subsequent assessment of the neutral ionization state at pH 7.0 directly resulted from the initial proximity of carboxylate groups of these residues. More importantly these two set of residues correspond to the putative location of polyamine binding site suggested by the NMR study of the CTCD of Kir3.1 (Osawa et al. 2009). For the purpose of my simulation, I decided to leave these residues in their charged state because I believed that this should be the ionization state allowing the polyamine-protein interaction and since in the crystallographic model, the conformation on E236 and D271 has been influenced by the low pH during the crystallization process, I expected that a rearrangement of the residues could be possible even in the conducting state. Later in the manuscript I will explain the role of the charged residues in my simulations and I will discuss the role of the polyamines binding to this site in the protein.

5.1.3 Modeling all atom PIP_2

Since the crystallographic analogue of the PIP_2 has aliphatic chains of only eight carbons it was necessary to decide what will be the particular type of the fatty acids and the configuration of the protonation of the phosphate in the all-atom model of the PIP_2 in the simulations. I chose to rely on the major PIP_2 type found in extracts of brain PIP_2 as used in the experimentation with Kir3.2 in reconstituted artificial membrane (Wang, Whorton, and MacKinnon 2014). The brain PIP_2 used in the work of Wang and colleagues is actually a mixture with predominant arachidate (20:4) and stearate (18:0) fatty acids (Avanti Polar Lipids: 840046), the same fatty acids were reported as constituents of the PIP_2 active on ion channels in a recent review article (D E Logothetis et al. 2015). To decide on the location of the proton on the 4'- or the 5'-phospate of the PIP_2 I visually inspected the C_8PIP2-protein contact network in the crystal structure Figure 2. The 5'-phosphate is within 3.2 Å contact range with

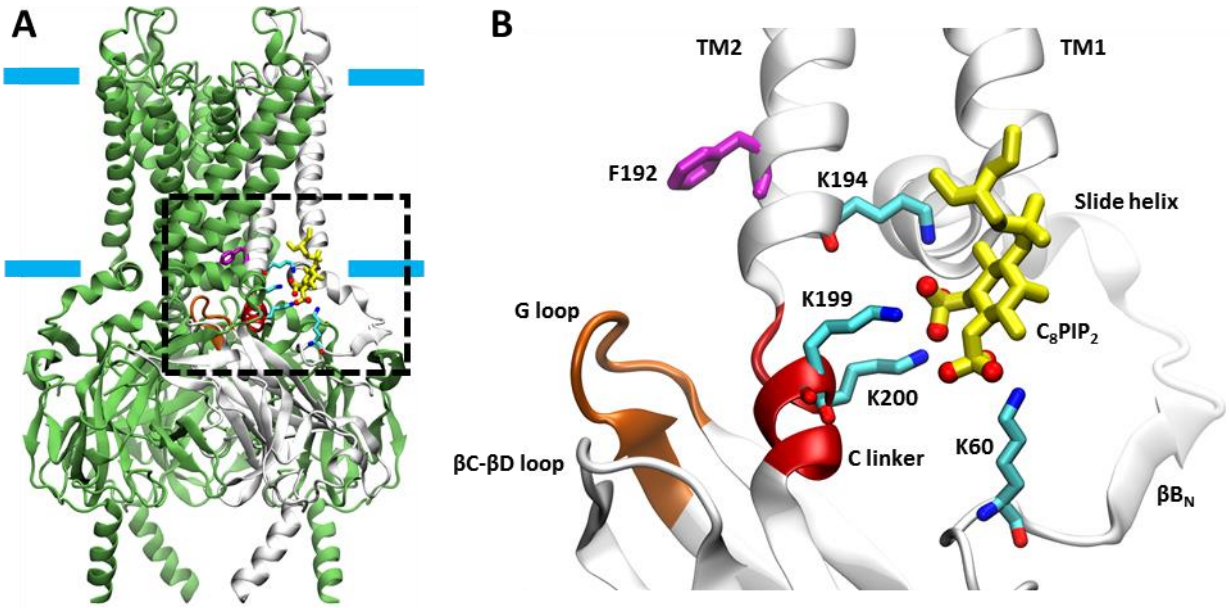

Figure 2: Interactions of PIP_2 4'- and 5'-phosphates with mouse Kir3.2 channel observed in the crystal structure PDB:4KFM. (A) The overall location of one PIP2 and its protein partners located tangent to the inner membrane leaflet (boxed region). (B) Enlarged view of the boxed region in (A) containing elements of only one subunit of the channel: C8PIP2 molecule (yellow sticks) whose 4'-phosphate oxygens (red spheres) are within 3.2 Å range of residues K60 and the 5'-phosphate within hydrogen-bonding range of residues K194, K199 and K200; F192 (violet sticks) constitutive of the HBC gate is in immediate proximity of the PIP2 binding site; a proline kink P195 at the end of the TM2 is located a small helix called the C linker or tether helix (red cartoon); the βH-βI loop (brown cartoon) constitutive of the G-loop gate is also located near the C linker containing the PIP2 binding site.

at least three donors of hydrogen bonds, the primary amine groups of the sidechains of residues K194, K199 and K200. Thus, the 5'-phosphate is not suitable to be modeled with a hydrogen bound to one of its oxygens because seemingly this phosphate group receives simultaneously three hydrogen bonds. The 4'-phosphate is left to harbor the charge-balancing hydrogen because its nearest neighbor is only the primary amine of the sidechain of K64.

After the topology of the PIP_2 had been decided, I equilibrated a patch for 5 ns with 124 POPC lipids and four PIP_2 (Stearate, Arachidate, L-α-Phosphatidyl-D-myo-Inositol 4,5-diphosphate; CHARMM forcefield nomenclature SAPI24 where "2" stands for 4',5'-diphosphate and "4" is the location of charge-balancing hydrogen at the 4'-phosphate). I took these four PIP_2 molecules with different conformations and aligned the phosphatidylinositol moieties to their equivalent in the C_8PIP_2 in the crystal structure. Another option would be to rebuild the aliphatic chains of the C_8PIP_2 to the desired stearate and arachidate by using the PSFGEN program, but I decided to impose explicitly different starting conformations to these molecules in contrast to the unchanged flattened conformations used as starting geometries by PSFGEN.

5.1.4 Modeling alcohol ligands in putative binding pocket in Kir3.2

The mapping of the putative binding pocket has been reviewed in the dedicated subsection of alcohol activation of the Kir3 channels. The fact that the studies mapping the binding site have pinpointed a single region important in the alcohol activation of Kir3 does not exclude multiple interaction sites on the protein, thus I searched the public RCSB database (Berman et al. 2000) where I found structures of alcohol-Kir beyond the PDB:2GIX cited in the work of Aryal et al. (Pegan et al. 2006; Aryal et al. 2009). The PDB:2GIX represents the methyl-pentane-diol (MPD) ligand bound to the CTDC of chicken Kir2.1. A complex between beta-mercaptoethanol and the CTCD of Kir3.1 (PDB:3VSQ, Inanobe and Kurachi, 2012, unpublished), was judged as irrelevant for my computational purpose because the complexing occurs by S-S bridging between the beta-mercaptoethanol and reduced cysteines of the protein. Lastly, a structure of ethanol (EtOH) bound to the CTCD of Kir3.2 complexes was thought as suitable to build the desired simulation setup, the PDB:3ATF (Inanobe, Nakagawa, and Kurachi 2011). In this structure ethanol is bound to two distinct parts of the CTCD, one is the putative binding pocket proposed by Aryal and colleagues and the other is on the surface of the CTCD near the distal C_{ter} helix.

After inspection of the crystallographic models, the MPD and the EtOH, the hydrophobic binding pockets appear superimposable with slight differences in the location of the ligands (Figure 3B), the amino acids of Kir2.1 contacting the MPD ligand are conserved in Kir3.2. For the generation of the model in Figure 3A, I decided to use the coordinates of the MPD ligand because experimentally it provides higher activation of the Kir3.2 channel. Thus, after aligning every one of the four regions constituting the alcohol binding pocket of Kir2.1 to its equivalent in Kir3.2, I simply copied the MPD ligand into the Kir3.2 CTCD. Then, I used homology modeling to restore part of the N_{ter} of mmKir3.2 which had equivalent coordinates in the CTCD of Kir2.1 because very importantly it interacts with the MPD ligand in the Kir2.1 crystal structure. I used a template modeling procedure to elongate the Kir3.2 by the mainchain of the peptide K52-R53-K54, the sidechains of these new residues were later generated by the PSFGEN program.

I have simulated the mmKir3.2 homotetramer in presence of different alcohols. The first alcohol to simulate the mmKir3.2 with was the MPD, as it was the one which was initially docked into the putative binding pocket and it provides strong experimental activation of the channel (Aryal et al. 2009). In other simulation setups I transformed the MPD molecule into two ethanol (EtOH) or propanol (PrOH) molecules. I decided to test other alcohol molecules because my impression from the MD trajectories with the MPD was such that this molecule was a bit large for the binding pocket because not all MPD molecules were remaining spontaneously inside the binding pocket for the entire simulation period (200-400 ns), even with imposed harmonic constraints of 1 kcal/mol/$Å^2$

acting as a function of the distance between the center of MPD and the sidechain of Y349. I will detail these results later.

When ethanol or propanol was simulated, these ligands were also harmonically constrained towards parts of the protein. Specifically, I used harmonic-wall constraints which are different from simple harmonic constraints of a distance between two centers. The imposed potential with wall-constraints is zero if the distance between both centers is below a threshold value, while harmonic distance constraints are always applied proportionally to the distance between the centers of the constrained partners. Thus, the shape of the potential of the harmonic-wall can be compared to the interior surface of a frustum standing on its upper base, where one can adjust the slope of the walls. The set of residues of the protein used to define the geometric center of the harmonic-wall constraints was constituted by the nearest residues surrounding the EtOH molecules observed in the PDB:3ATF. These residues are Y58-I244-L257-Y349, except P256 which interacts with the MPD ligand in the Kir2.1 (PDB:2GIX) and which was omitted because it is rather far from the EtOH location in the Kir3.2 crystal structure and whose interaction was in fact substituted by L257. In PDB:3GIX the hydrophobic pocket resembles a cage around the EtOH, three residues Y58-I244-L257 constitute a hydrophobic tunnel and the Y349 “closes” the hydrophobic pocket behind the EtOH.

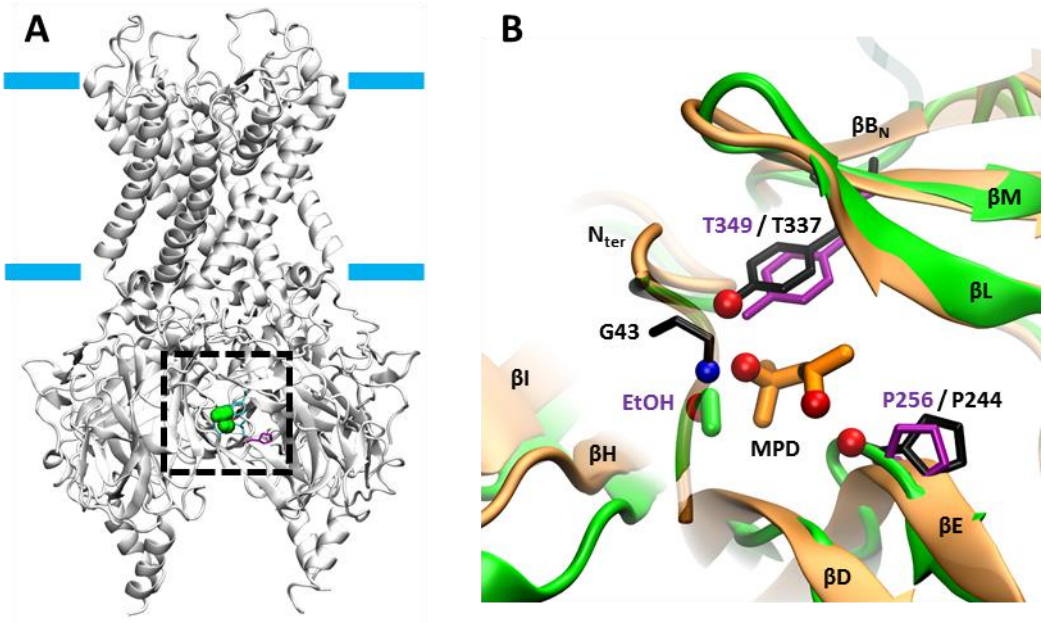

Figure 3: The alcohol binding pocket in Kir2.1 and in Kir3.2 is located at the inter-subunit interface involving the N_{ter} and the βD-βE strands of one subunit and the βL-βM strands of the adjacent subunit. (A) Overall location of the alcohol binding pocket in the mouse Kir3.2 channel with modeled one propanol molecule (green). (B) Superimposition of CTCD of Kir2.1 PDB:2GIX (ochre) and Kir3.2 PDB:3ATF (green), the represented region corresponds to the boxed region in panel A. The Cα atoms of residues in the displayed βD-βE and the βL-βM strands are aligned to RMSD of 1.05 Å². The methyl-pentanediol (MPD) present in the Kir2.1 crystal structure is represented as orange sticks Kir2.1 residues contacting the MPD ligand are shown as black sticks. Red and blue spheres represent oxygen and nitrogen atoms involved in hydrogen-bonding between the Kir2.1 and the MPD. The residues of Kir3.2 equivalent to the residues involved in the MPD-Kir2.1 complex are colored in magenta. The ethanol (EtOH) present in the hydrophobic pocket of Kir3.2 is represented in green. The Nter of Kir2.1 which does not have equivalent coordinates in the Kir3.2 structure is represented as a transparent loop in the middle of the representation and contains G43, one of the residues stabilizing the MPD.

5.1.5 *Solvation of the Kir3.2 model*

The last part of the setup was to select the simulation box constituents solvating the ligands-Kir3.2 complex. I decided to use a pure POPC bilayer to model the membrane and I set the KCl concentration to 600 mM, this high concentration is intended to speed up the occurrence of binding events of K^+ at the selectivity filter. Also, particular attention was laid on the placement of water molecules inside the vestibule of the channel and inside the selectivity filter. I used the program

SOLVATE to fill the vestibule with water. This procedure places individual water molecules by translation and rotation in order to maximally fill the available volume. After manual curation of the solvation obtained by SOLVATE, where I removed water from the protein-lipid interface and water that I judged inappropriately placed in protein crevasses, the vestibule between the site S0 of the selectivity filter and the residue G318 of the G-loop gate contained 94 water molecules. For me it was very important to maximally fill the vestibule with water in order to prevent a collapse of the vestibule which may occur at the beginning of the simulation, as the vestibule is closed at the selectivity filter and most often the sidechains of the methionine of the G-loop gate also close the water thus preventing the water exchange inside the TMV. Other ways of placing enough water inside the TMV are possible, such as iteratively displacing extra water molecules from the bulk inside the vestibule and leaving the system run with restraints on the protein and repeat this process until one detects constant expulsion of water from the vestibule corresponding to the equilibration accounting for the extra water added artificially. Another option is to run the system until a constant number of water molecules is found inside the vestibule while the protein is constrained to assure the permeability of the G-loop gate by either mutating sidechains or displacing them accordingly. The way I dealt with this issue is similar to the second option above. I did not quantify the amount of water remaining inside the TMV during each MD simulation that I ran. Depending on the interaction of the protein and the ligands in the simulation box, the TMV behaved in different ways, these observations are detailed in the following sections with the results of each simulation setup.

5.2 *Optimization of the simulation protocol*

In this section, I will briefly describe (no data shown) and discuss the preliminary tests I have performed. The set of test simulations led to the optimized molecular setup of the simulation box which was finally used to generate the data presented starting from section 5.3 in this chapter.

Just a quick remainder of the objective of the study and its starting point: we were interested to reproduce *in silico* the K^+ conductance of mmKir3.2 in order to establish a base-line computational protocol which could be used to simulate any other native or mutant Kir3 channel. We aim to tune our protocol to the K^+ conductance because this parameter is the easiest to study experimentally and most of the experimental data about Kir3 channels is obtained from electrophysiological experiments. As a starting point for the simulation of the molecular dynamics (MD) we decided to use the pore-conformation of mmKir3.2 observed in PDB:4KFM – in this model it is expected that under the influence of the complete set of physiological activators the channel is driven into a pre-activated state, but due to the lack of the physical presence of cell membrane in the crystallization assay the open state of the pore was not achieved.

The use of the entire crystallographic model PDB:4KFM was evaluated to be undesirable because of the large size of the simulated system including the four Gβγ dimers. Thus, we first simulated the mmKir3.2 pose in presence of PIP_2 and Na^+. Several short 10 ns unrestrained MD runs showed rapid change of conformation of the G-loop gate involving deflection of the sidechains of M313 which occluded the permeation pathway. Thus, we concluded that the removal of the Gβγ dimers destabilized the pore toward a closed state. We also attempted to prevent the “collapse” of the G-loop gate by implementing harmonic distance restraints on the applicable on the Cα atoms of M313 – the force constant was set to 4 kcal/mol/Å and the reference distance was that of the initial conformation. This attempt was also unsuccessful to maintain the G-loop open during another set of 10 ns MD runs. These results suggested that the PIP_2 and Na^+ ensemble positioned at the locations observed in the crystallographic model PDB:4KFM are not sufficient to maintain the pre-open conformation of the mmKir3.2 pore.

Following the lead of experiments which showed that small monovalent alcohols can activate the Kir3 channels we introduced the methyl-pentane-diol (MPD) ligand into the putative biding pocket mapped by the team of Slesinger 2009 (Aryal et al. 2009). The coordinates of the MPD were set by

homology to the co-crystal of MDP and CTCD of chicken Kir2.1 (PDB:2GIX). In the attempted unrestrained MD simulations of the mmKri3.2 pore supplemented with PIP_2, Na^+ and MPD – the MPD ligand tended to rapidly unbind from the binding pocket. We decided to simulate the rebinding of MPD to the protein by the implementation of harmonic distance constraints between the oxygen or hydrogen of the alcohol groups of MPD and the carbonyl oxygen of residue P256 and the alcohol group of residue Y349 – the force constant have been set to 1 kcal/mol/Å and the reference distance to 1.2 Å compatible with hydrogen-bonding interactions. This time MPD remained for longer periods of the simulations which lasted 100 ns the most. However, in these conditions the G-loop gate was as widely open as in the starting conformations only occasionally, suggesting that the PIP2, Na+ and MPD ensemble of partner to the channels is not optimal to induce the open state of the mmKir3.2 pore. Furthermore, when we simulated an inward K^+-driving-force using external electric field, we had to increase the membrane potential (V_m) to -1.3 V in order to observe inward K^+ permeations occurring at constant rate. We judged the setup of such a strong V_m irrelevant mainly because in other reports in the literature about simulation of K^+ conductance with wild-type KcsA are achieved with V_m between 400 and 600 mV (Jensen et al. 2013).

In the time we were performing the above described simulations, an article about structural study has been published extending the previous description of the presence in Kir2.1 of a secondary interaction site for anionic lipids (S. J. Lee et al. 2013; S.-J. Lee et al. 2016) – authors identified membrane-protein stabilizing properties of residue K64 in the slide helix of Kir2.1, whose presence correlated with increasing activity of the channel when perfusing excised inside-out patches with vesicles containing anionic lipids. Inspired by this report but also by the observation of strong positive potential developed by residue R73 in the slide helix of mmKir3.2 (data not shown) which is located at the equivalent position *i-1* in Kir2.1 K62, we modeled four POPG (1-palmitoyl-2-oleoyl-sn-glycero-3-phospho-(1'-rac-glycerol)) molecules in the lower leaflet of the membrane positioned in the vicinity of slide helix of the mmKir3.2 pore. We simulated the new ensemble mmKi3.2, PIP_2, Na^+, MPD and POPG following the restrained conditions described in the previous paragraph. We observed one of the unrestrained POPG molecules to interact for almost 100 ns with number of hydrogen-bonding partner from the slide helix, the other three POPG molecules in the same simulation rapidly defused in the membrane. The longest-lived non-restrained POPG-protein interaction (approximately 100 ns) has been identified to be between the POPG phosphate and the backbone nitrogen of residue T75, this observation has been used as basis for implementation of new harmonic distance restraints meant to favor the POPG rebinding to the slid-helix – the force of the restraints have been set to 2 kcal/mol/Å and the reference distance of the restraint have been set to 8.5 Å, while restraints have been implemented between the phosphorous atom of POPG and the backbone nitrogen of T75. In these conditions supplemented by simulated V_m= -700 mV, in one simulation out of three replicas, we obtained inward and outward K^+ permeations through the G-loop gate which was open with average bottleneck-diameter of 8 Å (when the outward permeations occurred). We found that the outward K^+ permeations were driven by the increased K^+ concentration immediately below the G-loop gate – this concentration of K^+ is driven by the presence of a number of negatively charged residues (see section 2.10), thus the positive electrostatic potential which is developed overwhelmed the effect of the applied external electric field and resulted in local outward driving-force of the K^+. In the other two simulated replicas simulated we obtained narrower G-loop conformations, hence we observed only inward K^+ transport.

From the above simulation we have identified that, the PIP_2 modeled initially near the TM2 helices often experience a slight displacement and it switches between positively charged partners form the TM2 to positively charged residues K64 and R60 in the N_{ter}. From there, we redesigned the simulation box in order to address two points of the previously observed molecular dynamics. First, we suspected that the newly established interactions between PIP2 and R60 residues could result in the gating of the HBC gate since the PIP_2 was not able to strongly interact with the partners in the TM2. We decided to model additional PIP2 molecules in order to "saturate" the R60 interaction site, thus

aiming to facilitate the PIP_2-TM2 interactions initially present in the starting crystallographic model. The second point aimed to remove the implementation of imposition of distance restraints between the slide helix of the protein and elements of the membrane. This point was addressed by addition of a third PIP_2 partner for each subunit, modeled near R73. This new simulation setup was tested in two replica simulations (*Simulation VII* and *Simulation VIII*) which are described in section 5.6 – it appeared to be favorable to maintain and extend open the mmKir3.2 gates.

In the following subsection of the chapter I report and discuss the results obtained with simulation-box setups with increasingly complexified set of ligands interacting with the mmKir3.2 pore.

5.2.1 Simulation protocol retained for investigating the dynamical control of the Kir3.2 gates

After the described above trials of simulation of Kir3.2 in presence of PIP_2, POPG and alcohol ligands, emerged the simulation box constituents reported in the last column of Table 2 which is the most complex ensemble of constituents tested to maintain the channel open during the simulation. In this setup the channel was simulated together with twelve PIP_2 molecules distributed at triplets of interaction sites found on each of the inter-subunit interfaces. The following is a fast overview of the atom constituents of different simulation boxes without presentation of any data which will be the subject of the following subsections.

The first site where PIP_2 was modeled is the canonical binding site, mapped experimentally and observed in the crystal structures of various Kir proteins (hereafter I call this site "Site 1"). This site is very potent because the PIP_2 interact simultaneously with five positively charged residues. Indeed, before I started tracking each individual hydrogen bond between the PIP_2 and the protein I was convinced that PIP_2 was not changing its behavior in the Site 1, since in all simulations without any bias the PIP_2 molecules always remained near the initial position. The picture became complex once the time-series of the hydrogen network had been pulled out from the trajectories. In total, the PIP_2 initially present in the Site 1 site could interact with 16 residues, these interactions are detailed in a dedicated subsection in the chapter. In short, the PIP_2 has the ability to establish only a limited amount of instantaneous interactions, it is straightforward to admit that there is a combinatorial pattern of PIP_2-protein interactions involving these 16 residues, which could be correlated to the obtained confirmation of the protein. Particularly, I noticed that the $_{(Site\ 1)}PIP_2$ can interact with the R60 which is located at the hairpin turn preceding the K64 residue in the N_{ter}. This residue does not interact with the PIP_2 in the crystal structure, but in my simulations as the N_{ter} approaches the membrane, the R60 comes closer to PIP_2 which is usually engaged in interaction with K64. Then, the PIP_2 may be slightly displaced and the 4'-phosphate establishes a long-lasting interaction with both R60 and K64. In such a configuration, the number of interactions between PIP_2 and K194, K199 and K200 decreased.

In order to better understand the pattern of PIP_2-protein interactions, I began saturating the biggest amount of possible PIP_2-protein interactions in the vicinity of Site 1. The reason behind this choice is that the PIP_2 is in limited amount in the plasma membrane but possibly it is not randomly distributed and one can imagine that several molecules can be "piled up" next to the protein if the energetics of such a crowding is favorable. Furthermore, it is not farfetched to assume that the PIP_2 can bind other parts of the protein prior to reaching the deeper Site 1. Thus, a second molecule of PIP_2 ($_{(Site\ 2)}PIP_2$) was modeled next to the one modeled as $_{(Site\ 1)}PIP_2$. This was done by simply mutating one POPC lipid occupying the area above K64 and R60 using the PSFGEN program to generate the all-atom model of the new $_{(Site\ 2)}PIP_2$ molecules. One could interpret Site 2 as secondary binding sites, thus admitting the simultaneous binding of PIP_2 to multiple sites with different valency on the channel, needed to increase the binding to Site 1. It is also probable that the parts of the protein observed to disengage a single PIP_2 from Site 1 are important for the inactivation of the channel. These two aspects will be investigated further in the chapter regarding the PIP_2-protein interaction hotspots.

Table 2: Molecular constituents of the simulation boxes in each test condition when the number of PIP_2 was varied, and the simulation protocol of the applied constraints used to prevent ligands from diffusing away from protein.

	Number of replicas	**2**	**2**	**2**	**2**
Simulation box constituents	**Box size (Å)** Number **POPC, POPG** Number **K^+ (600mM), Cl^-** Number **TIP3** water	100*100*160 288, 8 524, 545 42789	100*100*160 284, 8 524, 508 42805	100*100*160 280, 8 524,492 42821	100*100*160 276, 8 524, 476 42837
	Protein**: mmKir3.2 PDB:4KFM (I55...N382)** Homology modeling: **K52-R53-K54**	Yes Yes	Yes Yes	Yes Yes	Yes Yes
	Total number of PIP_2 in box **(a) Xray:** Canonical binding site **(b) R73:** Slide helix interaction site **(c) R60:** N_{ter} interaction site	**0** - - -	**4** **4** - -	**8** **4** **4** -	**12** **4** **4** **4**
	Total number of propanol (32 mM) **(d) I224:** Hydrophobic binding pocket	**28** **4**	**28** **4**	**28** **4**	**28** **4**
	Total number of Na^+ (23 mM) **(e) D228:** βC-βD loop binding site	**20** **4**	**20** **4**	**20** **4**	**20** **4**
		Applied collective variable to ligand-site			
Equilibration	**NPT ensemble:** 310K, 1atm, **Protein heavy atoms constraints:** **2** kcal/mol/Å²; total time **15ns** **2** to **0.4** kcal/mol/Å² (**-20% / 5ns)**; total time **20ns** **0.4** to **0** kcal/mol/Å² (**-10% / 1ns)**; total time **10ns**	(d), (e)	(a), (d), (e)	(a), (b), (d), (e)	(d), (e)
MD unrestrained protein NPT ensemble	Time= 0...400 ns Vm = 0 mV	(d), (e)	(a), (d), (e)	(a), (b), (d), (e)	(d), (e)
	Time= 400...600 ns **V_m = -700 mV***	(d), (e)	(a), (d), (e)	(a), (b), (d), (e)	(d), (e)
	Time= 600...800 ns V_m = -700 mV	End 800 ns	**(c)****, (d), (e)	(b), **(c)****, (d), (e)	End 800 ns
	Time= 800...1000 ns V_m = -700 mV	-	**1 replica*****	**1 replica*****	-

*List of atom groups used to set harmonic-wall distance constraints between PIP_2 and protein binding sites: atoms from the sugar ring, the 4'- and the 5' phosphates of PIP_2 used in all setups are C14 O4 P4 C15 O5 P5; (a) site **Xray** atom NZ of the sidechain of residue K194, threshold distance 8 Å and force constant 0.5 kcal/mol/Å²; (b) site **R73** atoms NE CZ NH1 NH2 of the sidechain of residue R73 and atoms N CA C O of the main chain of residue E74, threshold distance 4 Å and force constant 0.5 kcal/mol/Å²; (c) site **R60** atoms NE CZ NH1 NH2 of the sidechain of R60, threshold distance 4 Å and force constant 0.5 kcal/mol/Å². The atom groups used to restrain the propanol (PrOH) ligand towards the hydrophobic binding pocket: all atoms of the PrOH molecule were used, threshold distance 6 Å and force constant 0.5 kcal/mol/Å²; (d) site **I244** of the protein contained the sidechain heavy atoms of residues Y58 I244 L257 Y349. The atom groups used to restrain the Na^+ towards the binding site included: the Na^+ atom itself; (e) site **D228** the atom OD2 of D228, the atom O of R230 and atom O of S232, threshold distance 6 Å and force constant 0.2 kcal/mol/Å².*

** An external electric field is turned on; it was used to provide inward driving force to K^+. ** The stabilizing constraints on PIP_2 are switched from (a) to (c). *** Only one replica has been extended for additional 200 ns when the membrane potential was still applied but all ligand stabilizing collective variables have been turned off.*

A third PIP_2 was set to interact with residue R73 of the slide helix, which is interacting with POPG, as described above. Here once again I postulated that the R73 residue (hereafter termed "Site 3") is on a path used by the PIP_2 to approach the main binding site, Site 1. The supplementary interaction at Site 3 should be possible if the protein environment is enriched with PIP_2, always conceiving the experimentally impossible quantification of the exact number of PIP_2 in the vicinity of the channel upon its activation. It turned out that the $_{(Site3)}PIP_2$ interacting with the R73 is stable at this site, as only one molecule was seen leaving the interaction site in cumulated 1.6 µs unbiased simulations. Thus, in the simulation setup presented in the last column of Table 2 there was no need to implement distance restraint to keep the any of the PIP_2 molecules constantly in the vicinity of the protein at any of the three PIP_2 binding sites.

Next, other simulation boxes were assembled with reduced number of PIP_2 molecules. The channel was simulated in the total absence of PIP_2, with PIP_2 only in Site 1, and with PIP_2 in Site 1 and near the Site 2. In these simulations, all the PIP_2 molecules were constrained by a flat bottom harmonic potential which was inactive if the PIP_2 phosphates were within 6 Å from the side chain of positive residue of the interaction site, as detailed in the legend of Table 2. Although the PIP_2 in the previous simulations was interacting with the protein in a stable manner, I implemented the harmonic-wall constraints in order to better control and sample a desired subset of instantaneous PIP_2-protein interactions.

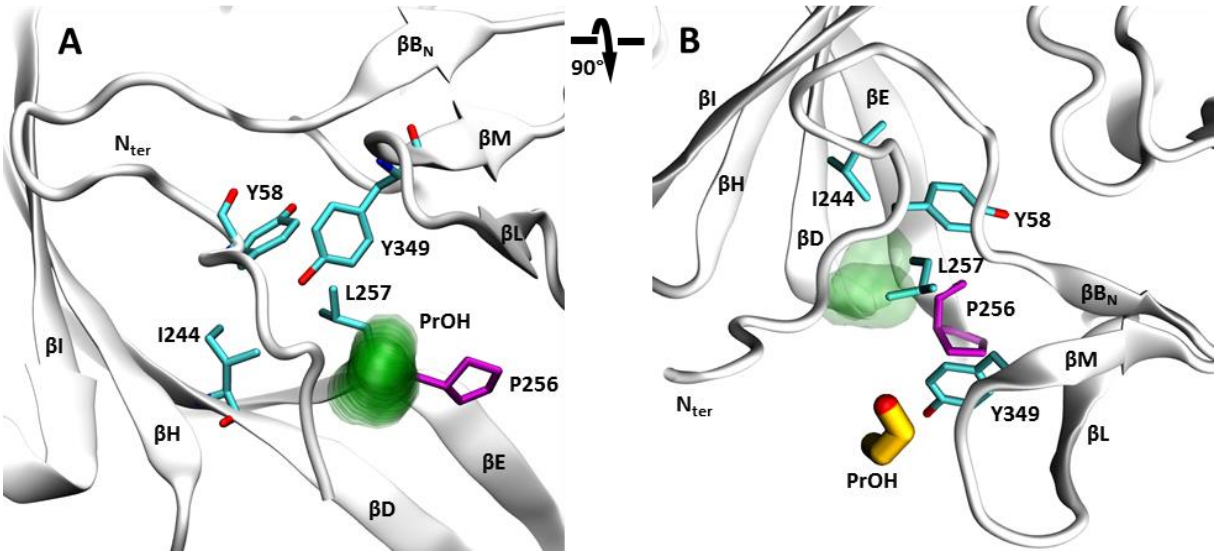

Figure 4: Simulated binding of alcohol in the hydrophobic binding pocket of mouse Kir3.2. (A) Side view of the hydrophobic binding pocket with bound propanol (PrOH), after 45 ns of equilibration simulation. Due to the constraining force applied during the equilibration of the heavy atoms of the protein, the displayed protein conformation is similar to the starting crystal structure PDB:4KFM. The view represents the same region as Figure 3B, only a slight rotation to the right and an upward tilt is applied for better visualization purposes. The imposition of the ten snapshots of PrOH (every 4.5 ns) is shown as green transparent surface. The residues contacting the ethanol in the crystal structure PDB:3ATF are displayed as cyan sticks. The residue P256 (magenta) was used as reference for the modeling of the methane-pentanediol (MPD) in the binding pocket, MPD molecules were transformed by deletion of atoms into PrOH in this simulation. (B) Top view of the hydrophobic binding pocket after 800 ns of simulation following the equilibration presented in panel A. The location of the PrOH molecule in the last snapshot is shown as yellow sticks. The average position of PrOH during this 800 ns simulation is represented by green transparent surface. The position of PrOH in panel A is the equivalent to the yellow stick representation in panel B, thus locations of pre-bound and bound PrOH can be appreciated, this observation evokes a role of Y349 as a gate keeper of the alcohol inside the binding pocket.

Figure 4 shows persistence of a restrained PrOH molecule in the hydrophobic binding pocket mapped from the position of the MPD ligand in the Kir2.1 CTDC (2GIX). In fact, in all simulations that I am presenting hereafter the PrOH has been constrained towards the geometric center of the hydrophobic residues which are the closest to the EtOH in the crystal structures of Kir3.2 CTCD (PDB:3ATF). The aim of this constraint was on the one hand to prevent the alcohol of diffusing from the binding pocket and on the other hand to observe if the PrOH ligand can bind as deep inside the

hydrophobic protein environment as the EtOH in the crystal structure. Regarding the first point, the harmonic-wall constraints with force constant of 0.5 kcal/mol/Å^2 were not absolutely efficient and in some of the simulations one or more PrOH diffused from the four binding pockets after various periods of persistence.

Regarding the second point, in all simulations the motion of the heavy atoms of the protein was constrained during the NPT ensemble equilibration of the simulated system. As it can be observed in the PDB:4KFM and in the particular snapshots shown in Figure 3B, the residues Y58 and I244 are screened by the Y349 residue. Thus, the PrOH could not reach those residues despite the imposed distance constraints (hereafter this location of PrOH is referred to as "in front of Y349"). This situation changed after approximately 20 ns of unrestrained simulation, when the Y349 can be seen displaced by a brief global motion of the βL-βM loop, thus the PrOH could move towards the I224 (in a location that I will call "behind Y349"). When the Y349 regained its previous position relative to the βD strand, it could "encage" the PrOH inside the binding pocket. The PrOH was also observed to oscillate between both locations in front and behind Y349. The persistence in front Y349 could be entirely attributed to the harmonic-wall distance constraints, but it is not true because the MPD was observed as persisting for some period in front of Y349 and a rebinding event of PrOH in front of Y349 was also spotted. The movement from in front to behind Y349 could also be partially favored by the harmonic-wall constraints. Nonetheless, this binding of PrOH could not be simply due to the imposed distance constraints because the force of the harmonic-wall constraint was switched off when the center of mass of PrOH was within 6 Å of the center of mass of the side chains of residues Y58-I244-L257-Y349. The measured distance between both positions in front and behind Y349 is about 6 Å. Thus, in all simulation snapshots, when the PrOH is observed behind the Y349, the alcohol is unrestrained and should be stabilized by favorable hydrogen bonding and hydrophobic interactions. The remaining transition from behind to in front of Y349 often coincides with a brief displacement of the βL-βM loop resembling an opening of the hydrophobic pocket (Figure 4B). It thus appeared that the position of PrOH in front and behind Y349 and the associated transitions between both states are not just the consequence of the harmonic well, but favorable stabilizing interaction were play and there were also protein conformational changes guiding the PrOH transitions in respect to Y349.

5.3 MD Kir3.2 in presence of propanol and Na^+

In this section I describe observation from the simplest simulation box setup that I used to access the PIP_2-protein interactions. It did not contain any PIP_2, but propanol and Na^+ were present and their positions were constraint by weak harmonic-walls to promote their interaction with the channel (Table 2). According to the widely accepted role of PIP_2, it was expected that, in these simulation conditions, the channel would undergo conformational changes leading to its closure at least at the HBC gate.

5.3.1 K^+ transport

Figure 5 shows K^+ movements across the TMD of the channel and the evolution of the G-loop and the HBC gates conformation in two replica simulations (*Simulation I* and *Simulation II*). During *Simulation I,* only one K^+ crossed the TMV in the inward direction. This event concerns the ion initially present in the S_{VEST} site of the filter, as the equilibration advanced this ion unbound the S5 and diffed inside the TMV. Near the end of the equilibration run, when the harmonic constraints on the protein were 0.4 kcal/mol/Å^2, K^+ bound back to the S_{VEST} and then after it progressed by one site as the filter configuration rearranged from w-w-K^+-K^+-w & K^+_{TMV} to w-K^+-K^+-ϕ-K^+ (where **w** indicates that the coordination site was occupied by water molecule, and **ϕ** indicates that the coordination site was unoccupied). In the following nanoseconds, the three K^+ configuration was broken by K^+ approaching the S0 site from the extracellular electrolyte bulk, without binding. After 10 ns the two K^+ configuration in the selectivity filter was restored, which released the ion from S4 back to S_{VEST} (Figure 1C). Simultaneously a new comer K^+ from the extracellular bulk bounded at S0 and then

rapidly moved to S1, causing the ion at S3 to transition at S4. This last transition seems to change the electrostatic potential in the TMV under the selectivity filter, resulting in the short-termed ejection of the K^+ from the TMV through the G-loop gate, this event occurred only 10 ns after the protein was completely released from the harmonic constraints. Until the end of the simulation the three K^+ configuration fluctuated, distributing ions between sites S1-S4 and leaving most of the time one of the sites unoccupied. 125 ns after the release of the constraints, the HBC gate closed and the TMV remained de-wetted at the level of V188 and F192. The G-loop gate in *Sim. I* reached minimal diameter between 150 and 400 ns, during this period the water column was still continuous at the level of the gate, but only individual water molecules were observed transiting through. Before and after this period the G-loop gate bottleneck delimited by the thioether groups of the sidechains of four M313 was sufficiently opened for outward permeating K^+. Undoubtably ions were pushed through by the increased concentration of K^+ between the E236 and D271 electronegative belts. These ions have been persisting in the G-loop gate region delimited by M313 and M319, they were partially dehydrated and oxygen coordination accounting for the missing water molecules was provided by the carbonyl oxygens of G318 and T317 (for details see section 5.3.2.2.2 and Figure 18).

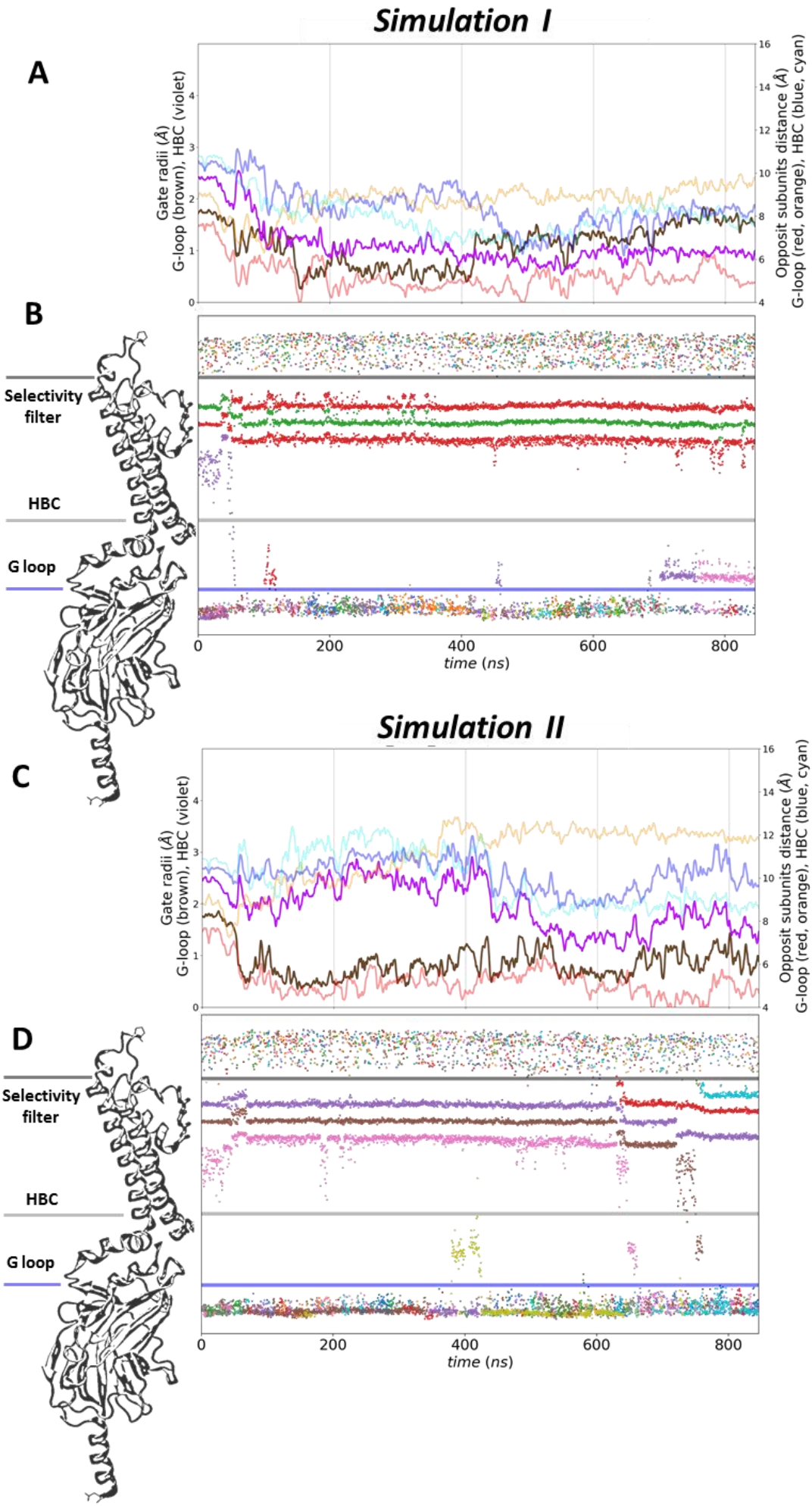

Figure 5: The pre-open Kir3.2 closes to K^+ impermeable state in absence of PIP_2. Observation in two replicas: Simulation I panel A and B; Simulation II panel C and D. Timeseries of snapshots taken every 0.4 ns are plotted as convoluted average using sliding window of 20 ns and a symmetric power law function x^n (n = ±6), the first 45 ns corresponds to the equilibration of the simulated system. (A, C) Timeseries of the opening of the G-loop gate (brown) and the HBC gate (magenta) is plotted to the left vertical axis. The measure of distance between pairs of atoms from diametrically opposite subunits is plotted to the right vertical axis: G318:0 carboxyl oxygen of the mainchain (red and orange); the geometrical center of the phenyl ring of F192 (blue and cyan). (B, D) Timeseries showing K^+ movement across a section of the pore extending between 10 Å below the Cα of residue M313 in the G loop, and 10 Å above the carbonyl oxygen of residue G158 in the selectivity filter. K^+ positions along the permeation pathway are plotted to the left vertical axis. Each individual ion is colored with the same color along the entire timeseries, due to limitation in the coloring scheme repeated colors for different ions exist in the plot. Watermark of part of the channel is shown on the right for easier localization of the gates in the plot.

5.3.2 Conformation of the K^+ permeation pathway

The above description of the trajectory mentioned multiple aspects of the molecular function of the Kir3 channels, some of the features of interest are: (i) the configuration of the K^+ occupancy in the filter at different levels of permeation; (ii) the conformation of the inner helix (TM2) upon closure and opening of the channel and the gating effector; (iii) the conformation of the G-loop gate; (iv) the conformation of β-globin like CTCD; (v) the occupancy of the binding sites by the corresponding ligands. The dynamical behavior of the channel supposes the possibility of different configurations of these structural elements when the channel is open and closed.

The first aspect has been described above and it is contradictory to the admitted water-K^+ alternating pattern occupying the selectivity filter. I will leave the discussion of this discrepancy for later sections of the chapter where I will describe how the pattern of water-K^+ in the selectivity filter changed among simulations in a PIP2 dependent manner. In Figure 6C is quantified the closing event of the selectivity filter in *Simulation I*. The reduction of the distance between the carbonyl oxygens constituting site S3 of the selectivity filter were also shown by MD simulations and in particular in the KcsA channel (Kratochvil et al. 2017). The authors identified residues F103 in the TM2 and R64 in the pore helix of KcsA as responsible for the pinching of the S4 site. The pattern of activation in KcsA channel involves the proximity of F103 to the selectivity filter and the distancing of R64 as the channel is open, while the reverse pattern is observed as the channel evolved in closed conformation. The equivalent positions in Kir3.2 are occupied by S143 and V183, thus no direct correspondence into this region could be made between the KcsA and the Kir3.2 channels. I will continue the investigation of the gating of the selectivity filter after the presentation of the dynamics of the transmembrane helix bundle.

5.3.2.1 Transmembrane helix bundle

The closure of the hydrophobic gate belonging to the inner helix in *Simulation I* is depicted in Figure 7. In this simulation the water column inside the TMV was first split by the sidechains of F192 and the subsequent conformational change observed in absence of PIP_2 brought the four residues V188 close enough to extend the de-wetting of the vestibule. The observed conformational changes in the TM2 and the residues active in the HBC gating are consistent with the data published by other researchers on the hydrophobic gating phenomenon of TMD in Kir channels (T. Jin et al. 2002; Aryal, Sansom, and Tucker 2015; X.-Y. Meng et al. 2016). The involvement of the V188 residue in the hydrophobic gating is also consistent with the observation in the crystallographic model of Kir2.2 (Hansen, Tao, and MacKinnon 2011). Furthermore, alanine and glycine mutants of Kir3.2 V188 have been identified and are used as a tool yielding constitutively open Kir3.2 channels (B. A. Yi et al. 2001). The dehydration of the TMV between G180 and F192 is not absolute in all frames of the 600-840 ns period analyzed in Figure 7, this is why in order to depict a discontinuous water column in the figure, the minimal probability of water occupancy was set to 20% (this value has been adopted for the subsequent representation monitoring the hydration of the TMV in other simulation setups and depicted in other figures). Thus, *Simulation I* clearly showed that there is a specific mechanism which oriented the V188 so that it extended the de-wetted portion of the TMV. Thus, the larger portion of dehydrated TMV increases the energy barrier which has to be crossed in order to allow water and ions to permeate through the vestibule. This provides an explanation of the role of the V188A and V188G mutants, whose constitutive activity is most likely due to an ineffective gating mechanism, rather than a stabilizing event of the open state of the channel.

To understand this closure mechanism, I have quantified the conformational changes occurring in the TM2 during *Simulation I* by monitoring the bending of secondary structure in the protein over time (Figure 8). Initially the TM2 helix has a kink in the region including residues L179-A185 (Figure 8D). The central residue G180 has been identified as the effector of the kink, corresponding to a glycine conserved among potassium channels (Mao et al. 2002; Rosenhouse-Dantsker and Logothetis 2006). As the simulation advances, the bend angle between I182-F186 decreased in all subunits. The bend angle involving residues preceding G180 (N_{ter} in respect to G180) also diminished in three subunits. It

can also be noticed that the curvature of the TM2 helix oscillates between the G180 and the extracellular side of the TM2 helix (residue G169).

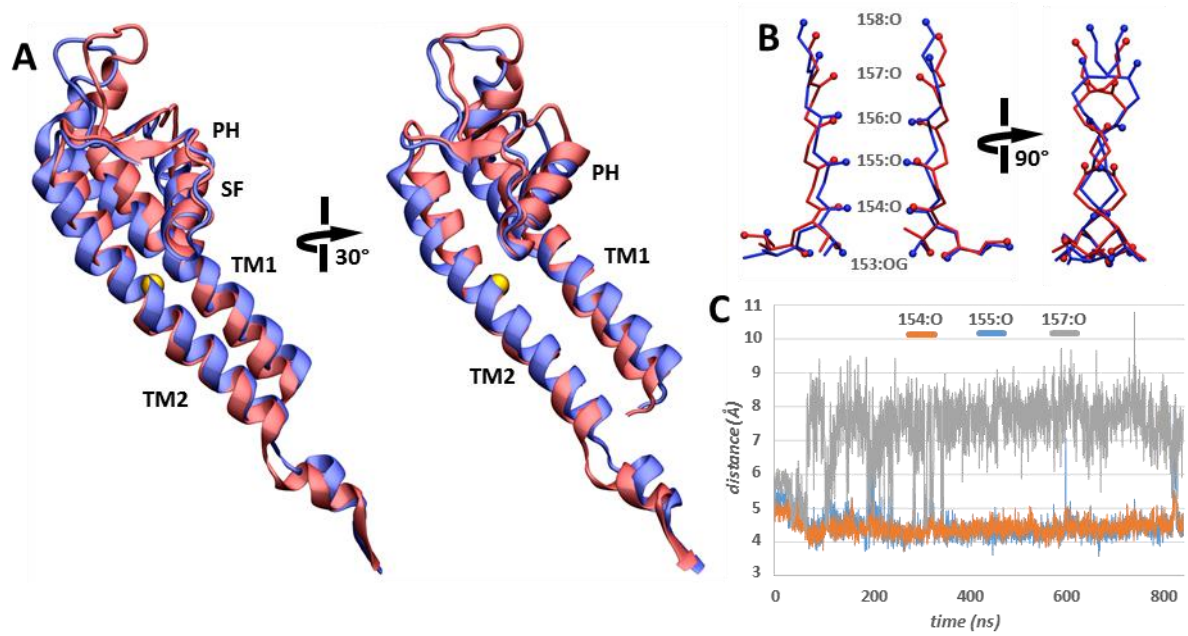

Figure 6: Closure of the selectivity filter of Kir3.2 in Simulation I. (A) Superimposition of two conformations of the transmembrane helices and the pore domain of subunit P4: at 0 ns (red) and at 845 ns (blue). (B) Superimposition of the backbone of residues constituting the selectivity filter in subunits P3 and P4. Position of oxygen atoms are indicated with spheres. (C) Timeseries of the distance between couples of carbonyls oxygen atoms presented in panel B.

Visual comparison of the evolution of the bending of TM2 between subunits does not evoke a simple "flattening" or a relocation of the initial G180 kink. If we consider couples of neighboring subunits, a marked asymmetry is distinguished between the bend maps of each of the four subunits. While the adjacent subunits P3-P2 display similar bend profiles along the simulation, the maximal bending in the lower half of the plots for subunits P4-P1 is different. The measured bend angle in the region G169-S177 markedly increased in subunit P4, this event coincides with the increased curvature of the pore helix in the same subunit occurring between residue S148 and residues E150 (Figure 8C). Then, if one considers the contacts between the N_{ter} half of TM2 in subunits P1 and P4, and the C_{ter} portion of the pore helix of subunit P4 (Figure 9D), it is easy to admit an inter-subunit cooperativity in the generation of the fluctuation of the pore helix in subunit P4. This hypothesis recovers the discussion of the events causing the pinching of the selectivity filter of the KcsA channel cited earlier. In this scope another recent computational study has identified another distance marker coinciding with the closure of the selectivity filter in KcsA. It has been demonstrated that the L40 in the TM1 of KcsA channel gets closer to the C_{ter} part of the pore helix and thus diminishes the amplitude of the fluctuations of the selectivity filter (Heer et al. 2017). According to protein sequence alignment the equivalent of the KcsA L40 in Kir3.2 is W114. Unfortunately, these residues are not located at the equivalent positions as one can verify by structural alignment of the crystallographic models of both channels. Indeed, the Kir3.2 W114 is located in the last most turn of TM1 exactly three turns closer to the extracellular side of TM1 than the KcsA L40. On the other hand, the structural equivalent of KcsA L40 is mmKir3.2 W106. The same region has been investigated in Kir3.4 by mutagenesis of the G175 (mmKir3.2 G180) and the significance of the interactions between the TM2 above residue G175 and the lower part of the pore helix has been demonstrated (Rosenhouse-Dantsker and Logothetis 2007).

5.3.2.2 Selectivity filter

At this point I have cited two published parts of the allosteric pathway activating the KcsA channel, I will refer to them in order to strengthen the hypothesis emerging from the observations of the simulations that I have made. Despite the fact that in *Simulation I* the channel is closed at the HBC

gate; it is possible that other parts of the pore are not in a completely closed state especially because of the presence of Na^+ and propanol in the respective binding pockets. I will describe the dynamics of the select filter and the adjacent protein environment.

At the end of *Simulation I*, two different states are observed in the pore helix domain. These states involve residue E152 and its partners which are topologically similar to the residues L40, F103 of the KcsA channel. The W106 of subunit P4 is observed in the *Simulation I* in contact with the pore helix of the same subunit. The inspection of the bend profile of TM1 in *Simulation I* once again reveals that the profiles of subunits P2 and P3 are more similar among them than the subunits P1 and P4. The initial strong bend angle in the region W114-Y118 persisted only in subunit P1, while in the other three subunits this pattern is rather intermittent. The diminished curvature in the W114-Y118 region in all subunits is accompanied by a bending in the region I97-T103, not observed in the initial conformation of the channel. Interestingly, the increased curvature in the W114-Y118 region coincides with the bending of the pore helix. The bending of the pore helix, on its turn coincides with changes of the rotamer state of E152 when the carboxyl group of the sidechain of the residue is rotated away from the originally faced TM helices, thus in some subunits it is found into the water filed TMV. In this particular rotamer state the E152 is observed establishing a hydrogen bond with W106 in the second part of the simulation, a representative conformation is shown in Figure 10. The rotation of the side chain of E152 is also accompanied by a sharp increase in the bending of the pore helix containing the E152. The increase in the bending on its turn is most probably operated by the substitution of alcohol groups of the side chains of S148 and T151 as donors of hydrogen bonds to the backbone carbonyls, respectively to residues A144 and F147 (Figure 10E). The implication of the sidechains of serine and threonine in the bending of alpha helices is documented in a statistical

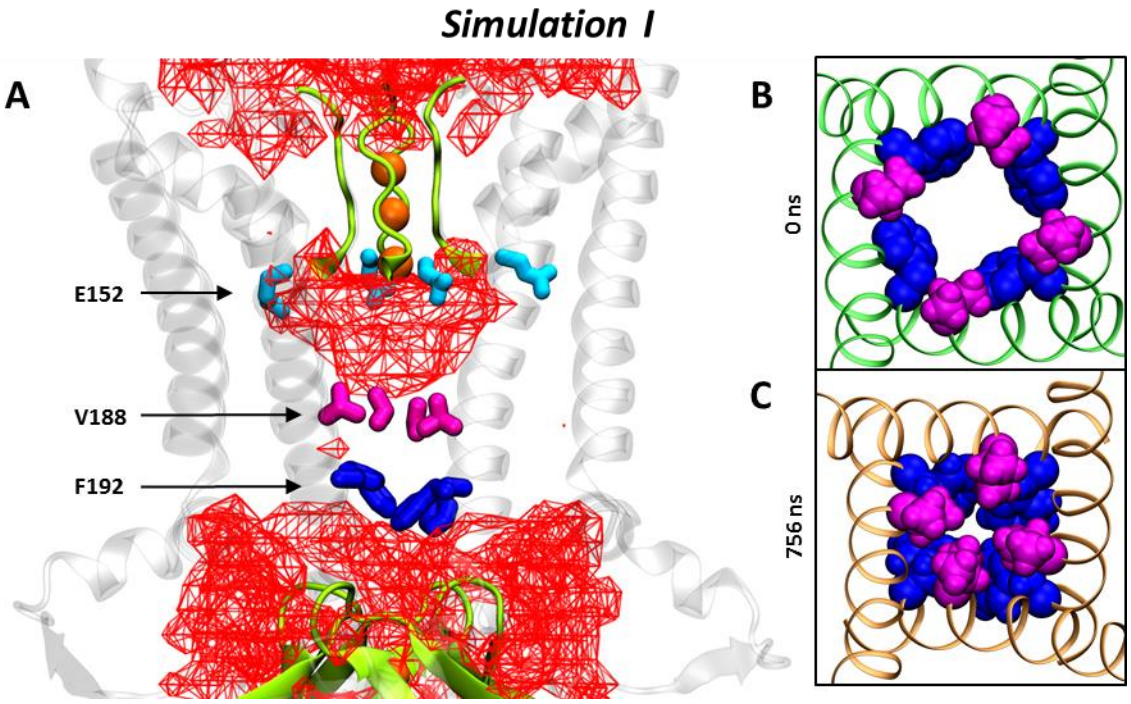

Figure 7: Closed conformation of the transmembrane vestibule of Kir3.2 in absence of PIP_2. (A) Sideview of the conformation of the TM vestibule and part of the CTCD of the channel are observed in a snapshot after 840 ns from Simulation I. The selectivity filter and the G-loop gate are highlighted with green. A mesh surface represents the probability >=20% of water occupancy in the time interval 600-840 ns from Simulation I. The hydrophobic gating inside the TM vestibule is operated by residues V118 (magenta) and F192 (blue). Three out of four E152 (cyan) in the pore helix are observed in the same conformation as in the crystallographic model PDB:4KFM. K^+ ions in the selectivity filter are shown as orange spheres. The representations of E152, V188, F192 and K^+ account for the average geometries in the 600-840 ns time interval, thus altered geometries of the sidechains of these residues can be noticed. (B) The starting conformation of the hydrophobic helix bundle crossing (HBC) gate seen from the selectivity filter. All atoms of V188 and F192 sidechains are shown as vdW spheres and colored accordingly to panel A. (C) The conformation of the HBC gate after 756 ns simulation. Represented atoms and coloring are same as in panel B.

investigation of crystal structures by Ballesteros and colleagues (Ballesteros et al. 2000). Here I report similar observations of threonine and serine in the gauche minus conformation simultaneously bending the pore helix at two consecutive turns of the alpha helix. This conformational change occurs in the part of the pore helix not exposed to the selectivity filter. Very importantly on the part of the pore helix interacting with the residues of the selectivity filter, the S148 and the T151 are flanking the E150.

The bending of the pore helix is very low and short-lived in subunit P3 as compared to subunits P1 and P4. As depicted in Figure 10F the sidechains of S148 and T151 interact with residues which are not contained in the pore helix. Thus, on the one hand there is data providing the possibility to investigate if the mechanism of the pore helix bending actually involves S148 and T151. And on the other hand, it is also interesting to access the effect of the pore helix bending, because it is evident that the conformation of the selectivity filter has evolved in respect to the staring conformation (Figure 6B, Figure 6C).

In Figure 11 the rotamer states of residue E152 observed in *Simulation I* are enumerated. Compared with the starting conformation from the crystallographic model, the equivalent rotamer state of E152 is when both dihedrals angles of the sidechain fall in the state centered at -180°. In the crystal, one of the oxygens from the carboxyl group of E152 is within 3.2 Å of the nitrogen in the indole group of W106, thus exhibiting propensity for hydrogen-bonding interaction. I will further refer to the combination of the dihedral angles χ_1 and χ_2 as the "rotamer states" of E152, denoted for example: *-180°/-180°*; where the first value is the χ_1 angle binned at -180° (±60°) and the second value is the χ_2 angle binned at -180° (±60°). The rotamer state -180°/-180° in *Simulation I* is predominant in subunits P2 and P3 and the second most populated state is the -180°/-60°. The second rotamer state resembles the first in the overall extended conformation of E152 towards the TM helices, despite the fact that the distance W106-E152 is increased. Subunits P2 and P3 display the lowest curvature of the TM1 helix in the region W114-Y118 and simultaneously in the pore helix. While the curvature of the pore helix resembles the initial conformation, the bending profiles of the TM1 are clearly different from the observed bending during the period of the equilibration when the protein has been held rigid (initial 45 ns in the timeseries). It appears that the migration of the bending peak in the TM1 is synchronized with the switching of the rotamer bin of χ_1 angle of E152 (Figure 8B and Figure 12). Indeed, considering subunit P1 the χ_1 angle is always in the -180° bin, and the bending peak persisted during the entire simulation between W144-Y118. Considering the P4 subunit where the minimization of the system has set the initial χ_1 of E152 to be in the -60° bin, the initial maximal bending has been displaced from W114-Y188 to the region I97-T103 for as long as the χ1 angel remained at in the -60° bin. Later on, when the χ_1 recovered the -180° bin the bending peak of the TM1 helix also recovered its initial location in the W114-Y118 region. The same synchronized oscillations of the TM1 maximally bended region and the χ_1 of E152 are observed in subunits P2 and P3. This data suggests that the rotamer state of E152 is influenced by the conformation of the TM1, and it is nicely in line with the report of the equivalent influence of the TM1 on the fluctuation of the selectivity filter (Heer et al. 2017).

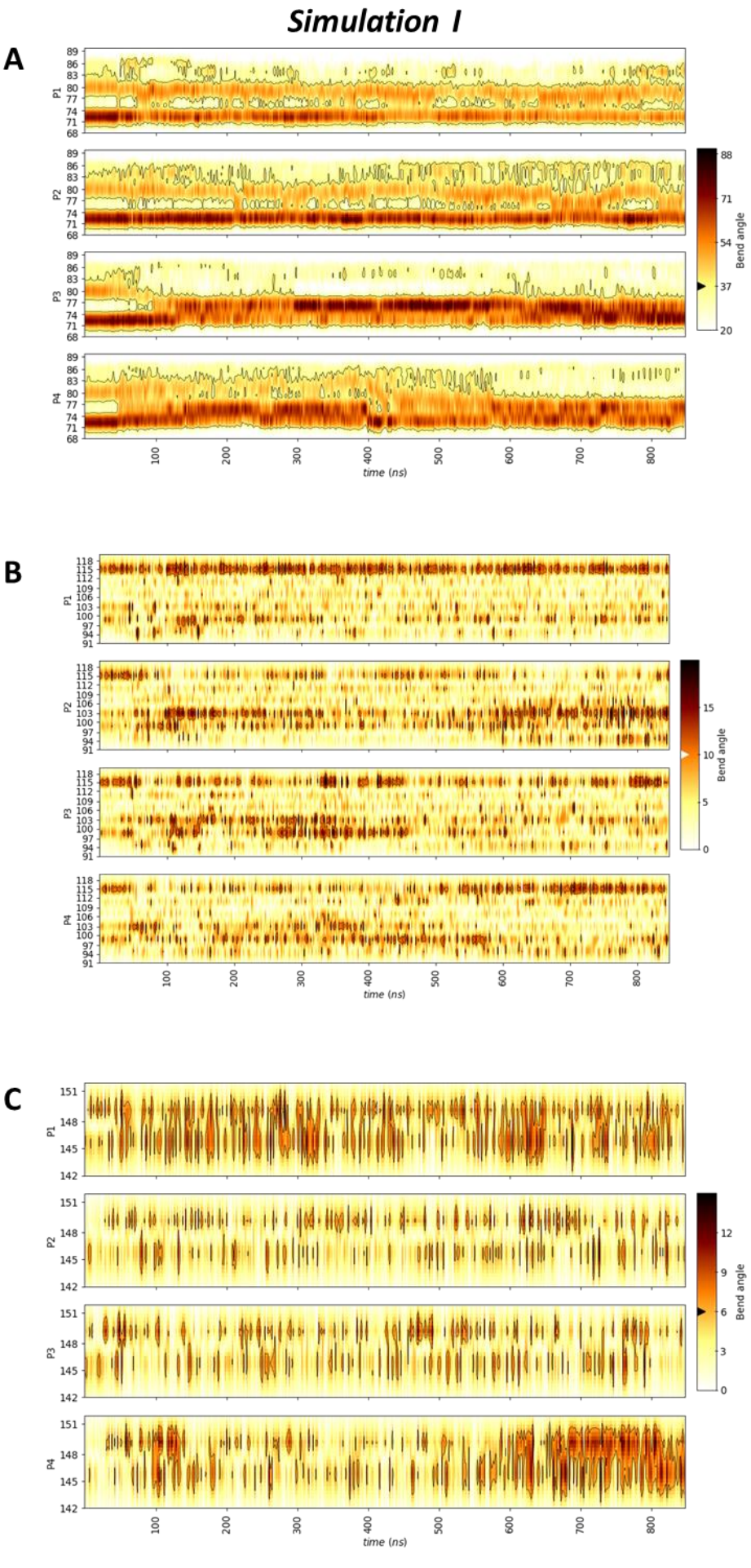
Simulation I
A
B
C
P1
P2
P3
P4
time (ns)
Bend angle

Simulation I

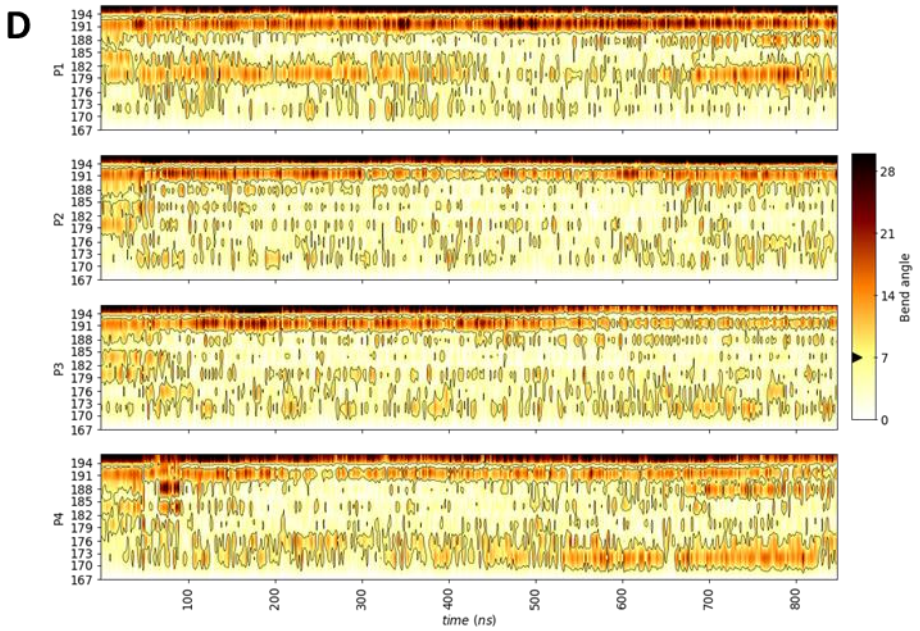

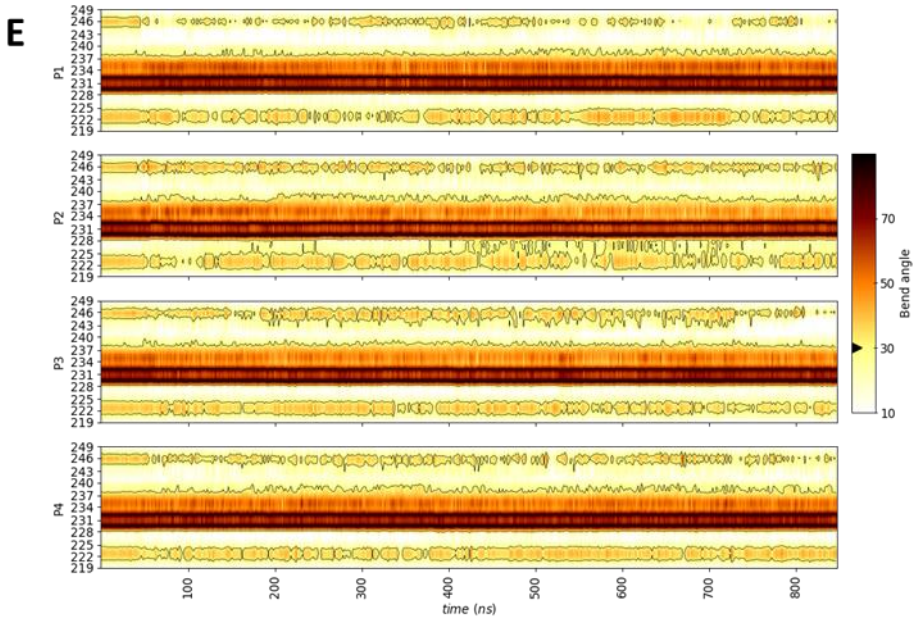

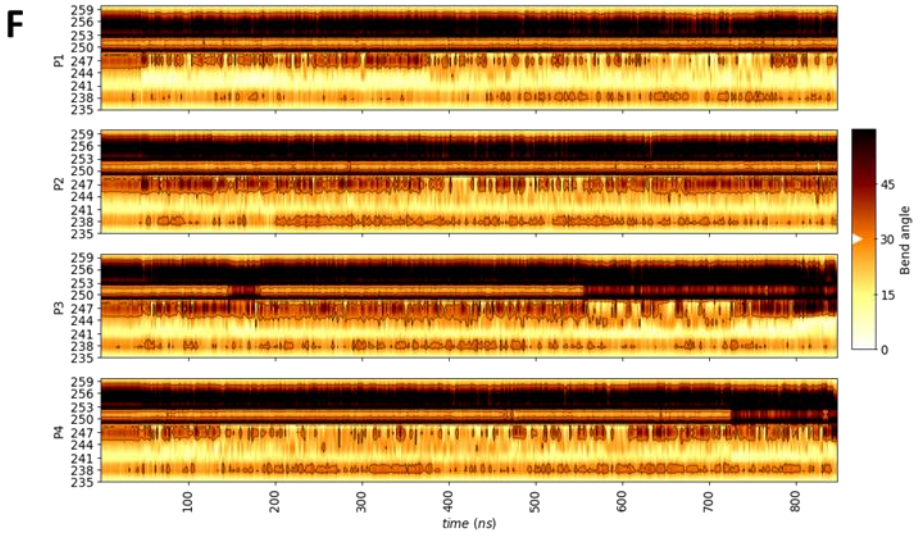

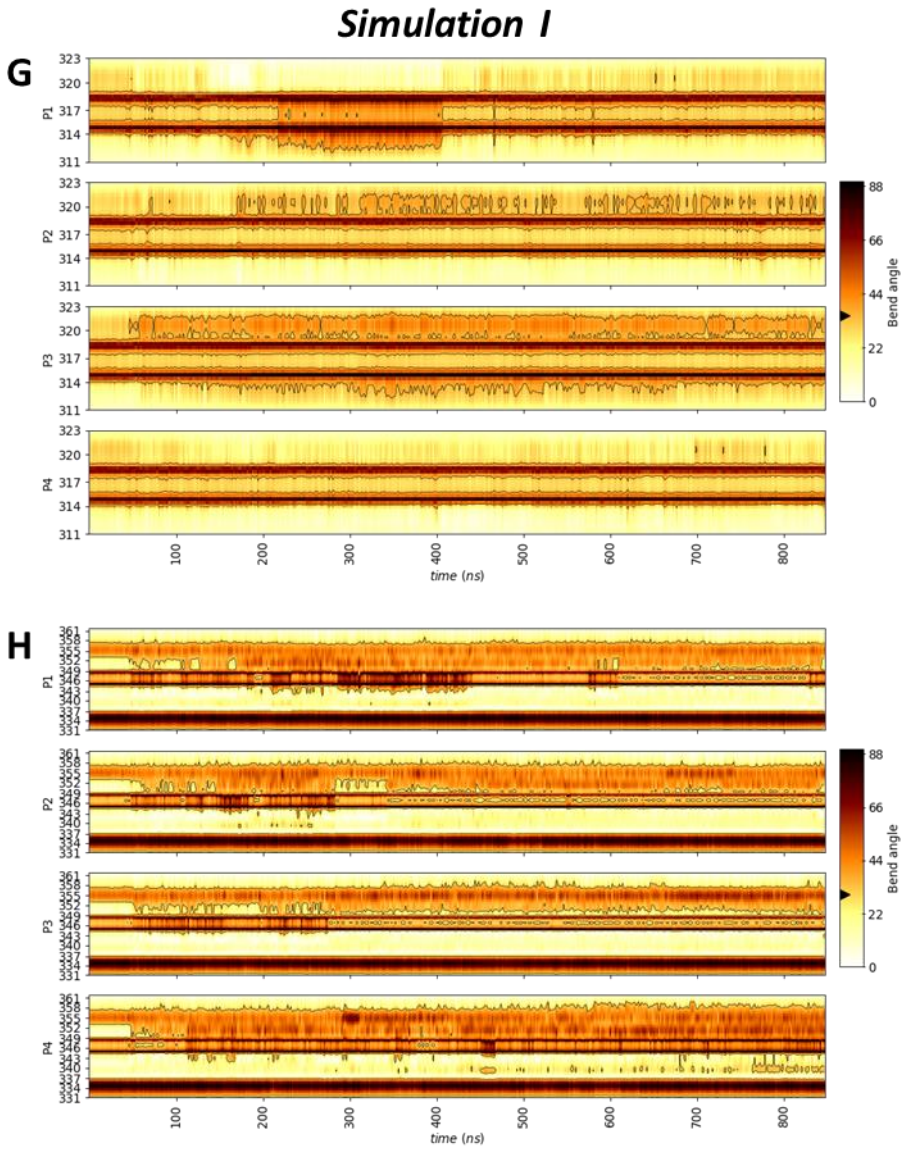

Figure 8: Evolution of the curvature of selected secondary structures in mouse Kir3.2 during simulation in absence of PIP2. The curvature measures as bend angle within four successive residues in each subunit is plotted as separate timeseries in each panel. A contour is drawn at a threshold value ***C*** *to facilitate the comparison between subunits (black/white marker in the color bar). The monitored secondary structure elements of Kir3.2 are: (A) βA strand and slide helix residues H69 to K90,* ***C****=37°; (B) TM1 residues W91 to R120,* ***C****=10°; (C) pore helix residues V142 to E152,* ***C****=6°; (D) TM2 residues P167 to S196,* ***C****=7°; (E) βC-βD strands and loop K219 to T249 ,* ***C****=30°; (F) βD-βE strands and loop residues V235 to T260,* ***C****=30°; (G) βH-βI strands and loop residues E311 to A323,* ***C****=35°; (H) βL-βM strands and loop residues R337 to T362,* ***C****=40°.*

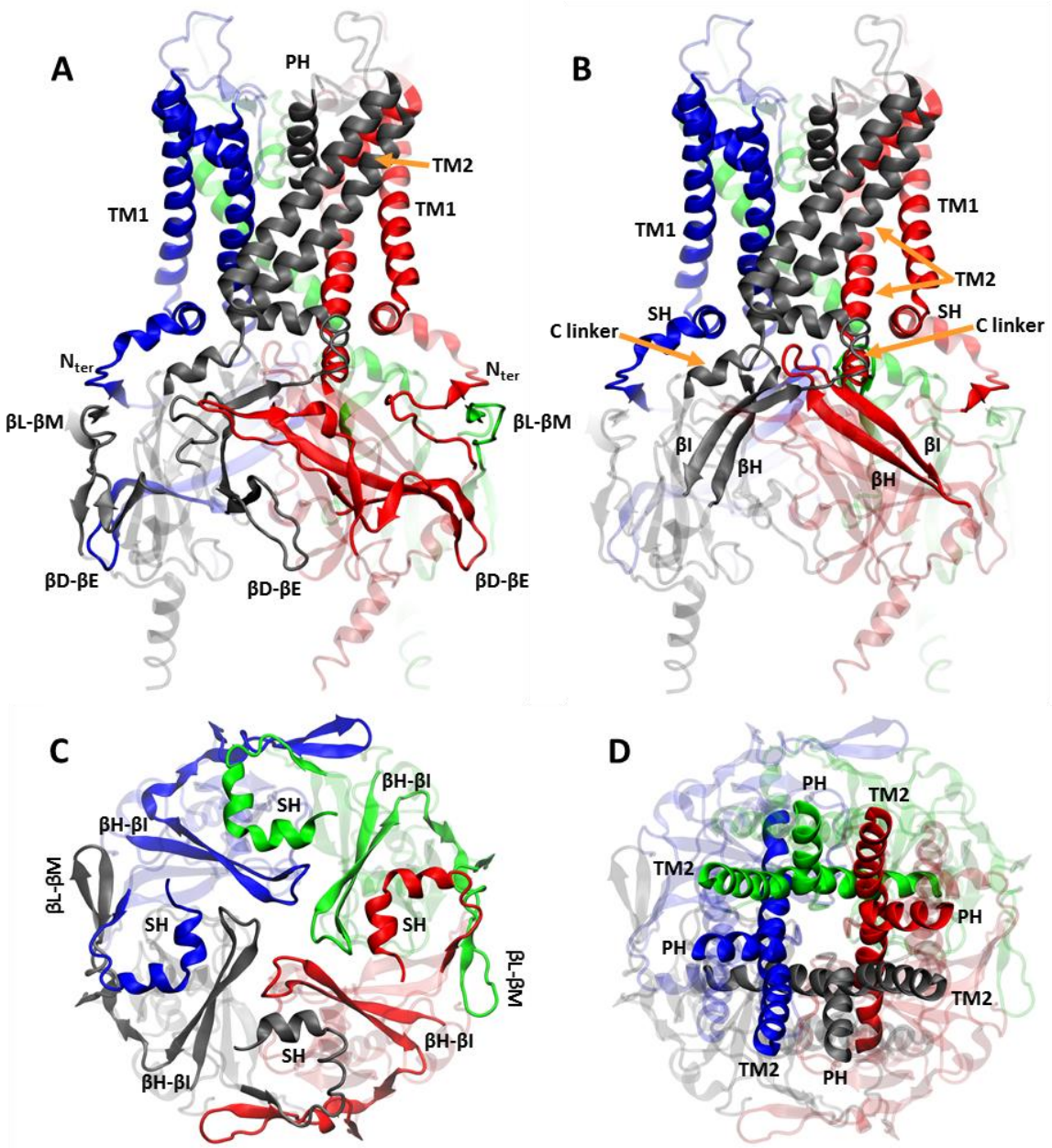

Figure 9: Topology of subset of secondary structures in Kir3.2. Selected secondary structures are shown as solid material in a cartoon representation of the channel with colored subunits: P1 in red; P3 in grey; P2 in blue; P4 in green. (A) Sideview emphasizing the proximity of N_{ter}, βL-βM loop and strands, and the βD-βE loop and strands. Also shown, the transmembrane helix bundle and the juxtaposition of the pore helix (PH). (B) Sideview emphasizing the superimposition between βH-βI loop and sheets, the C linker, and the slide helix (SH). (C) Extracellular view of the CTCD with emphasis on the physical contacts between βL-βM loop and strands, the N_{ter} and slide helix, and βH-βI loop and strands. (D) Extracellular view on the channel with emphasis on the two contacts that each pore helix has with two adjacent inner helices (TM2).

5.3.2.2.1 Identification of causal relationships in the dynamics of the region around the selectivity filter

Hereafter I will detail the investigation of the causality of the change of the conformation in the selectivity filter and the adjacent region. I have first identified residues alternatively interacting with E152 depending on its rotamer state. Then, the list of monitored hydrogen bonds was extended to the partners of the residues identified in the first place. A subset of these monitored contacts is reported in panel A of Figure 13. Subsequently, I used the collected timeseries of interatomic contacts to construct an interaction diagram based on the instantaneous correlation between the timeseries. The extracted distances have been correlated pairwise and the diagrams pointing to cause effect relations are presented in Figure 14.

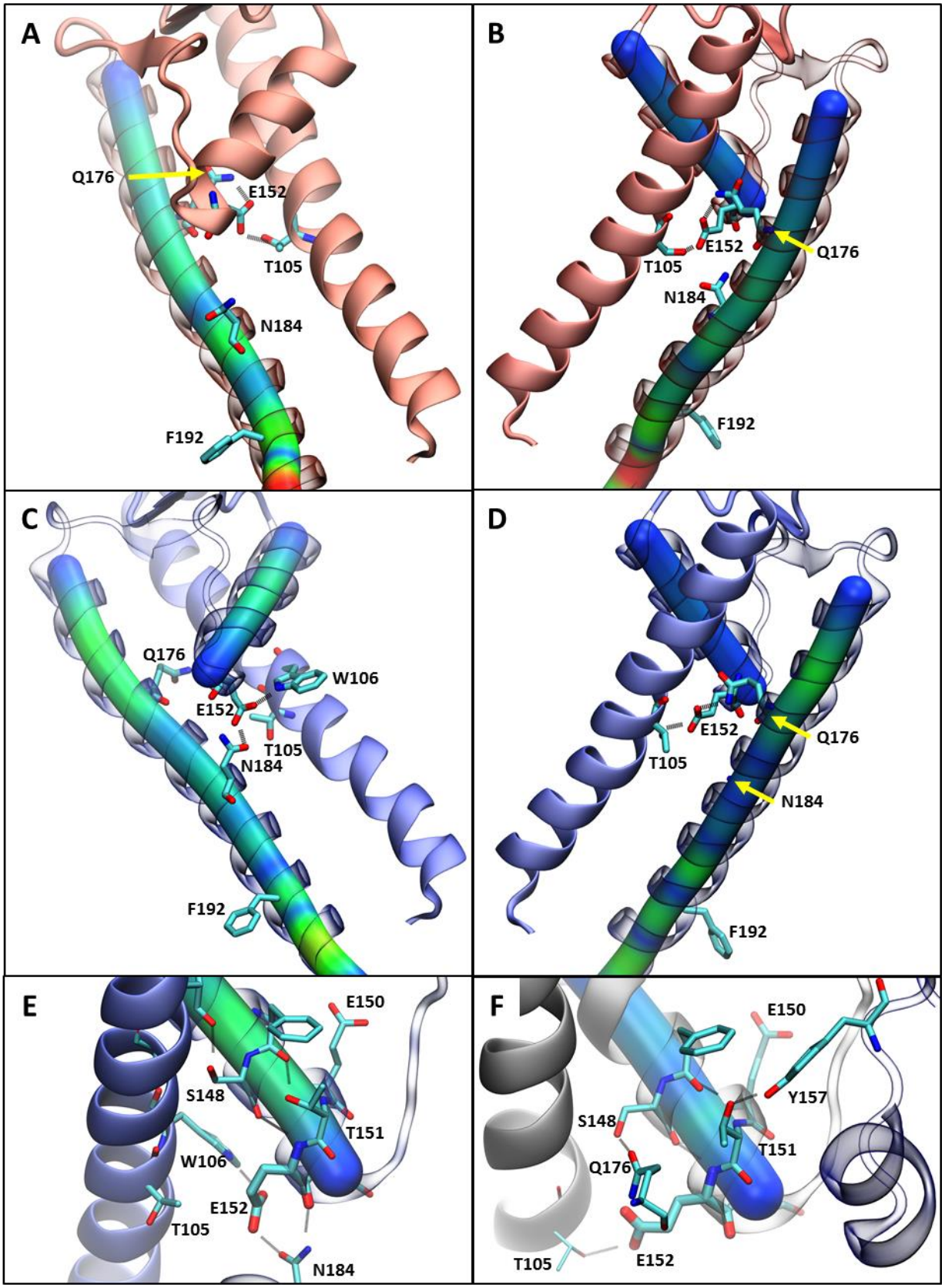

Figure 10: Conformational changes in the transmembrane helix bundle and in the pore helix in mouse Kir3.2. during simulated channel closure. Two conformations of the E152 are shown in both columns of panels. Panels on the left represent conformation in subunit P4 and panels on the right depict the diametrically opposite subunit P3, all conformations are from snapshots of Simulation I. Panels A and C represent subunit P4 viewed from the K^+ permeation pathway along the plane of the membrane. Panel E (subunit P4), and panels B, D and F (subunit P3) are representations of the respective subunits viewed from the membrane-protein interface along the plane of the membrane. Parts on the protein are set to transparent

for visualization of superimposed elements, in panels E and F the N_{ter} of TM2 is not represented to clear the view on the pore helix. The protein in all panels is colored in red for snapshots at the beginning and blue for the snapshots at the end on the simulation (in panel F the color is gray, nevertheless the time frame is equivalent to the one represented in panel E). The curvature of the helices in the panels is represented as a solid cylindrical surface, colored by rainbow gradient scaled on the bend angle range from 0° (dark blue) to 30° (red). (A) Hydrogen bonds between E152 and T105 and Q176. The conformation is observed 13 ns after the harmonic restraints on the protein where turned off. (B) The E152 hydrogen bonding T105 and Q176 in subunit P3. (C) Representative hydrogen bonding network of E152 in P4, where the E152 residue is observed with rotated carboxyl group of the sidechain away from the TM1 (snapshot at 738 ns after the equilibration). New hydrogen bond partners of E152 are T106 and N184. (D) The E152 in subunit P3 have preserved its initial conformation and hydrogen bond partners (snapshot 796 ns after the end of the equilibration). (E) Closeup on the E152 contacting W106 and N184 (760 ns after the equilibration). Hydrogen bond partners of residues S148 and T151 are also included. The carbonyl oxygen of the backbone of S148 interacts with the nitrogen of the backbone of E152, while the hydroxyl group of the sidechain of S148 substitutes the backbone nitrogen of S148 as donor of hydrogen bond to the carbonyl oxygen of A144. Similarly, the hydroxyl group of T151 is substituted as hydrogen donor in the alpha helix to the carbonyl oxygen of F147. (F) Closeup on E152 contacting T105 and Q176. Hydrogen bond partners of S148 and T151 are also shown. The side chain of S148 contacts Q176. And the sidechain of T151 contact Y157 of the adjacent subunit.

Based on my previous enquiry about the protonation state of the E152 residue, I have been particularly focused on this residue. Initial visual inspection of the MD trajectories was sufficient to spot the alternating rotamer states of the E152 residue. I have thus started collecting the hydrogen-bonding partners of the E152. These partners are relevant for the particular rotamer state of E152 as they are listed in Figure 11. The first impression of the collected timeseries was that they are quite different from one another, because even on a local scale, conformations including only several equivalent residues among the four subunits were not rotational four-fold symmetrical as one could expect for the homotetramer channel. The symmetry observed in these ns-scale simulations is not even a simple rotational two-fold, but rather a two-fold mirror-image symmetry. This is certainly due to the fact that at the simulated time laps the conformational changes generated in one part of the macromolecule have not been propagated very far, thus one can follow their propagation in a cooperativity fashion.

After the first immediate partners of the E152 have been identified, I collected the list of hydrogen bonds for the partners of these first level partners of E152, thus covering the majority of the hydrogen bond capable residues in the vicinity of the selectivity filter. Unfortunately, the hydrogen bond timeseries are very noisy and discontinuous depending on the threshold parameter used to collect the binary states (data not shown). Yet I decided to collect the interatomic distances of heavy atoms in the residues involved in the hydrogen bond network that I was investigating. The interatomic distances also produced noisy timeseries, nevertheless I applied convolution transformation of this data that provided me with smooth timeseries. For the transformation by convolution, I first digitized the distances in bins of 0.28 Å, then in order to give a lot of weight on the timesteps near the current timestep (t) I used a very sharp symmetric weighting function which shape was modeled by x^n with $n=14.95$ for $\{ x: (t-w/2) \leq x \leq t \}$ and $n=-14.95$ for $\{ x: t < x \leq (t+w/2) \}$. In order to avoid strong influence of local noise the weighting function was applied to a very large time window $w = 70$ *ns*. In reality, the weights declined to $5*10^{-3}$ for datapoints situated at ±14 ns from the current data point, meaning that the effective time window for the convolution has been of approximately 30 ns.

Representative plots of the original and the convoluted timeseries are presented in panel B of Figure 13. The following would serve as a remark and a disclaimer on the data preparation. The plotted data has been extracted from the convolution transformed timeseries in a manner that I have considered only timesteps in which the rotamer state of E152 in subunit P4 was -180°/-60°. Thus, the plotted data using this methodology could not be a continuous representation of the interatomic distances during the entire simulation, but it is a set of interatomic distances observed when another event took place. For the particular case of *Simulation I*, the data collected for the plot represents a nearly-continuous time laps, because as one can verify in Figure 12 the targeted rotamer state of E152 in subunit P4 is only observed in the period 620-845 ns, and there is a very short-life change near the beginning of this period. Regarding the original timeseries, it can be noted that there are

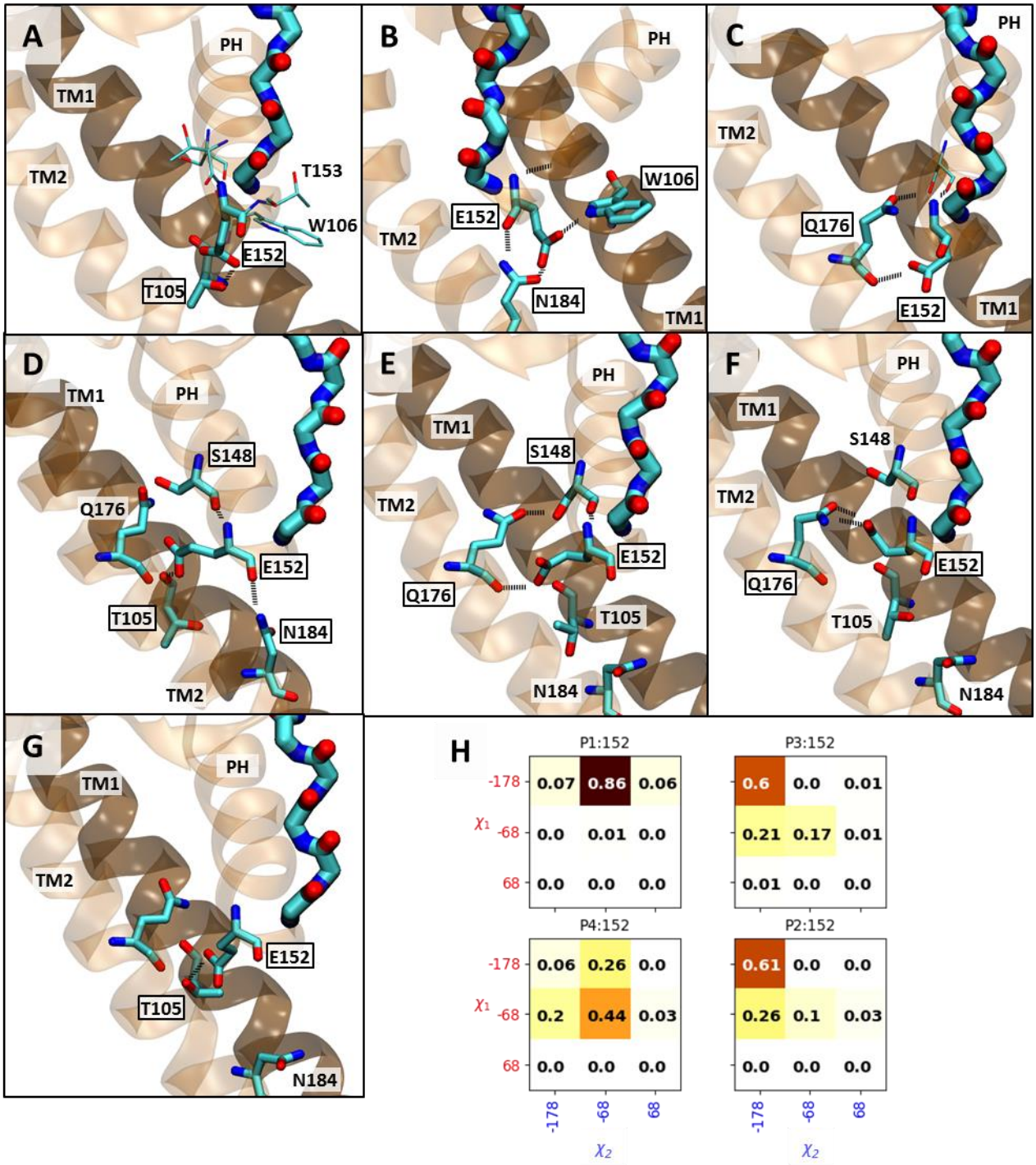

Figure 11: Rotamer states of the sidechain of residue E152 in mouse Kir3.2 observed by molecular dynamics simulation. In panels A-G all display conformations of E152 and the adjacent transmembrane region in subunit P3 during Simulation I. In panels A-G the mainchain of the selectivity filter is represented by the thickest sticks. E152 and residues engaged in hydrogen bond with E152 are represented in medium-thick sticks and indicated with boxed labels, while other residues common among the panels are displayed in thin sticks do not have boxed labels. (A) E152 χ_1: -180°, χ_2: -180°, contacts the alcohol group of T160. (B) E152 χ_1: -180°, χ_2: -60°, contacts the nitrogen in the indole group of W106 and establish double interaction with N184 via the carboxyl group of the sidechain and the carbonyl of the mainchain. (C) E152 χ_1: -180°, χ_2: 60°, contacts the carbonyl oxygen of the mainchain of Q176. (D) E152 χ_1: -60°, χ_2: -180°, contacts the mainchain of TM1 at the carbonyl of T105 and TM2 at the carboxamide group of N184. (E) E152 χ_1: -60°, χ_2: -60°, contacts the mainchain of TM2 at Q176. (F) E152 χ_1: -60°, χ_2: 60°, contacts Q176 engaging simultaneously both the amine and the carbonyl of the sidechain. (G) E152 χ_1: 60°, χ_2: -180°, contacts the alcohol of the sidechain of T105. (H) Average persistence of the rotamer states of the sidechain of E152 by subunit during Simulation I. The E152 in rotamer state χ_1: -180°, χ_2: -180° originally present in the 4KFM is the predominant conformation in only two subunits.

periods with reduced noise which corresponds to interaction events between both partners when the distance is low, and there are also periods of decreased noise when one of the partners interact with a third partner. The information of third-party interactions is lost once the original timeseries have been transformed, because it was contained in the standard deviation of the distance within the span of the sliding window. The subset of interatomic distances between T105-E152 used in panel B of Figure 13 shows the dynamical behavior of the E152. While the measured distance is stable in subunits P1 and P4, it displays a rapid displacement of the hydroxyl group of the sidechain of about 5 Å in subunits P2 and P3 which coincides with the change of rotamer state of the monitored E152 in these subunits.

I then proceeded to the linking of the different interactions of interest (Figure 13A) by computing the instantaneous correlation between the new data series. The Pearson correlation has been used rather than a cross correlation, because the datapoints of the compared distances have been sampled in a non-uniform timestep manner as described above. This gave me a correlation matrix, which has been used to construct the network diagrams in Figure 14. In the diagrams each node represents an interatomic contact as identified in Figure 13, an edge between two nodes is drawn if the Pearson correlation coefficient between the data series satisfies *abs(r) ≥ 0.5 (and abs(r) ≥ 0.375 in panel E)*. The threshold value 0.5 has been selected arbitrarily because at higher values the particular graph describing subunit P4 was mainly disconnected with very small subgraphs. Despite the fact that a coefficient of 0.5 means that we are able to infer the direction of the change of one of the data series from the other for only half the time, I believe that 50% is a good estimate of the correlation in the such multidimensional contact network. I have inspected the presented diagrams and compared every couple of data series, I noticed that very often the correlation of the change of values of two series rises by a slight increase of the collected values. This slight change would represent the propagation of a shock wave in the protein caused by a larger conformational change elsewhere in the macromolecule. Such an example can be observed in the representative traces in Figure 13, where in the first quarter of the data series of subunits P1 and P4 the instantaneous trends are very similar without an actual change of the state of binding of T105-E152. Such synchronized fluctuations are frequent in the data set that I am examining here (see Annex for all data points), and I will not discard them from my interpretation of the diagrams because this behavior is normally expected in the thermally driven dynamics of ensemble of small rigid bodies which constitute the integral protein macromolecule. Furthermore, during the detailed inspection of the diagrams of Figure 14 I did not encounter any aberrant or miss-leading correlation caught by the analysis and leading to a contradictory inference of the higher-level interactions.

Regarding the correlation involving P1 as the central subunit (Figure 14A) the diagram is moderately dense and fully connected including 11/15 nodes of subunit P1 and a total of 36 nodes. I did not make any measure of the topology of the network but it appears that the distance between N139-R160 (*id: 8*) is the most central node, followed by distances E152-N184 (*id: 3*), P1:157-P3:157 (*id: 5*) and N137-R160 (*id: 1*). The graph can be divided in two large subgraphs if one removes the nodes with ids 18, 25, 27, 37, 47 and 53, all of which do not belong to the subunit P1 but suggest an inter-subunit cooperativity as detailed hereafter. The graph involving the subunit P3 as central (Figure 14B) cannot be disconnected in similar manner because all nodes necessary to connect the network involve a distance to the subunit P3. This graph also contains a very large cluster where nodes with ids 34 and 47 are central. This large cluster is generated by the single oscillation of the distance between I105-E152 (*id: 47*) and W106-E152 (*id: 34*) observed in the subsets in panel B of Figure 13. Thus, the cluster caught the relation between the change of rotamer state of E152 in this subunit and gave the opportunity to pinpoint the generator event and also to track its consequences. The diagram of the subunit P4 is moderately populated and the less interconnected one among the those shown here. I believe the sparse network resulted from the relative stability of the data series involving the subunit P4, given that a unique rotamer state of E152 of this subunit has been used as reference to collect the data series. The diagram describing the subunit P2 contains the same

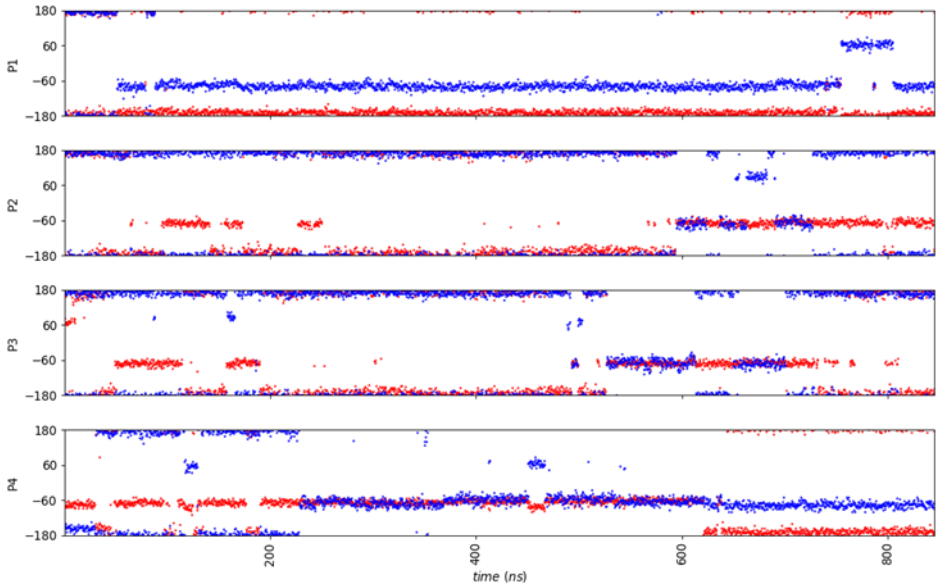

Figure 12: Timeseries of dihedral angles χ_1 and χ_2 of residue E152 of mouse Kir3.2 molecular dynamics simulation. Data representative of Simulation I; angle χ_1 (red) and angle χ_2 (blue) are measured every 400 ps.

number of nodes but has the most interconnected structure. It is likely that this is the reflection of a tight packing of the protein in this subunit, because the overall situation with this segment of the channel is that it is the less divergent from the initial structure in respect to those differences which were spotted in the remaining subunits.

In the following paragraphs I will use the notation *n~m* to designate the edge between node *n* and node *m*, where *n* and *m* are the identifiers of the interatomic distances given in panel A of Figure 13, moreover all interpretations of the order of the subunits suppose an observation from the extracellular site, thus the adjacent clockwise order of the subunits is: P1, P3, P2, P4 (Figure 9, Figure 13A). Figure 14 showed anti-parallel correlations between equivalent couples of contacts. For instance, in the couples of contacts *8~42* and *40~42*, the bending of the pore helix is alternatively correlated to the distance between the sidechains of N139 and R160 if the distance is measured in subunit P1 or in subunit P3. This pattern involves two adjacent subunits, its interpretation is that the change of rotamer state of R160 in subunit P3 leads to a contact with residue N139, this event is concomitant with the distancing of the alcohol group of S148 from the backbone of A144 in the pore helix in the same subunit and eventually influencing its bending state. Regarding the distance measured in P1 involving the N139 and R160, it is clear that the contacts between these two residues are observed in parallel with the contact between S148 and A144 in P3. Thus, it appears that the bending of the pore helix in P3 is alternatively influenced by the same type of conformational change but involving two different regions.

More combinations of antiparallel-correlated equivalent contacts among different subunits can be found in the diagrams in Figure 14. These patterns show that an orthogonal inter-subunit cooperativity is operated in the simulated system and suggest that dynamics of the system evolve in a dimer of dimer fashion. Other examples of anti-parallel cooperativity among adjacent subunits are: $^{-}$*2~34* and $^{+}$*18~34*, $^{+}$*8~42* and $^{-}$*40~42*, $^{-}$*9~31* and $^{+}$*25~31*, $^{+}$*17~42* and $^{-}$*33~42* (indexed – or + signs indicate the sign of the correlation coefficient for the particular couple of nodes). The nodes occurring in this list are: P1:E152:O~P1:W106:NE1 (*id: 2*), P1:N139:OD1~P1:R160:CG (*id: 8*), P1:N139:ND2~P3:R164:CG (*id: 9*), P2:N137:O~P2:R160:CG(*id: 17*), P2:E152:O~P2:N184:CG (*id: 18*), P2:N139:ND2~P4:R164:CG (*id: 25*), P2:E152:CD~P2:T105:OG1 (*id: 31*) , P3:N137:O~P3:R160:CZ (*id: 33*), P3:E152:CD~P3:W106:NE1 (*id: 34*), P3:N139:OD1~P3:R160:CZ (*id: 40*), P3:S148:OG~P3:A144:O (*id: 42*). Firstly, this listing is not symmetric, because there are no equivalents in all subunits for each couple of distances, and there is no occurrence of the subunit P4. Once again

A

	P1	P3	P2	P4
P1	S	N	O	P
P3	P	S	N	O
P2	O	P	S	N
P4	N	O	P	S

P1	P3	P2	P4	
0	32	16	48	SELF:137:ND2 | SELF:159:O
1	33	17	49	SELF:137:O | SELF:160:CZ
2	34	18	50	SELF:152:CD | SELF:106:NE1
3	35	19	51	SELF:152:O | SELF:184:CG
4	36	20	52	SELF:153:OG1 | NEXT:177:OG
5	37	21	53	SELF:157:O | OPPOSITE:157:O
6	38	22	54	SELF:160:CZ | NEXT:162:O
7	39	23	55	SELF:160:CZ | NEXT:164:CG
8	40	24	56	SELF:139:OD1 | SELF:160:CZ
9	41	25	57	SELF:139:ND2 | NEXT:164:CG
10	42	26	58	SELF:148:OG | SELF:144:O
11	43	27	59	SELF:150:O | SELF:155:N
12	44	28	60	SELF:150:CD | SELF:157:N
13	45	29	61	SELF:150:CD | SELF:160:NE
14	46	30	62	SELF:151:OG1 | SELF:147:O
15	47	31	63	SELF:152:CD | SELF:105:OG1

B

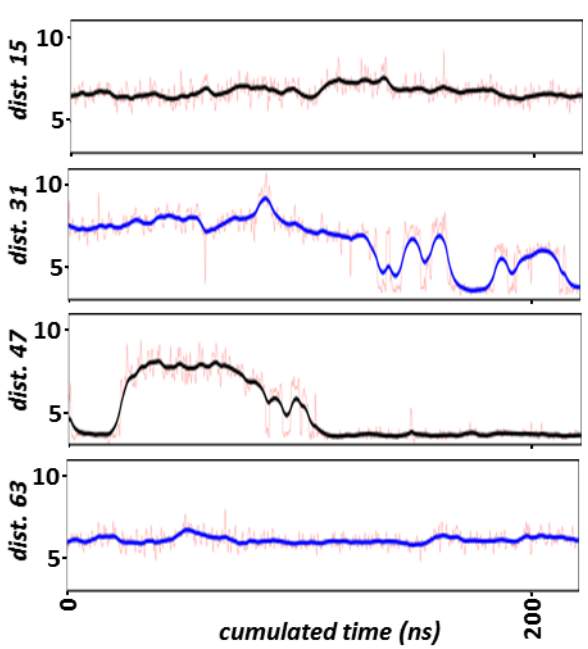

Figure 13: Atomic contacts monitored in the region of the selectivity filter of mouse Kir3.2 molecular dynamics simulation. Data representative of Simulation I. (A) The top four rows show the clockwise adjacency between the channel subunits viewed from the extracellular side (see section 4.2.4 for details). The five-columns table lists the identifiers (0 to 63) given to the timeseries of the interatomic distances; the last column details the interacting atoms. (B) Subset of the interatomic distance between E152:CD and T105:OG1 when the E152 rotamer state is the -180°/-60° in subunit P4. Interatomic distances have been collected every 400 ps (red curve) and have been convoluted by a very sharp symmetric function, the width of the time window was set to 70 ns and the parameter controlling the shape of the function was set to $x^{14.95}$. Then the convoluted timeseries have been sampled at the timesteps when the E152 rotamer state had the desired values. Example of the new timeseries is depicted in the four plots in the panel (the black and blue colors are without particular meaning).

this is the reflection of the skewed symmetry in which the conformation of the tetramer evolved. Secondly, due to the repetition of several distance identifiers, it is worth checking if those are not somehow aberrant or trivial data sets. For instance, the distances between R160 and N137 or N139 are always positively correlated because when R160 moves away from one of the asparagines it moves away from the other to because of their intrinsic proximity.

The first pair involves the rotamer states of E152 in subunit P1, P2 and P3. This pattern is the hallmark of the skewed symmetry that I have evoked earlier and similar datasets can be observed in panel B of Figure 13 as the timeseries involving E152 and T105 or W106 are very similar. The third couple involves on the one hand the proximity of the E152 and T105 in subunit P1, on the other hand it involves the proximity of the N_{ter} of the pore helix in subunit P1 or P2 and the N_{ter} of TM2 in the adjacent subunit, respectively P3 or P4. This pattern consists in the stabilization of the C_{ter} of the pore helix towards the TM1 in subunit P2, and the concomitant antiparallel distancing of the N_{ter} of pore helix in subunit P1 and the N_{ter} of TM2 of subunit P3 and the approach of the equivalent structure between P2 and P4 subunits. Lastly, the second and fourth couples involve the bending of the pore helix in the P3 subunit. The pattern concerning the second couple was detailed in the previous paragraph, concerning the fourth couple of distance the pattern is equivalent but this time it involves the subunits P2 and P3 instead of P1 and P3 on the side of the conformational change involving R160. Thus, the preserved distance between R160 and N137 or N139 in subunits P1, P2 and P3 is concomitant with the distancing of the sidechain of S148 from A144 in subunit P3. This leads to the conclusion that the weakly-bend state of the pore helix is promoted by the preserved proximity of the side chains of E150 and R160. This contact is observed in the crystal structure and all diagrams presented in panels A-D of Figure 14 show that this contact is positively correlated to the proximity of E152 and the adjacent T105. Thus, one should expect that the bending of the pore helix involving

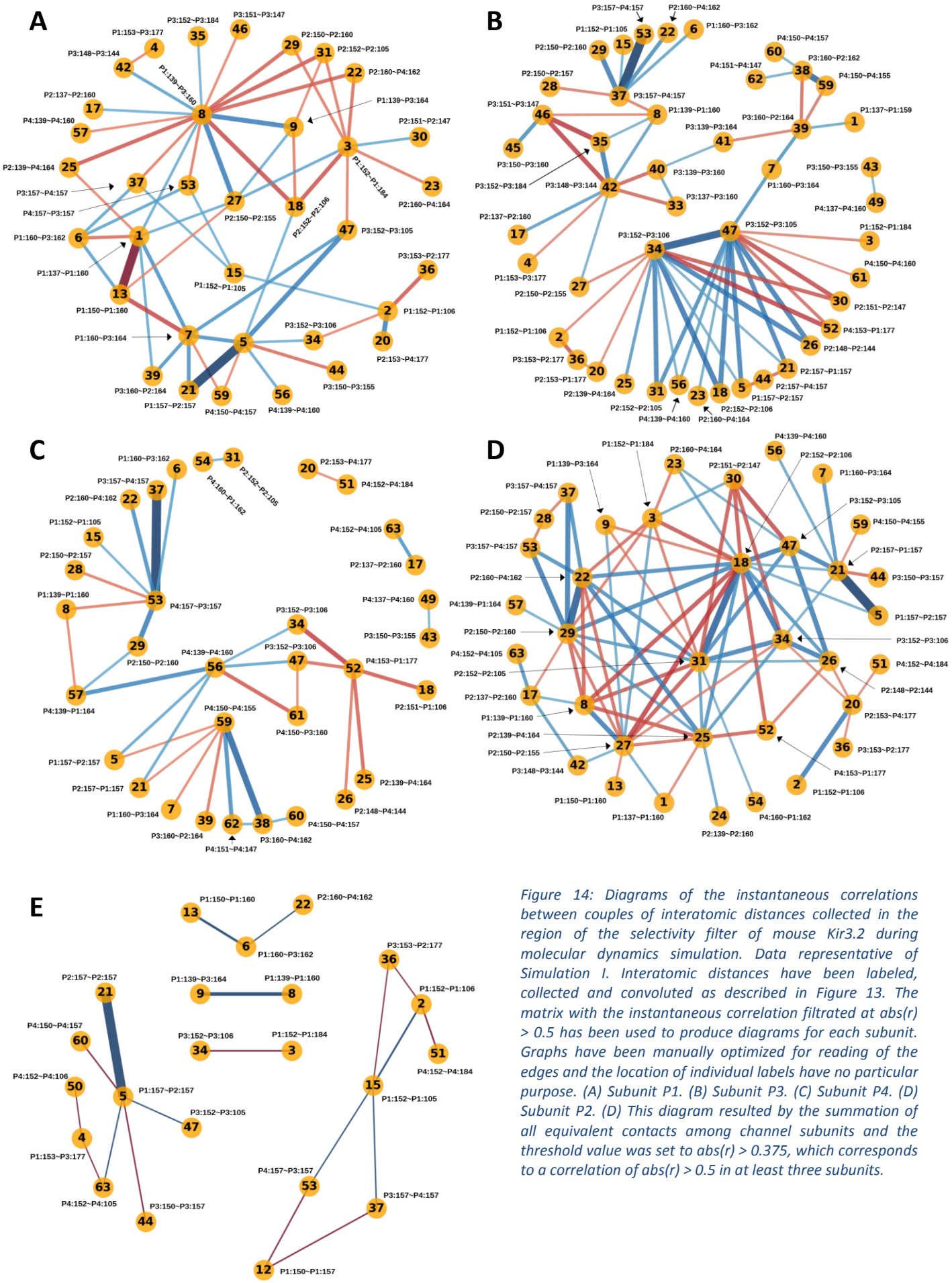

Figure 14: Diagrams of the instantaneous correlations between couples of interatomic distances collected in the region of the selectivity filter of mouse Kir3.2 during molecular dynamics simulation. Data representative of Simulation I. Interatomic distances have been labeled, collected and convoluted as described in Figure 13. The matrix with the instantaneous correlation filtrated at abs(r) > 0.5 has been used to produce diagrams for each subunit. Graphs have been manually optimized for reading of the edges and the location of individual labels have no particular purpose. (A) Subunit P1. (B) Subunit P3. (C) Subunit P4. (D) Subunit P2. (D) This diagram resulted by the summation of all equivalent contacts among channel subunits and the threshold value was set to abs(r) > 0.375, which corresponds to a correlation of abs(r) > 0.5 in at least three subunits.

residue S148 and the distance between E152 and T105 to evolve jointly in the same subunit. Unfortunately, this conclusion cannot be drawn from panel E of Figure 14 showing the diagram obtained from the averaged correlation matrix in respect to all subunits, because in this matrix no events with average below ¾ are caught. The stipulated positive correlation between contacts involving on the one hand E152 in the pore helix and T105 or W106 in the TM1, and on the other hand the proximity between E150 and R160, can be verified in panels A-B of Figure 14. Examples of similar couples of inter atomic distances referenced in Figure 13 are: *+7~47*, *+23~47*, *+29~31*, *+31~54*, *+17~63*, *+8~31*, *+7~47*. This list does not contain distances involving the subunit P1 pointed by P4, because by construction the rotamer state of E152 is stable and in the scope of the hypothesis that the change of this state will cause other measured distances to change, one should expect exactly that there will be no events correlated to the distance involving the E152 in subunit P4. Interestingly, the majority of the interatomic couples presented above involves two adjacent subunits, this observation is consistent with an inter-subunit cooperativity in the counterclockwise direction where the destabilization of the contact between E152 and T105 in one subunit will cause the motion of R160 away from E152 in the preceding subunit.

It is important to understand the effect on the conformation of the selectivity filter of this type of cooperativity and what is the event causing/regulating the E152 rotamer states. The last panel in Figure 14 shows the resulting consensus network (to a threshold *abs(r) = 0.375*) after averaging the diagrams shown in panels A-D. As the diagram is averaged, the interpretation of the presented relationships is centered at one subunit P1 and the adjacency of the neighboring subunits the labels of the measured distances follow the scheme corresponding to subunit P1 in panel A of Figure 13. This diagram contains two largest subgraphs which are populated by topologically equivalent pairs of atoms from different subunits. The diagram also contains the small parts which are disconnected from every other subgraph. The triplet network shows that the proximity between the R160 and E150 both in the current subunits is positively correlated to the proximity of the R160 of the opposite subunit and the I162 in the preceding subunit. This part of the diagram suggests that a cooperativity in the clockwise direction is operated from a subunit where R160 disengages the environment of E150 in the same subunit, leading to the destabilization of the equivalent contacts in the opposite subunit of the tetramer. The couple between nodes with ids 8~9 is a trivial one and it caught the repeated motion of R160 towards E164 in the preceding subunit. The couple of nodes 3~34 shows an anti-correlation deeper in the TM domain between adjacent subunits where both E152 experience rotamer dynamics. The first part of the interpretation of this relationship is that E152 is rotated in both subunits. The distancing of the E152 in the first subunit is concomitant with the contact between E152 and N184 in the previous subunit. This is the measure of the displacement of the C_{ter} of the pore helix towards the TM2 in one subunit, and the transmission to the conformational change until the next subunit where is favored the topologically and functionally equivalent destabilization of the interaction pore helix-TM1.

The two largest subgraphs in panel E are mirror images of one another with only one extra node in the left image. Here the relationship described for the nodes 3~34 is captured once again at 2~51, only this time it concerns the current subunit as receiving the conformational change from the bending of TM2 in the preceding subunit. The distance representing the destabilization of the pore helix-TM1 (*id: 2*) is also related to the approach of the TM2 of the opposite subunit to the C_{ter} of the subunit following the current one (*id: 36*). This relationship is equivalent to that of 2~51 and 3~34 and it is a third correlation from this dataset pointing to the link between the destabilization of the pore helix-TM1 and the bending of the TM2 helix. This link should be operated in a cooperative manner as suggested by the correlations between interatomic distances measured between equivalent positions closing an entire circle in the tetramer. The next node (id: 15) in the network is equivalent to node 2. Then the destabilization of pore helix-TM1 in the central subunit shows positive correlation in respect to the distancing of the carbonyls at the extracellular entrance of site S0 of the selectivity filter in both neighboring subunits. This correlation suggests an orthogonal

cooperativity in the transition of conformational change from one subunit where the TM1 changed conformations and loosened the interaction with the pore helix to the extracellular entrance of the selectivity filter of its neighboring subunits. The last correlation pointed by this diagram shows that the residue E150 interacts with the amine of the backbone of residue Y157 of the same subunit (id: 12) upon the enlargement of the site S0 in the orthogonal subunits. Thus, whatever the effect of the change of the conformation of the selectivity filter, it is stabilized by an interaction E150-Y157.

The subgraph on the left in panel E of Figure 14 is the mirror image of the subgraph just described. It contains the information of all the equivalent relationships involving the subunits in a shifted-reference manner. This graph strengthens the hypothesis of the inter-subunit cooperativity in the transmission of the conformational changes from the TM1 to the selectivity filter. To sum up on the diagram in panel E I will address the fact that it contains three disconnected members. I suggest that it is safe to connect the node *id: 13* to node *id: 2* for two main reasons. First, one can find several positive correlations between equivalents of these nodes in the diagrams focusing on single subunits (Figure 14A-D). Second, the events connected in panel E to both nodes occur simultaneously as observed in the timeseries of the pairwise distances (data not shown). Another possibility to draw the missing edges is to further decrease the *r* filtering threshold, but this option is considered undesirable since I am able to point to sufficient amount of facts ("simulated events") showing the missing links. Thus, I am led to my final interpretation of Figure 14.

The observed conformational change consists of the increase of distance with *id: 2* (and its equivalent) and leads to the rearrangement of the pore region and changes the opening along the selectivity filter. However, this rearrangement is only observed when the distance *id: 13* increases, because it involves the extraction of the sidechain of R160 from a hydrogen bond cage behind the selectivity filter and its rotation towards the N_{ter} of TM2 of the next subunit. This rotation is accompanied by a rearrangement in the pore helix and a partial β-stand containing R160. The pore helix which is just below the R160 and contained E150 undergoes a bending period when it is distorted by the interaction on its mainchain from the alcohols of S148 and T151. The participation in the bending of the pore helix by T151 requires that this residue disengages its interaction with Y159 releasing constraints on the middle of the selectivity filter in the preceding subunit and allowing it to bend in its turn. Since these phenomena were observed with enough evidence of inter-subunit cooperativity, despite the fact that the diagrams are sparse (do not contain equivalent observations among each individual panel) I believe that the described behavior taking place in the MD trajectory is of functional relevance and I will further refer to this interpretation as I am investigating its role.

At this point I described a phenomenon of rearrangement of the pore domain leading to the change of the conformation of the selectivity filter in respect to the starting conformation, the corresponding pore profile can be observed in Figure 15. Here I will discuss the possibilities of the fictional meaning of this rearrangement. The first option is that I may have obtained the unfortunate event of the unfolding of parts of the protein structure due to defects of the simulation protocol and/or the construction of the simulation box. In reality, I am pretty confident in my rejection of this option because I have observed this type of reorganization in the pore domain in repeatedly several simulations started from independently constructed simulation boxes (data not presented but described in the section on the optimization of the composition of the simulation box). Nevertheless, the most important argument against an unfolding-artefact of the pore domain being responsible for the observed pinched conformation of the GYG portion of the selectivity filter comes from crystallography. The pinched or collapsed state of the selectivity filter has been first observed in crystals of KcsA channel in low K^+ conditions (Y. Zhou et al. 2001). In this state the selectivity filter is occupied only by two K^+ in sites S1 and S4, water molecules are crystalized in sites S0 and S3, thus site S2 is unoccupied. The K^+-water occupancy in this crystal structure is not exactly the one that occurred in *Simulation I*.

The following references are relevant to provide me with an answer about the functional state observed in *Simulation I*. Previously, numerous studies have shown that the collapsed state of the filter in KcsA corresponds to an inactivation state which is reached after the opening of the activation gate in the intracellular end of the TMD (Cheng et al. 2011; Raghuraman et al. 2014; Heer et al. 2017; Tilegenova, Cortes, and Cuello 2017; Xu, Bhate, and McDermott 2017; Kratochvil et al. 2017). The transmission of the activation from the TM helix bundle to the selectivity filter is thus an established phenomenon in KcsA (Heer et al. 2017; Kratochvil et al. 2017). In the KcsA channel, the contact pore helix-TM1 is weakened upon activation while the contact pore helix-TM2 is straightened upon the closure of the channel. A similar function has been documented in Kir3.4, authors discovered a relationship between the modeled number of hydrogen bonds involving at the same time residue E147 (eq. mmKir3.2 E152) and the mutant at position G175X (ag. mmKir3.2 G180), versus the current amplitudes recorded with the corresponding mutants (Rosenhouse-Dantsker and Logothetis 2007). Then it is established that a rearrangement of the inter-residues contact network behind the selectivity filter causes the change in the conformation of the selectivity filter. Precisely, residues E71 and W67 contact the D80 in the wild-type KcsA channel. It has been demonstrated that the aromatic substitution of W67 to tyrosine has similar inactivating phenotype as the wild-type W67, on the contrary the substitution to phenylalanine has a non-inactivating phenotype as another well-known mutation the E71A (Cordero-Morales et al. 2006, 2011), similar observations has also been drawn for the potassium Shaker channel also using substitutions at the equivalent positions (Lueck et al. 2016). Thus, the interaction between a residue at the C_{ter} of the selectivity filter with residues in the pore helix is responsible for the inactivation of the above cited channels. The equivalent interaction has been studied in Kir3.1/Kir3.4, author has termed the interaction involving E150 and R160 “bowstring” (Dibb et al. 2003). Similar to the observation with KcsA the inability of the Kir3 mutant channel to establish this interaction resulted in either the diminished or abolished selectivity and inward rectification of the channel. Regarding the K^+ occupancy of the filter, Heer and colleagues computed PMF and found that upon binding of three K^+ to the selectivity filter the protein resides in an energetic minimum characterized by the highest possible binding energy for K^+. The authors interpretation of this potential well is that the K^+ permeation should be impeded contrary to the generally admitted interpretation that this is a conductive state (Heer et al. 2017). Taken together these reports point the role of the bowstring interaction toward the maintenance of the rigidity of the selectivity filter and implication in the inactivation phenomenon of the potassium channels.

Since in *Simulation I* the selectivity during the entire simulation is sustainably occupied by three K^+, which are located in sites S2, S3 and S4, it is reasonable to believe that the selectivity filter is in a high binding affinity for K^+ conformation. These three K+ were not initially present in these sites, the initial occupancy was set to K^+-K^+-x-K^+-K^+ exactly as the K+ is modeled in PDB:4KFM. Despite the described conformational changes behind the selectivity filter consistent with an inactivated state of the channel as suggested by the above paragraph, the filter in *Simulation I* is rather stable with RMSD:0.61 Å compared to the initial state. Thus the functional state of the channel by the end of this simulation should be “primed-closed” according to the nomenclature in the article by Heer and colleagues (Heer et al. 2017).

The observed rearrangements behind the selectivity filter resembling the entering in inactivated state described using Figure 14 however require an activation signal. It is possible for it to be provided by the binding of Na^+ and propanol to the cytoplasmic domain and further transmitted through TMD. Figure 15 shows the location of the bound ligands in the same time period analyzed in Figure 14. The vertical alignment of the location of Na^+ and propanol coincides with the residues E152 which were continuously found in rotamer state -180°/60° destabilizing the pore helix from the TM1 (Figure 12 and Figure 15). Thus, in line with the bibliographic references I admit that the selectivity filter has also partially adopted the inactivated conformation as suggested by the larger opening of site S0 (Figure 15A) in comparison with the profile of the selectivity filter in the original crystal structure (Figure 1) and the reduced distance between carbonyls of pairs of T154 and I155

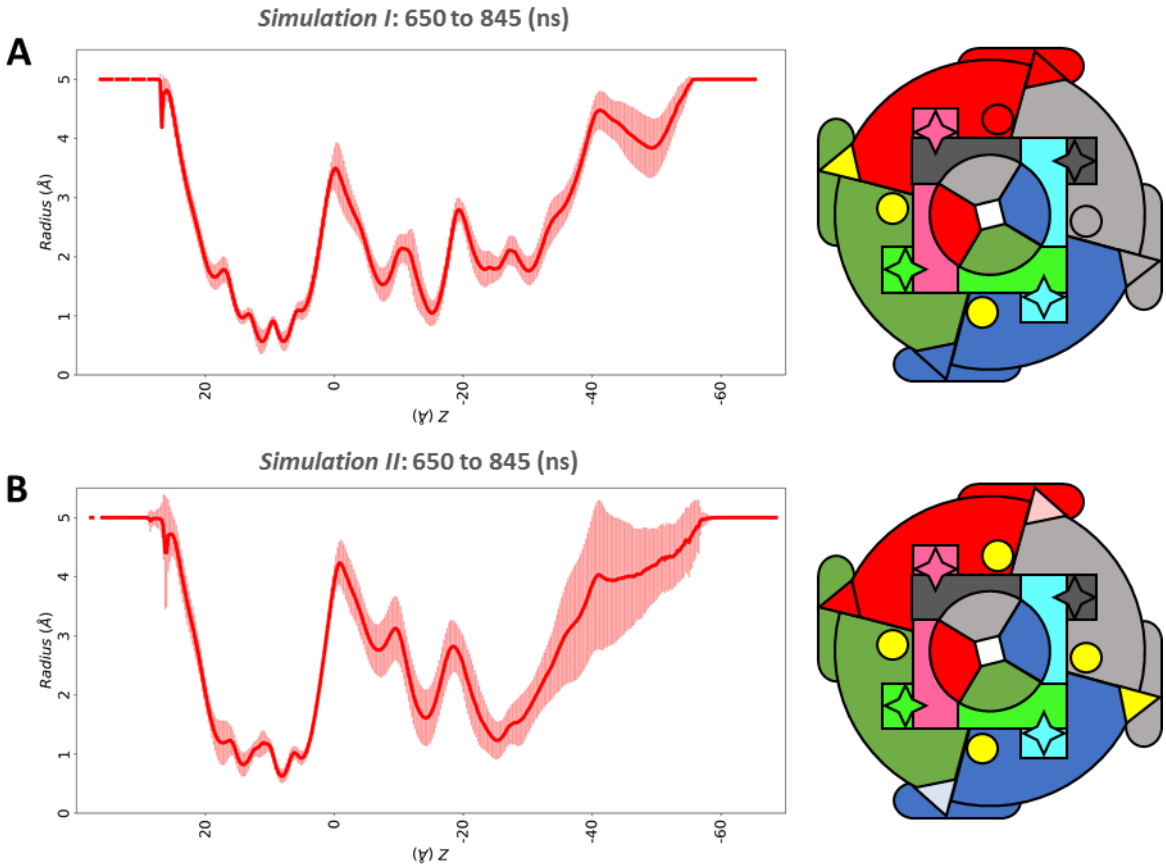

Figure 15: Profile of the pore lumen showing closure of mouse Kir3.2 in two molecular dynamic simulations. The panels on the left show the average (thick line) and the standard deviation (vertical bars) of the radius of minimum pore opening measured during the indicated periods sampled every 400 ps. The center of the TMD is aligned with coordinates Z_{axis} = 0 Å. The schematics on the right indicate the presence of ligands in the binding pockets of each subunit. The schematized adjacency corresponds to the extracellular view of the channel: the inner wheel symbolizes the selectivity filter and the turret domain, the rectangle bundle represents the TM domain, the outer wheel represents the cytoplasmic domain, the appendices on the outer wheel symbolize the βL-βM strands and loop. Protein subunits are colored: P1 in red, P3 in gray, P2 in blue, P4 in green. The ligands binding site of are indicated: PIP_2 (star), Na^+ (circle), propanol (triangle). If the ligand is present the corresponding symbol is colored yellow or with a lighter shade indicating the unbinding during the monitored time interval; if the site was completely empty during the entire period it is colored the same as the containing subunit.

(Figure 6C). In order to reconcile this idea with the previous paragraph I will discuss the fact of the increased interaction between the TM2 and the pore helix between residues E152~N184 which I think could prevail on the inactivation attempting to collapse the selectivity filter. This suggestion is interesting in the scope of activation-signal transition until the selectivity filter and the consequent entering in the inactivated state, are being independent and concomitant with the closure of the HBC gate. The data presented here also shows large portion of cooperativity between both mechanisms because the interaction E152~N184 present in the subunits where the inactivation of the selectivity filter is observed. This result is in line with the previous experimental and computational data and provides additional information on the mechanism called C-type inactivation occurring in Kir3.2 channels.

The pore profile observed in the last period of *Simulation II* depicts another interesting event in the dynamics of the selectivity filter (Figure 15B). One can easily notice that the central minimum in the region of the selectivity filter is not present in the profile from *Simulation II* compared to the one from *Simulation I*. Partially this profile corresponds to the "flipped" conformation of the carbonyl of residue I155 separating the sites S2 and S3 of the selectivity filter. This conformation is characterized by the change of dihedrals of the mainchain as represented in panel B of Figure 16, the angle φ from initially 90°-120° to 40°-50°, the angle ψ from about 100° to -80°. The existence of a flipped conformation of the carbonyl of the equivalent residue in other channels is a well-documented

phenomenon which is consistent with permeable selectivity filter and is characterized with lower binding affinity for K^+ compared to the initial state of the filter with all carbonyls oriented towards the lumen of the pore (Cheng et al. 2011; Raja and Vales 2009). In *Simulation II* the flipped conformation is observed only transiently. In most of the snapshots the carbonyl of residue I155 is indeed in an alternative conformation in respect to both the initial state and the state from *Simulation I*, but this conformation is not the "flipped" state. Indeed, the longest period of twisting of the filter is observed in subunit P3 where the angle φ switches between 120° to 90° and angle ψ switches from 120° to 160°. Simultaneously a more drastic change is observed for residue G156 in the same subunit, where angle ϕ changes from -120° to -60° and angle ψ from -120° to 160°. The beginning and the end of the persistence of these changes in the backbone torsion angles coincides with the time at which two K^+ which were leaked in the inward direction (Figure 5), thus depicting the reduction of the binding affinity of the selectivity filter towards K^+ as the carbonyl of residue I155 is turned away from the canter of the selectivity filter.

Interestingly during the complete flipping of the carbonyl of I155 in subunit P1 the sidechain of the I155 is also rotating (Annex *Simulation II*: 6), suggesting that the particular geometry of the isoleucine could be involved in a shaft-like motion controlling the widening of the filter at site S3. After inspection of the distances between the I155:Cδ and the sidechain of residues L173:Cβ, and I155:Cα and L173:Cα (Figure 16B), it was evident that the rotation of the sidechain of residue I155 is concomitant with the increase of the distance between atoms L173:Cγ and the I155:Cδ. Thus, I issued the hypothesis that the rotation of the sidechain of reissued L173 can compensate for the displacement of nearest the L173 in order to maintain the hydrophobic interaction involving sidechains of residues L149, I155, Y156 from on subunit and T151, L173 in subunit which is located counter-clockwise in the tetramer viewed from the extracellular side. It seems that the cost for the maintenance of this dehydrated environment is the displacement of the selectivity filter towards the "facing" TM2. On its turn, the enlargement of the selectivity filter is operated via the twist of the backbone displacing the K^+ coordinating carbonyls. This hypothesis could be tested by the I155V mutation which should abolish the ability of the TM2 subunit to generate changes in the nearby loop of the selectivity filter by attract the Cδ of residue at position 155.

It is noteworthy that valine residues constitute the equivalent interface in native KcsA channels, V75 and V94, equivalent respectively to I155 and L173 in mmKir3.2 Unfortunately, I was not able to find bibliographic references about the V76/V94 interaction in the KcsA channel. In Shaker channel the L461W mutation at the position equivalent to L173 in mmKir3.2 produces channels with gating properties very similar to the wild-type channel (Li-Smerin, Hackos, and Swartz 2000). On the behalf of the studies of Kir3 the exact same hypothesis is made in the base of recording of chimeric Kir3.1-Kir3.2 channels (Wydeven et al. 2012). Author observed that the bulkier substitution L173F causes the decrease in the recorded currents and hypothesized that the phenylalanine would push on the I155 resulting in the decrease of the opening of the selectivity filter. Further lines of evidence involve the L168 in Kir3.4 (eq. mmKir3.2 L173) whose pathological mutation L168R decrease the K^+ selectivity causing depolarization in native tissues (Choi et al. 2011). While it is clear that the substitution to arginine occurs at the codon level through a single nucleotide polymorphism (SNP) event, authors have speculated that in order to produce the non-selective phenotype the arginine could disturb a local salt bridge. The data I present in Figure 16 allows me to propose a molecular mechanism of action of this pathological mutation. First, one should expect faulty accommodation of the arginine sidechain into the unfavorable hydrophobic environment naturally accommodating the leucine residue. If the energetic barrier corresponding to the dehydration of the arginine could be somehow overcome, then the arginine sidechain will push on the isoleucine resulting in the collapse of the selectivity filter similar to the mutation L173W. Thus, the most probable explanation is that the significantly longer arginine sidechain fails to effectively interact with the I155, thus depriving the selectivity filter of the capacity to be stabilized in the conformation with all carbonyls towards the permeation pathway, i.e. to be stabilized in a high binding affinity conformation. Moreover, I do not

rule out the possible polar and/or ionic interactions which could be established involving the L173R mutant. For instance, the E147 (eq. E152 mmKir3.2) located at the very last turn of the pore helix is located within contact range of the mutant L168R in Kir3.4. can be verified by a very crude distance measurements in *Simulation II* where the sidechain of E152 adopted different rotamer sates and particularly the -60°/-60° (ANNEX *Simulation II*:5) in which the carboxyl group is rotated toward the TM2 of the same subunit. In brief, when the -60°/-60° rotamer state of E152 is observed, the distance between L173Cγ and E152Cδ evolves between 7 Å and 9 Å, and accounting for the bond length

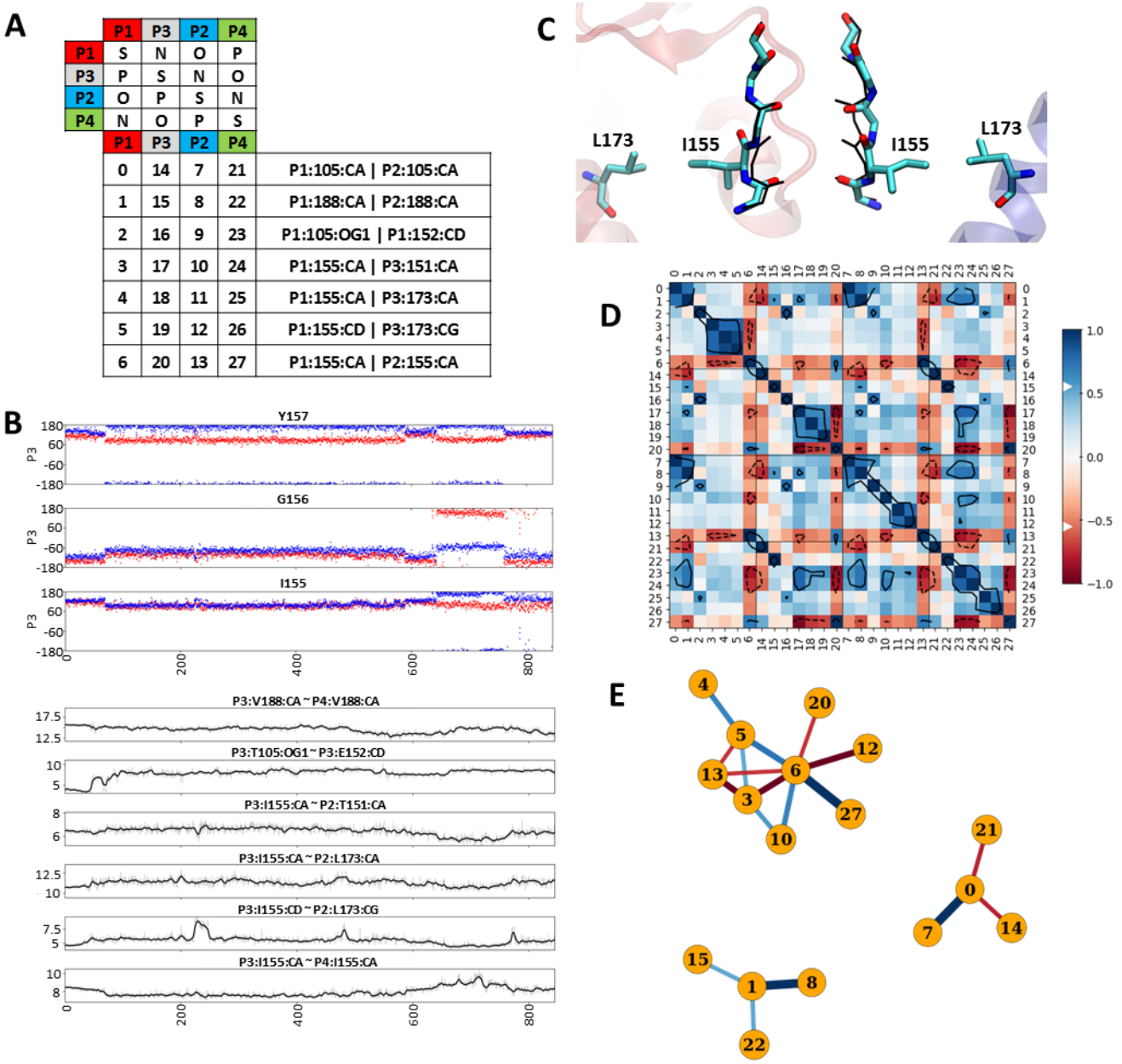

	P1	P3	P2	P4	
P1	S	N	O	P	
P3	P	S	N	O	
P2	O	P	S	N	
P4	N	O	P	S	
	P1	P3	P2	P4	
	0	14	7	21	P1:105:CA | P2:105:CA
	1	15	8	22	P1:188:CA | P2:188:CA
	2	16	9	23	P1:105:OG1 | P1:152:CD
	3	17	10	24	P1:155:CA | P3:151:CA
	4	18	11	25	P1:155:CA | P3:173:CA
	5	19	12	26	P1:155:CD | P3:173:CG
	6	20	13	27	P1:155:CA | P2:155:CA

Figure 16: Correlation of the conformation of the sidechain of I155, and the width of the central K^+-binding site in the selectivity filter of mouse Kir3.2 from molecular dynamics simulation. The input data for the correlation analysis is obtained from Simulation II sampled every 400 ps. (A) List of selected interatomic contacts involving the carbonyls of I155 and atoms of residues involved in hydrophobic contacts with the sidechain of I155. The table is assembled the same way as described in Figure 13. (B) The top panel contains the timeseries of backbone dihedral angles of some of the residues in the selectivity filter in subunit P3. The bottom panel contains timeseries of the interatomic distances involving residue I155 in the subunit P3. (C) Snapshot at time 716 ns when the carbonyls of residues I155 in two opposite subunits are simultaneously in the flipped state. The backbone of the selectivity filter of subunits P3 (on the right) and subunit P4 (on the left) at time 716 ns is represented with thick sticks, while the starting conformation is represented with thin black lines. Parts of TM2 and the selectivity filter in subunits P1 (red) and the TM2 in subunit P2 (blue) are shown as transparent cartoon drawings. The I155 in subunit P3 interacts with L173 in subunit P2, and the I155 in subunit P4 interacts with L173 in subunit P1. (D) Matrix containing the instantaneous correlation between the timeseries of interatomic distances indexed in panel A. The contours delimit areas with abs(r) ≥ 0.618. (E) Diagram summarizing the tetramer-wise interdependence between the monitored distances. The network is filtered to contain instances with abs(avg(r)) ≥ 0.55, colors and widths of the edges are proportional to the correlation factor displayed in panel D.

between E152Cδ and the oxygens of the carboxyl group which is 1.3 Å, updates the distance between the sidechains of E152 and L173 to be between 5.7 Å and 7.7 Å. As I have measured for different conformations of arginine residues in the simulation, the extra length to the sidechain provided by the L168R mutation should be between 3 Å and 3.8 Å (distance in arginine between Cγ to Cζ) plus 1.3 Å for the terminal Cζ-nitrogen bond, thus a distance between 4.3 Å and 5.1 Å. Thus, the hypothetical distance between E147 and L168R in Kir3.4 could be around 7.7 – 4.3 = 3.3 Å. Such a distance would allow an hydrogen bond or salt bridge to be established, in which conditions the channel could be further stabilized into a conformation allowing stronger fluctuations of the selectivity filer (see paragraph describing the interactions of E152 in *Simulation I* and the resulting changes in the contact network in the vicinity of the selectivity filter).

Thus, I would like to update my speculation on the effect which could have the I155V mutation in mmKir3.2. Despite the fact that, the sidechain of valine at position 155 is shorter than the one of the isoleucine, this substitution should still allow the L155V residue to interface L173 and to preserve the hydrophobic contacts behind the selectivity filter. The logical consequence is to expect a compensatory effect resulting in the enlargement of the S3 site of the selectivity filter. Thus, the I155V mutation should cause a more conductive phenotype by simply impeding the inactivated state of the selectivity filter, similar to the E70A mutation in KcsA channel for which the flipped carbonyls between sites S2/S3 is frequently observed in crystal structures.

One can also appreciate the relatively strong fluctuating profile of the pore in *Simulation II* compared to that from *Simulation I* (Figure 15, Annex *Simulation I*:2, Annex *Simulation II*:2). These larger fluctuations along the entire pore are potentially the reason for the obtained instability of the selectivity filter and the resulting leak of K^+ through the pore in *Simulation II*. This data is in line with reported experiments which have established that in K^+ channels the closed state of the pore is more rigid than the conductive state (Raghuraman et al. 2014; Kim et al. 2016). It is tempting to explain the larger fluctuations in *Simulation II* by the higher amount of ligand molecules persisting until the end of the 800 ns simulation, but in the same time I also observed that the dihedral angles inside the selectivity filter have changed upon the turning-on of the external electric field during the last 200 ns of the simulation. Thus, I will leave the interpretation of these result for the further paragraph where I will present more observation obtained in systems where PIP_2 was present in the simulation box.

5.3.2.2.2 Behavior of the cytoplasmic domain of Kir3.2 in absence of PIP_2 and in presence of stabilized Na^+ and propanol

In the set of simulations *Simulation I* and *Simulation II*, the dynamics of the channel have been exploited in absence of the membrane-constituent partner the PIP_2 lipids. On the other hand, based on available bibliographic references I have implemented the interaction between the mmKir3.2 channel and soluble partners which are potent to activate the channel in heterologous expression systems and as shown very recently in refined environment where purified channel is reconstituted in liposomes (see Chapter Introduction for exhaustive list of references).

In the case of the systems simulated without PIP_2 it is difficult to fully appreciate the effect of the Na^+ and the propanol on the channel because the K^+ permeation pathway has been primarily obstructed at the level of the HBC gate. Furthermore, the observed conformational changes in the CTDC are at least partially caused by the relaxation of the protein in response to the removal of the Gβγ proteins. The occupancy of the binding sites by Na^+ and propanol has not been constant. The average persistence of the ligands during non-overlapping periods is shown in (Annex Simulation I:3 and Simulation II:3). In *Simulation I* two of the initially bound Na^+ ions have rapidly changed location and stabilized for the subsequent 450 ns at a less buried interaction site, most probably it is the residues which are involved in the primarily coordination of the Na^+ before it could access the site where Na^+ is observed in the crystal structures. In this simulation, the propanol also was progressively unbounding from the putative binding site during the last 300 ns of simulation, and at the end only one site remained occupied by propanol and no rebinding events have been observed. In Simulation

II the Na+ ions remained in the initially populated binding site during the entire simulation. The propanol molecules were much more dynamically interacting with the channel. On one hand, the unbinding of the propanol from the putative binding sites started during the first 200 ns of simulation. Several unbinding and re-binding events can be observed in the figure, suggesting that the putative binding site has non-negligible affinity for the ligand. On the other hand, in this simulation multiple propanol molecules among those not constrained toward the putative binding sites of the channel (see chapter Methods) have interacted with the specific parts of the protein for periods longer than 1 ns. This is represented in the figure by the multiple contours delimiting shaded areas of integrated ligand density not overlapping with the *x/y* positions of the putative binding sites. In total, the stable binding of the Na^+ and the frequently changing number of interactions of propanol with the channel in *Simulation II vs*. *Simulation I*, could be the reason more fluctuating pore profile observed in *Simulation II*.

It is interesting to investigate the conformational changes occurring in the channel during the MD simulation. The simplest and straight forward method to use is the measure of RMSD. This method is highly dependent on the particular structure-alignment strategy that one will use. For instance, an alignment of all frames on the initial structure shows if the protein had stabilized after relaxation in response to the heating of the system. Indeed, in *Simulation I* the obtained plot (data not shown) showed a sharp increase of RMSD during the equilibration period when the constraints on the heavy atoms of the protein have been gradually decreased and the protein relaxed in response to the temperature, the obtained values for RMSD is about 2.5 Å. The subsequent part of the graph shows a trend of steady increasing RMSD from 2.3 to 3.8 Å which reflects that a constant evolution of the conformation of the channel was ongoing during this simulation (μ = 3.12 Å, σ = 0.41 Å). This observation is not surprising for the given simulated system, where the initial crystal structure is deprived of the experimental partners, the Gβγ proteins and is set to interact with a new variety of molecules. Furthermore, the simulated time is very short compared to the physiological timescales on which the channel operates, thus I did not expect to obtain a trajectory reached an equilibrium. The equivalent measure of RMSD in *Simulation II* showed the same global tendency of constant divergence from the starting conformation (μ = 2.92 Å, σ = 0.45 Å). In addition, this time apart from the general trend of increase there were discerned three seasonal-like oscillations of the RMSD lasting between 150 and 200 ns.

The next type of RMSD calculation I made is to investigate how spread is the conformational space in respect to an average conformation after the equilibration period. Thus, I obtained μ = 1.96 Å and σ = 0.23 Å for *Simulation I*, and μ = 1.79 Å and σ = 0.27 Å for *Simulation II*. The observed profiles of the plotted RMSD values along the time are also similar for both simulations. The similarities of the quantities in this analysis are good news showing overall structural stability of the starting structure and the reproducibility of the simulation protocol. The observed profiles of the RMSD along the time were also consistent in the times when deflections from the mean RMSD are observed and also in the directions of these deflections is the same in both simulations. The large oscillations of the RMSD are most probably due to the shock that I have applied to the systems during the simulation protocol, i.e. the time points at which were executed the switch-on of the external electric field and the switch-off of the constraints on the ligands (Table 2), while particular details of the oscillation profile could most probably resulted from the individual binding and unbinding invents of ligands and ions on the channels.

In order to quantify further the conformational changes in the CTCD, I use a method based on the computation of correlations between the fluctuations of each couple of interacting atoms. This metric represents the probabilities of the information transfer between couples of residues and has been developed to study the conformational changes in the tRNA-protein complexes (Sethi et al. 2009). Next, I performed an actual comparison of these correlation matrices between different periods of the same simulation, or between equivalent lapses of time from different simulations. For the comparison performed symmetrically-subtraction of one matrix from the other, mend to be the

first stage of contrasting the correlation profiles. This subtraction results in a set of new matrices which number is an entire multiple of the number of subunits of the channel, because all contact instances describing one subunit are subtracted from the equivalent contacts from every other subunit. Then I ranked each residual pairwise correlation in order to determine which contacts contribute the most for the difference of the observed contact networks (see Methods). This practice allows to efficiently recognize which parts of the macromolecule have diverged between the compared time lapses and/or simulation conditions.

For instance, as the G-loop gate changes conformation with the advance of the simulation, one would like to identify the molecular actors involved in the process. The time course of the radius of bottleneck of the G-loop gate in *Simulation I* is reported in panel A of Figure 5. This profile has three distinct features. First, during the equilibration the opening progressively shrinks with the release of the constraints on the protein and oscillates between 1 and 1.5 Å. During this event both pairs of opposite βI-βH loop behave symmetric *d* = 5-7 Å. The constriction occurred at the terminal methyl of residues M313 or M319 and the carbonyls of G318, all of which delimit the permeation pathway in the crystallographic model. Second, a nearly symmetric constriction developed right after the equilibration period and lasted for 100 ns. The constriction was operated by the rigid body fluctuation of the βI-βH strands and loop of each subunit, and the localized fluctuations of the carbonyls of residue G318 (Figure 17A). The backbone dihedral φ of G318 in subunits P1, P2 and P4 remained around 100°. While in subunit P3 it was rapidly switched to a state -125°, characterized with the retreated of the turn of the loop at the level of Cα from the permeation pathway and the rotation of the carbonyl oxygen from predominantly pointing towards the CTCD to be oriented in the plane parallel to the membrane. In the other three subunits the carbonyl oxygens of residue G318 were also exposed to the solvent inside the lumen of the gate, their fluctuation is more pronounced than that of the carbonyl oxygen of G318 in subunit P3 (Figure 17B) (dynamic data not shown). The third feature of the profile of the G-loop gate occurred at time 150 ns, it seems that the loops in subunit P1 and P2 get closer, while the other two loops in subunit P3 and P4 adopt more extended conformation. This drift of the bottleneck radius was accentuated during the time laps 200 ns to 420 ns, the visual inspection of the trajectory revealed that the βI-βH loop in subunit P1 adopted a unique conformation characterized by the increase of the curvature between the residues 314 and 318 (Annex *Simulation I*:4G). As a result, the part of the loop closest to the K^+ permeation pathway completely occluded the lumen of the G-loop gate. Then after, the conformation of this part of the loop in subunit P1 did come back to resemble the others three subunits. Nevertheless, the impression of two-fold symmetry of the G-loop gate given by the timeseries in panel B of Figure 5 is misleading. The visual inspection of the conformation shows that three subunit P1, P2 and P4 are spread evenly around the center of the opening of the gate, and that the subunit P3 is in a more extended conformation than the other three.

Very interestingly, in the last part of *Simulation I* despite the small radius of the bottleneck of the gate, several K^+ have been able to cross the gate constriction zone at the level of M313. K^+ moved first in the outward direction, then blocked by dehydrated environment caused by the closed HBC gate which in its turn recruited the hydrophobic sidechains of M319, the K^+ remained for up to 100 ns coordinated by the carbonyl oxygens of G318. Finally, the three K^+ are seen exiting the G-loop gate in the inward direction. (Figure 5B). A representative conformation of the G-loop gate during the coordination of a single K^+ ions is shown in Figure 18. This is a remarkable even in the sense that for a long part of the simulation a K^+ ion observed in a partially dehydrated state. During this event coordination oxygens are provided by the backbone of the individual loops constitutive of the G-loop gate and also interactions with the alcohol groups of threonine residues where observed. Moreover, presented conformation of the G-loop gate shows that the both there are three levels of constriction in the gate.

At the top and the bottom are located two “belts” of methionine residues, which able to independently split the water column along the permeation pathway. While in between is a located a

polar environment where numerous oxygen atoms provide coordination to K^+ in the expense to compensate for its dehydration, thus allowing to accommodate one K^+ ion inside a modular cavity otherwise too narrow to contain fully hydrated K^+ ion.

At this point the transport of K^+ inside the G-loop is due to two factors that I can point to. The first factor is that the observed conformations of the G-loop do not provide long term stabilization of the sidechains of residues M313. The sidechains of each one of the M313 is observed reaching the central zone of the permeation pathway, thus occluding it. Nevertheless, due at least to the thermal fluctuation the sidechains of M313 occasionally let water and ions to cross the M313 belt. Second, the local concentration of K^+ just below the M313 belt is very high, as there could be found up to five K^+ at different timepoints. This, K^+ crowded environment is favored by the negative electrostatic potential generated by the cluster of residues E236 which are modeled with charged carboxyl groups. The thermal agitation of the system allows occasionally a K^+ to be pushed through the M313 belt exploiting its fluctuation. These, observations may be linked to the relatively high basal activity of the Kir3 channels recorded in heterologous expression systems even when GPCRs are not expressed. These observations do not rule out the generally admitted hypothesis that the open conformation of the G- loop gate is extended enough to accommodate a fully hydrated K^+ ion. It is easy to admit that if the G-loop gate in physiological conditions is also conductive as it adopts conformations similar to the one observed at the end of *Simulation I*, the gate will allow higher K+ transport as it is extended further. Such extension of the G-loop gate could be imagined by simple rigid body motion of each loop, which will separate the sidechains of M313 enough for them to be unable to occlude the permeation pathway, without necessarily involving conformational changes to

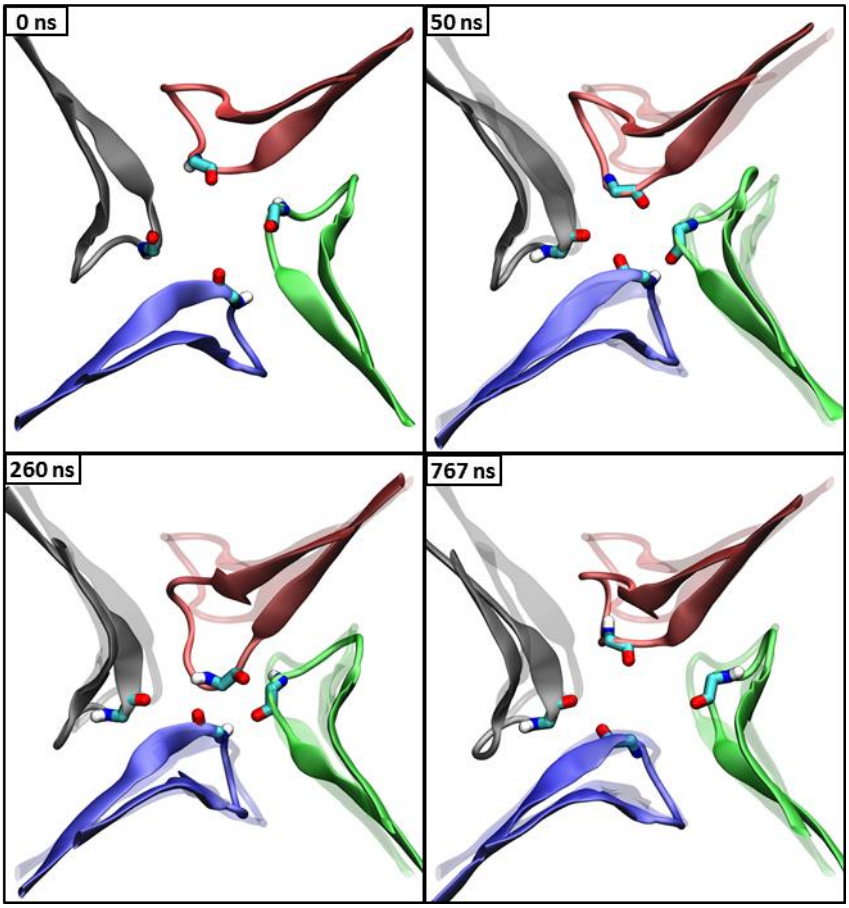

Figure 17: Different conformation of the G-loop gate of moue Kir3.2 from molecular dynamics simulation in absence of PIP_2. In all panels representing four snapshots taken at different times, the relative positions of residues 310 to 325 are represented by a solid material for the current time step, and as transparent material to compare with the starting conformation. Coloring of the protein subunits is consistent with Figure 9. All atoms of the Residue G318 are represented as solid stick.

stabilize the M313 residues away from the center of the pore. I will refer to this hypothesis in the subsequent sections of the manuscript as I present systems where PIP_2 has been modeled.

In Figure 18, one can also appreciate the proximity between the sidechains of residues F192 and the residues M319. The distance between the terminal methyl of residues M319 and the Cζ of residue F192 is between 4.5 and 6 Å, which is consistent with hydrophobic interactions. Indeed, the HBC gate is relatively stable at the end of the simulation (Annex *Simulation I*:2). In parallel, the region between residue F192 and M319 is not completely dehydrated in the last 250 ns of *Simulation I*, as depicted in panel A of Figure 7. Indeed, it seems that a de-wetting at the level of the M319 is not possible because even in the configuration with all four M319 sidechains extended towards the F192 residues, these residues do not "hermetically" confine a region from which water could be expelled by the decrease of entropy. If these hydrophobic interactions are permanent when the HBC gate is shut, they should have as an effect the further stabilization of the closed state of the HBC gate simply by decreasing its fluctuations. This observation rises the interest to observe if such hydrophobic interactions are present in simulations where the HBC gate are both open, these will be subject to

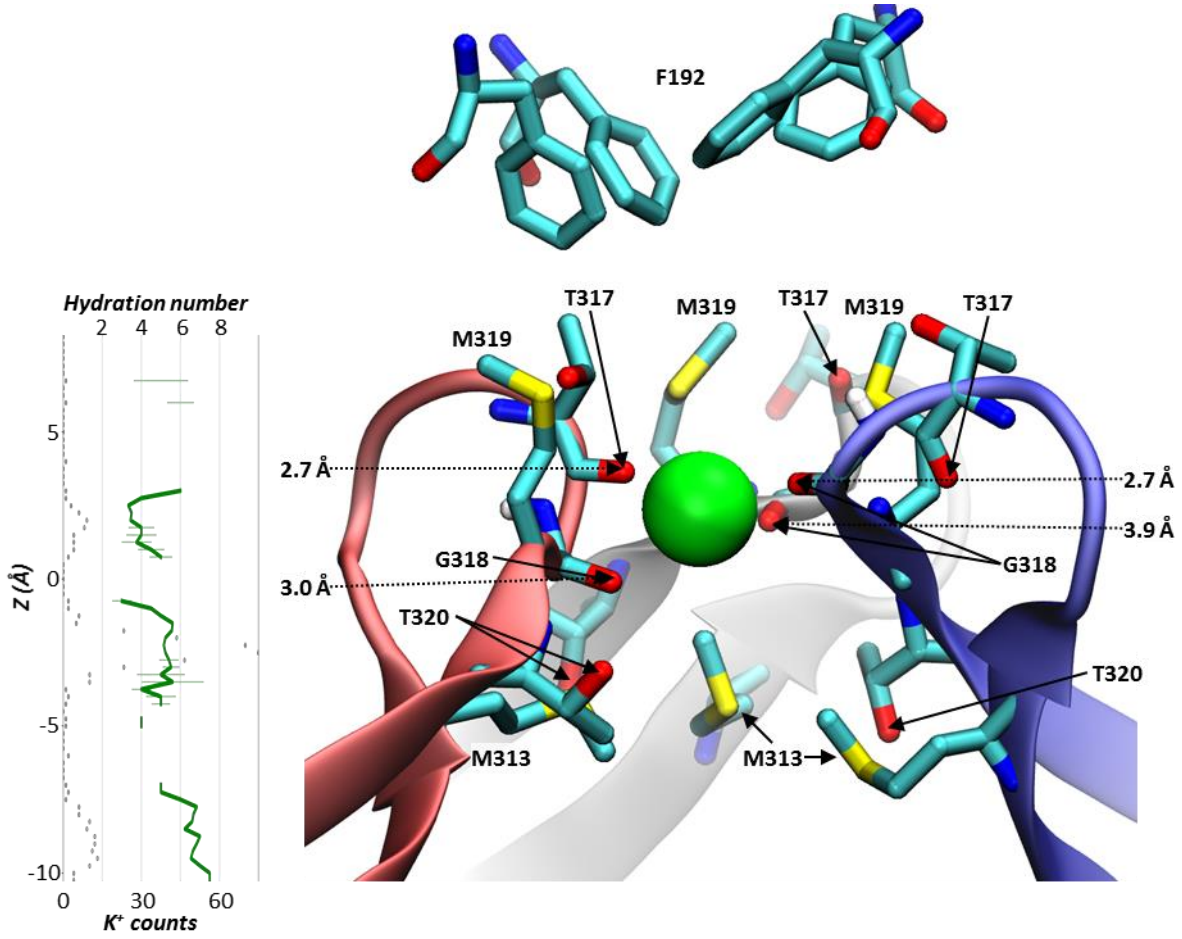

Figure 18: Conformation of the G-loop gate of mouse Kir3.2 during the coordination of a single K^+ observed when the HBC gate of the channel is closed during molecular dynamics simulation in absence of PIP_2. The snapshot of the conformation of the G-loop gate is taken at timestep 806 ns. The βI-βH loops in three subunits are represented as cartoon drawing, coloring of the protein subunits is consistent with Figure 9. A subset of main chain atoms and sidechains of residues lining the permeation pathway are represented as sticks. The K^+ ion (green sphere) is inside the lumen of the G-loop gate after it resided between residues M313 and M319 for 100 ns. The distance from the K^+ to the carbonyl oxygens substituting water molecules of the K^+ hydration shell is indicated by dashed arrows. (Plot inserted) K+ hydration number along the permeation pathway delimited by the G-loop gate. Individual hydration numbers have been sampled every 0.4 ns in the time laps 650 to 845 ns, the raw counts are reported on the bottom axis. The average hydration number of all K^+ ions is reported at the top vertical axis. The vertical axis is centered at the geometric center of the four Cα of residues G318.

investigation in when I present the results obtained with systems where PIP2 has been simulated.

I have further identified a correlation between the conformation of the sliding helix, the C-linker and the G-loop gate. Once again, I used the previously-mentioned strategy of subtraction of weighted contact networks computed for the first and the last 70 ns of *Simulation I*. Thus, I have found that the distance between Cα of residues D81 and R201 is positively correlated to the distance between Cα of diagonally opposite G318, one of which is in the same subunit as the considered R201 residue. A second, this time negative correlation involves the spacing between Cα of residues F83 and T317, and the distance between Cα of diagonally opposite G318, one of which is located in the counterclockwise subunit from the subunit where are located F83. In this case, the involved conformational change in the slide helix can be characterized by the increase of the angle through the Cα of Y78, D81 and T85 projected on to the plane of the membrane. As a result, the N_{ter} part of the slide helix is being displaced in the counterclockwise direction. Interestingly, at this point the propagation of the conformational effect is subject to conditional modulation. It is that, if the N_{ter} of the slide helix is found to be parallel to the membrane, it can no longer push on the C-linker located below, thus it allows the C-linker to be displaced away from the permeation pathway, corresponding to the decrease of the distance between the N_{ter} of the slide helix and the C-linker. This motion releases the steric restrains on the G-loop located immediately beneath the C-linker, thus allowing former to flicker away from the permeation pathway. The other option is that the slide helix is observed leaning on the C-linker, and in the case of the displacement of the slide helix in the counterclockwise direction it pushes on the C-linker which in its turn propagate the steric restriction onto the G-loop in the same subunit. Yet a third possibility is that the C-linker is not displaced towards the N_{ter} of the slide helix which may be favorably displaced towards the membrane, in this chase the G-loop below the C-linker is found to be in a constricted conformation, because it remains restrained by the C-linker. For the moment I will not discuss further these observations, but I will come back to the topic once I have presented the rest of the simulated systems in presence of PIP_2.

5.4 MD Kir3.2 in presence of PIP_2, propanol and Na^+

I have produced two independent trajectories (*Simulation III* and *Simulation IV*) of the same atomic system as used for *Simulation I* and *Simulation II* and supplemented with four PIP_2 molecules. The all-atom PIP_2 molecules were placed in the binding site where the short-chain PIP_2 is co-crystalized in PDB:4KFM. I order to better interpret the trajectories I would like to stress the varying conditions of the external constraints. First, the electric field which held the membrane potential at -70 mV at the beginning of the simulation was increased to -700 mV after 400 ns of simulation. Second, the harmonic distance constraints stabilizing the centers of the ligands towards the protein were also modulated: the constraints on the propanol and the Na^+ were maintained during 800 ns and then were turned off in Simulation IV, the center of 4',5'-phosphates of PIP_2 was initially constrained towards Cζ of K194 for 600 ns and then it was constrained only Cζ to R60 in both replicas. The stabilization of the PIP_2 towards different residue from the one seen interacting in the crystallographic model was dictated by the observed interaction of PIP_2 and the K60 in unrestrained simulations (data not shown). I suspected an inactivation effect on the G-loop gate and the HBC gate upon this interaction, thus the steering of the PIP_2 from K194 to R60 was meant to test this hypothesis.

The evolution of the opening of the G-loop and the HBC gates, and the K^+ transport over the time course of the simulations is shown in Figure 19. The gates, during the equilibration in both simulations, evolved similarly to what was observed for the simulations without PIP_2. The radius of both gates first decreased slightly with the release of the constraints on the protein and after the constraints have been complete switched-off the bottleneck of the G-loop gate shrined dramatically, while the bottleneck of the HBC gate extended in an anti-parallel manner in respect to the G-loop gate. I was very surprised to observe hydrophobic gating at the level of the HBC to occur despite the presence of stabilized PIP_2 in *Simulation III*. In panel A of Figure 19 this corresponds to the steep

decrease of the radius of the bottleneck of the HBC gate in the time laps 100 to 200 ns. This event gives very strong indication that the molecular system had a construction bias, because it did not reproduce the experimentally validated opening of the HBC gate in presence of PIP_2 inside the crystallographic binding pocket. Conversely, the hydrophobic gating did not occur in *Simulation IV*, giving the possibility to investigate why the pore failed to sustain the reopened state in *Simulation III*. Concerning the K+ transport through the pore of the channel, Simulation IV has been largely conductive compared to Simulation III, consistently with the closure of the HBC gate in *Simulation III*.

5.4.1 K^+ transport in the selectivity filter

Both replicas differed in the total amount of K^+ passing through the pore during the simulated trajectories. Only three ions have passed through the TMV in *Simulation III*, the impedance is most probably due to the hydrophobic gating of the HBC. The closed state of the HBC gate similarly to the observations in *Simulation I* is accompanied with reduced fluctuation of the selectivity filter (Annex *Simulation III*:6). The TMV in *Simulation IV* remained extended at least as much as in the starting conformation and allowed multiple K^+ permeation events to be observed while the constraints stabilizing the ligands in the CTCD were applied. Then after, the rate of transport of K^+ has decreased in the last 200 ns of the simulation. During this time laps the HBC gate conformation varies, large and rapid fluctuations are observed in the pore profile shown in panel D of Figure 19. These fluctuations are most probably related to the decrease of the total number of bound propanol and Na^+ ligands (Annex *Simulation IV*:3), concomitant to the switching of the constraints stabilizing the center of the 4'-, 5'-phosphates of PIP_2, from Nζ of K194 towards Cζ of R60.

It is interesting to observe the K^+ binding inside the selectivity filter which occurred in two different manners in relation with the differences of the fluctuation of the filter between *Simulation III* and *Simulating IV*. After the equilibration in *Simulation III* the selectivity filter adopted the pinched conformation which persisted until the end of the simulation. Apart for the time laps 50 to 150 ns when K^+ was bound to sites S0-S2-S4, during the rest of the simulation K^+ bound to site S2-S3 and S4. During the period 150 to 450 ns when the applied external electric field was very low, not much of a redistribution of K^+ in the filter occurred. In the subsequent period the K^+ ions in the filter were redistributed in the inward direction only twice. The first event occurred immediately after the membrane potential was set to -700 mV. Then, the K^+ expelled inside the TMV was blocked by the closed HBC gate. The second permeation of K^+ through the filter occurred during a period when the G-loop gate fluctuated. The closed HBC gate is most probably the reason for the low rate of K^+ during this simulation. It is that the closed state of the gate on one hand prevents the ions incoming in the TMV to continue towards the cytosol. On the other hand, the closed state of the HBC gate is concomitant with the pinched conformation of the selectivity filter, which is characterized with higher binding affinity for K^+. Thus, it seems that there is dual barrier opposing the K^+ transport in the inward direction.

Let's consider in more details the K^+ transport through the selectivity filter because the situations in both trajectories *Simulation III* and *Simulation IV* were distinctly different (Figure 19A, Figure 19C). In the first 100 ns after the equilibration period in *Simulation III*, one K^+ from the bulk stabilized in site S0, in the same time as the K^+ in the TMV migrated near the G-loop gate through the open HBC gate. Since the newcomer event preceded the displacement of the resident in the vestibule, I conclude that the newcomer has increased the electrostatic potential around the selectivity filter, thus repelling the K^+ inside the TMV towards the cytosolic gate. On its turn when the K^+ in the vestibule migrated towards the G-loop gate, it has decreased the electrostatic potential inside the vestibule immediately below the filter, and allowed the delocalization of the K^+ ions bound inside the filter to move one site in the inward direction (Annex *Simulation V*:11A). Thus, here is a nice example of the knock-on mechanism purely driven by electrostatic repulsion in the selectivity filter and the TMV, environments which in respect to the K^+ ions were initially electrically negative in the observed configurations.

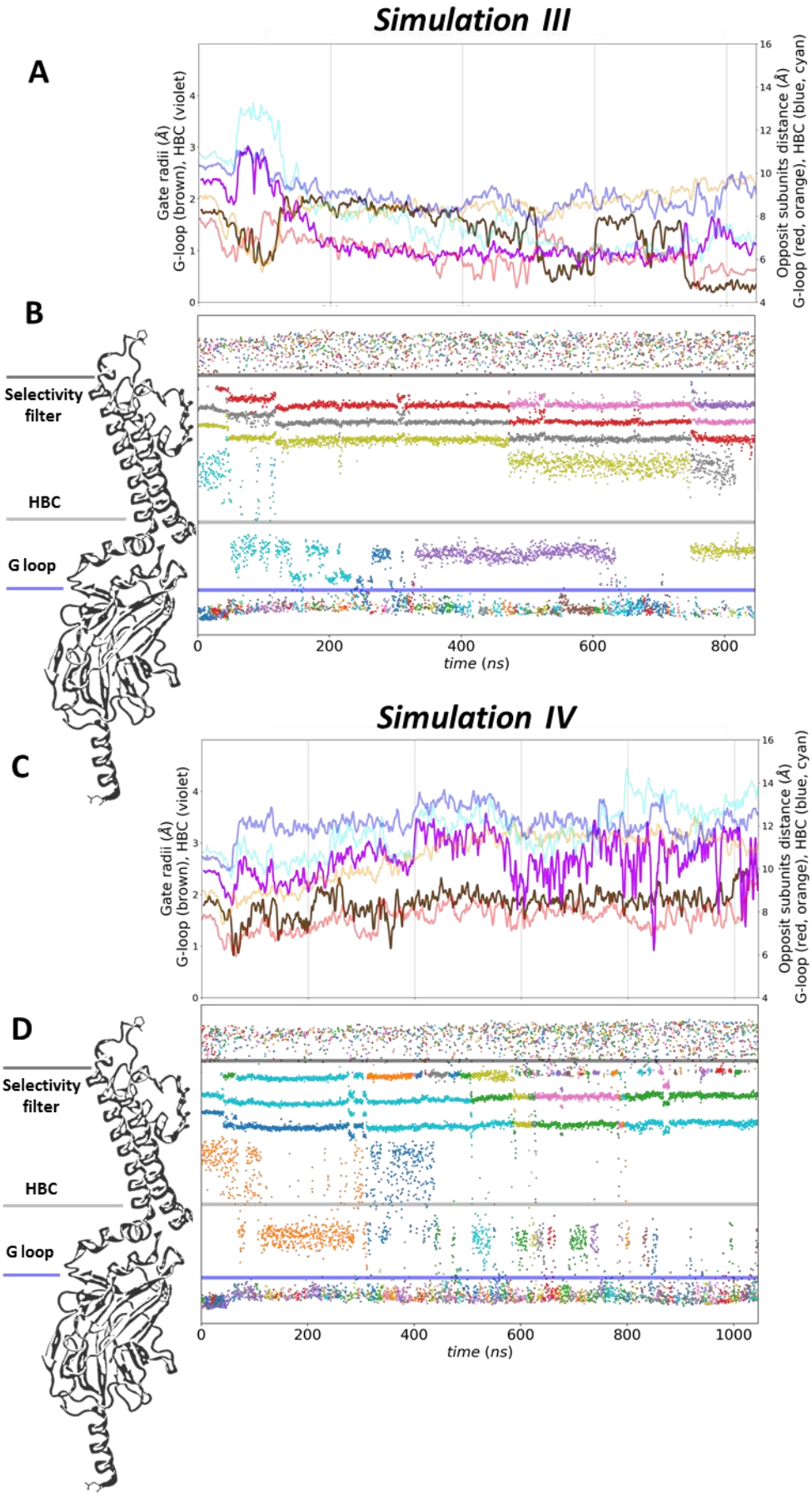

Figure 19: The pre-open mouse Kir3.2 in presence of PIP_2 modeled into the crystallographic binding sites (equivalent to PDB:4KFM), adopted alternative conformations of the TM vestibule during molecular dynamics simulation of two atomic-replica systems: Simulation III panel A and B; Simulation IV panel C and D. Timeseries are plotted for snapshots taken every 0.4 ns and plotted as convoluted average using sliding window of 20 ns and a symmetric power law function x^n (n=±6), the first 45 ns corresponds to the equilibration of the simulated system. (A, C) Timeseries of the opening of the G-loop gate (brown) and the HBC gate (magenta) is plotted on the left vertical axis. The distance between pairs of atoms from diametrically opposite subunits is plotted on the right vertical axis: G318:0 carboxyl oxygen of the mainchain (red and orange); the geometrical center of the phenyl ring of F192 (blue and cyan). (B, D) Timeseries showing K^+ movement across a section of the pore extending between 10 Å below the Cα of residue M313 in the G loop, and 10 Å above the carbonyl oxygen of residue G158 in the selectivity filter. K^+ positions along the permeation pathway are plotted on the left vertical axis. Each individual ion is colored with the same color along the entire timeseries, repeated color for different ions exist in the plot. Watermark of part of the channel is shown for easier localization of the gates in the plot.

Later on, the K^+ in the vestibule remained most of the time near the G-loop gate. This observation suggests an equilibration of the electrostatic potential in the volume between the S4 site and the

HBC gate when one K^+ is present in this region (Annex *Simulation V*:11B). The potential was probably close to 0 mV along the TM vestibule, therefore occasionally the K^+ in the vestibule approached the S4 site, before rapidly coming back to the G-loop gate. The potential barrier got rather higher near the S4 site, causing fast repeal of K^+ towards the G-loop gate. The behavior in time of the electrostatic potential around the selectivity filter also depends on the strength of the binding of K^+ in the filter. Thus, in a floppier filter K^+ ions inside could delocalize more easily in response to the approach of positive charges from outside the filter. In the time laps 70 to 140 ns, the opening of the filter mostly resembled the initial conformation (Annex *Simulation III*:2). Since the ions inside the filter did not move as the ion residing into the TMV approached the filter, it can be concluded that the binding affinity of this conformation of the filter for the particular K^+ occupancy is stronger that the repulsion generated by the incoming K^+ from the direction of the HBC gate. Then the latter simply bounced against the barrier generated by the occupied filter and it continued with similar velocity towards the G-loop gate.

Interestingly, this bouncing K^+ initially present in the TMV got caught between the G-loop and the HBC gates when the latter gate closed. In panel A of Figure 19 one can see that simultaneously with the closure of the HBC gate there was an inward delocalization of the K^+ from sites S1, S2/S3 and S4 to sites S2, S3 and S4. Indicating a change in the electrostatic potential inside the TMV and/or increase of the binding affinity of sites S2 and S3. Indeed, the profile of the pore in the time laps encompassing this event shows that the conformation of the filter changed to the "pinched" state and that it remained until the end of the trajectory (Annex *Simulation III*:3). This conformation is equivalent to the conformation observed in *Simulation I* and most probably corresponds to the inactivated conformation of the filter as discussed previously in parallel to numerous references from the literature. As the trajectory advanced, no global changes occurred in the conformation of the filter nor in the K^+ occupancy, until the applied voltage was increased. Approximately 50 ns after the external electric field was set to mimic V_m of -700 mV, there was an inward permeation event in the selectivity filter involving one newcomer K^+. As a result, the K^+ occupancy pattern in the selectivity filter did not change, but one K^+ from there on occupied the TMV between S4 and the closed HBC gate. The inward event was accompanied with a minor increase of the radius of the HBC gate, which probably is the reflection of the casual enlargement of the TM helix bundle. The fact that there was a new K^+ inside the vestibule suggests that the contribution of the external electric field is sufficiently strong to overcome the barrier set by the binding affinity for K^+ by the pinched conformation of the filter. Later, at time 750 ns another inward permeation was observed. This time, it seemed that the newcomer event in the selectivity filter was made possible by the passage of the K^+ residing in the TMV through the overall closed HBC gate, resulting in the decrease of the electrostatic potential in the vestibule below the site S4. A profile of the electrostatic potential at the time when the K^+ from above the HBC crossed the gate can be observed in Annex Simulation 3:11D – this profile shows the increase of the voltage difference between site S4 and the volume of the TMV immediately above the HBC gate once an ion occupying this volume continues its inward course. Thus, the inward K+ motion should be used as an "electrostatic piston" which by increasing the distance between the steady bound K+ into the filter and the K+ advancing inwardly, results into a pooling force on the K^+ occupying the most internal site of the selectivity filter.

The oriented motion of the K^+ inside the TMV when the transmembrane potential was simulated, suggests that the summed effect of the reaction field and the additional electric field efficiently generated a negative membrane potential distributed along the TMV. Because there were no obvious large conformational changes in the pore (Annex *Simulation III*:3), I conclude that the increase of driving force for K^+ was primarily caused by the external electric field, leaving opened the question of whether the conformation of the filter was genuinely conductive or the K^+ permeations were generated by external force breaching the existing energetic barriers in an otherwise closed/inactivated conformation of the filter.

The K^+ transport observed in *Simulation IV* was different. From the beginning of the simulation, K^+ occupancy in the selectivity filter followed the pattern K^+-W-K^+-W-K^+. The occurrence of a different K^+ occupancy pattern in the filter is concomitant with both a different conformation of the selectivity filter and an open HBC gate compared to *Simulation III*. Considering these differences, one should suspect that the conformation of the HBC gate influenced the mobility of the selectivity and hence the binding affinity for K^+. This hypothesis is virtually the same one as that I made in the previous section of the manuscript, based on observations of the system in absence of PIP_2 (*Simulation I* and *Simulation II*). Here again, I have found correlation between the flipped state of the filter at I155 and the distance between the sidechains I155 and L173 in two adjacent subunits. I linked this correlation to the conformation of the TMD which seemingly played role as a modulatory factor for the fluctuation of the selectivity filter. The correlation matrices quantifying the relationship between pairs of interatomic distances involving residue I155 and its contact partners are presented in Annex *Simulation III*:8 and Annex *Simulation IV*:8. The analysis made on the trajectory in *Simulation IV* showed several non-trivial correlations at a threshold as low as $r \geq 0.45$. I qualify a relationship as trivial if it explains a symmetric comparison, for instance the correlation between nodes 6 and 13 is trivial because the distances followed in both nodes are the same. The non-trivial correlations which were caught by the analysis showed that the distances between reference residues in TM1 and TM2 in both couples of diametrically opposed subunits behaved in a negatively correlated manner, for instance, nodes 0/1 vs. nodes 15/14 and nodes 0/1 vs. nodes 21/22, demonstrating once again C:2 symmetric processes in the tetramer. The analogue analysis made on the trajectory in *Simulation III* was much more informative, it was also very similar to the analysis made on the trajectory in Simulation II (Annex *Simulation II*:8). In *Simulation III*, a strong anti-correlation was observed between the distance Self:I155:CD~Next:L173:CG and the distance Self:I155:CA~Oposit:I155:CA. Although the equivalent anti-correlation was less strong in *Simulation IV*, it was also present in all subunits – giving to my hypothesis an additional line of evidence. Furthermore, the weaker correlation signal from *Simulation IV* suggested that when the helix bundle is larger, the fluctuating behavior of site S3 of the selectivity filter became stochastic, i.e. less directly driven by the L173 partner, in respect to situation of a more rigid structure when the HBC is closed.

A surprising observation was made in *Simulation IV*. At the time of approximately 325 ns, there was an inward permeation through the entire pore involving five K^+ ions (Figure 19D). The membrane potential at this point of the simulation was only -70 mV. At that moment, the G-loop and the HBC gate were open, allowing the rapid extraction of the K^+ previously present into the TMV. The most consequent fluctuation during the permeation took place in the HBC gate, which radius was extended by approximately 1 Å (Figure 19C), involving an increase in the distance between residues F192 in subunits P3 and P4. This could very well be the event which triggered the permeation. In fact, the fluctuation of the HBC gate preceded the inward displacement of K^+ in the filter. This observation is also in line with my previous assumption that the enlargement of the helix bundle increases the instability of the selectivity filter. Unfortunately, this was the only permeation of the kind that occurred at this membrane potential, among all of the different simulation setups I tested by varying the number of PIP_2 interacting with the channel. This rare event is promising and would definitively require to be investigated in longer simulation runs maintaining low membrane potential. If repetitive permeations were obtained with milder driving force, one would get evidence that the simulations where permeations are observed only at voltages -700 mV or higher, correspond to forced breaching of the barriers in a closed selectivity filter without necessarily involving the conformational changes which decrease the strength of interaction between the filter and the K^+.

By looking into more details, I found the possible effectors of the conformational changes. There were simultaneous changes in the backbone torsion angles which occurred in residues T154, I155, G156 and Y157 of subunit P1. At the same time, residue E152 in subunit P1 and residue E150 in subunit P3 also changed conformations. These changes involved parts of the protein which are vertically aligned and adjacent to each other due to the twist in the quaternary arrangement

between the channel subunits (Figure 9), thus providing one more line of evidence that the selectivity filter is allosterically linked to the conformation of the HBC gate.

By the end of *Simulation IV*, numerous K^+ transport events were observed with the increase of the driving force. This will be presented in more details in the next subsection, because the described phenomenon relies on both the conformation of the filter and on the HBC and G-loop gates. There is yet another issue which concerns the K^+-water alternation pattern in the selectivity filter in either situations, with or without K^+ transport. Some well-known aspects of K^+ transport need to be evoked to prepare further discussion on this topic: *i*) from electrophysiology it is well known that the amount of K^+ which crosses the channel is proportional to the driving force steering the ions in the inward or the outward direction; *ii*) several studies have confirmed that depending on the conformation of the selectivity filter, its binding affinity for K^+ is modulated. For instance, in *Simulation IV*, the K^+ was distributed in the selectivity filter following a different pattern in respect to *Simulation III*. The fact that the pattern K^+-W-K^+-W-K^+-W was obtained spontaneously in *Simulation IV* is very important. It suggests that the open state of the HBC gate caused fluctuation in the selectivity filter which in its turn lowered the binding affinity for K^+. The lower binding affinity would then allow the K^+-water alternation inside the filter to be established. It is then straightforward to state that the K^+ transport observed without K^+-water alternation taking place is less likely to be representative of the naturally occurring K^+ transport and it is most likely that it was made possible only because the driving force caused the K^+ to overcome the binding energy barrier of the constricted selectivity filter. This hypothesis is strengthened by the fact that both types of events were observed in atomic replica simulations using the exact same forcefield parameters, leading to consider that the only apparent difference was of conformational order.

5.4.2 Conformational changes involving the HBC and G-loop gates

After the K^+ permeated the selectivity filter, its course towards the cytosol could be blocked by the HBC gate. In the set of trajectories in *Simulation III* and *Simulation IV* two different situations are observed (Figure 19A, Figure 19C). In the first, the HBC gate closed approximately 100 ns after the constraints on the protein were released. The difference between the conformation of the bundles of TM2 in both simulations is clear when looking at the bending profiles of the helixes (Annex *Simulation III*:4D and *Simulation IV*:4D). It is important however to identify the cause of these differences. The difference which I discerned comes from the amount on hydrogen-bonding events detected over time between PIP_2 molecules and different parts of the protein. In *Simulation IV*, a PIP_2 molecule is constantly bound either to the TM2 or to the sliding helix of the same subunit in three of the subunits: P1, P3 and P4 (Annex *Simulation VI*:10). While in *Simulation III*, hydrogen bonds between TM2 and the PIP_2 were lost during the first 100 ns of the simulation and there was no evidence of compensation by the residues of the slide helix (Annex *Simulation III*:10). The effect of the decrease in PIP_2 interactions with TM2 and the slide helix can be followed in the profiles of the angles between consecutive residues (Annex *Simulation III*:4AD and Annex *Simulation IV*:4AD). By comparing the bend profiles of the slide helices between *Simulation III* and *Simulation IV*, it is obvious that when the bend angle 75-80 and 83-86 increased in *Simulation III*, the radius of the HBC gate decreased. On the contrary, the bend profile in *Simulation IV* resembled the initial one, having the strongest values for residues in the ranges 71-74 and 78-83. In *Simulation III*, this change in the slide helices was also concomitant with the loss of the bending of the TM2 (Annex Simulation III:4D), in line with the ideas of the importance of the TM2 central bending for the opening of the HBC gate (Jiang et al. 2002).

The changes in the slide helices described above are also correlated with the conformations of individual loops of the G-loop gate. In *Simulation III*, the initial bending measured between residues in the ranges 71-74 and 78-83 was displaced most strongly in subunit P4 and at the end of the simulation, it is almost entirely measured in the range 73-80. It is interesting to see that the βI-βH-loop which is under the slide helix of segment P4 had the conformation that occluded the permeation pathway the most. The conformation is equivalent to the one shown in Figure 17 for the

subunit P1 (the red subunit) at time 260 ns. Thus, in *Simulation III*, the bend angle between residues 319-322 in the G-loop of subunit P2 became nearly 0°, while the bend angle involving residues 312-314 increased markedly (Annex *Simulation III*:4G). The data also showed that the increase of the bend angle in individual βI-βH-loops involving residues in the ranges 312-314, 319-322, was concomitant with the enlargement of the lumen of the G-loop gate. This was the case of subunit P4 where the βI-βH-loop adopted a conformation displacing the loop away from the center of the permeation pathway. Despite the fact that this conformational change concerned only one subunit in this simulation, we believe that its identification is important and was fallowed in rest of the trajectories as potential reporter for the activation of the G-loop gate.

Somehow an equivalent process was also observed in *Simulation IV*. In this simulation, the G-loop gate remained open with a minimum diameter comparable to the starting one. The HBC gate also remained well extended. The maintained large diameters of the gates promoted rapid inward transport of the K^+ which flowed into the TMV from the selectivity filter. An enlargement of the diameter of the G-loop gate was observed numerous times when outward movement of K^+ occurred. It is noteworthy to remark that the binding of a newcomer K^+ at site S0 of the filter favored by increased negative membrane potential, was observed to be the limiting factor for a K^+ residing into the TMV to exit in the inward direction.

Two observations can thus be made: first, the K^+ awaited to exit the vestibule in the volume in between the HBC and the G loop; second, in *Simulation IV* and other simulations, the G-loop gate was sufficiently open to allow permeations of K^+ in the outward direction (against the driving force). Remarkably, these K^+ movements were against the direction of the driving force generated by simulated membrane potential -400 to -700 mV, suggesting that the voltage drop inside the TMV was flattened above the G loop. Indeed, in the profiles of the electrostatic potential when the voltage is turned on (Annex *Simulation IV*: 11) one can notice that the major part of the voltage drop was made on both sides of the selectivity filter. Moreover, it should also be noticed that the potential was more negative inside the TMV than immediately after the G-loop gate. This observation readily explains the spontaneous outward permeations of K^+ through the G-loop gate. The slight positive peak above the G-loop gate was generated by the sole K^+ found there, while the higher potential below the G-loop gate is produced by the numerous K^+ constantly occupying this volume. Three to five K^+ were recruited into this environment by E236. Without being coordinated in a stationary manner, K^+ ions exhibited a bouncing behavior. Thus, individual K^+ exploited the opening of the G-loop gate and from time to time an outward permeation of K^+ through the G-loop gate could be obtained. It is straightforward to deduce that this outward movement would be impossible if at the same time there was an inwardly permeating K^+ coming from the selectivity filter. This seems to be the case because there was no displacement of K^+ in the selectivity filter from S2/S3 to S4 which were simultaneous to outward permeation events of the G-loop gate, but all inward position changes of K^+ were concerted at all levels of the pore.

The contrast of the G-loop conformations between both simulations is promising to search for the allosteric link between different parts of the CTDC involved into the gating of the G-loop gate. If considering the already identified increase of bend angles involving residues in the ranges 312-314 and 319-322, it is clear that the same trend was also obtained in *Simulation IV*. Thus, except for subunit P1 where the G-loop remained in a conformation similar to the starting one, all other subunits displayed an increase in these two bend angles, causing the enlargement of the G-loop gate (Annex Simulation IV:4G). It is even evident that the predominant effect of the displacement of individual βH-βI loops was provided by the increase of bending at residues 319-323. This displacement of the βH-βI loops also coincided with the displacement of the HBC effector, the F192. By visual inspection of the trajectory, it could be seen that in respect to the starting conformation, in three subunits the HBC gate was larger at F192 and at the same time the βH-βI loop of the previous subunit was also displaced to enlarge the lumen of the pore.

The next hotspot of the protein which exhibited significant difference with the starting conformation in *Simulation III* and *Simulation IV* is the βC-βD loop and the adjacent N_{ter}, especially in the next subunit. For instance, in *Simulation III* this relation concerned subunits P2 and P4, it was easy to spot because P2 was the only subunits where at the end of the simulation the βC-βD loop did moved away from the center of the CTCD. In *Simulation IV*, the equivalent displacement occurred in subunits P1, P2 and P4, coinciding with the subunits where F192 of the HBC gate was displaced to enlarge the gate (see above). The conformational changes in the βC-βD loop and N_{ter} contact involved a reorientation of H69 and N231. N231 interacted with H68, H69 and with the PIP_2 or the membrane. H69 got more prominent into the βC-βD loop as the βC-βD loop was displaced toward the N_{ter}. These brief observations motivated a scrutiny of the interactions of the CTCD involved into the obtained dilatation of the G-loop gate.

By inspection of the inter-residue interactions along the layers of the dynamic interaction network (i.e. select ***m*** contacting residues from residue ***i***, then select ***n*** contacting residues for each ***m*** residue, and so on), I identified two sets of residues linked allosterically and spanning from the surface of the CTCD to the G-loop gate. The first network consists primarily of hydrophobic residues and crosses in-depth the superimposed β-sheets of the CTCD from the surface to the cytosolic gate of the channel. The second network runs on the surface of the CTDC tangent to the membrane, it involves mostly hydrogen-bonding interactions interlaced with hydrophobic contacts of the first network. These two allosteric pathways are grouped into a single one in the last sections of the chapter (section 5.7.2.2), however, they are discussed as separated allosteric elements in the following paragraphs.

The hydrophobic network is depicted in Figure 20. This network maintained the cohesion of the layers and permitted for a concerted motion of β-sheets as the βL-βM strands were displaced away from the center of the CTCD. This concerted motion is put to evidence by structural alignment of the TMD and the selectivity filter of the simulated channel to their initial state. In *Simulation IV* the G-loop gate opened at three subunits (P1, P2, P4), Figure 20 depicts the final conformational change of the central subunit (P4) among those three. Exploration of the conformational changes of the G-loop gate in central subunits P4 benefit by the conformational symmetry of its adjacent subunits P1 and P2.

The βL-βM strands are part of the Gβγ dimers binding surface. Upon G protein activation of the channel, this region was proposed to perform an upward motion towards the membrane and away from the βD-βE loop of the next subunit (X. Y. Meng et al. 2012b; Mahajan et al. 2013), this motion was validated by comparison of the further available crystallographic models of the full mmKir3.2 channel (see chapter Introduction subsection “The Gβγ-Kir3 interaction” for more details). Figure 20 shows a representation of a persistent upward conformation of the βL-βM strands. The βL-βM loop was additionally displaced away from the center of the CTDC under the influence of the continuously bound alcohol beneath it. The motion appeared propagated further as rigid body motion from the βL-βM strands towards the βA strand – in addition to the backbone interactions controlling the β-sheet formation, this structure was also stabilized by complementary hydrophobic interactions between V67 and V351, whose sidechains moved in concerted fashion and remained parallel during the most part of the simulation. In this region, F348 is located and it seems to be involved into pi-stacking parallel-displaced interactions with H68, as the side chains of these residues also evolved in

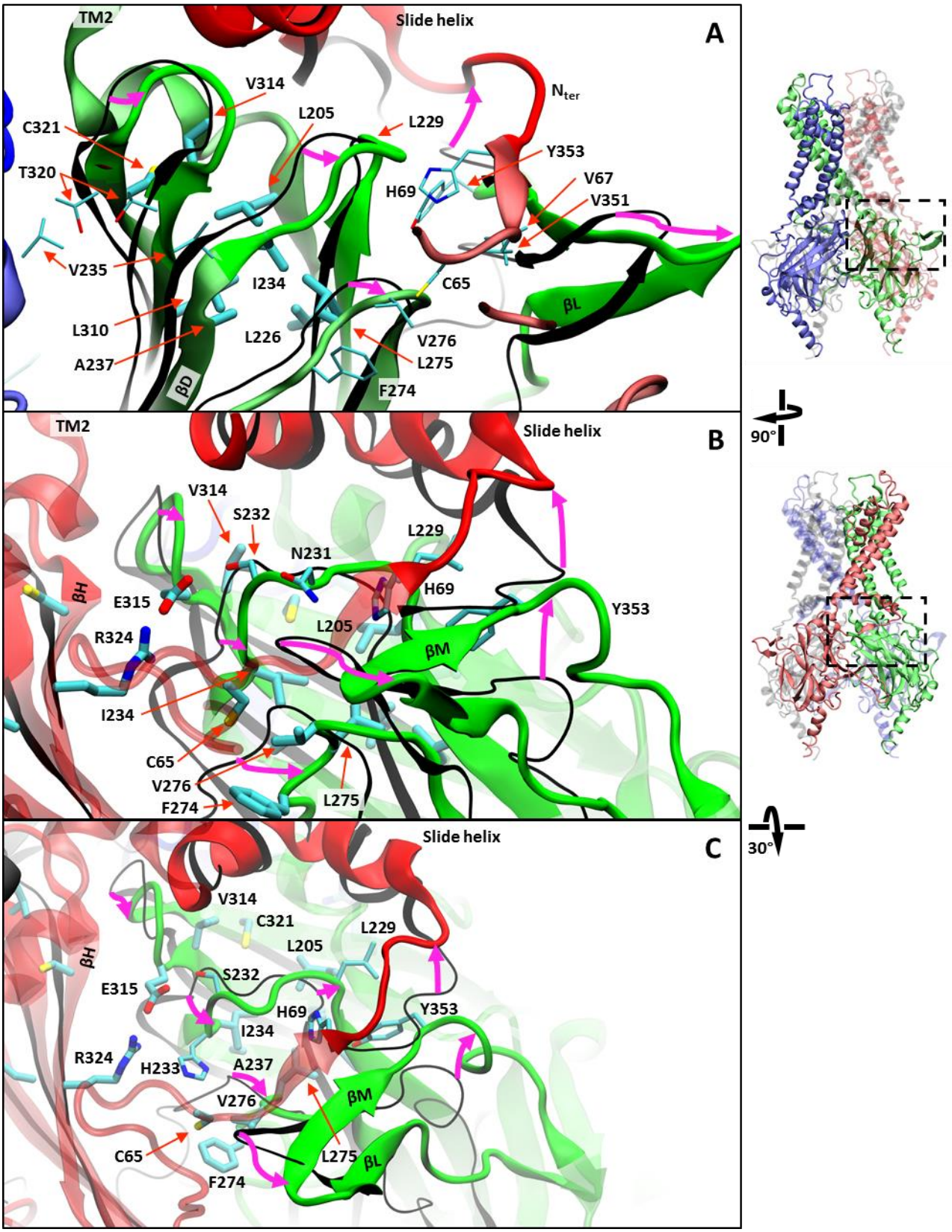

Figure 20: Displacement of superimposed β-sheets upon opening of the G-loop gate and the hydrophobic network connecting the $G_{\beta\gamma}$ binding site with the cytosolic gate represented in one subunit of mouse Kir3.2 during molecular dynamics simulation. The region of the CTDC represented in the panels corresponds to the boxed region on the channel miniatures on the right, the conformation of subunit P4 obtained after 1000 ns of Simulation IV is shown from different perspectives. The concerted displacement of the protein (green) in respect to its starting conformation (black trace) is pointed by curved arrows (magenta), the structural alignment is made on top of the starting conformation of the TM bundle, the pore helix and the selectivity filter. (A) View on the superimposed β-sheets in the cytoplasmic domain of subunit P4, subunit P1 (red) is removed for visibility on the subunit P4 (green). The two branches of hydrophobic network start at the right with residues V351 and Y353, and span until the βI and βH strands on the left. (B) View representing the same region as panel A after 90° rotation to the left. From this perspective the upward displacements of the βL-βM strands and the turn preceding the slide helix are most appreciable. (C) View of the region represented in panel B after 30° rotation of the channel away from the membrane. From this perspective is best seen the C321 in βH strand, which is the deepest residue of the represented hydrophobic network.

a parallel during long periods of the simulation (data not shown). F348 is interesting because it is not well conserved among the Kir family. For instance, in mmKir1.1 (constitutively opened channel) the equivalents of H68 and F348 are E73 and K317, which should favorably interact, suggesting that the proposed interaction in mmKir3.2 between H68 and F348 could be conservative element enhancing the cohesion in the βL-βM-βA β-sheet. On the C_{ter} side of the βM and the βA strands the hydrophobic network involved the T-shaped interaction between Y353 and H69. This last interaction provides additional strength into the integral β-sheet, but it also serves as a jump link to the next level of superimposed elements, the βC-βD loop. On the N_{ter} of the βA strand is located another residue, C65 linking the βA strand to the turn immediately before the N_{ter} of the βG strand – an interaction which is propagated towards the subsequent level of the β-globulin like CTCD (instead of simply stating the βG strand, I will refer to it as BF-βG coil in order to avoid confusion with the G-loop gate which is a completely different structure). Thus, the hydrophobic network splits into two volleys on both sides of the βA strand, this separation is best seen in Figure 20B.

During the simulation time, C65 remained within F274 and V275, thus coordinating the BF-βG coil in following the outward motion of the βL-βM-βA sheet. On the reverse side of the BF-βG coil, the L275 is oriented towards the center of the CTCD. L275 interacted with residues I234 and L226 in the βC-βD strand. This interaction was slightly deeper into the cytosol as compared to the interaction that H69 had with the βC-βD loop. Importantly, L275 and its partners constituted the "bottom" of the Na^+ binding site located under the arc of the βC-βD loop. Residue I234 in the βD strand serves as a transversal link to the second volley of the hydrophobic network involving residues in the βC strand, the C-linker and the βI strand. I234 also interacted with L226 and A237 in the βC-βD strands. Moreover, it interacted with L310 and V314 in the βH strand, thus extending the hydrophobic network to the base of the G-loop gate. The second volley of the hydrophobic network started at the Y353 interacting with H69 and then spread to the C_{ter} of βC strand, where Y353 interacted with the sidechain and the backbone of L229 and with D228 as a part of the hydrogen-bonding network. Near there, residue L205 was often within hydrophobic interaction range with residues L229 and C321. These last interactions closed both volleys of the hydrophobic network at the βI strand, thus encompassing the βH-βI loop (Figure 20C).

Before discussing into more in details the hydrophobic network and trying to make parallels with reports in the literature, I will present a second interaction network which involved mainly hydrogen-bonding interactions, and which appeared profoundly interlaced with the hydrophobic network presented just above. This network is presented in Figure 21, some of the partners in the hydrophobic network are also displayed to ease the impression of proximity between the partner residues. This network was also obtained by iterative search of partners starting from the Gβγ binding interface and up to the G-loop gate. The first partners found linking the βM and the βA strands to the βC-βD loop were the couples Y353 and L229, and H69 and N231, where only N231 was not involved into the hydrophobic network. The network then expanded until the βH-βI loop, from S232 forming transient interactions with E315, and from S232 also interacting with D88 in the slide helix. The βC-βD loop had additional permanent interaction with the slide helix via the R230/D81 and R230/D88 salt bridges. The last interaction which was observed permanently, independent of the conformation of the gates, was the D228/R201 salt bridge.

This last interaction is well-known because its ablation causes the Kir3.2 channel to enter a state of higher open probability which is insensitive to the protein activation pathway (Whorton and MacKinnon 2011). The proximity of the salt bridge to the experimentally observed Na^+ binding site, conjointly with the absence of acidic residue equivalent to D228 in Kir3.1 (insensitive to changes in intracellular Na^+ levels) and the highly active phenotype of the R201A mutants, served as a basis for the hypothesis that in Kir3.2 and Kir3.4 subunits, Na^+ will compete with the arginine from the C-linker for the aspartate of the βC-βD loop. The coordination of Na^+ at the aspartate would destabilize the C-linker and allows its displacement separately from the βC-βD loop, and both secondary structures would be able to move away from the K^+ permeation pathway, thus causing the G-loop gate to open

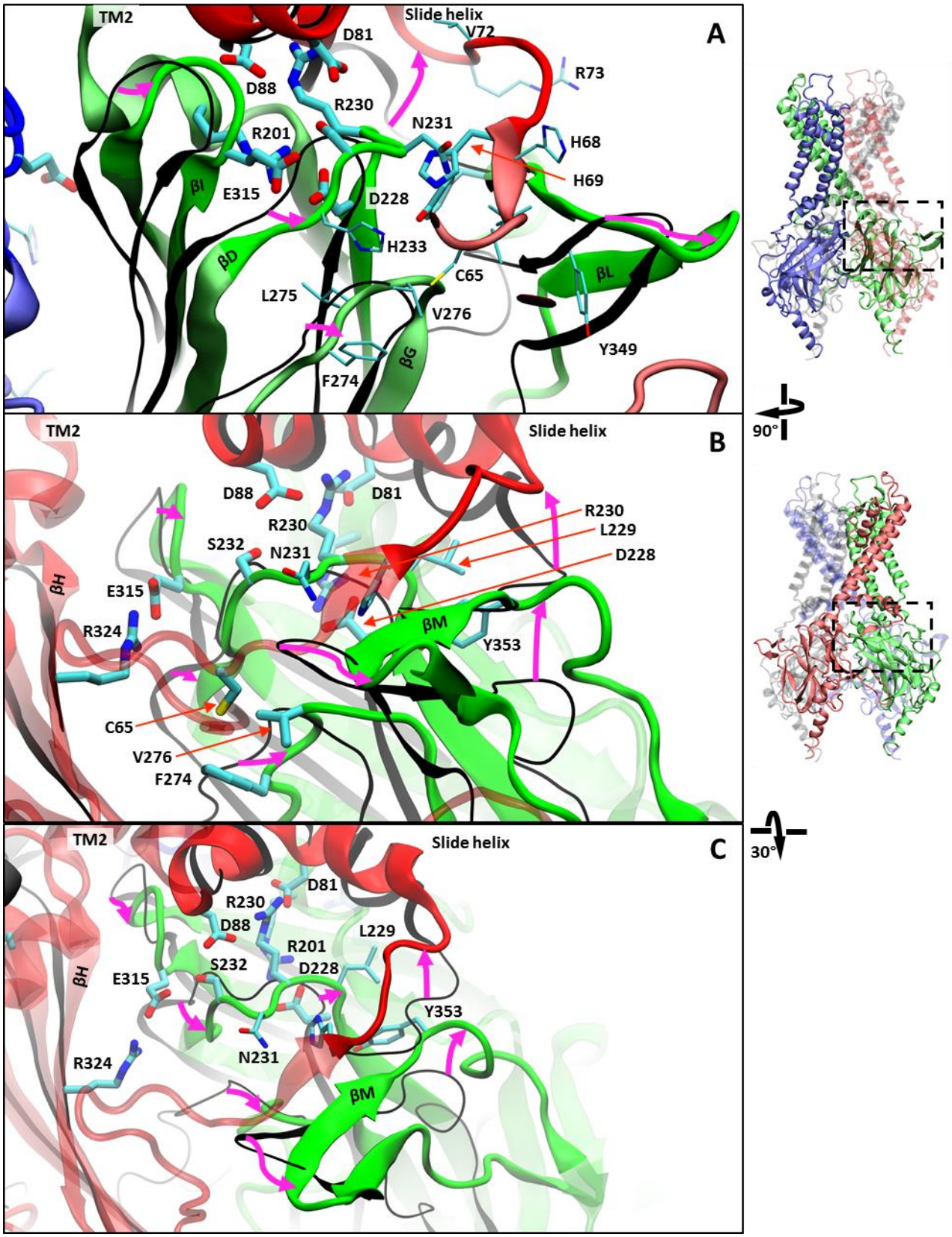

Figure 21: Displacement of superimposed β-sheets upon opening of the G-loop gate and the hydrogen-bonding network connecting the $G_{\beta\gamma}$ binding site with the cytosolic gate represented in one subunit of mouse Kir3.2 during molecular dynamics simulation. Same representation scheme as described in Figure 20. (A) View on the superimposed β-sheets in the cytoplasmic domain of subunit P4, subunit P1 (red) is removed for visibility on the subunit P4 (green). The hydrogen bond network starts at the βL-βM-βA sheet and it connects to the βC-βD loop via sidechain interactions to backbone interactions. Then, it splits towards the βI-βH loop, the Slide helix and the C-linker involving primarily sidechain interactions. (B) View representing the same region as panel A after 90° rotation to the left. From this perspective, the hydrogen bond network is seen parallel and located in the middle of both branches of the hydrophobic network described in Figure 20. (C) View of the region represented in panel B after 30° rotation of the channel away from the membrane. From this perspective can be appreciated the alignment between the salt-bridges connecting the βC-βD loop to the Slide helix ant to the C-linker.

in follow-back manner. It is regrettable that there is no crystal structure of the R210A mutant co-crystalized with Na^+ to actually confirm the role of Na^+ in the disengagement of the D228/R201 salt bridge, where one should expect that the Na^+ will be at least coordinated with the D228. In reality, in the available crystallographic models PDB:3SYQ and PDB:3SYP, one can visually track the effect of the R201A mutation to a twist of the βC-βD loop, which most probably accounted for the G-loop enlargement by the generated displacement of part of the βC-βD loop away from the βH-βI loop. In these models, H232 (in two subunits of 3SYP, in four subunits of 3SYQ) was attracted by D228, this local rearrangement suggested that D228 really needs a positive partner and H233 stepped into this role. Moreover, despite the absence of the D228/R201 salt bridge in both R201A mutant structures, the Cβ of A201 in the C-linker was always pointing at the position of the equivalent in R201, thus making it difficult to attribute the Na^+ binding to cause either of the proposed rearrangements resulting into the opening of the G-loop gate. Interestingly, in all simulations presented until now independent of the presence or the absence of K^+ transport through the G-loop gate, the salt bridge D228/R201 always remained stable and sustainably followed all the local fluctuations of the surrounding protein structures. This salt bridge was even sandwiched between two interacting couples: the hydrophobic interaction L205/I234, and the salt bridges D81/R230 and D88/R230. The crosslink of the three secondary structures suggested that they are functionally coupled, thus the motion of the βC-βD loop should be transmitted to the HBC gate through the C-linker via the salt bridge D228/R201, and the HBC gate could also affect the βC-βD loop by the reverse linkage. Then the R201A phenotype should be exceptional because it allows the displacement of the βC-βD loop and the opening of the G-loop gate. on the other hand, it would hardly represent a native active state of the channel because of the geometric/steric impairment between the C-linker and the βC-βD loop.

In order to strengthen my personal criticism of the hypothesis cited above, I invite the reader to follow the displacement of the G-loop shown in the insert of panel B in Figure 22. The more pronounced fluctuations of the G-loop of the subunit (P2 indicated by a blue bead) oriented towards the bottom of the figure coincided with the fluctuation of the slide helix located below (subunit P4 indicated by a green bead). In both simulations from which data was used to prepare Figure 22, all the salt bridges D228/R201 were always engaged, suggesting that the triple linkage between βC-βD loop and βH-βI loop, and βC-βD loop and the C-linker was most probably involved in the native mechanism opening the G-loop gate, rather than the uncoupling of the interaction between the βC-βD loop and the C-linker. Here I pointed to the fluctuation in the slide helix as a cofactor of the destabilization of the G-loop gate, this will be the subject of the simulation setup presented into the next subsection of the chapter.

Figure 22 shows the behavior of the I234 residue which was proposed to alter the PIP_2 affinity of Kir3 channels in respect to its equivalent leucine in Kir2.1. The mutation I234L was shown to sustainably decrease the rundown speed of the Kir3.4 homomeric channel and to increase the recovery rate after PIP_2 depletion by voltage dependent phosphatase (Zhang et al. 1999; Diomedes E. Logothetis et al. 2015; Ha et al. 2018). Let's consider the following expression:

$$R_{Kir3} = R_{sel.filt.} + R_{HBC\ gate} + R_{G\ loop}$$

The resistance of the channel is modeled as three resistances in series. Naturally, if the first two resistances are maintained constant, and the resistance of the G-loop is modulated, the additive resistance changes by exactly the amount by which the resistance of the G-loop has changed. It means that if the conformation of G-loop gate is altered and maintained to less obstructive states, the effect measured on the channel by modulation of the PIP_2 levels will be that of the HBC gate and the selectivity filter. Indeed, this is the case with the I223L mutation in Kir2.2, where the G-loop adopts the PIP_2 bound-like conformation in absence of PIP_2 (Hansen, Tao, and MacKinnon 2011). Then in my understanding, the higher apparent affinity for PIP_2 of the channel in the experiments of Hansen and colleagues does not necessarily indicate that the I234L mutation in channel

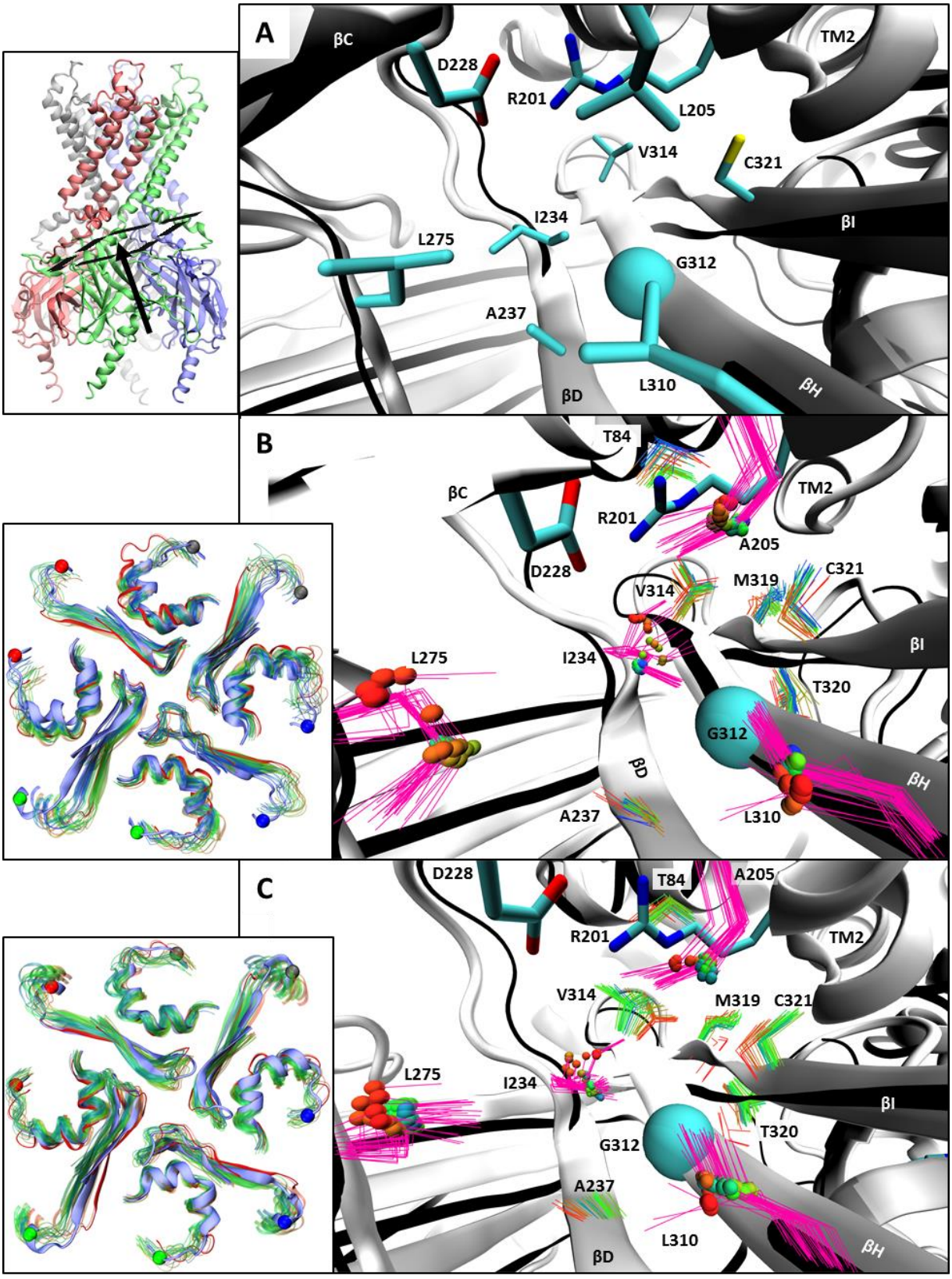

Figure 22: Core of a hydrophobic network inside the cytoplasmic domain controlling the G-loop gate of mouse Kir3.2; from two molecular dynamics simulations of systems evolved to closed and open G-loop gate states. Except for the first panel, the time progression is shown as a superimposition of drawings of the same secondary structure. Structural alignment is made on top of the starting coordinates of backbone of residues L205 I234 L275 L310 in the same channel subunit as the one used for the graphical rendering, snapshots are taken with a timestep of 40 ns and are colored using linear gradient red-green-blue. Elements followed in time include: Cγ and $Cγ_1$ atoms in leucine and iso-leucine residues shown as small spheres; the sidechains of residues T84, A237, V314, M319, T320 and C321 shown as lines. The Cα-Cβ-$Cγ_{(1)}$-Cδ bond in leucine and iso-leucine are drawn as purple lines, the Cα of G312 is shown as a van-der Waals sphere (cyan). Except for the first panel, the inserts to the left show the time progression of the residues preceding the slide helix in the range G70-K90, and the βH-βI strands in the range P300-S325. The Cα atoms of G90 and P300 are represented as van-der Waals spheres using color-code to indicate the names of the subunits as used in Figure 9. (A) Main residues of the hydrophobic network maintaining the cohesion between the BF-βG coil, the βD strand, the βH-βI strands, C-linker and the slide helix. The βH-βI loop of one subunit is observed in perspective along the β-strands confining the loop (boxed plane in the insert to the left). The same perspective is used for the representations in the other panels. (B) Closed G-loop gate in Simulation 0. (C) Open G-loop gate in Simulation IV.

Kir3.2(E152D) (critical note: E152D mutation decrease $R_{sel.filt.}$ in the above equation (B. A. Yi et al. 2001)) decrease the amount of PIP_2 needed to bound to the channel for its opening. Simply, similar effect on the current through the channel can be obtained when the G-loop gate closes less, which appears to be the case in Kir2.2(I223L).

Thus, I propose that the mutation L234 in Kir3.2 should be considered in a context relating it to the PIP_2 affinity of the channel and my hypothesis is that the function of the I234L mutation is to increase the coupling between the βC-βD loop and the βH strand, thus controlling the opening of the G-loop gate when Na^+ is bound under the arc of the βC-βD loop. This suggestion can be readily verified by recording of a G-loop gate mutant like M313A and/or M319A which would impair the ability of the G-loop gate to close, thus one could verify if the I234L mutation acts purely on the PIP_2 affinity or it is related to function of the G-loop gate. In panels B and C of Figure 22 are shown two predominant rotamer states found in two simulations. In panel B the bond $C\gamma_1$-Cδ of I234 was observed to its furthest from the βH strand. In this simulation the G-loop gate was closed and no K^+ transport was observed through the G-loop gate in the outward direction (Annex *Simulation 0*:1). In consequence, in panel B, one can see that the black trace marking the initial location of the βH strand is closer to the viewing point than the white trace which is representative of the location of the βH strand after 800 ns. The L275 residue was displaced in a lower position in respect to the starting position indicated by red beads. The distance between the βH loop at the center of panel B and the slide helix on top of it also appears to have increased. On the other hand, the contrary is observed in panel C representing the configuration of *Simulation IV* where numerous K+ ions crossed the G-loop gate in the outward and inward directions. In particular, the bond $C\gamma_1$-Cδ of the I234 residue is to its closest to G312 which appears to be the second hydrophobic partner for the sidechain of I234 in the βH strand. Thus, in Figure 22, I illustrate the bimodal behavior of residue I234. I think that in the case of the I234L mutation, the leucine independently on its rotamer state around the Cα-Cβ bond either of the $C\delta_1$/$C\delta_2$ atoms will occupy the volume next to the βH strand, thus providing constant hydrophobic interaction between the βC-βD loop and the βH strand. This hypothesis regarding I234 in mmKir3.2 can be confronted to crystallographic models of the homologous Kir2.2 channel. The native I223 in the apo-model of Kir2.2, as observed in PDB:3JYC (Tao et al. 2009), is oriented similarly as I234, shown in panel B of Figure 22. For L223 in Kir2.2(I223L) mutants, in absence (PDB:3SPJ) and in presence of PIP_2 (PDB:3SPH) (Hansen, Tao, and MacKinnon 2011), one of the Cδ atoms of the leucine occupies the same volume as the Cδ atom of I234 shown in panel C of Figure 22.

Until now the hydrophobic network I have observed in the simulations remains nicely in line with the records from the literature hypothesizing its existence (see section 2.6.2). However, an additional part of the interaction network propagating from the G protein binding site on Kir3.2 towards the G-loop gate (not present in the literature review), will be presented in the following subsections.

5.5 MD Kir3.2 in presence of PIP_2 interacting with two protein sites, propanol and Na^+

5.5.1 Modeling of additional PIP_2 interacting with the slide helix of mmKir3.2

In the previous subsection I suggested a relationship between the fluctuations of the slide helix and the conformation of the G-loop gate, here I will pursue with a subsection where I investigate the effect of the stability of the slide helix on the conformation of the gates of the channel.

The idea about the control of the gating of Kir channels upon stabilization of the slide helix is not new. It has been investigated experimentally, and I will mention only two examples. A potent increase in the activity of the bacterial KirBac1.1 channel was achieved by Enkvetchakul and colleagues, when hydrophobic decyl-MTS anchors were attached to cysteine mutants of specific residues of the slide helix of the channel (Enkvetchakul et al. 2007). These residues in KirBac1.1 are: V47, R49 and L51. Their positional equivalents in protein sequence alignment with mmKir3.2 are:

R77, L79 and D81. However, when visually inspecting these equivalents in a structural alignment (PDB:2WLL (Clarke et al. 2010) and PDB:3SYA (Whorton and MacKinnon 2011)), it is obvious that only KirBac R47 and V51 have positional equivalents in mmKir3.2, respectively L79 and I82, while KirBac1.1 R49 is aligned in-between T80 and D81, and only T80 displays a similar orientation of its sidechain. These residues in mmKir3.2 are among those that interact with the PIP_2 molecule via their backbones (and OH for T80), as observed in the crystallographic model PDB:3SYA. Thus, this reference did not provide me directly with new insight of the involvement of the slide helix into the activation of the Kir, but the idea that the slide helix is implicated in the process intrigued me. Moreover, the same authors showed that when decy-MTS was attached at position L56, corresponding to mmKir3.2 V87, the channel was almost completely silenced, this result showed that the three-turn slide helix is involved in both activation and deactivation of the cytosolic and the HBC gate of KirBac1.1.

In the meantime, I examined the amino acid sequence and the electrostatic properties of the slide helix of Kir3. My attention was retained by the glycine-serine insertion in Kir3.1 (G61 and S62), which is aligned with R73 in mmKir3.2 and with Q68 in Kir3.4. This glycine insertion would create an extra step into the helix, thus in conjunction with the serine it potentially causes a hinge at that site of the slide helix (Ballesteros et al. 2000). This region of the protein also contains the signature of cholesterol interaction propensity, this observation is very interesting in line with the experimental data showing the positive modulation of Kir3 currents upon increase of the membrane cholesterol concentration (see section 2.9.2 for more details). I scanned the slide helix and found two CARC signatures {***(R/K)X*$_{1\text{-}5}$*(Y/F)X*$_{1\text{-}5}$*(L/V)***} (Baier, Fantini, and Barrantes 2011; Rosenhouse-Dantsker et al. 2013). The first motif was found in the range R73/L79 {**R**et**Y**ry**L**}, and the second in the range L77/L89 {**R**yltdi**F**tt**LV**d**L**}. The hydrophobic residues of both motifs were oriented towards the lower leaflet of the membrane and the starting arginine was tangent to the membrane in the crystallographic model PDB:3SYA. Interestingly, the first of these cholesterol binding motifs partially aligns with the region of KirBac1.1 which upon decyl-MTS modification caused activation of the channel, as reported by

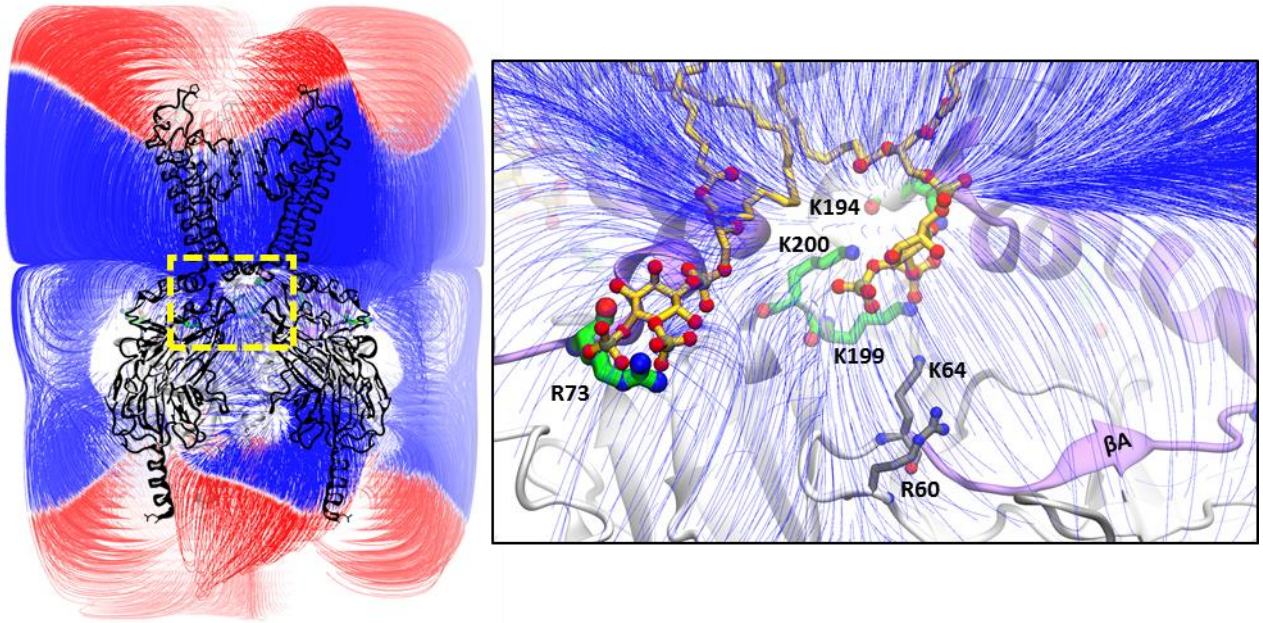

Figure 23 : Electrostatic contribution of mouse Kir3.2 to an all-atom simulation box and location of a putative secondary PIP_2 interaction site on the channel. The electric field lines derived from the average electrostatic potential generated by mmKir3.2 during 20 ns of constrained simulation are shown in the left panel. The potential threshold used for the graphic was ±51.4 mV. The right panel shows a zoom into the boxed region in the left panel. The location of the primary PIP_2 binding site corresponds to the one shown in ***Error! Reference source not found.****. The putative secondary binding site is represented by R73 and involves hydrogen-bonding interactions with other neighboring residues in the range N71 to R77. The slide helix and the preceding βA strand are colored in purple, the backbone of two PIP_2 molecules is colored in yellow and all heavy not carbon atoms are highlighted by colored spheres.*

Enkvetchakul in 2007 (Enkvetchakul et al. 2007), while the second region aligns with the region silencing KirBac1.1 upon modification. As a matter of speculation, if these sites in Kir3.2 are functional, it is possible that upon binding to the first site, cholesterol activates the channel, and then diffuses to the second more buried site where it takes part in an inhibitory mechanism.

This speculation put aside, the fact that there are multiple sequence characteristics in the side helix further increased my interest for this region. Next, I turned my attention to the electrostatics of this region. Figure 23 shows the field-lines profile of the electrostatic contribution of the channel into the simulation box. A potential of ±50 mV extends several nanometers around the channel. When focusing on the region of the protein with the highest emergence of field-lines, one can identify the PIP_2 binding site involving the cluster of positive residues of the TM1/TM2/C-linker. Further on I will term this PIP2 binding site "site 1" and a PIP2 molecule bound to it "$_{(Site\ 1)}PIP_2$". The residue K64 in the N_{ter} interacting with the $_{(site\ 1)}PIP_2$ seen in all available crystallographic models was seemingly in line with the field-lines emerging from the TM2. Interestingly, there was a swirl of field-lines emerging from R73 in the slide helix joining the positive potential generated from the TM2. This observation was very intriguing given the recent identification of a secondary binding site for anionic lipids on the slide helix of Kir2.1 channel (S.-J. Lee et al. 2016). The K64 implicated in Kir2.1 is only two positions after R73 in mmKir3.2, but these two residues had opposite orientations in respect to the center of the pore. In Kir2.1 K64 was oriented towards the βC-βD loop, while R73 in mmKir3.2 was oriented in a radially opposed direction from the permeation pathway (Figure 23). Despite these differences, I hypothesized that R73 could interact with PIP_2 molecules while the latter diffuse in the inner leaflet, and thus in addition to the PIP_2 molecules bound to the C-linker ($_{(Site\ 1)}PIP_2$).

This hypothesis had two rational pillars. First, the concentration of PIP_2 in native membranes is about 2%, but the true concentration in the vicinity of Kir3 upon channels activation might be much higher. Second, in line with the work of Lee and colleagues (S.-J. Lee et al. 2016), I simulated POPG lipids in the vicinity of R73 which spontaneously interacted with the slide helix of mmKir3.2 (data not shown). Unfortunately, the interactions were rather weak because most of the time POPG readily defused from the protein after 100 ns at most (data not shown). Nevertheless, these simulations showed the propensity of the region for interaction with anionic lipids. My further modifications of the simulation box were greatly encouraged by the results published by Stansfeld and coworkers, who clearly identified interactions between R50 of Kir6.2 (equivalent to R73 in mmkir3.2) and PIP_2 by a multiscale simulation protocol allowing the diffusion of PIP_2 towards the channel (Stansfeld et al. 2009). The pending questions then remained, what would be the stability of such additional interactions with R73, given that $_{(Site\ 1)}PIP_2$ should be in place, and what would be the effect of the additional interaction on the dynamics of the channel. Hereafter, the PIP_2 molecule modeled next to R73 will be termed "$_{(Site\ 3)}PIP_2$", and the R73 referred to as PIP_2 binding site will be termed "Site 3". The "Site 2" was termed to refer to residue R60 interacting with PIP_2. Indeed, this residue was observed to interact with PIP2 withdrawn from Site 1, as explained in the previous subsection and I decided to refer to it as to a separate PIP_2 binding site (see paragraph 5.2.1).

The simulation protocol is identical to the one already explained in section 5.4, except for the additional constraints between each of the four couples of $_{(Site\ 3)}PIP_2$ and the Cζ of R73 using the same parameters as those for $_{(Site\ 1)}PIP_2$ and Nζ of K194. Thus, in the beginning of the simulation the heavy atoms of the protein backbone were constrained by gradually decreasing harmonic potential (2 to 0 kcal/mol/Å) during 45 ns. The PROH and Na^+ ligands were constrained towards the centers of their binding sites by weak flat-bottom distance based harmonic potentials until 800 ns of simulation after equilibration. The $_{(Site\ 1)}PIP_2$ was constrained towards K194 (Site 1) for 600 ns, and after it was constrained towards R60 (Site 2) for 200 ns. The same constraints acted on $_{(Site\ 3)}PIP_2$ and R73 (Site 3) for 800 ns. After 800 ns of simulation in *Simulation VI*, all distance constraints on the PIP_2, PrOH and Na^+ were switched-off, and the simulation was continued for an additional 200 ns.

5.5.2 *Conformational changes towards open pore and associated increased K^+ transport*

In both simulations, the mmKir3.2 was permeant for K^+ in the inward direction once the membrane voltage was simulated at -700 mV (Figure 24). Interestingly, in *Simulation V*, a single Na^+ permeation in between 440 and 700 ns was observed. This permeation appears as a "gap" in the ion binding in panel A of Figure 24. After the Na^+ crossed the selectivity filter, it appears that the K^+ was able to permeate more thoroughly through the filter.

In *Simulation VI*, the K^+ crossed the selectivity filter in less ordered manner in respect to the K^+ binding configurations observed in the simulations presented until now. The lack of a strong pattern could be attributed to the enlarged conformation of the filter which appeared after 400 ns of simulation (Annex *Simulation VI*:2). As already discussed, the enlargement of the carbonyl cage around the permeating K^+ ions led to the decrease of the binding affinity of K^+ for each particular coordination site inside the filter. Thus, the time of residence of K^+ inside the filter was reduced in comparison to the other simulations shown in the previous subsections of the chapter – as numerous inward K^+ permeation took place in a period of 400 ns (Figure 24D).

In both simulations the HBC gate in the TMV adopted a more extended conformation than the starting one (Annex *Simulation V*:2, Annex *Simulation VI*:2). The enlargement in *Simulation V* occurred after the constraints on $_{(Site\ 1)}PIP_2$ were turned towards R60, while the G-loop gate simultaneously decreased its diameter. By inspecting the hydrogen-bonding between PIP_2 molecules and the channel, one can identify the correlation between the increase in the number of hydrogen bonds between PIP_2 and R60 and the increase in the opening of the HBC gate, while at the same time the number of hydrogen bonds counted on residues in the TM1, TM2 and the C-linker decreased (Annex *Simulation V*:10). As usual, the events in all subunits were not symmetric and this could be the reason explaining the observed rapid fluctuation of the HBC radius determined by the apex of the sidechains of F192 residues, despite the general enlargement measured at the Cα of F192 (Figure 24A). The same events were observed in *Simulation VI* (Annex *Simulation VI*:10). Nevertheless, the HBC gate remained larger in this simulation even before switching the constraints on $_{(Site\ 1)}PIP_2$ to be oriented towards R60. Compared to *Simulation V*, in this simulation one can observe more hydrogen bond counts at the TM2 and the C-linker, and less on the slide helix (Annex *Simulation VI*:10). It appears that the stabilization of the slide helix via $_{(Site\ 3)}PIP_2$ actually reduced the rapid fluctuations of the HBC gate. Without being the primary factor for the increase of the gate's radius, in most cases the higher hydrogen-bond counts on the slide helix are aligned in time with higher HBC gate radius. The primary factor for the increased HBC opening appeared to be the $_{(Site\ 1)}PIP_2$ interactions with TM1,TM2 and the C-linker, this observation is in line with the already established understanding of the PIP_2-$_{(Site\ 1)}$Kir interactions (Diomedes E. Logothetis et al. 2015; Lacin et al. 2017).

An interesting event was observed in *Simulation VI*, it started with changes in the backbone dihedral angle of residues G156 and G158 in almost all subunits of the tetramer after 420 ns of unrestrained simulation. In consequence, the sidechain of Y157 in subunit P2 rotated from -60° to 60° and engaged into a hydrogen-bond with E150 of the same subunit. The rotation of Y157 deprived the middle of the selectivity filter of subunit P2 from its inter-subunit interaction with the pore helix of the following subunit (P4). After approximately 50 ns, another change of the conformation of Y156 was observed, from 60° to -180°, which rotated its phenyl ring towards the extracellular bulk. This series of conformational changes occurred as the N-terminal side pore helix of subunit P2 was displaced by rigid body motion towards TM1 and TM2, and the angle of the helix relative to the plane of the membrane decreased. The motion of the pore helix constrained the selectivity filter motive of the subunit to move upwards, eventually displacing backbone carbonyls by the height of one K^+ coordination site towards the extracellular bulk: S4 of subunit P2 was aligned with S3 of the other subunits. The change in the position of Y157 was particularly marked. The sidechain of this residue approximately occupied the location where Y159 was initially, and interestingly, the major part of the hydrogen-bonding network behind the selectivity filter in subunit P2 was preserved except for a P2-P4 interaction involving P2:R160 and P4:I162 (interaction code 6, 22 in Annex *Simulation VI*:7), which

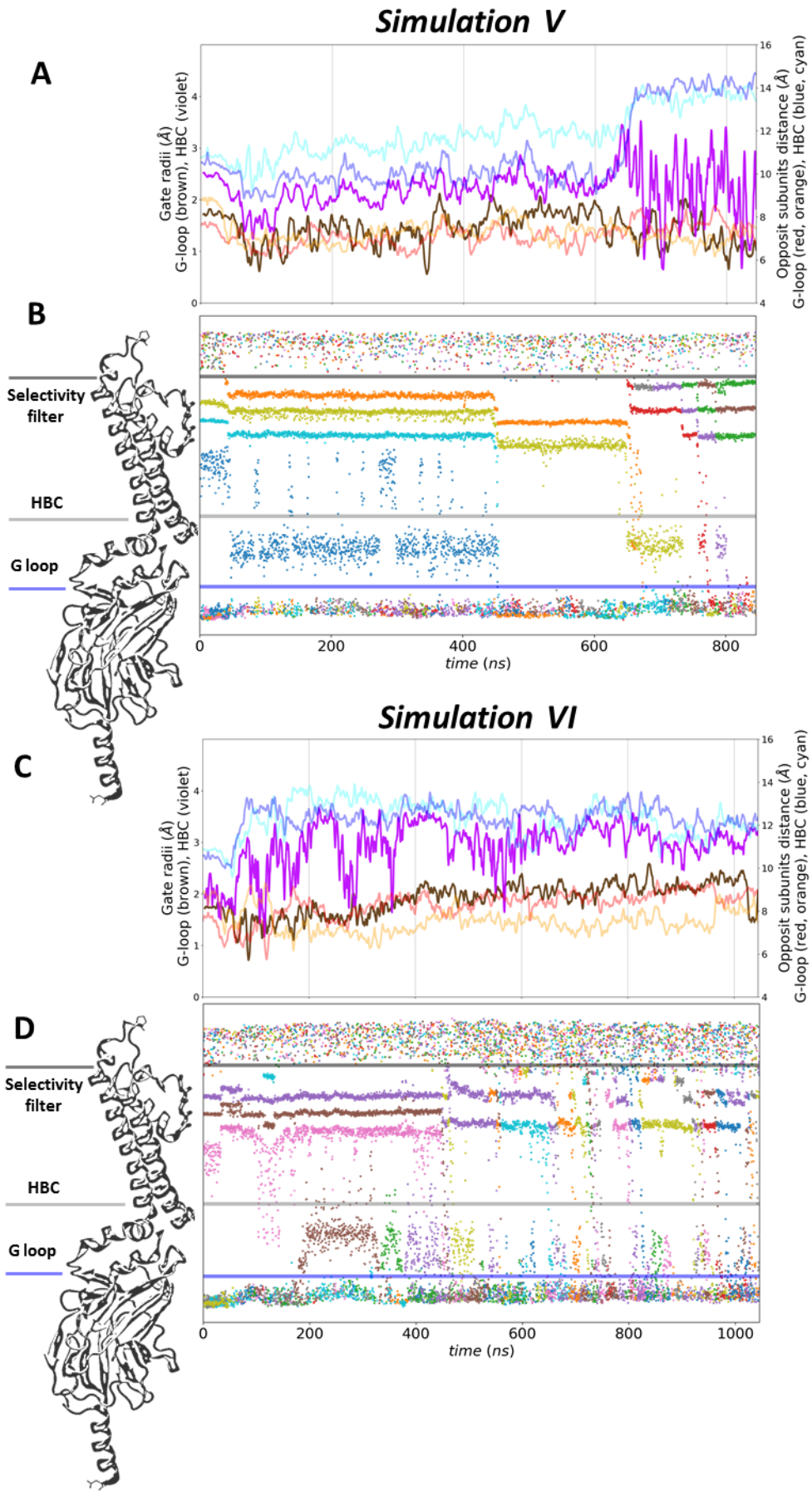

Figure 24: The pre-open Kir3.2 in presence of PIP_2 modeled into the crystallographic binding site and along the slide helix, adopted similar conformations of the TM vestibule during molecular dynamics simulation of two atomic-replica systems: Simulation V panel A and B; Simulation VI panel C and D. Timeseries are plotted for snapshots taken every 0.4 ns and plotted as convoluted average using sliding window of 20 ns and a symmetric power law function x^n (n=±6), the first 45 ns corresponds to the equilibration of the simulated system. (A, C) Timeseries of the opening of the G-loop gate (brown) and the HBC gate (magenta) are plotted on the left vertical axis. The distance between pairs of atoms from diametrically opposite subunits is plotted on the right vertical axis: G318:0 carboxyl oxygen of the mainchain (red and orange); the geometrical center of the phenyl ring of F192 (blue and cyan). (B, D) Timeseries showing K^+ movement across a section of the pore extending between 10 Å below the Cα of residue M313 in the G loop, and 10 Å above the carbonyl oxygen of residue G158 in the selectivity filter. K^+ positions along the permeation pathway are plotted on the left vertical axis. Each individual ion is colored with the same color along the entire timeseries, different ions however, can share the same colors. Watermark of part of the channel is shown for easier localization of the gates in the plot.

was exchanged with the interaction between P2:R160 and P4:D164 (interaction code 7, 23 in Annex *Simulation VI*:7). Despite the visually altered conformation of the filter, the K^+ permeation became less impeded, while preserving the single file nature of the permeation. In fact, the remaining three subunits still provided coordination sites with strong binding affinity for the K^+, which accounts for the observed stabilization of K^+ along the z-axis in the selectivity filter in panel D of Figure 24 after 450 ns of simulation. The particular enlargement of the selectivity filter can also be observed in the distance diagrams in Annex *Simulation VI*:8. The average of the correlation matrix based on these distances shows that the contacts involving E152 and the distance between the carbonyls of I155 are positively correlated across the tetramer, suggesting that the dissymmetric conformation of the filter was made possible thanks to the enlargement in the TM bundle, due to its initial enlargement which preceded the Y157 rotation by approximately 300 ns.

To further describe the effect of this conformational change of the selectivity filter I will focus on the electrostatic potential measure along the pore (Annex Simulation VI:10). One should notice the profound effect on the electrostatic potential at the level of the filter. At simulation time 1 µs the positive barrier inside the filter in respect to the extracellular entrance is about 100 mV. This magnitude of the potential is very close to E_K in physiological conditions. In comparison to the previous setup where few K^+ permeations were observed (Figure 19D and Annex *Simulation IV*:10) and where the potential difference inside the filter and the extracellular entrance was nearly 400 mV, the situation in *Simulation VI* is markedly different. This difference is due to the number of K^+ found in both simulations inside the selectivity filter, and this number of K^+ is dictated by the binding affinity of K^+ for the coordination sites which is directly influenced by the conformation of the filter itself.

The change of torsion angles of the glycine residues in the filter of the potassium channel was observed in MD simulations by other groups. Since, it has become common practice to constrain the torsion angles of the G156 and G158 equivalent residues (Jensen et al. 2010). These constraints are applied in order to prevent the filter to experience C-type inactivation events. However, the situation that I described in *Simulation VI* was very different because after the torsion angles of the glycine in the filter changed, the filter became overall more conductive. Thus, with the reserve that the observed conformation change is not an artifact, the data shown here suggests the existence of a fluctuating highly conductive state caught by *Simulation VI*. Significantly, this was not the only time this exact conformational change occurred in simulations I made with similar setup conditions. In the following subsections, I will present another simulation where this conformation was obtained, but in some other simulations (not part of the manuscript) where K^+ permeations were obtained, the displacement of one of the filter motives was also observed (data not shown due to differences in the atomic constituents of the simulation box: mmKir3.2 + $_{(Site\ 1)}PIP_2$ + $_{(Site\ 3)}$POPG + MPD + Na^+).

The additional PIP_2 near R73 in this set of simulations allowed the pore to remain conductive in both simulated systems. The general impression of this experiment is that the addition of PIP_2 stabilized the protein in open conformation.

5.6 MD Kir3.2 in presence of PIP_2 interacting with three protein sites, propanol and Na^+

5.6.1 Modification of the simulation protocol: saturation of all PIP_2 interaction sites

As I have already noticed during the simulation where the channel was in presence of unrestrained $_{(Site\ 1)}PIP_2$, I observed that, the PIP_2 switched partners to interact with residues K64/R60 in the N_{ter} (Site 2). Although, by observation of the trajectories it appeared that this change of interacting partners required only a minor displacement of the PIP_2, I had the impression that it was concomitant with conformational changes in the nearby element of the G-loop and the HBC gates. I tried to correlate the protein-PIP_2 distances or protein-PIP_2 hydrogen-bonding with the minimal radii

of the gates or the distances between diagonally opposed elements of the gates, but unfortunately, I was not able to detect unambiguous (cross-)correlation signals. Nevertheless, I decided to test the interaction of PIP_2 on Site 2, by "saturating" this site by adding PIP_2 molecules near each one of the four R60 of the mmKir3.2 tetramer.

Interestingly, almost all PIP_2 molecules interacted with the protein partners where I modeled them, and thus for the entire length of the simulation without any constraints between the PIP_2 and the protein. In *Simulation VIII*, the $_{(Site\ 3)}PIP_2$ modeled near R73 of subunit P3, remained near this residue only during the equilibration phase of the protocol. After approximately 70 ns of simulation this $_{(Site\ 3)}PIP_2$ diffused slightly along the slide helix and for the rest of the simulation it remained in hydrogen-bonding interaction with R77 at the same subunit – P3. In *Simulation VII* on the other hand, one of the $_{(Site\ 3)}PIP_2$ diffused from the slide helix of subunit P1 after approximately 700 ns of unrestrained simulation. The average ligand density during discrete time laps is reported in Annex *Simulation VII*:3 and Annex *Simulation VIII*:3, and the timeseries of the PIP2-protein hydrogen-bonding contacts in *Simulation VII*:9/10 and Annex *Simulation VIII*:9/10. These results suggest, first that the PIP_2 is a better partner that the POPG for the R73, and second that the vicinity of the mmKir3.2 is favorable for persistence of additional PIP_2 molecules apart those observed in the crystallographic models – Site 1.

5.6.2 Overview of the K^+ transport along the pore

The observed K^+ permeations and the measure of the gate bottlenecks are shown in Figure 25 for two atomic replicas: *Simulation VII* and *Simulation VIII*. In both simulations the channel was maintained with an open HBC gate, while the G-loop gates were observed in alternative conformations (Annex *Simulation VII*:2, and Annex *Simulation VIII*:2). While the conformations of the selectivity filter and the TM bundle were similar to those already detailed for simulated permeating systems with a lower amount of PIP_2 (see section 5.4 and 5.5), in both systems the channel allowed for a similar rate of inward permeations of K^+ across the selectivity filter.

In particular, during the last 100 ns, the K^+ ion permeating the selectivity filter were not stabilized into particular coordination sites as previously during this simulation (Figure 25B). The cause for this was the same displacement of the IGYG motif in one of the subunits towards the TM2 of the adjacent subunit as mentioned in the previous section (Section 5.5). In the region of the selectivity filter, the cascade of events started with the displacement of the TM2 of subunit P3, this displacement occurring after 500 ns of simulation can be observed through the distance between P1:I155:CD and P3:L173:CG in panel D of Annex Simulation VII-8. Shortly after, the backbone torsion angles of residues I155, G156 and Y157 began fluctuating, in particular these of G156 in all subunits which deviated from the starting conformation (Annex Simulation VII-6). As a consequence, the carbonyl oxygen of I155 in three subunits (and occasionally in all subunits) could be observed in the "flipped" state associated with lowered K^+ binding affinity for the S2-S3 sites. At time 760 ns, the IGYG motive of subunit P1 very rapidly approached the TM2 of subunit P3 which remained located further apart from the center of the permeation pathway in respect to the starting conformation. Thus, the opening of the selectivity filter was increased and at the same time, the distance between P1:I155:CD and P3:L173:CG came back to its initial values. This conformational change allowed the sidechain of Y157 to rotate and to be further oriented in the outward water bulk. The evolution of bend-profiles of secondary structures of the channel in *Simulation VII*, suggested that the event causing the extracellular side of TM2 to be displaced at time 500 ns, was the unbending of the TM2 helix at residues 182 to 185 in response to the conformational change of the slide helix in the same subunit (panels A and D in Annex Simulation VII-4). Interestingly, three out of four E152 were observed in the rotamer state χ_1 = -60° and χ_2 = -60° (Annex Simulation VII-5), also there were strong instantaneous correlations between the distances measured between residues in the region of the selectivity filter (Annex Simulation VII-8). Taken together once again, these observations point to the allosteric link between the cytoplasmic domain and the selectivity filter, which is operated through the TM bundle of the channel, with positive correlation once the HBC gate is in the open conformation.

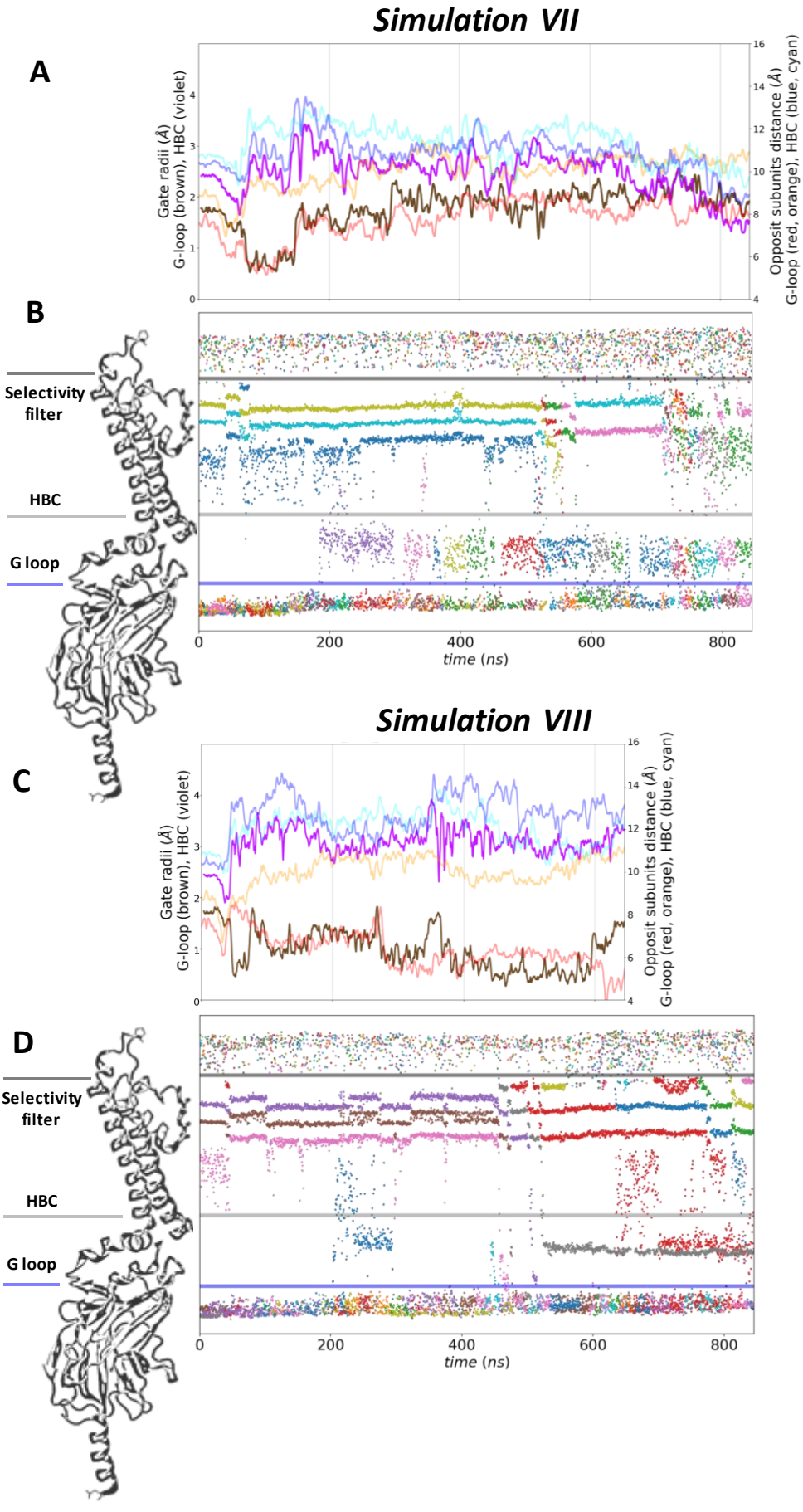

Figure 25: The pre-open Kir3.2 in presence of PIP_2 modeled into the crystallographic binding site, near the N_{ter} and along the slide helix, adopted similar conformations of the TM vestibule during molecular dynamic simulation of two atomic-replica systems: Simulation VII panel A and B; Simulation VIII panel C and D. Timeseries are plotted for snapshots taken every 0.4 ns and plotted as convoluted average using a sliding window of 20 ns and a symmetric power law function x^n (n=±6), the first 45 ns corresponds to the equilibration of the simulated system. (A, C) Timeseries of the opening of the G-loop gate (brown) and the HBC gate (magenta) are plotted on the left vertical axis. The distance between pairs of atoms from diametrically opposite subunits is plotted on the right vertical axis: G318:0 carbonyl oxygen of the mainchain (red and orange); the geometrical center of the phenyl ring of F192 (blue and cyan). (B, D) Timeseries showing K^+ movement across a section of the pore extending between 10 Å below the Cα of residue M313 in the G loop, and 10 Å above the carbonyl oxygen of residue G158 in the selectivity filter. K^+ positions along the permeation pathway are plotted on the left vertical axis. Each individual ion is colored with the same color along the entire timeseries, different ions however, can share the same color. Watermark of part of the channel is shown for easier localization of the gates in the plot.

The main conformational difference along the permeation pathway between both systems was observed at the G loop. Therefore, the cytosolic gate rapidly adopted a two-fold symmetric conformation in *Simulation VIII* and as a result, outward K^+ movements were prevented. However, this conformational change appeared without any significant impeding effect on the inward K^+ permeation. Furthermore, an interesting event was observed near the cytosolic gate in the second half of *Simulation VIII*. In panel D, one can observe that in the second half of the simulation, one K^+ was stabilized in between the HBC and the G-loop gates.

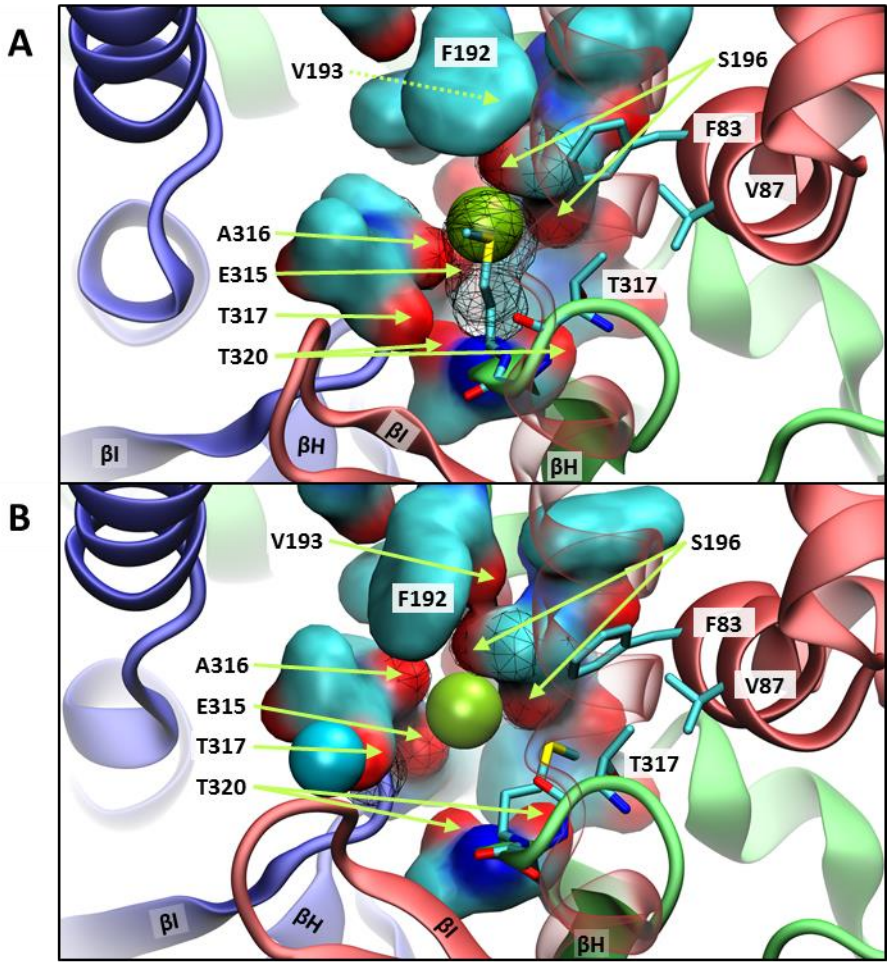

Figure 26: Pocket between adjacent βH-βI loops of mouse Kir3.2 with high K^+ affinity observed during molecular dynamics simulation. Snapshots are taken from the same simulation where one K^+ is stabilized by numerous carbonyl oxygens exposed once the TM bundle allows the permeable conformation of the HBC gate. The residues providing coordination to the K^+ ion (green) are represented as solid vdW surfaces, atoms found instantaneously within 4.5 Å of the K^+ ion are emphasized by a mesh (black) and all other carbonyls are indicated by arrows (green). A set of residues involved in hydrophobic contacts between the slide helix, the βI-βH loop and the F192 are represented as sticks. (A) Snapshot at time 607 ns, when the K^+ ion is blocked inside the pocket by the sidechain of M319. (B) Snapshot at time 845 ns, the pocket is open towards the TM vestibule.

Figure 26 shows the region where the K^+ remained stabilized at the interface of two subunits, with elements of the G-loop gate, the TM bundle and the slide helix providing a hollow volume abundantly lined with carbonyl oxygens. The figure shows two consecutive situations where the K^+ occupies the hollow volume behind the βH-βI loop of subunit P4 (green). In panel A the ion is isolated from the rest of the TMV by the side chain of M319, while in panel B the side chain of M319 is retreated away from the permeation pathway, thus providing continuous waterfilled volume to the trapped K^+. The motion of M319 is allowed by a change of the bending of βH-βI loop at the level of residues 318 to 321 (Annex *Simulation VIII*:4G), and as discussed later, the event causing this motion was the concomitant marked conformational change of the slide helix of subunit P4 (Annex

Simulation VIII:4A). Such stabilization of K^+ were often obtained in the MD trajectories I produced, seemingly a required conditions where that the G-loop gate allowed for inward K^+ transport and that the gate had a pronounced rhombic opening shape (data not shown in this report because obtained with different ligand constituents of the simulation box, i.e. MPD alcohol instead of PrOH and POPG constrained towards R73 instead of PIP_2).

5.6.3 Conformational changes which affected the gates of the mmKir3.2

5.6.3.1 Allosteric transmission of the conformational changes of the slide helix to the G-loop gate

The conformational change causing the expansion of the G-loop gate between subunits P3/P4 in *Simulation VIII* can be observed in Figure 27, all observations are referred to subunit P4. In panel A is depicted the overall displacement of the slide helix towards the inner membrane leaflet in respect to the starting structure. Also, it can be seen that the TM1 at its base was displaced to the right, which was the consequence of the preserved folding of the slide helix when it moved upwards. In panels A and D is also best seen the lateral displacement (towards the slide helix of the green subunit) of the C_{ter} of the TM2 helix and the proline kink of the C linker. In panels C and D are listed the residues which preserved the contact between the cytosolic ends of the TM1 and the TM2, by interlacing their

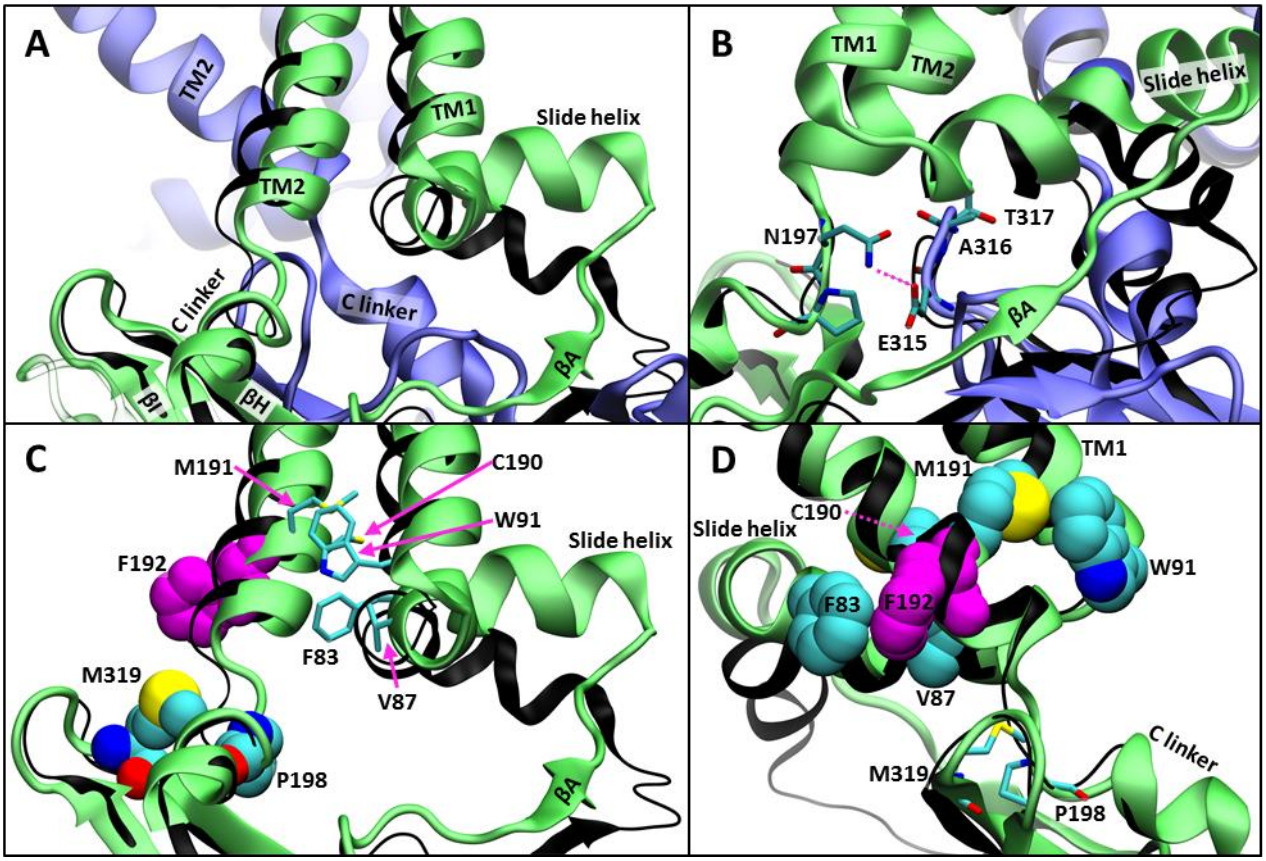

Figure 27: The blotting of the slide helix to the inner membrane layer allows the opening of the βH-Iβ loop in the same subunit mouse Kir3.2 during molecular dynamics simulation. Panels represent the conformation of the βH-Iβ loop, the TM1/TM2 and the slide helix in one subunit (P4 as green cartoon) obtained after 845 ns. The starting conformation of the subunit is represented with thinner cartoon trace (black). The starting and the final conformations of the pore were aligned by the backbone of the selectivity filter and the TM bundle, involving all four subunits. (A) Lateral view on the slide helix showing its 30° upward hinge-like motion. The represented region of the tetramer is the same as the one in the channels miniature in Figure 20. Several secondary structures are labeled to ease the interpretation of the rotated subunits in the other panels. (B) An interaction not present in any of the mmKir3.2 crystal structures appeared between the TM2 and the βH-Iβ loop of the anti-clockwise subunit. (C) Hydrophobic residues in the TM1 and the TM2 which are involved in the transduction of the displacement of TM1 to TM2 are represented as sticks. The gate residue F192 (magenta) is located at the same level as the hydrophobic residues linking TM1 and TM2. The G-loop gate residue M319 in subunit P4 and the allosterically-associated P198 are represented as vdW spheres (atom colors). (D) The residues listed in panel C are shown in a 90° clockwise rotation of subunit P4. Note the hydrophobic interactions between F83/C190/V87/M191/W91.

sidechains in hydrophobic contacts. As a result of the concerted TM1/TM2 displacement and the twist of the proline kink away from the G-loop gate, the sidechain of M319 appeared to rotate in order to occupy the volume where the P198 was located previously. The twist of the proline kink also created a novel contact between 197 and the βH-βI loop of the counterclockwise adjacent subunit (P2). This interaction is novel in respect to the published structures of mmKir3.2. The interaction P4:Q197-P2:E315 shown in panel B is representative of the rhombic opened G-loop gate, i.e. when the gate was extended at subunit P4, it required the proline kink of the same subunit to be displaced backwards from the gate, and at the same time the proline kink approached the βH-βI loop of the previous subunit. This conformation is the hallmark of an inter-subunit cooperativity, where the opening of the gate at one subunit increases the interactions of its controlling elements (C-linker including the proline kink) with the gate elements of the previous subunit. In fact, I observed this interaction in other simulations and in particular in *Simulation VII*, where Q197 contacted the carbonyl of A316 instead of E315. The reason for these two different partners of Q197 is alternative conformations of the gate between the rhombic vs. the four-fold symmetric opening of the G-loop gate. The Q197 contacted A316 when the gate was four-fold symmetric because the preceding βH-βI loop was also displaced away from the center of the pore, thus the E315 was out of reach of N198 and the carbonyl of A316 was available for the H-bonding interaction instead.

The involvement of Q197 in the interaction with the βH-βI loop of the previous subunit is of great interest because the equivalent of this residue in Kir1 and Kir2 channels is a lysine or an arginine. The equivalent-position residue to Q197 in the crystallographic models of Kir2.2 is R186, which interacted with PIP_2 (PDB:3SPG) and the R186A mutation decreased the apparent affinity for PIP_2 of the channel (Hansen, Tao, and MacKinnon 2011). The Kir2 channels are constitutively open channels in contrast to Kir3.2 channels. Thus, the previous paragraph exposes a putative new role for Q186 which no longer provides high PIP_2 affinity to the mmKir3.2, but rather helps to stabilize the apex of the G loop. Hence when the channel has bound PIP_2 at the TM2/C linker site (Site 1) and the G-loop gate is in extended conformation, Q186 can interact with the backbone of A316 thus stabilizing the open G-loop gate. On the other hand, when the G-loop gate is constricted, Q186 can interact with the side chain of E315 thus preventing the latter to establish a salt bridge with R324. In most cases, I observed the E315/R324 salt bridge when the G-loop gate was permeant, thus I suppose that the substitution of Q186 as a partner for E315 increases the stability of the constricted conformation of the G-loop gate.

5.6.3.2 Modulation of the G-loop gate affinity for K^+

Another aspect of the observed conformational changes involving the G-loop gate was caught in *Simulation VIII*. It concerns the increase of the number of oxygen atoms lining the lumen of the G-loop gate, the associated local changes of the electrostatic potential along the permeation pathway, and the influence these factors had on K^+ transport. In Figure 28 is shown the comparison between the atoms lining the lumen of the G-loop gate in different crystallographic models of Kir channels and those of mmKir3.2 obtained by MD simulation when the channel was modeled in presence of different amounts of ligands. The most extended conformation of the G-loop gate among the presented conformations of wild-type Kir channels is the one in panel D. Surprisingly, despite the absence of PIP2 in the experiment, the apo-Kir2.2 had the most extended G-loop gate and its HBC gate was not in a completely closed state, as was the case with the PPA-bound Kir2.2 (Hansen, Tao, and MacKinnon 2011). In this most extended G-loop gate conformation, it is easy to notice that the majority of hydrogen bond capable atoms lining the opening of the gate were oxygens, which was not the case for either of the mmKir3.2 crystallographic models. A similar conformation rich on water-exposed oxygens was obtained in *Simulation VIII* (panel B), where despite the two-fold symmetric opening of the G-loop gate, it appears that the represented environment was more prone to accommodate K^+ ions than the final conformation obtained in the apo-mmKir3.2 simulation shown in panel F. The conformation from panel F was more similar to that of the crystallographic models PDB:4KFM and PDB:3SYA. The conformation presented in panel D was somehow intermediate

between those of panels B and F, with major conformational changes of the HBC gate and yet a not completely constricted G-loop gate, where several oxygens atoms were oriented towards the center of the pore.

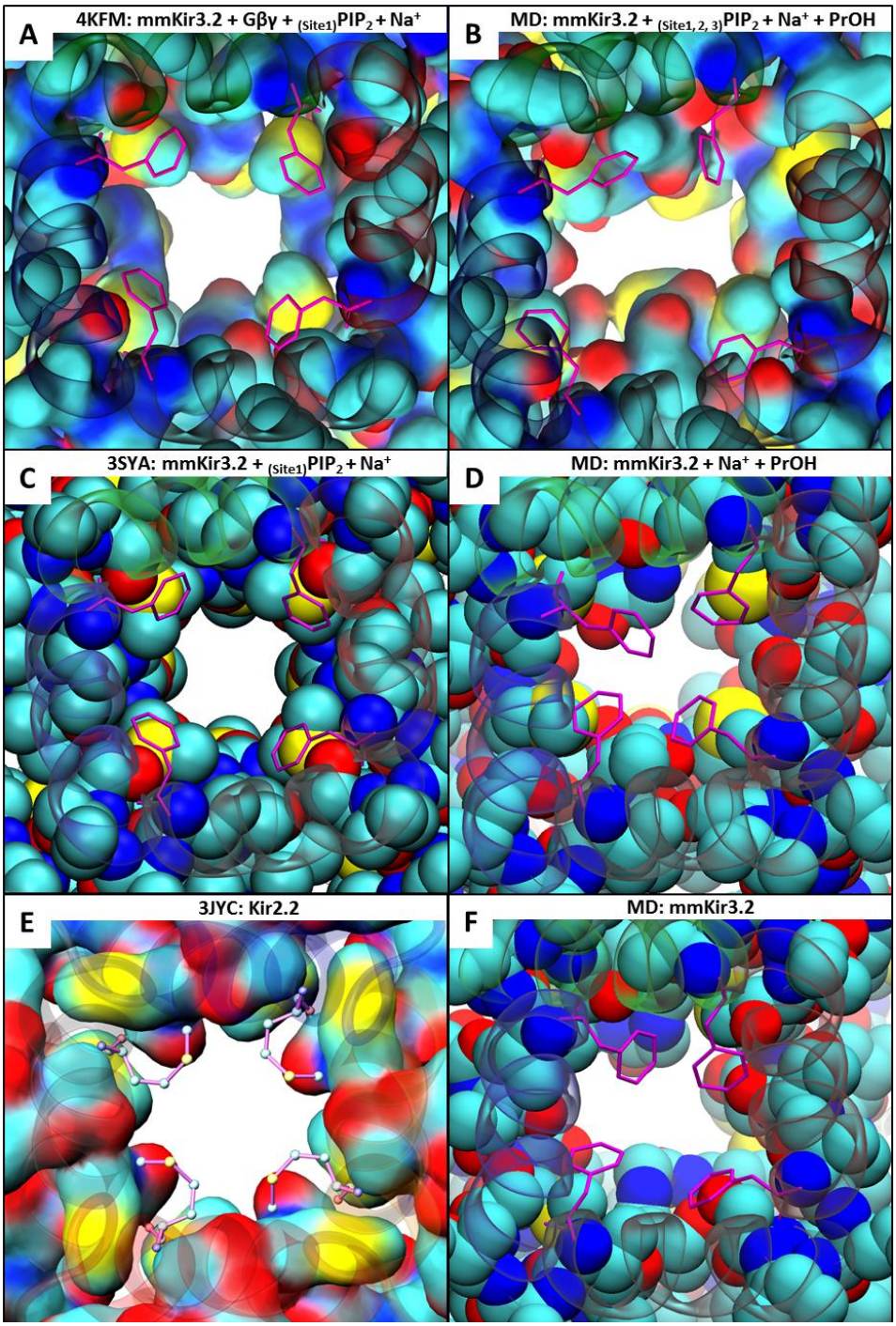

Figure 28: Change of the predominant atom types lining the lumen of the G-loop gate in Kir channels as the gate adopts more extended conformations during molecular dynamics simulation and from observation of crystallographic models. Conformations are taken from crystallographic models of Kir3.2, Kir2.2 (left column) and from snapshots at the last timestep of MD trajectories (right column). The non-hydrogen atoms of the residues of the βH-βI loops of the tetramer are represented either as vdW or surface volumes, viewed from the extracellular side. Except for the HBC gating residues represented as magenta sticks, the colors of all atoms are set to the standard coloring scheme. (A) From crystallographic model of mmKir3.2 in presence of Gβγ, C_8-PIP_2 and Na^+, PDB:4KFM. (B) At timestep 845 ns of Simulation VIII. (C) From crystallographic model of mmKir3.2 in presence of C_8-PIP_2 and Na^+, PDB:3SYA. (D) At timestep 845 ns of Simulation I. (E) From crystallographic model of apo Kir2.2 channels, PDB:3JYC. (D) At timestep 845 ns from simulation of mmKir3.2 in absence of any ligands (see section 5.7).

The set of conformations presented in Figure 28 suggests that upon relaxation of the G-loop gate, the protein-water interface at the G-loop gate got abundant with oxygen atoms which could decrease the local electrostatic potential and thus favor the visiting of this region of the pore by positively charged species such as K^+ ions and probably the rectification factors Mg^{2+} and polyamines. Moreover, this oxygen exposure was correlated with the presence of K^+ in the volume between the HBC and the G-loop gates (the lower transmembrane vestibule or LTMV). Thus, the most reasonable explanation for it should be that upon approaching of K^+ towards the βH-βI loops, the K^+ recruited oxygens for its coordination from its protein surroundings. A suggestion which can be deduced from the correlation between the increase of the electrostatic potential at the G-loop gate ($\boldsymbol{Z_{axis}}$: -20 to -30 Å in figure Annex *Simulation VII*:10) and the number of K^+ seen in the LTMV (Figure 25B). Therefore, suggesting that the local increase of the potential along the pore is generated by the presence of the K^+ and that the protein will respond in return. This could lead to the conclusion that the situation in panels B and D of Figure 28 could only reflect the presence of K^+ in the LTMV, rather than an induced open state conformational change adopted by the G-loop gate. Such a proposition appears bizarre because one would expect that the pore itself recruited the K^+ by somehow providing a suitable environment for the latter. In fact, this intuitive expectation continues to be true because in order for a K^+ to get inside the vestibule, the gates have to be open, and only then the protein could further provide accommodations to facilitate the transport of the K^+ ion. The factor which explains the abundance of oxygen in the G-loop gate among the conformations in Figure 28 taken from the simulations of mmKir3.2, is the presence of activator ligands interacting with the CTCD of the channel. While the absence of PIP_2 in *Simulation I* (panel D) caused the constriction of the HBC gate whose motion seemed to be accompanied by the sidechains of M319, the oxygen-reach profile remained visible in the pore below M319. On the other hand, the further K^+ unfavorable LTMV is depicted in panel F, where the G-loop gate was lined mostly by nitrogen atoms when the channel was simulated in absence of the intracellular ligands.

The hypothesis of an oxygen reach interface of the G-loop gate is strengthened by the crystallographic model of apo-Kir2.2 (PDB:3JYC) shown in panel E. There the G-loop gate was open with the 11.86 Å distance between carbonyl oxygens of A307, and represented the most oxygen abundant protein-water interface of the G-loop gate among the presented conformations. Thus, it is highly likely that in presence of the intracellular ligands, the protein-water interface of the G-loop gate was modified from lined by mostly nitrogen to mostly oxygen water-exposed atoms, and thus in conjunction with the presence of nearby PIP_2 neutralizing the strong positive potential of the cluster of lysine residues of the C-linker. Finally, these two factors could be responsible for the replenishment of the LTMV with K^+ in the outward direction. In such a case, as the simulation presented until here suggests, large G-loop conformational changes are not needed for K^+ transport to take place. On the contrary, a more prominent problem then is the gating of this region. This role seems to be played by the sidechains of residues M313 and M319 providing hydrophobic gating properties of the G-loop gate. The rapid rotation of M313 and M319, in and out of the lumen of the permeation pathway required only minor changes of the backbone torsion angles of residues G312 and G318. The LTMV was closed from the other side by the HBC gating residues F192 which are primarily regulated by the PIP_2 bound to the C-linker, but as I have suggested, modulation exerted at the slide helix could also be allosterically transmitted to the HBC gate.

5.6.3.3 Backtracking the allosteric pathways from the G-loop gate to the surface of the cytoplasmic domain of the mmKir3.2

In line with the allosteric hydrophobic network linking the βL-βM-βA sheet and the βI-βH loop described in section 5.4.2, I will present here another branch of the allosteric network that I observed running from the CTCD surface towards the G-loop gate.

In Figure 29 are presented the contact network involving the N_{ter} observed in two alternative configurations while the entire CTCD of the channel entered a two-fold symmetric conformational state. These two images are representative of the conformational state of the diametrically opposed

subunits in the tetramer, and they correlate with the conformation of individual βH-βI loops in the G-loop gate. Here I will start with the description of the subunits P3 and P4, between which was measured the longest diagonal of the G-loop gate. In these subunits, the N_{ter} was predominantly interacting with βI-βJ turn and the C_{ter} of the transitional two-turn helix (residues I294 to E302) located between the βG and the βH strands on the surface of the CTCD. The nearly terminal R53 contacted residues S330, T329 and P301, E302, E303, both set of residues being located at the base

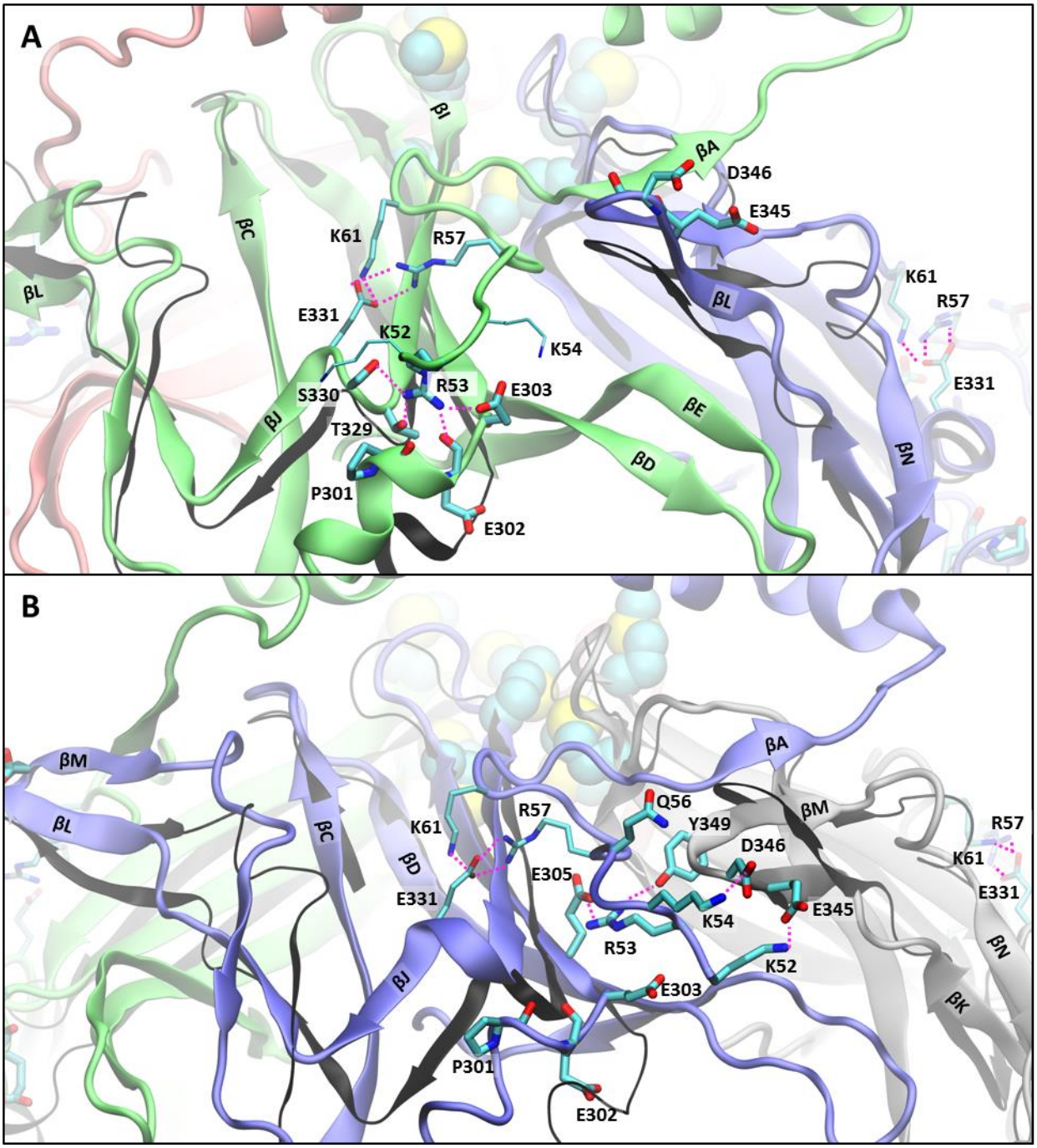

Figure 29: Modular organization of the inter-subunit interface in the βD-βE/βL-βM loops cleft-region of activated mouse Kir3.2 during molecular dynamics simulation. Snapshots are taken after 800 ns of Simulation VIII, and show the N_{ter} in two different configurations of interaction involving the cluster of basic residues K52-K61 and different parts of the CTCD. The actual conformation of the main chain is represented in colored cartoon, while selected parts of the CTCD at its initial coordinates is represented by thinner black cartoon. The N_{ter} basic residues establishing salt-bridge and hydrogen-bonding interactions and their all-times partners are represented by sticks, the methionine residues of the G-loop gate in the background are in vdW volume representation. The instantaneous hydrogen bond interactions are shown with dashed lines (magenta). (A) Focus on subunit P4. (B) Focus on subunit P2.

of the β-sheet containing the βH-βI loop. The observed displacement was counterclockwise and oriented away from the center of the CTCD. At this level of the subunits, the elements of the secondary structure were displaced by about the thickness of an α-helix, thus pulling on the base of the apex of the β-sheet containing the βH-βI loop and finally changing its apex conformation in a backward twist (Annex *Simulation VIII*:4G). While the most terminal K52 did not seem to have a hydrogen-bonding partner in the same subunit where R53 established the above described contacts – the K54 could interact with E303 and E305 or as shown in panel A, was oriented towards the intracellular aqueous bulk. In all these cases K52, R53 and K54 were sufficiently far from the βM-βM loop of the adjacent subunit, thus the N_{ter} did not restrained the βM-βM loop to move in the direction of the inner membrane leaflet. On the other hand, in subunits P1 and P2 (Figure 29B), the key difference was observed at residue R53 which rapidly stabilized to E305, thus causing K52 and K54 to approach the βM-βM loop. Once these three salt bridges were formed, the degree of freedom of the βM-βM loop was decreased and it was observed to adopt a position slightly lower than the starting one and markedly lower than the conformation obtained in subunits P3 and P4. Significantly, the residue important for function R57 in both configurations contact E331 in partnership with K61, which interaction is also observed in all crystallographic models of mmKir3.2. This interaction was also identified as mandatory for the function of other Kir6.2 (Cukras, Jeliazkova, and Nichols 2002). These two conformations of the N_{ter}, the adjacent βM-βM loop and the associated changes in the G-loop gate are in line with the accepted mechanism of activation of the CTCD of Kir3 channels (Diomedes E. Logothetis et al. 2015).

I tried to find a measure of distances in order to display an unambiguous correlation between the distances between opposite G-loop elements and associated N_{ter}/βL-βM loop distances, but I was not able to find a simple strong correlation which held for the entire length of the simulation (data not shown). This is an interesting result suggesting multivariate behavior which is difficult to be quantified given the unsymmetrical dynamics of the tetramer. What I was able to establish however, was that deflection (shocks) of the distance-timeseries were synchronized when measured within the G-loop gate, and within the surface of the CTCD including the N_{ter} and its contacting partners. This observation suggests that the shocks experienced by the contact network on surface of the CTCD were effectively transmitted to the G-loop gate, but the resulting effect on the G-loop gate is a combinatorial function of the interactions within the contact network at the time at which the shock occurred and the relaxation time laps between successive shocks. Clearly the dynamics of the CTCD of preactivated mmKir3.21 channel in presence of activator ligands resembles a neural network computing system, which solves the problem of the G-loop gate conformation – layer by layer, in a combinatorial progression in depth of the CTCD and until the cytosolic gate. I supposed that the chaotic nature of the molecular dynamics of the channels in presence of ligands should be less unambiguous in the case of the apo-mmKir3.2 because being that the experimentally measured open probability are generally low – the closure of the channel in absence of ligands appears be an unambiguous process.

5.7 MD KIR3.2 IN ABSENCE OF ANY SPECIFIC LIGANDS

Apart from the number of simulations in attempt to activate mmKir3.2 by using smaller ligands, a trajectory of the apo-mmKir3.2 was produced in order to establish the drift towards the closed state once the pre-activated model is released in absence of any activator partners. This simulation was required because apo-mmKir3.2 experimental models are not available, and it is important to be able to subtract the conformational changes undergone by the protein during its drift into the closed state from the dynamics observed in the simulations attempting to activate the channel.

5.7.1 *Overview of K^+ transport along the pore*

The evolution radii of the bottlenecks of the gates and the K^+ positions along the pore obtained when the channel was simulated in absence of any activator ligands (*Simulation 0*) is shown in Figure 30. An atomic replica of this setup was also simulated for 800 ns, in visual inspection it showed similar closure of the gates and absence of K^+ transport (data not shown due to unfinished analysis). An alternative distribution of K^+ is noticeable during the first 400 ns of unrestrained simulation when the membrane potential (V_m) was simulated to -70 mV, and the subsequent period when V_m = -700mV (Figure 30B). This observation of the inward movement of K^+ questions the finalization of the closure of the gates or at least the stabilization of the selectivity filter in high K^+ binding affinity conformation, and the fact that such configuration has enough stability to prevent K^+ permeation at -700 mV. After inspection of the trajectory, the two water-potassium patters in the selectivity filter are as follows (Figure 31B): (*i*) at time 55 ns w-K^+-ϕ-K^+-K^+, (ii) at 830 ns K^+-w-K^+-ϕ-K^+ & K^+ in the TMV close to S4. The first configuration occurred during the equilibration, right after the constraints on

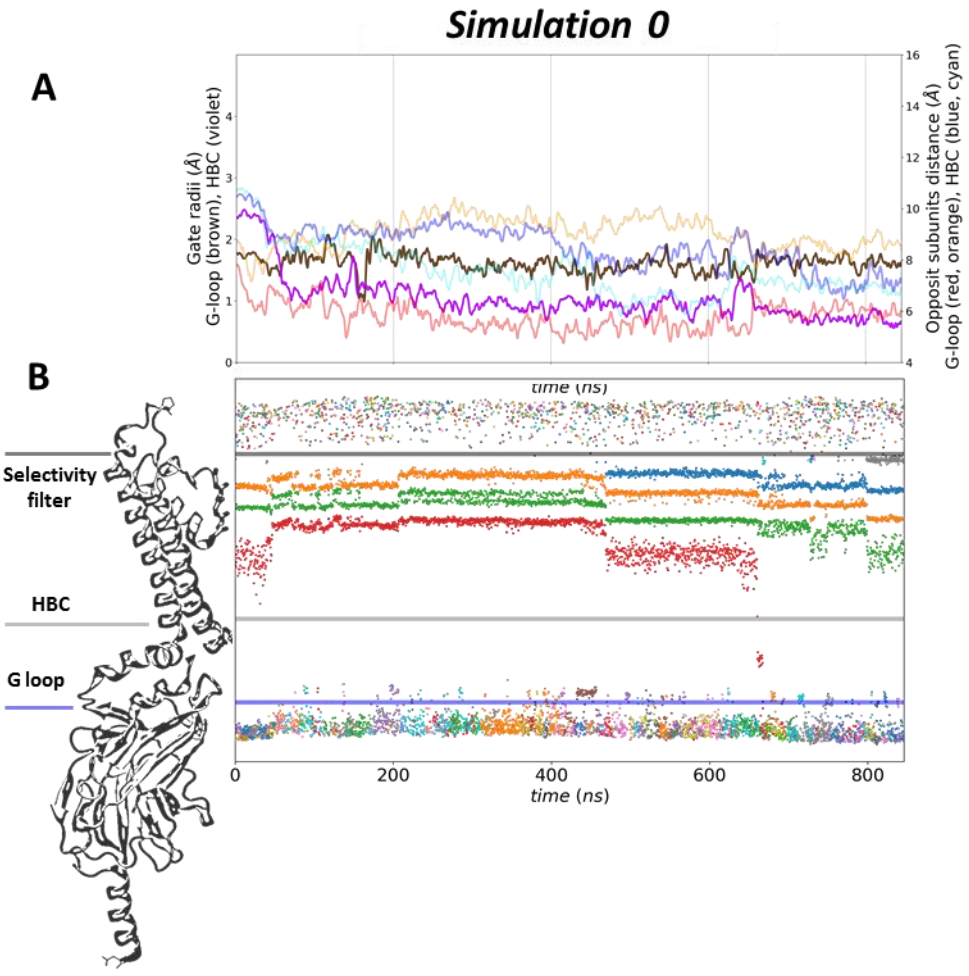

Figure 30: When molecular dynamics were simulated of the pre-open mouse Kir3.2 in absence of any ligands, the channel evolved rapidly into a closed state: Simulation 0 panel A and B. Timeseries are plotted for snapshots taken every 0.4 ns and plotted as convoluted average using sliding window of 20 ns and a symmetric power law function x^n (n=±6), the first 45 ns corresponds to the equilibration of the simulated system. (A) Timeseries of the minimum radius of the G-loop gate (brown) and the HBC gate (magenta) are plotted on the left vertical axis. The distance between pairs of atoms from diametrically opposite subunits is plotted on the right vertical axis: G318:0 carbonyl oxygen of the mainchain (red and orange); the geometrical center of the phenyl ring of F192 (blue and cyan). (B) Timeseries showing K^+ movement across a section of the pore extending between 10 Å below the Cα of residue M313 in the G loop, and 10 Å above the carbonyl oxygen of residue G158 in the selectivity filter. K^+ positions along the permeation pathway are plotted on the left vertical axis. Each individual ion is colored with the same color along the entire timeseries, repeated colors for different ions exist in the plot. Watermark of part of the channel is shown for easier localization of the gates in the plot.

the backbone were decreased to the final 0.1 kcal/mol/Å. This precise redistribution of K^+ was observed in every simulation described until here independently of the atomic constituents of the simulation box, suggesting that the true distribution of the K^+ in the crystallographic model could be of only three K^+, instead of K^+-K^+-K^+-K^+-K^+ modeled in PDB:4KFM. The displacement of the K^+ from S1 to S2 seems to be induced by the external electric force, thus it looks like this configuration of K^+ inside the filter is a waiting configuration for inward incomers, obtained in all simulations with simulated V_m = -70 mV. Therefore, the simulated membrane potential was not sufficient to move K^+ through the filter, and for a long time the filter did not stabilize additional K^+ at the extracellular S0, the potential barrier bulk/S0 was about 800 mV (Annex *Simulation 0*:10). Thus, in the initial conformation of the filter and when only -70 mV were applied across the filter, the filter was saturated by three K^+ in sites S1-S2/S3-S4, and this configuration was stable without any water molecules in between K^+ ions. It is interesting to notice that the TMV did not retake the K^+ from S4 despite the difference of -600 mV between S4/TMV. This observation increases the likelihood of this water-K^+ pattern to be a waiting configuration, observed all along the time laps 50-450 ns, especially because it repeated the observations of *Simulation I, II, III* where the channel adopted a closed state despite the presence of PIP_2 and/or the intracellular ligands.

The second redistribution of the water-K^+ pattern started right after the V_m was increased ten times, after timestep 445 ns. A newcomer K^+ was stabilized at S0 for a very short period followed by an inward displacement of the K^+ ensemble, the configuration in the filter became w-K^+-K^+-ϕ-K^+, and one K^+ left S4 for the TMV (Figure 31B boxed panel). Initially, the inward course of K^+ inside the TMV was interrupted by the closed HBC gate, where the hydrophobic gating phenomenon was already established. The subsequent change of the K^+ configuration along the pore was undoubtably due to electrowetting (Smirnov, Vlassiouk, and Lavrik 2011), causing the K^+ and its hydration shell to slide along the walls of the closed hydrophobic gate – while driven by the external electric force. The premise of the breach of the hydrophobic barrier can be observed in panel C of the supplementary

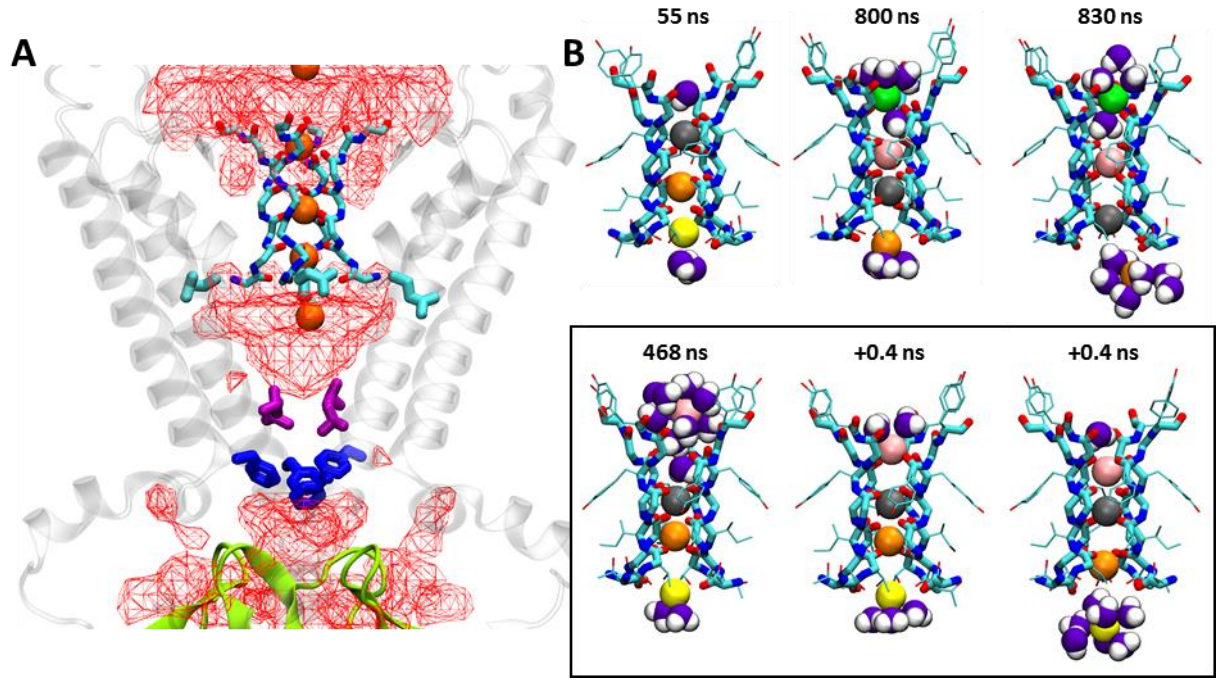

Figure 31: Water and K^+ distribution along the pore observed during molecular dynamics simulation of mouse Kir3.2 in absence of specific ligands. (A) Water occupancy at threshold ≥20%. The TM and the sliding helices of two subunits (gray) and the G-loop gate (green) are shown in cartoon representation. Sidechains of residues E152 (cyan), V188 (violet) and F192 (blue), and the backbone of the selectivity filter are represented by sticks at their conformation after 800 ns of unrestrained simulation. (B) Configuration of the water-K^+ pattern in the selectivity filter at different timesteps of simulation. The selectivity filter residues are shown as sticks, the backbone atoms are emphasized by thicker representation. K^+ are shown as colored spheres (black, green, pink, yellow) where each color allows to track unique atoms, the water is also represented by vdW spheres for the oxygen and the hydrogen respectively (purple, white). The lower boxed panel shows the inward permeation of one K^+ and the involved water exclusion from site S1.

figure Annex *Simulation 0*:10, the potential barrier of the HBC gate was actually inexistent, while the measured potential at *z* = 0 Å is higher than the potential of the gate itself, at *z* = -10 Å.

Thereafter, another event of stabilization of K^+ was observed around timestep 800 ns, this time the ion remained for a longer period in S0, and it was involved in significant redistribution of the ions inside the filter (Figure 31B). It was favored by the preliminary progression of K+/K+/K+ from sites S1/S2/S4 to site S2/S3/S4 (same as the waiting state suggested earlier), and the subsequent progression of these ions to sites S2/S4/TMV which occurred simultaneously with the binding of the new K^+ in S0. This new K^+-w-K^+-ϕ-K^+ pattern appeared as another waiting state, which this time was impeded by the closed HBC gate. Here the profile of the electrostatic potential along the filter and the vestibule was notably different from the previous timepoints (Annex *Simulation 0*:10D). The positive barrier provided by the HBC gate was low, <50 mV. The biggest difference was observed in the electrostatic potential inside the filter, where the major peak was about 650 mV at S3/S4, and a lower peak of 550 mV was measured at S0. This profile is quite different from the profile of the previous timepoint, where the major peak was located at S1 and was >1000 mV. This redistribution of the positive potential from S1 to S0 in addition to the barrier of the closed HBC was most likely the reason for the arrest of the inward K^+ movement. Finally, I am inclined to qualify the K^+-w-K^+-ϕ-K^+ pattern as activated because it is equivalent in K^+ distribution and the magnitude of the electrostatic profile as the one obtained in *Simulation IV*, where significant amount of K^+ inwardly permeated the pore when the HBC gate was open.

5.7.2 Conformational changes which affected the gates of mmKir3.2

As expected in absence of PIP_2, the HBC gate experienced rapid closure and did not recover its opening during the simulation (Figure 30A). The gate closed at F192 after 30 ns of unrestrained simulation, and the V188 sealed the permeation pathway 400 ns later (Annex *Simulation 0*:2). The HBC gate maintained the hydrophobic gating effect for 80 % of the simulation (Figure 31A).

5.7.2.1 Conformational changes of the G-loop gate and lookup for causality

Interestingly, the G-loop gate kept the value of the minimal opening radius all along the simulation (Figure 30A). The G-loop gate remained impermeable for the outward K^+, but allowed the single inward K^+ permeation to occur very rapidly (Figure 30B). The dissymmetry measured between the closest atoms of the backbone (G318:O) was small compared to simulations where K^+ transport was obtained in presence of activating partners (*Simulation IV, V, VI, VII, VIII*). On the other hand, it was similar to the replicas obtained in presence of PrOH and Na^+ but without PIP_2, indicating that the presence of intracellular ligands effectively modified the dynamics of the G-loop gate. From the results of this simulation, one can also notice that the minimal opening being equivalent to the one of the initial structures also indicated that the G-loop gate in the crystallographic model was in a closed state. This suggestion is not directly related to the minimal measured radius of the gate but rather to the environment of the lower TMV. A representative image of the G-loop conformation is reported in panel F of Figure 28. This conformation was only partially different from that of the starting crystallographic model because two of the βH-βI loops oriented the carbonyl oxygens towards the permeation pathway, these were elements of subunits P3 and P4. Nevertheless, the fact that the K^+ which permeated at timestep 660 ns was not stabilized for a long time in the LTMV is in line with my previous hypothesis based on observations that K^+ remains for a long period if the G-loop gate exposes oxygen atoms to the water filled lower TMV – instead of nitrogen atoms. Thus, the fast expel of the K^+ at time 660 ns suggested an unfavorable potential for the K^+ in the lower vestibule.

In addition to the previously presented exploration of the conformational changes of the G-loop gate, further search into the details of the conformational dynamics of the gate was merited. In fact, except for a brief period (including simulation time 148 to 158 ns) during which one sidechain of M319 in subunit P1 rotated to occlude the permeation pathway, the measure of the minimal radius of the G-loop gate was determined by the distance between residues G318 (the backbone of the

gate), involving either the carbonyl oxygen or the Cα of these residues. Since the closure of the gate was deprived by the fast component provided by residues M319, or M313 which sidechains were also in larger extension than the initial conformation, there is a possibility to track the reason for the alternative exposure of T317:O and T318:N atoms on diametrically opposed βH-βI loops.

The initial conformation being – T318N exposed towards the water in the lower TMV – it seemed to me that an increase in the distance between opposite G318:O atoms would coincide with the exposure of T317:O. In order to find evidence, I looked at the conformation of the βD-βE/βL-βM loops cleft- region, because it is admitted that this region controls the G-loop gate (Diomedes E. Logothetis et al. 2015). In *Simulation 0*, the N_{ter} including residues K52 to K54 predominantly contacted the βH-βI strands in three subunits (P1, P3, P4), similarly to the representation in panel A of Figure 29. On the other hand, the conformation of the N_{ter} of subunit P2 resembled the representation in panel B of Figure 29. The predominant conformations were contrary to what I had suggested (in section 5.6.3.3) about the role of the contacts between the N_{ter} and the βH-βI strands, in the sense that I supposed that these conformations were primary determinants for the conformation of the βH-βI loop. Figure 32 regroups measures of the radial pair distribution (*g(r)*) of the average distance between atomic centers, measured in three simulations (the specific protein conformations are redundant with those in Figure 29). In the first two columns one can follow the proximity of the N_{ter} - either to the adjacent βH-βI strands, either to the adjacent βL-βM loop. The first set of peaks in each panel observed at radii <4.5 Å were compatible with hydrogen-bonding contacts between the charged sidechains of these residues. Thus, they indicate that in *Simulation VII* all four residues R53 interacted more frequently with E303 in the βH strand, than with the residues in the βL-βM loop. These readings also show that residue R53 in subunit P2 was not interacting with D246 (no peak near 4.5 Å in the second column) – in fact, it was interacting with E305 (peaks between 6 Å and 8 Å in the first column), thus the N_{ter} of subunit P2 was also most frequently interacting with the βH strand, as suggested by the weakness or the absence of the peaks at 4.5 Å in the second. In *Simulation VII*, the R53 in subunits P1 and P2 also interacted predominantly with E305, and to a lesser extent with E303 in subunit P1, while R53 in subunits P3 and P4 interacted alternatively with E303 in the same subunit and with D346 in the adjacent subunit. Interestingly, based on these repeated observations a rule about the role of the N_{ter} could be constructed. Thus, when R53 interacted with E305 there were two possibilities for the stabilization of residues K52 and K54 – either K52/54 interacted with E302/E303, or they interacted with E345/D346. Respectively in the first case, only one of the residues 52/54 interacted with βH at the time, due to the geometry of the N_{ter}. While in the second case, most of the interactions with the βL-βM loop started with K54 and possible further recruitment of K52. Yet, a third option was the observation of R53 interacting with the βL-βM loop, while K52/K54 interacted with the base of the βH strand, this case being equivalent to the interaction R53/βH strand and K52/K54/βL-βM loop. Taken together these observations extend my previous observations of bi-modal stabilizing interactions involving the N_{ter} and alternatively the base of the βH strand or the βL-βM loop – placing residue R53 as a pivot in this mechanism.

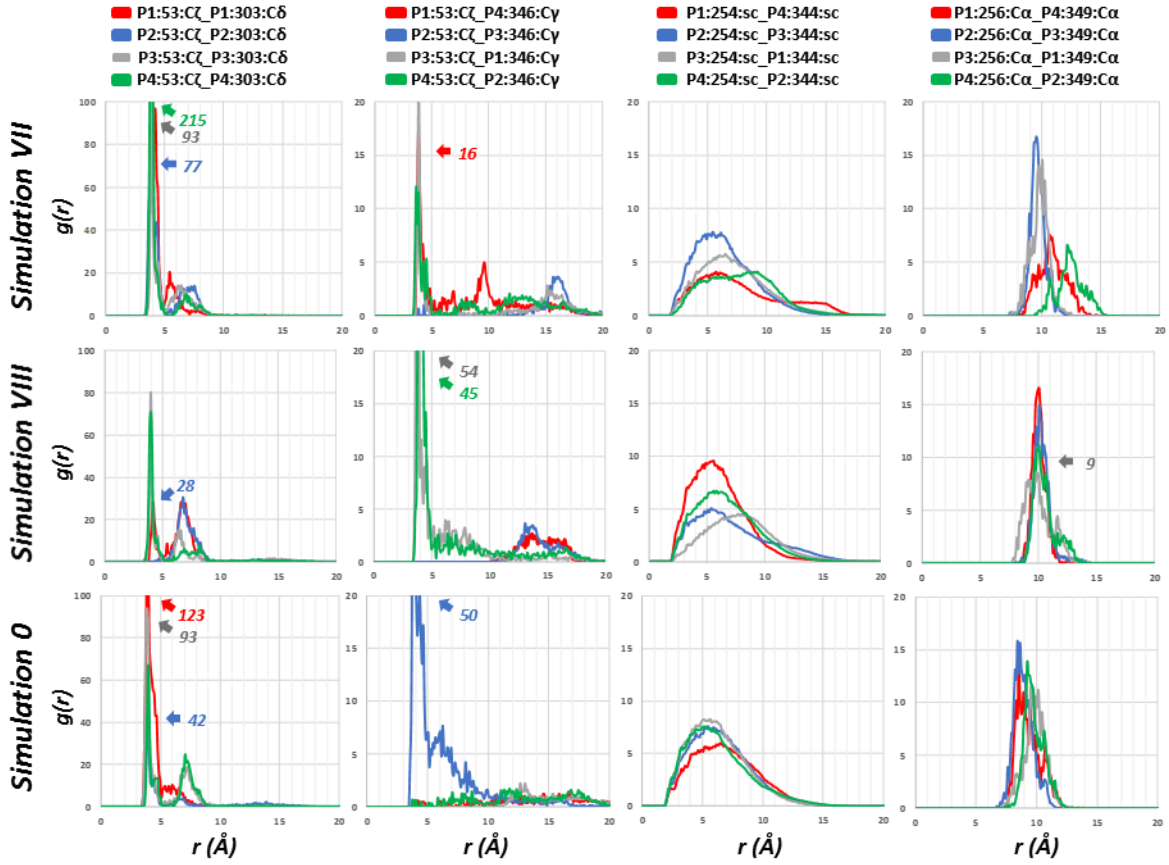

*Figure 32: Subset of differing contacts in the βD-βE/βL-βM cleft-region of mouse Kir3.2, from molecular dynamic simulation of systems with varied ligand compositions. The plots of radial pair distribution function g(r), are used to discriminate between atomic contact propensities. The first two rows in the table are computed from 800 ns simulation of mouse Kir3.2 + $_{(Site\ 1,\ 2,\ 3)}PIP_2$ + Na^+ + PrOH, the third row uses 800 ns trajectory of mouse Kir3.2 without any ligands. The pairwise distances used for computation of g(r) are indicated as names of the columns – individual centers are in the format (subunit identifier):(residue number):(atom name) and (sc) stands for sidechain, thus the computation involved average over all sidechain atoms. g(r) was normalized using cell with size 30*30*30 Å and periodic boundary conditions.*

Panels in the third column of Figure 32 follow the hydrophobic interactions between F254 and L344 in adjacent subunits. These residues are important for the binding of the Gβγ and take a central place in the currently accepted model (Diomedes E. Logothetis et al. 2015). The measures in the fourth column involve the couple P256/Y349, which interact with the alcohol in GIRK channels and are equivalent to residues involved in the coordination of the MPD in the crystal structure of Kir2.1 (Pegan et al. 2006; Aryal et al. 2009; Toyama et al. 2018). In the presented distributions the computation of the average among all sidechain atoms of adjacent F244 and L344, caused the curves to be less noisy and without any prominent peaks. The overall observation is that the distributions from both simulations made in presence of PrOH and where the G-loop gate have conducted K^+, are leveled downwards and spread to longer distances. Despite the apparent differences between simulations with and without PrOH, I did not identify direct causality between these distributions, the state of the N_{ter} binding either to βH strand or to βL-βM loop, and the profile of the bottlenecks of the G-loop gate in the three simulations.

I think this particularity is due to the removal/absence of the Gβγ which eventually released the βD-βE loop, and as I have observed, this structure became rather floppy in all simulations. Thus, the measures using the distances between the Cα atoms of P256 and Y349, also showed only little premises of conditional dependences in line with the model of activation of the G-loop gate (Diomedes E. Logothetis et al. 2015).

For instance, in *Simulation VII*, R53 of subunit P2 was the least stabilized towards the base of the βH strand, at the same time the βL-βM loop adopted a lower conformation than initially – as a result, the distance between the P265/Y349 decreased to 9.5 Å and the F254/L344 contacted more frequently. The next highest peak is the one of P256 in subunit P3, the N_{ter} of subunit P3 did not stabilize next to the βH strand for long period, and interacted frequently with the βL-βM-loop. Surprisingly, the βH-βI loops in these subunits exhibited the largest displacement away from the permeation pathway and since this displacement followed the direction of the displacement of the βL-βM loop, I think that the correlation in presence of alcohol is inversed compared to the model by Mahajan and coworkers (Mahajan et al. 2013; Diomedes E. Logothetis et al. 2015). The N_{ter} of subunits P1 and P4 often interacted with both the βH strands and the adjacent βL-βM loops. Moreover, the βL-βM loops adopted a new conformation where most of the loops were slightly displaced towards the βD-βE loops and away from the center of the CTCD because of the presence of the PrOH beneath it. This new conformation caused the sidechains of F254 and L344 to rotate and to lose contact. These rearrangements contributed to the maintain of the initial distance between the βD-βE/βL-βM loops but were not reflected in the third and the fourth columns of Figure 32 – instead, there were significant shifts to the left of the distributions involving subunits P1 and P4. Thus, the measure of the proximity of these residues important for function was not in agreement with the observed extended conformation of the G-loop in *Simulation VII*. On the other hand, the stabilization of PrOH and Na^+ seems to have helped for the fluctuations in the βD-βE/βL-βM loops cleft-region, and it is possible that the conformational changes that resulted in these secondary structures were transmitted until the G-loop gate which remained extended – contrary to the results obtained in *Simulation 0*.

In *Simulation VIII*, the observed profiles in the first two columns of Figure 32 pointed to a two-fold symmetric conformation of the CTCD – while the profile in the third column resembles that of *Simulation VII*, thus further inspection of the conformation of the cleft region is required in order to correlate these measures with the conformation of the G-loop gate. The gate was predominantly occluded by the sidechains of residues M319, but residues M313 were also involved, this resulted in the maintained short bottleneck radius (Figure 25C). The distances between the opposite G318 at the apex of the βH-βI loops were short between subunits P1 and P2 and long between subunits P3 and P4. The N_{ter} in subunits P3 and P4 fluctuated between the βH strands and the βL-βM loops. Moreover, in these subunits the βD-βE loops moved closer to the inner leaflet than they did at the beginning of the simulation, while the opposite occurred in subunits P1 and P2. In parallel, the βL-βM loops in subunits P1 and P2 remained far from the βD-βE loops of subunits P3 and P4, and the opposite was obtained for the other two couples of cleft regions. Unfortunately, the proximity between the βD-βE/βL-βM loops between subunits P2 and P3 was not caught in the distribution (P2:254:sc_P3:344:sh), because these sidechains rotated away from each other. Furthermore, the proximity between all four couples of βD-βE/βL-βM loops was established by the end of the simulation. Thus, the only difference which still correlated with the G-loop gate and the cleft region remained the displacement of the βD-βE loops in respect to the initial configuration. This requirement is the same as in the model by Meng and coworkers (X. Y. Meng et al. 2012b), but in my understanding in presence of PrOH, the βD-βE loop becomes the leading component. Thus, the βL-βM loop can still remain close to the βD-βE loop but the latter needs to move towards the inner leaflet in order to activate the βH-βI loop in the same subunit.

5.7.2.2 Allosteric pathways controlling the G-loop gate

Since the methodology implied for the analysis shown in Figure 32 is based on (and is restricted by) the user knowledge for the selection of distances to be analyzed, I will present the results from the methodology described in section 4.2.2.3, which allows to compare the ensemble of local conformational changes in the protein over time and to compare those from different simulations. This particular analysis was made by comparing periods of *Simulation VII*/*Simulation VIII* vs. *Simulation 0*. The time lap for the analysis was chosen to be the last 70 ns before the release of the

weak stabilizing constraints on the ligands used in *Simulation VII* and *Simulation VIII*. I chose this period because it could provide less-variable conformation ensembles for the analysis, compared to the increased ligand diffusion observed after the release of the constraints. In addition, I used one more set of coordinates from each simulation containing the time laps 317-387 ns as a mean to introduce depth and some noise into the input data. The notion of pure noise applying to the cases when the data should be uncorrelated, is refuted by the fact that the data came from the same simulations, thus the inherited conformational effects brings additional depth to the analysis. The maps presented in Figure 33 contain sets of automatically filtered Cα-Cα contacts which differed within the couples *Simulation VII*/*Simulation 0* and *Simulation VIII*/*Simulation 0* at period 564-634 ns. The comparison was made by a first stage operation of a symmetrical subtraction of the contact networks. It consisted of the subtraction of the contact network (N_C) of each protein subunit in the control condition (*Simulation 0*) from each of the contact networks (N_T) of each subunit in the test conditions (simulations with ligands). The second filtering stage consisted in a PCA dimensionality-reduction procedure, which used the residual of the Cα-Cα contacts as variables for the comparison N_T vs. N_C. Given the four input data sets and the four by four subtractions between subunits, I obtained 96 eigenvalues and the 85 % of cumulative variance was reached by including 11 of them. The final stage of the analysis consisted in selecting those Cα-Cα contacts which contributed the most to the 85 % cumulative variance. To do so, I simply filtered out every contact below an arbitrary threshold applied to a vector assembled from the loadings provided for each Cα-Cα contacts along the 11 retained eigenvalues. In other words, this procedure is different from iteratively sorting 11 lists of loadings – it consists in first finding the longest distance in an 11-dimensional space, and retaining variables which satisfy the condition to be above the applied threshold portion in respect to this maximal distance. The threshold was manually optimized to be 85 % (for Simulation VII) and 87.5 % (for Simulation VIII), until the returned lists contained residues of interest described in the previous subsections of this manuscript (for instance Figure 13, Figure 20, Figure 21, Figure 22, Figure 29). The initial lists using *Simulation VII*/*Simulation 0* contained 8700 Cα-Cα contacts ($i_T - i_C$), after the subtraction and filtering remained 426 instances which had value $abs(i_T - i_C) > 0.62$ – still too many contacts to scrutiny manually; the subsequent PCA and 85 % loadings-based filtering retained only 77 Cα-Cα contacts. The equivalent quantities for the couple simulation VIII/Simulation 0 were respectively 8820, 399 and 70. Thus in Figure 33 I report the top 1.13% (for Simulation VII) and 1.26% (for Simulation VIII) of Cα-Cα contacts which allow to discriminate between average conformational states from simulations with ligands and a simulation without ligands. This methodology appeared very powerful to pinpoint the conformational changes without using a single structural alignment. Yet it remained to verify that these selected contacts made sense in the context of what is already known about Kir3 dynamics.

Before starting the description of the panels of the figure, I will explain what the edges of the networks mean in these particular cases. First, in the control condition, it should be expected the observation of a rearrangement in response to the removal of the crystallographic partners Gβγ, $_{(Site\ 1)}PIP_2$, Na^+ and the detergent DDM which was crystalized in-between the βA and the slide helix. As a result, the HBC gate closed very quickly, while the G-loop gate opening remained the same, thus indicating that the conformational changes in the CTCD were not of large magnitude. In the test, conditions were supplemented with PIP_2 at two additional sites and the removal of Gβγ was supposedly compensated by the presence of PrOH, while the DDM was also removed. In *Simulation VII*, the G-loop gate remained extended and allowed inward and outward transport of K^+, while in *Simulation VIII*, only inward transport was observed through the two-fold symmetric G-loop gate – the HBC gate in both simulations remained open and no hydrophobic gating was observed. Thus, it should be expected to detect conformational changes in the CTCD which differ between both test simulations, and between *Simulation VIII* and *Simulation 0*. Then, all purple edges in the differential contact network will highlight the Cα-Cα couples which remained or came close together within 4.5 Å (cut-off criterion for interacting residues) in the test condition, and were lost or simply were absent in the control condition. The inverse interpretation is straightforward for the orange edges in respect

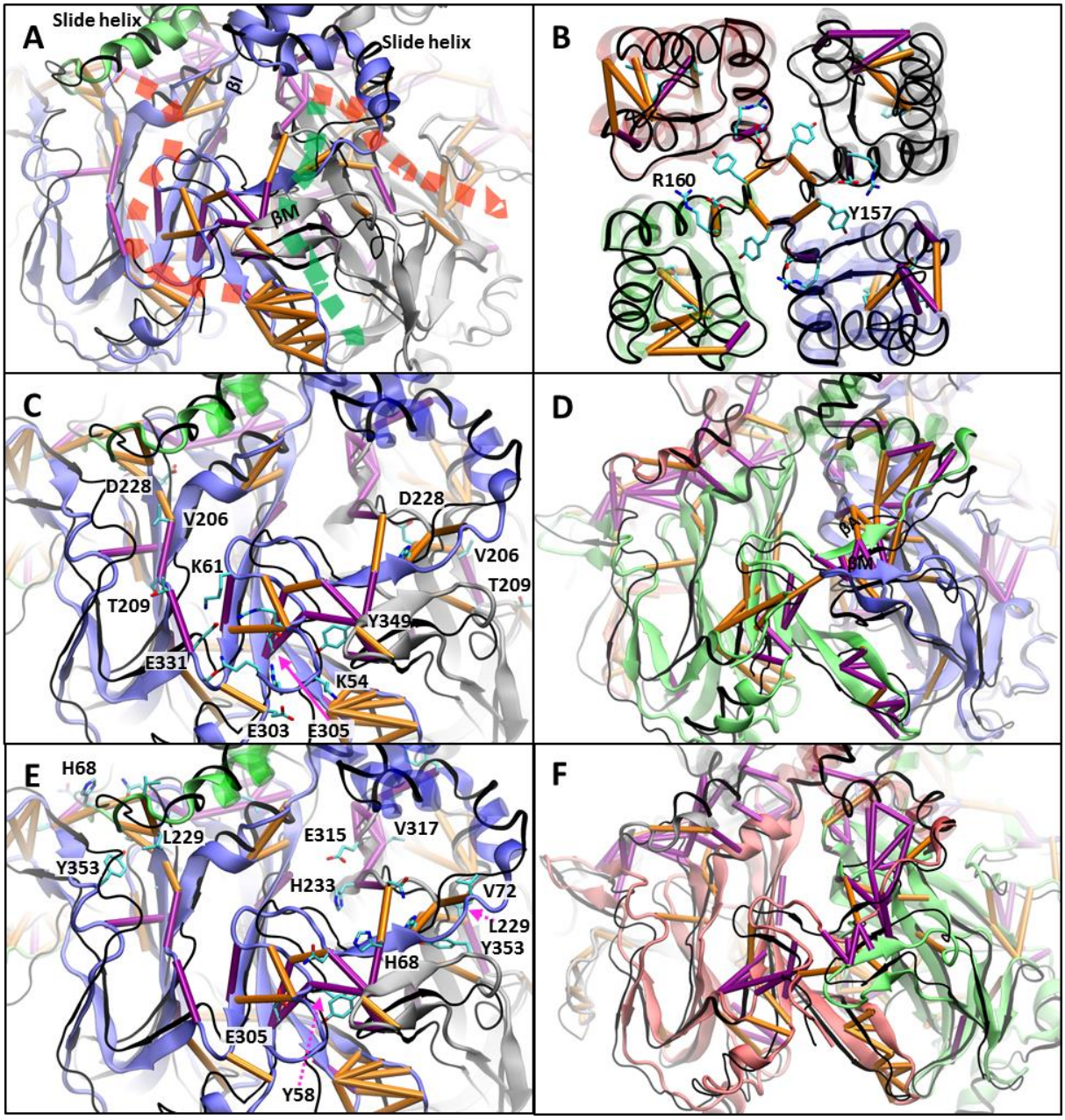

Figure 33: Molecular dynamics simulations of mouse Kir3.2 in presence of a variable number of ligands, suggest the existence of two allosteric pathways controlling the G-loop gate from within the βD-βE/βL-βM cleft region. All panels except B represent one of the inter-subunit interfaces in the CTCD viewed along a tilted perspective from the plane of the membrane. Panel B represents the extracellular part of the tetramer and approximately the upper half of the TM bundle domain, viewed from the extracellular side. In each panel are superimposed two conformations – Test and Control – obtained after approximately 600 ns in presence or in absence of ligands. The test condition conformations from simulation with $_{(Site\ 1,\ 2,\ 3)}PIP_2 + Na^+ + PrOH$ are shown as thick cartoon drawings colored according to the protein segment scheme (P1:red, P2:blue, P3:grey, P4:green). The control condition conformations from simulations without any ligands are shown as ribbon drawing (black). Subset of the differential contact network is shown as vertices drawn between Cα atoms. The represented maps show differences between the control and the test conditions after significance filtering: the contacts absent in the test vs. control condition (orange), contacts absent in the control vs. test condition (purple). The differential contact network was computed using the time laps 564-634 ns from each test and control simulations. (A) Both allosteric pathways are highlighted (red and green) on the map obtained by the comparison using test(Simulation VII) and control(Simulation 0) conditions and significance threshold of 85 % difference. (B) Extracellular view on the same map as used in panel A, showing a relaxation of the selectivity filter in Simulation VII. (C) Same map as panel A, with accent on residues intervening in the allosteric pathway involving N_{ter}/βH/βI/βB/βC-βD loop/βH-βI loop. (D) Map obtained by the comparison using Test(Simulation VIII) and Control(Simulation 0) and representing the P4/P2 segments interface. The significance threshold for differentiation was set to 87.5 %. (E) Same map as panel A, with accent on residues intervening in the allosteric pathway involving βM/βA/βC-βD loop/βH-βI loop. (F) Same map as panel D with accent on the P1/P4 segments interface.

to the control and the test conditions. To remove the ambiguity on the interpretation brought by the possible absence of a contact in one simulation, but it being displayed in the network since it had a counterpart in the other condition, I implemented and used a cunning parameter allowing to display only the active Cα-Cα couples – which have remained close to each other in one or the other simulation.

In panel A of Figure 33 two allosteric pathways running through the CTCD of mmKir3.2 are highlighted. In fact, in the panel the totality of the differential contact map between *Simulation VII*/*Simulation 0* is represented, and it is really surprising that the major differences between these two conditions are located in the regions that I previously discussed in the manuscript. It is even more surprising that while I was making this analysis and I decreased the cut-off, until the emitted list contained residues that I was looking for – the final result appeared rather structured. I interpret the presented map as allosteric pathways because it is composed of a continuous reorganization running from the βD-βE/βL-βM cleft region, through adjacent secondary to finally reach the G-loop gate. Interestingly, there appears to be two subnetworks involved. The first is highlighted by the red dotted line and is detailed in panel C. Briefly, after the cleft where Gβγ and alcohol bind to the CTCD, the reorganization spread in the clockwise direction through the N_{ter} turn (residues 57 to 66) towards the base of the βH strand and the terminus of the βI strand. These transmissions involved the decrease of the distance between the βM and the βA strands, which probably caused the N_{ter} turn to approach the βH-βI strands and the βI-βJ coil. Interestingly, in this region got isolated the slat-bridge R57/K61/E331 which is known to be important for function in Kir6.2 (Cukras, Jeliazkova, and Nichols 2002). Also, the N_{ter} turn approached the βI strand at its second half, this region is interesting because βI strand exposed only the flattened surface of the backbone without any prominent sidechains, and the apex of the N_{ter} turn has a convenient geometry to also expose a flat surface to the βI strand, thus both structures can freely slide one on top of the other. After the node at E313, the allosteric pathway jumped and advanced by three nodes (T209, S208, V206) on the C-linker. At this point the unfolding of the C linker coil was detected, which in partnership with the pooling measure between E331/T209 and S208/V206 drew back the C-linker away from the βC and the βI strands. I believe that this mechanism is involved in the releases of the stoical constraints on the G-loop gate, I will term it “counter-clockwise pulling on the C-linker”.

Panel D contains visualization of the replica comparison *Simulation VIII*/*Simulation 0*, where the left subunit (P4: green) has an open, and the subunit of the right (P2: blue) has closed components of the two-folded symmetric G-loop gate. Interestingly, despite the lack of an exact match between the edges in panel B and panel D, both networks had the same starting configuration at the N_{ter}/E331 interactions, then the network in panel D was interrupted until the drawback of the C-linker from the βC strand. In the conformation presented in panel D, the relief of the satirical constraints on the βI strand in subunit P4 (green) was operated by the upward motion of the slide helix of the same subunit, as discussed in section 5.6.3.1 and presented in Figure 27. Panel F displays the subunit with the constricted G-loop component on the left (P1: red). Here the N_{ter}/E331 interactions were increased, and the slide helix of subunit P3 moved against the CTCD and had multiple nodes which came closer to the C-linker and the TM of subunit P2. All these elements could explain the increased steric constraints of the βH-βI loop of subunit P1.

The second allosteric pathway is highlighted in green in panel A of Figure 33 and is detailed in panel E. Remarkably, as it turned out, this pathway was already entirely discussed in section 5.4.2 and was displayed in Figure 21 and Figure 22. What is really astonishing here is the very close resemblance between the data presented in the opened state *Simulation VI* and the present pathway displayed in panel E. The details in panel E show the βM and the βA strands moving closer to one another, the separation between βA and βC-βD loop, and the contacts between the βC-βD loop and the βH-βI loop. These rearrangements of the CTCD are in perfect agreement with the state of the art functional model for the activation of the G-loop gate (Diomedes E. Logothetis et al. 2015). Furthermore, the contrasts between the simulations with and without ligands are higher in panel D and panel F. There

is clearly a ramification of the pathway which is determined by the conformation of the N_{ter} intracellular part of the channel. While the slide helix of subunit P1 (red) was tightly laying on the intracellular C_{ter} domain of subunit P4, the slide helix of subunit P4 was markedly moved towards the membrane – probably involving the loosening of the interactions between N71/D352 and R73/N354 (data not shown), which residues were initially interacting in the vicinity of the only displayed orange edge between the βM/βA strands in panel D. The slide helix of subunit P4 also lost interactions with the C-linker and the βC-βD loop of subunit P2, but since the C-linker of subunit P2 did not move upwards to follow the motion of the above slide helix, the steric constraints on the βH-βI strand and loop were maintained and the G-loop gate remained constricted at subunit P2.

As a final piece of evidence, capable of explaining the two-folded geometry of the G-loop gate in *Simulation VIII*, I will evoke the contacts of residue R53 and E305 or E303 – they were already discussed in section 5.6.3.3 and displayed in Figure 29 in the scope of *Simulation VIII*. Here I will refer to the differential analysis *Simulation VIII*/*Simulation 0*, and link the N_{ter} conformations and the βH-βI loop in the same subunits. Since in the control simulation the CTCD domain exhibited fewer changes in comparison to the initial structure, the observed strong interaction in panel F between the node at E331 and its partners would be a hallmark of the constricted βH-βI loop in subunit P1. On the other hand, in this conformation, R53 established a salt bridge with E305, which is located closer to the G-loop gate than the alternative possible partner for R53, the residue E303. The R53/E305 contact was also concomitant to the separation of the base of the βH-βI β-sheet. Taken together these observations indicate that the switching of the R53 salt bridge from E305 to E303 allowed the N_{ter} to pull more efficiently on the C_{ter} of the βH strand, and since the βI strand is superimposed on the βH strand in the slab where R53 interact with the latter – the βI sheet was push-bended away from the N_{ter}, an event which conformational signal was caught by the analysis method and represented with the orange edges between the N_{ter} and the coil containing residue E313. On the contrary, the R53/E305 salt bridge might simply serve as a lock for the bending mechanism by pulling on the βI strand towards the N_{ter}.

In this paragraph I would like to come back to the observation that the backbone nitrogen of residues T317 was exposed to the water column when the G gate closed in *Simulation 0*. To provide evidence of the involvement of the distal N_{ter} in the fine-tuning of the conformation of the G-loop gate I will examine distinct points along the allosteric pathways in the CTDC that I have just described. The starting-point data for this argumentation is presented in Figure 34. This time, I measured distances beyond the reach of the methodology used to produce the differential contact maps shown in Figure 33. The majority of timeseries in Figure 34 display the two-fold symmetric conformational change that the CTCD experienced during this simulation. These changes can be traced clockwise from the distal N_{ter} (Figure 34P, Q) up to the βH-βI strands (Figure 34J, L, M) and to the G-loop gate (Figure 34B), and also in the counter-clockwise direction, from the βA strand (Figure 34R) up to the βD strand (Figure 34D) – but did not include the βC strand (Figure 34G), nor the second half of the slide helix (Figure 34E). The two-fold symmetry measured at the C linkers (Figure 34F, H) should be attributed to the clock-wise pathway in accordance with the measures displayed in Figure 33 and the provided discussion (see above).

I have to underline the apparent correlation between the measures at the βC strand (Figure 34G), the slide helix (Figure 34E) and the HBC gate (Figure 34C) – while in this situation of absent PIP_2 molecules, the fluctuation of the HBC gate remained uncorrelated from the C-linker (Figure 34F, H). These observations suggest that on the behalf of the CTCD, it is mostly the βC loop which could be involved in the control of the HBC gate. These results are compatible with the demonstrated priming of the channel by Na^+, i.e. the increase of PIP_2 affinity of the channel in presence of Na^+ reported in the literature (see section 2.4). Interestingly, the proline kink P198 seemed to uncouple the clock-wise pathway after the C linker from the HBC gate, leading to the suggestion that the intra-subunit pathway controls the flickering of the G-loop gate through the displacement of the C linker back-away from the βH-βI loop and towards the slide helix. Nevertheless, this process remained

mechanically dependent on the inter-subunit pathway, because despite the observed slight extension of the G-loop gate at two opposite subunits, the absence of Na^+ did not provide the

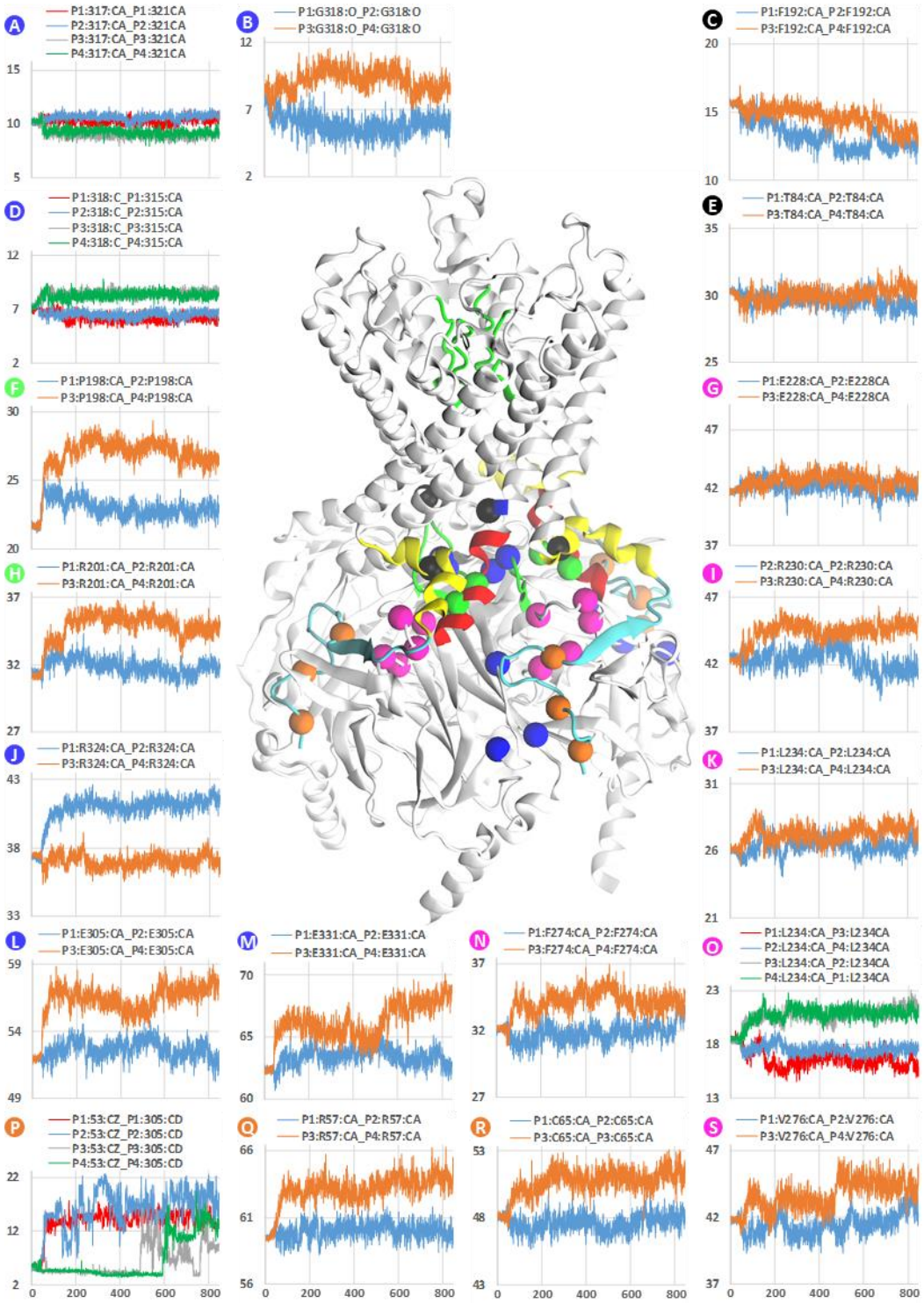

Figure 34: Timeseries of inter-atomic distances from a molecular dynamics simulation of mouse Kir3.2 in absence of any ligands. All graphics except panels A, D, O, P, follow distances between Cα atoms of diametrically opposite equivalent residues in the tetramer. Panels A and D follow distances between atoms in the same βH-βI loop across all subunits. Panel O captures the two-fold symmetry of the tetramer by following the distance between equivalent Cα atoms in the center of the CTCD across adjacent subunits. Panel P follows the distance between the sidechain of residue R53 in the distal N_{ter} and the inner-most glutamate (E305) of the βI strand that R53 interacts with. The channel is represented by cartoon drawing (white) where some elements are emphasized: N_{ter} (cyan), slide helix (yellow), C-linker (red) selectivity filter and βH-βI loop (green). The overall localization of the centers used for construction of the timeseries is indicated in two adjacent subunits by colored beads centered at the coordinates of each Cα of the involved residues. The Cα color scheme group residues by secondary structure and by allosteric pathway: the intra-subunit pathway involving the N_{ter} (orange), the βH-βI strands (blue), the C-linker (green) and the βH-βI loop (blue); the inter-subunit pathway involving the Nter (orange), the βF-βG loop and the βC-βD loop (magenta), the βH-βI loop (blue) and the HBC gate (black).

necessary amplitude of the conformational change (to observe outward motion of K^+) through the allosteric link between the βC-βD and the βH-βI loops. This hypothesis was backed by the union of both conditions – βC-βD interaction with elements of the G-loop gate and the C-linker displacement – attained for brief periods of the trajectories in *Simulation I* and *Simulation II* (in presence of Na^+ and PrOH).

The ensemble of conformational changes described in this section encompassed in one hand, the generator event of interaction between the N_{ter} with residue E303 and the subsequent allosteric conformational transition along the pathway detailed in panel C of Figure 33. It seems to operate an intra-subunit control of βH-βI loop – by cooperativity between push-bending of the βH-βI β-sheet, and by the pull-back of the C-linker. The second pathway, traced in red in panel A and detailed in panel E of Figure 33, seems to operate inter-subunit cooperativity through the upward motion of the slide helix which releases constraints on the C-linker of the anti-clockwise subunit. However, the motions of the slide helix also appeared to have an influence on the number of interactions measured between the βA/slide helix and the βC-βD loop which is a central element in the mechanism proposed by Logothetis and colleagues (Diomedes E. Logothetis et al. 2015).

5.8 MD Kir3.2 in presence of Gβγ dimers, PIP_2 and Na^+

After I successfully reproduced the opening of the gates of mmKir3.2 in a series of simulations – where I complexified the conditions of ligands interacting with the channel, I decided to complete the set of simulations with the results of the dynamics of the integral initial crystallographic model – mmKir3.2 co-crystalized with Gβγ, PIP_2 and Na^+ (Whorton and MacKinnon 2013). If the magnitude and the appearance of the opening were similar or equivalent to those already presented in the previous sections, this last data set could serve to validate the previously presented trajectories and to strengthen the hypothesis I have made so far.

The simulation setup for the simulation of the crystallographic assembly used the exact same simulation parameters as previously. Exceptions were the size of the simulation box, which was extended in the *xy*-plane to accommodate the Gβγ dimers, and the content of Na^+ and PIP_2 was set to only four molecules of each. The Na^+ and the $_{(Site\ 1)}PIP_2$ were constrained during the entire simulation towards the respective crystallographic binding pockets using the parameter indexed *e* and *a* in Table 2. The membrane potential was set to -70 mV during the 60 ns equilibration period, and increased to -700 mV during the subsequent 600 ns of simulation with unrestrained protein. The code of this simulation in the following chapter will be *Simulation IX*.

5.8.1 Conformational changes of the selectivity filter, the HBC and the G-loop gates, and associated K^+ transport

The structure appeared nonconductive during the equilibration (Figure 35B). Therefore, immediately after the switching-off of the protein constraints and the increase of the simulated membrane potential there was a redistribution of the K^+ inside the selectivity filter: from w-K^+-K^+- ϕ-w & $_{TMV}K^+$ to K^+-w-K^+-ϕ-K^+. This last configuration was maintained during the next 140 ns when seven K^+ were transported in the inward direction through the selectivity filter and exited the G-loop gate. This K^+ binding profile was characterized by a higher positive potential measured across the sites of the selectivity filter as compared to the measure taken at time step 220 ns (Annex *Simulation XI*:11A, 11B). The conformational changes in the selectivity filter associated with the decrease of the binding affinity for potassium involved two processes. At sites S2/S3, during the entire simulation the flipping of the carbonyl oxygens of residues I155 and those of G156 was observed (Annex *Simulation IX*:6). Furthermore, the affinity of site S0 appeared to have decreased due to the displacement of the carbonyls of residue Y159 – this process however did not involve an isolated backbone torsion change in S0. Rather the outer half of the filter, including sites S0/S1, experienced a rigid body twist starting at G156 (S2). The evolution of the opening of the filter can be followed in the pore profiles displayed in Annex *Simulation IX*:2. While the rotation of the upper-half of the backbone of the filter

around G156 was observed in the nonconductive pore which was the result of the pinching of S2 (Annex *Simulation I*:2), here it is clear that the flipping of the carbonyl of I156 was involved in the decrease of the stabilization influence of the pinched S2. Thus, this simulation simultaneously caught two mechanisms, whose joint contribution decreased the global binding affinity of the selectivity filter, and as a result they increased the conductance of the filter.

The opening of site S2 of the selectivity filter was concomitant with the persistent opening of the HBC gate (Figure 35A), which implied that the TM bundle was enlarged in comparison to the nonconductive states observed in other simulations. Nevertheless, the enlarged TM bundle had an influence on the selectivity filter. I had already found a correlation between the displacement of the TM helices and the flipping of the carbonyl oxygen of I156 in simulations without the Gβγ dimers (see section 5.3.2.2.1 and Figure 16), and verified that the same correlation could be traced in *Simulation IX* (data not shown).

The TMV remained only transiently occupied by K^+ in the first 400 ns – in the following 200 ns it accommodated two to three K^+ which were trapped mostly in the lower TMV because of the closure of the G-loop gate. One K^+ ion (not always the same ion), remained stabilized by the oxygen-reach surface exposed by the removal of the sidechain of C319 of subunit P4 – representing the very same

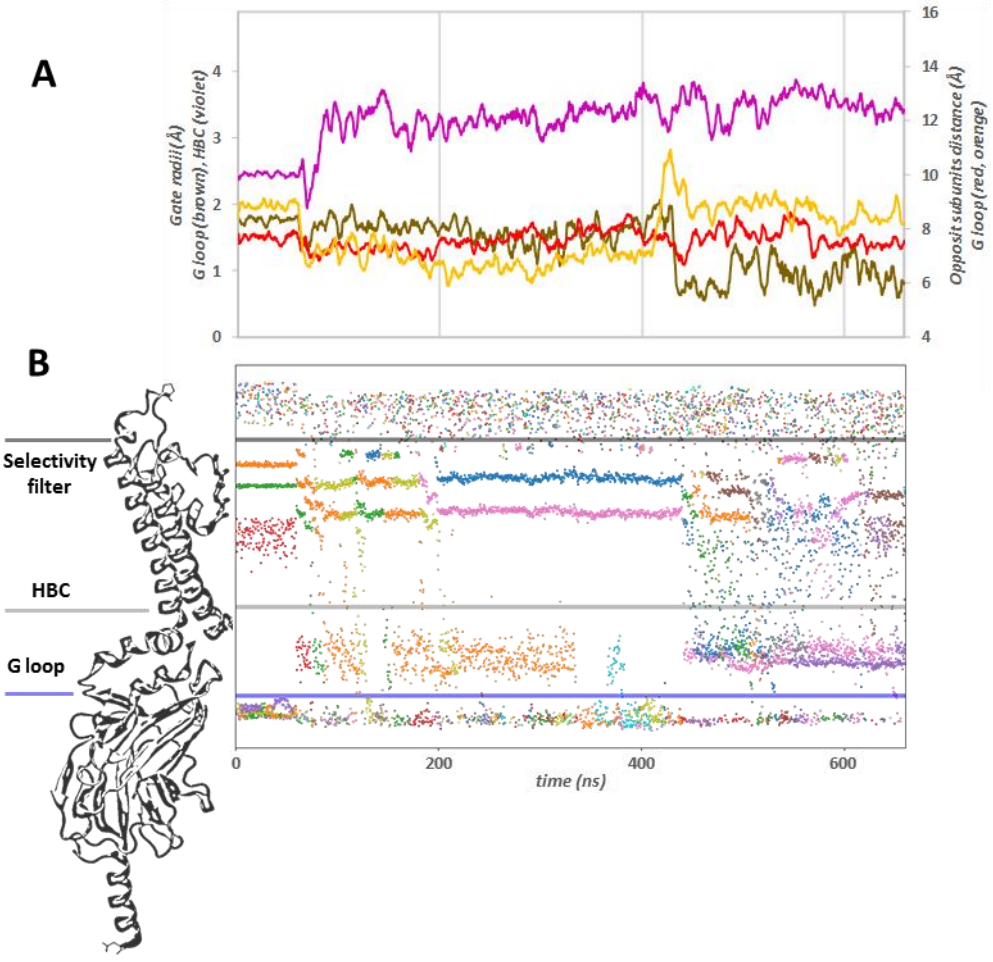

Figure 35: The HBC and the G-loop gates of the pre-open mouse Kir3.2 stabilized by Gβγ, PIP_2 and Na^+, opened during molecular dynamic simulation. Inside de main text this atomic system is referred to as Simulation IX. Timeseries are plotted for snapshots taken every 0.4 ns and plotted as average using a sliding window of 4 ns, the first 60 ns corresponds to the equilibration of the simulated system. (A) Timeseries of the minimum radius of the G-loop gate (brown) and the HBC gate (magenta) are plotted on the left vertical axis. (B) Timeseries showing K^+ movement across a section of the pore extending between 10 Å below the Cα of residue M313 in the G loop, and 10 Å above the carbonyl oxygen of residue G158 in the selectivity filter. K^+ positions along the permeation pathway are plotted on the left vertical axis. Each individual ion is colored with the same color along the entire timeseries, duplicate color for different ions exist in the plot. Watermark of part of the channel is shown for easier localization of the gates in the plot.

event as the one described in Figure 26. The G-loop gate was remarkably stable for the first 400 ns of the simulation, allowing rapid inward progression of K^+ incoming from the selectivity filter. Thereafter, a single sidechain of C319 occluded the permeation pathway and thus, the K^+ efflux in the inward direction from the lower TMV was severely impeded. Remarkably, this conformational change was very rapid and initially involved only a rearrangement in several of the backbone torsion angles along the βH-βI loop of subunit P4, rather than a rigid body motion of the gate itself.

In the scope of the closure of the G-loop gate, I was able to pinpoint the conformational change that occurred in subunit P4 to the rolling-out of the distal N_{ter}. Hereafter is the description of these conformational changes, which evolution was correlated to the change in the βH-βI loop in subunit P4 (Figure 36C, D). Before the rearrangement of the G-loop gate, residue R53 interacted with E303 approaching it from the plane of the membrane (Figure 36A) – an interaction that I termed "above-R53/E303". In this configuration, R53 equally engaged residue E305 and extended until T329 and S330 in the βI-βJ turn – the same conformation was obtained in other simulations (Figure 29A). At time 340, the rearrangement involving the interactions N_{ter}-βH strand began. Residue R53 decoupled from E303, and rotated in the opposite direction entering in hydrogen-bonding interaction with the alcohol of the sidechain of residue S246. At the same time, the backbone of K54 followed the displacement of R53 and rotated the sidechain K54 to interact with E305. The closure of the G-loop gate occurred during this period at simulation time 420 ns. To a smaller extent, the interaction R53 with the βD strand resembled the set of strong interactions involving three slat-bridges between the distal N_{ter}, the βH strand and the βL-βM loop, discussed in section 5.6.3.3 and pictured in Figure 29B.

In the scope of this mechanism, I would like to speculate that the interaction R53/S246 in mmKir3.2 could be equivalent to a hypothetical couple E(Q)30/K222 in mm(hs)Kir6.2 – a channel which is constitutively closed and thus would require a more stable interaction to maintain the G-loop gate shut. Residue K222 was probed in the study by Shyng and colleagues (Shyng et al. 2000), where authors found a PIP_2-insensitve phenotype of the K222A mutant. Their conclusion was that K222 would be involved in PIP_2 binding. Such a conclusion seems straightforward when one forgets that the channel of the Kir family have three gate-like elements, and the closure of any one of them will provide negative readings for the other two elements. Of course, this study was made in the total absence of representative structure of the Kir6.2 channel, thus the authors could not know that K222 is located some 2.5 nm from the membrane – hence interactions with PIP_2 seem impossible. Thus, I do not criticize the sited study, but rather I want to stress the fact that it is often forgotten that the response of the Kir channels is multi variate. Finally, if my hypothesis about the N_{ter}-βD contact involved in the G-loop opening is right, then it shouldn't be of no surprise that when this interaction is abolished and it results in the closure of the G-loop gate – any following addition of PIP_2 to the channel will always produce PIP_2-insensitive phenotype.

The conformational change of the N_{ter} continued after visiting S246 – lastly R53 approached the coil located after the βH strand. The novel interaction R53/E302 was established at time 510 ns and was further stabilized by interaction R53/E303 (Figure 36B) – in the legend of Figure 36 I termed this interaction "below-R53/E303", referring to the relative position of the R53:Cζ in respect to E303:Cδ. Meanwhile, K54 additionally stabilized the N_{ter} towards the βH strand at E305. Hence, this configuration was the same as the one observed in subunit P1 in *Simulation 0*, where the βH loop was markedly constricted (see section 5.7.2 and Figure 30A).

Taken together these observations allowed me to deepen my understanding of the generator-event of the intra-subunit allosteric pathway that I had started to describe in section 5.7.2.2. The summary of the events would be the following: in the first case of the interaction above-R53/E303, the distal N_{ter} helped by the βI-βJ coil pulled on the base of the βH strand towards the plane of the membrane, thus having a positive effect on the global upward motion of the CTCD towards the membrane and hence, on the opening of the G-loop gate; while during the interaction below-R53/E303, the distal N_{ter} was pushing the Hβ strand away from the plane of the membrane, thus causing the CTDC to

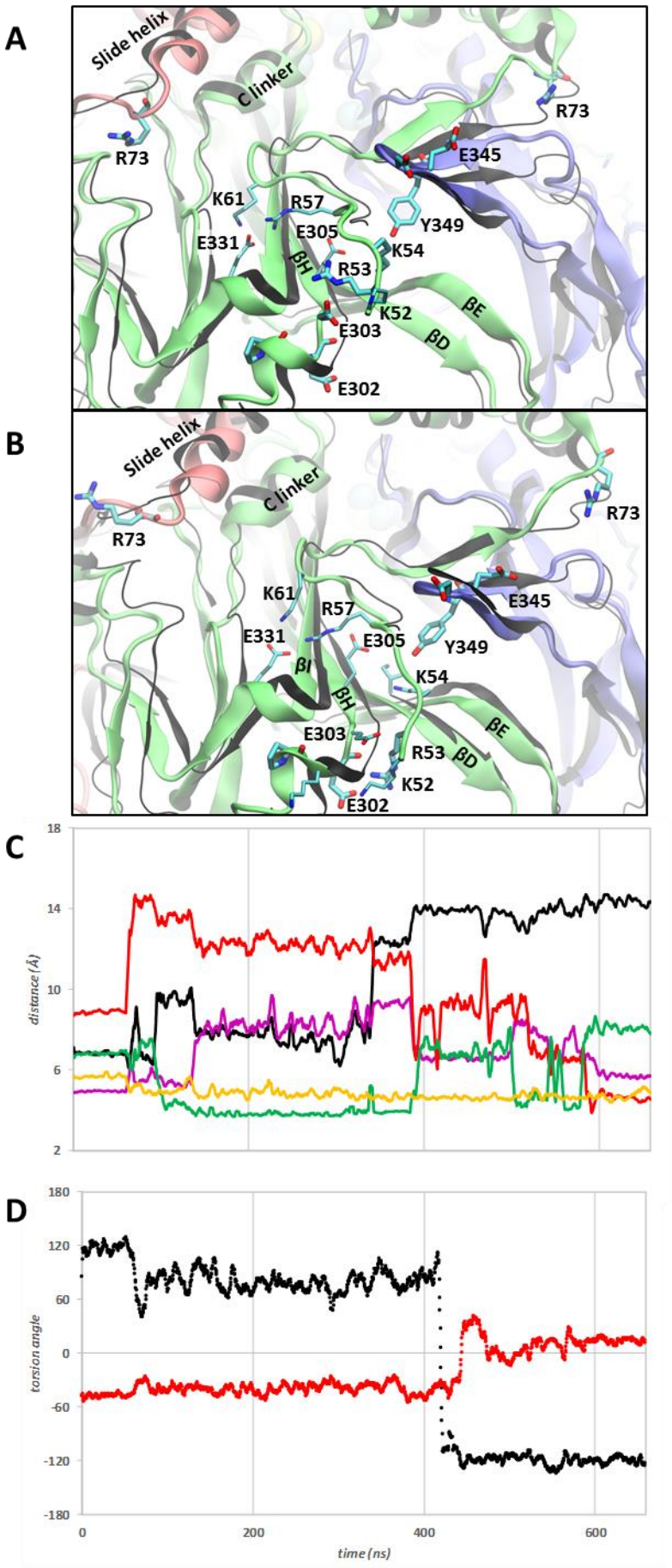

Figure 36: Alternative conformations of the distal N_{ter} of mouse Kir3.2 correlate with bending of the apex of the βH-βI loop in the same channel subunits; results from unrestrained molecular dynamics simulation of the mouse Kir3.2 channel interacting with Gβγ dimers, Na^+ and PIP_2 molecules. (A) Snapshot at timestep 335 ns. The R53 contacts the βH strand from above residue E303. (B) Snapshot at timestep 640 ns. The N_{ter} is rolled-out along the βH strand and the subsequent coil, and now R53 interacts with residue E303 from below. (C) Timeseries of interatomic distances: P4:R53:Cζ and P4:N56:Cα (black), P4:R53:Cα and P4:E303:Cα (purple), P4:R53:Cζ and P4:E302:Cδ (red), P4:R53:Cζ and P4:E303:Cδ (green), P4:R56:O and P4:E303:Cδ (orange). (D) Timeseries of the backbone torsion angles of residue C319 in subunit P4: ψ (black), φ(red). Timeseries in panels C and D were collected every 0.4 ns and averaged with a sliding window of 5 ns.

move downwards from the membrane and resulting in the closure of the G-loop gate. Furthermore, as the ensemble of simulation presented until now has shown – the closure of the G-loop gate implicated three distinct combinations of interactions seen in every subunit where the βH-βI loop closed, hence: *(i)* interaction between R53 and E302 was simultaneous with K54/E305, *(ii)* interaction R53/S246 was simultaneous with K54/E305, *(iii)* interaction R53/E305 was simultaneous with K52/E345 and K54/D346. The allosteric transmission until the G-loop gate in *Simulation IX* was obtained in a similar fashion and in correlation with simulations from the previous chapters – especially *Simulation 0* and *Simulation VI*, showing that the protocols I used to simulate the mmKir3.2 channel in absence of Gβγ allowed the channel to close at the G-loop gate by a mechanism similar to the one observed here in presence of Gβγ.

5.8.2 Novel interpretation of the R201A activating mutation

Taken together, the results presented in the subsections of this chapter and their interpretation allow me to propose an alternative interpretation for the mechanism of the D228N and the R201A activating mutations (Whorton and MacKinnon 2011), and the role of the Na^+ binding to the Kir3.2 channel.

As a reminder, the R201A mutation uncouples the βC-βD loop and C-linker by abolishing the native salt-bridge interaction between these two structures – the conformational effect of this mutation is observed in two crystallographic models: the apo state PDB:3SYP and the PIP_2 bound state PDB:3SYQ (Whorton and MacKinnon 2011). Neither of these two structures showed the channel in a completely open conformation. From the inspection of PDB:3SYQ model, it became clear that the opening of the lumen of the G-loop gate is provoked by the motion of the βH-βI loop led by the displacement of matter in the βC-βD loop. In the crystallographic model, the side chain of H233 occupied the location reserved for the side chain of R201 in the wild-type and this irrespectively of the various ligands bound to the channel: Na^+ (PDB:3SYO), Na^+ & PIP_2 (PDB:3SYA), Na^+ & PIP_2 & Gβγ (PDB:4KFM). This rearrangement of the βC-βD loop opened the G-loop gate at M313 but was not concomitant to any significant changes in the C-linker, which remained perfectly superimposable between the R201A mutant and wild-type structures. Moreover, the Cα and the Cβ of A201 and R201 in these models always pointed to the βC-βD loop.

Here I will resume some of the information provided in the reference, about the currents from whole-cell recordings. The mmKir3.2(R201A) provided a maximum recorded current (I_{max}) comparable to the wild-type channel – -0.3 µA, while the fraction of the current developed by the acetylcholine (*Ach*) stimulation was about 10 to 20 % of I_{max} for the R201A mutant, and it was 90 % for the wild-type. Thus, because it is admitted that the I_{max} should be a finite quantity when experiments are made in the same conditions, one of the possible conclusions and the one adopted by the authors about the observed difference between both conditions, was that the R201A mutation caused the channel to be more frequently open in the basal experimental conditions, i.e. without Gβγ stimulation but in presence of cytosolic of Na^+ and PIP_2. Hence, the R201A mutant was more frequently open in the basal state, it had the same I_{max} as the wild-type, while the D228N mutant was more active when stimulated by the G-proteins and it appears that its basal currents (I_{basal}) were slightly higher than I_{basal} of the wild-type. The I_{max} of the D228N mutant was about 2.5 times higher than the wild-type and R201A, while this channel kept the property for Gβγ to provide 80 % of I_{max}. Thus, the effect of the D228N mutation was to increase the conductance of the G-protein activated state, and had only a small influence on the basal state. Most probably this effect comes from the decreased coupling of the βC-βD loop and the C-linker. The structure of the mmKir3.2(D228N) mutant is only weakly informative on the matter because it was obtained in absence of Na^+, and shows the pore in a closed state resembling the one of PDB:3SYP. Furthermore, in PDB:3SYC, the G-loop gate was also closed at M313 probably due to the lack of rearrangement in the βC-βD loop and the subsequent effect on the βH-βI loop as observed in PDB:3SYP. The binding of PIP_2 in mmKir3.2(R201A) also had an effect on the conformation of the HBC gate. This condition was expected and easily verified by inspection of the crystal structures. The distance between the Cα

atoms of opposite F192 in PDB:3SYA was 15.29 Å vs. 14.61 Å in PDB:3SYO, while in PDB:3SYP it was 13.37 Å, in PDB:3SYQ it was 16.40 Å in the PIP_2-bound subunits and it was 13.27 Å in subunits lacking PIP_2. Thus, the PIP_2 binding in PDB:3SYQ extended not only the G-loop gate but also the HBC gate. Based on this comparison, authors imagined that if four PIP_2 bound the mmKir3.2(R201A) mutant channel, this would open the HBC gate to at least 8 Å – merely enough to allow hydrated K^+ to cross the gate. By supplementing the reading of the article by Whorton and MacKinnon with the profiles of the pore opening of the crystal structures (**Error! Reference source not found.**B), one can visualize how the PIP_2 serves as the major factor controlling the HBC gate – comparison between PDB:3SYC and PDB:3SYA. In the case of R201A mutant, the gate was tightly closed in PDB:3SYP, and the addition of PIP_2 in two sites on the C-linker extended the HBC gate in a two-fold symmetric conformation to finally approach the conformation of the wild-type channel in presence of PIP_2 (PDB:3SYA). Nevertheless, this 2D flattening of the profile caused the loss of a significant amount of information, thus requiring deeper inspection of the models.

On the other hand, the situation of the G-loop gate is much more complex and also particularly related to the presence of PIP_2. In PDB:3SYP, the G-loop gate was the least open among all crystal structures whose pore profiles are presented in **Error! Reference source not found.**B. This result was not straightforward because one could expect that the R201A mutation changed the G-loop gate given the higher I_{basal} and conversely the low *Ach* contribution to I_{max}. However, if one considers not only the apparent positive effect on the opening of the G-loop gate by the R201A mutation, but also takes into account differences between the conformations of PDB:3SYQ vs. PDB:3SYP, the interpretation for the constricted gates seen in PDB:3SYP is that the conformation of the G-loop gate is also under the major influence of the bound PIP_2. In fact, in PDB:3SYQ the G-loop gate had a pronounced two-fold symmetric conformation, and just like the HBC gate, the opening was in phase with the two PIP_2 molecules bound to C-linker of the channel. Namely, the presence of C_8-PIP_2 modeled at diametrically opposite subunits (say P1 and P2) was concomitant with the extended conformations of the backbone and the sidechains of M319 in the same subunits. The interpretation made by the authors about the observed two-fold symmetry of PDB:3SYQ was that, due to peculiarities of the crystal formation, the PIP_2 bound only two subunits of the channel. From here on, authors hypothesized an opening of 13 Å of the G-loop gate in the case of the simultaneous binding of four PIP2 to the C-linker. In the end, since these two mutations tweaked the channel conductance and the residues R201 and D228 were located near the Na^+ binding site observed in PDB:3SYA and PDB:3SYO, authors proposed that in native Kir3.2 channels the Na^+ binding would disrupt the D228/R201 salt-bridge and thus would cause the channel to be more active in presence of PIP_2 and Gβγ. In the following paragraphs of the subsection, I will argue against the Na^+ induced disruption of the D228/R201 salt-bridge in the action mechanism of native Kir3.2 channels.

In my understanding, what happens to the βC-βD loop in presence of Na^+ when R201A abrogates the coupling of the C-linker and the βC-βD loop, remains an open question. In order to reinforce my version of the facts, I will first stress the alarming presence of low-resolution electron density in the omitted density map, near K64 in both subunits where PIP_2 was not modeled in the final model (Figure 37). I allow myself to speculate that these densities near the K64 in two of the subunits could correspond to weakly stabilized C_8-PIP_2. These densities were not accounted for in the final model and thus were not taken into account in the authors interpretation of the final model. One can easily spot that the conformations of K64 were different across the tetramer in PDB:3SYQ – in subunits where C_8-PIP_2 was modeled, the sidechain of K64 was seen parallel to the plane of the membrane, while in subunits without modeled PIP_2 analogue, the sidechains of K64 pointed upward from the N_{ter} towards the omitted densities shown in Figure 37. If my suggestion is right, then this could be direct evidence that the absence of Na^+ in the crystallization setup resulted in the decrease of the PIP_2 binding affinity of the critical site including K199, K200 and K194 in the C-linker and the TM2. Since the PIP_2 binding was positively influenced by Na^+ (see the introduction for extended list of references), it would be very interesting to have had a crystallographic structure like PDB:3SYQ in

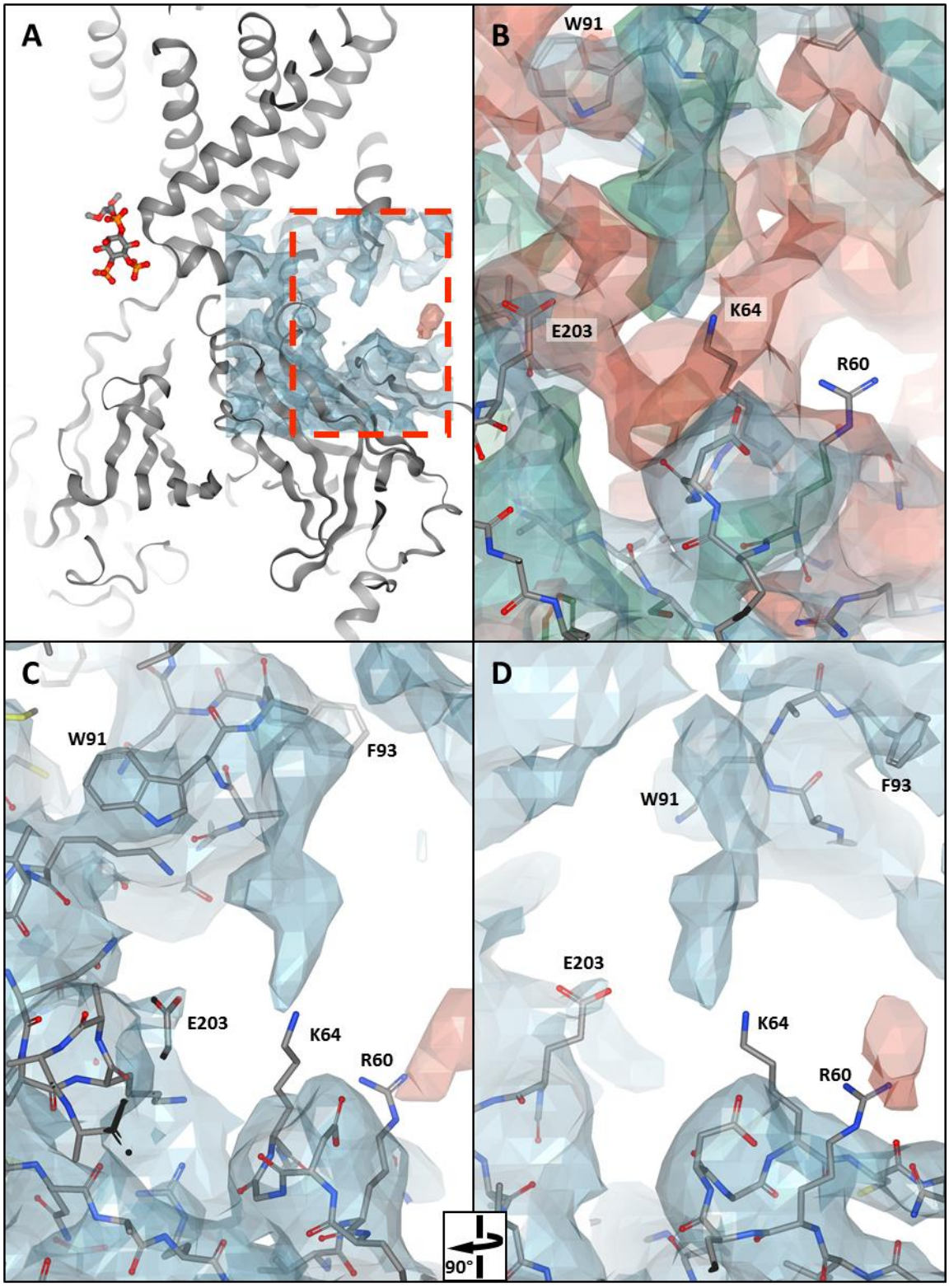

Figure 37: Subsets from difference and composite electronic-density maps of PDB:3SYQ (Whorton and MacKinnon, Cell, 2011) showing electron densities not accounted for in the final model near K64. (A) Fraction of 2Fo-Fc map (contour 0.4σ) centered at the expected PIP_2 binding pocket in one of the mouse Kir3.2 subunits where no bound C_8-PIP_2 is modeled. The final model of the channel is shown as a cartoon drawing, and one of the C_8-PIP_2 molecules is shown in sticks representation. (B) Zoom-in on the boxed region of panel A, showing overlaid Fc-Fc (contour 0.8σ) and 2Fo-Fc (contour 0.4σ) maps. (C) Zoom-in on the boxed region of panel A, showing the 2Fo-Fc map (contour 0.4σ). (D) Same representation as panel C, after 90° rotation to the left around the normal of the membrane and centered at the Nζ atom of K64. Rendering was made using the online facilities of RCSB PDB website (www.rcsb.org).

presence of Na^+. However, the conformations of PDB:3SYQ strongly suggest that the binding of the PIP_2 at the C-linker decreased certain steric constraints on the βH-βI strands (and the TM2 containing the HBC gate), hence allowing the displacement of the βH-βI loop away from the center of the permeation pathway. Consistently, in my own work (exposed in the previous sections), I explored the possibility of PIP_2 bound at K64/R60 (Site 2) and not fully bound to the C-linker (Site 1). I have implemented constraints meant to move $_{(Site\ 1)}PIP_2$ towards $_{(Site\ 2)}PIP_2$ in *Simulations III*, *IV*, *V*, *VI* and I explicitly saturated the R60/K64 interaction site with additional PIP_2 in *Simulations VII*, *VIII* (see the dedicated subsections of the chapter). These manipulations of the simulated systems allowed me to observe conformational changes which provided me with the bases for speculation on the existence of intra-subunit allosteric pathway involving the N_{ter}, the βH-βI strands and the C-liner.

Given the previous discussion, I will now invite my own interpretation of the facts about the role of the Na^+ binding to the channel and the particular role of the R201A and the D228N mutations. The mechanism which I propose for the events concerning the Na^+ binding to mmKir3.2 is the following: the Na^+ bound to the vault of the βC-βD loop where it mostly interacted with carbonyl oxygens, as a result the volume between the βC-βD loop and the βA strand swells because the Na^+ ion have to keep some of its hydration shell as it is most certainly repelled by the sidechain of H69; the Na^+ binding causes the βC-βD loop to approach and stabilize the N-terminus of the βH-βI loop, thus opening the constriction of the G-loop gate at the M313. A similar remark about the swelling of the volume between the βA strand and the βC-βD loop could be made regarding the H69Q mutation which also increases the magnitude of the recorded currents (Inanobe et al. 2010), while the contrary remark would be possibly addressed to the substitution Kir3.4(H64F) which causes loss of the channel activity (He, Yan, Zhang, et al. 2002). In this last case, the effect could be attributed to a gate-keeping role played by the phenylalanine (H64F) preventing the hydrated Na^+ to stabilize in its binding site – I make this suggestion simply by drawing a parallel from protein sequence involving the couple F59/K219 in Na^+ insensitive channel Kir2.1. In Kir3.2, the βC-βD loop at the end of the rearrangement was maintained by the D228/R201 salt-bridge to the C-linker, but there was also a significant stabilizing contribution due to the T204/L229 and V206/L229 hydrophobic interfaces. Equally, the βC-βD loop was stabilized to the slide helix by the R230/D81 salt-bridge and the L229/V72 and L229/Y78 hydrophobic interfaces and the R230/Y78 cation-π interaction. These interactions combined with the Na^+ ligation to the βC-βD loop would push the C-linker and the slide helix slightly towards the membrane. At this point the C-linker would be more prone to interact with PIP_2 molecules approaching or already in place in the crystallographic binding pocket, hence Na^+ would increase the PIP_2 affinity of the channel (Wang et al. 2016). The sum of the Na^+ and the PIP_2 binding in the wild-type mmKir3.2 are schematized in panel D of Figure 38, the description of these events was made on the basis of the crystallographic models PDB:3SYO for the Na^+ binding and PDB:3SYQ for the NA^+ and PIP_2 binding, as well I have referred to information from the literature and to my own observations of the simulated trajectories where the mmKir3.2 channel was set in presence of various combinations of activator partners (see the previous sections in this chapter).

The next step of the model described in Figure 38 is the Gβγ binding, I think this triggered the intra-subunit allosteric pathway starting at the N_{ter} and propagated until the C-linker and the G-loop gate. In this series of events, the C-linker jointly with the distal N_{ter} were further moved towards the membrane and by pulling on the βH-βI loop/strands allowed M319 at the apex of the G-loop gate to be displaced away from the center of the pore (Figure 38A). On the contrary, the energy of the downwards return of the C-linker which pushed the apex of the G-loop gate towards the closed state is tuned by the D228/R201 salt-bridge. I assume that this strong interaction prevented the long-lasting opening of the G-loop gate in contrast to the D228N or the R201A mutations (see discussion below). In panel A, the return of the C-linker downwards is represented by a solid red arrow, which should evoke the finite strength in this mechanism acting in the wild-type channel. Thereafter, as demonstrated by *Simulation 0*, once the bound G-proteins, Na^+ and PIP_2 were completely removed from the channel, the gates closed rapidly (Figure 38G). However, the consideration of the

interaction of PIP_2 bound only to K64/R60 (whose shadow can be observed in PDB:3SYQ (Figure 37), and an interaction which persistently occurred in the simulations that I made) strongly suggests that the closure of the G-loop and the HBC gate could be achieved by a mild displacement of the PIP_2 towards the channel's N_{ter}. Based on these findings I predict that the mmKir3.2 channel uses a negative self-feet-back mechanism to close the G-loop and the HBC gate, independently from the Gβγ and PIP_2 depleting pathways present in parallel in the cell.

I now turn my focus to the D228N mutant. Since Na^+ and PIP_2 were sufficient to activate atrial Kir3 channels (Mintert et al. 2007) and since the mmKir3.2(D228N) increases I_{basal} (Whorton and

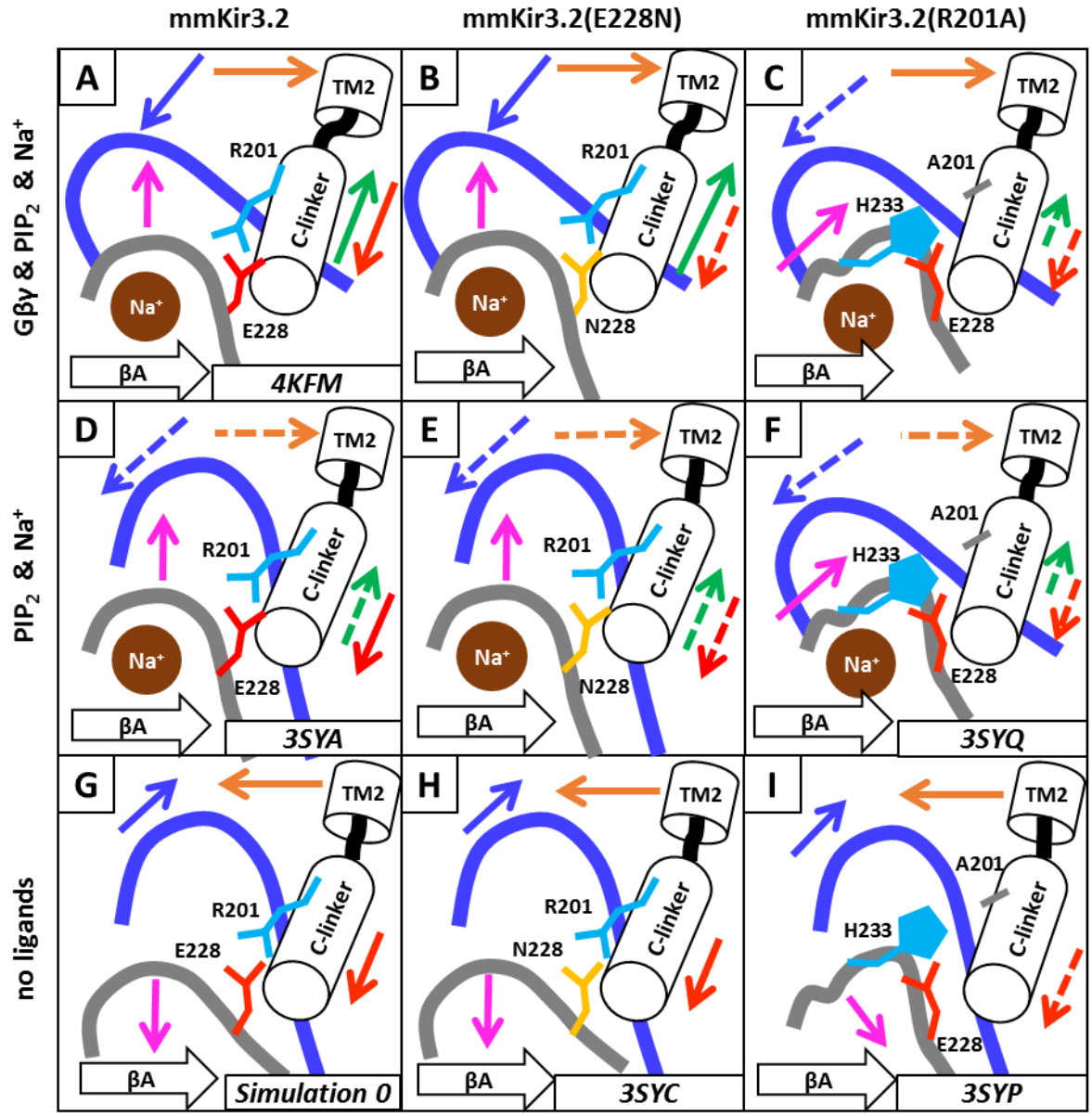

Figure 38: Putative mechanism of activation of the HBC and the G-loop gates of mouse Kir3.2, derived from results of molecular dynamic simulations, crystallographic models and whole cell recordings. The trace schematics embraces the interactions between the βC-βD loop (grey), the βH-βI loop (blue), the N-terminus of the TM2 helix and the C-linker in the same subunit. The direction of motion of secondary structures observed in each condition from experimental models or the simulations is represented by solid arrows, while the dashed style arrows indicate the putative direction of the motion deduced by the results of experimental recordings. The arrow colors are used as follows: βC-βD loop (magenta), βH-βI loop (blue), HBC gate (orange), C-linker in presence of Gβγ (green) and immediately after Gβγ unbound (red). Question marks near an arrow mean that the direction of the motion was deduced from the recorded phenotype presented in the study by Whorton and MacKinnon in 2011, where the R201A and D228N mutants were reported.

MacKinnon 2011), it follows that the D228N mutation in Kir3.2 increases the entropy of the C-linker – similar to the native Kir3.1 monomers do in the atrial channels (Touhara, Wang, and Mackinnon 2016). Hence, I suppose that in the basal state, mmKir3.2(D228N) also bound Na^+ and PIP_2 (Figure 38E), I think this is true because the G-loop gate in PDB:3SYC was very narrow in comparison to PDB:3SYO – suggesting that the D228N mutation was not sufficient to modify the gate by itself. The recorded increase of I_{basal} of mmKir3.2(D228N) (Inanobe et al. 2010; Whorton and MacKinnon 2011), requires however the opening of the G-loop gate which, I think, was made possible by low-amplitude fluctuations of the C-linker (schematized by dashed green and red arrows in Figure 38E). The magnitude of these fluctuations remained minor compared to the subsequent stabilization of the C-linker during the simulation in presence of G-proteins. Notably, I suppose that the conformational changes of the activation are the same as in the wild-type channel, this is schematized by a solid green arrow in panel B of Figure 38. There is a rational line that backup my suggestion, it appears to me that the length of the atomic material organized between Cα at position 228 and Cα at position 201 is of significant importance – indeed, it is the same in the wild-type and in the D228N mutant and provided large activation during *Ach* application, while in the R201A mutant this length is constitutively reduced and could not be efficiently used to induce large rigid-body motion displacing the C-linker. In consequence, the R201A mutant exhibit I_{basal} similar to I_{max}, but also I_{max} of R201A channels is dramatically reduced compared to the native mmKir3.2, taken together these facts suggest that the increased I_{basal} of R201A mutant is primarily due to the uncoupling of the C-linker from the βC-βD loop, while the decreased channel conductance can be easily attributed to the defect of the mechanism displacing the C-linker suggested above (Figure 38C, F). Furthermore, I would like to state a probable cause for the apparent increase of the unitary conductance of mmKir3.2(D228N). I suppose that suitable explanation can be make if one considers an increase of the open probability of this mutant channel. It is indeed, easy to admit that the N228 would increase the entropy of the C-linker and in consequence it should decrease the probability of the "back-journey" of the C-linker downwards to interact βC-βD loop and hence to push on the Hβ-Iβ loop – resulting in a delay in the closure of the G-loop gate. This mechanism explains the increased I_{basal} of the mmKir3.2(D228N), and also nicely predicts that in presence of Gβγ – the C-linker would be further stabilized towards the membrane (which contains PIP_2, and will increase the affinity of the cannel for PIP_2 – in fact this is not a pure prediction because this behavior is documented elsewhere (Inanobe et al. 2010)) resulting in the experimentally observed thorough increase of the current during the *Ach* stimulation of the mmKir3.2(D228N).

A study has been recently published providing additional evidence against the initial hypothesis that the conformation states generated by the R201A mutant are to be native-like (Adney et al. 2015). The aim of this study was to shed light on whether S196 is involved in the PKC-induced inhibition of Kir3.2 channels. Authors tested phosphorylation-like mutant S196E and the phosphorylation site neutralizing mutant S196Q and they found that the S196E mostly preserved the amplitude of the recorded basal current and led to a slight decrease of the PKC induced inhibition of the channel, while the S196Q caused the channel to conduct only a small fraction of the native current, but markedly increased the rate of the inhibition after PKC stimulation. Authors also found that the S196E mutation was not PIP_2 mimetic, because when the PIP_2 levels in the membrane were decreased by inhibition of the phosphoinositol-4-kynaze, the mutant channel had decreased conductance falling in the range of the wild-type channel. Additionally, authors performed MD modeling which showed that S196E (as well as the phosphoserine (SEP)) competed with D228 and eventually coordinated R201, leading to the rearrangement of the HBC gate to increase the minimal opening of the gate – unluckily, these predictions were not successfully validated experimentally by the attempted exchange of the positions of the salt bridge partners (S196R/R201E). Eventually, authors proposed that S196 is constitutively phosphorylated but that it is not modified during activation of PKC which results in the inhibition of the channel, the putative interaction SEP196/R210 would thus limit the inhibition which would be operated on some other, unknown direct phosphorylation target. Despite the promising interpretation of the obtained results in the light of

the activating mechanism of the channel, a critical view on this study should be made because authors simultaneously implemented great number of mutations (up to three E152D, R201A, D228N) in an undoubtably functionally critical region. Very importantly, the use of the E152D in all subsequent constructs inserts a major bias due to the fact that it is suspected that this residue tweaks the PIP_2 affinity of the channel (Adney et al. 2015), while in my opinion this mutation destabilizes the helix bundle in the closed state, thus it seems that the activation of the channel is obtained at lower PIP_2 concentrations – which eventually is the same as to measure the increase of the apparent PIP_2 affinity and oversimplify the underlaying process. While S196Q/E mutations reasonably approached the volume of the proposed SEP196 and could preserve the protein from locally repacking – except for the electrostatic compensation as demonstrated by the reorientation of the sidechain of R201 to interact with SEP196 or E196 – authors did not point to any rearrangements in the region where the D228/R201 interaction was initially before R201 rotated to interact with E196 or SEP196. If the lack of such a repacking around D228 can be justified by the shortness of the simulations, there is no information about the fate of Na^+ which could delocalize on a faster timescale and expectedly interact with the sidechain of D288 – in line with the mechanism accepted in the research community. Moreover, such a rearrangement would further open the G-loop gate, as can be expected in projection with the conformation observed in the crystallographic model PDB:3SYQ, where in presence of PIP_2 and absence of the sidechain of R201, it could be seen that H233 interacted with D288, causing important changes in the βC-βD and the βH-βI loops. It is also unclear why the proposed constitutive phosphoserine at position 196 was not caught in the crystallographic models obtained from proteins produced in *P. pastoris* (Whorton and MacKinnon 2011, 2013). Authors also missed to demonstrate any result of modeling of the Kir3.2(SEP196, D228N) mutant which experimental conductance is increased by two-fold compared to the wild-type – in this modeling one should expect to observe the SEP196/R201 interaction in absence of the competitive contribution of D228. Despite the very tempting conclusions drawn from this study, I think that due to the high risk of obtaining divergent phenotypes simply by mutations in the region of the channel gates and subsequently miss-correlating them to a distant process such as PKC inhibition, an additional work could benefit by the insight that my work provided about multiple PIP_2 binding sites – to first establish a irrefutable baseline for the wild type and subsequently and parsimoniously model the effect of SEP196/R201 in the background of the native D228. I think this is important because the modeling reported by the authors showed a very strong two-fold symmetric distortion of the HBC gate with final minimal opening incompatible with water and K^+ permeation. In comparison, in *Simulation V* and *Simulation VI* I obtained better results regarding the opening of the HBC gate using stabilization of the slide helix mediated by additional PIP_2, thus the mechanism presented in Figure 38 constructed in the ignorance of the SEP196 could represent yet another possibility in the apparently huge conformational space of Kir3.2 channel.

5.9 *Conclusion and perspectives for application and future research*

Since we desired to investigate the molecular dynamics of Kir3 channels, we oriented our approach to first establish a reproducible protocol for the activation of an experimentally determined structure of a channel in this family. A reasonable approach ought to use the most representative crystallographic model available to date. The co-crystal of a mouse homotetrameric Kir3.2 with Gβγ dimers of the heterotrimeric G-protein, Na^+ and PIP_2, gave the opportunity to appreciate a Kir3.3 channel in its pre-activated conformational state. The ease to use this model as a starting point for the study was dictated by the fact that in comparison to the other crystallographic models of Kir3.2 channels, it required the least amount of reconstruction of unresolved parts of the channels.

The simulation of the full crystallographic model PDB:4KFM embedded into a POPC bilayer and solvated into a saline solution filled simulation box (*Simulation IX*) showed a channel conformation remaining similar to the initial state for approximately 400 ns, thus suggesting high stability of the channel in presence of the particular combination of partners. It also allowed K^+ to permeate in the

inward direction in agreement with the experimental behavior, while the Kir3.2 channel was interacting with Gβγ, PIP_2 and Na^+. When inspecting the produced dynamics in more details, I detected that after the crystal-packing bias was removed (release of the constraints on the protein after equilibration), a rapid opening of the HBC gate occurred, and it was maintained until the end of the simulation. The structure was conductive until a point in the last third of the simulation, when the G-loop gate stopped the inward K^+ flux, a closure which was sufficiently operated at one sole subunit. A replica simulation not presented in this report was started with the same atomic constituents– it was run for only 200 ns (data not shown). Regrettably, at the beginning of this simulation the G-loop gate got rapidly occluded by a single sidechain of a M319 residue which took a conformation not frequently seen in the previous simulations we performed. Due to the low yield of simulated time, it was decided not to extend this simulation and wait for the gate to recover a permeant conformation.

The opposite to the molecular setup with the full crystallographic model included the Kir3.2 channel in absence of any ligands (*Simulation 0*). The simulation of this system also produced a straightforward conformational change in accordance with the functional experimental behavior of the channel. The HBC gate closed very rapidly, an associated stabilization of the selectivity filter was observed, and the G-loop gate also adopted a hermetic conformation. These results confirmed the power of simulation methodology to reproduce experimental features of the Kir3.2 channel.

The computational productivity with the full crystallographic model was and remained a concern for us during this project. Indeed, the reproduced conductive phenotype with the full crystallographic model was great news, but it came to a relatively high computational cost due to the size of the system – and in reality, it was only attempted at the very end of the work on the project once our computer had done simulating the other systems presented below. In order to increase productivity, we thought about accelerated-sampling methods like the application of boost potentials or steered dynamics. In both cases, we needed specific knowledge of the unbiased dynamics of the system first. Back in the days, the full crystallographic model was simulated with a productivity of 6 ns/day, and taking into account the required periods for queuing at the cluster we were using, the continuation of the project in such conditions appeared unacceptable. Regrettably, we did not have a well-established testing protocol yet, and we did not attempt the application for dedicated computational time in the scope of HPC sharing initiatives like the Partnership for Advanced Computing in Europe (PRACE). Regarding the simulation protocol itself, the use of steered dynamics was not a novelty to the research field, because soon before we started this project, a study was published where a homology model of Kir2.1 in the closed state was steered by 500 kcal/mol applied on special parts of the channel towards another homology model representing an open state of the channel (J. Li et al. 2015a). However, we wanted to avoid the use of such drastic conditions and most importantly the use of homology modeling based on conformations of the protein with unproven relevance to the function of the wild-type channel – thus the steered dynamics methodology did not become our principal choice.

While seeking to stimulate the opening of the channel when G-proteins were removed, we decided to go by another rout – allowing us to speed up the calculation by reducing the size of the system to cut roughly by half the number of atoms in the simulation box in comparison with the requirements for the full PDB:4KFM, respectively 191K vs. 446K atoms. Such a strategy did not seem far-fetched with regard to the expectation of opening the channel, because there was at least one experimental option – a functional mutation activating the channel without explicit G-protein stimulation, R201A (Whorton and MacKinnon 2011). We disliked this option too, first because it would have repeated the approach of Li and coworkers (J. Li et al. 2015a) and second, the simulation of an activating mutant would most probably have influenced the modeling of other mutations that we were seeking to investigate, such as Kir3.1(F317S) (Chan et al. 1996). We eventually decided to “go all in” on an alternative hypothesis – partially verified by previous experimental research. Thus, we began to simulate mmKir3.2 with small alcohol molecules into a hydrophobic pocket, mapped experimentally

by both functional and mutagenesis studies, and by X-ray crystallography of the CTCD of Kir3.1 co-crystalized with ethanol, and the CTCD of Kir2.1 crystalized with methyl-pentane-diol. Based on the assumption that PIP_2, Na^+ and alcohol would be sufficient to activate the channel, we constructed a simulation box and further implemented a number of combinations of parameters, including restraints on the alcohol ligand because it was diffusing too fast from the binding pocket, and also changing the magnitude of the external electric field providing the driving force for the K^+ through the pore. The results, though, were not conclusive and the channel mostly conducted K^+ when an exaggerated driving force was provided by the simulated membrane potential of 1.3 V.

The next generation of the molecular setups of the simulation box turned out to be remarkably fruitful. At the beginning, our attention was drawn to the recently identified secondary binding site for anionic lipids in the homologous Kir2.2 channel (S. J. Lee et al. 2013). Remarkably, the position of the secondary binding site first shown by docking of different lipids coincides with the location of the DDM detergent molecule observed in the crystallographic model PDB:4KFM. At first sight, the observation seemed hardly exploitable in the scope of our project, but the same team has more recently published a study where a functional mutation favoring the protein-membrane interactions was implemented in this region of interest (S.-J. Lee et al. 2016). We thus investigated the possibility that there might be an equivalent secondary site at the slide helix of Kir3.2 channel for interaction with negatively charged lipids in the intracellular leaflet of the cell membrane. Indeed, by increasing interactions between the slide helix and the membrane, for the first time, we were able to observe spontaneous K^+ crossing the G-loop gate in the outward direction, which was a straightforward suggestion that the gate was open.

In total we tested five different combination of ligands interacting with mmKir3.2. In addition to lipid partners, in all conditions (except for the apo-state *Simulation 0*) weakly constrained Na^+ and alcohol were modeled in each binding site on the tetramer. First, in direct transposition of the data published by Lee and coworkers about Kir2.1, we added POPG lipids into the setup of our simulation box already containing $_{(Site\ 1)}PIP_2$, Na^+ and alcohol methyl-pentane-diol (MPD). Despite the observed spontaneous capacity of interaction with the slide helix, the POPG required continued weak harmonic restraints (2 kcal/mol/Å) to remain near the slide helix during the entire simulated period of 400 ns. As a result, the G-loop gate was observed permeant in both directions (data not shown). Thereafter, we substituted the additional POPG by PIP_2 and the alcohol MPD with propanol (PrOH) – we observed that the PIP_2 interacted stably with residue R73 without requiring an external force. In parallel, we noticed that the PIP_2 interacting freely with the C-linker could be deviated to interact more frequently with R60 and K64 in the N-terminus, thus destabilizing the HBC gate connected to the concerned C-linker. These observations led us to implement two combinations where PIP_2 interacted with different sites of the channel, these sites were: C-linker (Site 1), N-terminus (Site 2), and slide helix (Site 3). In one of the setups, in addition to the $_{(Site\ 1)}PIP_2$, four more PIP_2 molecules were conditioned near residues R73 (replica simulations *Simulation V* and *Simulation VI*). In the other setup, a total of twelve PIP_2 were placed near the C-linker, slide helix and N_{ter} of each subunit (replica simulations *Simulation VII* and *Simulation VIII*). The other two molecular setups consisted of the simulation of Kir3.2 without PIP_2 but with Na^+ and PrOH (*Simulation I* and *Simulation II*), and with additional $_{(Site\ 1)}PIP_2$ (*Simulation III* and *Simulation IV*).

In accordance with the experiments, our simulation showed that the transport of K^+ through the transmembrane vestibule required interactions between PIP_2 and the C-linker of the channel. In the absence of $_{(Site\ 1)}PIP_2$, the hydrophobic gating phenomenon occurred in less than 100 ns when the channel was simulated without any additional partners, and the closure of the HBC gate took approximately 400 ns in simulation where only Na^+ and PrOH partnered the channel. Interestingly, the closure of the HBC gate was generally slower than the closure of the G-loop gate – the presence of long hydrophobic sidechains borne by M313/M319 at two levels of the gate conferred higher entropy to the G-loop gate compared to the HBC gate where the sidechains of residues F192 and V188 were displaced by rigid body motions of the TM2. Moreover, the gating involving M313 or

M319 occurred in different modes depending on the presence of PIP_2 interacting with the C-linker. In absence of PIP_2, residue M313 was also involved in the gating phenomenon, while when PIP_2 molecules were interacting with the C-linker, it was M319 which most often blocked the gate. In fact, in all simulations, the measured bottleneck of the G-loop gate first shrunk under the effect of the sidechains of M319 entering the permeation pathway and in the cases when PIP_2 was present, the gate most often recovered an open conformation. Remarkably, in almost all permeant conformations of the G-loop gate, we identified a skewed to two-fold symmetric organization of the backbone of the gate. In these conditions, without the gating intervention from M313/M319, the gate remained permeant even at a bottleneck radius measure below the generally admitted requirement for the hydrated K^+.

We highlighted the fact that the inward transport through the G-loop gate occurred even when the G-loop gate was not widely extended. Surprisingly, the transport was facilitated by dehydration of the transported K^+ which was operated by carbonyl and alcohol oxygen atoms lining the G-loop gate (Figure 18) – conditions somehow resembling the selectivity filter of the potassium channels. We further identified that these conditions could be changed either by the occlusion of the lumen of the gate by the hydrophobic sidechains of M313/M319, or by conformational dynamics leading to the substitution of the suggested oxygens by the exposure of nitrogen atoms from the backbone of the βH-βI loops. Thus, in our simulations, in the event of inwardly permeating K^+, we were not convinced that the channel was in a fully activated state. This uncertainty had a multivariate foundation – once the HBC gate was hydrated and the driving force allowed the inwardly delocalization of K^+ from the selectivity filter into the TMV, the subsequent K^+ transport through the G-loop gate was almost never obtained. On the other hand, the transport in the outward direction was only observed when the G-loop gate was in an extended conformation. The outward transport of K^+ occurred when the hydrophobic sidechains of all M313/M319 were off the permeation pathway and the centers of the carbonyl oxygens of G318 from opposite subunits were distant for at least 8 Å from one another. Thus, both diagonals of the gate fluctuated around 8 Å in the four-fold symmetric conformations and when a two-fold symmetry of the diagonals was involved, the shortest diagonal had to be of 8 Å for the outward K^+ transport to occur. However, these conformations never resembled the expected 13 Å symmetric opening of the G-loop gate, suggested from the projection of the largest opening of the G-loop gate observed in the two-fold symmetric conformation of mmKir3.2(R201A) activating mutant (Whorton and MacKinnon 2011). We think that the observed dehydration of inwardly transported K^+ through the G-loop gate is of fundamental importance; thus, we allow ourselves to speculate that this phenomenon could contribute to the inward K^+ transport recorded experimentally – which is the major functional feature exploited to study Kir channels.

The incorporations of additional PIP_2 beyond the canonical PIP_2 interacting with the C-linker resulted in a pattern of increase of the open gate conformations. On the one hand, interactions with R73 could be possible only with Kir3.2 among the members of the Kir3 sub-sub-family – and would potentially explain why Kir3.2 homomers are recorded as electrically more active than other homomeric assemblies of the Kir3 proteins. These novel interactions are hard to be ruled out as unphysiological, especially in the light of the recent publication of the study by Glasser and colleagues, where Kir3.2 was activated in a reconstituted artificial membrane environment by the combination of PIP_2, NA^+ and EtOH (Glaaser and Slesinger 2017). Put aside whose work preceded the other, these conditions experimentally replicated our simulation box and we believe serve as validation to our findings. On the other hand, the presence of additional $_{(Site\ 2)}PIP_2$ implemented in *Simulation VII* and *Simulation VIII* led to the prevention of the depletion of Site 1. One way to analyze it would be to claim that at very high concentrations of PIP_2 into the membrane it would saturate Site 2 and thus the channel would undergo a high open probability phase. This suggestion could also be true as it is hard to imagine and even harder to confirm that during a burst of activity of the Kir3 channel, there could only be exactly four PIP_2 molecules in its vicinity. However, another way to think about the functional role of the increased interactions of PIP_2 with the N_{ter} would be as follows:

during the activation burst, $_{(Site\ 1)}$PIP2 interacts with the C-linker, the activation of the channel requires also alcohol or G-proteins which cause the N_{ter} to move towards the membrane and to approach Site 1, eventually residues R60 and K64 engage $_{(Site\ 1)}PIP_2$ which loses tight contacts with the C-linker and in consequence, the HBC gate becomes destabilized – this is a perfect example of an auto-negative-feedback loop. Remarkably, we were able to find experimental confirmation of this hypothesis (Figure 37) in the dated raw data of the crystallographic model PDB:3SYQ (Whorton and MacKinnon 2011).

We also explored in depth the conformational dynamics obtained by the various molecular setups. We found correlations between dynamical phenomena and the activated/open and the inactivated/gated channel conformations. In the main text of the manuscript, multiple pieces of evidence led to the emergence of two important hallmarks of the allosteric activation of the Kir3.2 channel. The first one involves the control of the selectivity filter through the interactions of the pore helix with the TM bundle. As it has already been shown and suggested elsewhere, this coupling between the filter and the TM bundle appears to be a common mechanism among K^+ channels. Furthermore, this observation is in line with the proposed mechanism for the opening of the HBC by the PIP_2 (J. Li et al. 2015a). Observation from our data showed that the enlargement of the TM bundle under the influence of the binding of PIP_2 led to the increase of the entropy of the selectivity filter, which most probably decreased the binding affinity of the filter for the encaged K^+. Thus, the flickering of the filter allowed the K^+ transport to take place in all simulation setups where at least $_{(Site\ 1)}PIP_2$ was present. It is important that our data has captured this behavior and that we have been able to identify it correctly by the use of the in-house implemented analysis scripts (using standard libraries to handle MD trajectories and standard libraries for scientific data analysis). The second group of observations highlighted a pathway of conformational rearrangements leading to the control of the cytosolic and the hydrophobic gates (Figure 20, Figure 21, Figure 27, Figure 29, Figure 33, Figure 34). Importantly, since the release of the conformational constraints on the selectivity filter are under the influence of the TM bundle, the identified allosteric pathway stimulating the G-loop gate and the HBC gate appears to be a unifying activation mechanism encompassing all the functional gating elements of the Kir3.2 channel.

The allosteric mechanism in the CTCD that we observed appears to have two components propagating from interaction sites involving simultaneously three adjacent subunits. These two components can be arbitrarily separated as shown in the filtered differential contact-maps that we produced. However, their reunion into a common center where their action appears to be projected on the G-loop and the HBC gates of the central subunit in the considered triplet. The separation of the allosteric components is allowed by the fact that two adjacent G-protein binding sites are involved simultaneously; thus, it appears that both components of the allosteric pathways are independently controlled while spanning the CTCD part of one subunit in the Kir3.2 homotetramer at the time. It would be convenient to refer to both allosteric pathways as left and right with respect to the C-linker of the central subunit – both the pathways are depicted in panel A of Figure 33, where both the left (green) and the right (red) are highlighted in the subunit colored in grey, while only the right pathway is represented in the clockwise-standing blue subunit. Interestingly, in MD trajectories that were simulated, we identified that the conformation of the highly flexible distal N-terminus was very important for the outcome of the right pathway, while at the same time this pathway appeared to be under the positive influence of the binding of the Na^+ ion inside the dedicated binding pocket – which is located in the left allosteric pathway. This proposed reunion and quasi-subordinance of the right under the left pathways, is in adequacy with the current understanding of the role of the Na^+ ions which potentates the affinity for G-proteins of the Kir3.2 homotetramers (Wang et al. 2016) and parallel to the increase of the apparent affinity for PIP_2 (Rosenhouse-dantsker et al. 2014).

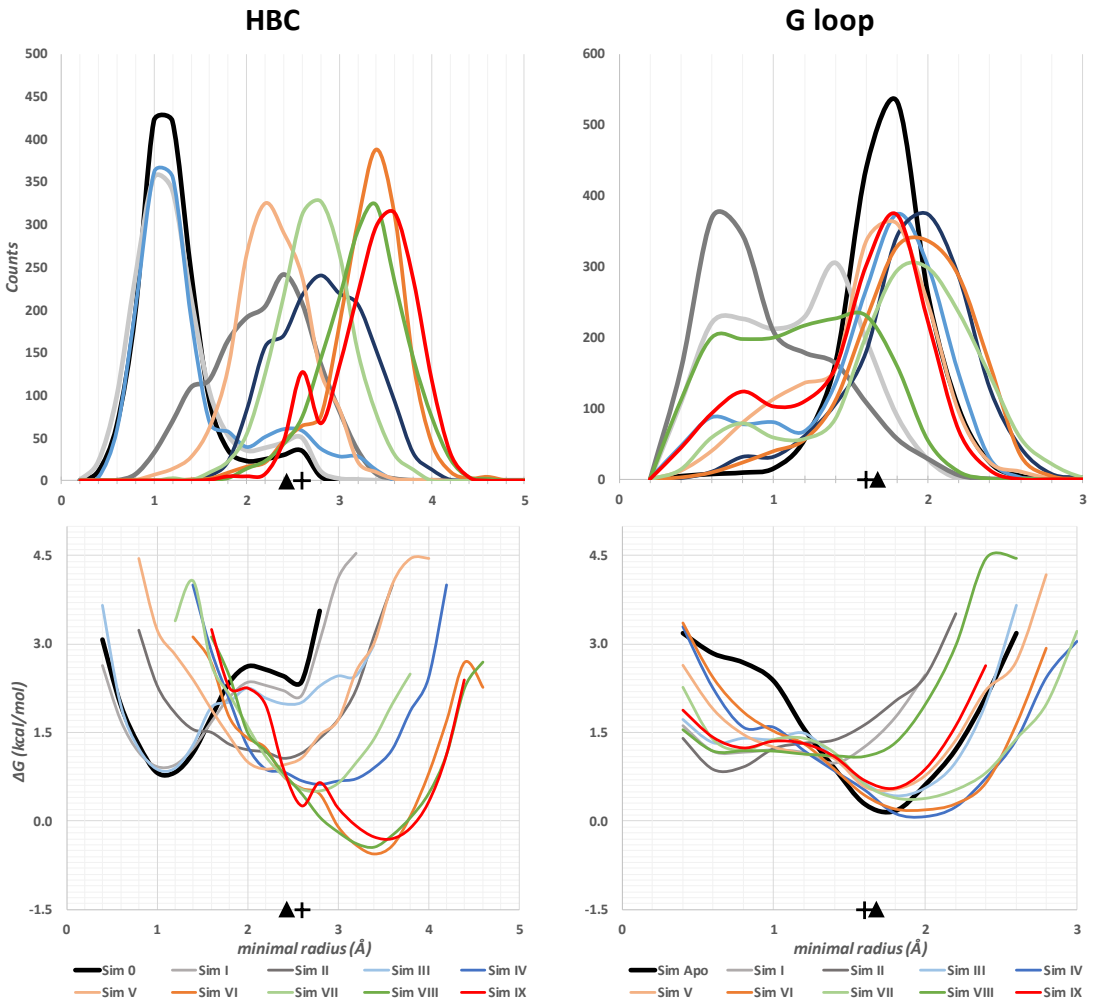

Figure 39: Histograms and the associated free energy profiles of the minimal radii of the HBC and the G-loop gates, obtained by MD simulation of mmKir3.2. In each simulation box setup, channel's starting conformation was taken from PDB:4KFM and the number of ligands PIP_2, Na^+ and PrOH interacting with the channel vas varied. Sim 0: no ligands. Sim I, II: Na^+ and PrOH. Sim III, IV: $_{(Site\ 1)}PIP_2$, Na^+ and PrOH. Sim V, VI: $_{(Site\ 1)(Site\ 2)}PIP_2$, Na^+ and PrOH. Sim VII, VIII: $_{(Site\ 1)(Site\ 2)(Site\ 3)}PIP_2$, Na^+ and PrOH/ Sim IX: simulation of the configuration of PDB:4KFM, i.e. mmKir3.2, Gβγ, $_{(Site\ 1)}PIP_2$, Na^+. The initial minimal radii are marked on the x axis by triangle (black): HBC gate r= 2.43 Å, G-loop gate r= 1.68 Å. The threshold radii discriminating between open (N_{open}) and closed states (N_{closed}) used for the ΔG calculation is marked on the x axis by a plus sign (black): HBC gate r= 2.6 Å, G-loop gate r= 1.6 Å. The free energy calculation was made by histogram method with bins of width dr= 0.2 Å, using the formula $\Delta G = -kT*ln(N_{bin}/N_{closed})$.

An overall conclusion about our results with the various molecular setups that we tested ought to be made highlining the fact that we were able to obtain activation profiles corresponding to that one would expect based on the current knowledge about the role of the activator small-molecules partnered with the Kir3.2 channels. We summarize the evolution of the dynamics of the G-loop and the HBC gates observed in all independent trajectories we have produced. Apart from the histograms of the measured minimal radii of the gates, we show a one-dimensional energy profile obtained by application of Boltzmann weighting to the later histograms. Except for one of the simulations where we modeled $_{(Site\ 1)}$PIP2 interacting with the channel, in all simulations the opening of the HBC gate was in agreement with the trend that $_{(Site\ 1)}$PIP2 is required for the opening of the HBC gate. However, we observed three modes of this opening. The first corresponding to the closed gate was obtained in absence of PIP2. The second mode was permeant and characterized by an opening similar to that of the starting structure. The third opening profile was characterized by an even greater opening than the starting conformation. Interestingly, the second and the third configurations of the HBC gate

were obtained when the channel interacted with the entire set of canonical activator partners (Simulation IX) or when we modeled PIP_2 molecules in addition to the $_{(Site\ 1)}PIP_2$. From the energic profile, it follows that the binding of the G-proteins, the $_{(Site\ 1)}PIP_2$ and the Na^+ drives the complex into a conformation which is separated from the closed state by at least -2.5 kcal/mol. Our data showed that similar separation of conformational states can be obtained when $_{(Site\ 3)}PIP_2$ interacts with R73 in the slide helices of the channels, but cannot be observed with only $_{(Site\ 1)}$PIP2 and ethanol, thus our hypothesis about the favorable interactions between the slide helix and the membrane, got additional evidence from the characterization of the energetic profile of the opening of the HBC gate. The equivalent profiling of the G-loop gate however present less clear separation between the simulations, demonstrating a mostly fluctuating behavior of the G-loop gate, which can be explained by the additional degrees of freedom of the residues in this gate as compared with the HBC gate. Moreover, it appeared that independently with the presence of activator molecules interacting with the Kir3.2, the G-loop can adopt both closed and opened conformations, what can be exploded by the low amplitude of the energy barrier between (> -1.5 kcal/mol) as observed in lower right panel of Figure 39 – interestingly, the small magnitude of the presented separation can be assigned easily to the rapid motions of the sidechains of residues M313 and M319.

Our work on this project was an overall success over the initial goals – the *in silico* activation of a Kir3 channel and the profound exploration of the mechanics of its molecular function. Significantly, we were able to optimize a set of conditions where by increasing the number of interactants with the channel we obtained a crescendo activation-like dynamic behavior. We made several observations related to and in adequation with independently published data mostly from experimental studies. Our main finding remained the insight that the Kir3.2 channel has multiple interaction sites for the integral membrane messenger lipid PIP_2 – beyond the well-known binding site on the C-linker and its close environment. Surprisingly, the observations that we made at a theoretical level of evidence have been indirectly confirmed experimentally by a very recent independent study (Glaaser and Slesinger 2017). Some of the interactions that we observed outside Site 1 had already been mentioned in other theoretical studies, but our work detailed for the first time the role of these and other completely novel PIP_2-Kir3.2 interactions, apparently having important roles in the activation and the inactivation paradigms of the molecular function of Kir3 channels. These findings could become useful to guide future experimental research. Regrettably, we were not able to reliably reproduce the conductive phenotype of the simulated channel – we identify two factors for the unfulfillment of this goal. First, our simulations were not long enough to explore the convergence of the conductance. And second, we did not use the most-advanced models to describe the K^+-protein interaction, such as the modern Drude polarizable force field (Hui Li et al. 2015). Thus, further efforts are required to efficiently reproduce the conductive phenotype of the Kir3, most probably by using finer-tuned forcefields to describe the interactions between the selectivity filter and the permeating K^+, however, we believe that such future endeavors would directly benefit from the molecular setup that we optimized for the activation of the Kir3.2 channel in absence of the G-protein activation.

6 Design of light-gated Kir3 channels: Results and discussion

A variety of strategies for the optical control of proteins are documented to date as being successfully used to control specifically ion channels (Banghart et al. 2004; Essen and Koert 2008; Gorostiza and Isacoff 2008; Cosentino et al. 2015; Moreau et al. 2017; Trads et al. 2017). To create photosensitive Kir3 channels, we chose to implement the strategy consisting in the labeling of these channels with photoisomerizable tethered ligands (PTLs) (Gorostiza and Isacoff 2008). In extension to the seminal use of tethered K^+ channel blockers (Blaustein et al. 2000), this technique has been successfully applied for the reversible photo-blocking of the selectivity filter of numerous potassium channels (Banghart et al. 2004; Fortin et al. 2011) and even for the activation of P2X2 channels by introduction of reversible conformational bias (Lemoine et al. 2013).

The successful application of the PTL technique to achieve reversible photo-control of Kir3 channels requires the labeling of native or engineered residues suitably located to use the geometry of the photo-sensitive ligand whose isomerization could introduce the desired change in the channels function. Thus, several parameters need to be simultaneously accounted for, while changes in each of them allow to explore different routes of optimization. Namely, parameters are: the geometry of the PTL, the particular functionalization of the PTL, the labeled position on the protein, additional protein engineering.

In this project we could not follow the most optimal designer route which is to cast the geometry and the chemistry of the PTL to fit specifically into a targeted region of the protein. This type of design can be greatly accelerated using computational techniques to rationalize the compounds design. Unfortunately, the results and the interpretations of the MD simulations from the first project did not come rapidly enough to supplement the available crystallographic models with expected interpretations of the dynamics of Kir3 in order to guide the rational design of new PTL compounds.

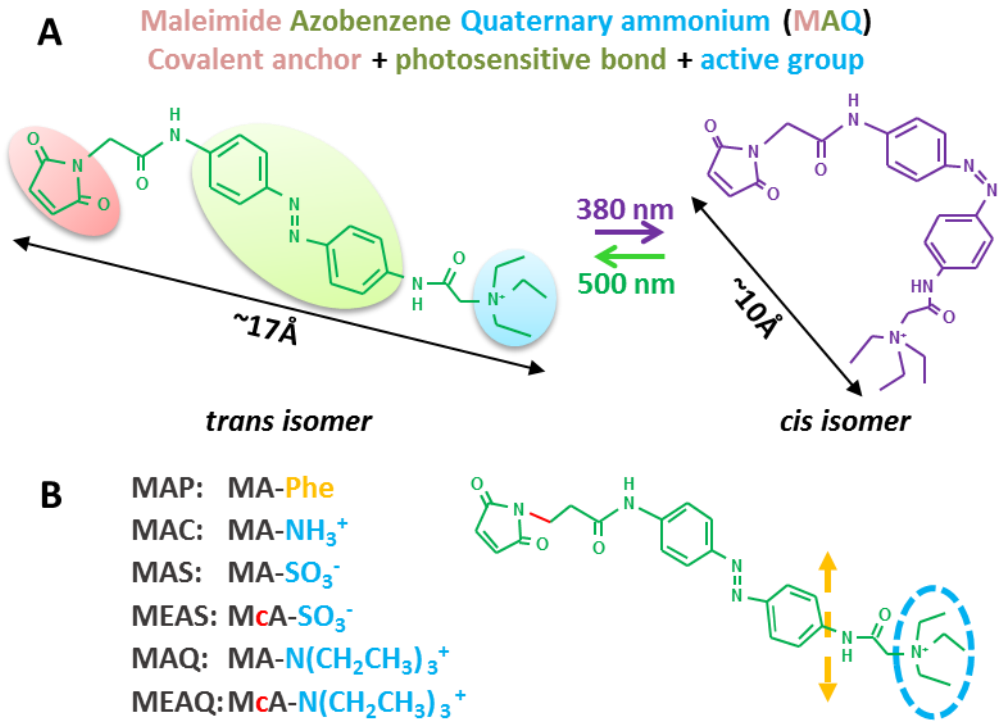

Figure 40: Photoisomerizable tethered ligands (PTLs) used in the project. (A) Schematics of the isomerization of MAQ tether. (B) List of all tested PTLs. The variable elements of the molecules are highlighted in the molecule name and in the 2D structure: functional groups (blue or orange), additional covalent bonds in the linker (red).

Furthermore, such rational-design scheme would have required considerable investments in computation, chemicals synthesis and time, above what we were able to provide for this side-project. We decided to use a limited number of PTL molecules which were already in our possession. The protocol used in this work consisted of a rationally-guided position selection and cysteine mutagenesis in order to iteratively test various PTLs (from a small compound library) for their ability to cause light-induced reversible changes in the function of Kir3 channels.

A PTL suitable for the assays according to our experimental strategy was already available in our lab – the maleimide-azobenzene-quaternary ammonium (MAL-AZO-QA or MAQ) (Figure 40A), originally developed by the Isacoff team (Banghart et al. 2004) – and was used successfully by my colleagues to photo-block engineered Kir6.2 channel (C. R., M. V., unpublished data). Later on, we acquired commercially available smaller photo-sensitive tethers commonly used as quenchers in fluorescence essays – the 4-phenylazophenylmaleimide (4-PAPM or MAP) (O'Malley and McDonald 1994). And more recently, our collaborator Guillaume Sandoz from the University of Nice generously provided us with four more PTLs. Eventually, we assembled a library of MAQ-like PTLs having different lengths and terminal function (Figure 40B). This collection of PTLs allowed us to test several molecules using the same batch of cells heterologously expressing the protein variants to study.

6.1 SELECTION OF POSITIONS FOR CYSTEINE MUTAGENESIS

The easiest way to covalently label a protein with a ligand is to target a reduced cysteine with a maleimide moiety (Baslé, Joubert, and Pucheault 2010). The reaction is spontaneous and irreversible at biological conditions (pH 6.5 - 7.5 and room temperature), it leads to the formation of a thioether bond by a Michal reaction mechanism involving the nucleophilic addition of the unsaturated alkene group of the maleimide to the nucleophilic thiol group of a cysteine on the protein side (Nanda and Lorsch 2014).

The initial step in the project was to select amino acids in the protein and to modify them using molecular biology to cysteines where the PTLs were to be grafted. The main challenge though was to find suitable positions for CYS mutation which would simultaneously be accessible to the tether and target a functionally important regions in the channel. Even before constituting the final PTL library, we already had a clear idea of the region of the protein to target. Since protein labeling is made by soaking the Xenopus oocytes or the cultured cells in a medium containing the PTL only for a brief period (max. 1 hour), we knew that the labeling would only be effective towards the extracellular region of the Kir3 channels – perhaps extending to the TM region close to the extracellular bulk provided possible diffusion of the PTLs into the cell membrane. The Kir3 proteins we chose to work with were the monomers of the human cardiac Kir3.1/Kir3.4 channel, because these proteins are commonly used in our lab and they have activated mutants allowing the expression of active homomeric channels, namely: hsKir3.1(F137S) (Chan et al. 1996) and hsKir3.4(S143T) (Vivaudou et al. 1997).

The first two positions tested were the positions which allowed the control by light of the Kir6.2 channel (C.R., and M.V., unpublished data). These target residues in Kir6.2 resemble those used to photo-block the Shaker channel and subsequently transposed to other channels (Banghart et al. 2004; Fortin et al. 2011). In hsKir3.1 these positions are A115 and G118, while in hsKir3.4 they are V121 and Q124. In mmKir3.2, whose crystallographic models were used as reference for the 3D structure-based decision making, these residues are I126 and P129. There are a number of mismatches near these residues between the Kir3 and the Kir6.2 sequences (Figure 41A). There are signs that the apex of the turret is differentially folded in Kir3 and Kir6.2 because proline-kink in both homologues is distant by four residues (P102 in mmKir6.2 and P129 in mmKir3.2). Thus there are doubts about the exact correspondence between the residues providing the best photo-block in Kir6.2 and where they might be in Kir3.We decided to start with the two positions in Kir3.1, A115 and G118 whose relative positions are presented in the mmKir3.2 channel in panel B of Figure 41. In this

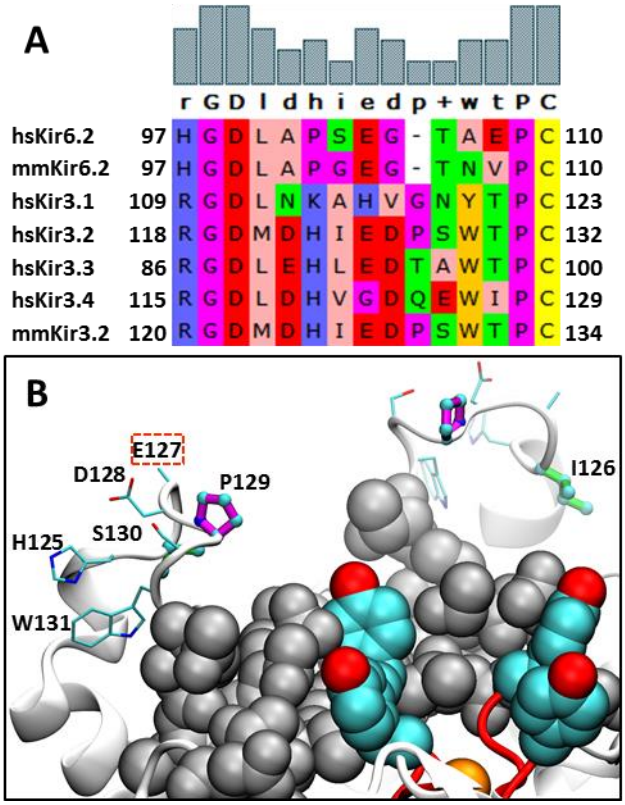

Figure 41: Model of Kir3.2 serving as reference to choose position for engineered cysteine mutations in Kir3.1. (A) Multiple-sequence alignment of part of the turret regions of Kir3 and Kir6.2 proteins showing the poor sequence homology in this region. (B) View of the turret region of two subunits of mmKir3.2 (PDB:4KFM) showing the relative position of the CYS mutations in the turret of hsKir3.1: hsKir3.1 A115 eq. mmKir3.2 I126 (green), hsKir3.1 G188 eq. mmKir3.2 P129 (magenta). Other residues of the turret are shown as thinner sticks. The label of residue E157 is boxed (red) to emphasize the lack of coordinates for the sidechain. The residues around the selectivity filter (red) are presented as vdW volume (grey) and the "gate keeper" residue Y159 is highlighted by standard coloring of the atoms.

representation it can be noticed that among all the residues in the apex of the turret of Kir3.2, all the residues in the range I126 to S130 are potentially suitable to test the grafted MAQ, because upon the presumed dynamical conformational changes of the turret region, they could orient their sidechains towards the filter. At the time I decided to wait for results of the MD modeling of mmKir3.2 to better understand the dynamics of this region, and the mutation to cysteine of the remaining residues was left aside to be tested later – regrettably I did not have time to continue working on them. A posteriori, in the light of the newly available electron-microscopy model of Kir6.2 (Martin et al. 2017) it seems that the position of residue S130 of mmKir3.2 is better aligned with the second best photo-blocking residue found in Kir6.2 (C. R., and M. V., unpublished data).

We were quite confident that the positions in the turret described above, if successful, would enable photo-blocking of the Kir3 channel. A much more attractive perspective was to achieve photo-activation of the channel. A recent reference showed such control for the P2X2 channel (Lemoine et al. 2013). The authors managed to activate the channel by labeling the V48 residue which is part of an inter-α-helices hydrophobic interaction network. Thus, a rule of thumb was set to select candidate positions for the cysteine mutagenesis in Kir3 – residues should be involved in inter-2D-structure interfaces in order to allow the effective transmission of conformational changes due to isomerization of the PTL. Finally, I reproduced already published results describing a "twist-to-open" collective motion predicted to be one of the largest during the opening of Kir family members (Bahar et al. 2010). This computation was made using only the mmKir3.2 crystallographic model, rather than homology models of Kir3.1 and Kir3.4 because the specificity of the construction of the elastic network accounted only for Cα atoms. Therefore, the Cα-Cα networks of the template mmKir3.2

were equivalent to those of the homology models due to the extremely high sequence identity among the Kir3 sub-family. The twist-to-open collective motion of mmKir3.2 appears to be best modeled by the first normal mode (mode 1). After filtering the contribution of each Cα in mode 1, I observed that the amplitude of the predicted displacement diminished with the increase of the depth inside the membrane towards the inner membrane leaflet (Figure 42A).Thus an additional rule for the selection of the positions of cysteine mutations became that only residues as deep as the third α-helix turn from the extracellular side of both TM helices should be considered. The last rule I tried to satisfy was to avoid an area of radius 17 Å around the extracellular entrance of the selectivity filter because I did not want yet to obtain a photo-blocking by binding of the MAQ to the filter.

It seemed difficult to effectively label a cysteine introduced deep into the TM domain because of the dense packing of the helix bundle. For this reason, all selected residues were located along the membrane-protein interface (assuming accessibility by the extracellular PTL solution) and not deeper than the third α-helix turn of the TM helices. The list of positions chosen which at least partially satisfied the above stated rules is presented as labels of the table in panel B of Figure 42. This table presents the entire space of possible mutagenesis experiments and functional tests. The tested constructs are marked as "+" or "-" signs, representing the success or the failure to record functional channels.

6.2 *FUNCTIONAL TESTS OF CYSTEINE MUTANTS*

The cysteine mutations (codon: *tgt*) were implemented into cDNA (cloned into *pXoom* vector) of the wild-type Kir3.1, Kir3.4 or the over-activated Kir3.1(F137S), Kir3.4(S143T) templates by a standard single site-oriented mutagenesis protocol and after amplification and purification from *XL10-Gold®* cells. They were systematically confirmed by Sanger sequencing of the entire coding sequences. The cDNAs were transcribed *in vitro* to single-stranded RNA (mRNA) and stored solubilized in RNAase-free demineralized water at -80 °C. Before microinjection into *Xenopus laevis* oocytes, the stock solutions were diluted to deliver 0.1-2.5 ng of mRNA/oocyte. mRNAs for the human δ-opioid and m2-muscarinic receptors were prepared (by other team members) and used in the same manner to deliver 2.5ng of mRNA/oocyte. The injected oocytes were incubated at 19 °C for 24-72 hours to allow the expression of the channels and the co-expressed GPCR.

The electrophysiology protocol used was simple. A representative trace of a TEVC recording obtained with this protocol is shown in panel C of Figure 42. The membrane potential was iteratively stepped to: 0 mV for 1 sec, -50 mV for 1 sec, 0 mV for 1 sec, 50 mV for 1 sec and 0 mV for 1 sec. This sequence of potentials constituted a "sweep". The iteration through the "sweep" protocol allowed to measure with a period of 5 sec the evolution of the K^+ permeability of the membrane. The 1-s duration of the voltage steps was much slower than the timescales of the channel gating and the period required for the rectification phenomenon to take place, enabling reliable measurements at all three membrane potentials. The steps at 0 mV, the expected reversal potential in our conditions, served to establish the zero-current. They also provided a transition between both extreme voltages of the protocol. The steps at +50 mV served to assess the leakiness of the membrane. If the strongly-rectifying Kir3 channels are predominant, the +50-mV current should be much smaller than the -50-mV current. In that case, we retained the oocyte and analyzed the -50-mV current. Hence, during one recording of the same oocyte, we obtained multiple pieces of information about the tested channel by varying the membrane potential, but we also manipulated the bath compositions. Initially oocytes were bathed into low [K^+ 2 mM] buffer which provided the zero-current level of the oocyte – all the other solutions contained [K^+ 91 mM]. The second bath fixed the equimolar K^+ distribution on both sides of the membrane, and gave the basal activity of the channels. Thereafter, we applied GPCR-agonist-containing buffers to trigger Gβγ-stimulation of the Kir3 channels. Subsequently, we could record agonist-washing kinetics and at the end of the protocol, the oocytes were exposed to [Ba^{2+} 3mM] as a means to quantify the current specific to the potassium channels. This last step is rather sensitive because it supposes that the membrane resistance was unchanged from the beginning of the

experiment, i. e. the membrane was still tightly sealed around the microelectrodes and no further leak developed. We should also note that the current responses to various solutions was rather slow because full solution exchange in our setup required nearly 60 sec to get rid of all traces of a previous compound from the chamber.

A

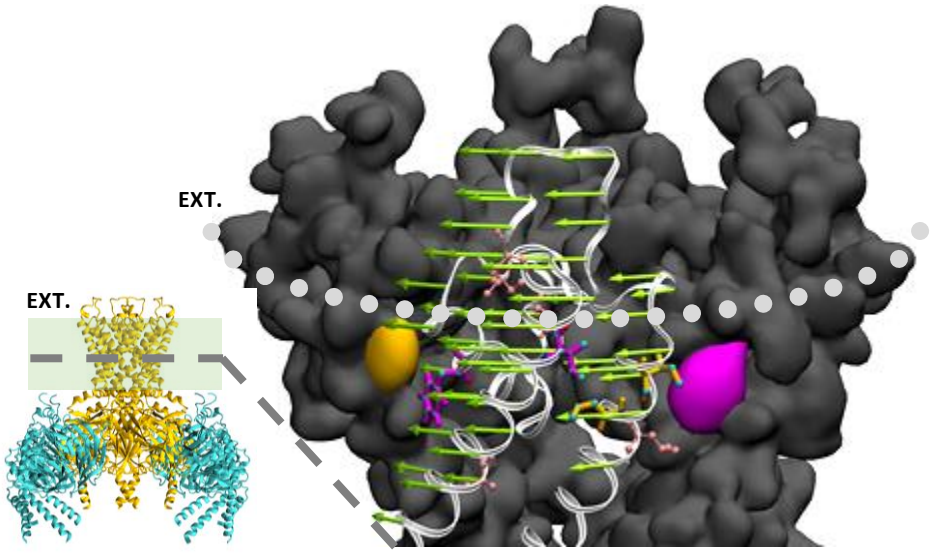

B

Kir3.1	M101	I105	L112	A115	G118	F130	F134	D153	I159	L161
Kir3.1		+		+	+		+			
Kir3.1(F137S)	+	+		+	+	-		-	-	+
Kir3.4	**I107**	**I111**	**L118**	**V121**	**Q124**	**F136**	**F140**	**E159**	**I165**	**L167**
Kir3.4		+					+			
Kir3.4(S143T)		+	+			+		+	+	+

C

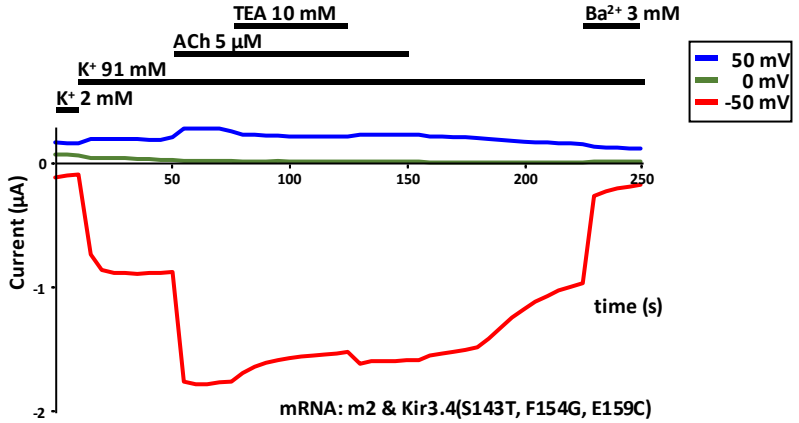

Figure 42: Most Kir3 cysteine mutants were expressed and functional. (A) External view of the mmKir3.2 model. The slowest collective mode predicted is represented in one subunit by green arrows. The displayed contributions are filtered by amplitude >3.5 Å. Several residues at positions selected for mutagenesis are shown as sticks in the mmKir3.2 channel - orange and magenta coloring is used to highlight the involvement of these residues in interfaces between secondary structures of the tetramer. (B) Summary of the cysteine mutations introduced in Kir3.1, Kir3.1(F137S), Kir3.4 and Kir3.4(S143T). "+" and "-" signs in the table represent the ability to detect currents of a given mutant: cysteine mutations introduced in Kir3.1(F137S) and Kir3.4(S143T) proteins were tested as homotetramers, cysteine mutations introduced in the wild-type Kir3.1 or Kir3.4 subunits were tested by co-expressing wild-type Kir3.4 and Kir3.1, respectively, to reconstitute Kir3.1/Kir3.4 heterotetramers where only two subunits should bear the cysteine mutations. (C) Representative TEVC recording from an oocyte expressing the m2-muscarinic receptor and the homomeric Kir3.4(S143T, F154G, E159C) channel. Recording was performed using repeated "sweeps" of 5 s., where membrane potential was sequentially stepped to 0 mV, -50 mV, 0 mV, 50mV and 0 mV for 1 s.

The post-injection expression period varied for different constructs. For some of them, the oocytes were massively dying after 48 hours or recordings were showing important leak currents, suggesting that the overexpression of some mutant channels was malignant for the oocytes. Consequently, to optimize the recording conditions, I diminished the amounts of injected mRNA and the incubation time before proceeding to the functional testing.

Some of the constructs reported with a "-" sign in Figure 42 had low current levels such as Kir3.1(F137S, F130) and Kir3.1(F137S, D153), while the construct Kir3.1(F137S, I159C) had current recorded at -50 mV equal to the current recorded at 50 mV (suggesting loss of rectification) – these constructs were not considered for the next PTL-testing stage.

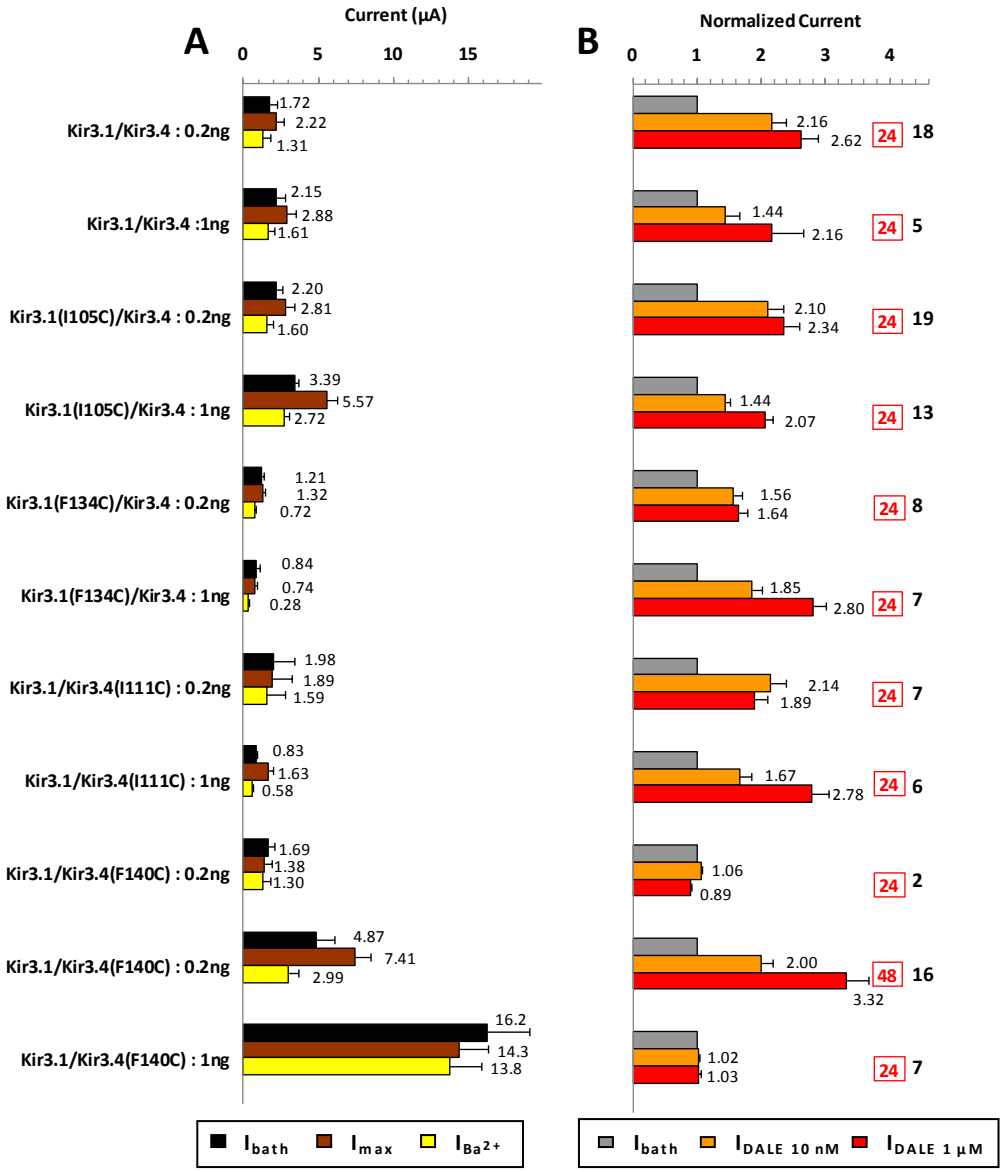

Figure 43: Functional testing in Xenopus oocytes of heterotetrameric Kir3.1/Kir3.4 channels with cysteine mutations in one subunit. The amount of mRNAs injected per oocyte, in ng, is indicated in the construct names. G-protein activation was elicited by 10 nM and 1 µM [D-Ala^2-Leu^5]-enkephalin (DALE) acting on co-expressed δ-opioid receptors (injected mRNA: 0.2 ng/oocyte). Recordings were performed using ND$_{96}$ (Nathan Dascal buffer [K$^+$ 92 mM], pH 7.42) extracellular buffer. Membrane potential was -50 mV. (A) Average current levels at different steps of the protocol: (I_{bath}) basal activity prior to agonist-induced stimulation, (I_{max}) maximal current obtained during recording of the basal activity or the agonist induced stimulation, ($I_{Ba^{2+}}$) current inhibited by a 60-sec application of potassium channel blocker [Ba^{2+} 3 mM]. (B) Currents normalized to the basal current I_{bath}. Incubation time after mRNA injection in hours (red) and number of oocytes used are indicated next to histogram bars. In both panels, the values of the computed averages are indicated next to the error bars representing the standard error of the mean (SEM).

In the following paragraphs I will describe in more details the results of the functional testing of all considered cysteine mutants. Hereafter, for convenience, I will refer to the mutants Kir3.1(F137S) as Kir3.1S, and Kir3.4(S143T) as Kir3.4T.

6.2.1 Cysteine mutations in wild-type Kir3.1 and Kir3.4

I started with a small batch of positions and introduced cysteine mutations in the wild-types Kir3.1 and Kir3.4. These mutations can be classified as avoiding the turret region of the channel. The average currents and the normalized currents (with respect to the basal activity) recorded at different experimental conditions are reported in Figure 43. The same response to the higher concentration of agonist was observed independently of the amount of mRNA of the wild-type channel. However, the current density was increased by nearly 30 % with the increase of the mRNA used, and there was a significant difference in responses to the lower concentration of the agonist ($p < 0.005$), suggesting that the increase of channels in the membrane also increased the recorded basal activity. The I105C mutation in Kir3.1 had no discernable effect on the channel in comparison to wild-type Kir3.1. Hence, the increase of the mRNA concentrations used coincided with the same significant decrease of the activation obtained with the lower agonist concentration ($p < 0.05$). The profile of normalized currents reported for the mutation F134 in Kir3.4 was slightly different from those of the wild-type. Here again, when a lower amount of Kir3 mRNA was injected, the difference between the low-dose and the high-dose agonist activation was smaller. However, the apparent decrease in agonist activation in presence of the Kir3.1(F134C) subunit in the heterotetramer was not statistically significant. This mutant however, required to increase the amount of mRNA (2.5ng/oocyte) to obtain a basal current density (-6.76 µA/oocyte; ±1.19 µA; n = 16) comparable to that of the wild-type channel 24 hours after injection. In parallel, the current increase was not accompanied by an increasing dose-response agonist activation (DALE 0.01 µM: 1.65; ±0.08; DALE 1 µM: 1.67; ±0.11) (data not shown in graphical representation). This data followed the same trend as previously reported constructs, suggesting that the expression of the GPCR was slower than that of Kir3 channels and was most probably the reason for the changes in the agonist-induced responses. The two cysteine mutations in the Kir3.4 subunit equivalent to the mutations in Kir3.1 described above resembled strongly the Kir3.1-counterparts when the quantities of injected mRNA (1ng/oocyte) were increased. However, when using 0.2 ng/oocyte, the Kir3.4(I111C) mutant exhibited an inverse dose-response pattern. This observation was not novel to our laboratory, and other members of our team have been making important efforts to shed light on the mechanism of this phenomenon. On the other hand, the Kir3.4(F134C) mutation, like the Kir3.1(F134C), hindered the agonist-induced activation at 24 hours after injection. However, Kir3.1/Kir3.4(I111C) channels were very active the next day, while increasing the amount of injected mRNA, as observed previously, increased basal activity and induced the loss of potency of the agonist-induced activation - making it difficult to properly compare the recorded phenotype with the wild-type.

Despite the number of interesting observations and the even greater number of arising ideas that the preliminary results suggested for further functional exploration of the novel cysteine mutants, we simply decided to pursue the work through cysteine scanning towards the PTL testing phase, concentrating on the cysteine mutants which we were able to record and whose phenotypes resembled the native Kir3 channels.

I also tested cysteine mutations in the turret region. These were implemented only in the Kir3.1 subunit and functional tests were made using the δ-opioid receptor (data not shown) and the m2 receptor (Figure 44). The mutant channels showed the same agonist-induced stimulations as the wild-type, which suggested that these mutations were not critical for gating. The agonist responses of these constructs after labeling with MAQ are also included in the figure. Despite the lower current levels recorded with this batch of oocytes (discussed in section 6.3), it appeared that the response to ACh stimulation did not change in these conditions.

Soon after, these first results about functional testing became available and I had doubts about their interpretation. The problem laid in the fact that there was no certainty that the recorded currents were actually generated by heteromeric channels rather than homomeric channels. This is because we did not have a rapid and reliable means to evaluate if the conducting channels were the heterotetramers we wanted them to be. In fact, in the literature, there are reports about mutant monomeric Kir3 channels. For instance, currents can be recorded from: Kir3.4 homomers, or from mutation-activated monomers like Kir3.1(F137S) and Kir3.4(S143T) (Chan et al. 1996; Vivaudou et al. 1997). Thus, in case of low functional expression as indicated by low basal activity, there were at least two possibilities: either the mutation was expressed into the desired heterotetrameric channel and it caused a change in function, or the heterotetrameric channels did not assemble and we observed currents form the wild-type Kir3.4 homomeric channels or from homomers of the particular mutant we were co-injecting. Thus, I decided to postpone further implementation of cysteine mutants into the wild-type Kir3.1 or Kir3.4 subunits because the functional testing of these mutant channels was less important than to first identify proteins sensitive to the PTL labeling. We also had a limited quantity of compounds and I had to be parsimonious in the testing approach.

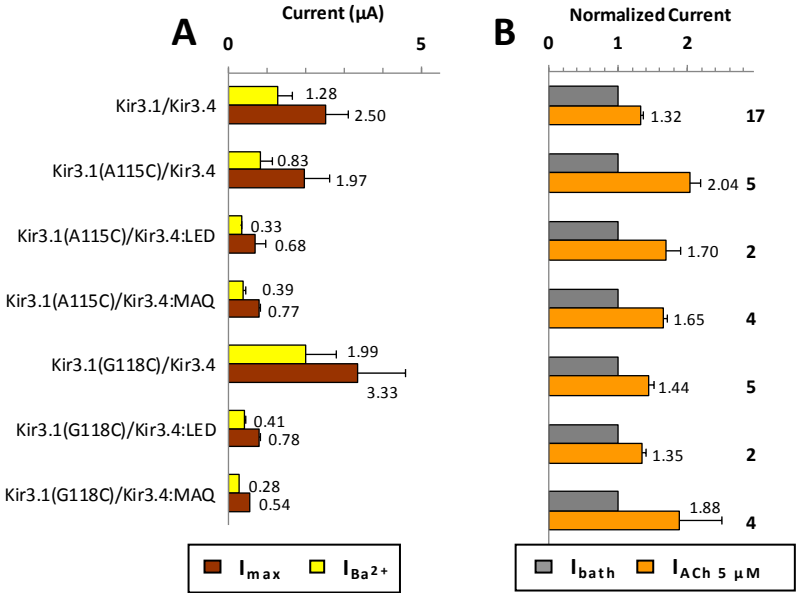

Figure 44: Functional testing in Xenopus oocytes of cysteine mutants implemented in the turret region of the Kir3.1 subunit in the heterotetrameric Kir3.1/Kir3.4 channel. 2.5 ng of mRNAs were injected per oocyte and oocytes were recorder 48 hours later. G-protein activation was elicited by 5 µM acetylcholine (ACh) acting on co-expressed m2 receptor (injected mRNA: 0.2 ng/oocyte). Panels A and B follow the representation scheme of Figure 43: Functional testing in Xenopus oocytes of heterotetrameric Kir3.1/Kir3.4 channels with cysteine mutations in one subunit. The amount of mRNAs injected per oocyte, in ng, is indicated in the construct names. G-protein activation was elicited by 10 nM and 1 µM [D-Ala²-Leu⁵]-enkephalin (DALE) acting on co-expressed δ-opioid receptors (injected mRNA: 0.2 ng/oocyte). Recordings were performed using ND_{96} (Nathan Dascal buffer [K^+ 92 mM], pH 7.42) extracellular buffer. Membrane potential was -50 mV. (A) Average

6.2.2 *Cysteine mutations in homomeric Kir3.1(F137S) and Kir3.4(S143T) channels*

In order to make non-ambiguous interpretations of the functional results obtained from the Kir3 cysteine mutants (see section 6.2.1), I decided to switch to two activated homomeric channels as templates: Kir3.1(F137S) and Kir3.4(S143T). Thus, I expected to better pinpoint important hotspots for PTL-modulation in the homotetrameric Kir3 channels and, after that, to return to the native subunits in order to verify if the effect still persisted. Another change in the rational-design strategy was to not duplicate CYS mutations at equivalent positions in both monomer types, i.e., the first batch of mutations would probe a larger number of positions along the Kir3 quaternary structure. This was done just to go faster in the screening assays, assuming equivalence between the corresponding positions in the Kir3.1 and Kir3.4 monomers. Later work would complete the exhaustive testing of all equivalent positions in both monomers. The list of positions that were mutated to cysteine in either Kir3.1S of Kir3.4T is shown in panel B of Figure 42.

Results are shown in Figure 45. As already mentioned in Figure 42, three of the Kir3.1S mutations (F130C, D153C, I159C) did not yield channels similar enough to the reference constructs and thus were not considered for PTL-testing (Figure 45 A, B). While all these CYS mutant channels had small maximal currents at -50 mV (I_{max}), they also appeared to have an agonist-induced activation similar to that of the Kir3.1S homotetramers and greater than that of the non-injected oocytes – although the T-test did not confirm this assumption for all three constructs. On the other hand, the quantification

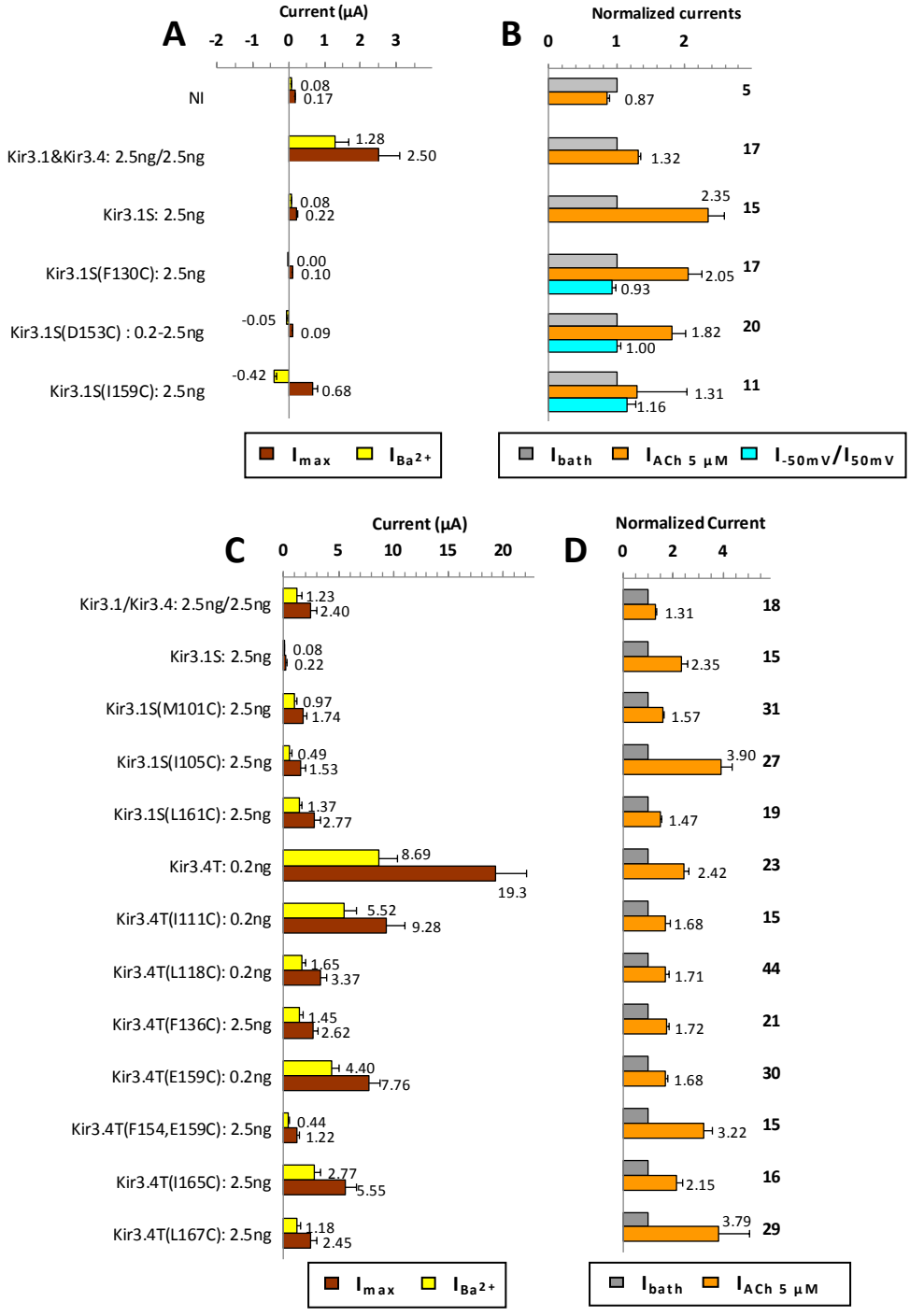

Figure 45: Functional tests in Xenopus oocytes of Kir3.1S and Kir3.4T with mutations to cysteine mutants in the TM helix bundle. The amount of mRNAs injected per oocyte are indicated next to construct names. Oocytes were recorded 24 hours after injection for the Kir3.4T constructs, 48 to 72 hours for the Kir3.1S constructs. G-protein activation was elicited by 5 µM acetylcholine (ACh) acting on co-expressed m2 receptor (injected mRNA: 2.5 ng/oocyte). Panels A and B follow the representation scheme of Figure 43 (see for details).

of rectification ($I_{(-50mV)}/I_{(50mV)}$) in the case of these mutations showed weaker rectification than Kir3. So, there is evidence for the heterologous expression of channels after injection of the mRNA of mutants Kir3.1S(F130C), Kir3.1S(D153C) and Kir3.1(I159C), but it appears that these channels diverge from the Kir3 phenotype.

Results for the remaining CYS mutants are shown in panels C and D in Figure 45. The overall impression from these results is that constructs involving the Kir3.1 subunit were less expressed in the membrane – in line with the findings about the predominate degradation instead of maturation of the channels constituted only of Kir3.1 subunits (Zylbergold et al. 2014), while the Kir3.4T CYS mutants had reduced activity. The agonist-induced currents were in line with those for the wild-type and the homomeric template channels.

An interesting observation was that the agonist-induced response was more pronounced when the maximum recorded currents were lower – as in Kir3.1S, Kir3.1S(I105C), Kir3.4T(F154G, E159C) and Kir3.4T(L167C). This observation is in line with the quantitative modeling made by Yakubovich and colleagues (Yakubovich et al. 2015). However, this trend was not applicable to channels Kir3.4T, Kir3.4T(I111C), Kir3.4(L118C) and Kir3.4T(F136C).

All Kir3.1S CYS mutants had increased currents compared to Kir3.1S (Figure 45 C, D). By comparing CYS mutations at equivalent positions between Kir3.1S and Kir3.4T, one could notice that Kir3.1(I105C) and Kir3.4(L167C) exhibited similar phenotypes with high agonist-induced activation, and Kir3.1(L161C) and Kir3.4(I111C) showed similar phenotype of lower agonist-induced activation. This suggests switched location of equivalent functional elements. Indeed, when compiling information from the literature with the results I obtained, I developed the impression that this region could bind some kind of a partner and that the effect of these interactions with the TM helices would be transmitted to the pore helix and eventually result in changes of the flickering of the selectivity filter. First, the C-terminus of the TM1 in hsKir3.1, mmKir3.2 and hsKir3.4 contains all residues of the CRAC cholesterol binding motive {$\boldsymbol{(R/K)X_{1-5}(Y/F)X_{1-5}(L/V)}$} (Hua Li and Papadopoulos 1998; Epand 2006), and except for within hsKir3.1 the CCM cholesterol binding motive {$\boldsymbol{(W/Y)(I/V/L)(K/R)}$} on one helix and {$\boldsymbol{(F/Y/R)}$} the second helix) (Hanson et al. 2008) is also partially present in the region of the above cited mutations in mmKir3.2 and hsKir3.4. Interestingly, the expected partner from a second helix to complete the CCM motive could be either a glutamate or a leucine at positions E168 or L172 in mmKir3.2, and E163 or L167 in hsKir3.4 – the CCM motive in hsKir3.1 was broken by T108. Second, in other potassium channels this region is involved in specific binding of lipids: anionic lipids in KcsA channels (Deol et al. 2006), Kv1.3 channels (van der Cruijsen et al. 2013), Kv1.2 channels (Long et al. 2007). Third, as discussed previously, the introduction of CYS in hsKir3.1S and hsKir3.4T in this region had an effect on the conductance of the channel. Taken together these facts suggest that this inter-subunit interface in Kir3 channels might be involved in interactions with a partner in the upper leaflet of the membrane and as suggested by the double occurrence of cholesterol binding motives this partner could eventually be cholesterol, thus bringing the count of putative cholesterol binding sites to two (see section 5.5.1).

6.3 TESTING THE PTL-INDUCED LIGHT-SENSITIVITY

I proceeded to investigate the ability of the different PTLs to label the CYS mutants and to impart light sensitivity. I worked with eleven CYS mutants and five PTL molecules. The testing scheme does not constitute a full combinatorial explorations 11x5 because I had a limited supply of all molecules except MAQ and PAM.

The labeling efficiency of the channels expressed in *Xenopus* oocytes was addressed indirectly from the effect of the illumination with λ=380 nm (λ_{380}) and λ=500 nm (λ_{500}) during TEVC recording of the treated oocytes. However, now is the time to make a very important remark concerning the TEVC recording protocol and the light stimulation of the oocytes. In fact, in order to light-stimulate the oocytes, our recording chamber was illuminated with a collimator-terminated optic fiber. In these

conditions, only a portion of the oocyte was illuminated and the illuminated surface depended on a number of parameters. The angle of incidence of the light beam and the refraction index of the perfusing buffers, along with LED power output determined the illumination power per area of the oocyte surface – these parameters were not explicitly investigated but they were the same among all recordings. However, we were certain that the conditions were sufficient to induce isomerization of the azobenzene moiety because we obtained the expected effect and strength of photo-blocking with a light-inhibited Kir6.2(CYS) channel labeled with MAQ. The next set of parameters are particularly user dependent. For instance, the height of the buffer inside the perfusion chamber is controlled by a manually placed aspiration gauge varying in the vertical axis, thus not exactly

Table 3: Normalized current changes induced by illumination with λ=380 nm and λ=500 nm of oocytes expressing various CYS mutant Kir3 channels labeled with the indicated PTLs. The changes in normalized current subtracted by the standard error which are greater than 0.2 are highlighted in green.

PTL	Construct	Normalized currents[1]	
		ΔI_{base} 380 nm vs. 500 nm	ΔI_{base} 500 nm vs. 380 nm
MAQ 10µM	non-injected	1.03 (±0) n=2	0.94 (±0) n=2
	Kir3.1S(M101C)	1.01 (±0) n=14	1.01 (±0) n=10
	Kir3.1S(I105C)	0.99 (±0.01) n=11	1.01 (±0.02) n=10
	Kir3.1S(A115C)	1.01 (±0) n=3	1.01 (±0) n=3
	Kir3.1S(G118C)	1.02 (±0) n=3	0.99 (±0) n=3
	Kir3.1S(L161C)	1 (±0.01) n=5	
	Kir3.4T(I111C)	1 (±0) n=8	0.99 (±0.01) n=8
	Kir3.4T(L118C)	1.01 (±0.01) n=3	1 (±0) n=3
	Kir3.4T(F136C)	1 (±0.01) n=10	1.01 (±0) n=8
	Kir3.4T	0.99 (±0.01) n=3	0.99 (±0.01) n=3
	Kir3.4T(E159C)	** 1.07 (±0.01) n=35	** 0.93 (±0.01) n=34
	Kir3.4T(F145G/E159C)	** 1.16 (±0.03) n=23	** 0.87 (±0.02) n=23
	Kir3.4T(I165C)	1 (±0) n=2	1 (±0) n=2
	Kir3.4T(L167C)	1.01 (±0) n=7	1 (±0) n=7
MAC	non-injected	1.05 (±0.02) n=2	1.06 (±0) n=2
	Kir3.4T(E159C)	1.02 (±0.01) n=5	0.98 (±0) n=3
	Kir3.4T(I165C)	1 (±0) n=3	0.99 (±0) n=3
	Kir3.4T(L167C)	1.05 (±0.04) n=8	0.99 (±0.01) n=6
MAS	Kir3.1S(M101C)	1 (±0) n=6	1.01 (±0.01) n=6
	Kir3.1S(I105C)	0.99 (±0.01) n=5	0.98 (±0.01) n=5
	Kir3.1S(L161C)	1 (±0) n=3	1 (±0) n=3
	Kir3.4T(L118C)	1.01 (±0.01) n=6	1 (±0) n=6
	Kir3.4T(F136C)	0.98 (±0.01) n=5	0.99 (±0.01) n=4
	Kir3.4T(E159C)	1 (±0) n=6	1.01 (±0) n=6
$MEASO_3^-$	Kir3.1S(I105C)	0.99 (±0.01) n=3	1 (±0) n=2
	Kir3.4T(L118C)	0.99 (±0) n=9	0.99 (±0) n=9
	Kir3.4T(F136C)	0.99 (±0) n=14	0.99 (±0.01) n=13
	Kir3.4T(E159C)	0.99 (±0) n=8	1.01 (±0) n=8
PAM 10µM	non-injected	0.92 (±0.06) n=2	0.98 (±0.01) n=2
	Kir3.4T(I111C)	0.98 (±0.01) n=7	1.01 (±0.02) n=7
	Kir3.4T(E159C)	1 (±0) n=4	1.01 (±0.01) n=4
	Kir3.4T(I165C)	0.99 (±0.01) n=2	0.99 (±0) n=1
	Kir3.4T(L167C)	1 (±0) n=6	1 (±0) n=4

[1] ΔI_{base} λ_1 vs. λ_2: is the ratio of I_{base} recorded at λ_1 and normalized by the average I_{base} recorded at λ_2 before and after the application of λ_1. I_{base} refers to recordings of oocytes perfused with control buffer, thus I_{base} is a measure of the basal activity of the channels.

identical between all experiments. The other two parameters that I tried to standardize to the best of my ability are the orientation of both poles of the oocyte to the vertical axis and the particular position of the oocyte into the perfusion chamber. Thus, each oocyte was brought to the wall of the chamber opposite to the entry of the prefusion buffer and the cell was turned with the animal (dark) pole up. Nevertheless, despite all these efforts, the major portion of the oocyte membrane was not efficiently illuminated because of the curvature of the oocyte. Thus, in case of a photo-block induced by the relaxed state of the PTL (*trans-state*), the whole cell current levels should be inferior to those recorded with the untreated oocytes. This situation is favorable for the observation and quantification of light-induced changes because the channels remaining in the dark are blocked and do not contribute to the recorded currents. On the other hand, if the trans state of the PTL induced activation of the channels, or no or partial photo-blocking, channels on the dark side will stay open and will contribute to a large background current, thus reducing the relative effect of light on the whole-cell current.

Results on the effects of illuminations at λ_{380} and λ_{500} are shown in Table 3. Although these results only describe currents recorded with the control buffer, the observed effects on agonist-induced currents were similar in relative amplitude (data not shown). Only a few of the tests listed in Table 3 actually present light-sensitive amplitude changes. Among those, small changes were observed with non-injected oocytes, possibly due to a photoelectric effect (Kozai and Vazquez 2015), rather than a PTL or light induced modification of the oocytes. Except for mutation E159C, the rest of the constructs reported in Table 3, presented light-induced changes of the recorded currents with amplitude greater than 2% once the standard error was subtracted. For all these cases, there is no certainty that channels were labelled. We had no biochemical assay to test labeling efficiency and could only rely on light-induced changes to confirm labeling. I tried to compare currents and normalized currents before and after the PTL labeling of the oocytes. Unfortunately, there were few experiments reproducing the exact same incubation protocol, thus a sufficient number of repeats was not available for proper statistical assessment. This is very important for such a comparison because the expression of the channels is fast and I observed that generally, oocytes recorded in the morning had considerably less currents that the same batch recorded in late afternoon – and I normally first recorded few oocytes of each batch to verify channel expression early in the day and several hours later oocytes of the same batches were labeled with PTL and tested . The same also applies to the comparison between the normalized agonist-induced activation which as previously discussed is also sensible to the proportion of expressed GPCRs and channels – which have different expression kinetics. Apart from comparing different oocytes before and after labeling, in theory the efficiency of the labeling can be verified by direct recording while the oocyte is being perfused with a PTL containing buffer – this experiment is possible in the limit of the longevity of the impaled oocyte being recorded and in general the longest recording I was able to obtain without PTL was about 20 minutes long, which is roughly half of the incubation time used for labeling. An experiment of this type would be interesting because it could decipher whether or not the PTL induces light-insensitive (not reversible by light-induced isomerization) functional changes of the CYS mutant Kir3 channels. Nevertheless, such experiments were not performed, and it was not possible to determine whether light insensitivity was due to poor labeling or lack of block.

The only construct that showed a significant amount of current reversibly modified by both light wavelengths was the Kir3.4S(E159C) mutant labeled with MAQ or MAC. The activity of this construct was increased by λ_{380} illumination, and this increase was fully reversed by λ_{500} illumination. One cannot be sure if the actual phenomenon is photo-unblocking or photo-activation of the channel because both phenotypes would have equivalent recording profiles. With MAC labeling, effects were similar but smaller than with MAQ. This could be due to the smaller terminal function of the MAC compound – three methyl on the quaternary ammonium, instead of three ethyl in the MAQ compound. This suggests that the bulkier ethyl terminated compound could be stabilized by additional hydrophobic contacts, in line with published data about KcsA channels (Lenaeus et al.

2005). This hypothesis is weak because the residues stabilizing the TEA in KcsA channel are TYR (Y82), but the equivalent residues in hsKir3.4 are VAL (V156). There could be hydrophobic contacts but of minor stabilizing extent if the four TYR residues form a hydrophobic cage around the extracellular entry of the selectivity filter – more favorable for TEA than one formed by four VAL residues. I describe later additional modifications of the mmKir3 channels based on the possible hydrophobic stabilization of the MAQ tether at the selectivity filter.

In summary, our results were contrasted. Reversible light-induced activation of the channel was not obtained. Our observations indicated that the transmembrane domain is not an easy target when making use of a weakly-hydrophobic PTL designed for labeling an extracellular target on the protein. We detected no evidence of a grafted PTL in Kir3 constructs with CYS mutation in the TM domain. In contrast, there was a positive hit for a reversible light-induced photo-blocking: Kir3.4T(E159C) labeled with MAQ or MAC. The distance between the E159 residue and the extracellular entrance of the selectivity filter appears compatible with the binding of MAQ in the trans state to the mouth of the selectivity filter, and its release in the cis state.

6.4 Optimization of Kir3.4(E159C)

Photo-block of Kir3.4(E159C) is far from complete and needed to be improved. For the Kir6.2(CYS) mutant, the 380nm-light-induced block of whole-cell currents was about 90 %, indicating that the majority of Kir6.2(CYS) channels, including those located in the area of the oocytes inaccessible for light illumination, were blocked by the trans-state of the MAQ. Since the MAQ appears to act on the selectivity filter, we attempted to optimize the Kir3.4(E159C) construct in this direction following a rational design argumentation. To our knowledge, there are no evidence of an effect of TEA on Kir3 channels in the literature, implying that the intrinsic binding affinity of these channels for extracellular TEA is very low. Significantly, the tethering of the MAQ causes a large increase of the local concentration of quaternary ammonium (QA) at the entrance of the selectivity filter, and a high probability of QA binding to the channel. Thus, when comparing the results obtained Kir6.2(CYS) and Kir3.4(E159C), assuming similar local QA concentrations, QA binding to the Kir3.4 selectivity filter is systematically weaker to that of Kir6.2(CYS). Hence, we tried to identify the molecular factor(s) responsible for this weakening of the binding affinity.

Panel A of Figure 46 shows multiple sequence alignments of the region of the selectivity filter of Kir6.2 and Kir3 proteins including the positions equivalent to Kir3.4(E159). The entrance of the selectivity filter of Kir6.2 includes residue G135, the equivalent of which in Kir3 channels is either a bulky aromatic Y/F or a positive residue H. Both these cases are very different from what is known and has been observed about KcsA and other potassium channels (Shaker, Kv1.3, Kv3.1, Kv7.2, SK2) blocked by extracellular TEA or extracellular MAQ-modifications (Andalib et al. 2004; Lenaeus et al. 2005; Fortin et al. 2011). All these channels have an aspartate residue at position *i+1* of the conserved GYG motive. This aspartate residue is often observed in the crystal structures as pointing towards the pore helix, thus exposing its backbone at the entrance of the selectivity filter. It could be speculated that the withdrawal of the sidechain of the aspartate which is observed in the inactivated conformation of the KcsA channel would provide additional volume for the extracellular TEA to dock at the end of the filter. The local negative electrostatic contribution of this aspartate could also increase the apparent binding affinity of KcsA channel for TEA. For Kir3, the residue at position *i+1* of the GYG motive of the filter is a bulky Y/F/H which always points towards the intracellular bulk in the crystallographic models of mmKir3.2. We hypothesized that the residue at position *i+1* of the GYG motive could act as a “gate-keeper” of the extracellular entrance of the selectivity filter. This hypothesis seemed increasingly relevant in the light of the lateral alignment of the apex of the sidechain of D164, the apex of Y159 and the entrance of the selectivity filter (Figure 46B). Moreover, the sidechain of Y158 blocked the “view” on the filter from D164 because of its more important height relative to a straight line between D164 apex and the filter entrance.

We decided to modify the extracellular entrance of the selectivity filter of Kir3 channels to resemble that of the Kir6.2 channel. The modification consisted in the mutation Y148G in Kir3.1, and F154G in Kir3.4. The results of the functional tests of Kir3.4T(F154G, E159C) are in panels C and D of Figure 47. We were unable to characterize the constructs Kir3.4T(F154G) nor Kir3.1S(Y154G) which gave undetectable currents. The maximal currents (I_{max}) obtained with the construct Kir3.4T(F154G, E159C) were lower than I_{max} of Kir3.4T(E159C). This observation could be due to a lower quality of mRNA, which I could not resynthesize because of lack of time. It could also arise from interference of the introduced mutation with channel gating. In rare oocytes having a nice aspect during manipulation (shape, color, absence of cytosolic leak when impaled), I observed that the inward rectification of Kir3.4T(F154G,E159C) was preserved. For instance: -1.00 µA at -50 mV and 0.33 µA at 50 mV in iso-molar condition of high 92 mM K^+; while the selectivity towards Na^+ was also maintained: -0.014 µA at -50 mV and 0.29 µA at 50 mV with 92-mM extracellular Na^+. The set of raw data requires to be extended with additional recordings and also further statistical exploration needs to be applied in order to quantify precisely the rectification and the selectivity of this triple mutant. However, the preliminary data indicated preservation of the native phenotype in terms of rectification and selectivity (data not shown).

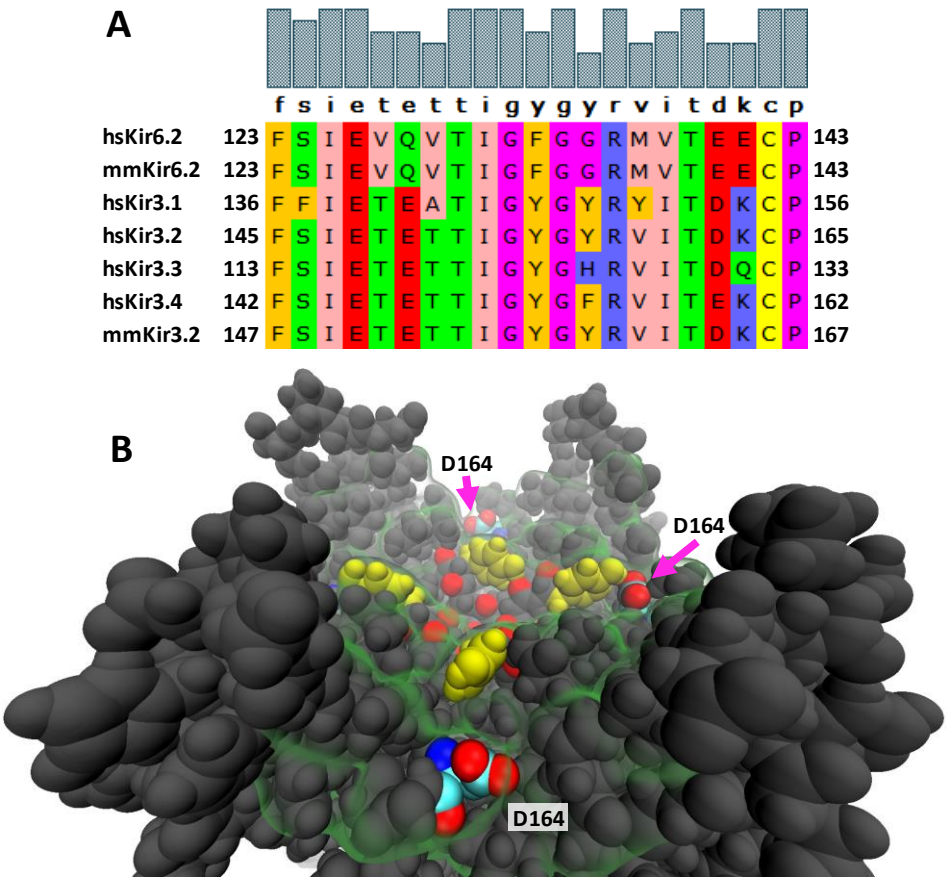

Figure 46: The extracellular entrance of the selectivity filter of Kir3 is "guarded" by bulky sidechains. (A) Multiple sequence alignment between Kir6.2 and Kir3 in the region around the selectivity filter going from the middle of the pore helix until the N-terminus of the TM2 helix. (B) Extracellular view of the turret region and the selectivity filter of the pre-activated mmKir3.2 (PDB:4KFM). The perspective of the view is set to represent the viewpoint from the sidechain of residue D164 towards the selectivity filter. All atoms of the model are represented as Van der Waals spheres and accent is put on: oxygens lining the solvent-exposed selectivity filter (red), Y159 (yellow), D164 standard atom coloring. A transparent surface (green) delimits the area within 17 Å of the carbonyl oxygen of all G158.

Regarding the effect of the light modulation of the MAQ-modified triple mutant Kir3.4T(F154G, E159C) there were some good news. In fact, the removal of the bulky sidechain near the entrance of the filter led to a three-fold increase in the amplitude of the light-sensitive component of the currents recorded in basal or Ach-induced conditions (Figure 47B, D). These results confirmed that the MAQ interacted with the selectivity filter rather than inducing conformational changes in the channels, somehow resulting in a change in activity.

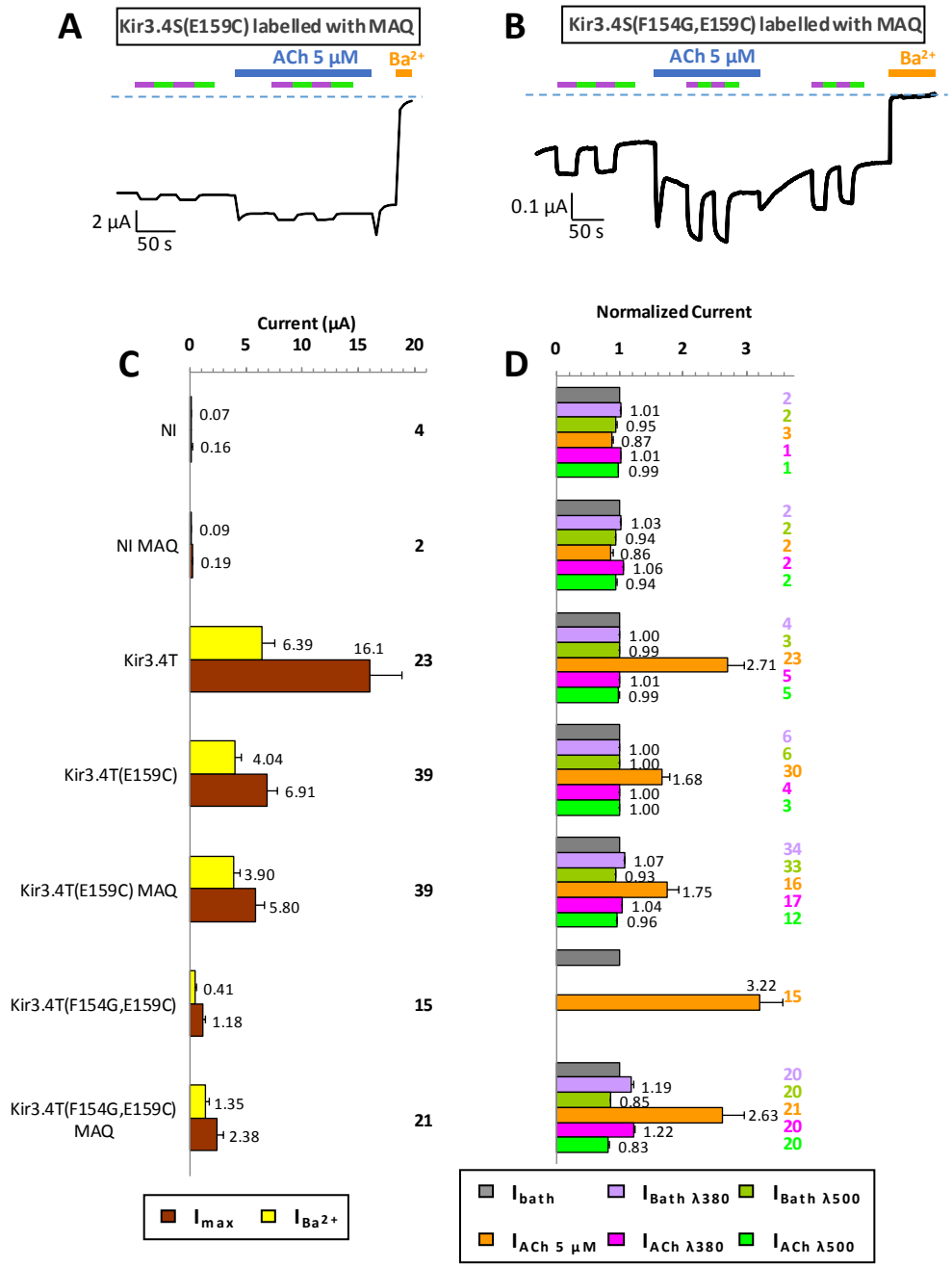

Figure 47: The mutant Kir3.4T(F154G, E159C) labeled with MAQ displays a solid block by 500-nm light, which is relieved by 380-nm light. (A) Representative recording of Kir3.4T(E159C). The recording was made in high extracellular K^+ 92 mM buffer at -50 mV. The current modulated by light was ~10 % of the Ba^{2+}-sensitive current. (B) Representative recording of Kir3.4T(F154G, E159C). The current modulated by light was ~60 % of the Ba^{2+}-sensitive current. (C) Maximal and Ba^{2+} currents of non-injected oocytes and Kir3.4 homomers, with and without MAQ labeling. (D) Normalized currents before and during ACh application, before and during illumination at 380 nm and 500 nm. I_{bath} λ380 and I_{bath} λ500 are normalized with respect to I_{bath}, while I_{ACh} λ380 and I_{ACh} λ500 are normalized with respect to I_{ACh}.

An interesting conclusion about the efficiency of the MAQ labeling protocol can be made regarding the very low standard error of the normalized currents (in the range of 0.003 to 0.03) describing the light-stimulated conditions obtained with Kir3.4T(E159C) and Kir3.4T(F154G, E159C). It indicates that regardless of the variability of the amount of expressed channels among different cells or the particular channel phenotypes, the statistics showed that the labeling with MAQ was a stable experimental parameter, as well as the fraction of the oocyte surface effectively illuminated during the experiments. These observations confirmed that the intact oocytes expressing engineered channels labeled with PTLs can be used as a rapid and easy way to the screening of designer channels for optogenetics.

6.5 *Conclusion and perspectives for application and future research*

In this project we aimed to design light-modulated Kir3 channels. As far as we know, light-sensitive Kir channels have never been reported. This objective is motivated by the possibility to use the enhanced spatial and temporal control afforded by light stimulation to study the physiological role of native Kir3 channels by co-expression with the light-gated channels. Such studies are not possible with a pharmacological approach, because such an approach lacks space and time specificity. It also requires specific modulators which do not exist for Kir3 channels.

Because our laboratory has some growing expertise in application of photo-switchable tethered ligands (PTLs) for optogenetics, we adopted this strategy for this project. The PTL technique is particularly suitable for designing novel optogenetic constructs because the CYS-mutations required for the PTL labeling of the targeted proteins cab introduced rapidly with modern molecular-biology protocols and the functional testing and the characterization of potential light-sensitive phenotypes of the newly-designed channels is straight forward using the current electrophysiological equipment.

The first stage of the development required to select positions for the implementations of the CYS-mutations in the Kir3 channels of interest. We examined several crystallographic models of Kir3.2 (Whorton and MacKinnon 2011, 2013) and a series of homology models of Kir3.1, Kir3.4 and Kir3.1/Kir3.4 channels that used the crystallographic models as templates. The CYS-mutants were selected with two constraints: First, the cysteine should be accessible for labeling with extracellular PTL, and second, the PTL attached to the cysteine should have a good chance of affecting channel function through pore block or induction of conformational disturbances. The first constraint is not difficult to respect. The second constraint imposes some rational design, and a good part of trial-and-error.

Therefore, all selected positions for the CYS-mutants were located along the protein sequence of the Kir3 subunits exposed to or very close to the extracellular medium (Figure 42A, B). In total we selected ten distinct positions along the Kir3 subunit, we tested twenty CYS-mutants implemented in Kir3.1 and Kir3.4 wild-type or mutation-activated Kir3.1S and Kir3.4T subunits (Chan et al. 1996; Vivaudou et al. 1997) (for details see section 6.1). Only three of the Kir3.1S CYS-mutant did not yield detectable currents, while all other CYS-mutants had characteristics similar to the parental constructs (wild-type or mutation-activated) (Figure 42B).

During the stage of light-sensitive phenotype characterization, all expressing CYS constructs were tested with the MAQ tether. This compound was developed in a pioneering study on the Shaker channel and was optimized to target the extracellular vestibule of the Shaker potassium channel (Banghart et al. 2004). MAQ has geometric compatibility with its tethering to the apex of the channel turret and in the trans-state it extends to electrostatically interact with the selectivity filter yielding a reversible photo-block of the channel. We effectively tested two CYS-mutants aligned with functional photo-blocking positions in Kir6.2 (unpublished results from our lab using the MAQ tether) which eventually aligns near the original Shaker position. None of the Kir3.1S(A115C) and Kir3.1S(G118C) were photo-sensitive. We then attempted to induce conformational disturbance using the same MAQ tether. Only MAQ-labeled Kir3.4T(E159C) was responsive to changing light illumination.

Unfortunately, we cannot rule out the relevance of the other positions for the conformational change induction because we are not able to assess the labeling efficiency of the MAQ tether (and the other PTLs) when the CYS-mutation is partially buried in the plane of the membrane. Further PTL labeling was subject to compromise because time constraints and the limited supplies of the PTLs (Figure 40) required to choose arbitrary which CYS-mutants to test (Table 3). The selections aimed for repulsion effect by combination of the electrostatics of the PTL functional-group and the electrostatic environment of the CYS-mutation. In this series of tests Kir3.4T(E159C) was the sole construct which had light-sensitive phenotype with the lysine-like MAC tether, but this phenotype was weaker than the one observed with MAQ.

Instead of attempting to find ways to measure the labeling efficiency of the buried CYS-mutations, we concentrated on optimizing the phenotype of the Kir3.4T(E159C), the single positive hit in the project at the moment. We came up with the truncation of the aromatic sidechain of the residue at the extracellular entrance of the selectivity filter. The rationale for this manipulation came from sequence and structure observations of Kir3 vs. Kir6, KcsA and Shaker channels. Indeed, the suggested aromatic residues are only present in Kir3 (Figure 46) (but also aromatic or histidine in Kir1.1, Kir2.1 and Kir2.3) and we suspected that they could prevent the MAQ from fully interacting with the selectivity filter. This reasoning proved to be correct because the Kir3.4T(Y154G, E159C) mutant was much more sensitive to block by the 500nm light-induced cis conformation of MAQ (Figure 47).

In conclusion, our results demonstrate that the Kir3 unsensitivity to extracellular TEA, and therefore MAQ, is most probably conferred by the aromatic side chains of the residues immediately preceding the selectivity filter coordination sites – F150 in Kir3.1 and Y154 in Kir3.4. The modification of the extracellular entrance of the selectivity filter allowed for stronger interaction of the MAQ tether with the selectivity filter. Hence, the Kir3.4T(Y154G, E159C) mutant constitutes the first light-modulated Kir3 channel, and could form the basis for other light-gated Kir channels.

7 BIBLIOGRAPHY

Adney, S. K., J. Ha, X.-Y. Meng, T. Kawano, and D. E. Logothetis. 2015. "A Critical Gating Switch at a Modulatory Site in Neuronal Kir3 Channels." *Journal of Neuroscience* 35 (42): 14397–405. https://doi.org/10.1523/JNEUROSCI.1415-15.2015.

Alagem, Noga, Semen Yesylevskyy, and Eitan Reuveny. 2003. "The Pore Helix Is Involved in Stabilizing the Open State of Inwardly Rectifying K+ Channels." *Biophysical Journal* 85 (1): 300–312. https://doi.org/10.1016/S0006-3495(03)74475-0.

Andalib, Payam, Joseph F Consiglio, Josef G Trapani, and Stephen J Korn. 2004. "The External TEA Binding Site and C-Type Inactivation in Voltage-Gated Potassium Channels." *Biophysical Journal* 87 (5): 3148–61. https://doi.org/10.1529/biophysj.104.046664.

Aryal, Prafulla, Hay Dvir, Senyon Choe, and Paul a Slesinger. 2009. "A Discrete Alcohol Pocket Involved in GIRK Channel Activation." *Nature Neuroscience* 12 (June): 988–95. https://doi.org/10.1038/nn.2358.

Aryal, Prafulla, Mark S.P. Sansom, and Stephen J Tucker. 2015. "Hydrophobic Gating in Ion Channels." *Journal of Molecular Biology* 427 (1): 121–30. https://doi.org/10.1016/j.jmb.2014.07.030.

Bahar, Ivet, Timothy R Lezon, Ahmet Bakan, and Indira H Shrivastava. 2010. "Normal Mode Analysis of Biomolecular Structures: Functional Mech Membrane Proteins." *Chemical Reviews* 110 (3): 1463–97. https://doi.org/doi: 10.1021/cr900095e.

Baier, Carlos J., Jacques Fantini, and Francisco J. Barrantes. 2011. "Disclosure of Cholesterol Recognition Motifs in Transmembrane Domains of the Human Nicotinic Acetylcholine Receptor." *Scientific Reports* 1 (1): 69. https://doi.org/10.1038/srep00069.

Bakan, Ahmet, Lidio M Meireles, and Ivet Bahar. 2011. "ProDy: Protein Dynamics Inferred from Theory and Experiments." *Bioinformatics* 27 (11): 1575–77. https://doi.org/10.1093/bioinformatics/btr168.

Ballesteros, Juan A, Xavier Deupi, Mireia Olivella, Eric E.J. Haaksma, and Leonardo Pardo. 2000. "Serine and Threonine Residues Bend α-Helices in the X1=g− Conformation." *Biophysical Journal* 79 (5): 2754–60. https://doi.org/10.1016/S0006-3495(00)76514-3.

Banghart, Matthew, Katharine Borges, Ehud Isacoff, Dirk Trauner, and Richard H Kramer. 2004. "Light-Activated Ion Channels for Remote Control of Neuronal Firing." *Nature Neuroscience* 7 (12): 1381–86. https://doi.org/10.1038/nn1356.

Baslé, Emmanuel, Nicolas Joubert, and Mathieu Pucheault. 2010. "Protein Chemical Modification on Endogenous Amino Acids." *Chemistry and Biology* 17 (3): 213–27. https://doi.org/10.1016/j.chembiol.2010.02.008.

Berlin, Shai, Vladimir A. Tsemakhovich, Ruth Castel, Tatiana Ivanina, Carmen W. Dessauer, Tal Keren-Raifman, and Nathan Dascal. 2011. "Two Distinct Aspects of Coupling between Gα i Protein and G Protein-Activated K + Channel (GIRK) Revealed by Fluorescently Labeled Gα I3 Protein Subunits." *Journal of Biological Chemistry* 286 (38): 33223–35. https://doi.org/10.1074/jbc.M111.271056.

Berman, H M, J Westbrook, Z Feng, G Gilliland, T N Bhat, H Weissig, I N Shindyalov, and P E Bourne. 2000. "The Protein Data Bank." *Nucleic Acids Research* 28 (1): 235–42. https://doi.org/10.1093/nar/28.1.235.

Bernèche, Simon, and Benoît Roux. 2002. "The Ionization State and the Conformation of Glu-71 in the KcsA K+ Channel." *Biophysical Journal* 82 (2): 772–80. https://doi.org/10.1016/S0006-

3495(02)75439-8.

———. 2005. “A Gate in the Selectivity Filter of Potassium Channels.” *Structure* 13 (4): 591–600. https://doi.org/10.1016/j.str.2004.12.019.

Blaustein, R O, P a Cole, C Williams, and C Miller. 2000. “Tethered Blockers as Molecular ‘tape Measures’ for a Voltage-Gated K+ Channel.” *Nature Structural Biology* 7: 309–11. https://doi.org/10.1038/74076.

Bodhinathan, Karthik, and Paul A Slesinger. 2013. “Molecular Mechanism Underlying Ethanol Activation of G-Protein-Gated Inwardly Rectifying Potassium Channels.” *Proceedings of the National Academy of Sciences* 110 (45): 18309–14. https://doi.org/10.1073/pnas.1311406110.

Bukiya, Anna N., Catherine V. Osborn, Guruprasad Kuntamallappanavar, Peter T. Toth, Lia Baki, Gregory Kowalsky, Myung J. Oh, Alex M. Dopico, Irena Levitan, and Avia Rosenhouse-Dantsker. 2015. “Cholesterol Increases the Open Probability of Cardiac KACh Currents.” *Biochimica et Biophysica Acta (BBA) - Biomembranes* 1848 (10): 2406–13. https://doi.org/10.1016/j.bbamem.2015.07.007.

Bukiya, Anna N., and Avia Rosenhouse-Dantsker. 2015. “Hypercholesterolemia Effect on Potassium Channels.” In *Hypercholesterolemia*, 595. InTech. https://doi.org/10.5772/59761.

———. 2017. “Synergistic Activation of G Protein-Gated Inwardly Rectifying Potassium Channels by Cholesterol and PI(4,5)P2.” *Biochimica et Biophysica Acta - Biomembranes* 1859 (7): 1233–41. https://doi.org/10.1016/j.bbamem.2017.03.023.

Bunemann, M., M. Frank, and M. J. Lohse. 2003. “Gi Protein Activation in Intact Cells Involves Subunit Rearrangement Rather than Dissociation.” *Proceedings of the National Academy of Sciences* 100 (26): 16077–82. https://doi.org/10.1073/pnas.2536719100.

Chan, K W, J L Sui, M Vivaudou, and D E Logothetis. 1996. “Control of Channel Activity through a Unique Amino Acid Residue of a G Protein-Gated Inwardly Rectifying K+ Channel Subunit.” *Proceedings of the National Academy of Sciences of the United States of America* 93 (24): 14193–98. https://doi.org/10.1073/pnas.93.24.14193.

Charmandari, Evangelia, Amalia Sertedaki, Tomoshige Kino, Christina Merakou, Dax A. Hoffman, Michael M. Hatch, Darrell E. Hurt, et al. 2012. “A Novel Point Mutation in the KCNJ5 Gene Causing Primary Hyperaldosteronism and Early-Onset Autosomal Dominant Hypertension.” *The Journal of Clinical Endocrinology & Metabolism* 97 (8): E1532–39. https://doi.org/10.1210/jc.2012-1334.

Chen, J, M DeVivo, J Dingus, A Harry, J Li, J Sui, D J Carty, J L Blank, J H Exton, and R H Stoffel. 1995. “A Region of Adenylyl Cyclase 2 Critical for Regulation by G Protein Beta Gamma Subunits.” *Science (New York, N.Y.)* 268 (5214): 1166–69. https://doi.org/10.1126/science.7761832.

Cheng, Wayland W L, Jason G McCoy, Ameer N Thompson, Colin G Nichols, and Crina M Nimigean. 2011. “Mechanism for Selectivity-Inactivation Coupling in KcsA Potassium Channels.” *Proceedings of the National Academy of Sciences of the United States of America* 108 (13): 5272–77. https://doi.org/10.1073/pnas.1014186108.

Choi, M., U. I. Scholl, P. Yue, P. Bjorklund, B. Zhao, C. Nelson-Williams, W. Ji, et al. 2011. “K+ Channel Mutations in Adrenal Aldosterone-Producing Adenomas and Hereditary Hypertension.” *Science* 331 (6018): 768–72. https://doi.org/10.1126/science.1198785.

Clancy, Sinead M., Catherine E. Fowler, Melissa Finley, Ka Fai Suen, Christine Arrabit, Frédérique Berton, Tohru Kosaza, Patrick J. Casey, and Paul A. Slesinger. 2005. “Pertussis-Toxin-Sensitive Gα Subunits Selectively Bind to C-Terminal Domain of Neuronal GIRK Channels: Evidence for a

Heterotrimeric G-Protein-Channel Complex." *Molecular and Cellular Neuroscience* 28 (2): 375–89. https://doi.org/10.1016/j.mcn.2004.10.009.

Clarke, Oliver B., Alessandro T. Caputo, Adam P. Hill, Jamie I. Vandenberg, Brian J. Smith, and Jacqueline M. Gulbis. 2010. "Domain Reorientation and Rotation of an Intracellular Assembly Regulate Conduction in Kir Potassium Channels." *Cell* 141 (6): 1018–29. https://doi.org/10.1016/j.cell.2010.05.003.

Claydon, T.W., S.Y. Makary, K.M. Dibb, and M.R. Boyett. 2004. "K+ Activation of Kir3.1/Kir3.4 and Kv1.4K+ Channels Is Regulated by Extracellular Charges." *Biophysical Journal* 87 (4): 2407–18. https://doi.org/10.1529/biophysj.103.039073.

Cordero-Morales, Julio F., Luis G. Cuello, Yanxiang Zhao, Vishwanath Jogini, D. Marien Cortes, Benoît Roux, and Eduardo Perozo. 2006. "Molecular Determinants of Gating at the Potassium-Channel Selectivity Filter." *Nature Structural & Molecular Biology* 13 (4): 311–18. https://doi.org/10.1038/nsmb1069.

Cordero-Morales, Julio F., Vishwanath Jogini, Sudha Chakrapani, and Eduardo Perozo. 2011. "A Multipoint Hydrogen-Bond Network Underlying KcsA C-Type Inactivation." *Biophysical Journal* 100 (10): 2387–93. https://doi.org/10.1016/j.bpj.2011.01.073.

Cosentino, C., L. Alberio, S. Gazzarrini, M. Aquila, E. Romano, S. Cermenati, P. Zuccolini, et al. 2015. "Engineering of a Light-Gated Potassium Channel." *Science* 348 (6235): 707–10. https://doi.org/10.1126/science.aaa2787.

Cruijsen, E. A. W. van der, D. Nand, M. Weingarth, A. Prokofyev, S. Hornig, A. A. Cukkemane, A. M. J. J. Bonvin, et al. 2013. "Importance of Lipid-Pore Loop Interface for Potassium Channel Structure and Function." *Proceedings of the National Academy of Sciences* 110 (32): 13008–13. https://doi.org/10.1073/pnas.1305563110.

Cukras, Catherine A., Iana Jeliazkova, and Colin G. Nichols. 2002. "Structural and Functional Determinants of Conserved Lipid Interaction Domains of Inward Rectifying Kir6.2 Channels." *The Journal of General Physiology* 119 (6): 581–91. https://doi.org/10.1085/jgp.20028562.

D'Avanzo, Nazzareno, Krzysztof Hyrc, Decha Enkvetchakul, Douglas F. Covey, and Colin G. Nichols. 2011. "Enantioselective Protein-Sterol Interactions Mediate Regulation of Both Prokaryotic and Eukaryotic Inward Rectifier K+ Channels by Cholesterol." Edited by Maria A. Deli. *PLoS ONE* 6 (4): e19393. https://doi.org/10.1371/journal.pone.0019393.

Dascal, N, W Schreibmayer, N F Lim, W Wang, C Chavkin, L DiMagno, C Labarca, B L Kieffer, C Gaveriaux-Ruff, and D Trollinger. 1993. "Atrial G Protein-Activated K+ Channel: Expression Cloning and Molecular Properties." *Proceedings of the National Academy of Sciences of the United States of America* 90 (21): 10235–39. http://www.ncbi.nlm.nih.gov/entrez/query.fcgi?cmd=Retrieve&db=PubMed&dopt=Citation&list_uids=8234283%5Cnhttp://www.pnas.org/content/90/21/10235.full.pdf.

Delemotte, Lucie, Franois Dehez, Werner Treptow, and Mounir Tarek. 2008. "Modeling Membranes under a Transmembrane Potential Modeling Membranes under a Transmembrane Potential" 112 (April): 5547–50. https://doi.org/10.1021/jp710846y.

Deng, Wu, Anna N. Bukiya, Aldo a. Rodríguez-Menchaca, Zhe Zhang, Clive M. Baumgarten, Diomedes E. Logothetis, Irena Levitan, and Avia Rosenhouse-Dantsker. 2012. "Hypercholesterolemia Induces Up-Regulation of K ACh Cardiac Currents via a Mechanism Independent of Phosphatidylinositol 4,5-Bisphosphate and Gβγ." *Journal of Biological Chemistry* 287 (7): 4925–35. https://doi.org/10.1074/jbc.M111.306134.

Deol, Sundeep S., Carmen Domene, Peter J. Bond, and Mark S.P. Sansom. 2006. “Anionic Phospholipid Interactions with the Potassium Channel KcsA: Simulation Studies.” *Biophysical Journal* 90 (3): 822–30. https://doi.org/10.1529/biophysj.105.071407.

Dibb, Katherine M, Thierry Rose, Samy Y Makary, Thomas W Claydon, Decha Enkvetchakul, Robert Leach, Colin G. Nichols, and Mark R Boyett. 2003. “Molecular Basis of Ion Selectivity, Block, and Rectification of the Inward Rectifier Kir3.1/Kir3.4 K + Channel.” *Journal of Biological Chemistry* 278 (49): 49537–48. https://doi.org/10.1074/jbc.M307723200.

Doyle, Declan A, Morais Cabral, Richard A Pfuetzner, Anling Kuo, Jacqueline M Gulbis, Steven L Cohen, Brian T Chait, and Roderick Mackinnon. 1998. “The Structure of the Potassium Channel: Molecular Basis of K+ Conduction and Selectivity.” *Science* 280 (5360): 69–77. https://doi.org/10.1126/science.280.5360.69.

Du, Xiaona, Hailin Zhang, Coeli Lopes, Tooraj Mirshahi, Tibor Rohacs, and Diomedes E. Logothetis. 2004. “Characteristic Interactions with Phosphatidylinositol 4,5-Bisphosphate Determine Regulation of Kir Channels by Diverse Modulators.” *Journal of Biological Chemistry* 279 (36): 37271–81. https://doi.org/10.1074/jbc.M403413200.

Enkvetchakul, Decha, Iana Jeliazkova, Jaya Bhattacharyya, and Colin G. Nichols. 2007. “Control of Inward Rectifier K Channel Activity by Lipid Tethering of Cytoplasmic Domains.” *The Journal of General Physiology* 130 (3): 329–34. https://doi.org/10.1085/jgp.200709764.

Epand, Richard M. 2006. “Cholesterol and the Interaction of Proteins with Membrane Domains.” *Progress in Lipid Research* 45 (4): 279–94. https://doi.org/10.1016/j.plipres.2006.02.001.

Epshtein, Yulia, Arun P Chopra, Avia Rosenhouse-Dantsker, Gregory B Kowalsky, Diomedes E Logothetis, and Irena Levitan. 2009. “Identification of a C-Terminus Domain Critical for the Sensitivity of Kir2.1 to Cholesterol.” *Proceedings of the National Academy of Sciences* 106 (19): 8055–60. https://doi.org/10.1073/pnas.0809847106.

Essen, Lars-Oliver, and Ulrich Koert. 2008. “Ion-Channel Engineering.” *Annual Reports Section “C” (Physical Chemistry)* 104: 165. https://doi.org/10.1039/b703980h.

Fagerberg, Linn, Björn M. Hallström, Per Oksvold, Caroline Kampf, Dijana Djureinovic, Jacob Odeberg, Masato Habuka, et al. 2014. “Analysis of the Human Tissue-Specific Expression by Genome-Wide Integration of Transcriptomics and Antibody-Based Proteomics.” *Molecular & Cellular Proteomics* 13 (2): 397–406. https://doi.org/10.1074/mcp.M113.035600.

Feng, Liang, Ernest B. Campbell, Yichun Hsiung, and Roderick MacKinnon. 2010. “Structure of a Eukaryotic CLC Transporter Defines an Intermediate State in the Transport Cycle.” *Science* 330 (6004): 635–41. https://doi.org/10.1126/science.1195230.

Fortin, D. L., T. W. Dunn, A. Fedorchak, D. Allen, R. Montpetit, M. R. Banghart, D. Trauner, J. P. Adelman, and R. H. Kramer. 2011. “Optogenetic Photochemical Control of Designer K+ Channels in Mammalian Neurons.” *Journal of Neurophysiology* 106 (1): 488–96. https://doi.org/10.1152/jn.00251.2011.

Frenkel, Daan, and Berend Smit. 2002. *Understanding Molecular Simulation*. Elsevier. https://doi.org/10.1016/B978-0-12-267351-1.X5000-7.

Fürst, Oliver, Colin G. Nichols, Guillaume Lamoureux, and Nazzareno D’Avanzo. 2014. “Identification of a Cholesterol-Binding Pocket in Inward Rectifier K + (Kir) Channels.” *Biophysical Journal* 107 (12): 2786–96. https://doi.org/10.1016/j.bpj.2014.10.066.

Gilman, Alfred G. 1987. “G Proteins: Transducers of Receptor-Generated Signals.” *Annual Review of Biochemistry* 56 (1): 615–49. https://doi.org/10.1146/annurev.bi.56.070187.003151.

Glaaser, Ian W., and Paul A. Slesinger. 2015. *Structural Insights into GIRK Channel Function*. *International Review of Neurobiology*. 1st ed. Vol. 123. Elsevier Inc. https://doi.org/10.1016/bs.irn.2015.05.014.

———. 2017. "Dual Activation of Neuronal G Protein-Gated Inwardly Rectifying Potassium (GIRK) Channels by Cholesterol and Alcohol." *Scientific Reports* 7 (1): 4592. https://doi.org/10.1038/s41598-017-04681-x.

Glykos, Nicholas M. 2006. "Software News and Updates Carma: A Molecular Dynamics Analysis Program." *Journal of Computational Chemistry* 27 (14): 1765–68. https://doi.org/10.1002/jcc.20482.

Gordon, John C., Jonathan B. Myers, Timothy Folta, Valia Shoja, Lenwood S. Heath, and Alexey Onufriev. 2005. "H++: A Server for Estimating PKas and Adding Missing Hydrogens to Macromolecules." *Nucleic Acids Research* 33 (Web Server): W368–71. https://doi.org/10.1093/nar/gki464.

Gorostiza, Pau, and Ehud Y. Isacoff. 2008. "Nanoengineering Ion Channels for Optical Control." *Physiology* 23 (5): 238–47. https://doi.org/10.1152/physiol.00018.2008.

Grubmüller, Helmut, and Volker Groll. 2013. "SOLVATE." München, Germany: Theoretical Biophysics Group, Institut für Medizinische Optik, Ludwig-Maximilians-Universität München. https://www.mpibpc.mpg.de/274092/07-License.

Gumbart, James, Fatemeh Khalili-Araghi, Marcos Sotomayor, and Benoît Roux. 2012. "Constant Electric Field Simulations of the Membrane Potential Illustrated with Simple Systems." *Biochimica et Biophysica Acta - Biomembranes* 1818 (2): 294–302. https://doi.org/10.1016/j.bbamem.2011.09.030.

Ha, Junghoon, Yu Xu, Takeharu Kawano, Tyler Hendon, Lia Baki, Sumanta Garai, Andreas Papapetropoulos, Ganesh A. Thakur, Leigh D. Plant, and Diomedes E. Logothetis. 2018. "Hydrogen Sulfide Inhibits Kir2 and Kir3 Channels by Decreasing Sensitivity to the Phospholipid Phosphatidylinositol 4,5-Bisphosphate (PIP2)." *Journal of Biological Chemistry* 293 (10): 3546–61. https://doi.org/10.1074/jbc.RA117.001679.

Haider, Shozeb, Syma Khalid, Stephen J. Tucker, Frances M. Ashcroft, and Mark S P Sansom. 2007. "Molecular Dynamics Simulations of Inwardly Rectifying (Kir) Potassium Channels: A Comparative Study." *Biochemistry* 46 (12): 3643–52. https://doi.org/10.1021/bi062210f.

Hansen, Scott B., Xiao Tao, and Roderick MacKinnon. 2011. "Structural Basis of PIP2 Activation of the Classical Inward Rectifier K+ Channel Kir2.2." *Nature* 477 (7365): 495–98. https://doi.org/10.1038/nature10370.

Hansen, Scott B. 2015. "Lipid Agonism: The PIP2 Paradigm of Ligand-Gated Ion Channels." *Biochimica et Biophysica Acta (BBA) - Molecular and Cell Biology of Lipids* 1851 (5): 620–28. https://doi.org/10.1016/j.bbalip.2015.01.011.

Hanson, Michael A, Vadim Cherezov, Mark T Griffith, Christopher B Roth, Veli-Pekka Jaakola, Ellen Y.T. Chien, Jeffrey Velasquez, Peter Kuhn, and Raymond C Stevens. 2008. "A Specific Cholesterol Binding Site Is Established by the 2.8 Å Structure of the Human B2-Adrenergic Receptor." *Structure* 16 (6): 897–905. https://doi.org/10.1016/j.str.2008.05.001.

He, Cheng, Xixin Yan, Hailin Zhang, Tooraj Mirshahi, Taihao Jin, Aijun Huang, and Diomedes E. Logothetis. 2002. "Identification of Critical Residues Controlling G Protein-Gated Inwardly Rectifying K+channel Activity through Interactions with the Bγ Subunits of G Proteins." *Journal of Biological Chemistry* 277 (8): 6088–96. https://doi.org/10.1074/jbc.M104851200.

He, Cheng, Xixin Yan, Hailin Zhangţ, Tooraj Mirshahiţ, Taihao Jinţ, Aijun Huang, and Diomedes E Logothetisţ. 2002. “Identification of Critical Residues Controlling G Protein-Gated Inwardly Rectifying K+ Channel Activity through Interactions with the Bγ Subunits of G Proteins*.” *J. Biol. Chem.* 277 (8): 6088–6096. https://doi.org/10.1074/jbc.M104851200.

He, Cheng, Hailin Zhang, Tooraj Mirshahi, and Diomedes E. Logothetis. 1999. “Identification of a Potassium Channel Site That Interacts with G Protein Bγ Subunits to Mediate Agonist-Induced Signaling.” *Journal of Biological Chemistry* 274 (18): 12517–24. https://doi.org/10.1074/jbc.274.18.12517.

Heer, Florian T, David J Posson, Wojciech Wojtas-Niziurski, Crina M Nimigean, and Simon Bernèche. 2017. “Mechanism of Activation at the Selectivity Filter of the KcsA K+ Channel.” *ELife* 6 (October): e25844. https://doi.org/10.7554/eLife.25844.

Heginbotham, Lise, Zhe Lu, Tatiana Abramson, and Roderick Mackinnon. 1994. “Mutations in the K + Channel Signature Sequence.” *Biophys J.* 66 (4): 1061–67. https://doi.org/10.1016/S0006-3495(94)80887-2.

Hibino, Hiroshi, Atsushi Inanobe, Kazuharu Furutani, Shingo Murakami, Ian Findlay, and Yoshihisa Kurachi. 2010. “Inwardly Rectifying Potassium Channels: Their Structure, Function, and Physiological Roles.” *Physiology Reviews* 90: 291–366. https://doi.org/10.1152/physrev.00021.2009.

Hille, Bertil, Eamonn J. Dickson, Martin Kruse, Oscar Vivas, and Byung Chang Suh. 2015. “Phosphoinositides Regulate Ion Channels.” *Biochimica et Biophysica Acta - Molecular and Cell Biology of Lipids* 1851 (6): 844–56. https://doi.org/10.1016/j.bbalip.2014.09.010.

Horvath, Gabriella A., Yulin Zhao, Maja Tarailo-Graovac, Cyrus Boelman, Harinder Gill, Casper Shyr, James Lee, et al. 2018. “Gain-of-Function KCNJ6 Mutation in a Severe Hyperkinetic Movement Disorder Phenotype.” *Neuroscience* 384: 152–64. https://doi.org/10.1016/j.neuroscience.2018.05.031.

Huang, Chou-Long, Siyi Feng, and Donald W. Hilgemann. 1998. “Direct Activation of Inward Rectifier Potassium Channels by PIP2 and Its Stabilization by Gβγ.” *Nature* 391 (6669): 803–6. https://doi.org/10.1038/35882.

Humphrey, William, Andrew Dalke, and Klaus Schulten. 1996. “VMD: Visual Molecular Dynamics.” *Journal of Molecular Graphics* 14 (1): 33–38. https://doi.org/10.1016/0263-7855(96)00018-5.

Inanobe, Atsushi, Atsushi Nakagawa, and Yoshihisa Kurachi. 2011. “Interactions of Cations with the Cytoplasmic Pores of Inward Rectifier K + Channels in the Closed State.” *Journal of Biological Chemistry* 286 (48): 41801–11. https://doi.org/10.1074/jbc.M111.278531.

Inanobe, Atsushi, Atsushi Nakagawa, Takanori Matsuura, and Yoshihisa Kurachi. 2010. “A Structural Determinant for the Control of PIP2 Sensitivity in G Protein-Gated Inward Rectifier K+ Channels.” *Journal of Biological Chemistry* 285 (49): 38517–23. https://doi.org/10.1074/jbc.M110.161703.

Ivanova-Nikolova, T T, and G E Breitwieser. 1997. “Effector Contributions to G Beta Gamma-Mediated Signaling as Revealed by Muscarinic Potassium Channel Gating.” *The Journal of General Physiology* 109 (2): 245–53. http://www.pubmedcentral.nih.gov/articlerender.fcgi?artid=2220061&tool=pmcentrez&rendertype=abstract.

Jensen, Morten Ø, David W Borhani, Kresten Lindorff-Larsen, Paul Maragakis, Vishwanath Jogini, Michael P Eastwood, Ron O Dror, and David E Shaw. 2010. “Principles of Conduction and

Hydrophobic Gating in K+ Channels." *Proceedings of the National Academy of Sciences of the United States of America* 107 (13): 5833–38. https://doi.org/10.1073/pnas.0911691107.

Jensen, Morten Ø, Vishwanath Jogini, Michael P Eastwood, and David E Shaw. 2013. "Atomic-Level Simulation of Current–Voltage Relationships in Single-File Ion Channels." *The Journal of General Physiology* 141 (5): 619–32. https://doi.org/10.1085/jgp.201210820.

Jespersen, T., M. Grunnet, K. Angelo, D.A. Klærke, and S.-P. Olesen. 2002. "Dual-Function Vector for Protein Expression in Both Mammalian Cells and Xenopus Laevis Oocytes." *BioTechniques* 32 (3): 536–40. https://doi.org/10.2144/02323st05.

Jiang, Youxing, Alice Lee, Jiayun Chen, Martine Cadene, Brian T Chait, and Roderick MacKinnon. 2002. "The Open Pore Conformation of Potassium Channels." *Nature* 417 (6888): 523–46. https://doi.org/10.1038/417523a.

Jin, Taihao, Luying Peng, Tooraj Mirshahi, Tibor Rohacs, Kim W. Chan, Roberto Sanchez, and Diomedes E. Logothetis. 2002. "The Bγ Subunits of G Proteins Gate a K+channel by Pivoted Bending of a Transmembrane Segment." *Molecular Cell* 10 (3): 469–81. https://doi.org/10.1016/S1097-2765(02)00659-7.

Jin, Weili, and Zhe Lu. 1998. "A Novel High-Affinity Inhibitor for Inward-Rectifier K + Channels †." *Biochemistry* 37 (38): 13291–99. https://doi.org/10.1021/bi981178p.

Jo, Sunhwan, Taehoon Kim, and Wonpil Im. 2007. "Automated Builder and Database of Protein/Membrane Complexes for Molecular Dynamics Simulations." Edited by Adam Yuan. *PLoS ONE* 2 (9): e880. https://doi.org/10.1371/journal.pone.0000880.

Jo, Sunhwan, Taehoon Kim, Vidyashankara G. Iyer, and Wonpil Im. 2008. "CHARMM-GUI: A Web-Based Graphical User Interface for CHARMM." *Journal of Computational Chemistry* 29 (11): 1859–65. https://doi.org/10.1002/jcc.20945.

John, Scott A., Lai-Hua Xie, and James N Weiss. 2004. "Mechanism of Inward Rectification in Kir Channels." *The Journal of General Physiology* 123 (5): 623–25. https://doi.org/10.1085/jgp.200409017.

Kahanovitch, Uri, Vladimir Tsemakhovich, Shai Berlin, Moran Rubinstein, Boaz Styr, Ruth Castel, Sagit Peleg, et al. 2014. "Recruitment of Gβγ Controls the Basal Activity of G-Protein Coupled Inwardly Rectifying Potassium (GIRK) Channels: Crucial Role of Distal C Terminus of GIRK1." *The Journal of Physiology* 592 (24): 5373–90. https://doi.org/10.1113/jphysiol.2014.283218.

Kilambi, Krishna Praneeth, and Jeffrey J. Gray. 2012. "Rapid Calculation of Protein PKa Values Using Rosetta." *Biophysical Journal* 103 (3): 587–95. https://doi.org/10.1016/j.bpj.2012.06.044.

Kim, Dorothy M., Igor Dikiy, Vikrant Upadhyay, David J. Posson, David Eliezer, and Crina M. Nimigean. 2016. "Conformational Heterogeneity in Closed and Open States of the KcsA Potassium Channel in Lipid Bicelles." *The Journal of General Physiology* 148 (2): 119–32. https://doi.org/10.1085/jgp.201611602.

Kobayashi, Toru, Kazutaka Ikeda, Hiroshi Kojima, Hiroaki Niki, Ryoji Yano, Tohru Yoshioka, and Toshiro Kumanishi. 1999. "Ethanol Opens G-Protein-Activated Inwardly Rectifying K+channels." *Nature Neuroscience* 2 (12): 1091–97. https://doi.org/10.1038/16019.

Kozai, Takashi D. Y., and Alberto L. Vazquez. 2015. "Photoelectric Artefact from Optogenetics and Imaging on Microelectrodes and Bioelectronics: New Challenges and Opportunities." *Journal of Materials Chemistry B* 3 (25): 4965–78. https://doi.org/10.1039/C5TB00108K.

Krapivinsky, G., E. A. Gordon, K. Wickman, B. Velimirović, L. Krapivinsky, and D. E. Clapham. 1995.

"The G-Protein-Gated Atrial K+channel IKAchis a Heteromultimer of Two Inwardly Rectifying K+-Channel Proteins." *Nature* 374 (6518): 135–41. https://doi.org/10.1038/374135a0.

Kratochvil, Huong T, Michał Maj, Kimberly Matulef, Alvin W Annen, Jared Ostmeyer, Eduardo Perozo, Benoît Roux, Francis I Valiyaveetil, and Martin T Zanni. 2017. "Probing the Effects of Gating on the Ion Occupancy of the K + Channel Selectivity Filter Using Two-Dimensional Infrared Spectroscopy." *Journal of the American Chemical Society* 139 (26): 8837–45. https://doi.org/10.1021/jacs.7b01594.

Kubo, Y, E Reuveny, P A Slesinger, Y N Jan, and L Y Jan. 1993. "Primary Structure and Functional Expression of a Rat G-Protein-Coupled Muscarinic Potassium Channel." *Nature* 364 (6440): 802–6. https://doi.org/10.1038/364802a0.

Kurata, Harley T., Alejandro Akrouh, Jenny B W Li, Laurence J. Marton, and Colin G. Nichols. 2013. "Scanning the Topography of Polyamine Blocker Binding in an Inwardly Rectifying Potassium Channel." *Journal of Biological Chemistry* 288 (9): 6591–6601. https://doi.org/10.1074/jbc.M112.383794.

Kutzner, Carsten, Helmut Grubmüller, Bert L. De Groot, and Ulrich Zachariae. 2011. "Computational Electrophysiology: The Molecular Dynamics of Ion Channel Permeation and Selectivity in Atomistic Detail." *Biophysical Journal* 101 (4): 809–17. https://doi.org/10.1016/j.bpj.2011.06.010.

Lacin, Emre, Prafulla Aryal, Ian W. Glaaser, Karthik Bodhinathan, Eric Tsai, Nidaa Marsh, Stephen J. Tucker, Mark S.P. Sansom, and Paul A. Slesinger. 2017. "Dynamic Role of the Tether Helix in PIP 2 -Dependent Gating of a G Protein–Gated Potassium Channel." *The Journal of General Physiology* 149 (8): 799–811. https://doi.org/10.1085/jgp.201711801.

Lee, Jumin, Xi Cheng, Jason M. Swails, Min Sun Yeom, Peter K. Eastman, Justin A. Lemkul, Shuai Wei, et al. 2016. "CHARMM-GUI Input Generator for NAMD, GROMACS, AMBER, OpenMM, and CHARMM/OpenMM Simulations Using the CHARMM36 Additive Force Field." *Journal of Chemical Theory and Computation* 12 (1): 405–13. https://doi.org/10.1021/acs.jctc.5b00935.

Lee, Sun-Joo, Feifei Ren, Eva-Maria Zangerl-Plessl, Sarah Heyman, Anna Stary-Weinzinger, Peng Yuan, and Colin G. Nichols. 2016. "Structural Basis of Control of Inward Rectifier Kir2 Channel Gating by Bulk Anionic Phospholipids." *The Journal of General Physiology* 148 (3): jgp.201611616. https://doi.org/10.1085/jgp.201611616.

Lee, Sun Joo, Shizhen Wang, William Borschel, Sarah Heyman, Jacob Gyore, and Colin G. Nichols. 2013. "Secondary Anionic Phospholipid Binding Site and Gating Mechanism in Kir2.1 Inward Rectifier Channels." *Nature Communications* 4: 1–12. https://doi.org/10.1038/ncomms3786.

Lemoine, D., C. Habermacher, A. Martz, P.-F. Mery, N. Bouquier, F. Diverchy, A. Taly, F. Rassendren, A. Specht, and T. Grutter. 2013. "Optical Control of an Ion Channel Gate." *Proceedings of the National Academy of Sciences* 110 (51): 20813–18. https://doi.org/10.1073/pnas.1318715110.

Lenaeus, Michael J, Magdalini Vamvouka, Pamela J Focia, and Adrian Gross. 2005. "Structural Basis of TEA Blockade in a Model Potassium Channel." *Nature Structural & Molecular Biology* 12 (5): 454–59. https://doi.org/10.1038/nsmb929.

Lesage, Florian, Fabrice Duprat, Michel Fink, Eric Guillemare, Thierry Coppola, Michel Lazdunski, and Jean Philippe Hugnot. 1994. "Cloning Provides Evidence for a Family of Inward Rectifier and G-Protein Coupled K+ Channels in the Brain." *FEBS Letters* 353 (1): 37–42. https://doi.org/10.1016/0014-5793(94)01007-2.

Levitan, Irena. 2009. "Cholesterol and Kir Channels." *IUBMB Life* 61 (8): 781–90.

https://doi.org/10.1002/iub.192.

Lewohl, Joanne M, Walter R Wilson, R Dayne Mayfield, Susan J Brozowski, Richard A Morrisett, and R Adron Harris. 1999. “G-Protein-Coupled Inwardly Rectifying Potassium Channels Are Targets of Alcohol Action.” *Nature Neuroscience* 2 (12): 1084–90. https://doi.org/10.1038/16012.

Li-Smerin, Yingying, David H Hackos, and Kenton J Swartz. 2000. “A Localized Interaction Surface for Voltage-Sensing Domains on the Pore Domain of a K+ Channel.” *Neuron* 25 (2): 411–23. https://doi.org/10.1016/S0896-6273(00)80904-6.

Li, Hua, and Vassilios Papadopoulos. 1998. “Peripheral-Type Benzodiazepine Receptor Function in Cholesterol Transport. Identification of a Putative Cholesterol Recognition/Interaction Amino Acid Sequence and Consensus Pattern 1.” *Endocrinology* 139 (12): 4991–97. https://doi.org/10.1210/endo.139.12.6390.

Li, Hui, Van Ngo, Mauricio Chagas Da Silva, Dennis R. Salahub, Karen Callahan, Benoît Roux, and Sergei Yu. Noskov. 2015. “Representation of Ion–Protein Interactions Using the Drude Polarizable Force-Field.” *The Journal of Physical Chemistry B* 119 (29): 9401–16. https://doi.org/10.1021/jp510560k.

Li, Junwei, Shouqin Lü, Yuzhi Liu, Chunli Pang, Yafei Chen, Suhua Zhang, Hui Yu, et al. 2015a. “Identification of the Conformational Transition Pathway in PIP2 Opening Kir Channels.” *Scientific Reports* 5 (1): 11289. https://doi.org/10.1038/srep11289.

———. 2015b. “Identification of the Conformational Transition Pathway in PIP2 Opening Kir Channels.” *Scientific Reports* 5 (1): 11289. https://doi.org/10.1038/srep11289.

Logothetis, D E, V I Petrou, M Zhang, R Mahajan, X Y Meng, S K Adney, M Cui, and L Baki. 2015. “Phosphoinositide Control of Membrane Protein Function: A Frontier Led by Studies on Ion Channels.” *Annu Rev Physiol* 77: 81–104. https://doi.org/10.1146/annurev-physiol-021113-170358.

Logothetis, Diomedes E., Rahul Mahajan, Scott K. Adney, Junghoon Ha, Takeharu Kawano, Xuan Yu Meng, and Meng Cui. 2015. *Unifying Mechanism of Controlling Kir3 Channel Activity by G Proteins and Phosphoinositides*. *International Review of Neurobiology*. 1st ed. Vol. 123. Elsevier Inc. https://doi.org/10.1016/bs.irn.2015.05.013.

Logothetis, Diomedes E, Yoshihisa Kurachi, Jonas Galper, Eva J Neer, and David E Clapham. 1987. “The Bγ Subunits of GTP-Binding Proteins Activate the Muscarinic K+ Channel in Heart.” *Nature* 325 (6102): 321–26. https://doi.org/10.1038/325321a0.

Lomize, Mikhail A., Irina D. Pogozheva, Hyeon Joo, Henry I. Mosberg, and Andrei L. Lomize. 2012. “OPM Database and PPM Web Server: Resources for Positioning of Proteins in Membranes.” *Nucleic Acids Research* 40 (D1): D370–76. https://doi.org/10.1093/nar/gkr703.

Long, Stephen B., Xiao Tao, Ernest B. Campbell, and Roderick MacKinnon. 2007. “Atomic Structure of a Voltage-Dependent K+ Channel in a Lipid Membrane-like Environment.” *Nature* 450 (7168): 376–82. https://doi.org/10.1038/nature06265.

Lueck, John D., Adam L. Mackey, Daniel T. Infield, Jason D. Galpin, Jing Li, Benoît Roux, and Christopher A. Ahern. 2016. “Atomic Mutagenesis in Ion Channels with Engineered Stoichiometry.” *ELife* 5 (OCTOBER2016): 1–16. https://doi.org/10.7554/eLife.18976.

Luján, Rafael, and Carolina Aguado. 2015. “Localization and Targeting of GIRK Channels in Mammalian Central Neurons.” *International Review of Neurobiology* 123: 161–200. https://doi.org/10.1016/bs.irn.2015.05.009.

Lüscher, Christian, and Paul a Slesinger. 2010. “Emerging Concepts for G Protein-Gated Inwardly Rectifying (GIRK) Channels in Health and Disease.” *Nature Reviews Neuroscience* 11 (5): 301–15. https://doi.org/10.1038/nrn2834.Emerging.

Lyskov, Sergey, Fang-Chieh Chou, Shane Ó Conchúir, Bryan S. Der, Kevin Drew, Daisuke Kuroda, Jianqing Xu, et al. 2013. “Serverification of Molecular Modeling Applications: The Rosetta Online Server That Includes Everyone (ROSIE).” Edited by Vladimir N. Uversky. *PLoS ONE* 8 (5): e63906. https://doi.org/10.1371/journal.pone.0063906.

Mahajan, Rahul, Junghoon Ha, Miao Zhang, Takeharu Kawano, Tohru Kozasa, and Diomedes E. Logothetis. 2013. “A Computational Model Predicts That Gbg Acts at a Cleft Between Channel Subunits to Activate GIRK1 Channels.” *Science Signaling* 6 (288): ra69–ra69. https://doi.org/10.1126/scisignal.2004075.

Mao, Jinzhe, Lilly Li, Maurine McManus, Jianping Wu, Ningren Cui, and Chun Jiang. 2002. “Molecular Determinants for Activation of G-Protein-Coupled Inward Rectifier K + (GIRK) Channels by Extracellular Acidosis.” *Journal of Biological Chemistry* 277 (48): 46166–71. https://doi.org/10.1074/jbc.M205438200.

Martin, Gregory M, Craig Yoshioka, Emily A Rex, Jonathan F Fay, Qing Xie, Matthew R Whorton, James Z Chen, and Show-Ling Shyng. 2017. “Cryo-EM Structure of the ATP-Sensitive Potassium Channel Illuminates Mechanisms of Assembly and Gating.” *ELife* 6 (January). https://doi.org/10.7554/eLife.24149.

Mase, Yoko, Mariko Yokogawa, Masanori Osawa, and Ichio Shimada. 2012. “Structural Basis for Modulation of Gating Property of G Protein-Gated Inwardly Rectifying Potassium Ion Channel (GIRK) by i/o-Family G Protein α Subunit (Gα i/O).” *Journal of Biological Chemistry* 287 (23): 19537–49. https://doi.org/10.1074/jbc.M112.353888.

Masotti, Andrea, Paolo Uva, Laura Davis-Keppen, Lina Basel-Vanagaite, Lior Cohen, Elisa Pisaneschi, Antonella Celluzzi, et al. 2015. “Keppen-Lubinsky Syndrome Is Caused by Mutations in the Inwardly Rectifying K+channel Encoded by KCNJ6.” *American Journal of Human Genetics* 96 (2): 295–300. https://doi.org/10.1016/j.ajhg.2014.12.011.

Mayfield, Jody, Yuri A. Blednov, and R. Adron Harris. 2015. *Behavioral and Genetic Evidence for GIRK Channels in the CNS: Role in Physiology, Pathophysiology, and Drug Addiction*. *International Review of Neurobiology*. 1st ed. Vol. 123. Elsevier Inc. https://doi.org/10.1016/bs.irn.2015.05.016.

Medovoy, David, Eduardo Perozo, and Benoît Roux. 2016. “Multi-Ion Free Energy Landscapes Underscore the Microscopic Mechanism of Ion Selectivity in the KcsA Channel.” *Biochimica et Biophysica Acta (BBA) - Biomembranes* 1858 (7): 1722–32. https://doi.org/10.1016/j.bbamem.2016.02.019.

Meng, Xuan-Yu, Shengtang Liu, Meng Cui, Ruhong Zhou, and Diomedes E. Logothetis. 2016. “The Molecular Mechanism of Opening the Helix Bundle Crossing (HBC) Gate of a Kir Channel.” *Scientific Reports* 6: 29399. https://doi.org/10.1038/srep29399.

Meng, Xuan Yu, Hong Xing Zhang, Diomedes E. Logothetis, and Meng Cui. 2012a. “The Molecular Mechanism by Which PIP2 Opens the Intracellular G-Loop Gate of a Kir3.1 Channel.” *Biophysical Journal* 102 (9): 2049–59. https://doi.org/10.1016/j.bpj.2012.03.050.

———. 2012b. “The Molecular Mechanism by Which PIP2 Opens the Intracellular G-Loop Gate of a Kir3.1 Channel.” *Biophysical Journal* 102 (9): 2049–59. https://doi.org/10.1016/j.bpj.2012.03.050.

Mintert, Elisa, Leif I. Bösche, Andreas Rinne, Mathias Timpert, Marie Cécile Kienitz, Lutz Pott, and Kirsten Bender. 2007. “Generation of a Constitutive Na+-Dependent Inward-Rectifier Current in Rat Adult Atrial Myocytes by Overexpression of Kir3.4.” *Journal of Physiology* 585 (1): 3–13. https://doi.org/10.1113/jphysiol.2007.140772.

Mirshahi, Tooraj, Liliane Robillard, Hailin Zhang, Terence E. Hébert, and Diomedes E Logothetis. 2002. “Gβ Residues That Do Not Interact with Gα Underlie Agonist-Independent Activity of K + Channels.” *Journal of Biological Chemistry* 277 (9): 7348–55. https://doi.org/10.1074/jbc.M109999200.

Mitchell, Michael R, and Stanislas Leibler. 2018. “Elastic Strain and Twist Analysis of Protein Structural Data and Allostery of the Transmembrane Channel KcsA.” *Physical Biology* 15 (3): 036004. https://doi.org/10.1088/1478-3975/aa9906.

Miyake, M., M. J. Christie, and R. A. North. 1989. “Single Potassium Channels Opened by Opioids in Rat Locus Ceruleus Neurons.” *Proceedings of the National Academy of Sciences* 86 (9): 3419–22. https://doi.org/10.1073/pnas.86.9.3419.

Moreau, Christophe J., Jean Revilloud, Lydia N. Caro, Julien P. Dupuis, Amandine Trouchet, Argel Estrada-Mondragón, Katarzyna Nieścierowicz, Nicolas Sapay, Serge Crouzy, and Michel Vivaudou. 2017. “Tuning the Allosteric Regulation of Artificial Muscarinic and Dopaminergic Ligand-Gated Potassium Channels by Protein Engineering of G Protein-Coupled Receptors.” *Scientific Reports* 7 (February): 41154. https://doi.org/10.1038/srep41154.

Mulatero, Paolo, Philipp Tauber, Maria Christina Zennaro, Silvia Monticone, Katharina Lang, Felix Beuschlein, Evelyn Fischer, et al. 2012. “KCNJ5 Mutations in European Families with Nonglucocorticoid Remediable Familial Hyperaldosteronism.” *Hypertension* 59 (2): 235–40. https://doi.org/10.1161/HYPERTENSIONAHA.111.183996.

Nanda, Jagpreet S., and Jon R. Lorsch. 2014. “Labeling of a Protein with Fluorophores Using Maleimide Derivitization.” In , 79–86. https://doi.org/10.1016/B978-0-12-420070-8.00007-6.

Nishida, Motohiko, Martine Cadene, Brian T Chait, and Roderick MacKinnon. 2007. “Crystal Structure of a Kir3.1-Prokaryotic Kir Channel Chimera.” *The EMBO Journal* 26 (17): 4005–15. https://doi.org/10.1038/sj.emboj.7601828.

Nishida, Motohiko, and Roderick MacKinnon. 2002. “Structural Basis of Inward Rectification: Cytoplasmic Pore of the G Protein-Gated Inward Rectifier GIRK1 at 1.8 Å Resolution.” *Cell* 111 (7): 957–65. https://doi.org/10.1016/S0092-8674(02)01227-8.

North, R Alan, John T Williams, Annmarie Surprenant, and Macdonald J Christie. 1987. “Mu and Delta Receptors Belong to a Family of Receptors That Are Coupled to Potassium Channels.” *Proceedings of the National Academy of Sciences* 84 (15): 5487–91. https://doi.org/10.1073/pnas.84.15.5487.

O’Malley, S M, and Melisendra J. McDonald. 1994. “Steady State Fluorescence Energy Transfer Measurements of Human Alpha Apohemoglobin Structure.” *Biochemical and Biophysical Research Communications* 200 (1): 384–88. https://doi.org/0006-291X/94.

Olsson, Mats H M, Chresten R Søndergaard, Michal Rostkowski, and Jan H Jensen. 2011. “PROPKA3: Consistent Treatment of Internal and Surface Residues in Empirical p K a Predictions.” *Journal of Chemical Theory and Computation* 7 (2): 525–37. https://doi.org/10.1021/ct100578z.

Onufriev, Alexey V., and Emil Alexov. 2013. “Protonation and PK Changes in Protein–Ligand Binding.” *Quarterly Reviews of Biophysics* 46 (02): 181–209. https://doi.org/10.1017/S0033583513000024.

Osawa, Masanori, Mariko Yokogawa, Takahiro Muramatsu, Tomomi Kimura, Yoko Mase, and Ichio Shimada. 2009. “Evidence for the Direct Interaction of Spermine with the Inwardly Rectifying Potassium Channel.” *The Journal of Biological Chemistry* 284 (38): 26117–26. https://doi.org/10.1074/jbc.M109.029355.

Pegan, Scott, Christine Arrabit, Paul A. Slesinger, and Senyon Choe. 2006. “Andersen’s Syndrome Mutation Effects on the Structure and Assembly of the Cytoplasmic Domains of Kir2.1.” *Biochemistry* 45 (28): 8599–8606. https://doi.org/10.1021/bi060653d.

Pegan, Scott, Christine Arrabit, Wei Zhou, Witek Kwiatkowski, Anthony Collins, Paul A. Slesinger, and Senyon Choe. 2005. “Cytoplasmic Domain Structures of Kir2.1 and Kir3.1 Show Sites for Modulating Gating and Rectification.” *Nature Neuroscience* 8 (3): 279–87. https://doi.org/10.1038/nn1411.

Pfaffinger, Paul J., Jennifer M. Martin, Dale D. Hunter, Neil M. Nathanson, and Bertil Hille. 1985. “GTP-Binding Proteins Couple Cardiac Muscarinic Receptors to a K Channel.” *Nature* 317 (6037): 536–38. https://doi.org/10.1038/317536a0.

Phillips, James C., Rosemary Braun, Wei Wang, James Gumbart, Emad Tajkhorshid, Elizabeth Villa, Christophe Chipot, Robert D. Skeel, Laxmikant Kalé, and Klaus Schulten. 2005. “Scalable Molecular Dynamics with NAMD.” *Journal of Computational Chemistry* 26 (16): 1781–1802. https://doi.org/10.1002/jcc.20289.

Raghuraman, H., Shahidul M. Islam, Soumi Mukherjee, Benoit Roux, and Eduardo Perozo. 2014. “Dynamics Transitions at the Outer Vestibule of the KcsA Potassium Channel during Gating.” *Proceedings of the National Academy of Sciences* 111 (5): 1831–36. https://doi.org/10.1073/pnas.1314875111.

Raja, Mobeen, and Elisabeth Vales. 2009. “Changing Val-76 towards Kir Channels Drastically Influences the Folding and Gating Properties of the Bacterial Potassium Channel KcsA.” *Biophysical Chemistry* 144 (3): 95–100. https://doi.org/10.1016/j.bpc.2009.06.006.

Ramos-Hunter, Susan J., Darren W. Engers, Kristian Kaufmann, Yu Du, Craig W. Lindsley, C. David Weaver, and Gary A. Sulikowski. 2013. “Discovery and SAR of a Novel Series of GIRK1/2 and GIRK1/4 Activators.” *Bioorganic and Medicinal Chemistry Letters* 23 (18): 5195–98. https://doi.org/10.1016/j.bmcl.2013.07.002.

Rebois, R. Victor, Mélanie Robitaille, Céline Galés, Denis J Dupré, Alessandra Baragli, Phan Trieu, Nathalie Ethier, Michel Bouvier, and Terence E Hébert. 2006. “Heterotrimeric G Proteins Form Stable Complexes with Adenylyl Cyclase and Kir3.1 Channels in Living Cells.” *Journal of Cell Science* 119 (Pt 13): 2807–18. https://doi.org/10.1242/jcs.03021.

Rifkin, Robert A., Stephen J. Moss, and Paul A. Slesinger. 2017. “G Protein-Gated Potassium Channels: A Link to Drug Addiction.” *Trends in Pharmacological Sciences* 38 (4): 378–92. https://doi.org/10.1016/j.tips.2017.01.007.

Riven, Inbal, Eli Kalmanzon, Lior Segev, and Eitan Reuveny. 2003. “Conformational Rearrangements Associated with the Gating of the G Protein-Coupled Potassium Channel Revealed by FRET Microscopy.” *Neuron* 38 (2): 225–35. https://doi.org/10.1016/S0896-6273(03)00193-4.

Robertson, J. L., L. G. Palmer, and Benoît Roux. 2012. “Multi-Ion Distributions in the Cytoplasmic Domain of Inward Rectifier Potassium Channels.” *Biophysical Journal* 103 (3): 434–43. https://doi.org/10.1016/j.bpj.2012.06.023.

Robertson, Janice L, Lawrence G Palmer, and Benoît Roux. 2008. “Long-Pore Electrostatics in Inward-Rectifier Potassium Channels.” *The Journal of General Physiology* 132 (6): 613–32.

https://doi.org/10.1085/jgp.200810068.

Rohacs, T., Coeli M B Lopes, Taihao Jin, Pavan P Ramdya, Z. Molnar, and Diomedes E Logothetis. 2003. “Specificity of Activation by Phosphoinositides Determines Lipid Regulation of Kir Channels.” *Proceedings of the National Academy of Sciences* 100 (2): 745–50. https://doi.org/10.1073/pnas.0236364100.

Rosenhouse-Dantsker, Avia, Edgar Leal-Pinto, Diomedes E. Logothetis, and Irena Levitan. 2010. “Comparative Analysis of Cholesterol Sensitivity of Kir Channels: Role of the CD Loop.” *Channels (Austin, Tex.)* 4 (1): 63–66. http://www.ncbi.nlm.nih.gov/pubmed/19923917.

Rosenhouse-Dantsker, Avia, and Diomedes E. Logothetis. 2006. “New Roles for a Key Glycine and Its Neighboring Residue in Potassium Channel Gating.” *Biophysical Journal* 91 (8): 2860–73. https://doi.org/10.1529/biophysj.105.080242.

———. 2007. “Potassium Channel Gating in the Absence of the Highly Conserved Glycine of the Inner Transmembrane Helix.” *Channels* 1 (3): 189–97. https://doi.org/10.4161/chan.4475.

Rosenhouse-Dantsker, Avia, Sergei Noskov, Serdar Durdagi, Diomedes E. Logothetis, and Irena Levitan. 2013. “Identification of Novel Cholesterol-Binding Regions in Kir2 Channels.” *Journal of Biological Chemistry* 288 (43): 31154–64. https://doi.org/10.1074/jbc.M113.496117.

Rosenhouse-Dantsker, Avia, Sergei Noskov, Huazhi Han, Scott K. Adney, Qiong Yao Tang, Aldo A. Rodríguez-Menchaca, Gregory B. Kowalsky, et al. 2012. “Distant Cytosolic Residues Mediate a Two-Way Molecular Switch That Controls the Modulation of Inwardly Rectifying Potassium (Kir) Channels by Cholesterol and Phosphatidylinositol 4,5-Bisphosphate (PI(4,5)P2).” *Journal of Biological Chemistry* 287 (48): 40266–78. https://doi.org/10.1074/jbc.M111.336339.

Rosenhouse-dantsker, Avia, Jin L Sui, Qi Zhao, Radda Rusinova, Zhe Zhang, and Diomedes E Logothetis. 2014. “A Sodium-Mediated Structural Switch That Controls the Sensitivity of Kir Channels to PIP2” 4 (10): 624–31. https://doi.org/10.1038/nchembio.112.A.

Roux, Benoît. 2005. “ION CONDUCTION AND SELECTIVITY IN K + CHANNELS.” *Annu. Rev. Biophys. Biomol. Struct* 34: 153–71. https://doi.org/10.1146/annurev.biophys.34.040204.144655.

Sadja, Rona, Karine Smadja, Noga Alagem, and Eitan Reuveny. 2001. “Coupling Gβγ-Dependent Activation to Channel Opening via Pore Elements in Inwardly Rectifying Potassium Channels.” *Neuron* 29 (3): 669–80. https://doi.org/10.1016/S0896-6273(01)00242-2.

Sakmann, B, A Noma, and W Trautwein. 1983. “Acetylcholine Activation of Single Muscarinic K+ Channels in Isolated Pacemaker Cells of the Mammalian Heart.” *Nature* 303 (5914): 250–53. https://doi.org/10.1038/303250a0.

Sali, A, and T L Blundell. 1993. “Comparative Protein Modelling by Satisfaction of Spatial Restraints.” *Journal of Molecular Biology*. https://doi.org/10.1006/jmbi.1993.1626.

Sarvazyan, Noune a, Ann E Remmers, and Richard R Neubig. 1998. “Determinants of Gi1alpha and Beta Gamma Binding. Measuring High Affinity Interactions in a Lipid Environment Using Flow Cytometry.” *The Journal of Biological Chemistry* 273 (14): 7934–40. http://www.ncbi.nlm.nih.gov/pubmed/9525890.

Schreibmayer, Wolfgang, Carmen W. Dessauer, Dmitry Vorobiov, Alfred G. Gilman, Henry A. Lester, Norman Davidson, and Nathan Dascal. 1996. “Inhibition of an Inwardly Rectifying K+ Channel by G-Protein α-Subunits.” *Nature* 380 (6575): 624–27. https://doi.org/10.1038/380624a0.

Sethi, A., J. Eargle, A. A. Black, and Z. Luthey-Schulten. 2009. “Dynamical Networks in TRNA:Protein Complexes.” *Proceedings of the National Academy of Sciences* 106 (16): 6620–25.

https://doi.org/10.1073/pnas.0810961106.

Shrivastava, Indira H., and Ivet Bahar. 2006. “Common Mechanism of Pore Opening Shared by Five Different Potassium Channels.” *Biophysical Journal* 90 (11): 3929–40. https://doi.org/10.1529/biophysj.105.080093.

Shyng, Show-Ling, Catherine A Cukras, Jane Harwood, and Colin G Nichols. 2000. “Structural Determinants of Pip 2 Regulation of Inward Rectifier K ATP Channels.” *The Journal of General Physiology* 116 (5): 599–608. https://doi.org/10.1085/jgp.116.5.599.

Smart, Oliver S., Joseph G. Neduvelil, Xiaonan Wang, B. A. Wallace, and Mark S P Sansom. 1996. “HOLE: A Program for the Analysis of the Pore Dimensions of Ion Channel Structural Models.” *Journal of Molecular Graphics* 14 (6): 354–60. https://doi.org/10.1016/S0263-7855(97)00009-X.

Smirnov, Sergei N., Ivan V. Vlassiouk, and Nickolay V. Lavrik. 2011. “Voltage-Gated Hydrophobic Nanopores.” *ACS Nano* 5 (9): 7453–61. https://doi.org/10.1021/nn202392d.

Sohn, Jong-Woo, Ajin Lim, Suk-Ho Lee, and Won-Kyung Ho. 2007. “Decrease in PIP 2 -Channel Interactions Is the Final Common Mechanism Involved in PKC- and Arachidonic Acid-Mediated Inhibitions of GABA B -Activated K + Current.” *The Journal of Physiology* 582 (3): 1037–46. https://doi.org/10.1113/jphysiol.2007.137265.

Søndergaard, Chresten R., Mats H. M. Olsson, Michał Rostkowski, and Jan H. Jensen. 2011. “Improved Treatment of Ligands and Coupling Effects in Empirical Calculation and Rationalization of p K a Values.” *Journal of Chemical Theory and Computation* 7 (7): 2284–95. https://doi.org/10.1021/ct200133y.

Stansfeld, Phillip J, Richard Hopkinson, Frances M Ashcroft, and Mark S P Sansom. 2009. “PIP 2 -Binding Site in Kir Channels: Definition by Multiscale Biomolecular Simulations.” *Biochemistry* 48 (46): 10926–33. https://doi.org/10.1021/bi9013193.

Sui, J. L., Jérme Petit-Jacques, and Diomedes E Logothetis. 1998. “Activation of the Atrial KACh Channel by the Beta,Gama Subunits of G Proteins or Intracellular Na+ Ions Depends on the Presence of Phosphatidylinositol Phosphates.” *Proceedings of the National Academy of Sciences* 95 (3): 1307–12. https://doi.org/10.1073/pnas.95.3.1307.

Tang, Qiong-Yao, Trevor Larry, Kalen Hendra, Erica Yamamoto, Jessica Bell, Meng Cui, Diomedes E Logothetis, and Linda M Boland. 2015. “Mutations in Nature Conferred a High Affinity Phosphatidylinositol 4,5-Bisphosphate-Binding Site in Vertebrate Inwardly Rectifying Potassium Channels.” *Journal of Biological Chemistry* 290 (27): 16517–29. https://doi.org/10.1074/jbc.M115.640409.

Tao, X., J. L. Avalos, J. Chen, and R. MacKinnon. 2009. “Crystal Structure of the Eukaryotic Strong Inward-Rectifier K+ Channel Kir2.2 at 3.1 A Resolution.” *Science* 326 (5960): 1668–74. https://doi.org/10.1126/science.1180310.

Tesmer, John J.G., David M. Berman, Alfred G. Gilman, and Stephen R. Sprang. 1997. “Structure of RGS4 Bound to AlF4−-Activated Giα1: Stabilization of the Transition State for GTP Hydrolysis.” *Cell* 89 (2): 251–61. https://doi.org/10.1016/S0092-8674(00)80204-4.

Tilegenova, Cholpon, D Marien Cortes, and Luis G Cuello. 2017. “Hysteresis of KcsA Potassium Channel’s Activation– Deactivation Gating Is Caused by Structural Changes at the Channel’s Selectivity Filter.” *Proceedings of the National Academy of Sciences* 114 (12): 3234–39. https://doi.org/10.1073/pnas.1618101114.

Tipps, Megan E., and Kari J. Buck. 2015. *GIRK Channels: A Potential Link Between Learning and Addiction*. *International Review of Neurobiology*. 1st ed. Vol. 123. Elsevier Inc.

https://doi.org/10.1016/bs.irn.2015.05.012.

Touhara, Kouki K., Weiwei Wang, and Roderick Mackinnon. 2016. “The GIRK1 Subunit Potentiates G Protein Activation of Cardiac GIRK1/4 Heterotetramers.” *ELife* 5 (April 2016): 1–12. https://doi.org/10.7554/eLife.15750.

Toyama, Yuki, Hanaho Kano, Yoko Mase, Mariko Yokogawa, Masanori Osawa, and Ichio Shimada. 2018. “Structural Basis for the Ethanol Action on G-Protein–Activated Inwardly Rectifying Potassium Channel 1 Revealed by NMR Spectroscopy.” *Proceedings of the National Academy of Sciences* 115 (15): 3858–63. https://doi.org/10.1073/pnas.1722257115.

Trads, Julie B, Jessica Burgstaller, Laura Laprell, David B Konrad, Luis de la Osa de la Rosa, C. David Weaver, Herwig Baier, Dirk Trauner, and David M Barber. 2017. “Optical Control of GIRK Channels Using Visible Light.” *Organic & Biomolecular Chemistry* 15 (1): 76–81. https://doi.org/10.1039/C6OB02153K.

Vanommeslaeghe, K., E. Hatcher, C. Acharya, S. Kundu, S. Zhong, J. Shim, E. Darian, et al. 2009. “CHARMM General Force Field: A Force Field for Drug-like Molecules Compatible with the CHARMM All-Atom Additive Biological Force Fields.” *Journal of Computational Chemistry* 31 (4): NA-NA. https://doi.org/10.1002/jcc.21367.

Varon, Dalia, Nathan Dascal, Tatiana Ivanina, Carmen W Dessauer, and Sagit Peleg. 2002. “G(Alpha)(i) Controls the Gating of the G Protein-Activated K(+) Channel, GIRK.” *Neuron* 33 (1): 87–99. https://doi.org/10.1016/S0896-6273(01)00567-0.

Velasco, Ezequiel Marron Fernandez de, Nora McCall, and Kevin Wickman. 2015. *GIRK Channel Plasticity and Implications for Drug Addiction*. *International Review of Neurobiology*. 1st ed. Vol. 123. Elsevier Inc. https://doi.org/10.1016/bs.irn.2015.05.011.

Vivaudou, Michel, Kim W. Chan, Jin Liang Sui, Lily Y. Jan, Eitan Reuveny, and Diomedes E. Logothetis. 1997. “Probing the G-Protein Regulation of GIRK1 and GIRK4, the Two Subunits of the K(ACh) Channel, Using Functional Homomeric Mutants.” *Journal of Biological Chemistry* 272 (50): 31553–60. https://doi.org/10.1074/jbc.272.50.31553.

Vivaudou, Michel, Zlatomir Todorov, Gina Catalina Reyes-Mejia, and Christophe Moreau. 2017. “Ion Channels as Reporters of Membrane Receptor Function: Automated Analysis in Xenopus Oocytes.” In , 1635:283–301. https://doi.org/10.1007/978-1-4939-7151-0_15.

Vlugt, T J H, J P J M van der Eerden, M Dijkstra, B Smit, and D Frenkel. 2009. *Introduction to Molecular Simulation and Statistical Thermodynamics*. *Computer*.

Walsh, Kenneth B., Elaine A. Gay, Bruce E. Blough, and David W. Geurkink. 2017. “N-(2-Methoxyphenyl) Benzenesulfonamide, a Novel Regulator of Neuronal G Protein-Gated Inward Rectifier K+channels.” *European Journal of Pharmacology* 815 (September): 233–40. https://doi.org/10.1016/j.ejphar.2017.09.020.

Wang, Weiwei, Kouki K. Touhara, Keiko Weir, Bruce P. Bean, and Roderick MacKinnon. 2016. “Cooperative Regulation by G Proteins and Na+ of Neuronal GIRK2 K+ Channels.” *ELife* 5 (April 2016): 1–15. https://doi.org/10.7554/eLife.15751.

Wang, Weiwei, Matthew R. Whorton, and Roderick MacKinnon. 2014. “Quantitative Analysis of Mammalian GIRK2 Channel Regulation by G Proteins, the Signaling Lipid PIP2 and Na+ in a Reconstituted System.” *ELife* 3: e03671. https://doi.org/10.7554/eLife.03671.

Wei, A. D. 2005. “International Union of Pharmacology. LII. Nomenclature and Molecular Relationships of Calcium-Activated Potassium Channels.” *Pharmacological Reviews* 57 (4): 463–72. https://doi.org/10.1124/pr.57.4.9.

Wen, Wandong, Wenjun Wu, Ian M. Romaine, Kristian Kaufmann, Yu Du, Gary A. Sulikowski, C. David Weaver, and Craig W. Lindsley. 2013. “Discovery of ‘molecular Switches’ within a GIRK Activator Scaffold That Afford Selective GIRK Inhibitors.” *Bioorganic and Medicinal Chemistry Letters* 23 (16): 4562–66. https://doi.org/10.1016/j.bmcl.2013.06.023.

Wen, Wandong, Wenjun Wu, C. David Weaver, and Craig W. Lindsley. 2014. “Discovery of Potent and Selective GIRK1/2 Modulators via ‘molecular Switches’ within a Series of 1-(3-Cyclopropyl-1-Phenyl-1H-Pyrazol-5-Yl)Ureas.” *Bioorganic and Medicinal Chemistry Letters* 24 (21): 5102–6. https://doi.org/10.1016/j.bmcl.2014.08.061.

Whorton, Matthew R., and Roderick MacKinnon. 2011. “Crystal Structure of the Mammalian GIRK2 K+ Channel and Gating Regulation by G Proteins, PIP2, and Sodium.” *Cell* 147 (1): 199–208. https://doi.org/10.1016/j.cell.2011.07.046.

———. 2013. “X-Ray Structure of the Mammalian GIRK2–Bγ G-Protein Complex.” *Nature* 498 (7453): 190–97. https://doi.org/10.1038/nature12241.

Wickman, Kevin D., Jorge A. Iñiguez-Lluhi, Philip A. Davenport, Ronald Taussig, Grigory B. Krapivinsky, Maurine E. Linder, Alfred G. Gilman, and David E. Clapham. 1994. “Recombinant G-Protein Bγ-Subunits Activate the Muscarinic-Gated Atrial Potassium Channel.” *Nature* 368 (6468): 255–57. https://doi.org/10.1038/368255a0.

Wydeven, Nicole, Daniele Young, Kelsey Mirkovic, and Kevin Wickman. 2012. “Structural Elements in the Girk1 Subunit That Potentiate G Protein – Gated Potassium Channel Activity” 2012. https://doi.org/10.1073/pnas.1212019110/-/DCSupplemental.www.pnas.org/cgi/doi/10.1073/pnas.1212019110.

Xu, Yunyao, Manasi P. Bhate, and Ann E. McDermott. 2017. “Transmembrane Allosteric Energetics Characterization for Strong Coupling between Proton and Potassium Ion Binding in the KcsA Channel.” *Proceedings of the National Academy of Sciences* 114 (33): 8788–93. https://doi.org/10.1073/pnas.1701330114.

Yakubovich, Daniel, Shai Berlin, Uri Kahanovitch, Moran Rubinstein, Isabella Farhy-Tselnicker, Boaz Styr, Tal Keren-Raifman, Carmen W Dessauer, and Nathan Dascal. 2015. “A Quantitative Model of the GIRK1/2 Channel Reveals That Its Basal and Evoked Activities Are Controlled by Unequal Stoichiometry of Gα and Gβγ.” *PLoS Computational Biology* 11 (11). https://doi.org/10.1371/journal.pcbi.1004598.

Yi, B.Alexander, Yu-Fung Lin, Yuh Nung Jan, and Lily Yeh Jan. 2001. “Yeast Screen for Constitutively Active Mutant G Protein–Activated Potassium Channels.” *Neuron* 29 (3): 657–67. https://doi.org/10.1016/S0896-6273(01)00241-0.

Yi, Fei, B M Denker, and E J Neer. 1991. “Structural and Functional Studies of Cross-Linked Go Protein Subunits.” *The Journal of Biological Chemistry* 266 (6): 3900–3906. http://www.ncbi.nlm.nih.gov/pubmed/1899868.

Yin, Daxu, and Alexander D. MacKerell. 1998. “Combinedab Initio/Empirical Approach for Optimization of Lennard-Jones Parameters.” *Journal of Computational Chemistry* 19 (3): 334–48. https://doi.org/10.1002/(SICI)1096-987X(199802)19:3<334::AID-JCC7>3.0.CO;2-U.

Yokogawa, Mariko, Masanori Osawa, Koh Takeuchi, Yoko Mase, and Ichio Shimada. 2011. “NMR Analyses of the Gβγ Binding and Conformational Rearrangements of the Cytoplasmic Pore of G Protein-Activated Inwardly Rectifying Potassium Channel 1 (GIRK1).” *Journal of Biological Chemistry* 286 (3): 2215–23. https://doi.org/L.

Yow, Tin T., Elena Pera, Nathan Absalom, Marika Heblinski, Graham Ar Johnston, Jane R. Hanrahan,

and Mary Chebib. 2011. “Naringin Directly Activates Inwardly Rectifying Potassium Channels at an Overlapping Binding Site to Tertiapin-Q.” *British Journal of Pharmacology* 163 (5): 1017–33. https://doi.org/10.1111/j.1476-5381.2011.01315.x.

Zhang, Hailin, Cheng He, Xixin Yan, Tooraj Mirshahi, and Diomedes E. Logothetis. 1999. “Activation of Inwardly Rectifying K+ Channels by Distinct PtdIns(4,5)P2 Interactions.” *Nature Cell Biology* 1 (3): 183–88. https://doi.org/10.1038/11103.

Zhao, Qi, Abla M. Albsoul-Younes, Peng Zhao, Tohru Kozasa, Yasuko Nakajima, and Shigehiro Nakajima. 2006. “Dominant Negative Effects of a Gβ Mutant on G-Protein Coupled Inward Rectifier K+ channel.” *FEBS Letters* 580 (16): 3879–82. https://doi.org/10.1016/j.febslet.2006.06.016.

Zhou, W., C. Arrabit, S. Choe, and P. A. Slesinger. 2001. “Mechanism Underlying Bupivacaine Inhibition of G Protein-Gated Inwardly Rectifying K+ Channels.” *Proceedings of the National Academy of Sciences* 98 (11): 6482–87. https://doi.org/10.1073/pnas.111447798.

Zhou, Yufeng, João H. Morais-Cabral, Amelia Kaufman, and Roderick MacKinnon. 2001. “Chemistry of Ion Coordination and Hydration Revealed by a K+ Channel–Fab Complex at 2.0 Å Resolution.” *Nature* 414 (6859): 43–48. https://doi.org/10.1038/35102009.

Zylbergold, Peter, Rory Sleno, Shahriar M Khan, Ashley M Jacobi, Mark A Belhke, and Terence E. HÃ©bert. 2014. “Kir3 Channel Ontogeny - the Role of Gβγ Subunits in Channel Assembly and Trafficking.” *Frontiers in Cellular Neuroscience* 8 (April). https://doi.org/10.3389/fncel.2014.00108.

8 ANNEX

8.1 SUPPLEMENTARY FIGURES LEGENDS

Below are the legends of supplementary figures referred in the main text to as "Annex Simulation M:NP". Where "M" is the numeric code of each molecular dynamic simulation (see Table 2) and "N" is the supplementary figure number and "P" is the panel alphabetic identifier. These legends are compatible for set of supplementary figures presenting timeseries and other analysis about each simulation run.

Figure 1

A) Position of K^+ along the pore during the simulation. The z-axis coordinates over time of a K^+ ion are considered for plotting if the ion persists inside a cylinder with a 10 Å radius and is aligned with the permeation pathway along the pore – sampling is made every 0.4 ns. The representation of each K^+ is colored with the same color during the entire time laps, multiple K^+ can be assigned the same color. Please note that the vertical axis spans only part of the simulation box, thus the top and bottom edges of the graphic-range do not behave as periodic boundary conditions.

B) Measure of the opening of the G-loop and the HBC gates over time. The radii of the bottlenecks of the G loop (brown) and HBC (purple) gates are plotted to the left vertical axis – sampling is made every 0.4 ns. Distances measured between specific atom centers of diametrically opposite residues in each gate are plotted to the right vertical axis: P1:G318:O~P2:G318:O (red) and P3:G318:O~P4:G318:O (orange) in the G loop gate; P1:F192:CZ~P2:F192:CZ (blue) and P3:F192:CZ~P4:F192:CZ (cyan) in the HBC gate. All timeseries are convoluted with a symmetric power-law function x^n with width t = 20 ns, where n = -6 *for* $\{ x: (t-w/2) \leq x \leq t \}$ and n= 6 *for* $\{ x: t < x \leq (t+w/2) \}$.

Figure 2

Evolution of the average radii of opening along the pore. The pore-profiles are computed from ensembles of conformations sampled every 0.4 ns in consecutive 70 ns bins. The resolution of the analysis along the pore axis plotted to the horizontal axis is 0.5 Å. The averages (solid colored line) and the standard deviation (thin vertical bars) of the measures in the time-bin are plotted to the vertical axis for each position along the pore of the channel.

Figure 3

Average occupancy of ligand measured in non-overlapping time bins with sampling of 0.4 ns. The representations are built as projections of the average occupancy obtained from integration along the normal to the plan of the membrane of the voxels (0.5 $Å^3$) in strata of various thicknesses depending on the monitored ligands, as follows: for Na^+ consider the atomic radius $2 * VdW(Na^+) = 4.54$ Å; for PrOH consider the length if the molecule $(dist(O1, C3) + 2 * VdW(C) + 2 * VdW(O) = 3.25 + 2 * 1.7 + 2 * 1.5$ Å $= 9.65$ Å; for PIP_2 consider $2 * VdW(P) = 3.6$ Å. The time average was computed from data sampled every 0.4 ns, and per-voxel/per-frame weighting was applied to adjust the units of the representation (1/$Å^3$/ns). The final values for PrOH and PIP_2 exceed 1 because several atoms were used for the data collection, thus PrOH occupancy was monitored on the basis of all heavy atoms of the molecule, while the PIP_2 occupancy was obtained on the basis of both 4' and 5' phosphorous atoms. Please note that the scale of the darkening is not the same for all bins concerning the same ligand – this was made on purpose, aiming at facilitating the observation of the residual occupancy when a ligand was not frequently in the binding site. The first bin is a good estimate of the maximum occupancy that could be measured along the trajectory.

Figure 4

Profile of the curvature of the selected secondary structures of the channel (see Figure 8). The time profile of the curvature was obtained as series of measures of the angle between eight consecutive Cα atoms using the VMD plugin Bendix (Dahl, Chavent, and Sansom 2012), analyzed conformations were sampled every 4 ns. Residue numbers are reported to the left vertical axis, the horizontal axis represents simulation time. The panels on the right of each bend profile represent the instantaneous correlation between the timeseries of the bend angle for each residue and the timeseries of the radii of the bottlenecks of the G loop (brown) and the HBC gate (purple), timeseries were prepared as described in Annex Simulation:1B. A) βB strand and slide helix. B) TM1. C) Pore helix. D) TM2. E) βC-βD strands and loop. F) βD-βE strands and loop. G) βH-βI strands and loop. H) βL-βM strands and loop.

Figure 5

Evolution of the dihedral angles in the sidechains of E150 and E152 in each subunit of the tetramer. The bottom panel contains the percent distribution of each dihedral state *s:*(χ_1, χ_2) of residue E152 in each one of the subunits.

Figure 6

Timeseries of the backbone-dihedral angles of residues T154, I155, G156, Y157 from the selectivity filter in each protein subunit.

Figure 7

Diagrams of the instantaneous correlations between couples of interatomic distances collected in the region of the selectivity filter for a subset of snapshots when a particular rotamer state of residue E152 was observed. The set of monitored distances is reported in panel A of Figure 13. The collected data constituted noisy timeseries (for examples see Figure 13B), this data was filtered by convolution transformation. Convolution and preprocessing were made as follows: firstly data was digitized in bins of 0.28 Å; secondly in order to give a lot of weight on the timesteps near the current timestep (t) a very sharp symmetric power-law function x^n was used to weigh the snapshots in the sliding window (w) with $\mathrm{n} = 14.95$ for $\{\mathrm{x}: (\mathrm{t} - \mathrm{w}/2) \leq \mathrm{x} \leq \mathrm{t}\}$ and $\mathrm{n} = \text{-}14.95$ for $\{\mathrm{x}: \mathrm{t} < \mathrm{x} \leq (\mathrm{t} + \mathrm{w}/2)\}$. In order to avoid strong influence of local noise, the weighting function was applied to a large time window of 70 ns. In reality, the weights declined to $5*10^{-3}$ for datapoints situated at ±14 ns from the current data point, meaning that the effective time window for the convolution was of approximately 30 ns. The next step of the analysis consisted to extract a subset of interatomic distances for each time step when the rotamer state of interest of E152 was observed (see each Annex: Figure 7 for the particular E152 rotamer state). A pairwise-matrix of instantaneous correlation was computed for all possible couples of interatomic distances in the extracted data. Finally, the correlation matrix was filtered to retain only correlation with $abs(\mathrm{r}) > 0.5$, the remaining data was used to produce diagrams for each subunit (panels A-E). The presented graphs were manually optimized to allow the visualization of the largest number of edges between nodes, thus individual positions of each node and the length of the edges do not contain further information. However, the thickness of edges is proportional to $abs(r)$, edges representing $r < 0$ are red while edges representing $r > 0$ are blue. (A) Subunit P1. (B) Subunit P3. (C) Subunit P4. (D) Subunit P2. (E) Average diagram resulting from summation of all equivalent contacts among the four channel subunits – this time the threshold value was set to $abs(\mathrm{r}) > 0.375$, which corresponds to a correlation of $abs(\mathrm{r}) > 0.75$ in at least three subunits, and $abs(r) = 1$ for the fourth subunit which is supported by the initial frame selection by E152 rotamer state.

Figure 8

Correlation of the conformation of I155, and the width of the central K^+ binding site of the selectivity filter of Kir3.2. The ensemble of interatomic distance that was monitored is listed in panel A, see Figure 13 of the main text for explanations on how to read the table. The data describing the

interatomic distances was manipulated the same manner as described in (Figure 13, Figure 14 and Annex: Figure 7). See panel C of each figure for the specific threshold used for the correlation diagrams.

Figure 9* and *Figure 10

Timeseries of PIP_2-protein hydrogen bonds. Data presented in *Annex: Figure* 9 is a subset of the data presented in Annex: *Figure* 10. Data for the detection of the hydrogen-bonds was collected every 0.08 ns and hydrogen-bond were assigned if the angle between the partners was $ang < 30°$ and the distance was $d < 3.5$ Å. The left column of panels shows the number of hydrogen-bonds counted on individual residues of PIP2 binding site (regrouping residues from different subunits). The right column of panels shows the number of hydrogen-bonds counted on named secondary structures, these secondary structures gather the following residues: N_{ter} residues 60 to 71 (**N-t**), slide helix residues 72 to 80 (**S-h**), slide helix and TM1 residues 88 to 92 (**TM1**), TM2 residue K194 (**TM2**), C-linker residues 194 to 203 (**C-l**), βC-βD loop and βM strand residues 231 and 354 (**C-D|M**). The height of each lane is normalized between all subunits **(# Norm** on top of the left and the right columns of panels). The time-profiles of the bottlenecks of the G-loop (brown) and the HBC (violet) gates are plotted to the right vertical axis.

Figure 11

Profile of the electrostatic potential along the normal to the membrane computed for discontinuous time bins. The left column of panels shows the integration along different cylinder radii in the *x*-*y* plane of the effective electrostatic profile Φ (see section 4.2.2.2 of the main text). The cylinder radii vary between 0.75 (red) to 10 Å (green) with step of 0.25 Å. The right column of panels shows a slice of Φ in *x*-*z* plane and aligned with the center of the permeation pathway of the channel. The time bin and the simulated membrane potential are reported on top of each panel.

8.2 SIMULATION 0

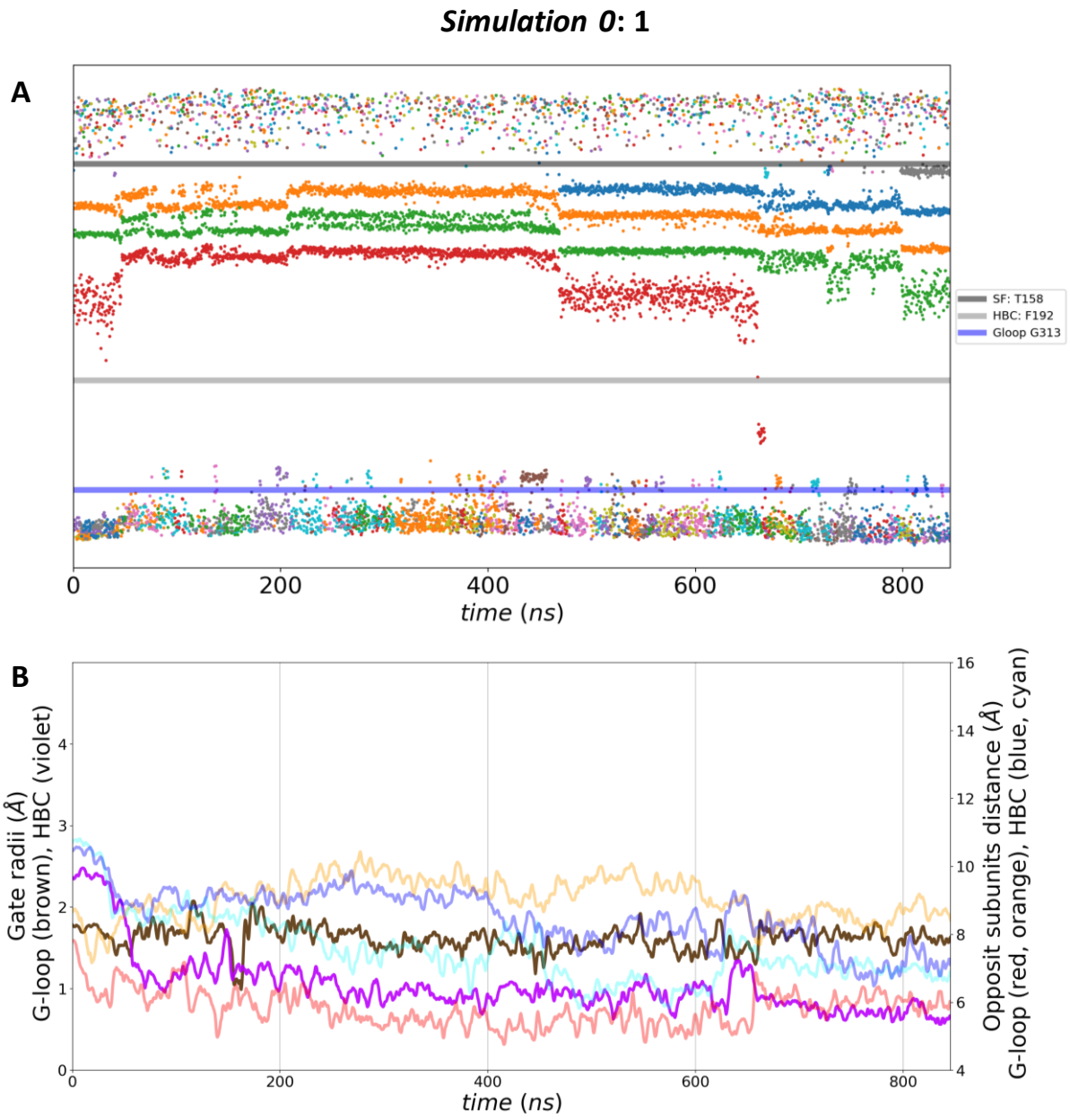

Simulation 0: 2

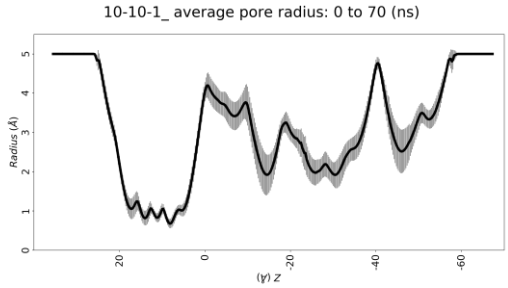

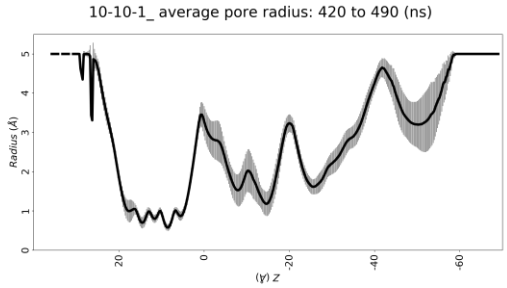

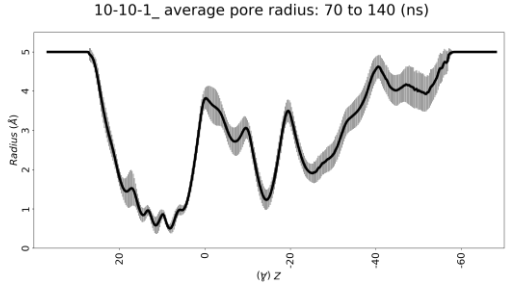

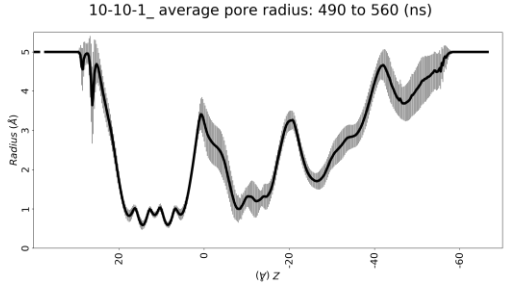

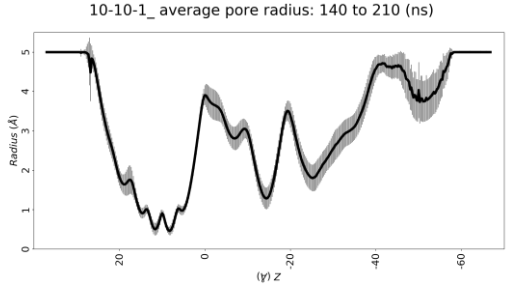

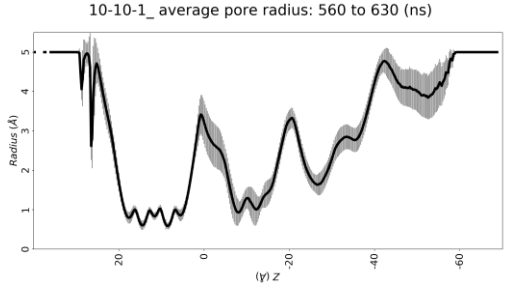

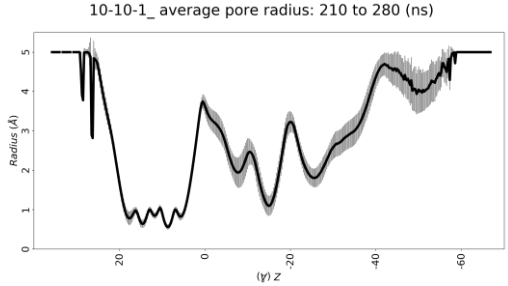

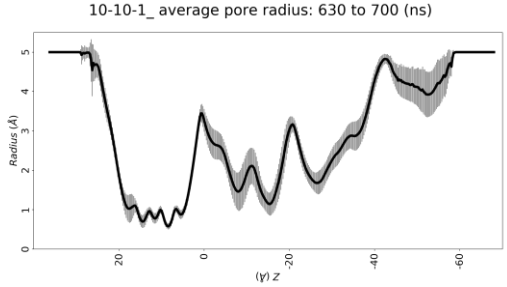

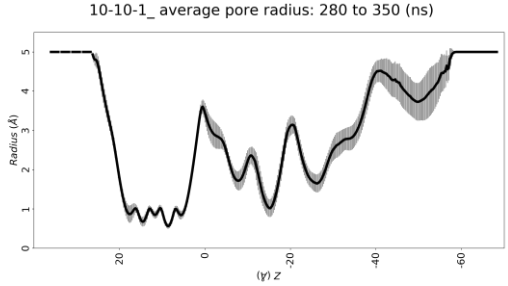

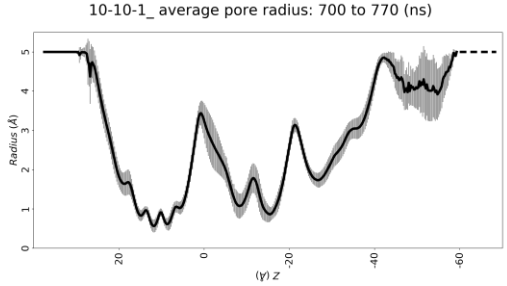

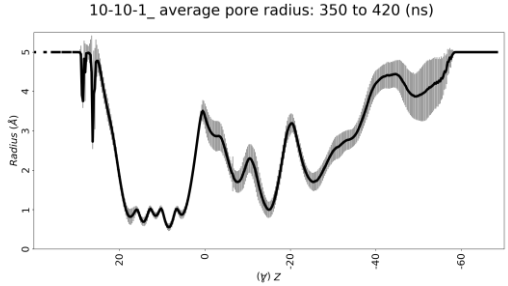

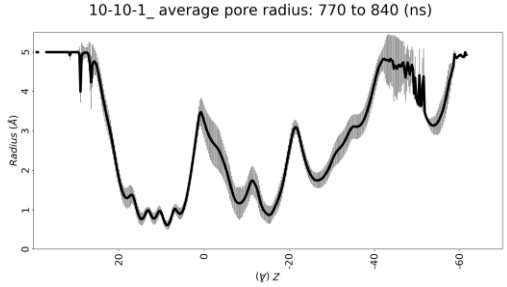

Simulation 0: 10

Average electrostatic potential along the pore

Electrostatic potential in the simulation box *(Y_{axis}= 0)*

A

50 to 70 ns; V_m= -0,07 *(Volts)*

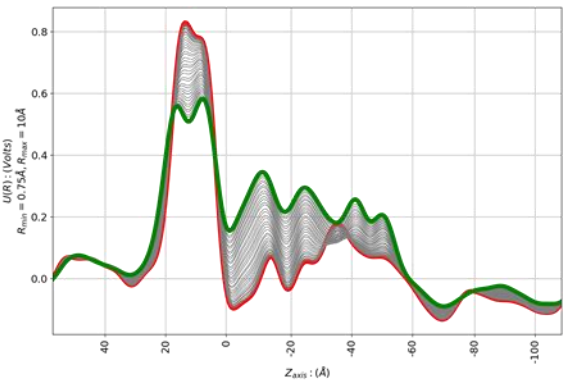

50 to 70 ns; V_m= -0,07 *(Volts)*

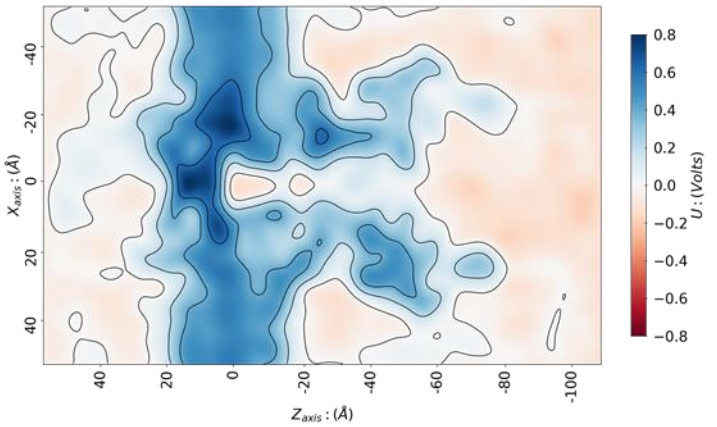

B

420 to 440 ns; V_m= -0,07 *(Volts)*

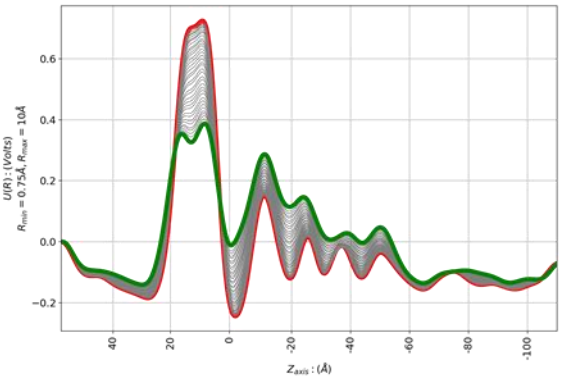

420 to 440 ns; V_m= -0,07 *(Volts)*

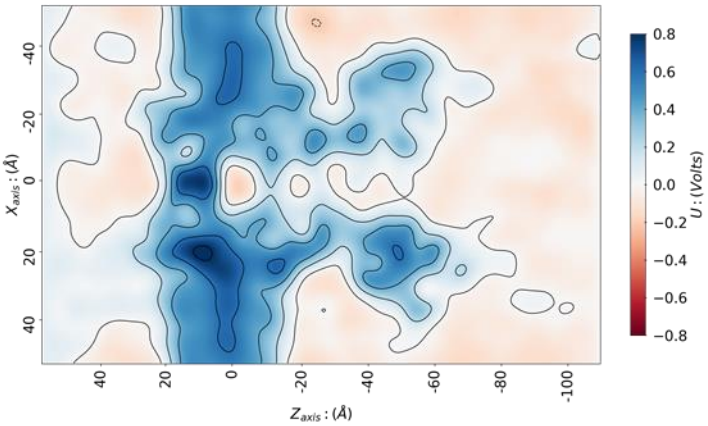

C

620 to 640 ns; V_m= -0,7 *(Volts)*

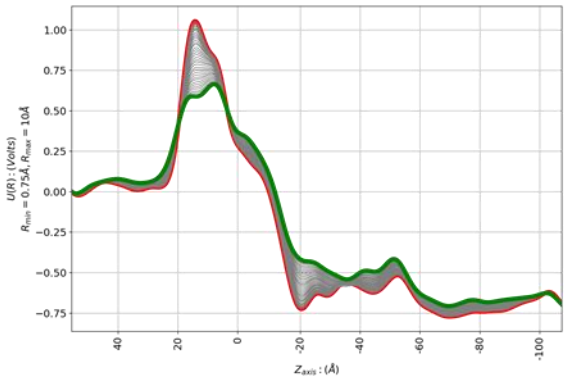

620 to 640 ns; V_m= -0,7 *(Volts)*

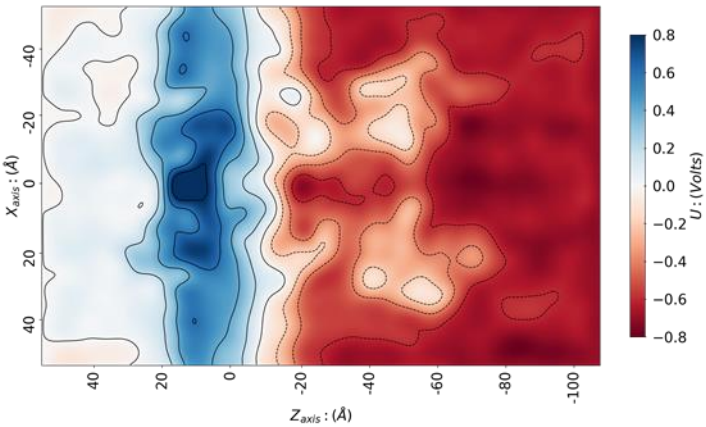

D

820 to 840 ns; V_m= -0,7 *(Volts)*

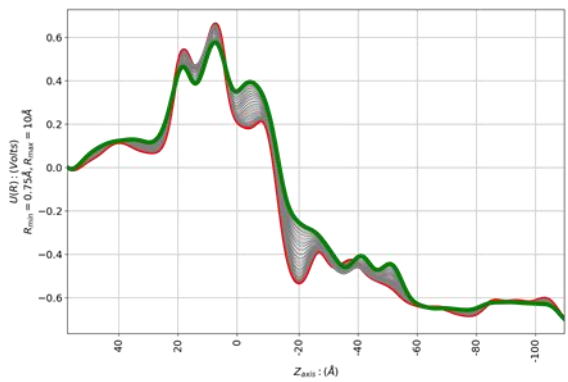

820 to 840 ns; V_m= -0,7 *(Volts)*

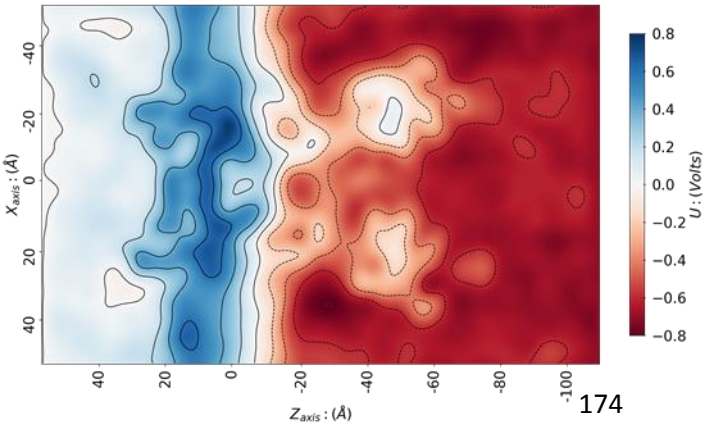

8.3 SIMULATION I

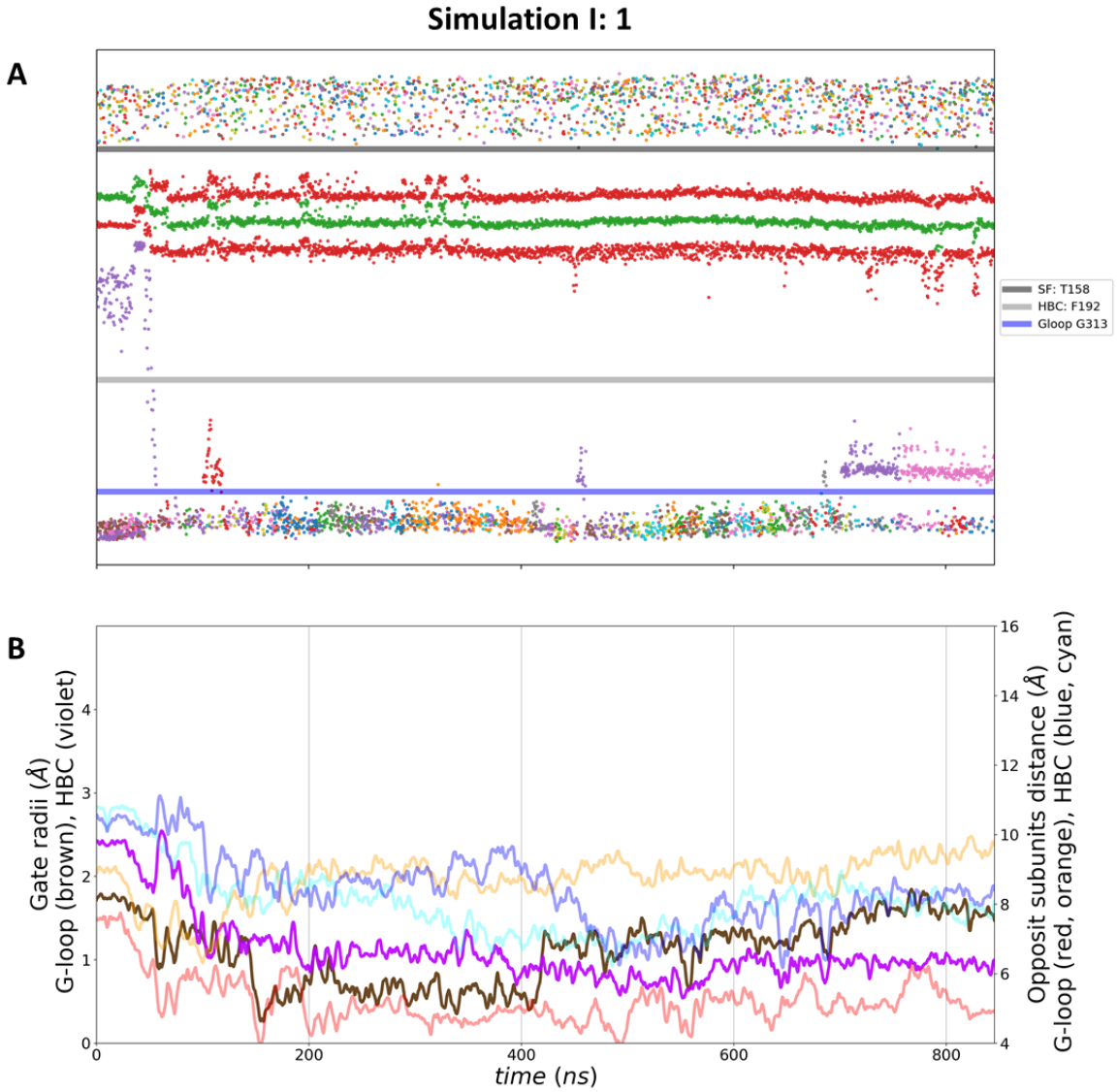

Simulation I: 2

10-7-1_ average pore radius: 0 to 70 (ns)

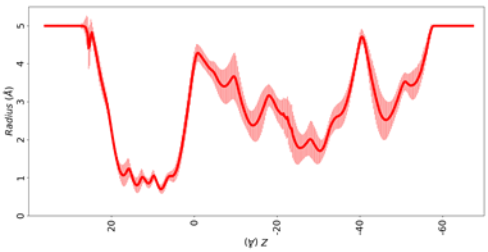

10-7-1_ average pore radius: 420 to 490 (ns)

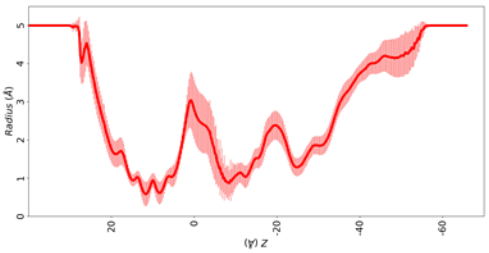

10-7-1_ average pore radius: 70 to 140 (ns)

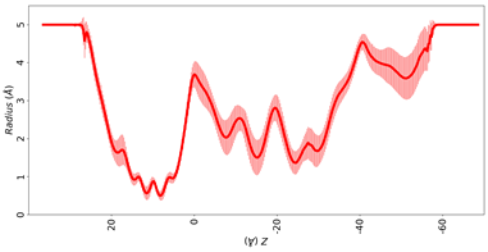

10-7-1_ average pore radius: 490 to 560 (ns)

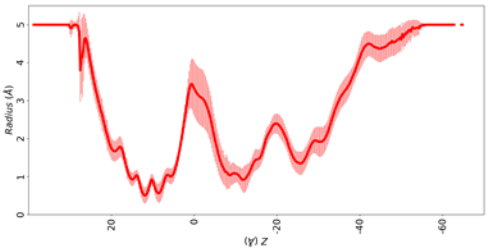

10-7-1_ average pore radius: 140 to 210 (ns)

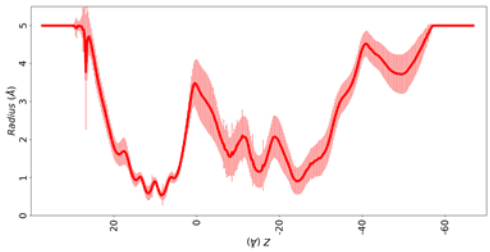

10-7-1_ average pore radius: 560 to 630 (ns)

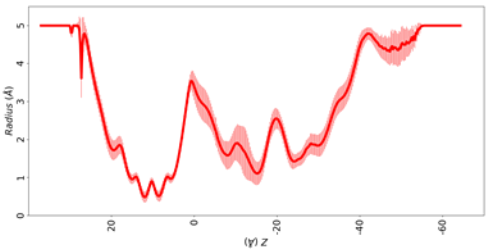

10-7-1_ average pore radius: 210 to 280 (ns)

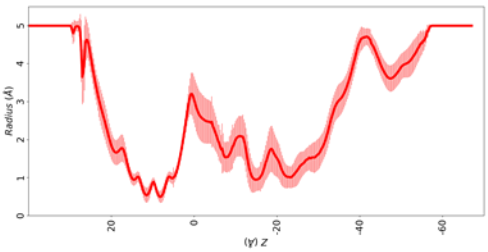

10-7-1_ average pore radius: 630 to 700 (ns)

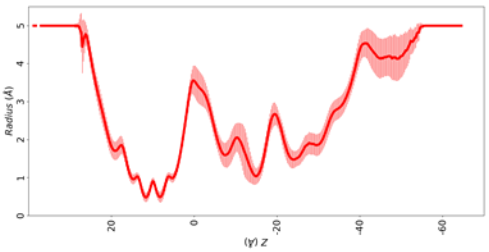

10-7-1_ average pore radius: 280 to 350 (ns)

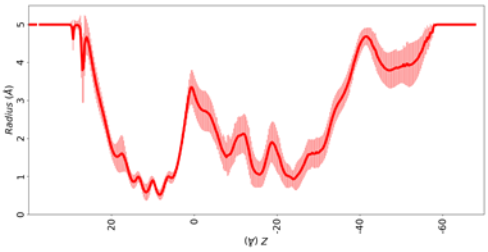

10-7-1_ average pore radius: 700 to 770 (ns)

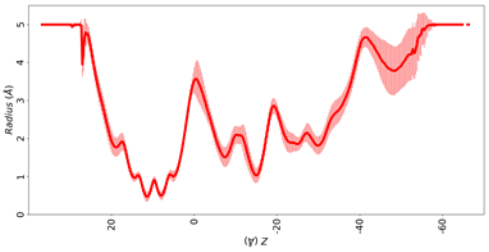

10-7-1_ average pore radius: 350 to 420 (ns)

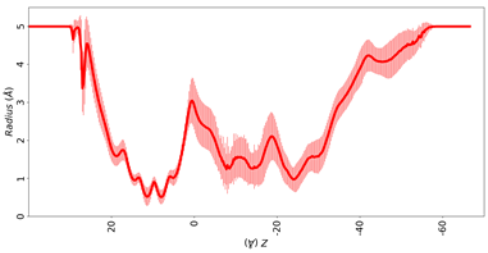

10-7-1_ average pore radius: 770 to 840 (ns)

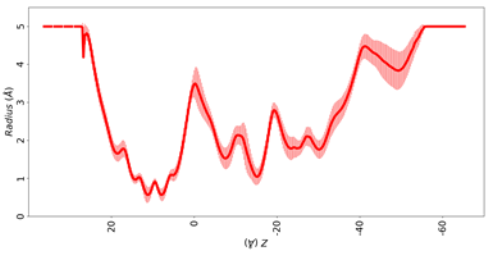

Simulation I: 3

Occupacy in binding sites during time interval: 0..70 (*ns*)

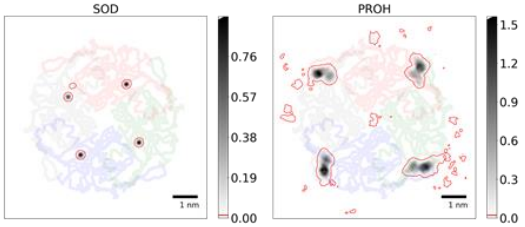

Occupacy in binding sites during time interval: 422..492 (*ns*)

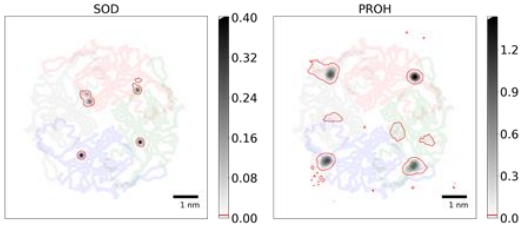

Occupacy in binding sites during time interval: 70..140 (*ns*)

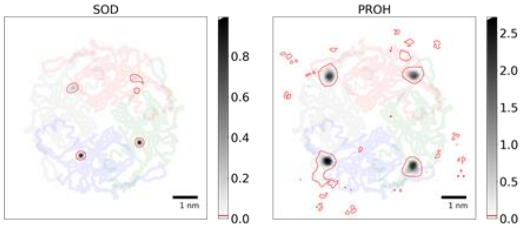

Occupacy in binding sites during time interval: 492..563 (*ns*)

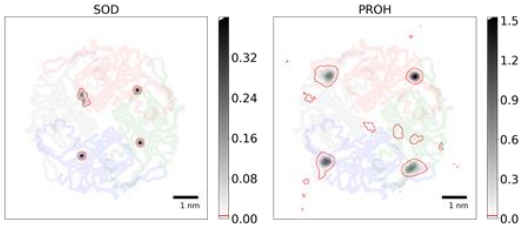

Occupacy in binding sites during time interval: 140..211 (*ns*)

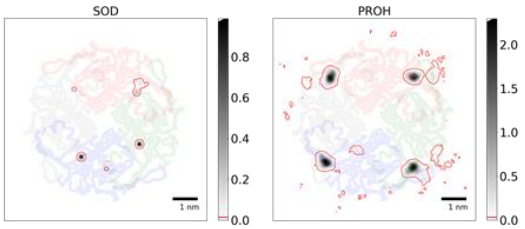

Occupacy in binding sites during time interval: 562..633 (*ns*)

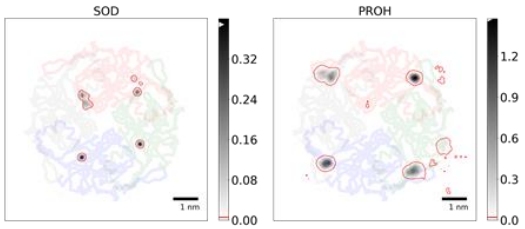

Occupacy in binding sites during time interval: 210..281 (*ns*)

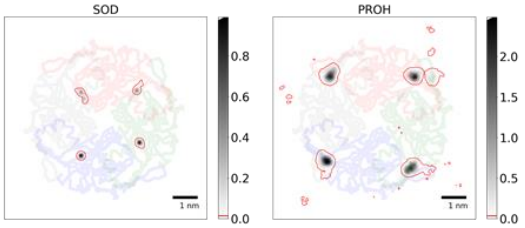

Occupacy in binding sites during time interval: 633..704 (*ns*)

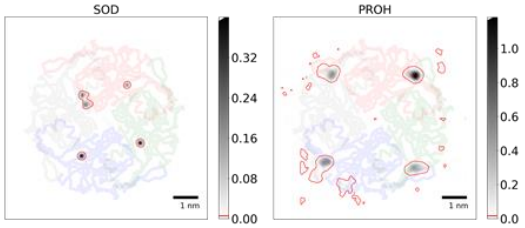

Occupacy in binding sites during time interval: 281..352 (*ns*)

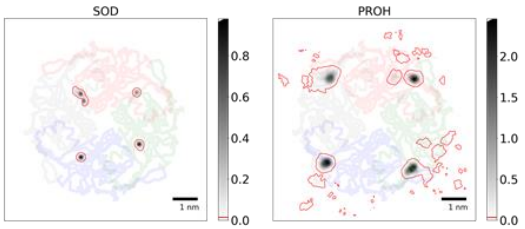

Occupacy in binding sites during time interval: 703..774 (*ns*)

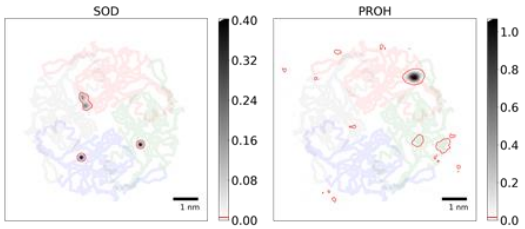

Occupacy in binding sites during time interval: 351..422 (*ns*)

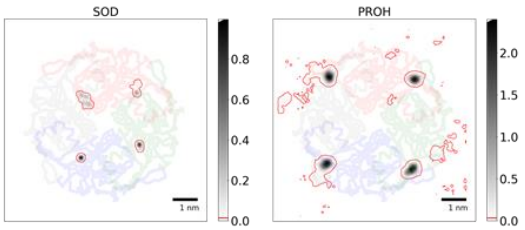

Occupacy in binding sites during time interval: 774..844 (*ns*)

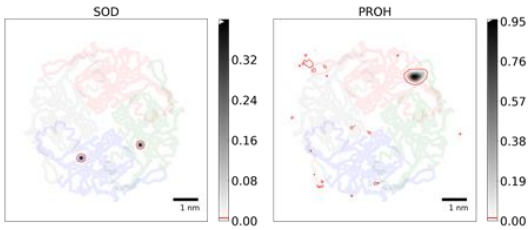

Simulation I: 4

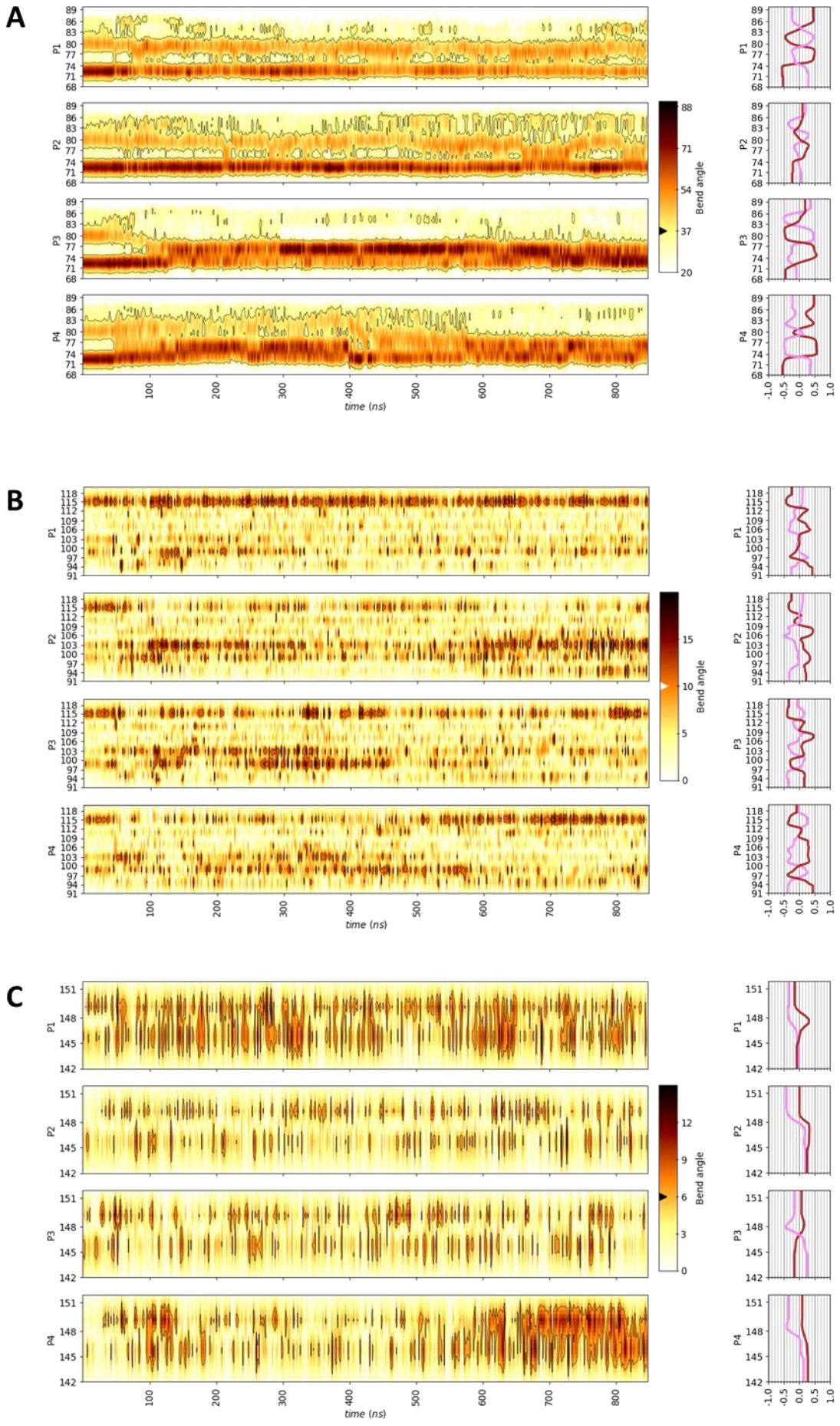

Simulation I: 4

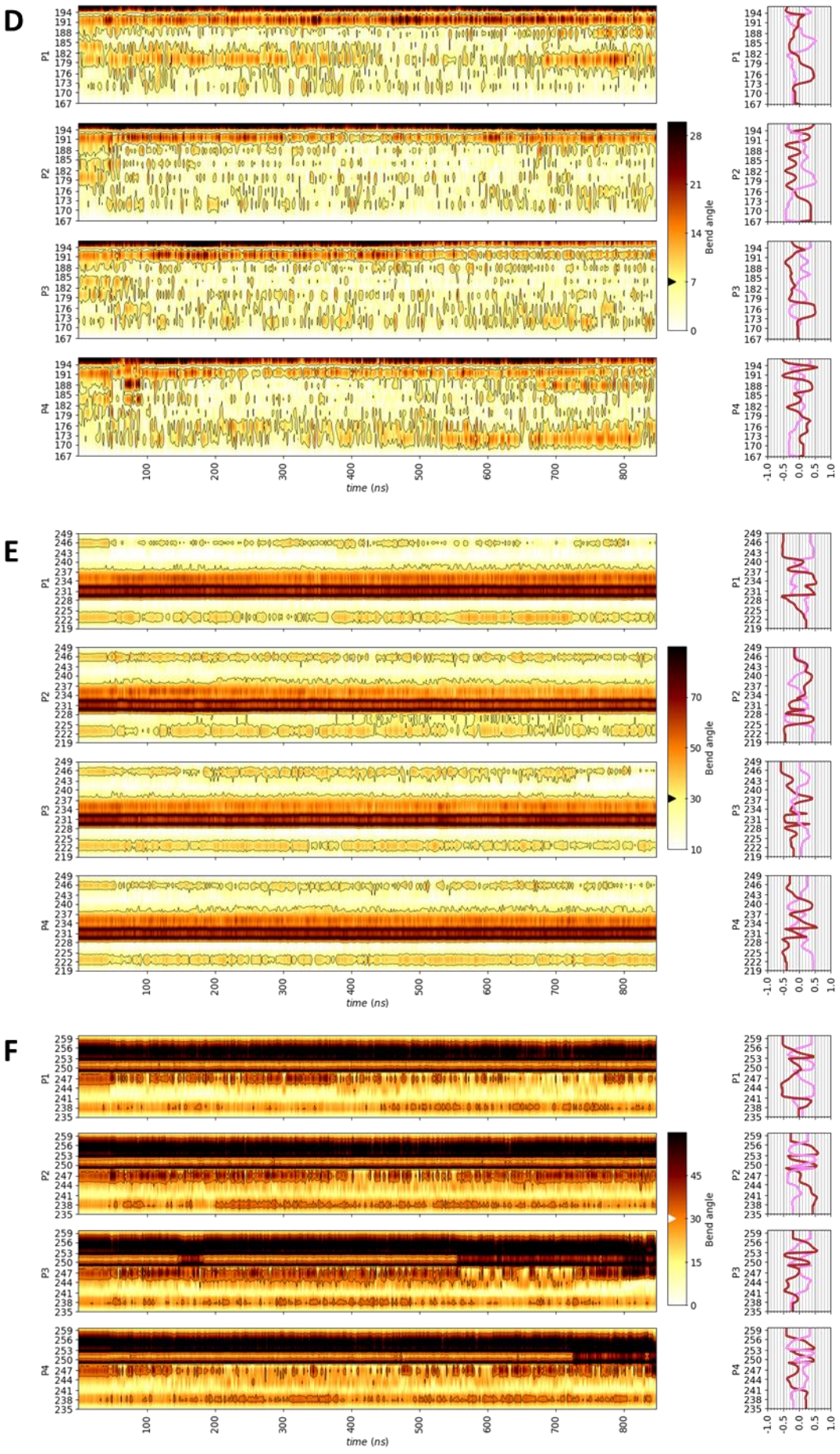

Simulation I: 4

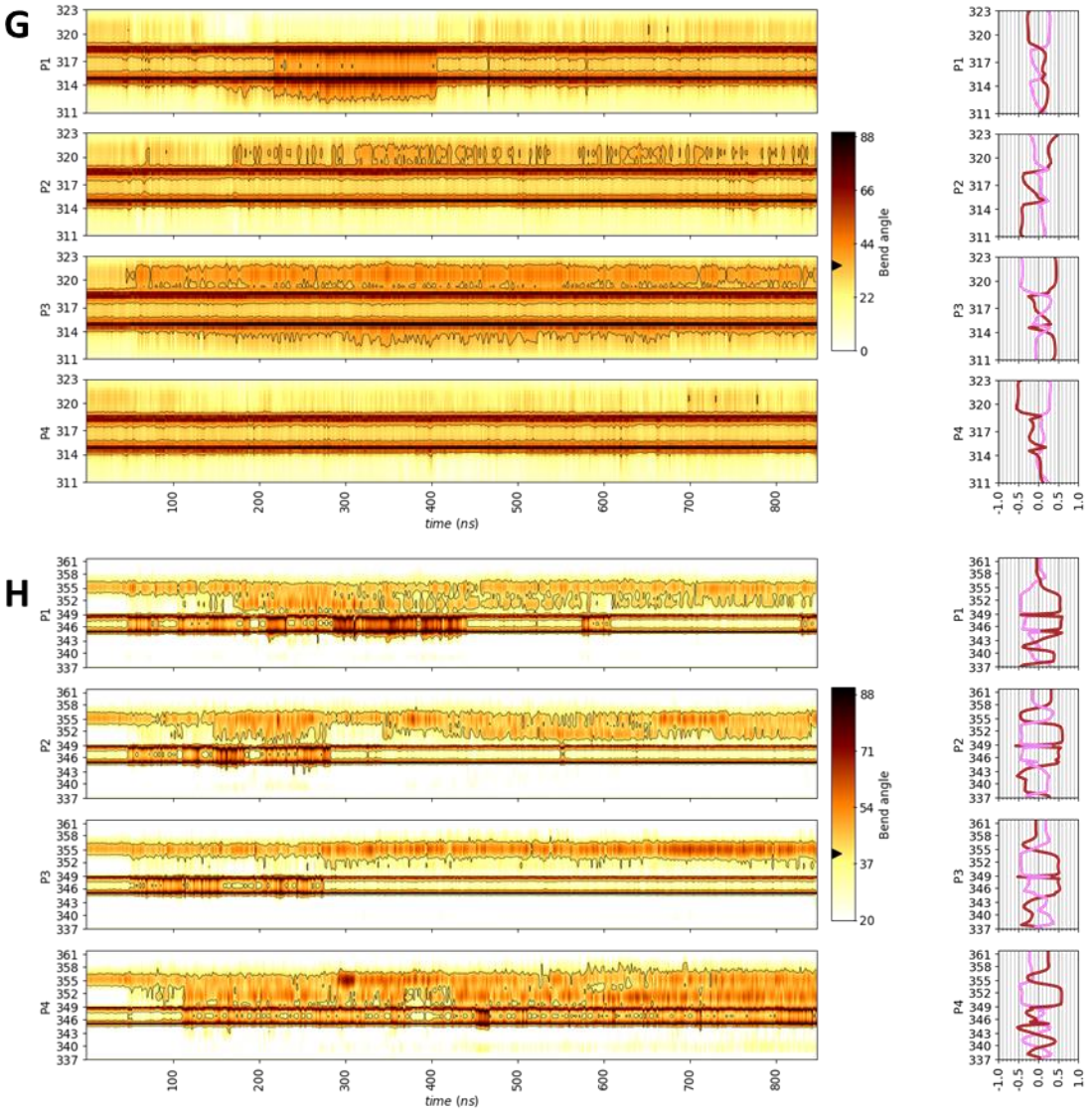

Simulation I: 5

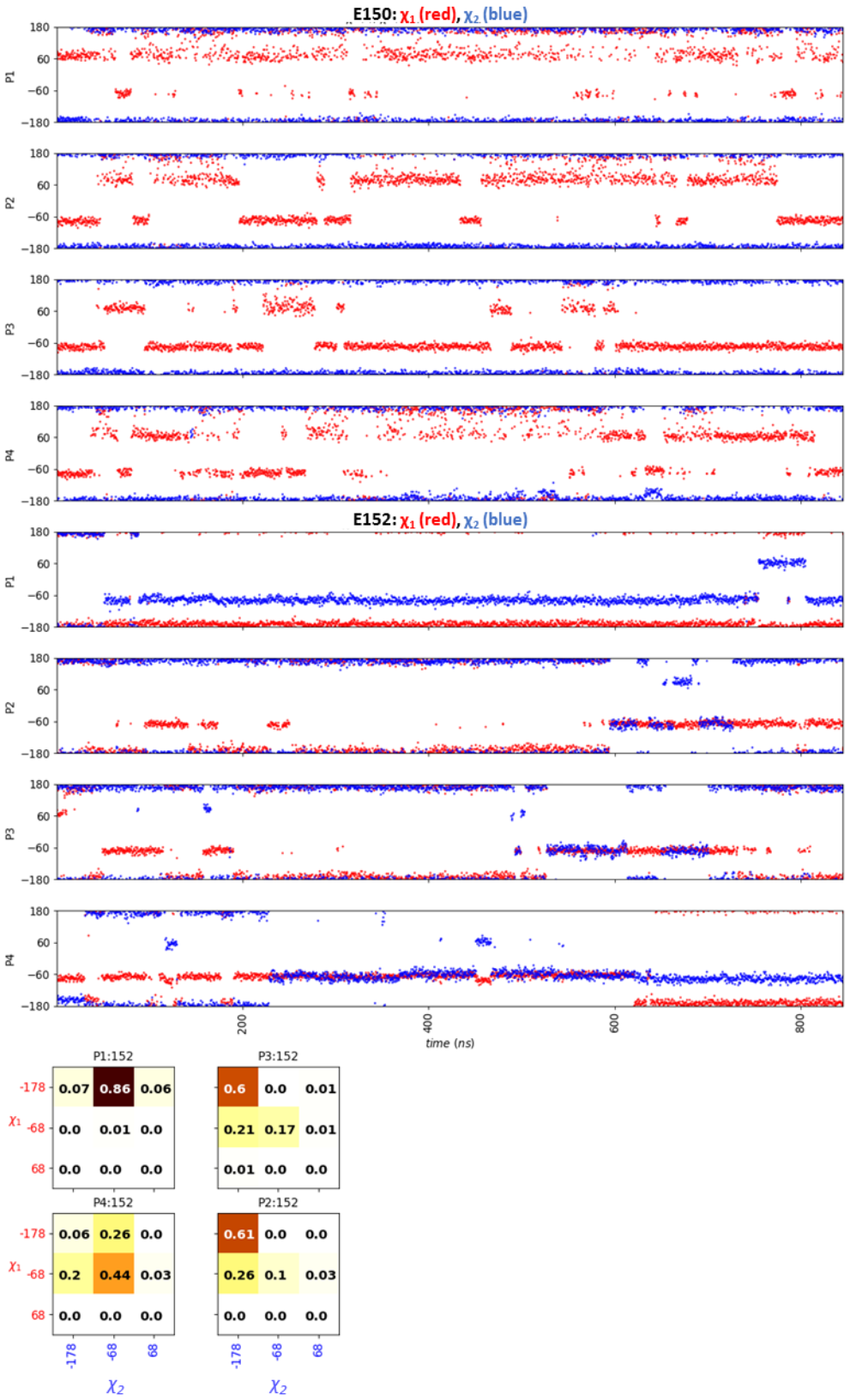

Simulation I: 6

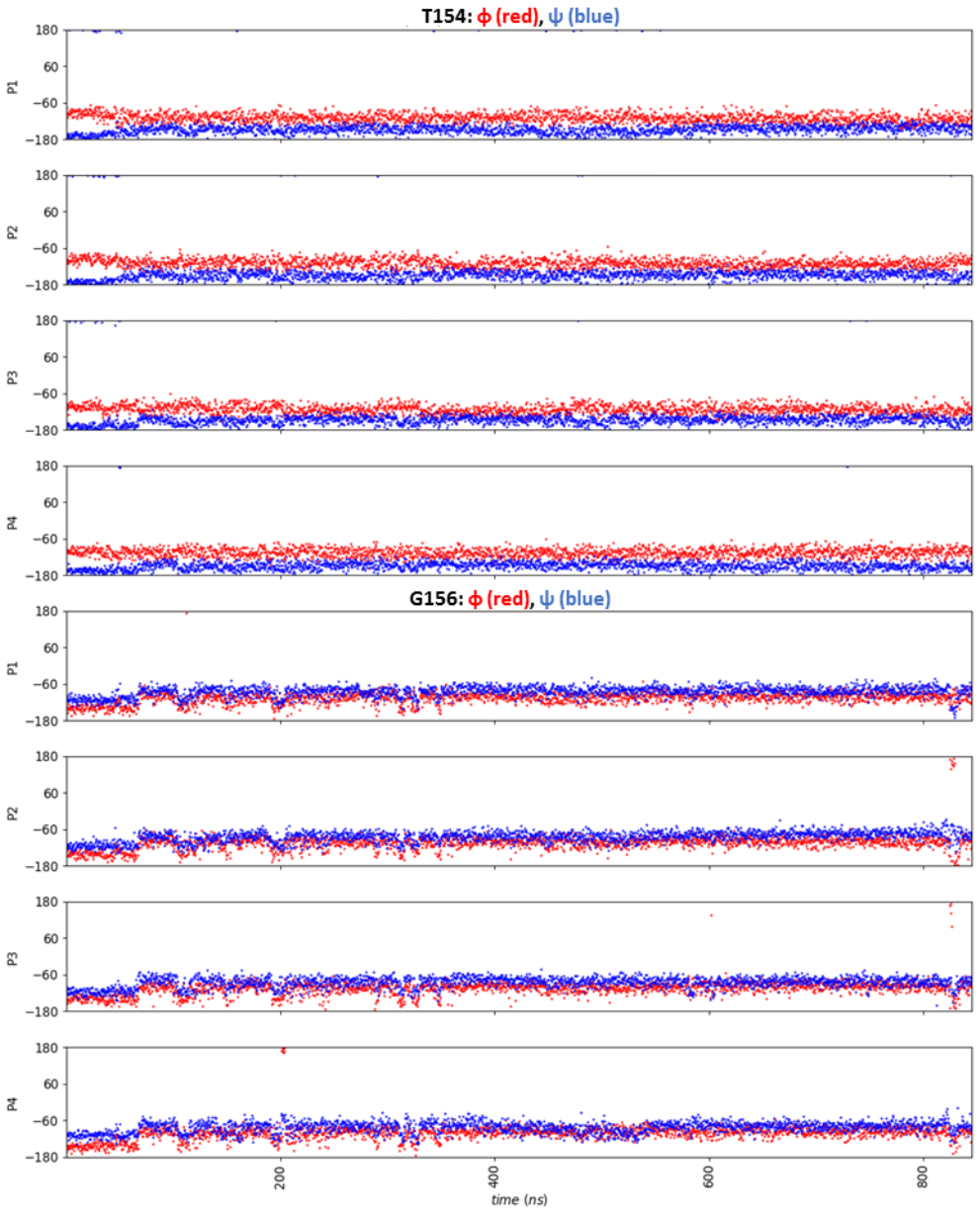

Simulation I: 6

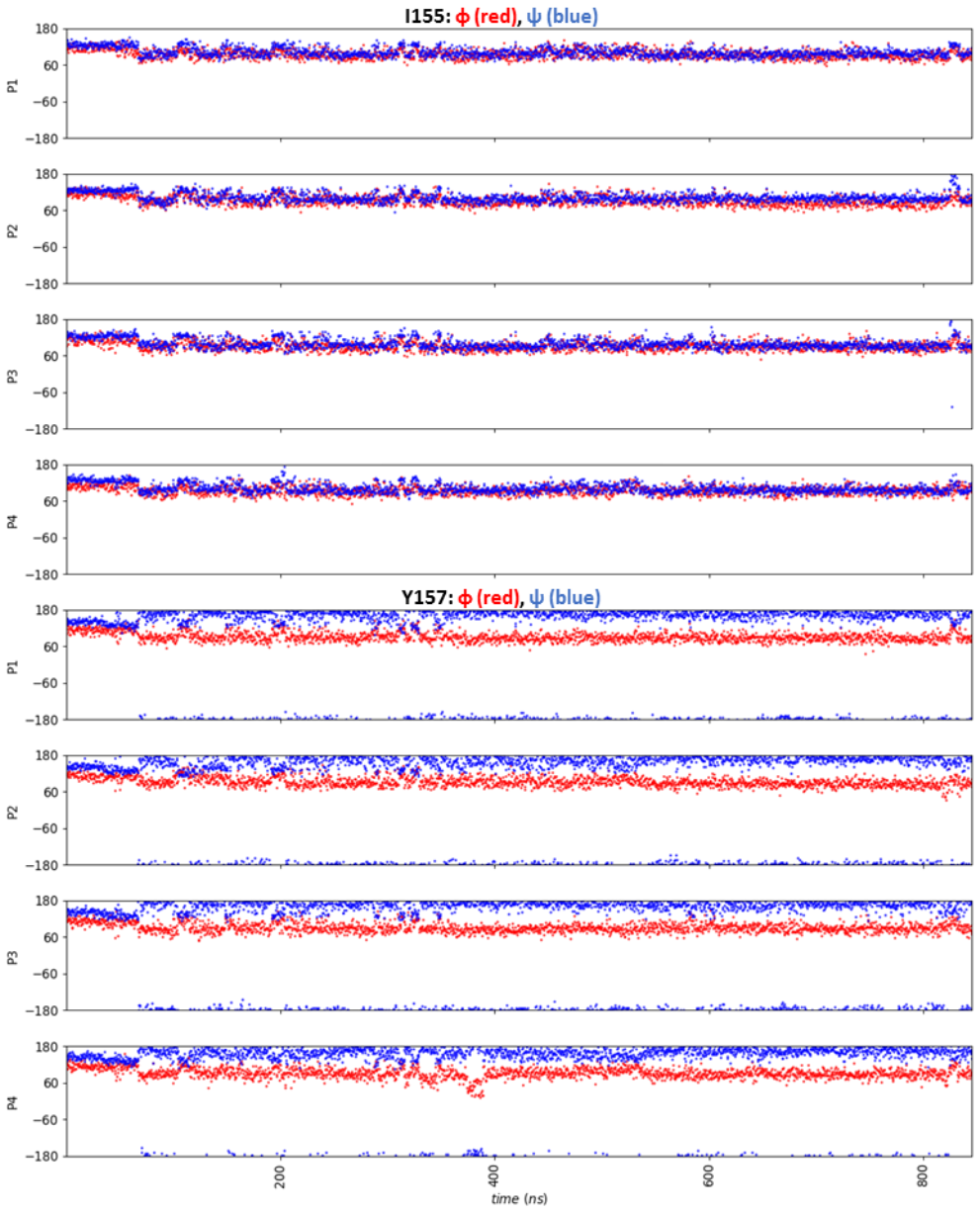

Simulation I: 6

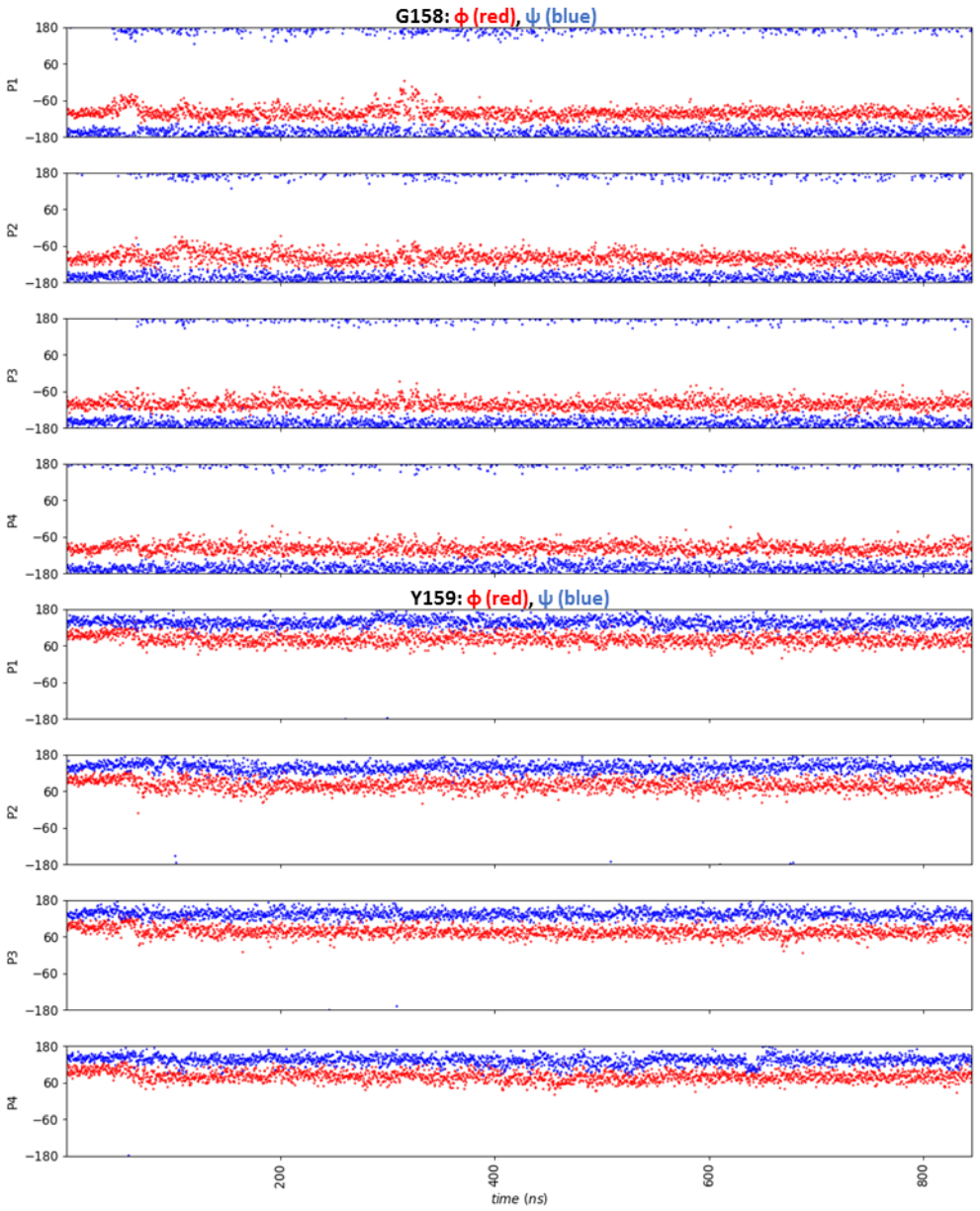

Simulation I: 7

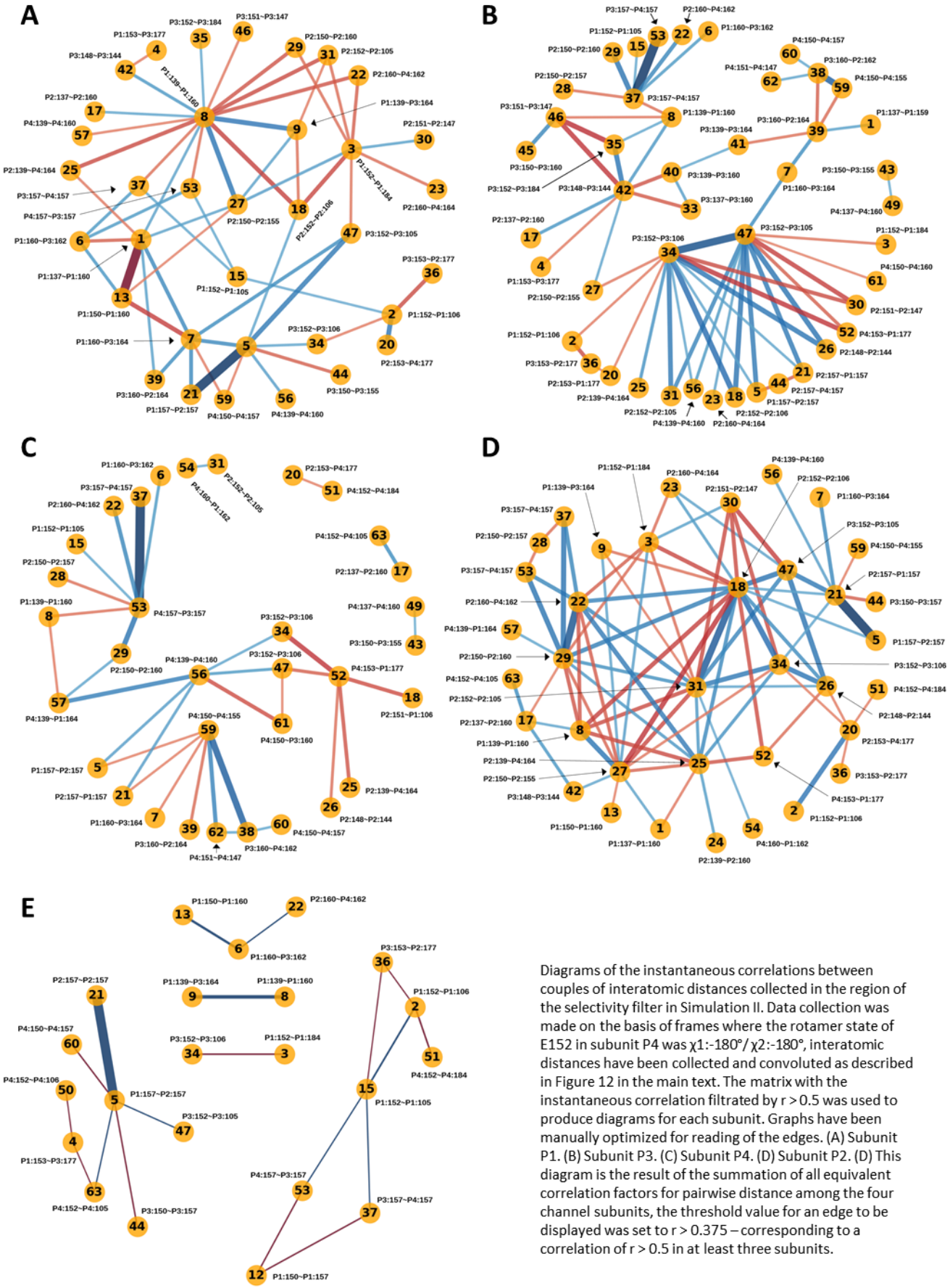

Diagrams of the instantaneous correlations between couples of interatomic distances collected in the region of the selectivity filter in Simulation II. Data collection was made on the basis of frames where the rotamer state of E152 in subunit P4 was χ1:-180°/ χ2:-180°, interatomic distances have been collected and convoluted as described in Figure 12 in the main text. The matrix with the instantaneous correlation filtrated by r > 0.5 was used to produce diagrams for each subunit. Graphs have been manually optimized for reading of the edges. (A) Subunit P1. (B) Subunit P3. (C) Subunit P4. (D) Subunit P2. (D) This diagram is the result of the summation of all equivalent correlation factors for pairwise distance among the four channel subunits, the threshold value for an edge to be displayed was set to r > 0.375 – corresponding to a correlation of r > 0.5 in at least three subunits.

Simulation I: 11

Average electrostatic potential along the pore | **Electrostatic potential in the simulation box *(Y_{axis}= 0)***

A

50 to 70 ns; V_m= -0,07 *(Volts)*

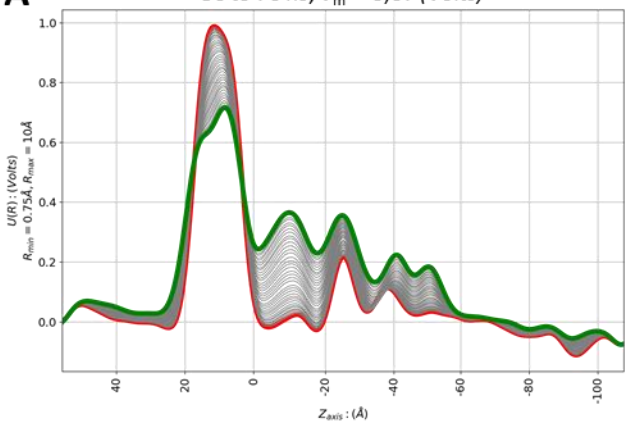

50 to 70 ns; V_m= -0,07 *(Volts)*

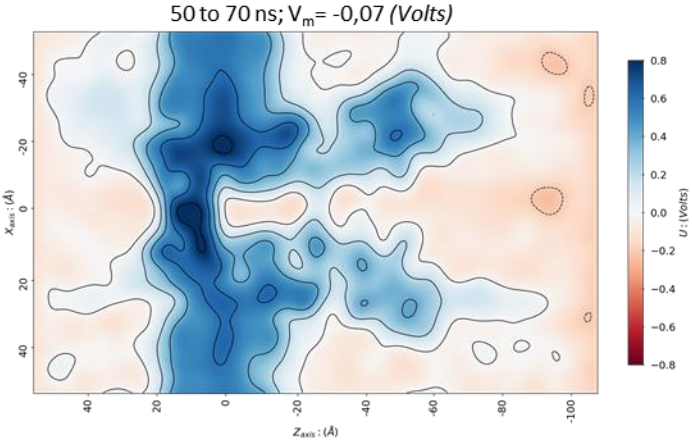

B

420 to 440 ns; V_m= -0,07 *(Volts)*

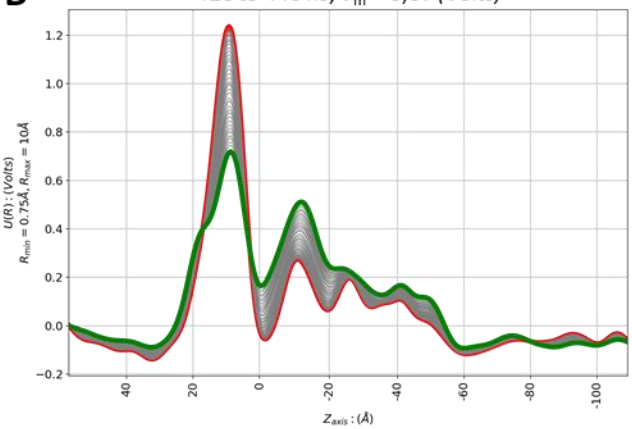

420 to 440 ns; V_m= -0,07 *(Volts)*

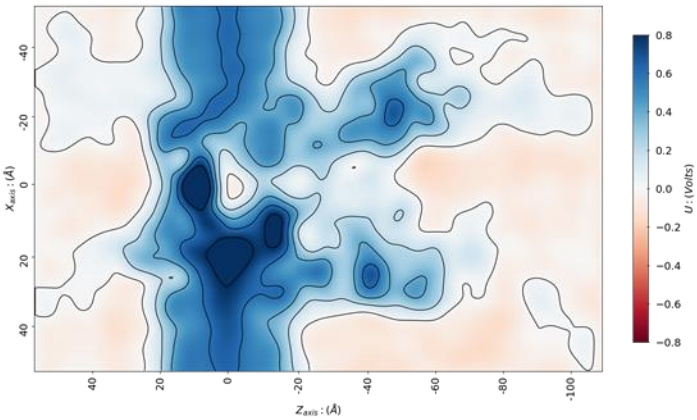

C

620 to 640 ns; V_m= -0,7 *(Volts)*

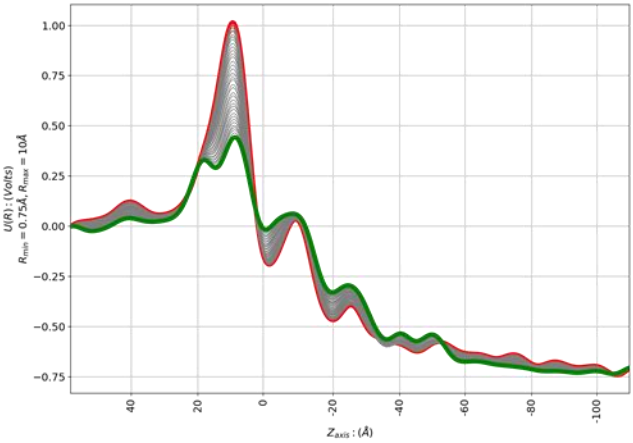

620 to 640 ns; V_m= -0,7 *(Volts)*

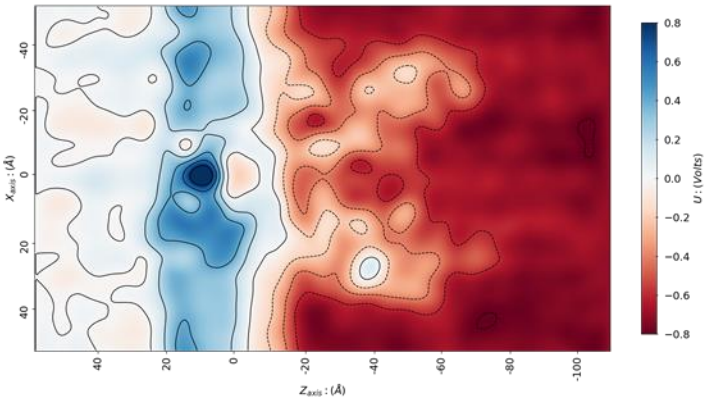

D

820 to 840 ns; V_m= -0,7 *(Volts)*

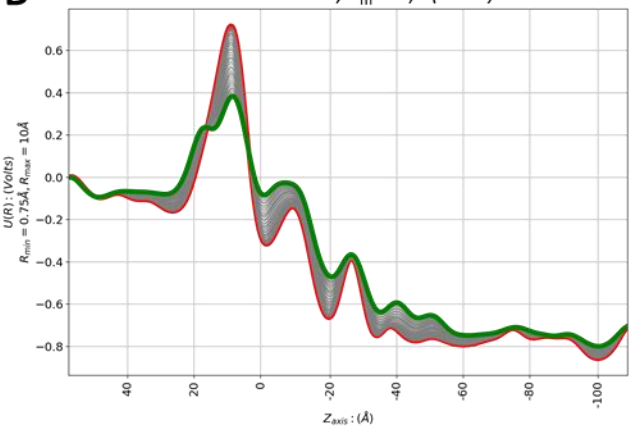

820 to 840 ns; V_m= -0,7 *(Volts)*

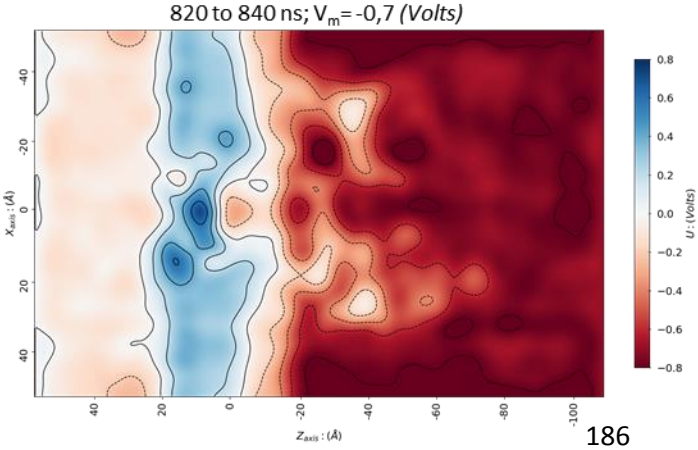

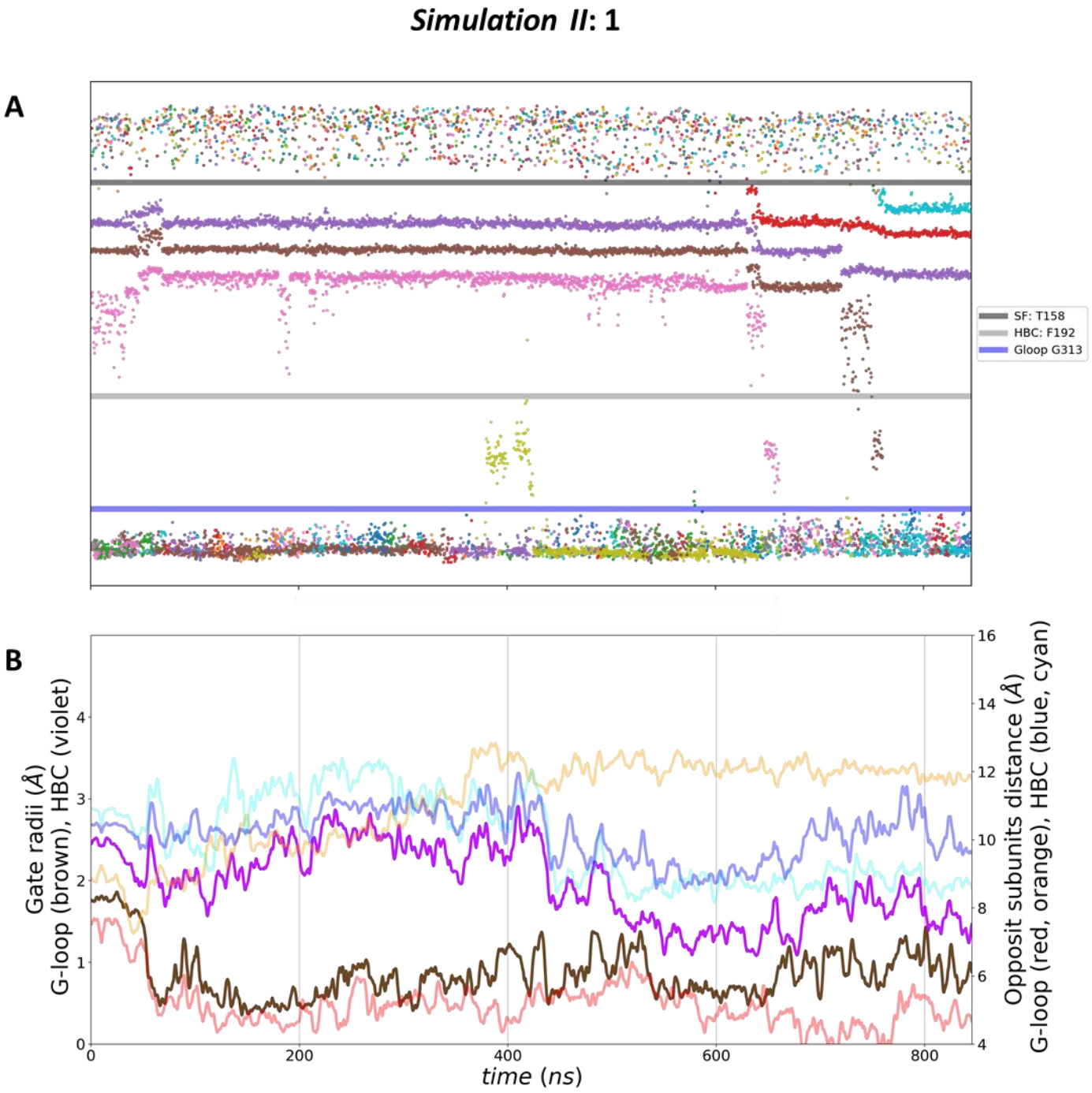
Simulation II: 1
A
SF: T158
HBC: F192
Gloop G313
B
Gate radii (Å)
G-loop (brown), HBC (violet)
Opposit subunits distance (Å)
G-loop (red, orange), HBC (blue, cyan)
time (ns)
0
200
400
600
800
0
1
2
3
4
4
6
8
10
12
14
16

Simulation II: 2

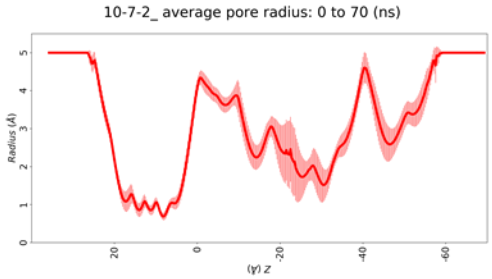

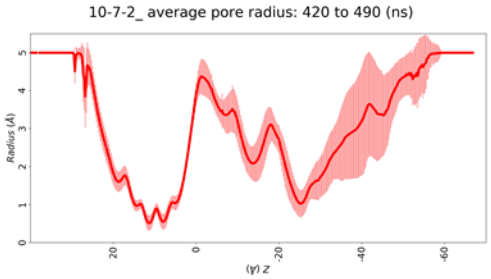

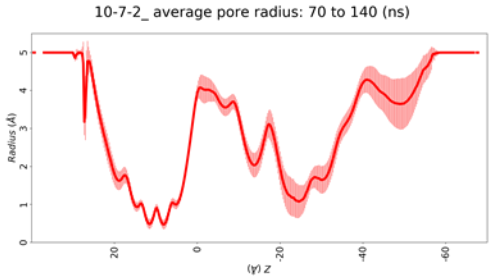

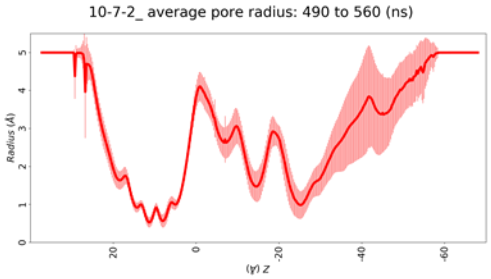

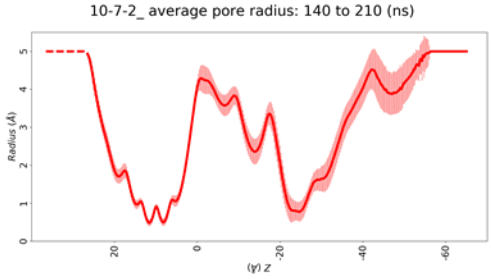

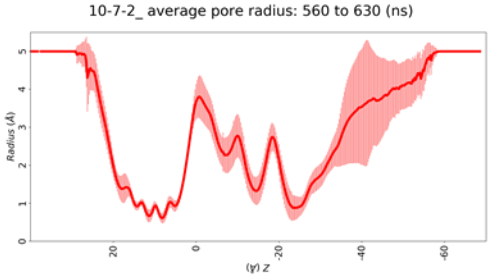

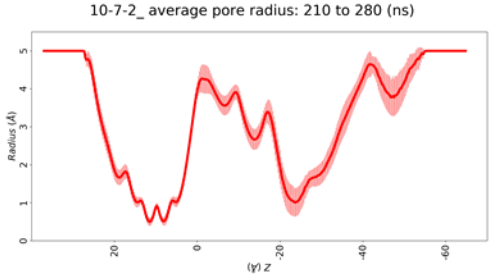

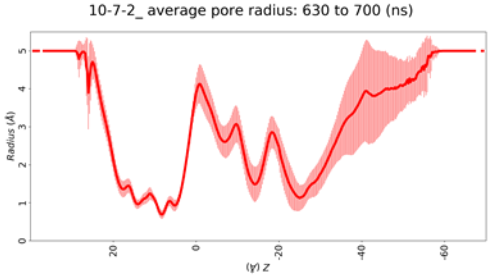

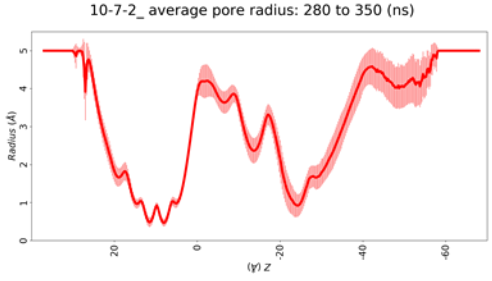

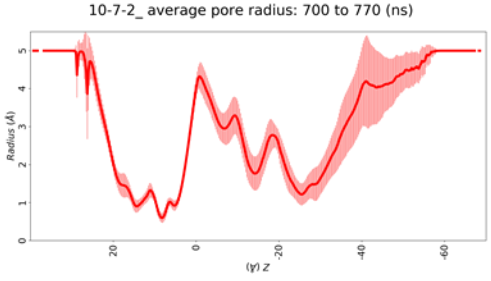

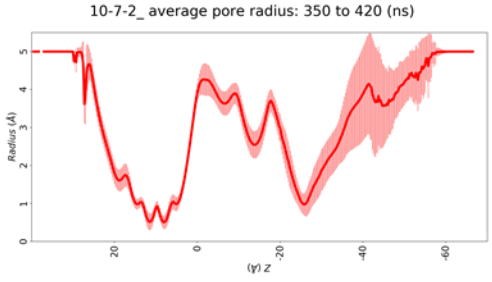

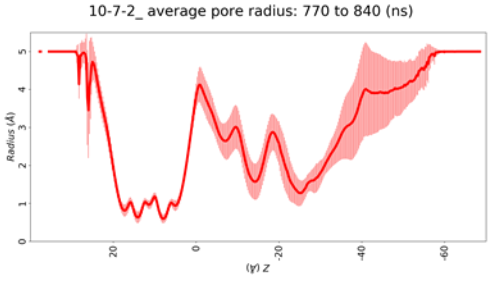

Simulation II: 3

Occupacy in binding sites during time interval: 0..70 (*ns*)

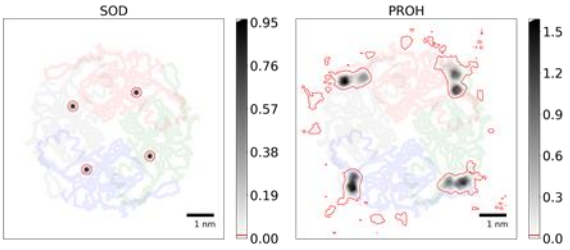

Occupacy in binding sites during time interval: 422..492 (*ns*)

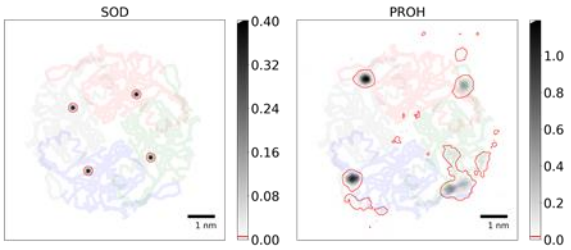

Occupacy in binding sites during time interval: 70..140 (*ns*)

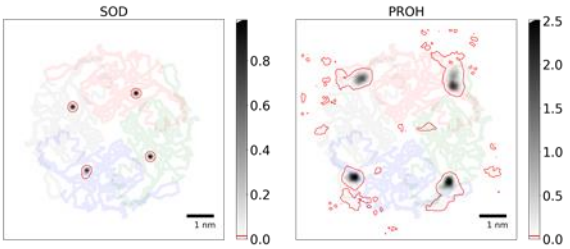

Occupacy in binding sites during time interval: 492..563 (*ns*)

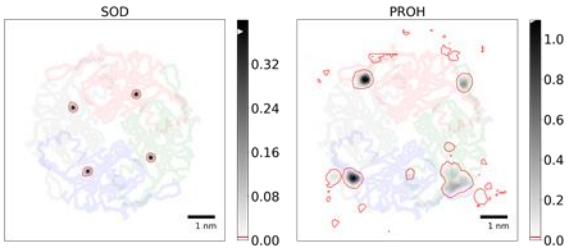

Occupacy in binding sites during time interval: 140..211 (*ns*)

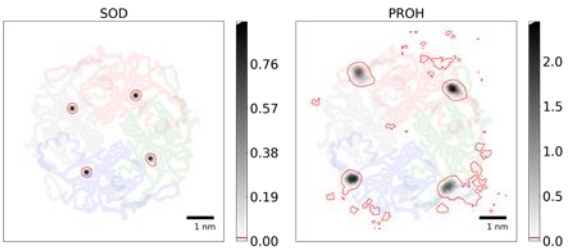

Occupacy in binding sites during time interval: 562..633 (*ns*)

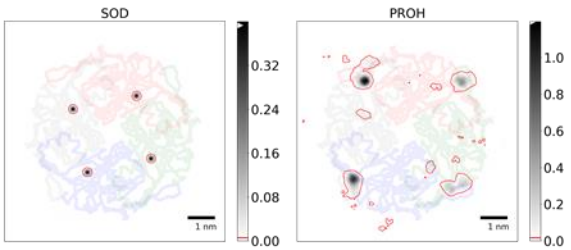

Occupacy in binding sites during time interval: 210..281 (*ns*)

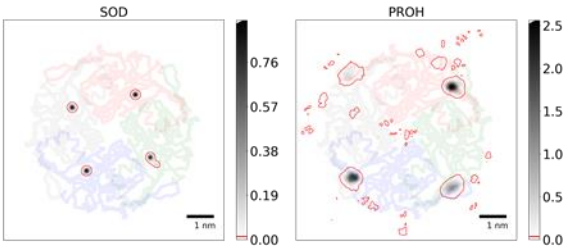

Occupacy in binding sites during time interval: 633..704 (*ns*)

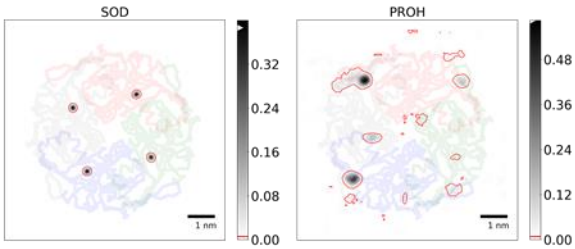

Occupacy in binding sites during time interval: 281..352 (*ns*)

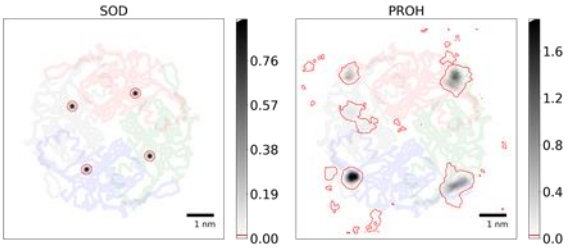

Occupacy in binding sites during time interval: 703..774 (*ns*)

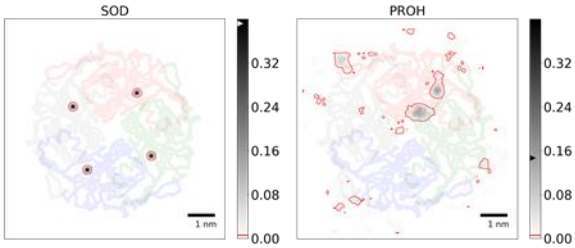

Occupacy in binding sites during time interval: 351..422 (*ns*)

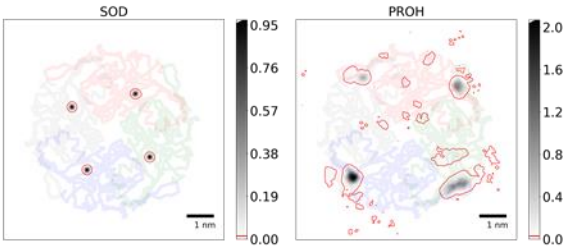

Occupacy in binding sites during time interval: 774..844 (*ns*)

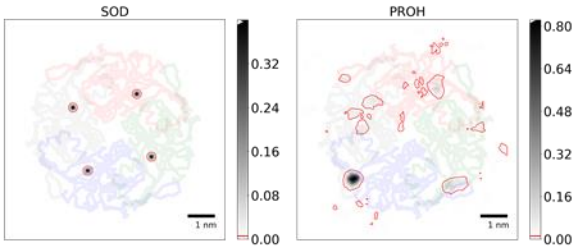

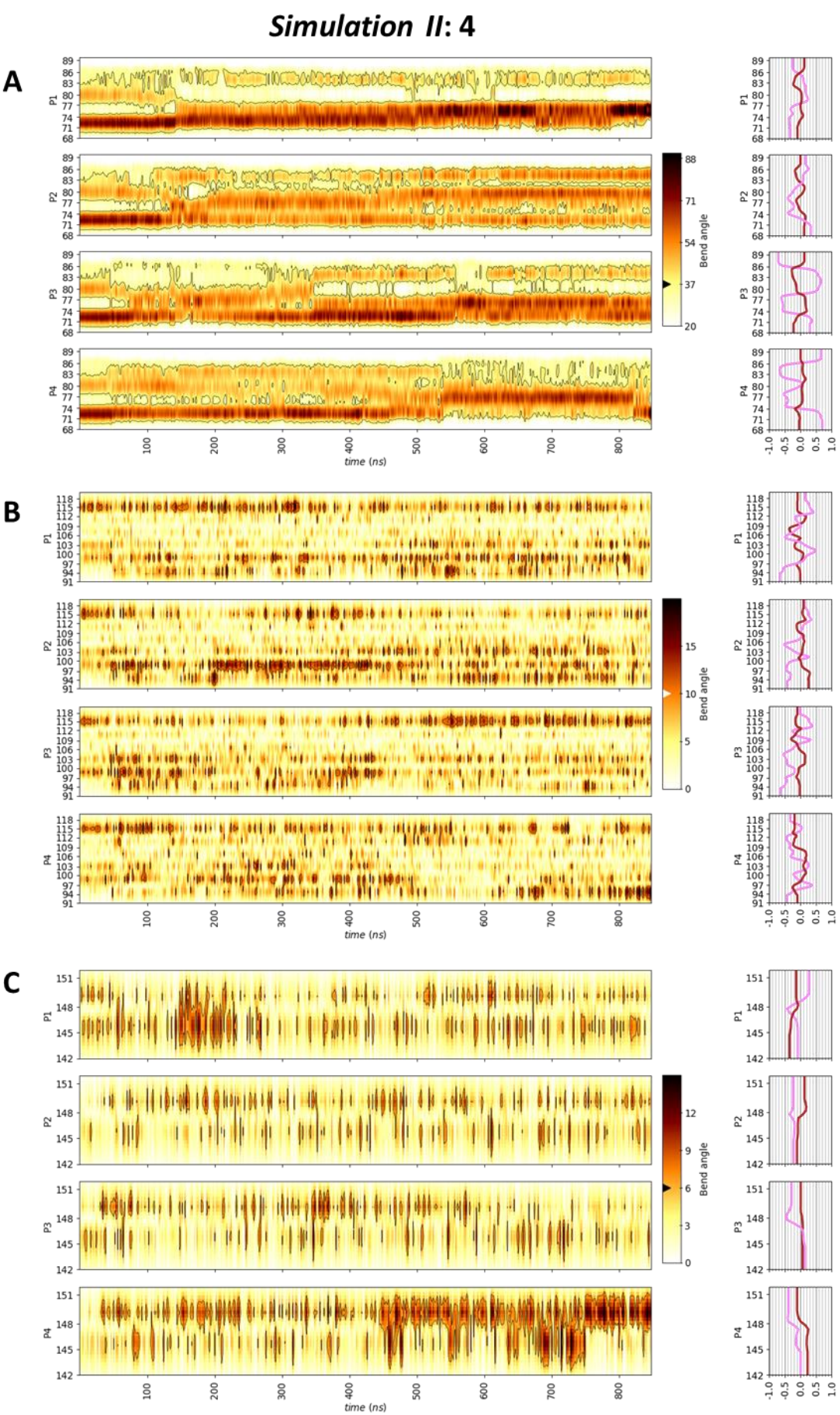
Simulation II: 4
A
B
C
P1
P2
P3
P4
time (ns)
Bend angle

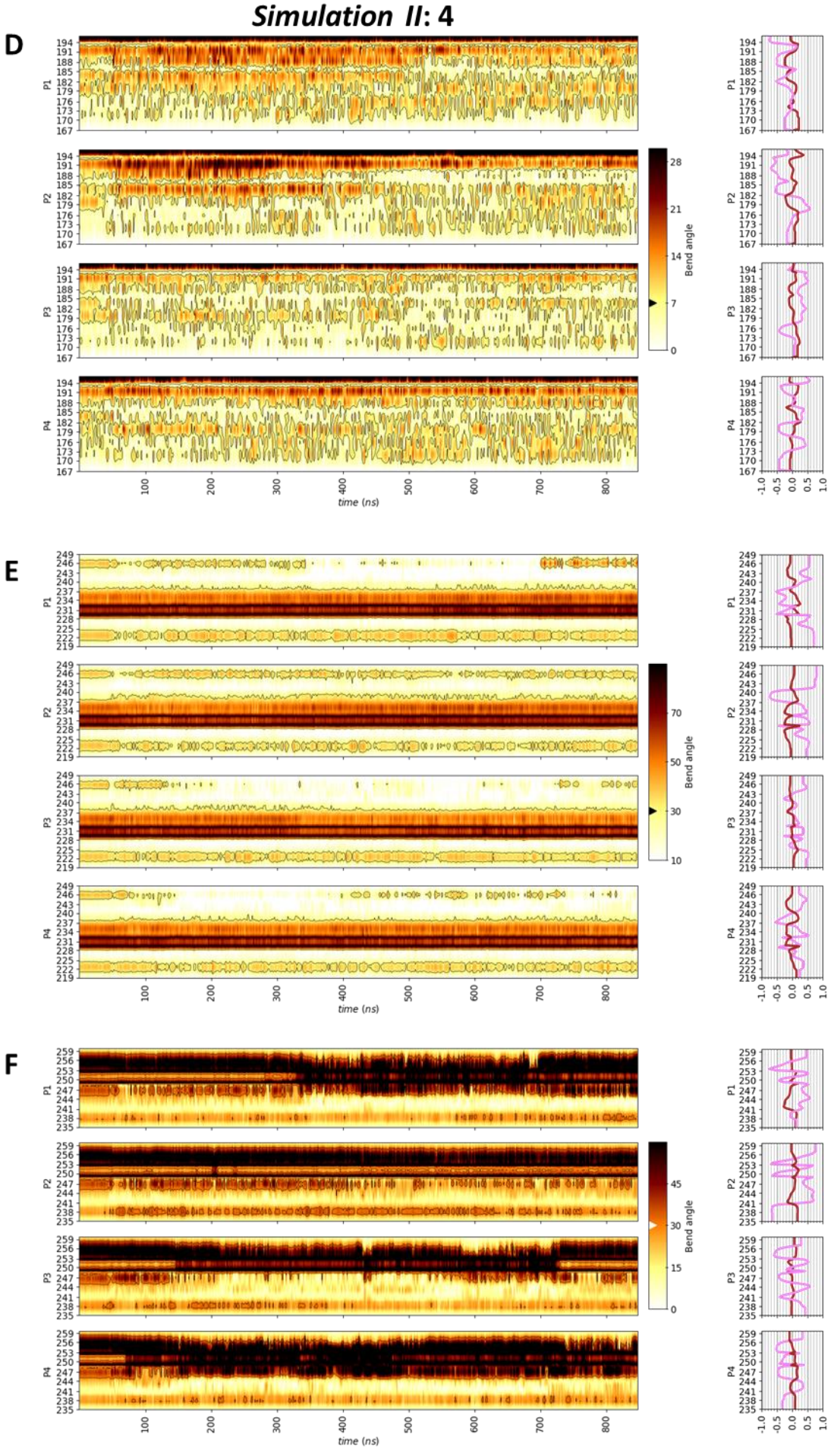
Simulation II: 4
D
E
F
P1
P2
P3
P4
Bend angle
time (ns)

Simulation II: 4

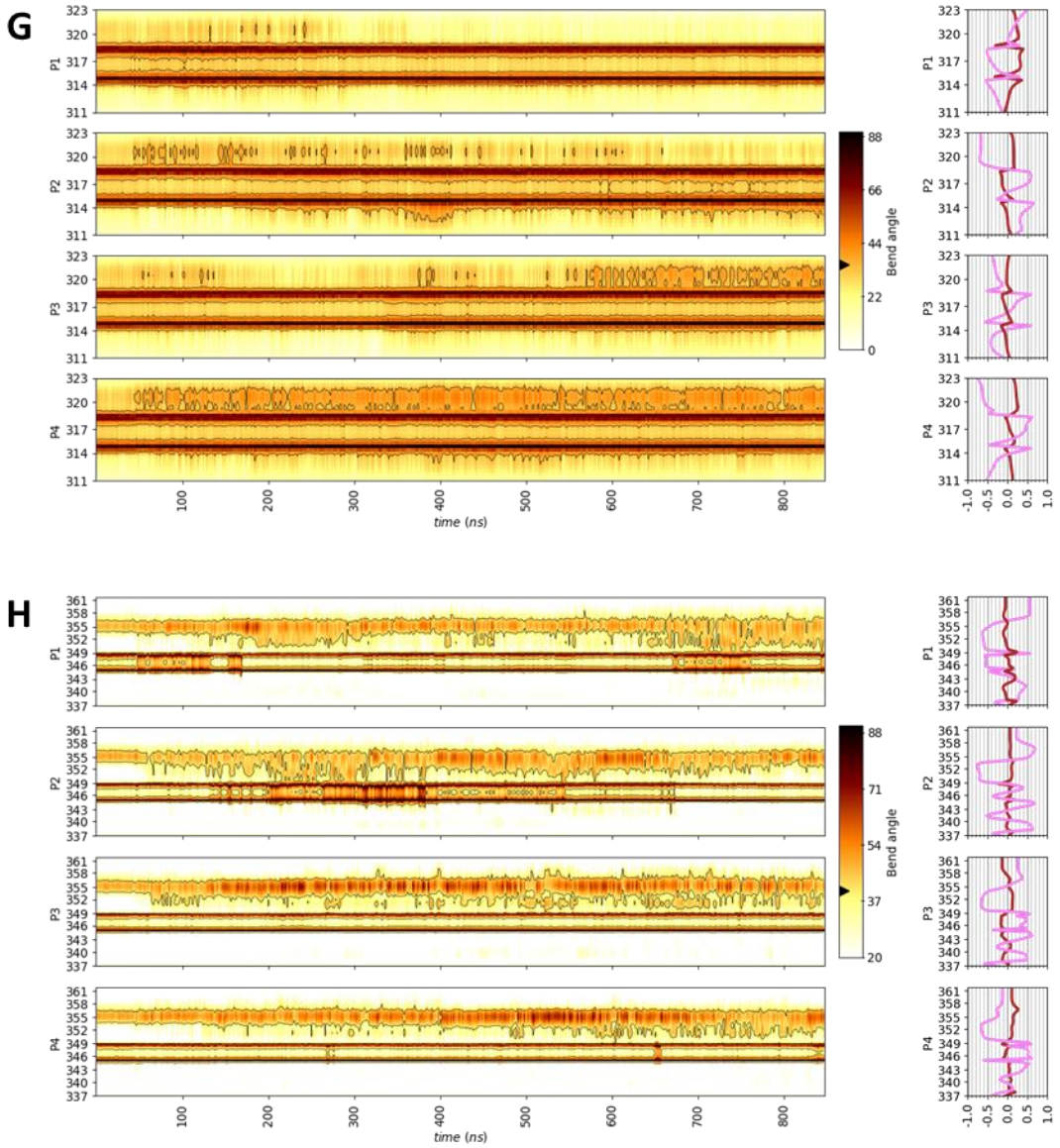

Simulation II: 5

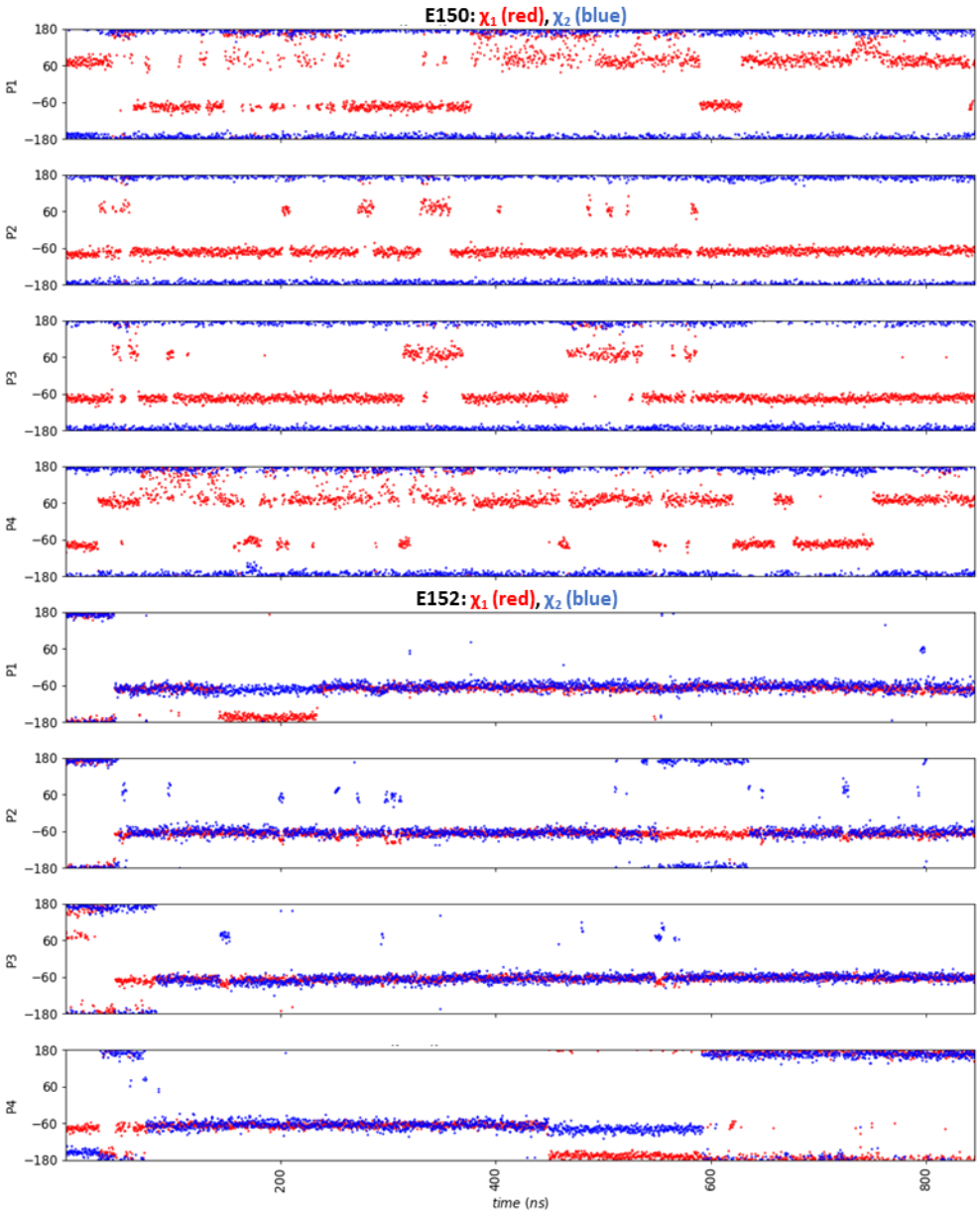

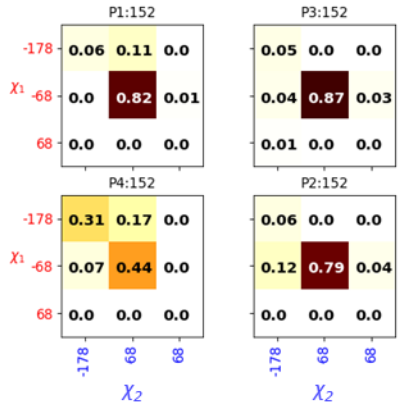

Simulation II: 6

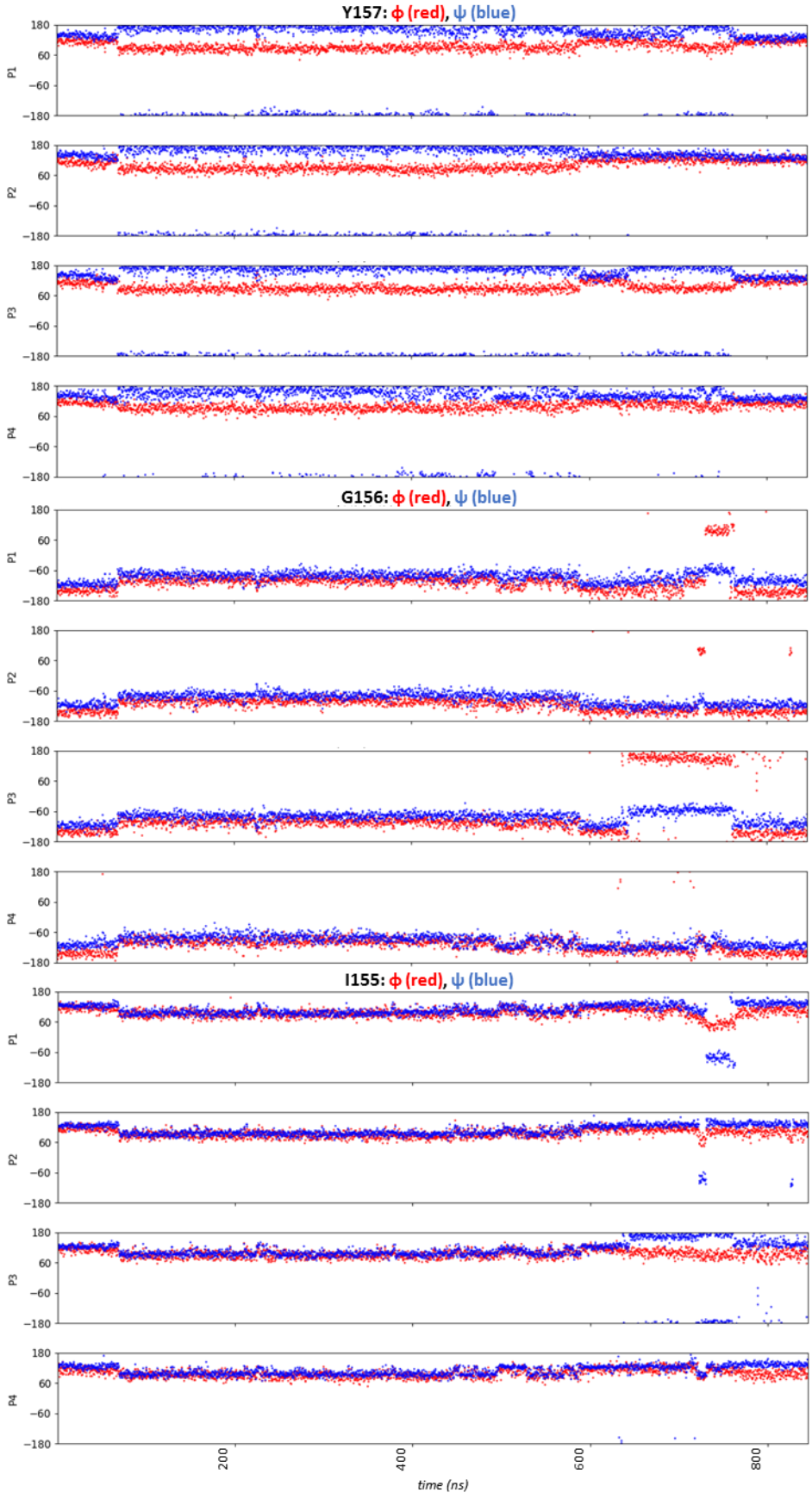

Simulation II: 7

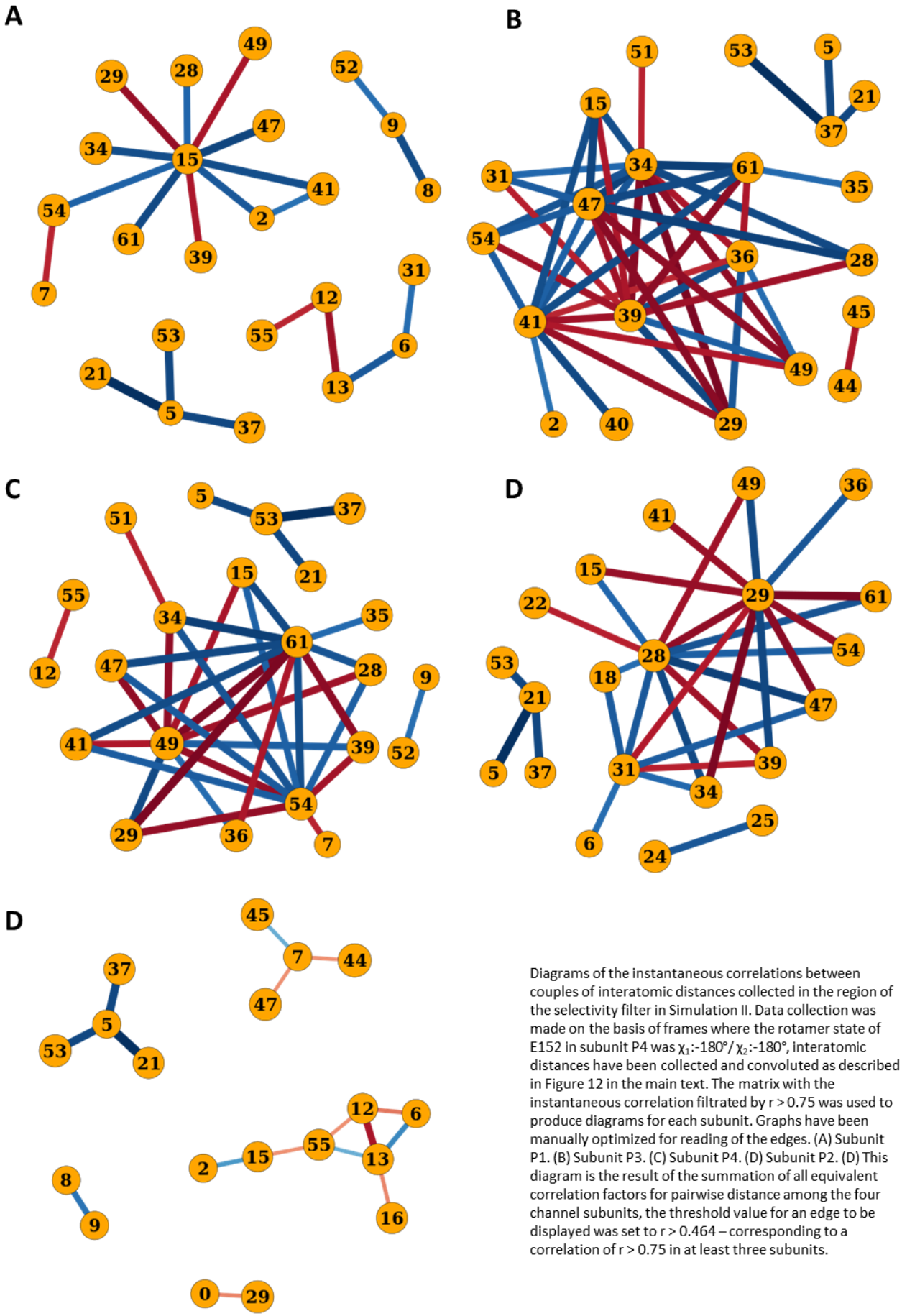

Diagrams of the instantaneous correlations between couples of interatomic distances collected in the region of the selectivity filter in Simulation II. Data collection was made on the basis of frames where the rotamer state of E152 in subunit P4 was χ_1:-180°/ χ_2:-180°, interatomic distances have been collected and convoluted as described in Figure 12 in the main text. The matrix with the instantaneous correlation filtrated by $r > 0.75$ was used to produce diagrams for each subunit. Graphs have been manually optimized for reading of the edges. (A) Subunit P1. (B) Subunit P3. (C) Subunit P4. (D) Subunit P2. (D) This diagram is the result of the summation of all equivalent correlation factors for pairwise distance among the four channel subunits, the threshold value for an edge to be displayed was set to $r > 0.464$ – corresponding to a correlation of $r > 0.75$ in at least three subunits.

Simulation II: 8

A

	P1	P3	P2	P4
P1	S	N	O	P
P3	P	S	N	O
P2	O	P	S	N
P4	N	O	P	S

P1	P3	P2	P4	
0	14	7	21	P1:105:CA | P2:105:CA
1	15	8	22	P1:188:CA | P2:188:CA
2	16	9	23	P1:105:OG1 | P1:152:CD
3	17	10	24	P1:155:CA | P3:151:CA
4	18	11	25	P1:155:CA | P3:173:CA
5	19	12	26	P1:155:CD | P3:173:CG
6	20	13	27	P1:155:CA | P2:155:CA

B

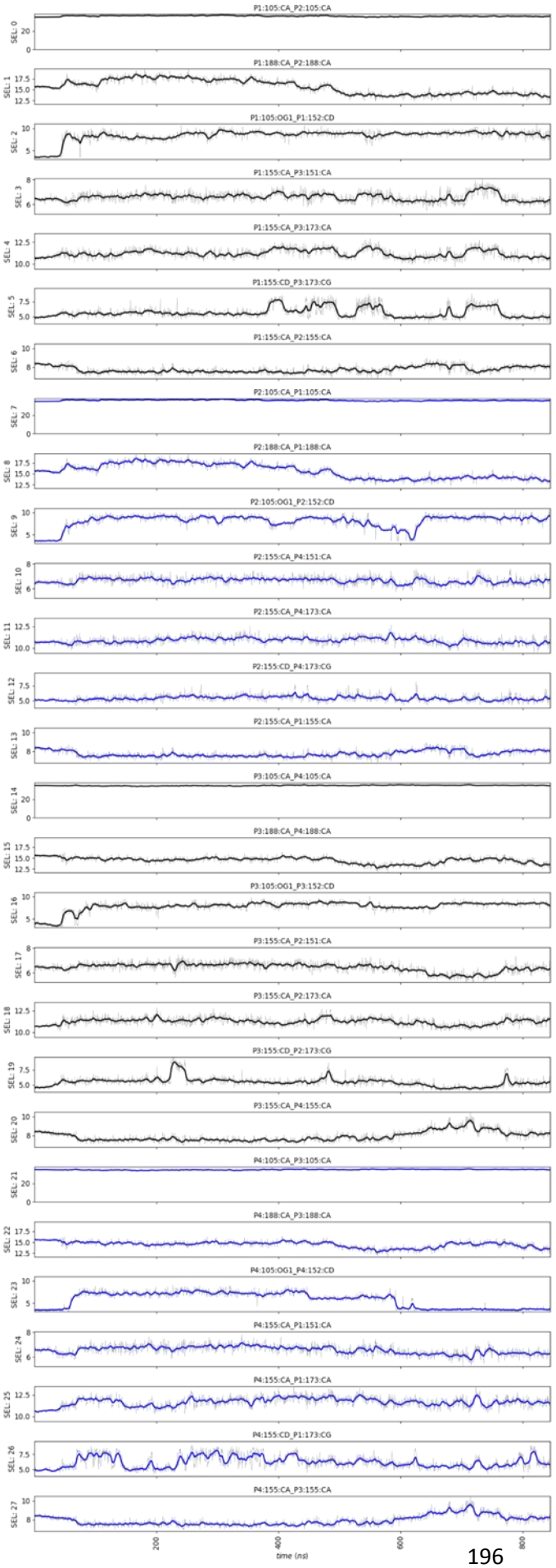

C

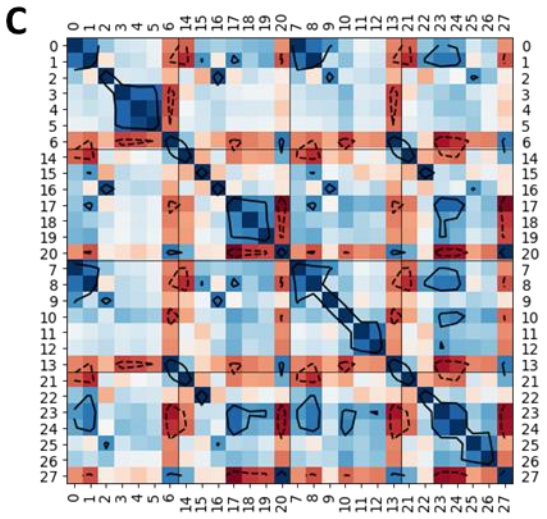

D Network threshold $r \geq 0.55$

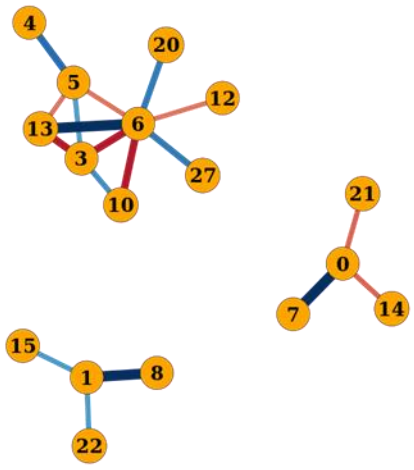

Simulation II: 8

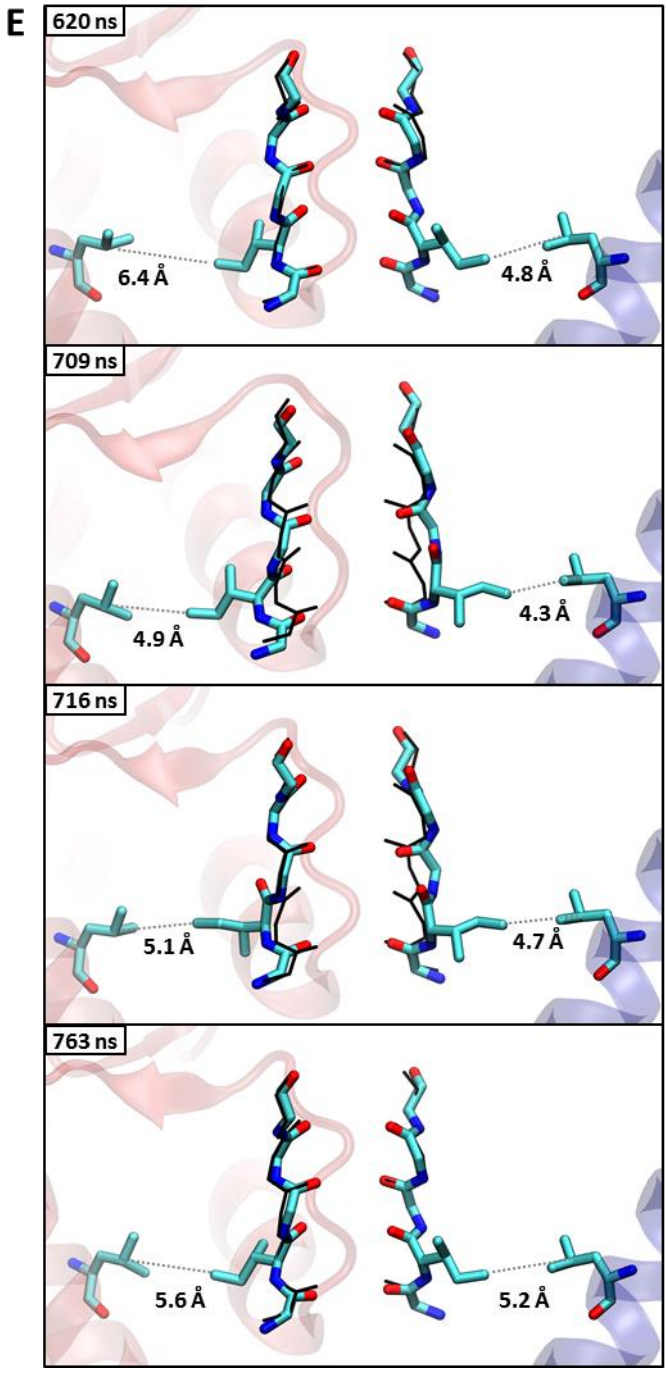

Simulation II: 11

Average electrostatic potential along the pore | **Electrostatic potential in the simulation box (Y_{axis}= 0)**

A

50 to 70 ns; V_m= -0,07 *(Volts)*

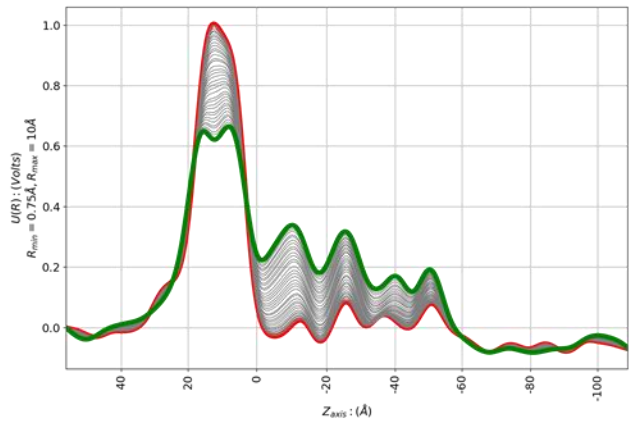

50 to 70 ns; V_m= -0,07 *(Volts)*

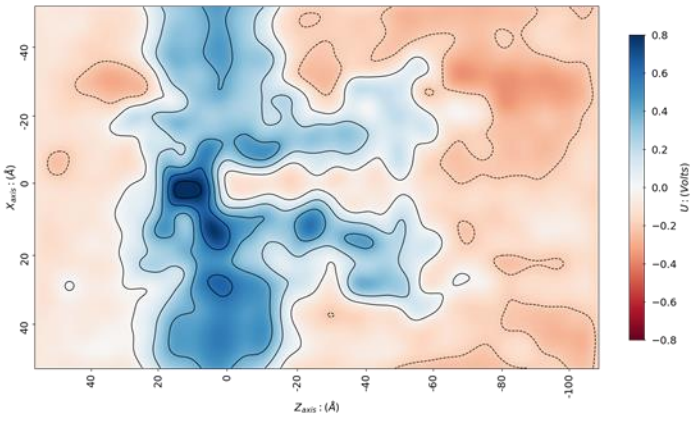

B

420 to 440 ns; V_m= -0,07 *(Volts)*

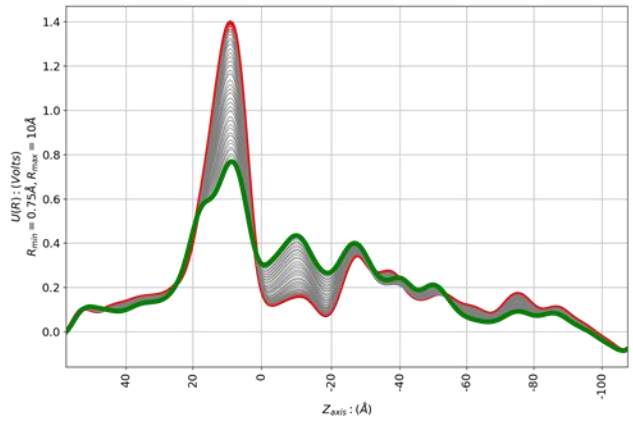

420 to 440 ns; V_m= -0,07 *(Volts)*

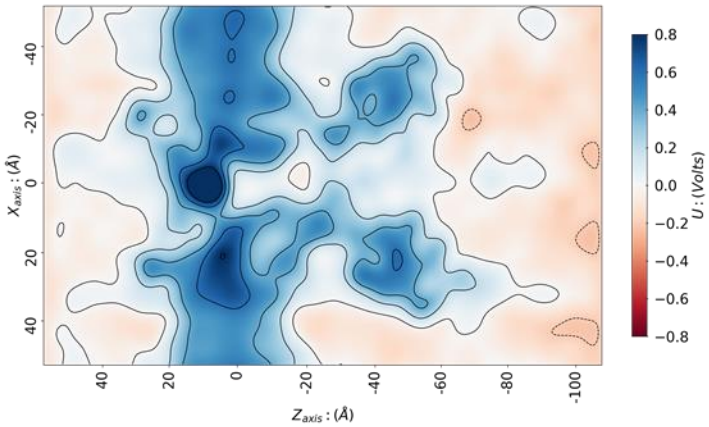

C

620 to 640 ns; V_m= -0,7 *(Volts)*

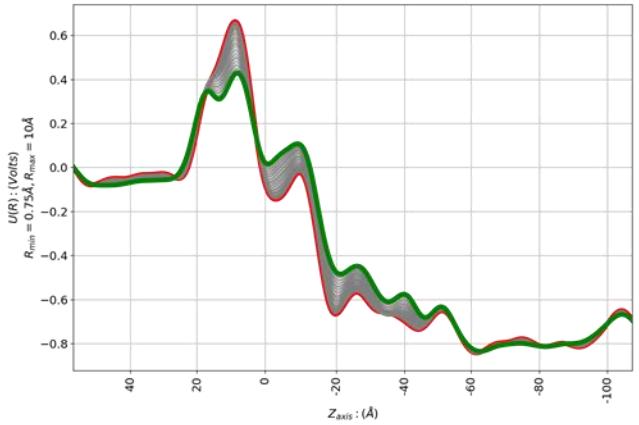

620 to 640 ns; V_m= -0,7 *(Volts)*

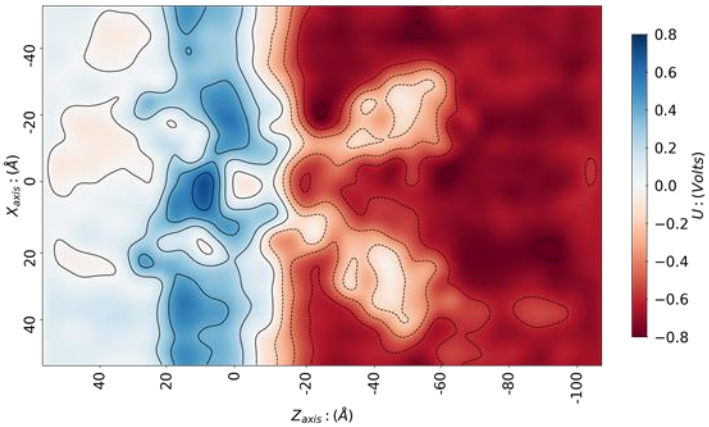

D

820 to 840 ns; V_m= -0,7 *(Volts)*

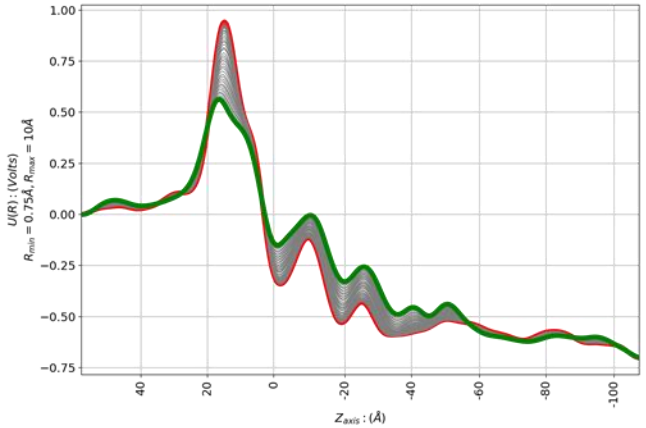

820 to 840 ns; V_m= -0,7 *(Volts)*

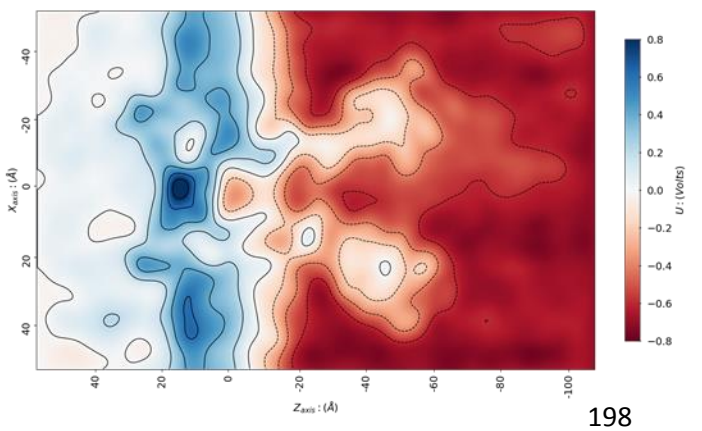

8.5 SIMULATION III

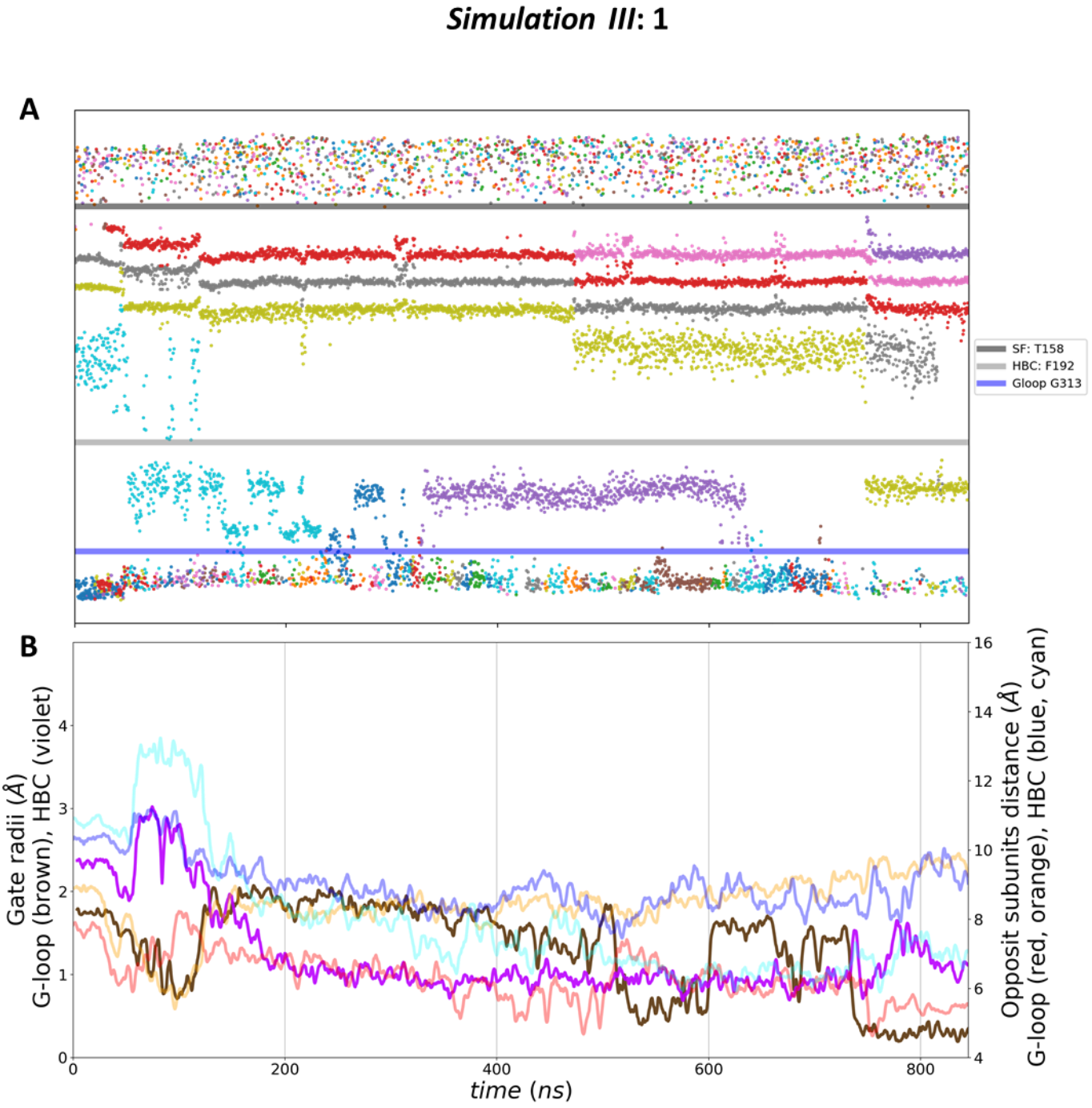

Simulation III: 2

10-8-1_ average pore radius: 0 to 70 (ns)

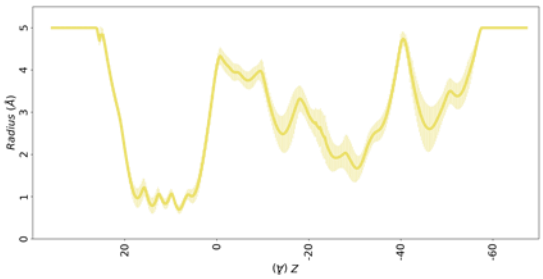

10-8-1_ average pore radius: 420 to 490 (ns)

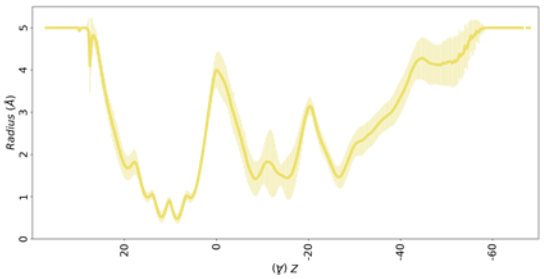

10-8-1_ average pore radius: 70 to 140 (ns)

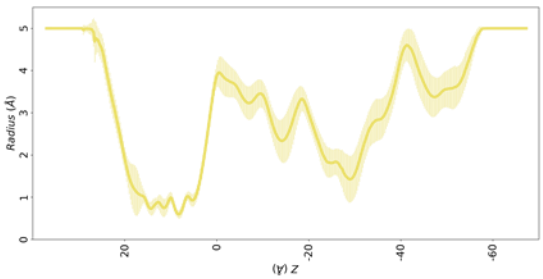

10-8-1_ average pore radius: 490 to 560 (ns)

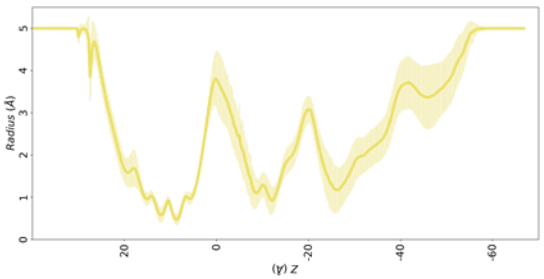

10-8-1_ average pore radius: 140 to 210 (ns)

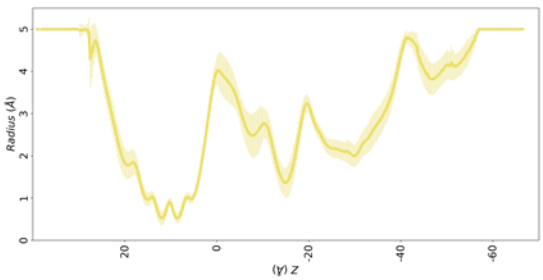

10-8-1_ average pore radius: 560 to 630 (ns)

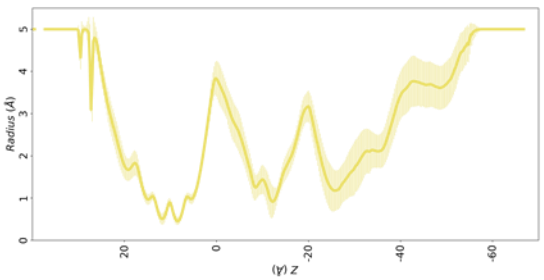

10-8-1_ average pore radius: 210 to 280 (ns)

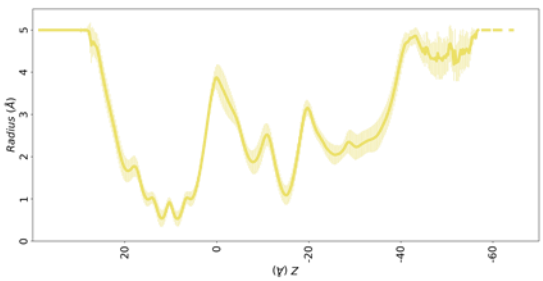

10-8-1_ average pore radius: 630 to 700 (ns)

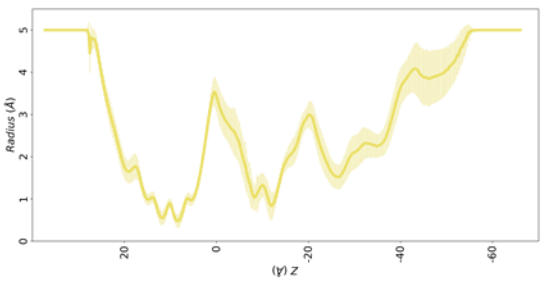

10-8-1_ average pore radius: 280 to 350 (ns)

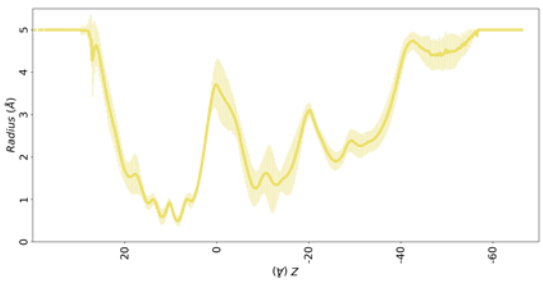

10-8-1_ average pore radius: 700 to 770 (ns)

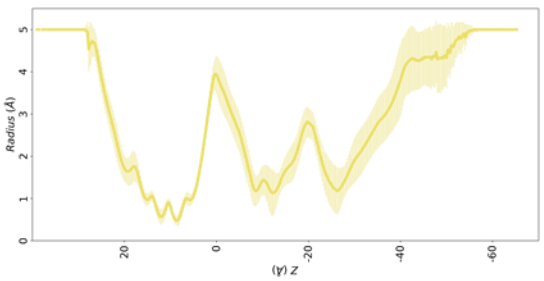

10-8-1_ average pore radius: 350 to 420 (ns)

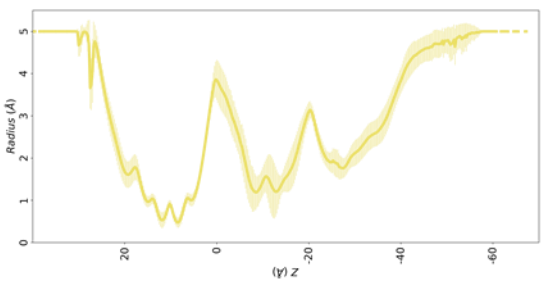

10-8-1_ average pore radius: 770 to 840 (ns)

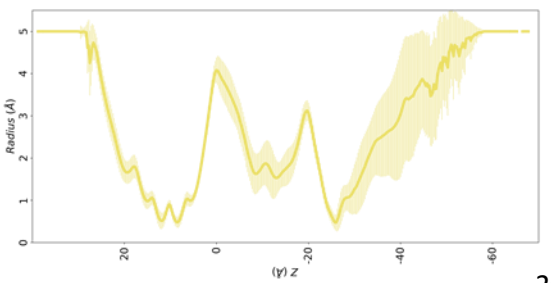

Simulation III: 3

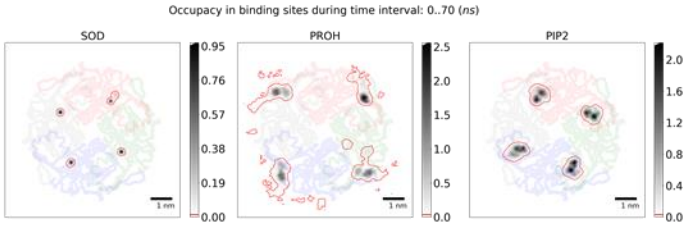

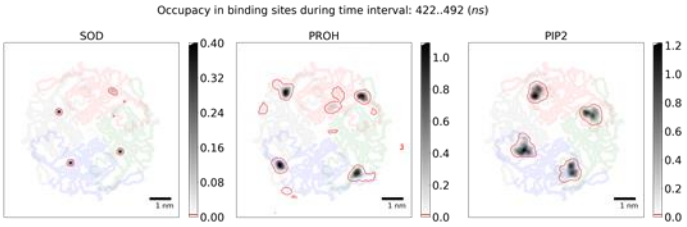

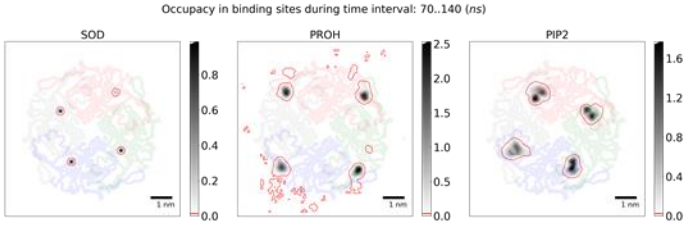

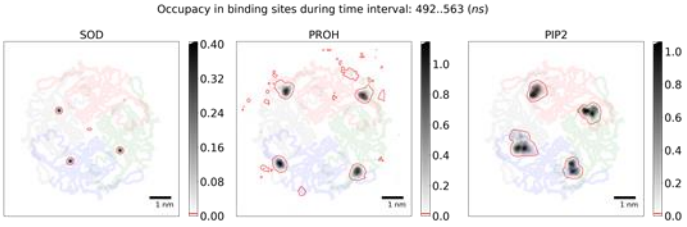

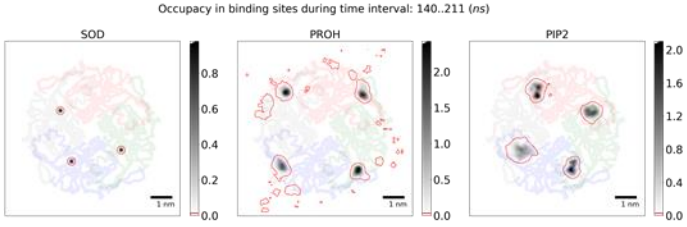

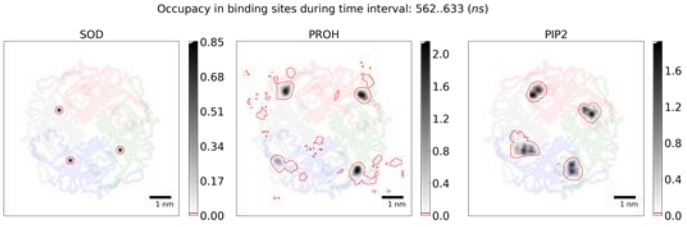

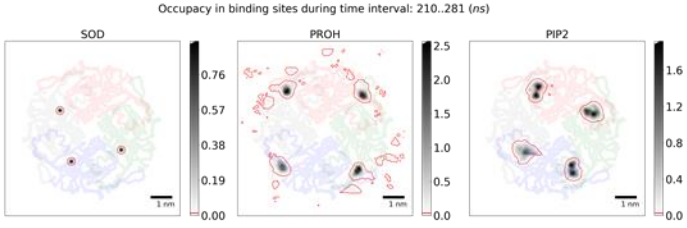

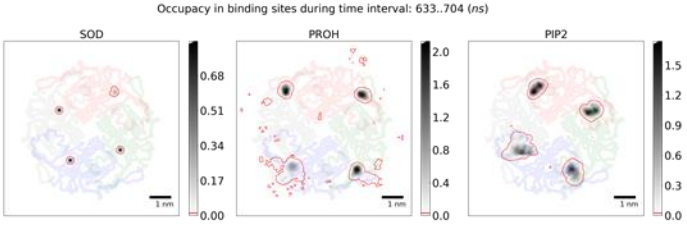

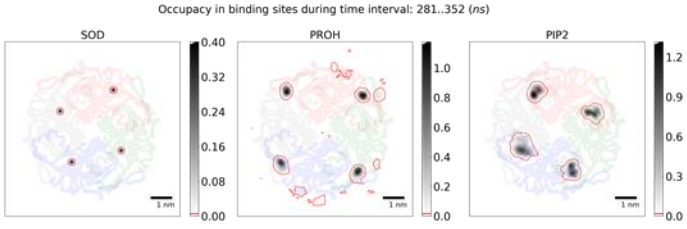

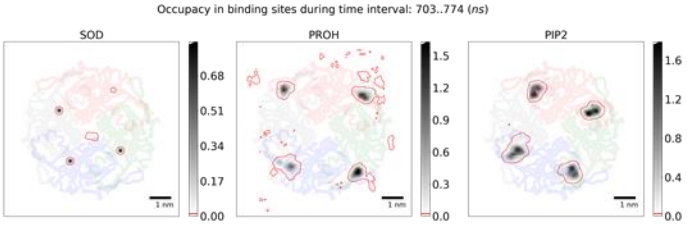

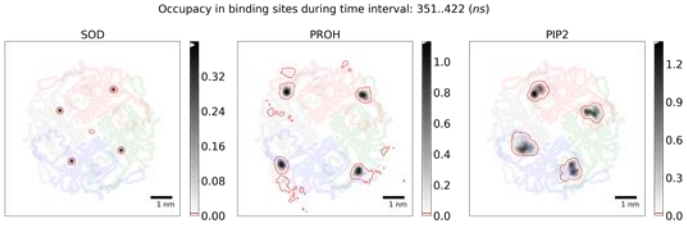

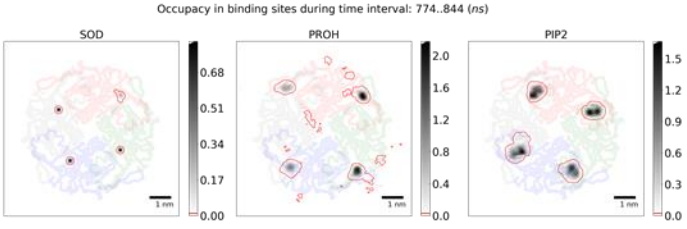

Simulation III: 4

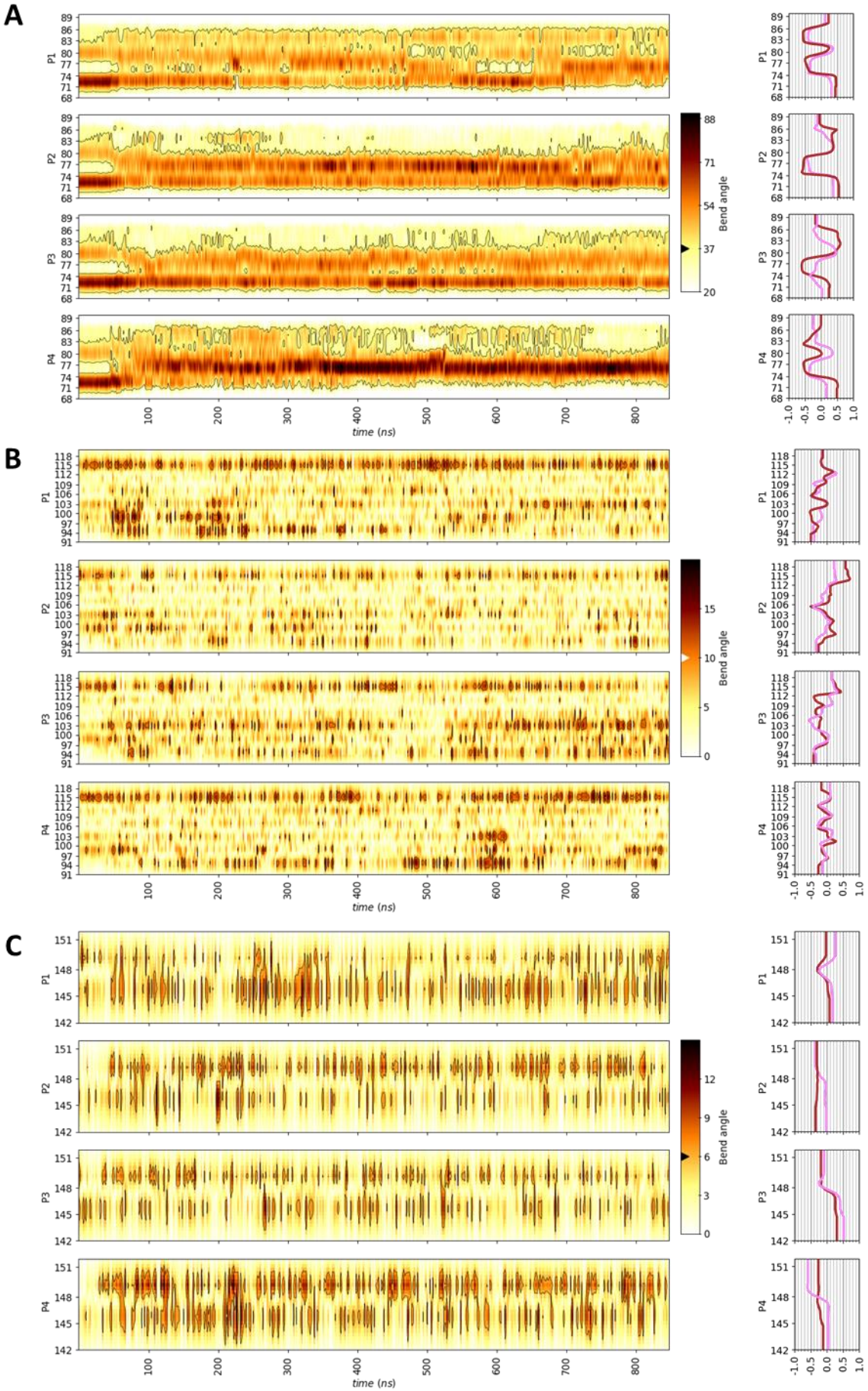

Simulation III: 4

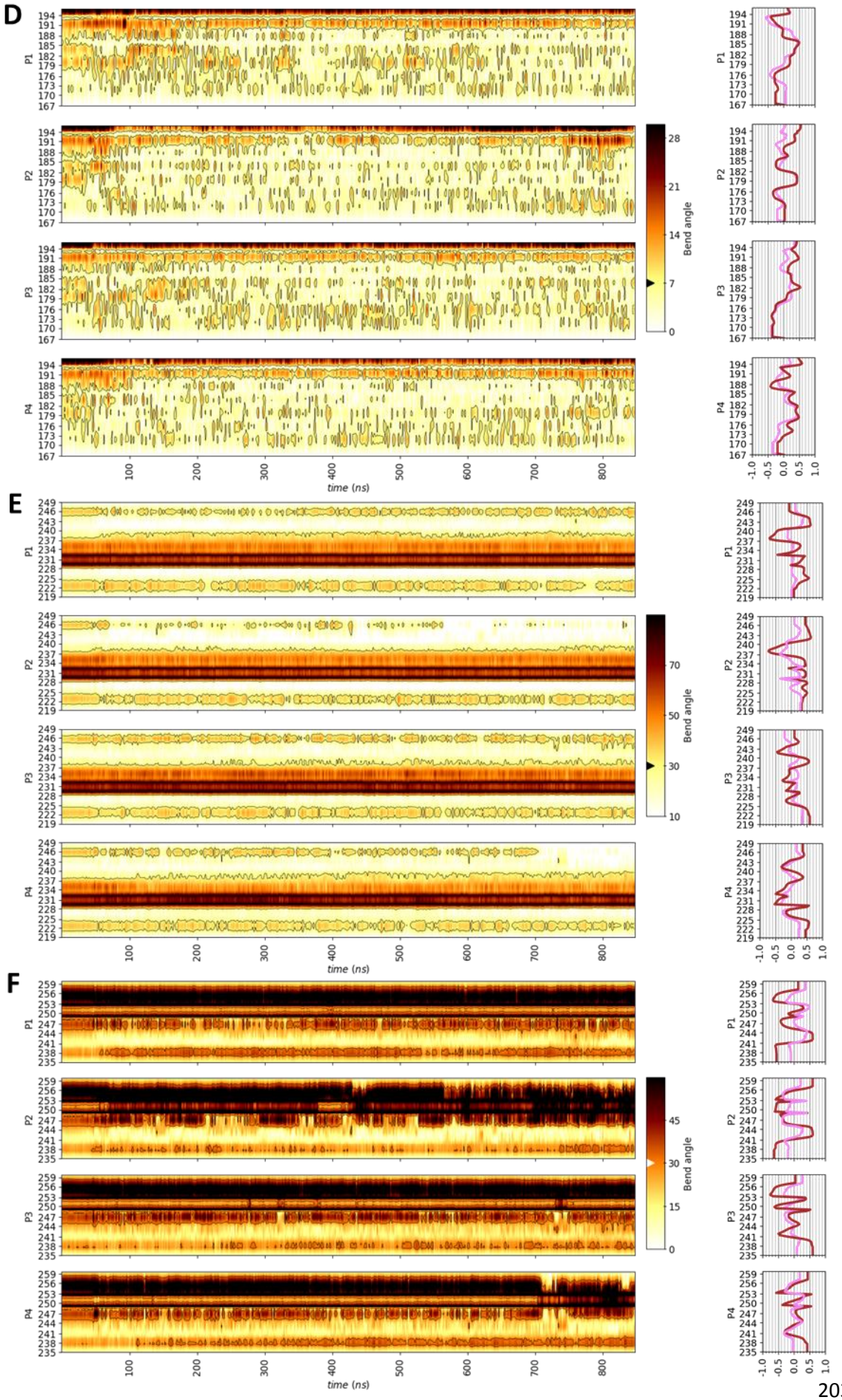

Simulation III: 4

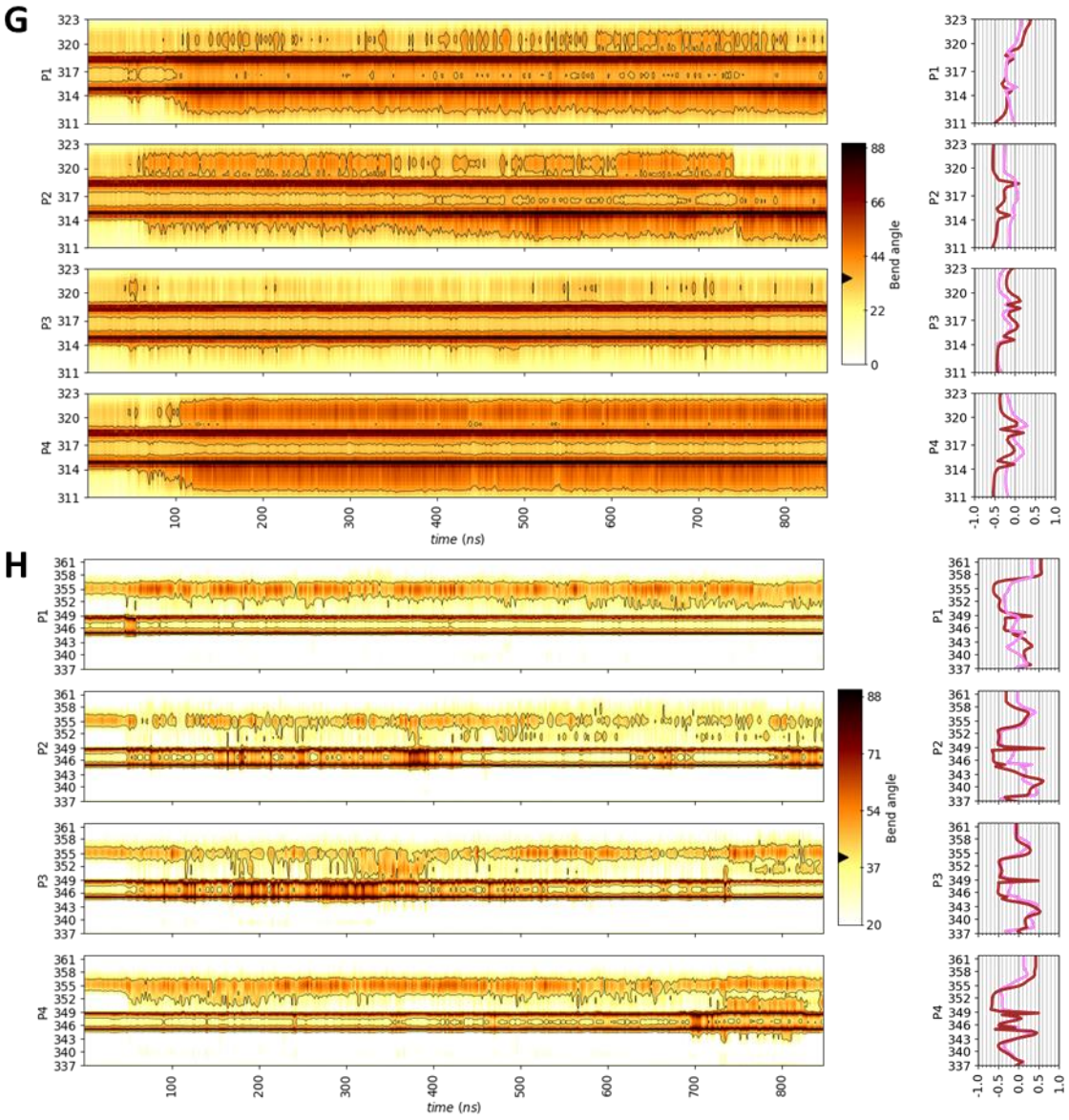

Simulation III: 5

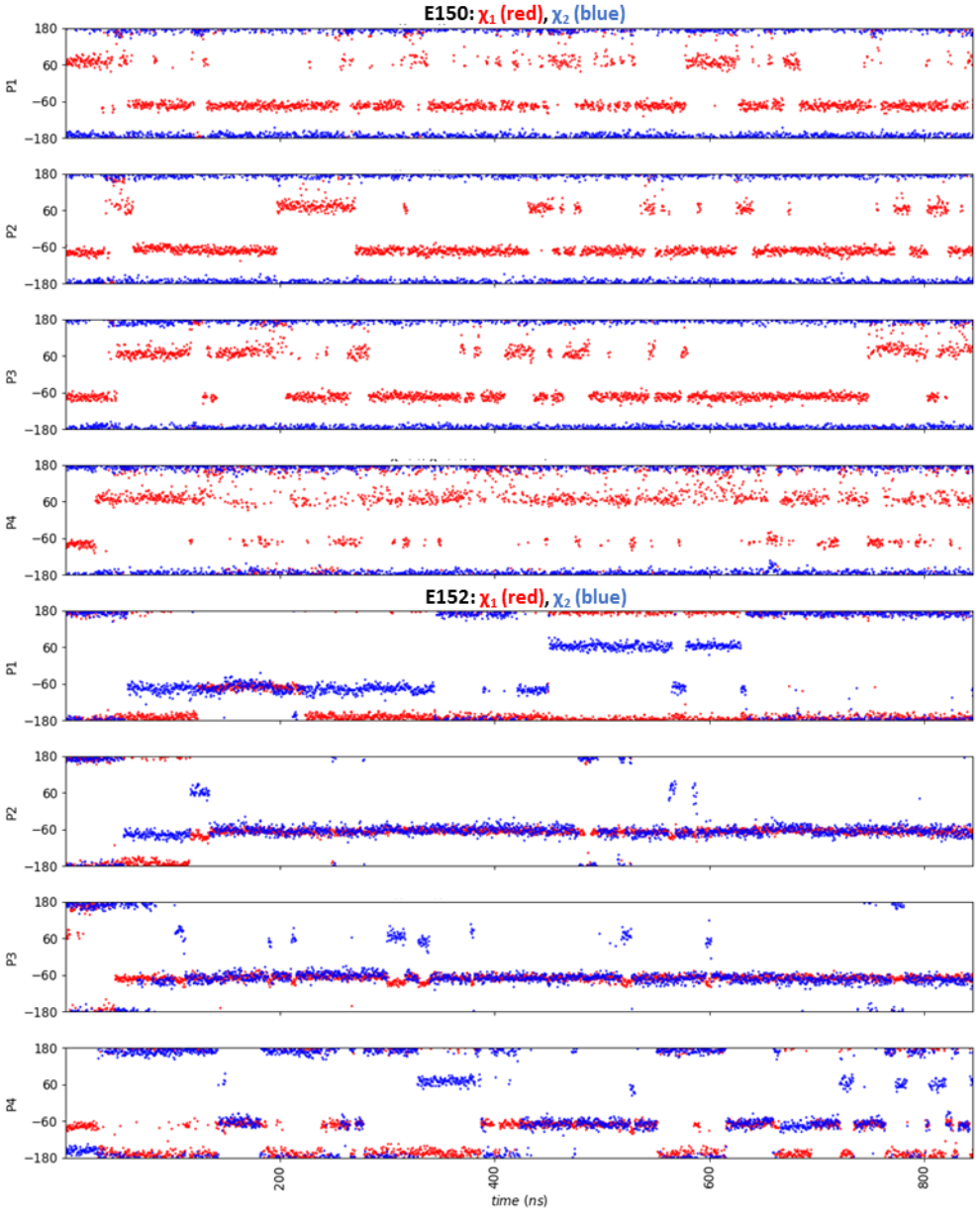

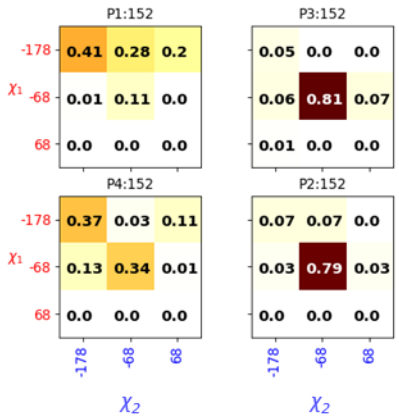

Simulation III: 6

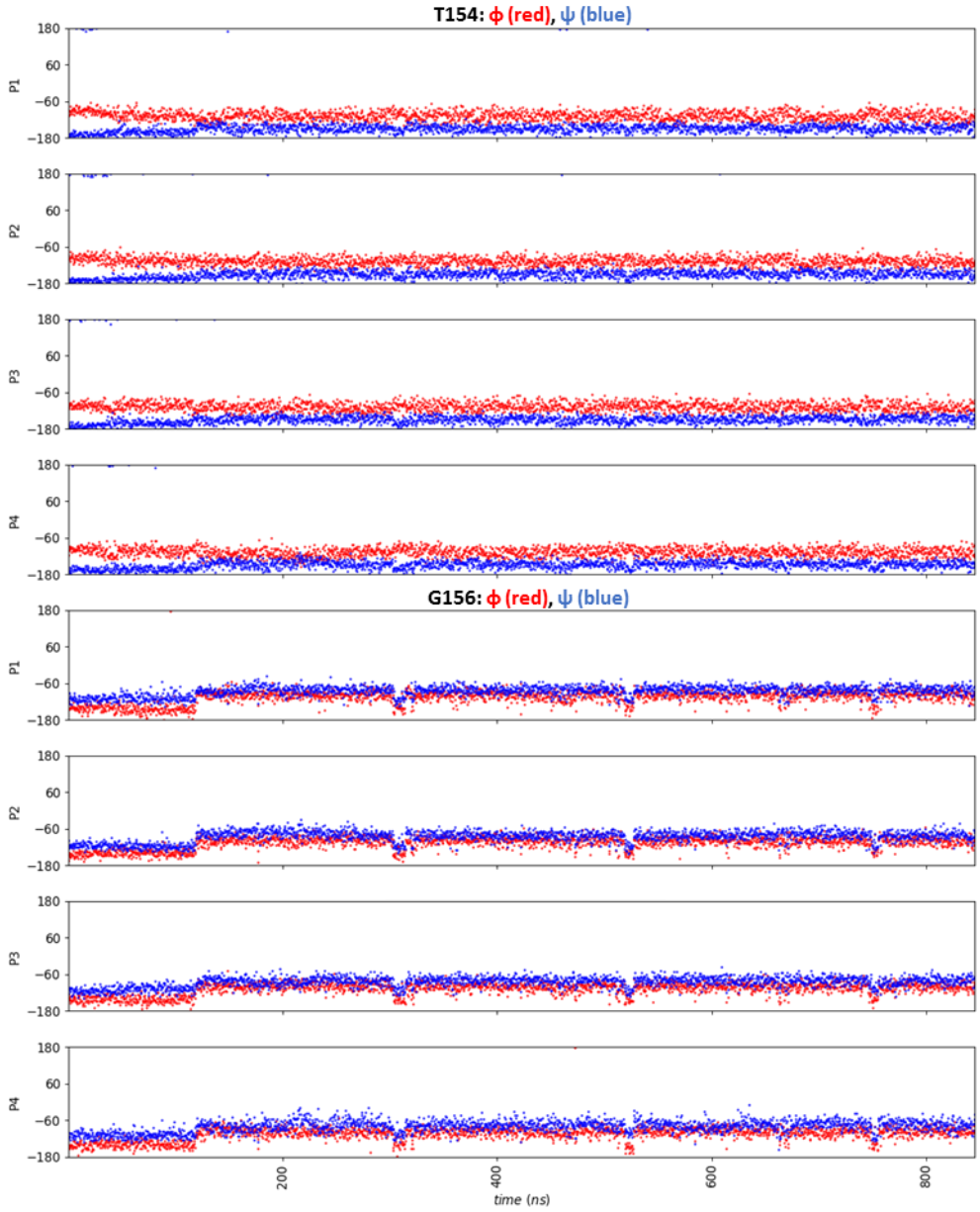

Simulation III: 6

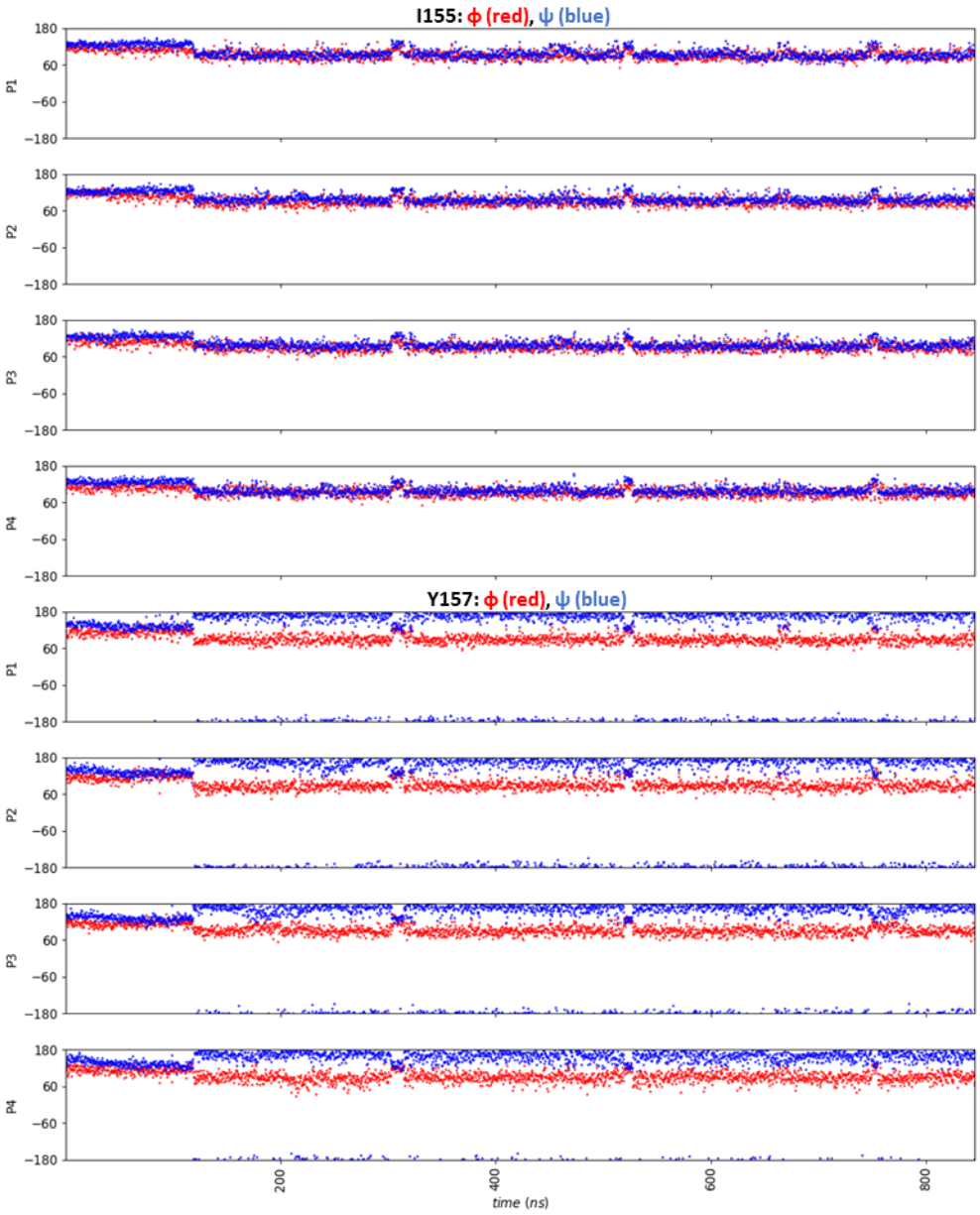

Simulation III: 6

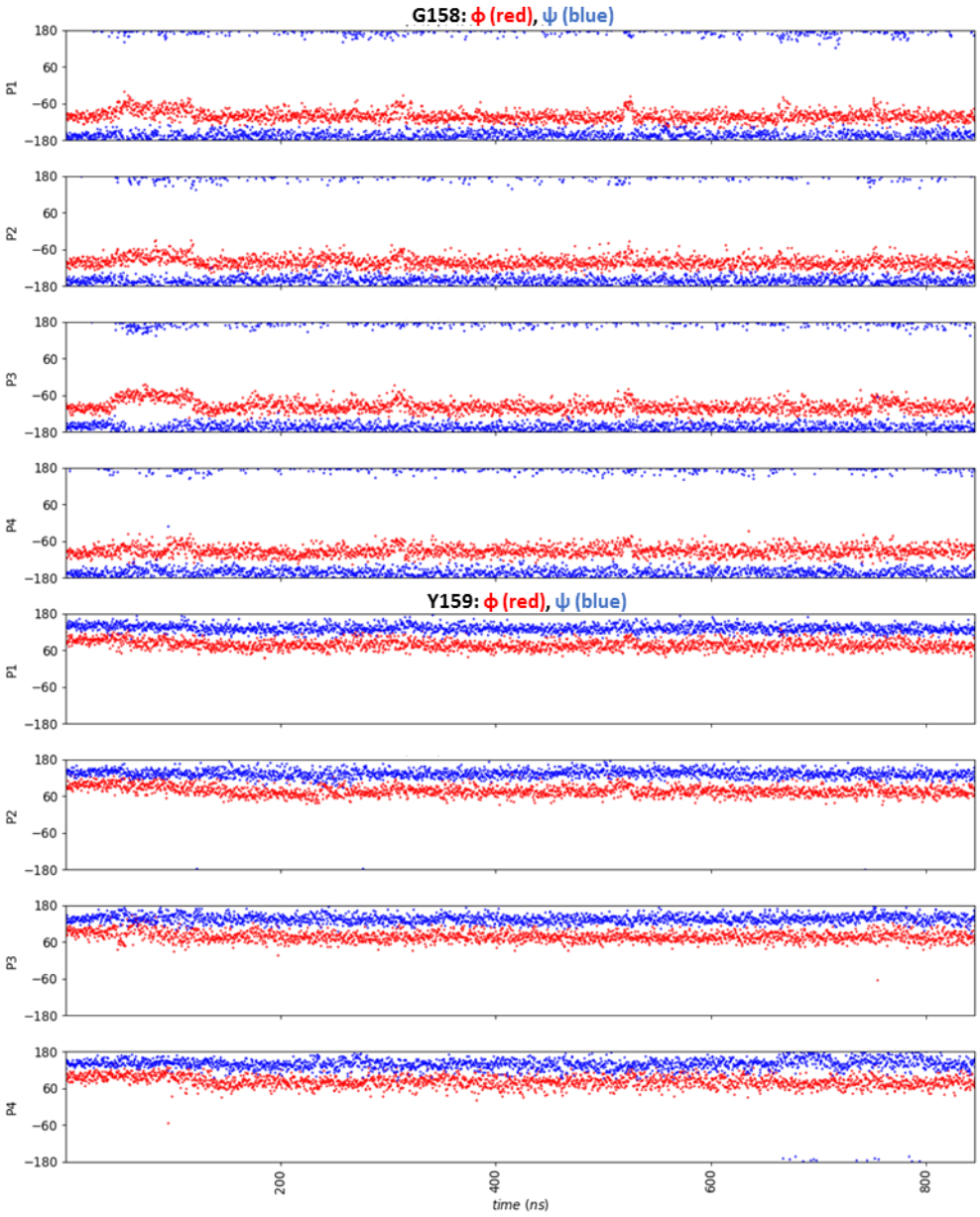

Simulation III: 7

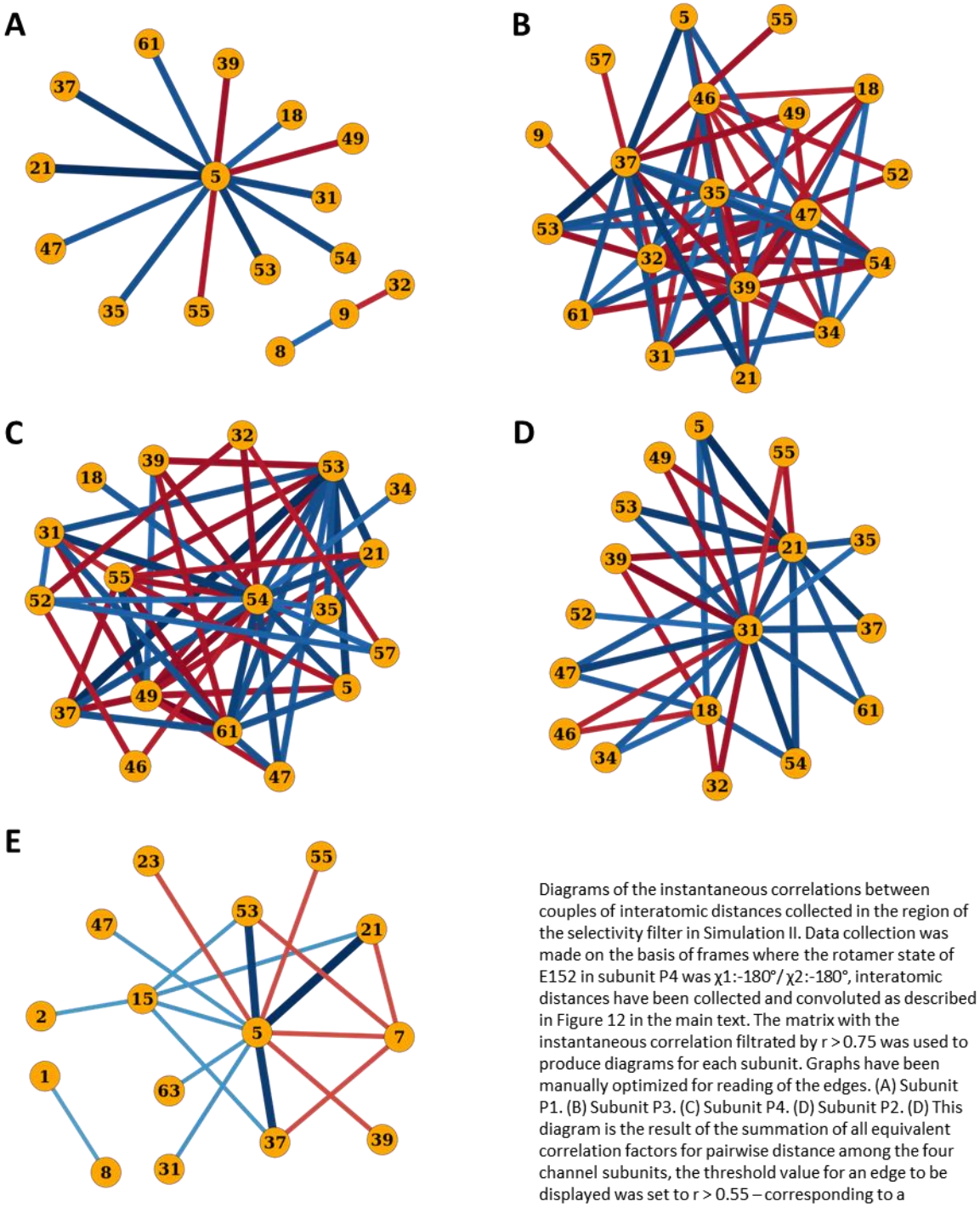

Diagrams of the instantaneous correlations between couples of interatomic distances collected in the region of the selectivity filter in Simulation II. Data collection was made on the basis of frames where the rotamer state of E152 in subunit P4 was χ1:-180°/χ2:-180°, interatomic distances have been collected and convoluted as described in Figure 12 in the main text. The matrix with the instantaneous correlation filtrated by r > 0.75 was used to produce diagrams for each subunit. Graphs have been manually optimized for reading of the edges. (A) Subunit P1. (B) Subunit P3. (C) Subunit P4. (D) Subunit P2. (D) This diagram is the result of the summation of all equivalent correlation factors for pairwise distance among the four channel subunits, the threshold value for an edge to be displayed was set to r > 0.55 – corresponding to a correlation of r > 0.82 in at least three subunits.

Simulation III: 8

A

	P1	P3	P2	P4
P1	S	N	O	P
P3	P	S	N	O
P2	O	P	S	N
P4	N	O	P	S

P1	P3	P2	P4	
0	14	7	21	P1:105:CA | P2:105:CA
1	15	8	22	P1:188:CA | P2:188:CA
2	16	9	23	P1:105:OG1 | P1:152:CD
3	17	10	24	P1:155:CA | P3:151:CA
4	18	11	25	P1:155:CA | P3:173:CA
5	19	12	26	P1:155:CD | P3:173:CG
6	20	13	27	P1:155:CA | P2:155:CA

B

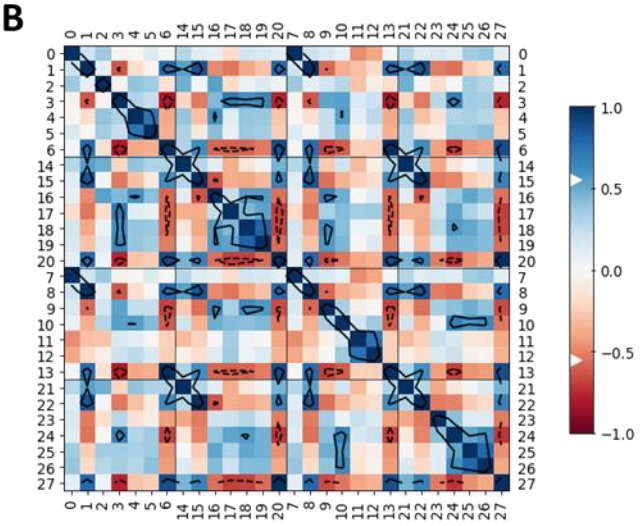

C

Network threshold $r \geq 0.618$

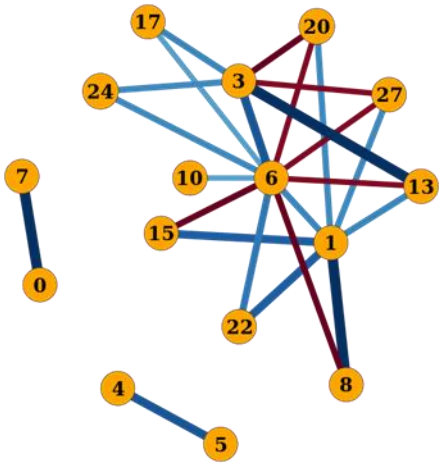

D

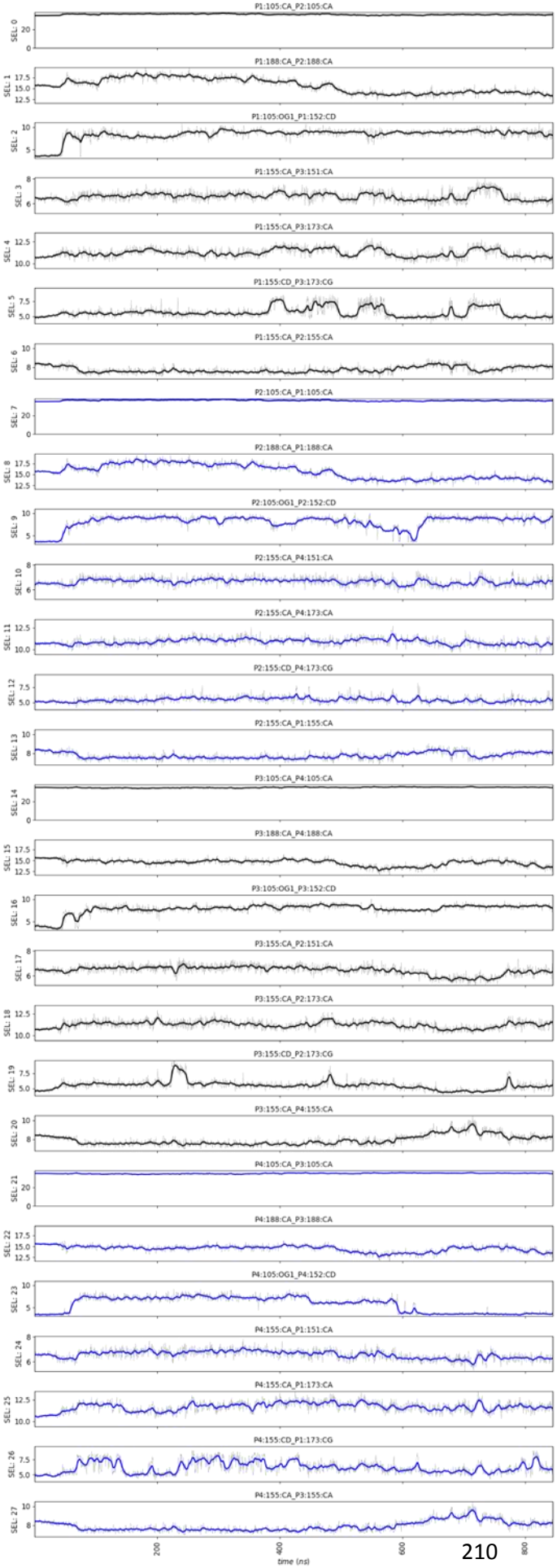

Simulation III: 9

Norm: #4

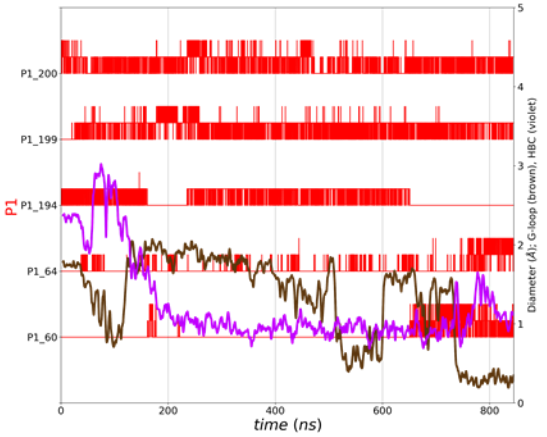

Norm: #4

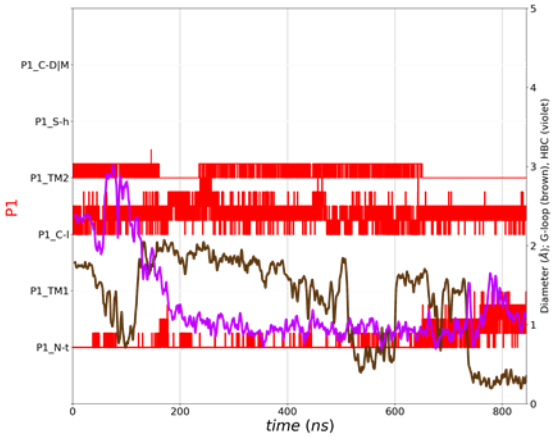

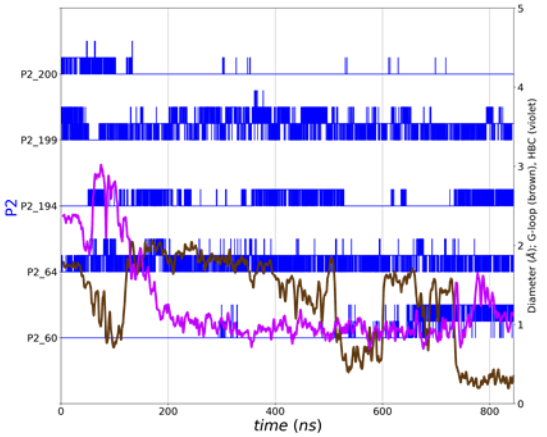

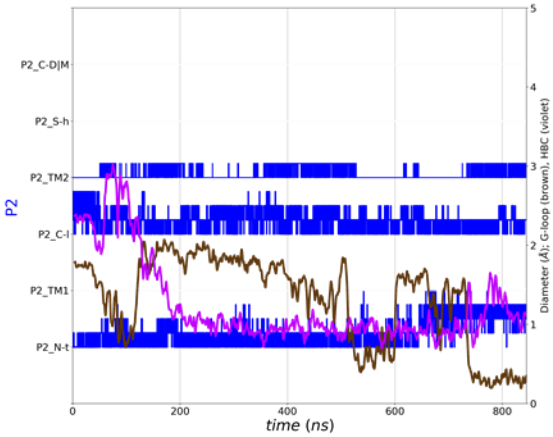

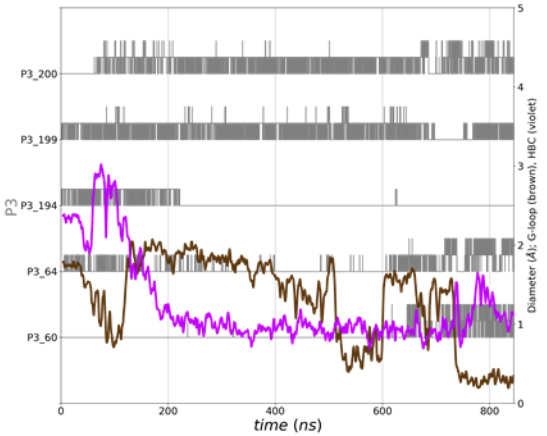

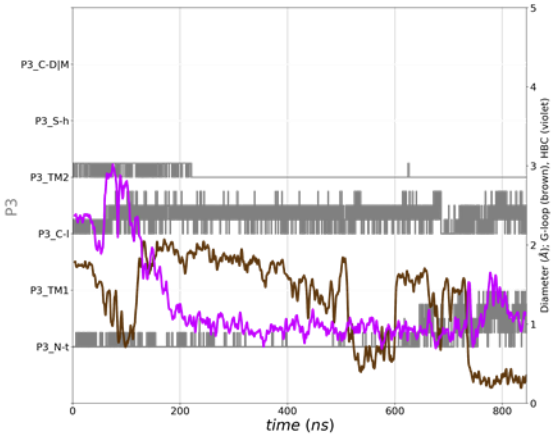

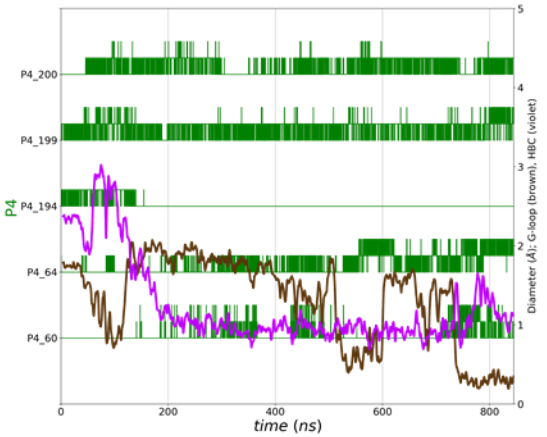

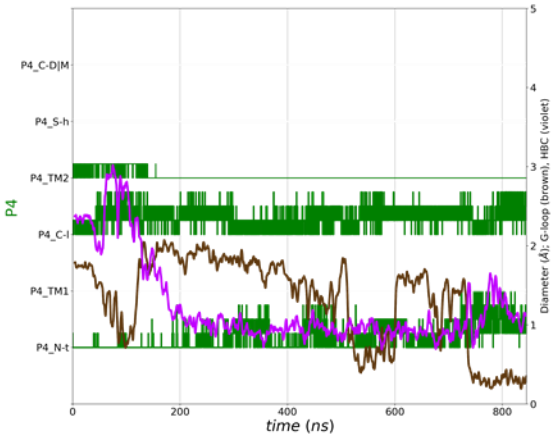

Simulation III: 10

Norm: #4

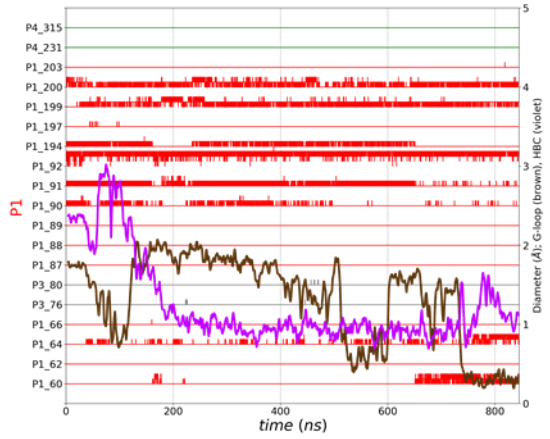

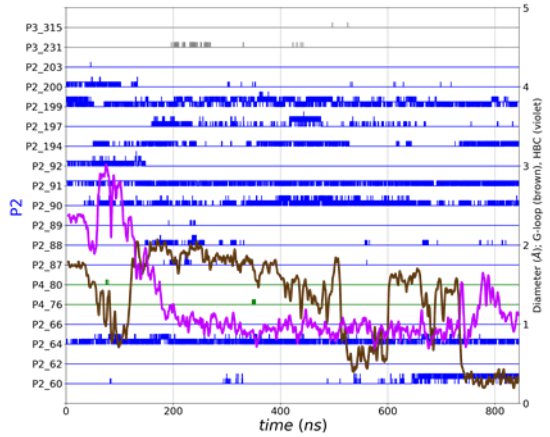

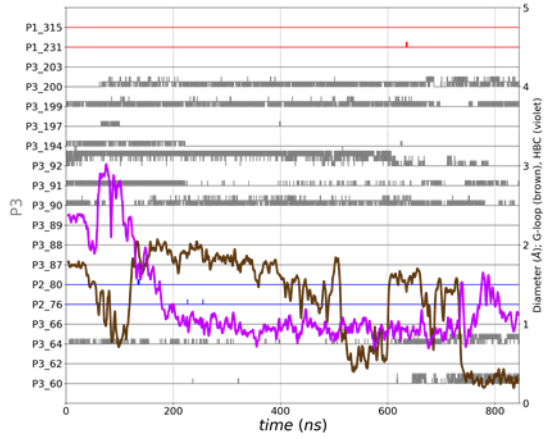

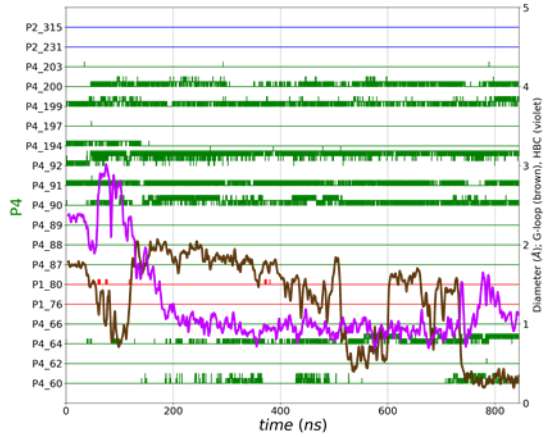

Norm: #7

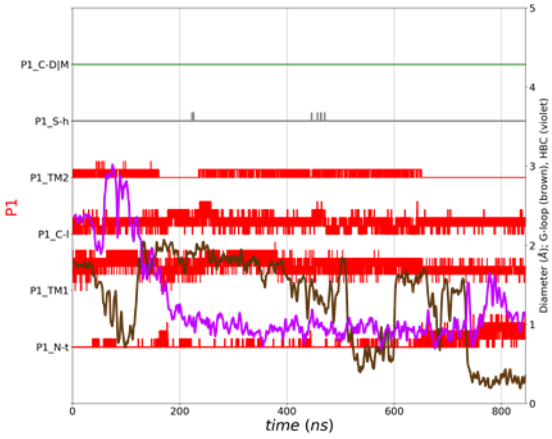

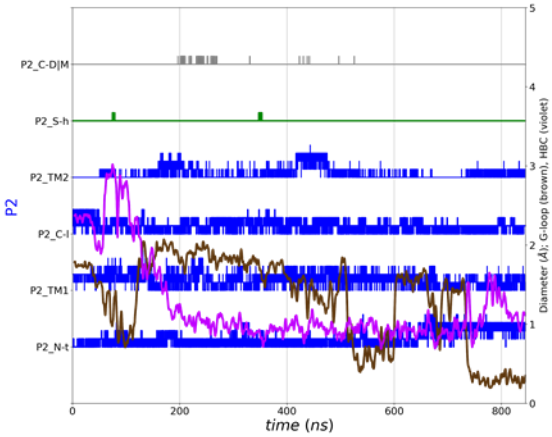

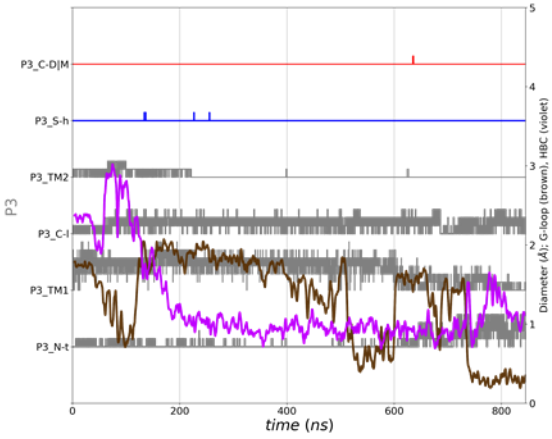

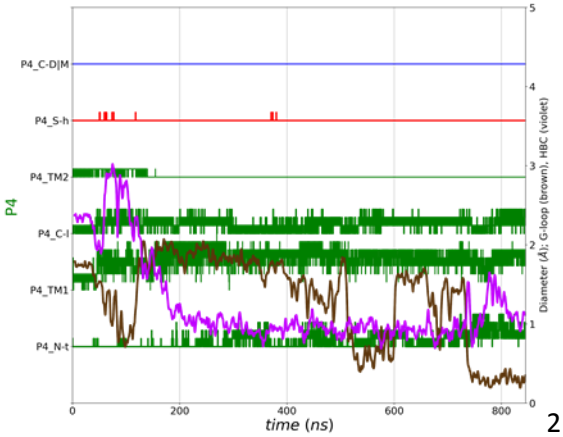

Simulation III: 11

Average electrostatic potential along the pore | **Electrostatic potential in the simulation box (Y_{axis}= 0)**

A

50 to 70 ns; V_m= -0,07 (Volts)

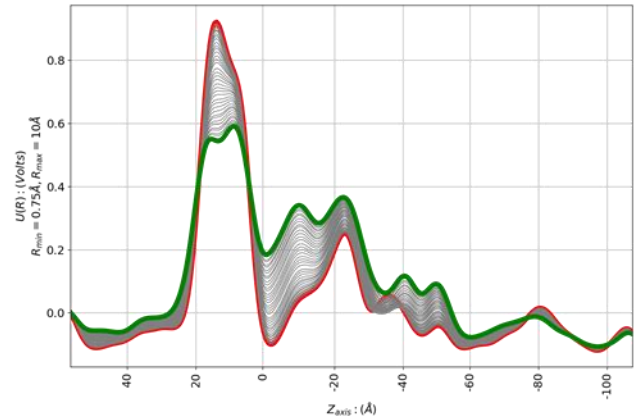

50 to 70 ns; V_m= -0,07 (Volts)

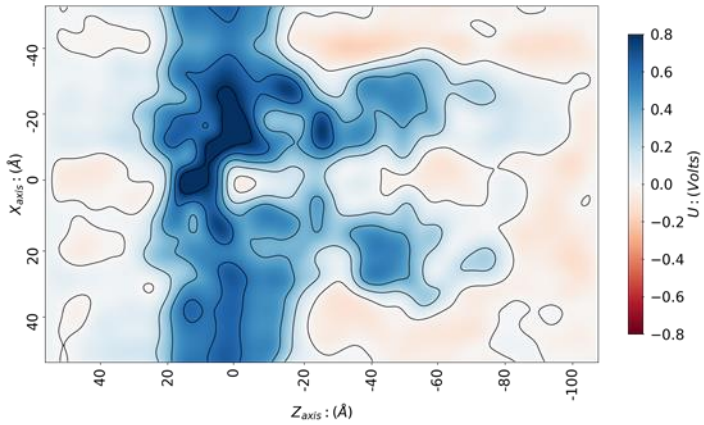

B

420 to 440 ns; V_m= -0,07 (Volts)

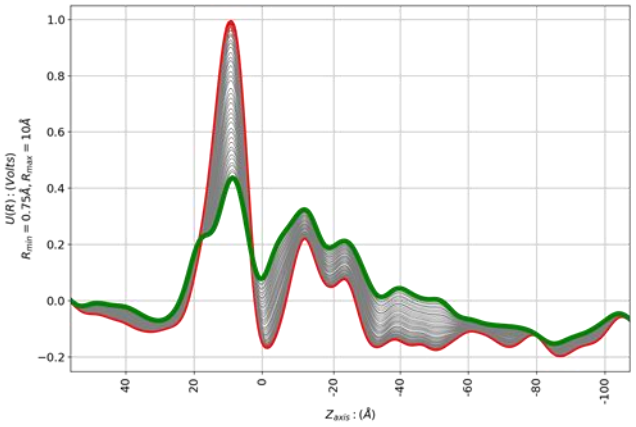

420 to 440 ns; V_m= -0,07 (Volts)

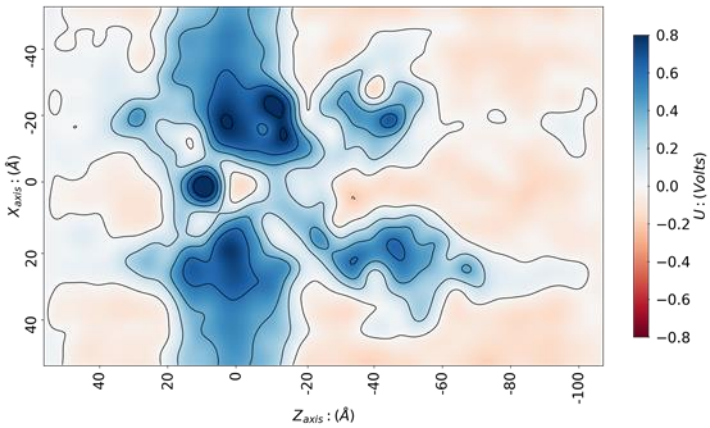

C

620 to 640 ns; V_m= -0,7 (Volts)

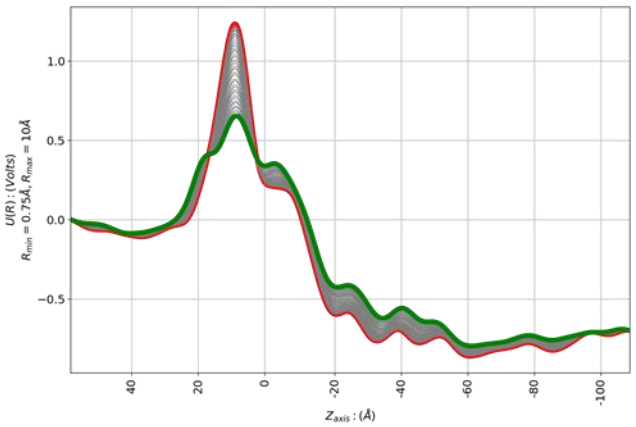

620 to 640 ns; V_m= -0,7 (Volts)

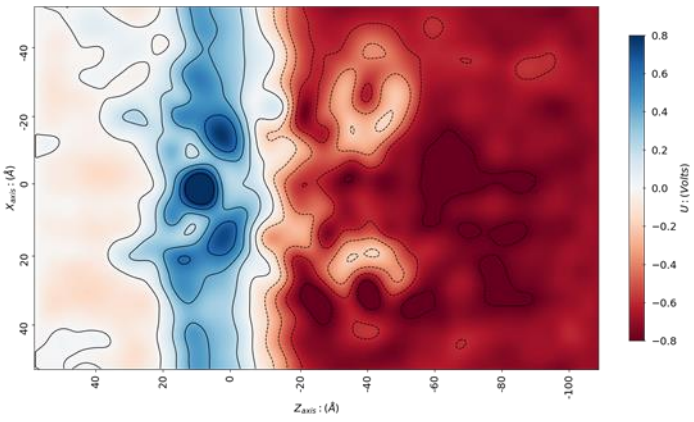

D

820 to 840 ns; V_m= -0,7 (Volts)

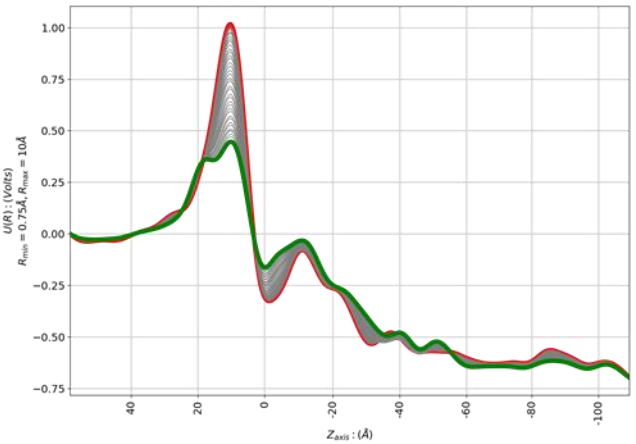

820 to 840 ns; V_m= -0,7 (Volts)

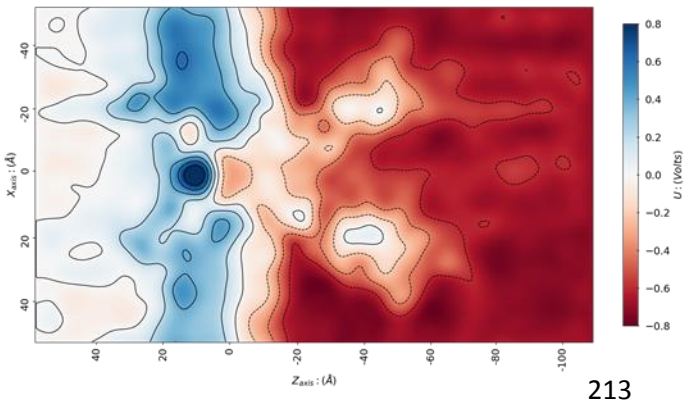

8.6 SIMULATION IV

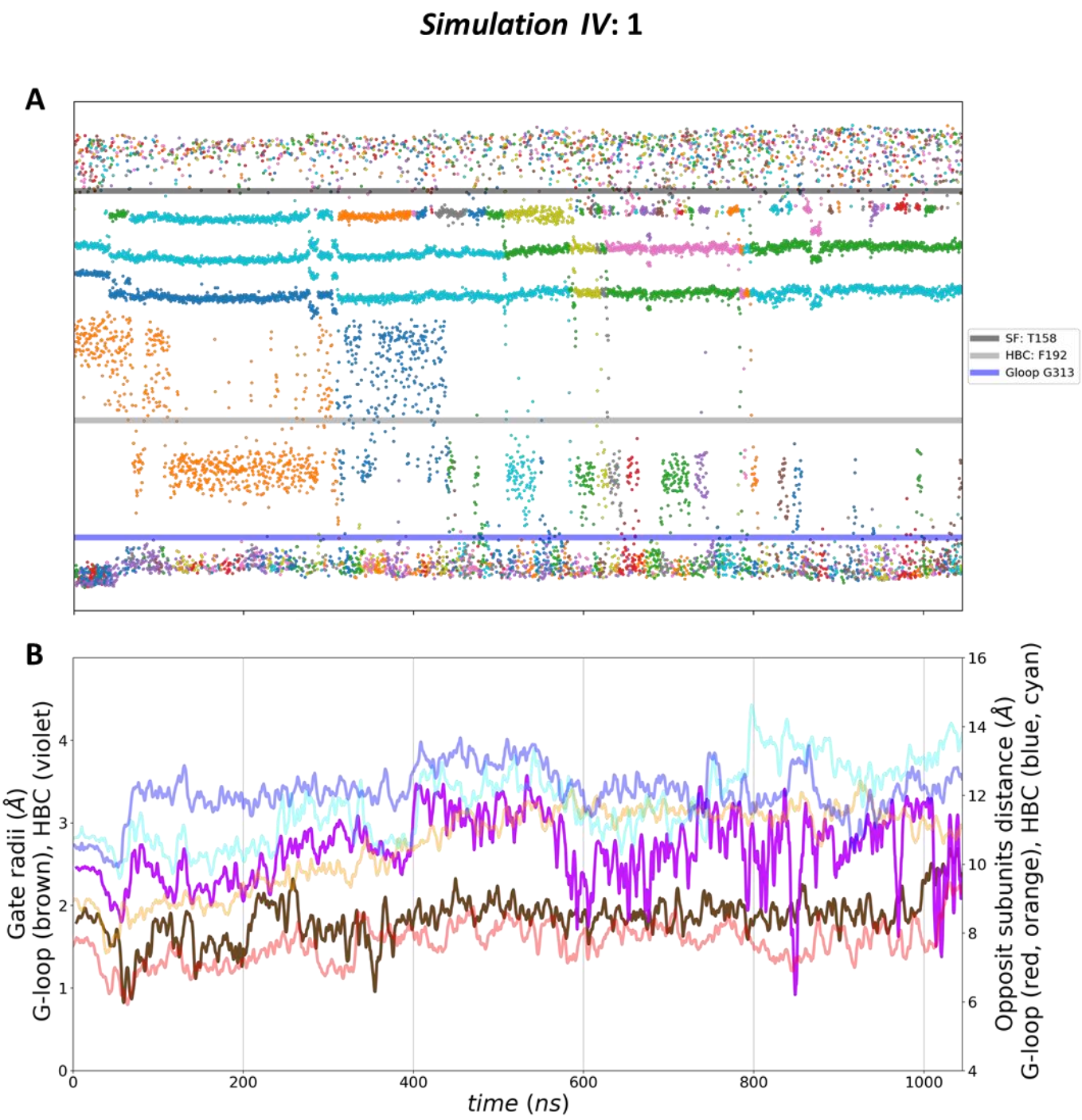

Simulation IV: 2

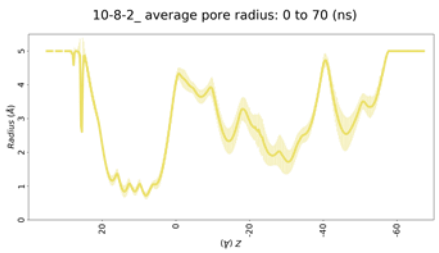

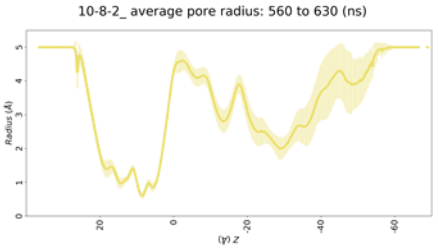

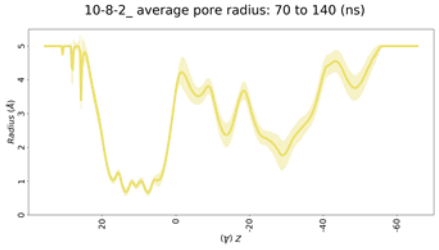

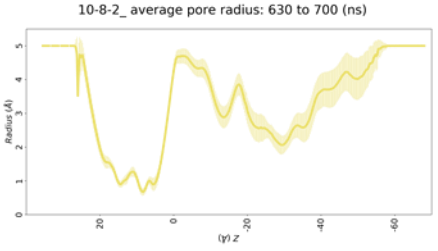

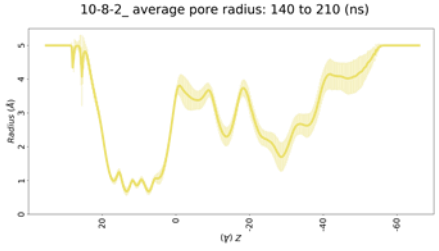

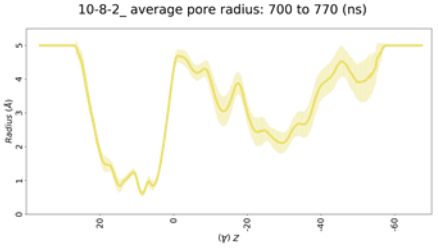

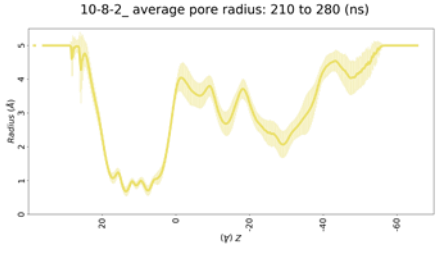

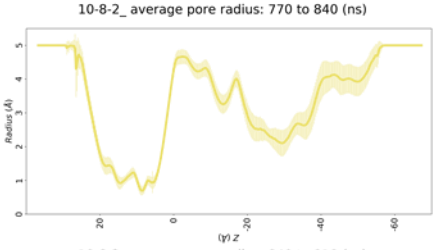

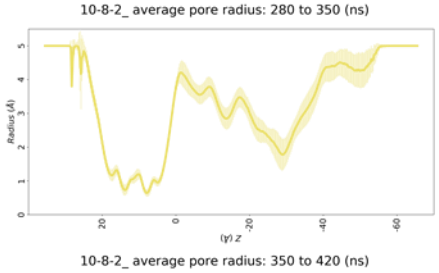

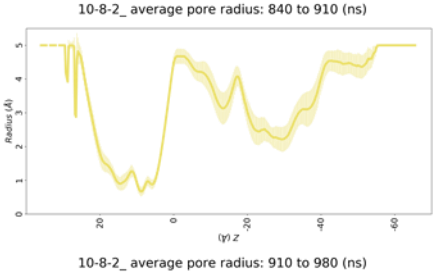

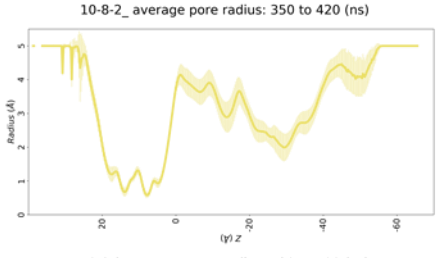

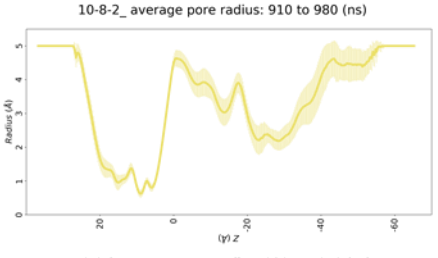

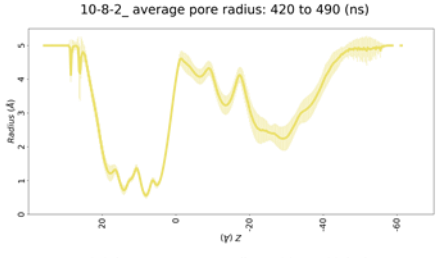

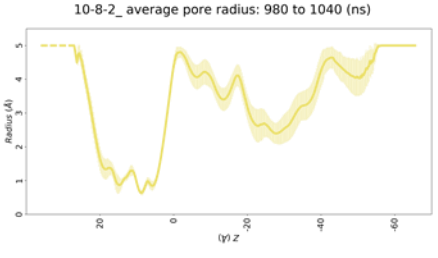

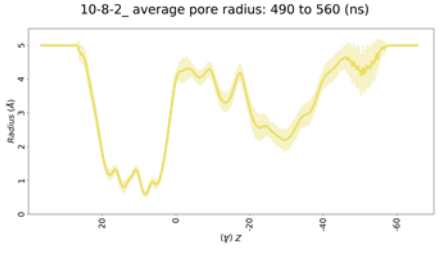

Simulation IV: 3

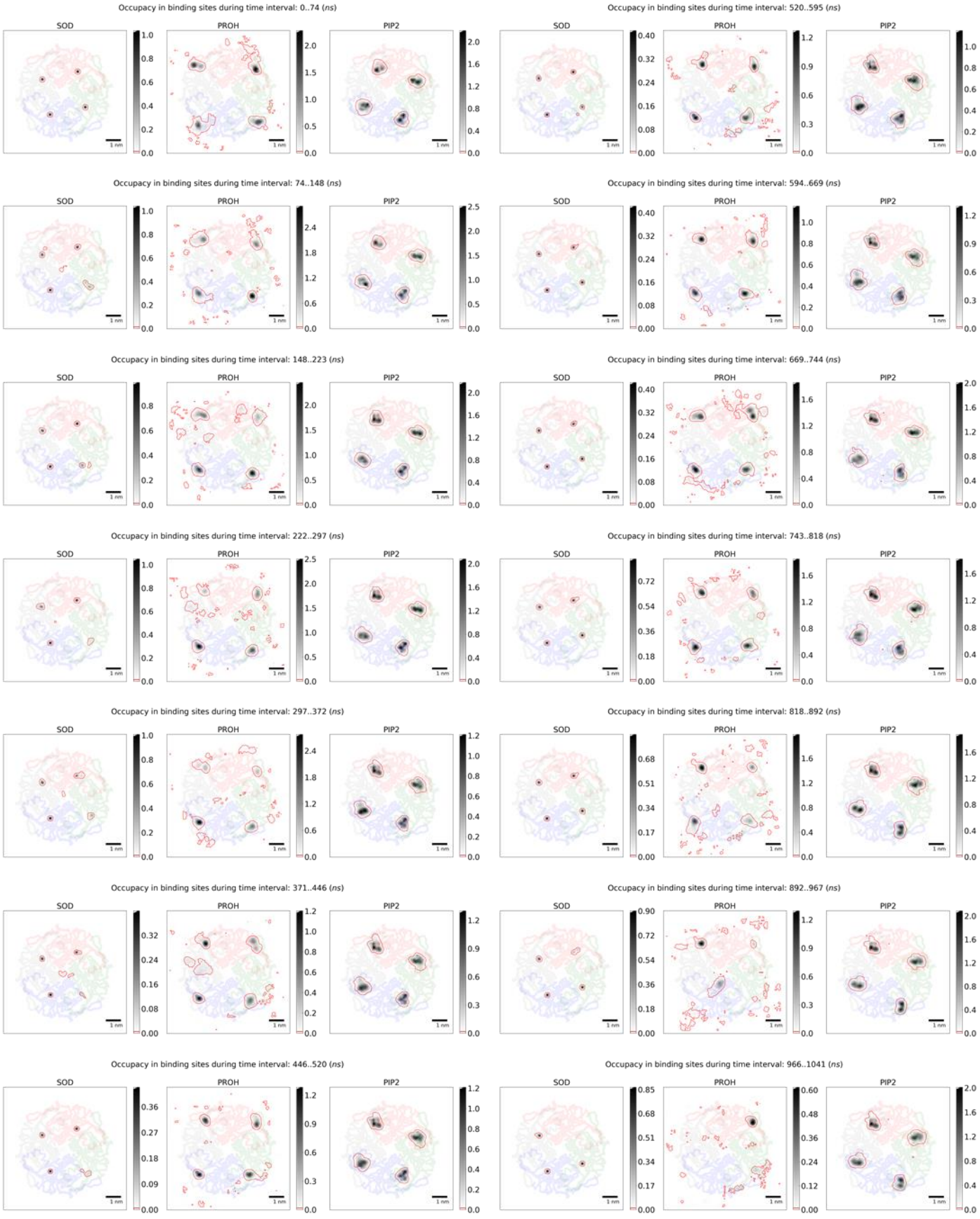

Simulation IV: 4

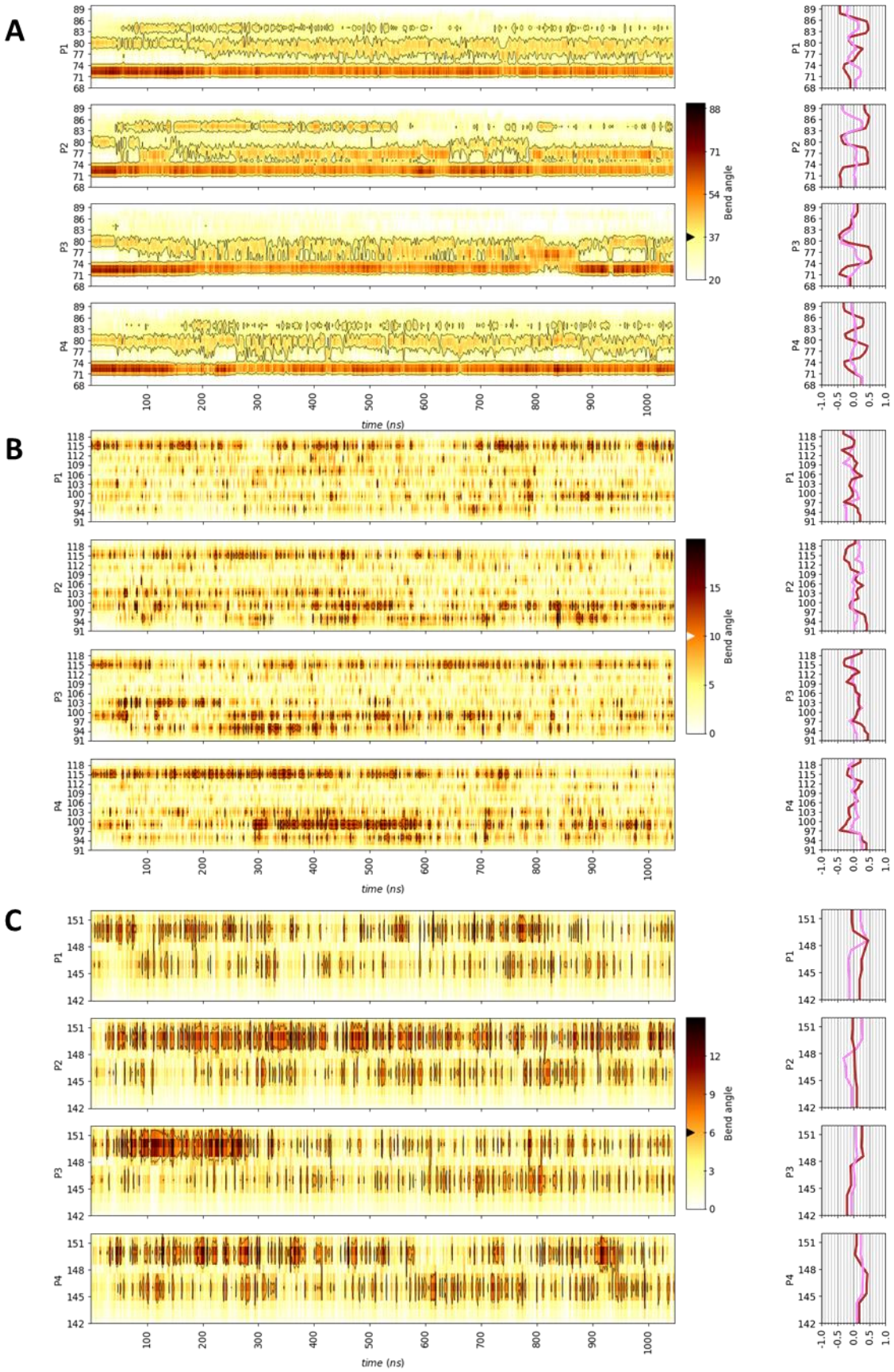

Simulation IV: 4

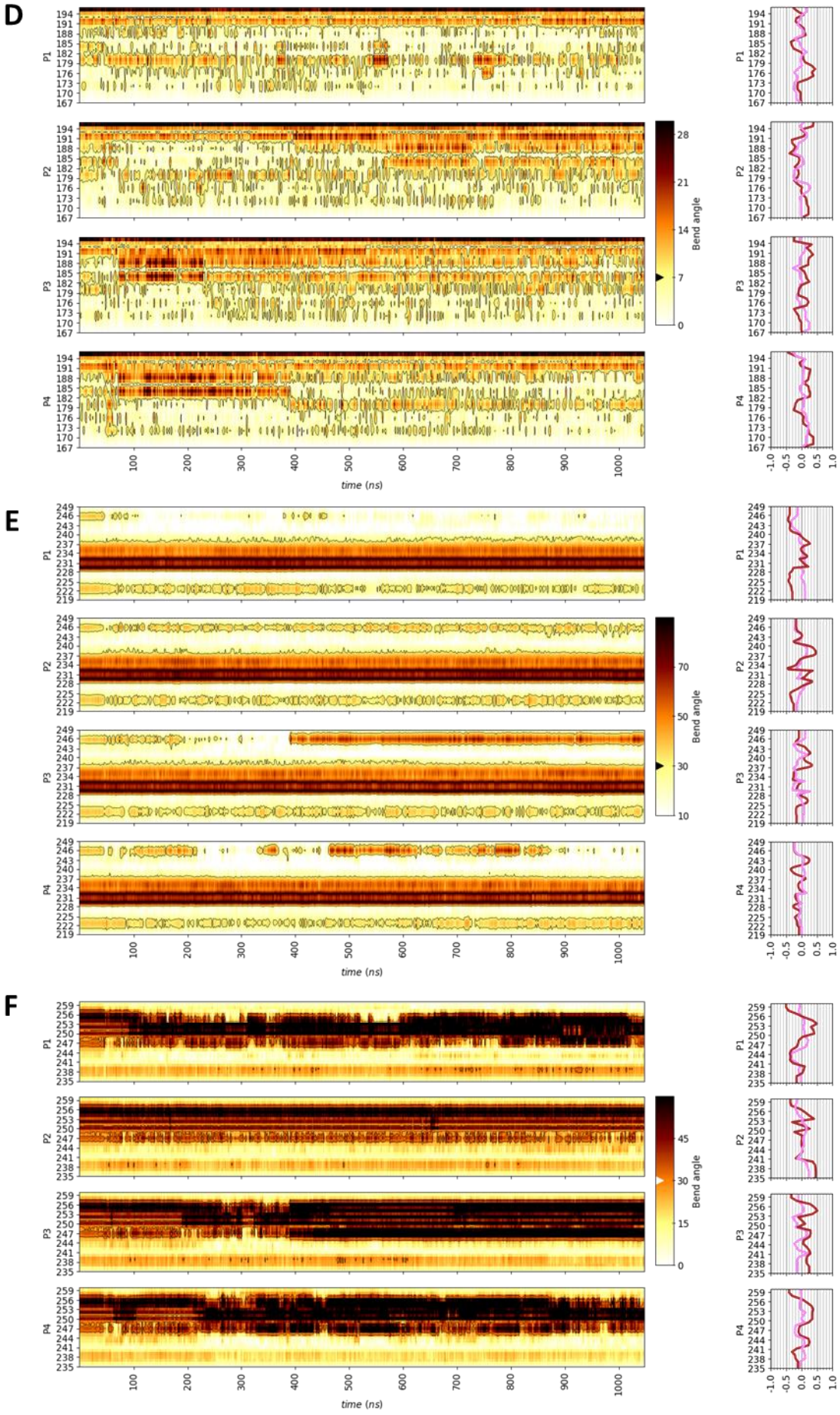

Simulation IV: 4

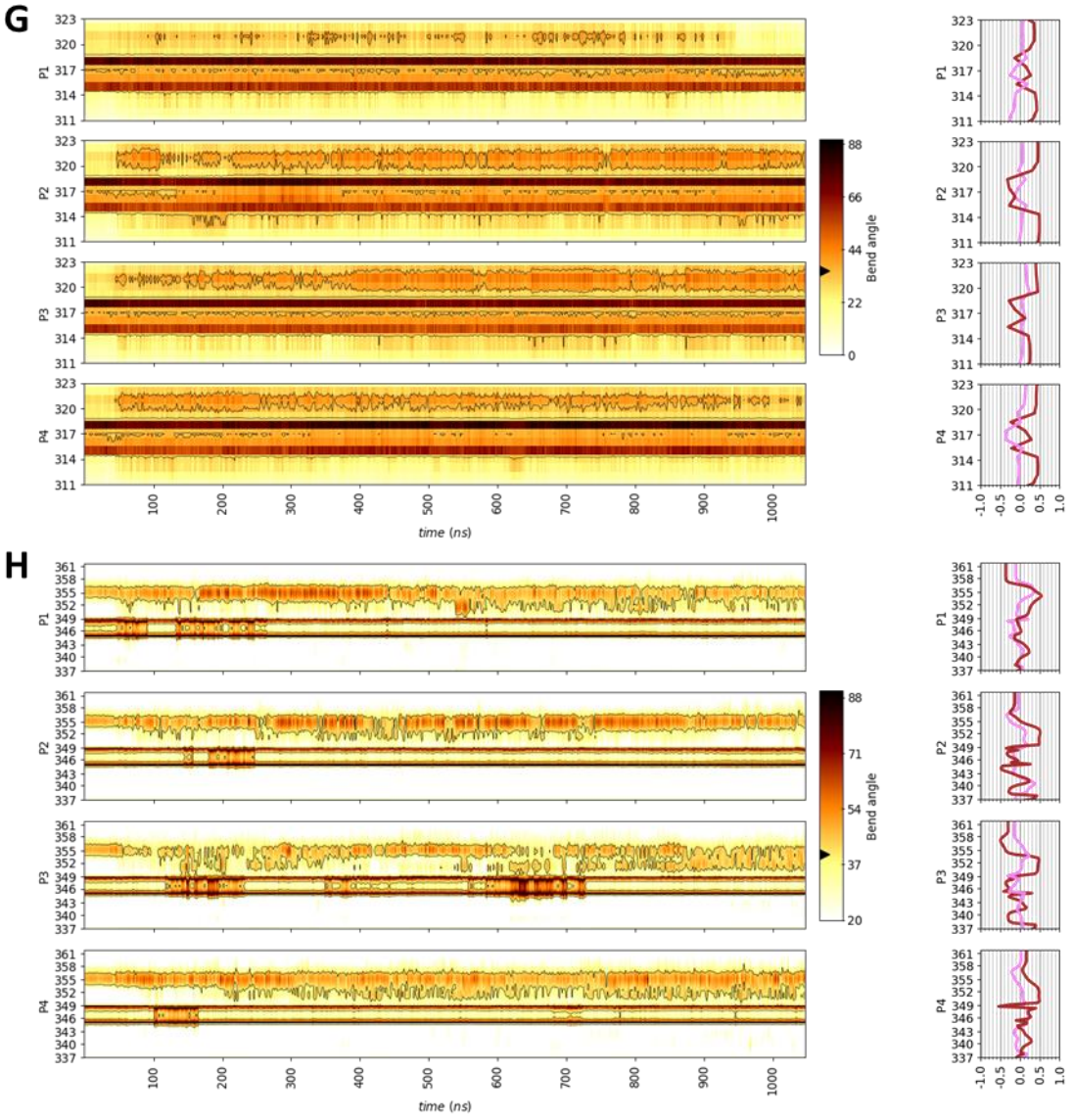

Simulation IV: 5

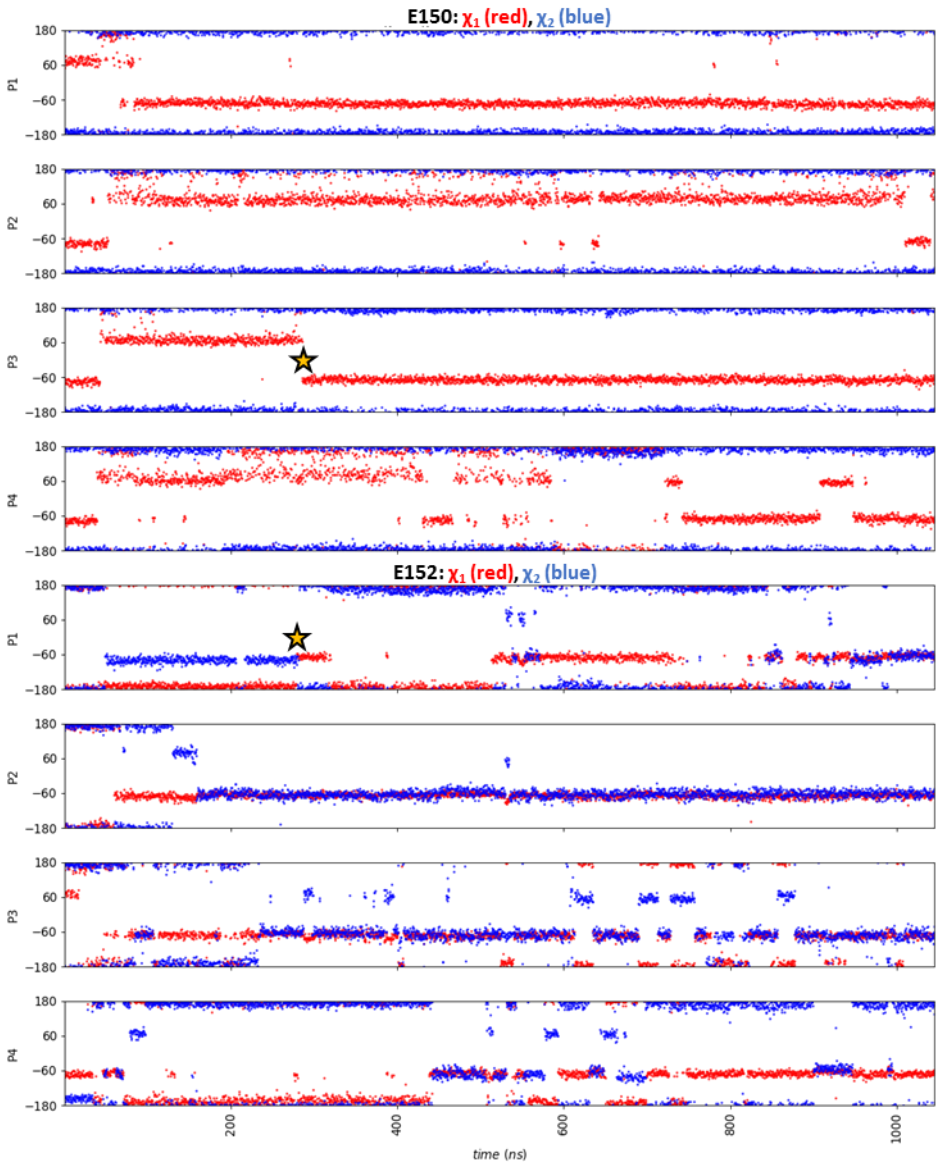

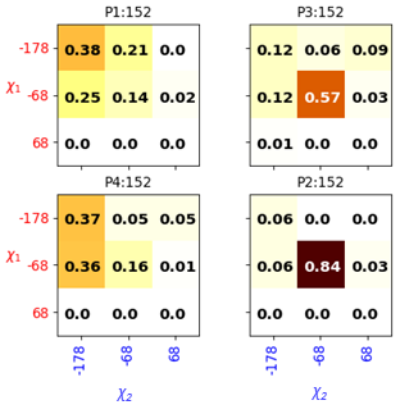

Simulation IV: 6

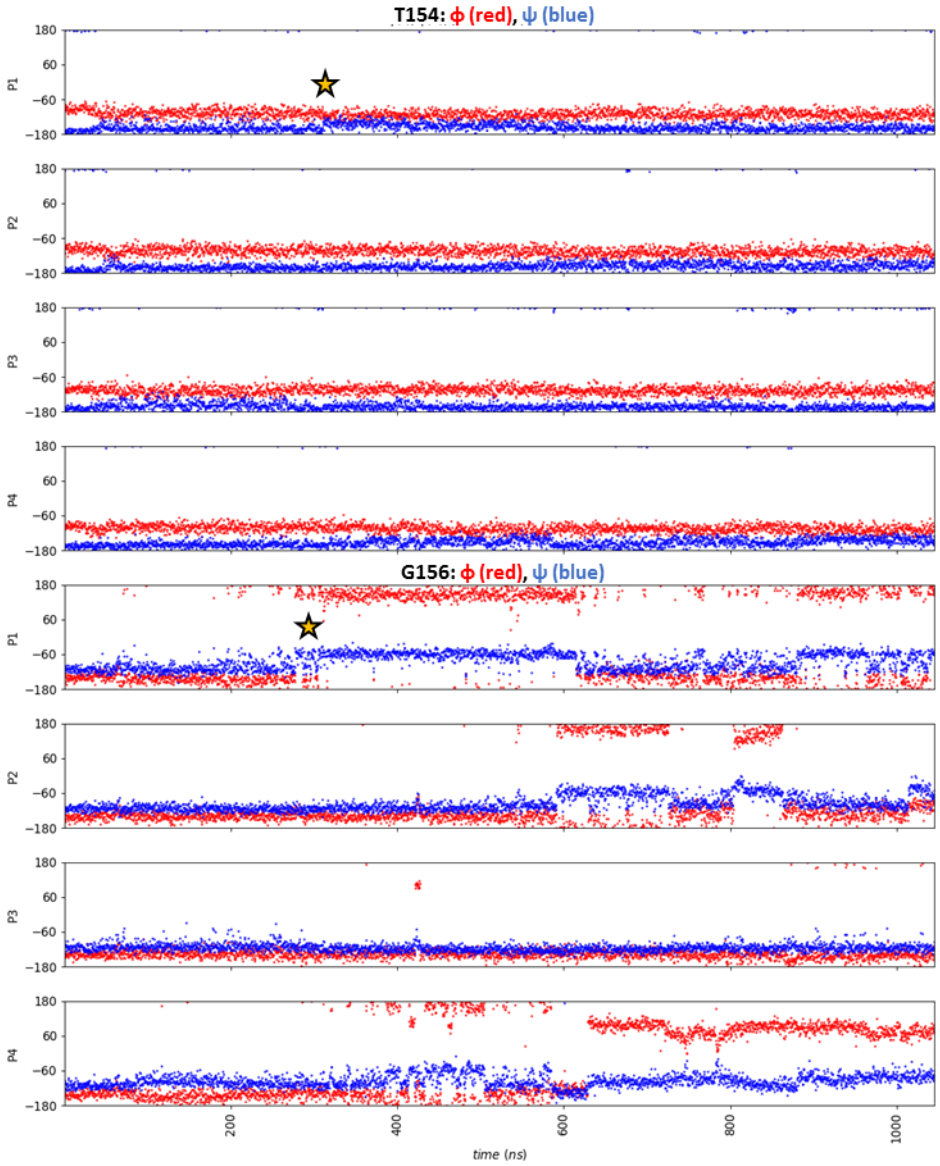

Simulation IV: 6

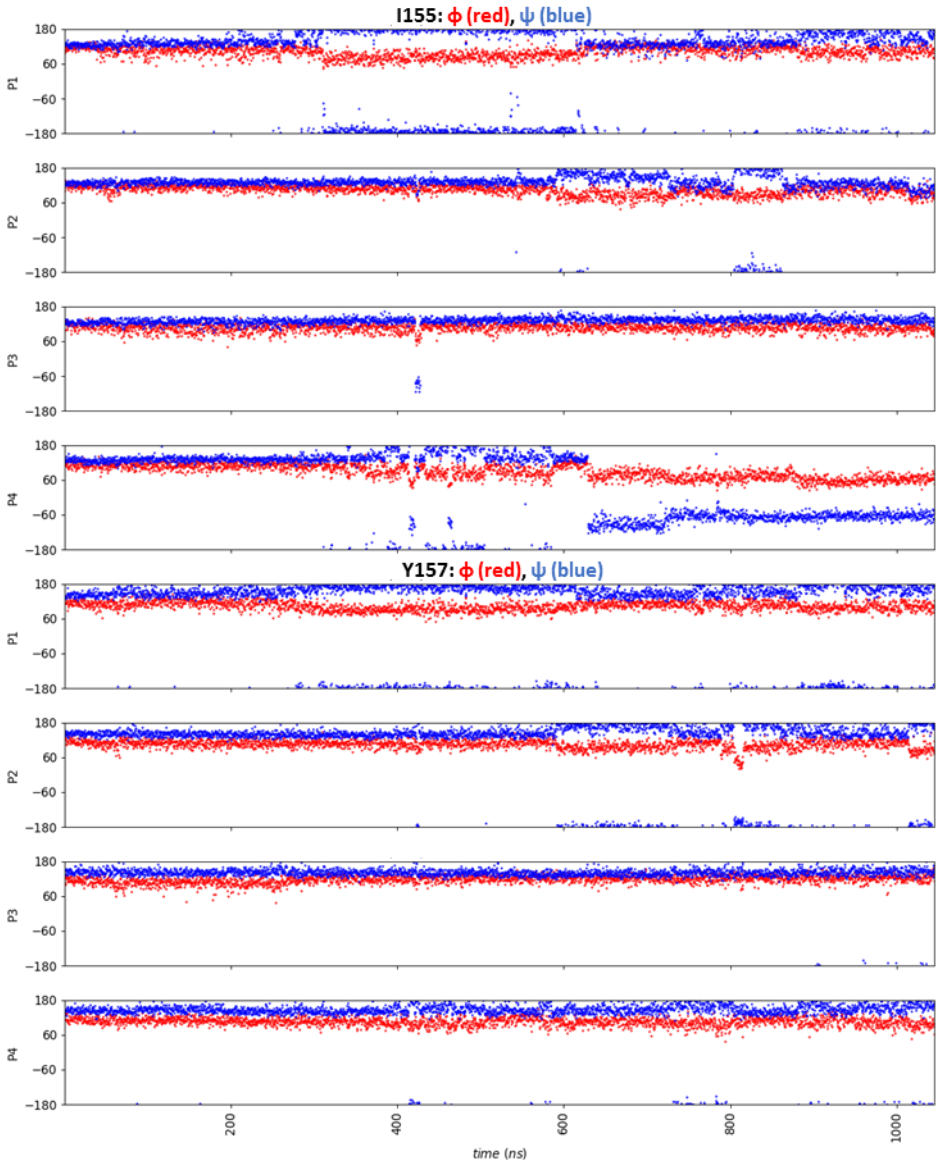

Simulation IV: 6

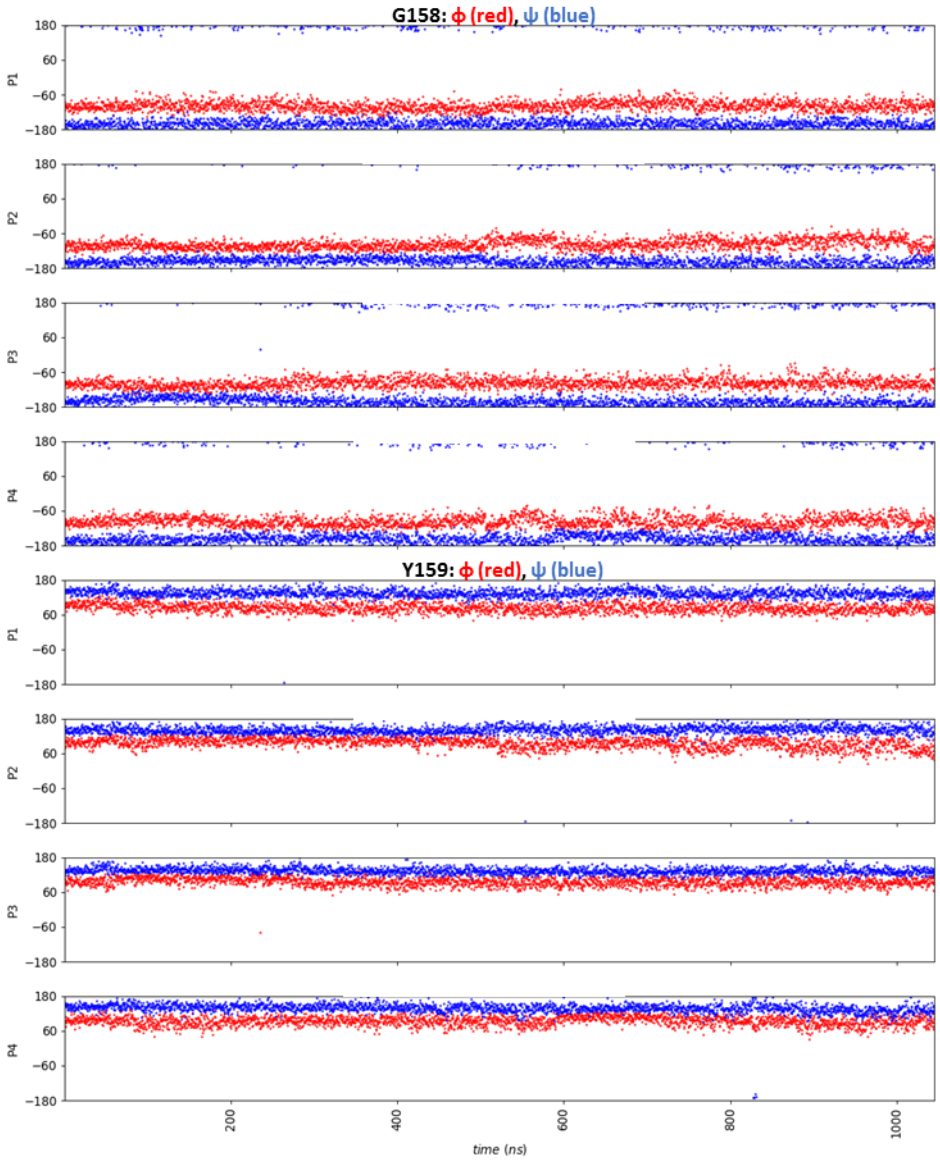

Simulation IV: 7

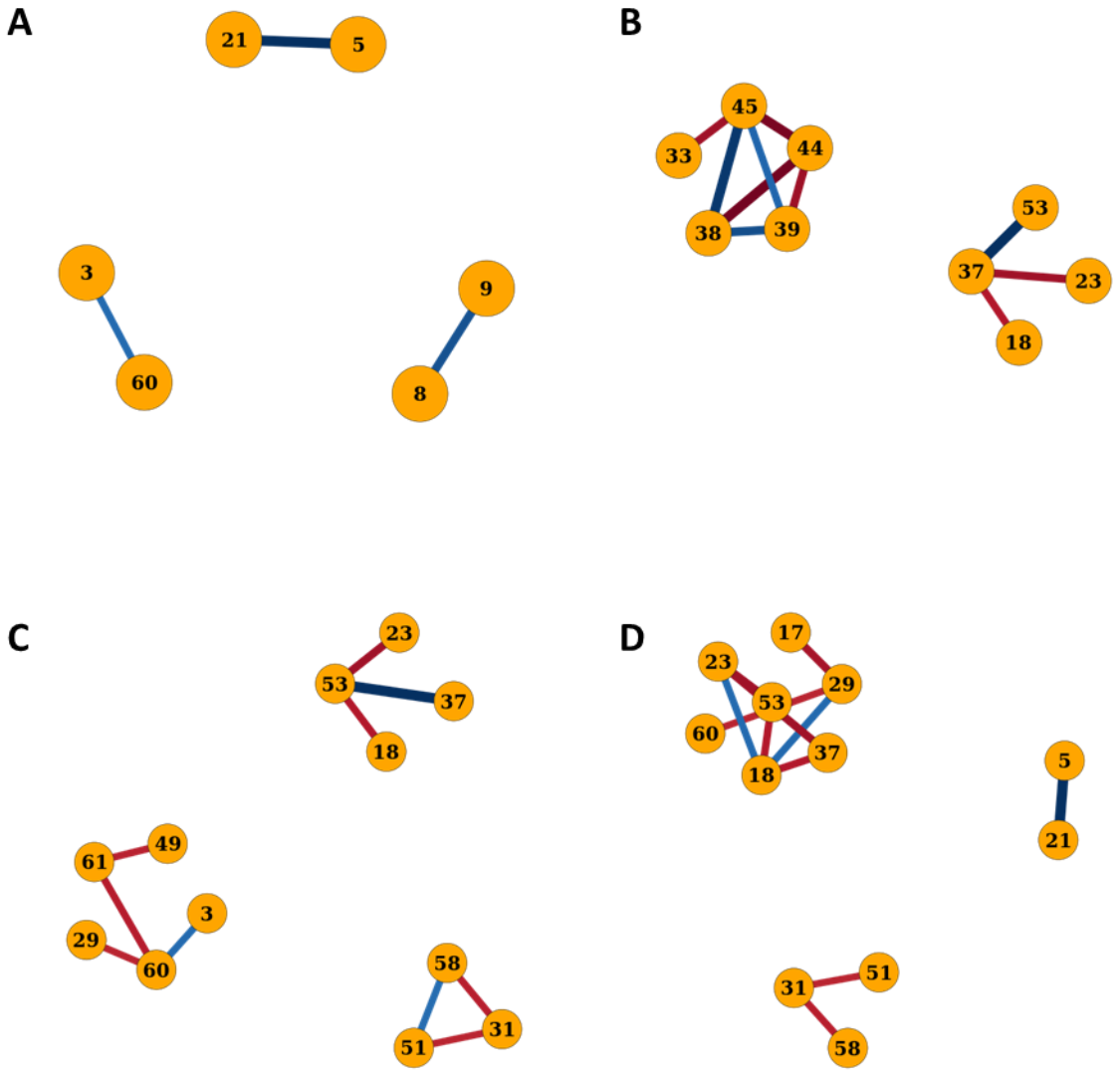

Diagrams of the instantaneous correlations between couples of interatomic distances collected in the region of the selectivity filter in Simulation II. Data collection was made on the basis of frames where the rotamer state of E152 in subunit P2 was χ1:-60°/ χ2:-60°, interatomic distances have been collected and convoluted as described in Figure 12 in the main text. The matrix with the instantaneous correlation filtrated by r > 0.75 was used to produce diagrams for each subunit. Graphs have been manually optimized for reading of the edges. (A) Subunit P1. (B) Subunit P3. (C) Subunit P4. (D) Subunit P2. (D) This diagram is the result of the summation of all equivalent correlation factors for pairwise distance among the four channel subunits, the threshold value for an edge to be displayed was set to r > 0.375 – corresponding to a correlation of r > 0.72 in at least three subunits.

Simulation IV: 8

A

	P1	P3	P2	P4
P1	S	N	O	P
P3	P	S	N	O
P2	O	P	S	N
P4	N	O	P	S

P1	P3	P2	P4	
0	14	7	21	P1:105:CA | P2:105:CA
1	15	8	22	P1:188:CA | P2:188:CA
2	16	9	23	P1:105:OG1 | P1:152:CD
3	17	10	24	P1:155:CA | P3:151:CA
4	18	11	25	P1:155:CA | P3:173:CA
5	19	12	26	P1:155:CD | P3:173:CG
6	20	13	27	P1:155:CA | P2:155:CA

B

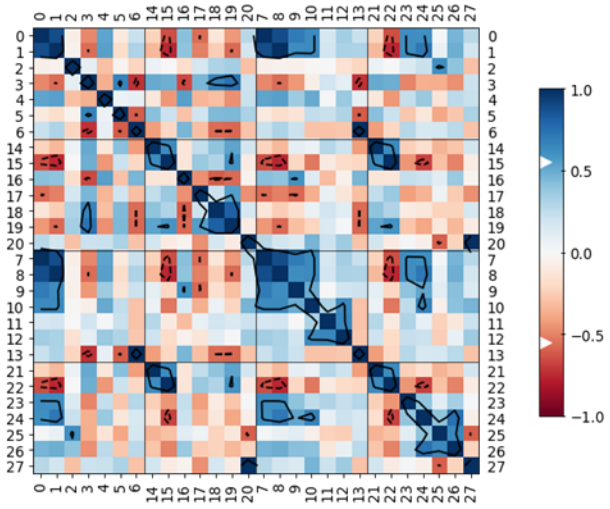

C

Network threshold $r \geq 0.45$

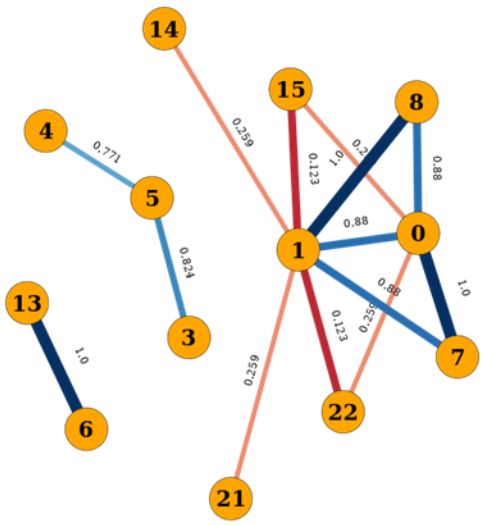

D

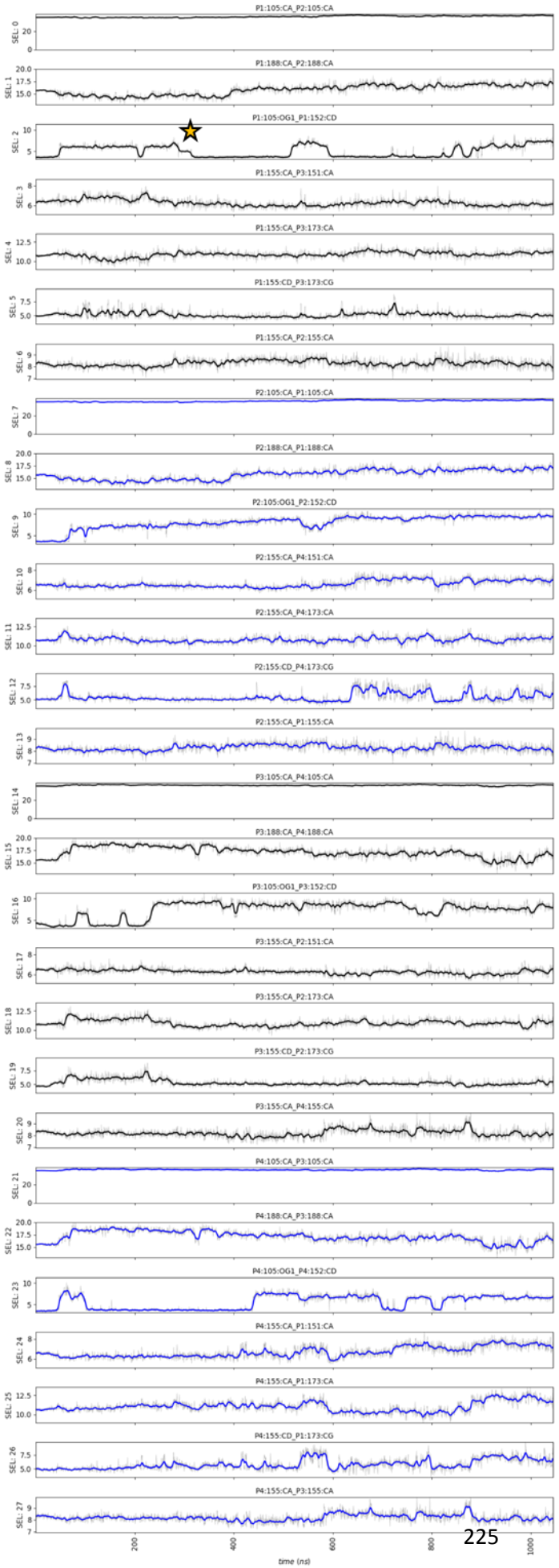

Simulation IV: 9

Norm: #3

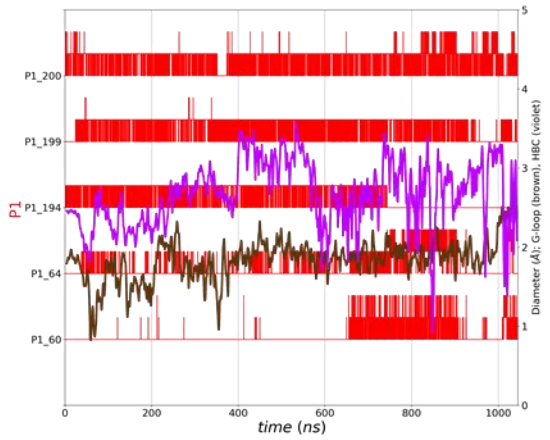

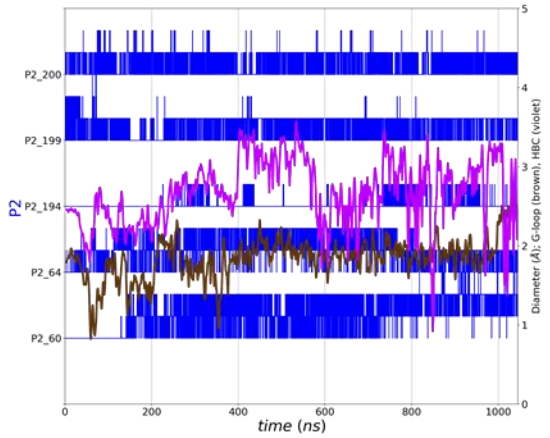

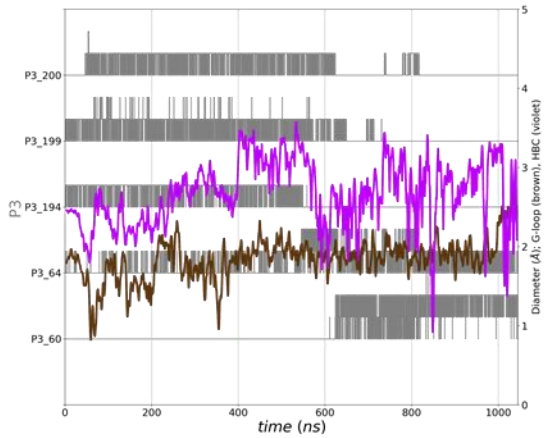

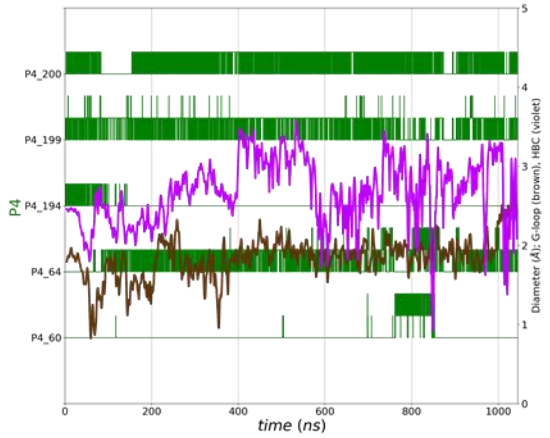

Norm: #4

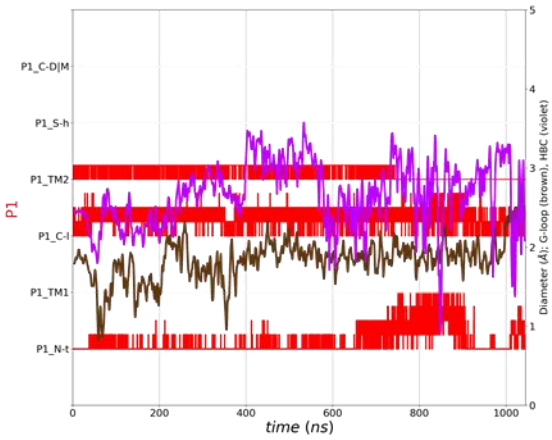

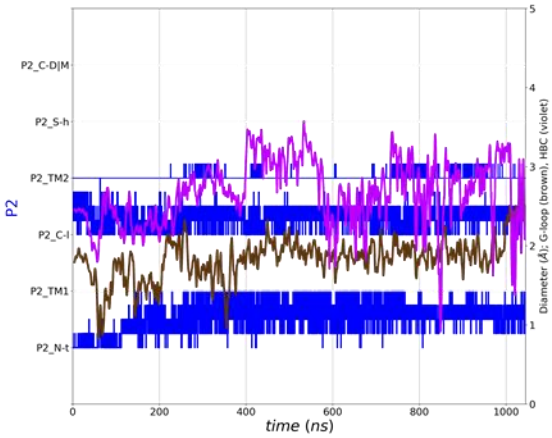

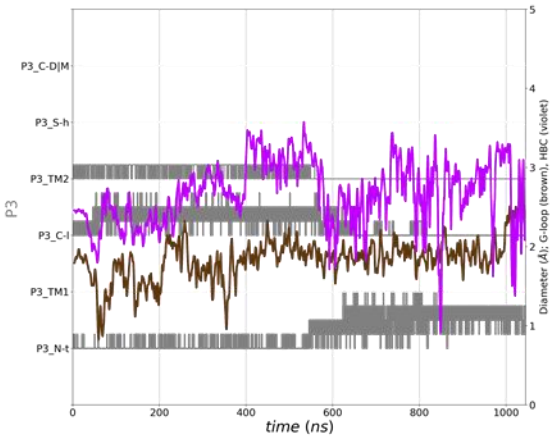

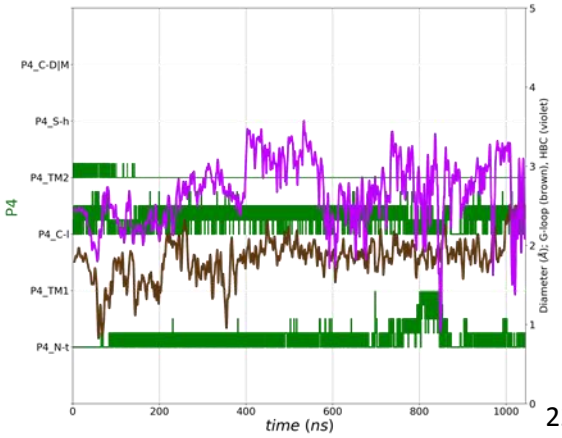

Simulation IV: 10

Norm: #3

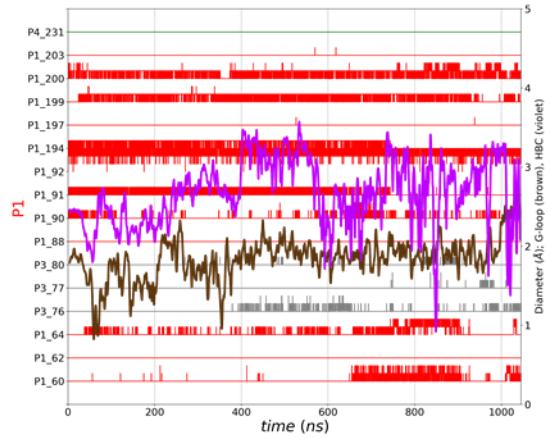

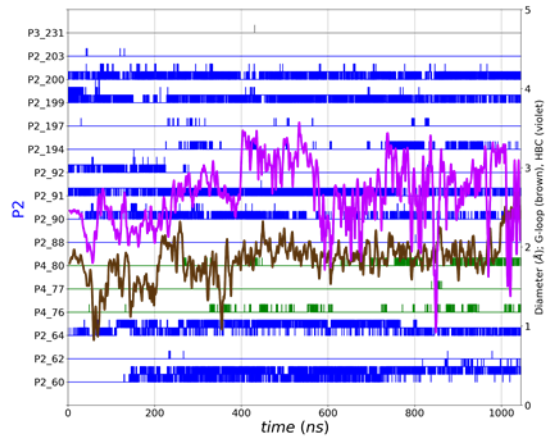

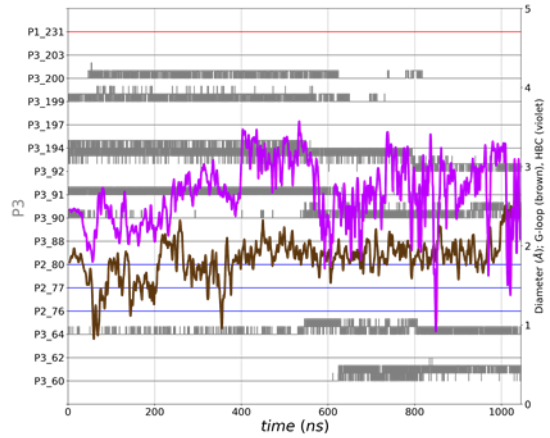

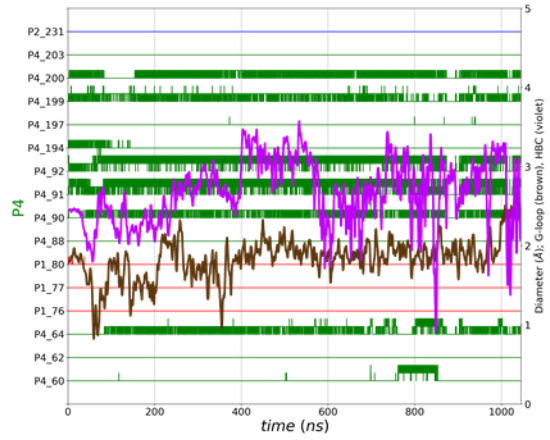

Norm: #6

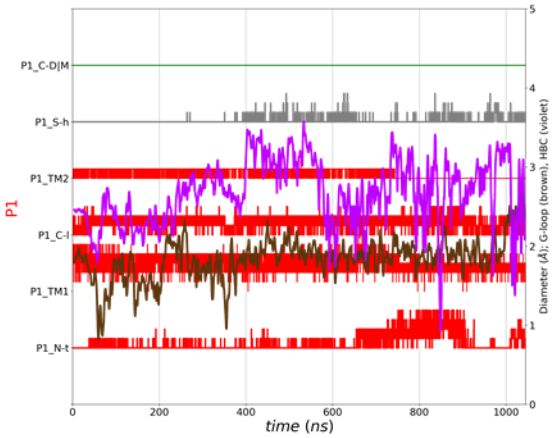

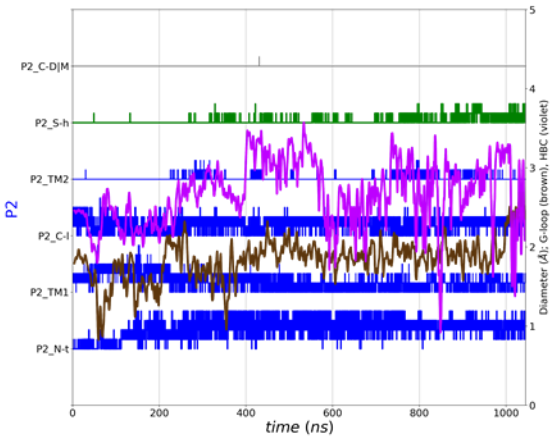

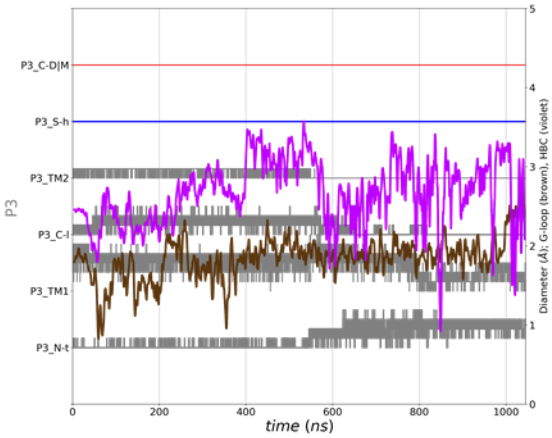

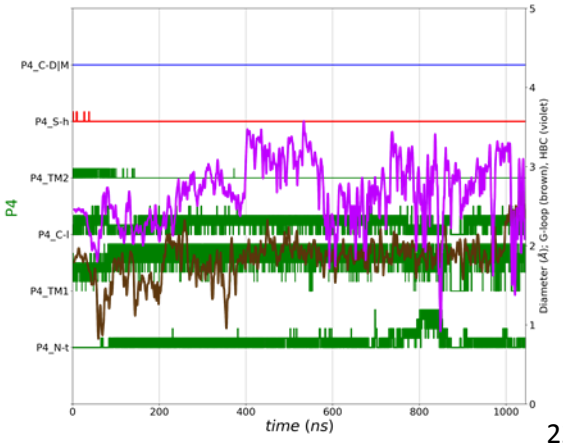

Simulation IV: 11

Average electrostatic potential along the pore | **Electrostatic potential in the simulation box *(Y_{axis}= 0)***

A

50 to 70 ns; V_m= -0,07 (Volts)

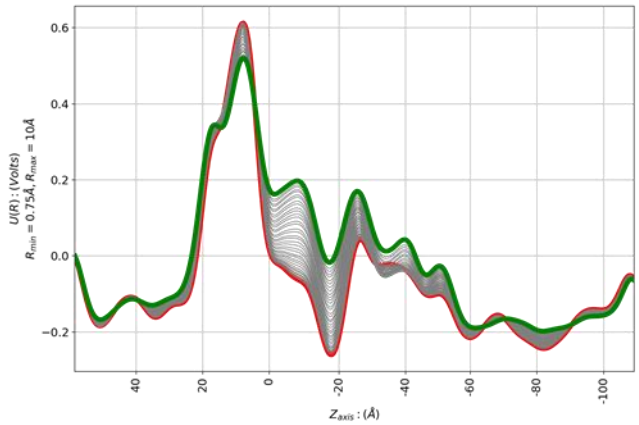

50 to 70 ns; V_m= -0,07 (Volts)

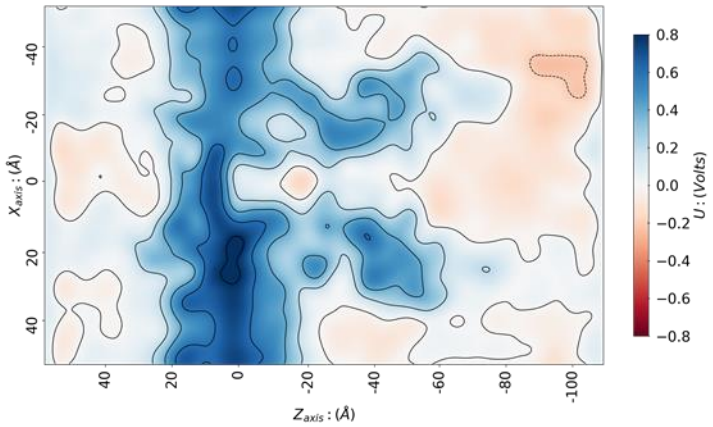

B

420 to 440 ns; V_m= -0,07 (Volts)

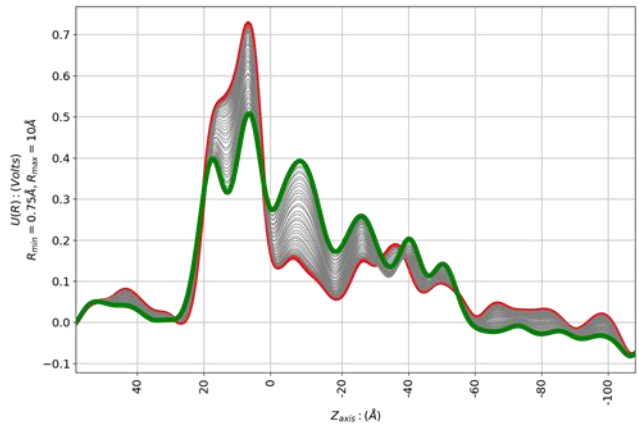

420 to 440 ns; V_m= -0,07 (Volts)

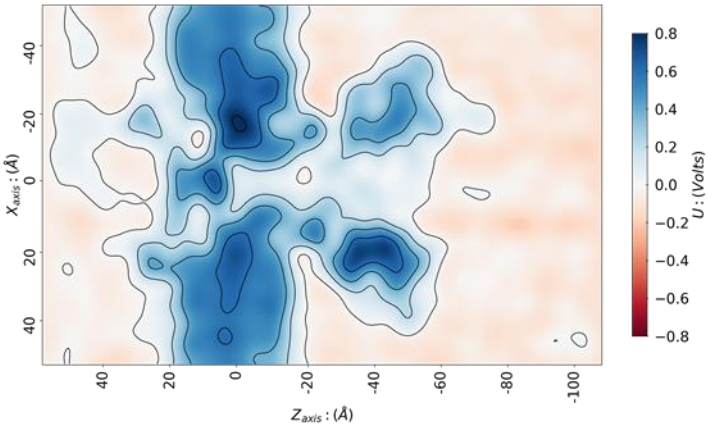

C

620 to 640 ns; V_m= -0,7 (Volts)

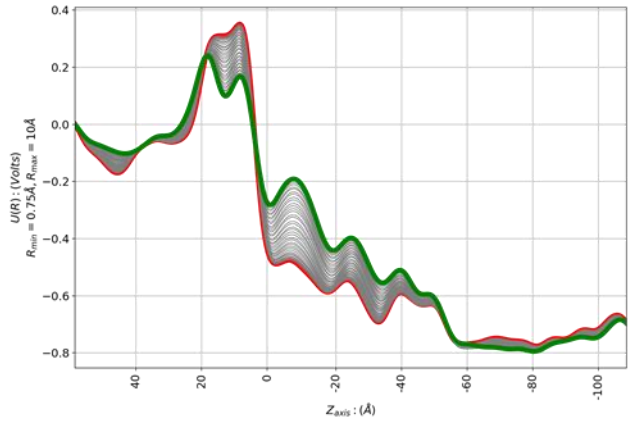

620 to 640 ns; V_m= -0,7 (Volts)

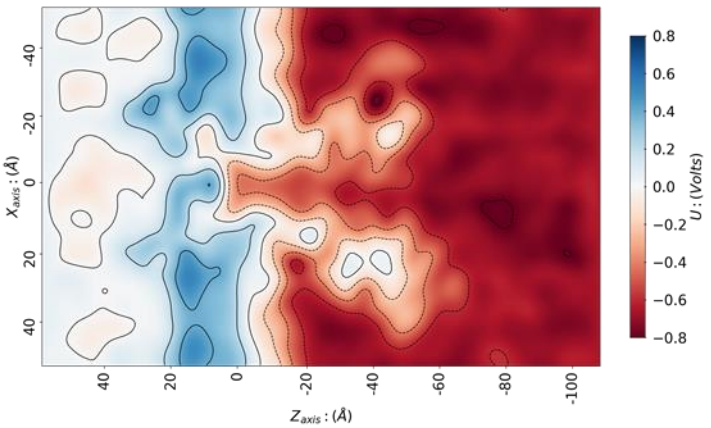

D

820 to 840 ns; V_m= -0,7 (Volts)

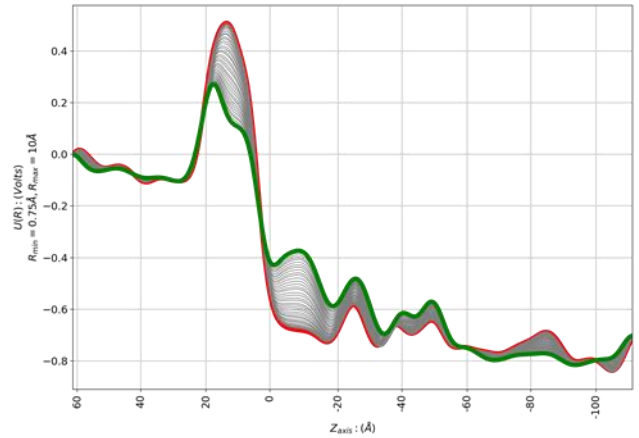

820 to 840 ns; V_m= -0,7 (Volts)

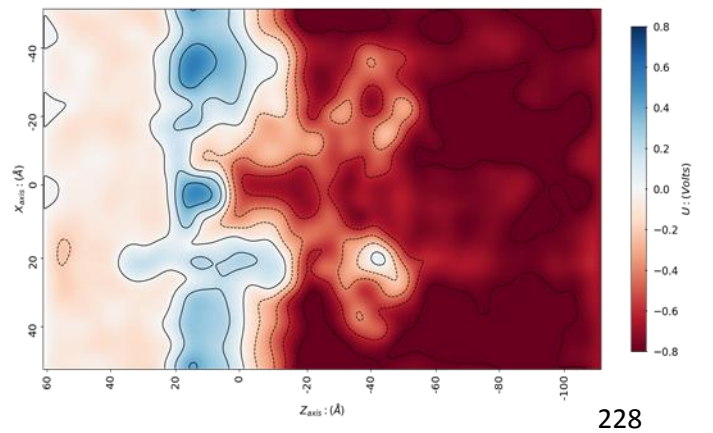

8.7 SIMULATION V

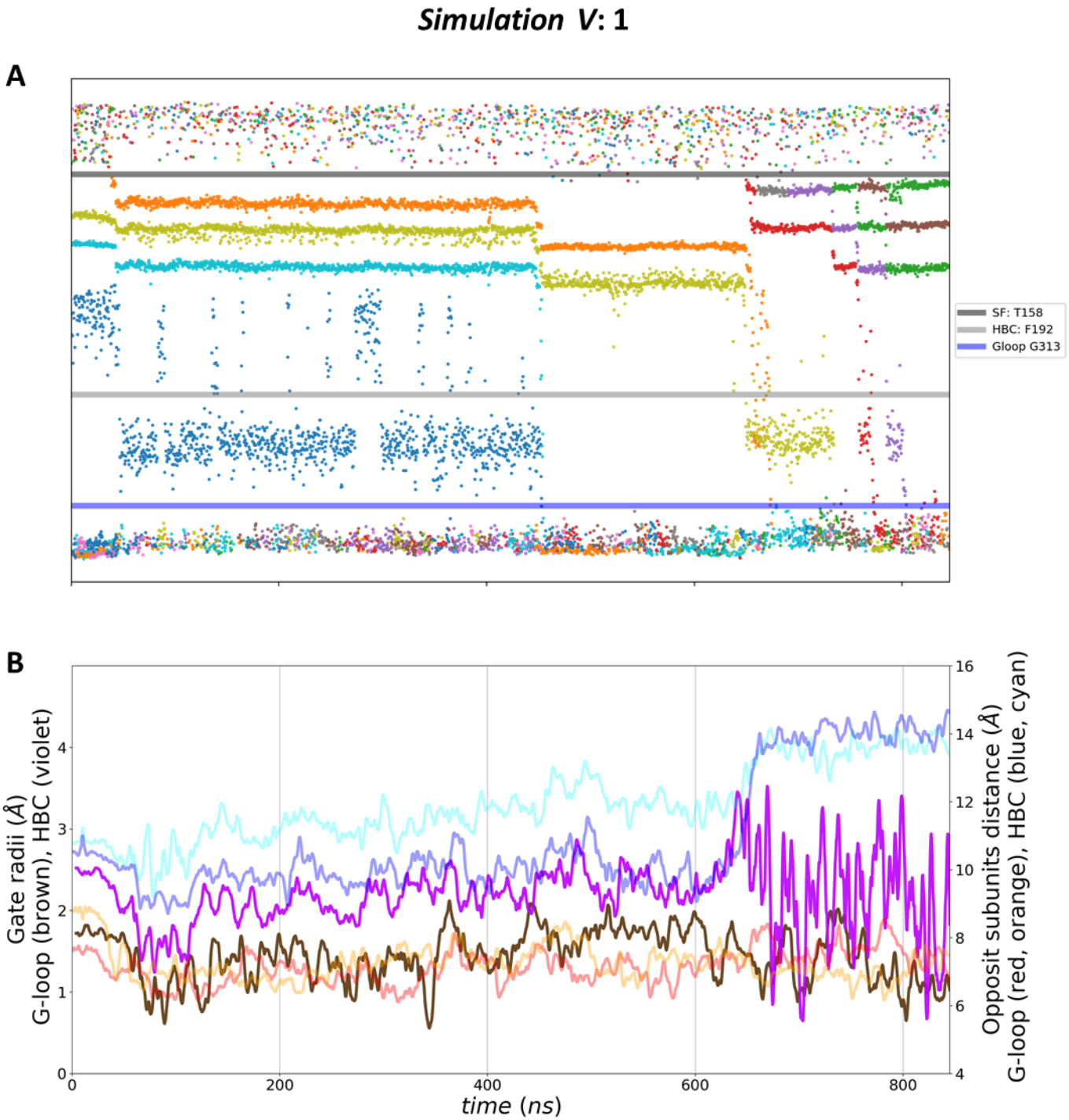

Simulation V: 2

10-9-1_ average pore radius: 0 to 70 (ns)

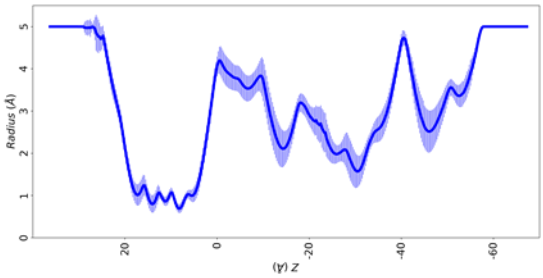

10-9-1_ average pore radius: 420 to 490 (ns)

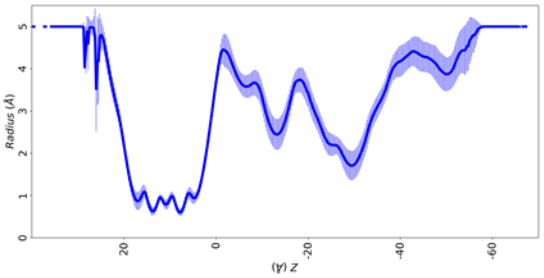

10-9-1_ average pore radius: 70 to 140 (ns)

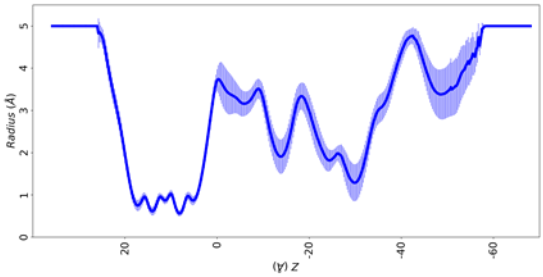

10-9-1_ average pore radius: 490 to 560 (ns)

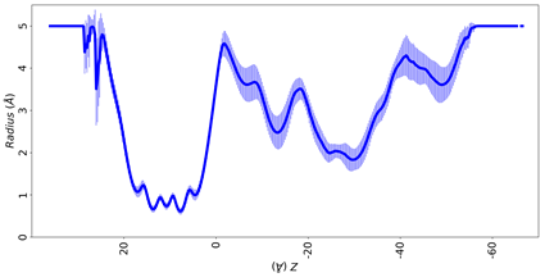

10-9-1_ average pore radius: 140 to 210 (ns)

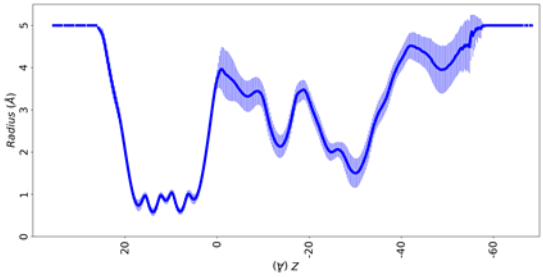

10-9-1_ average pore radius: 560 to 630 (ns)

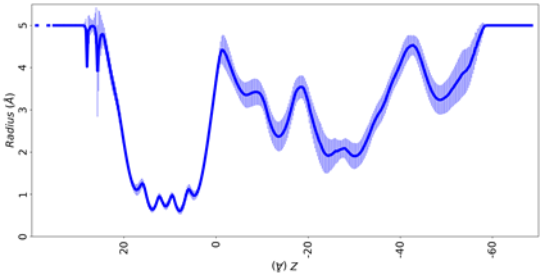

10-9-1_ average pore radius: 210 to 280 (ns)

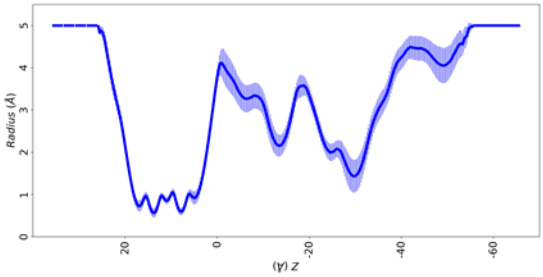

10-9-1_ average pore radius: 630 to 700 (ns)

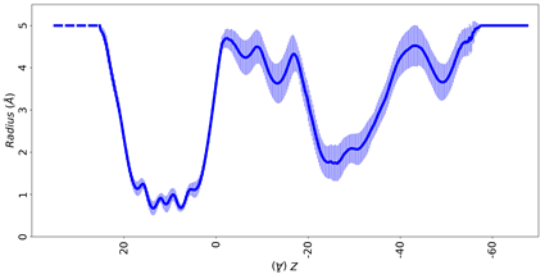

10-9-1_ average pore radius: 280 to 350 (ns)

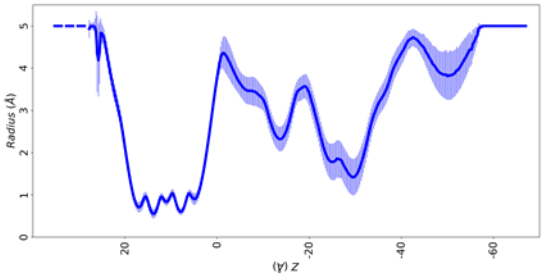

10-9-1_ average pore radius: 700 to 770 (ns)

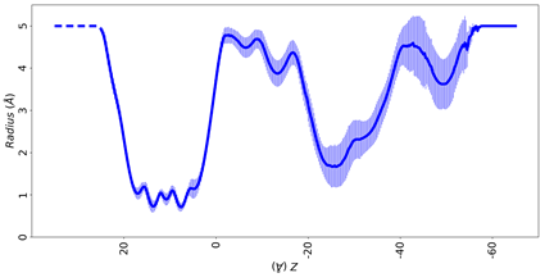

10-9-1_ average pore radius: 350 to 420 (ns)

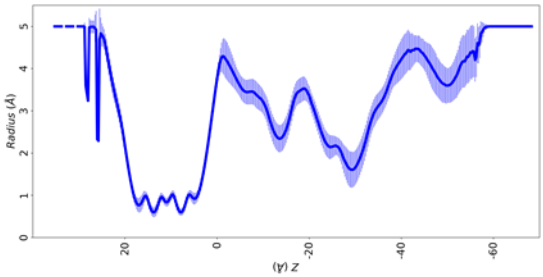

10-9-1_ average pore radius: 770 to 840 (ns)

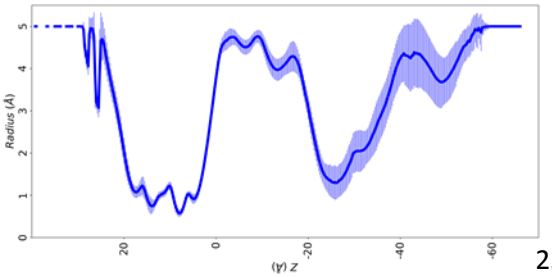

Simulation V: 3

Bad averaging: signal is 70*0.4 times underestimated

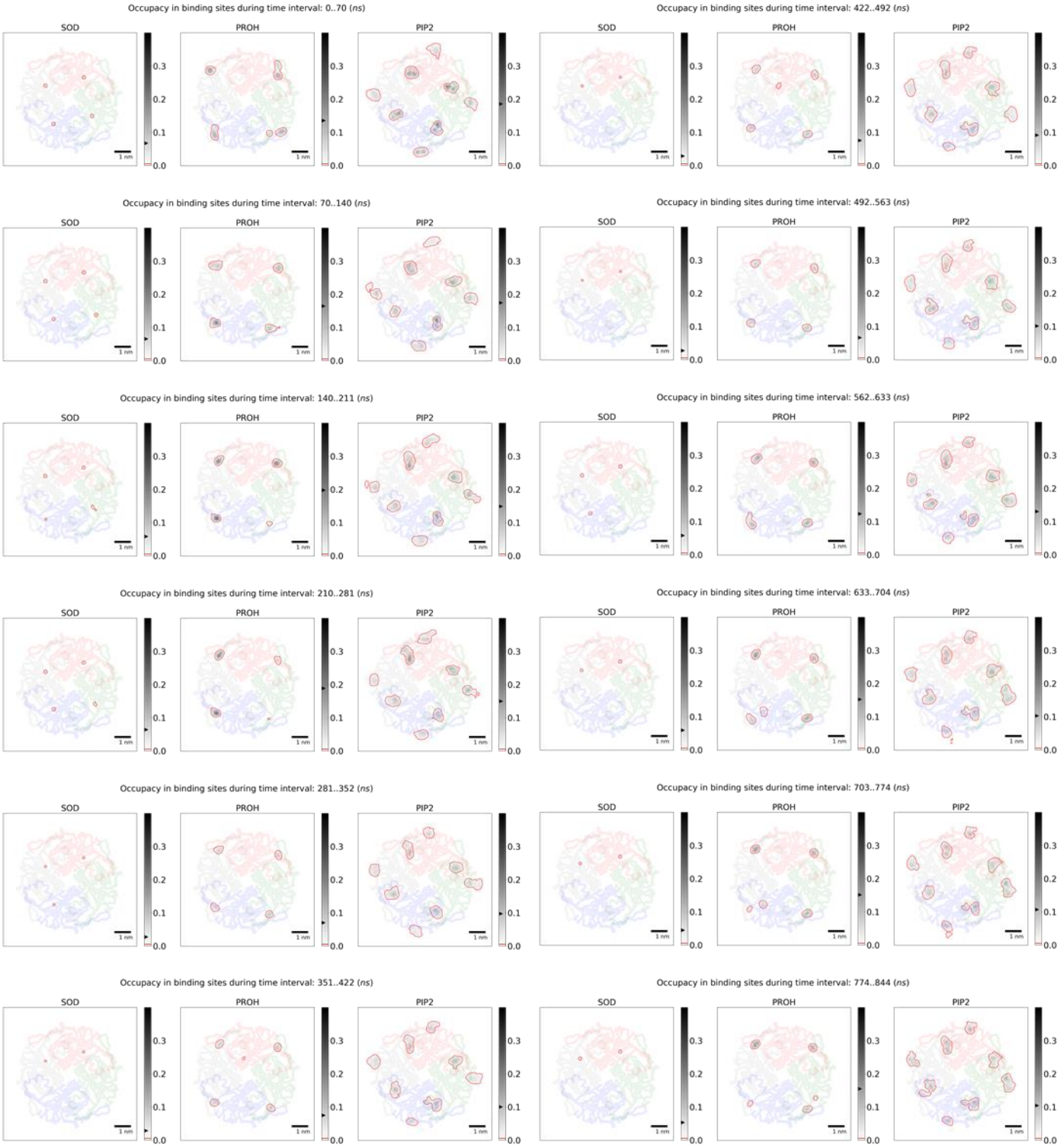

Simulation V: 4

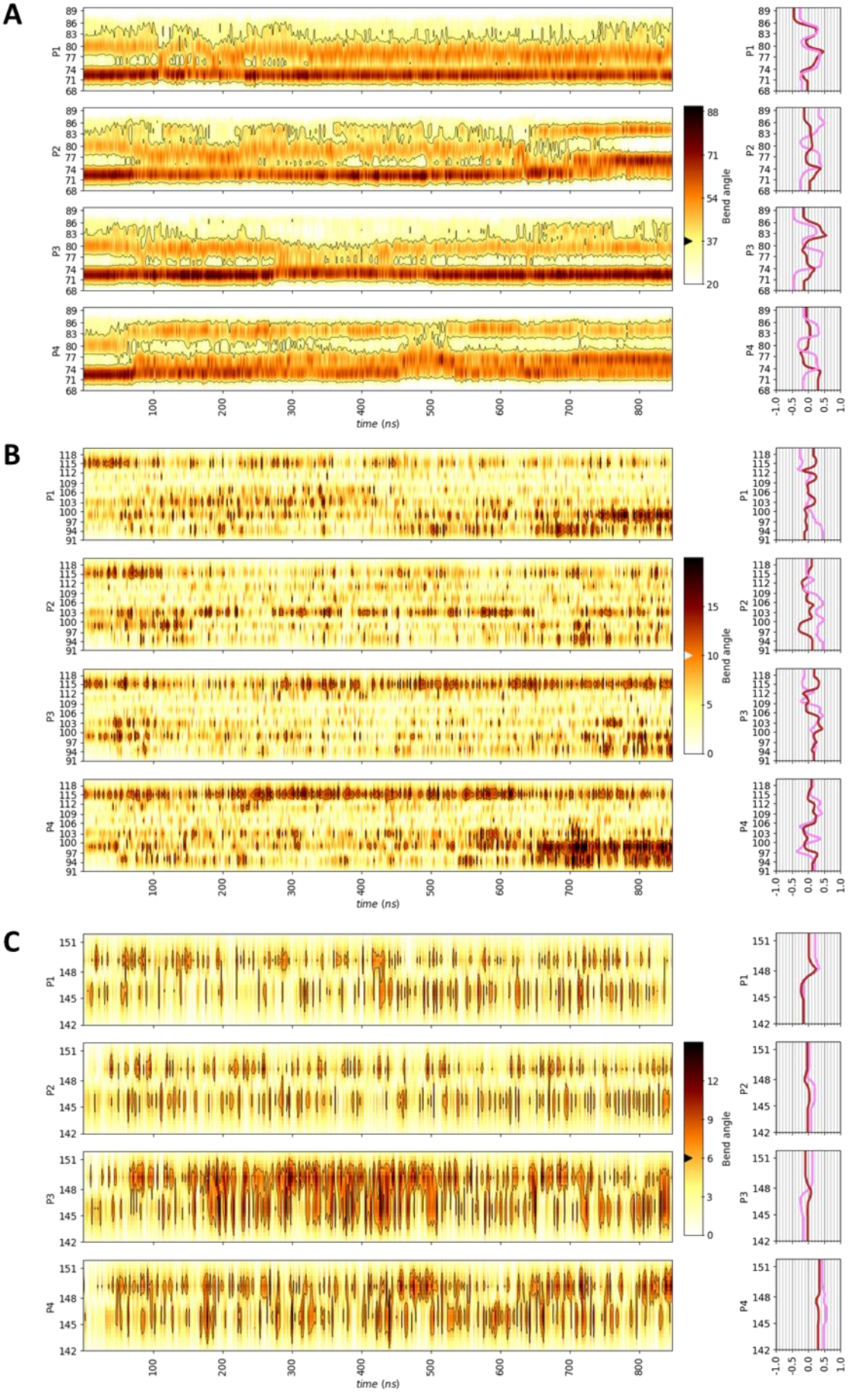

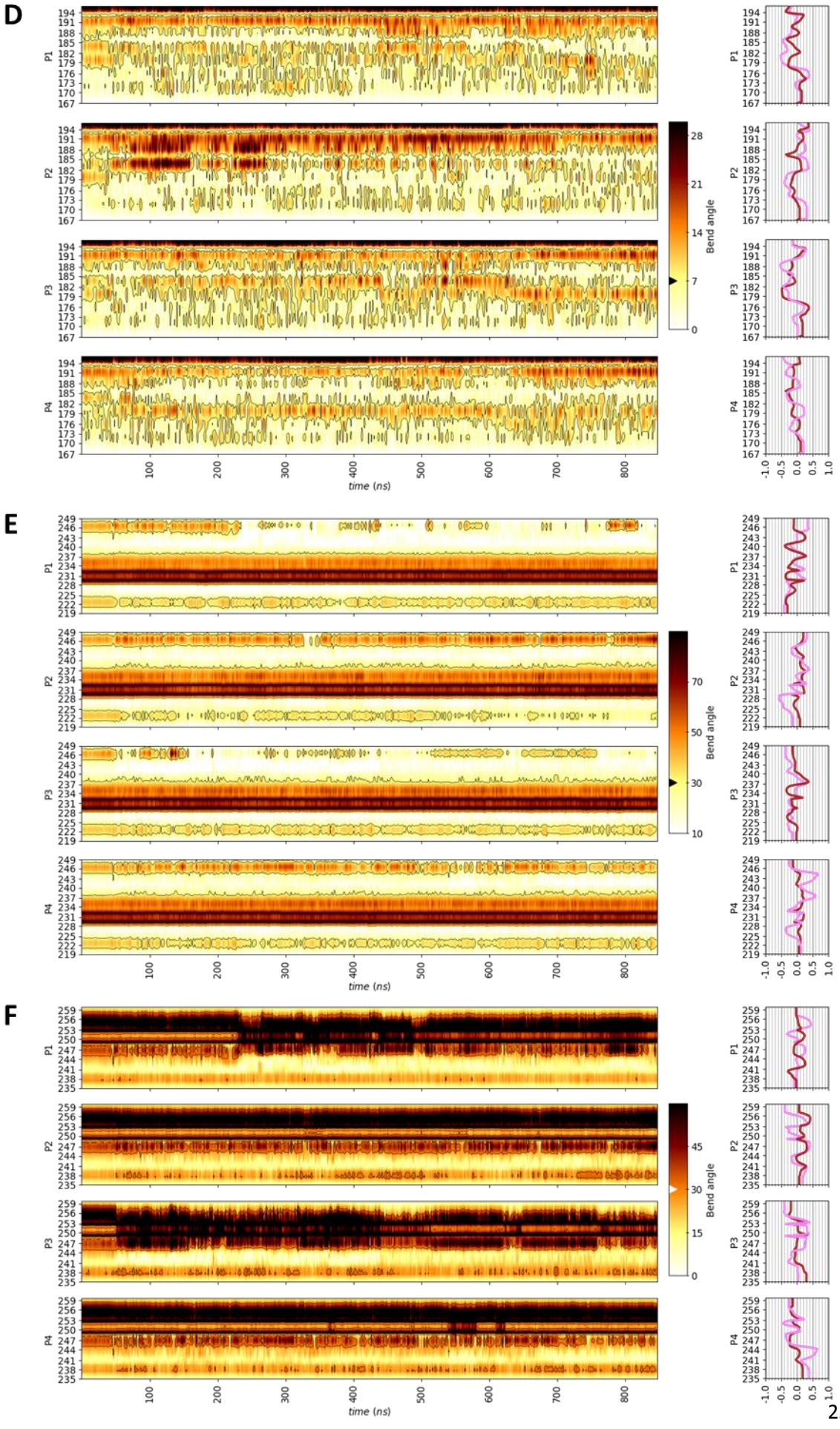
D
E
F
P1
P2
P3
P4
Bend angle
time (ns)

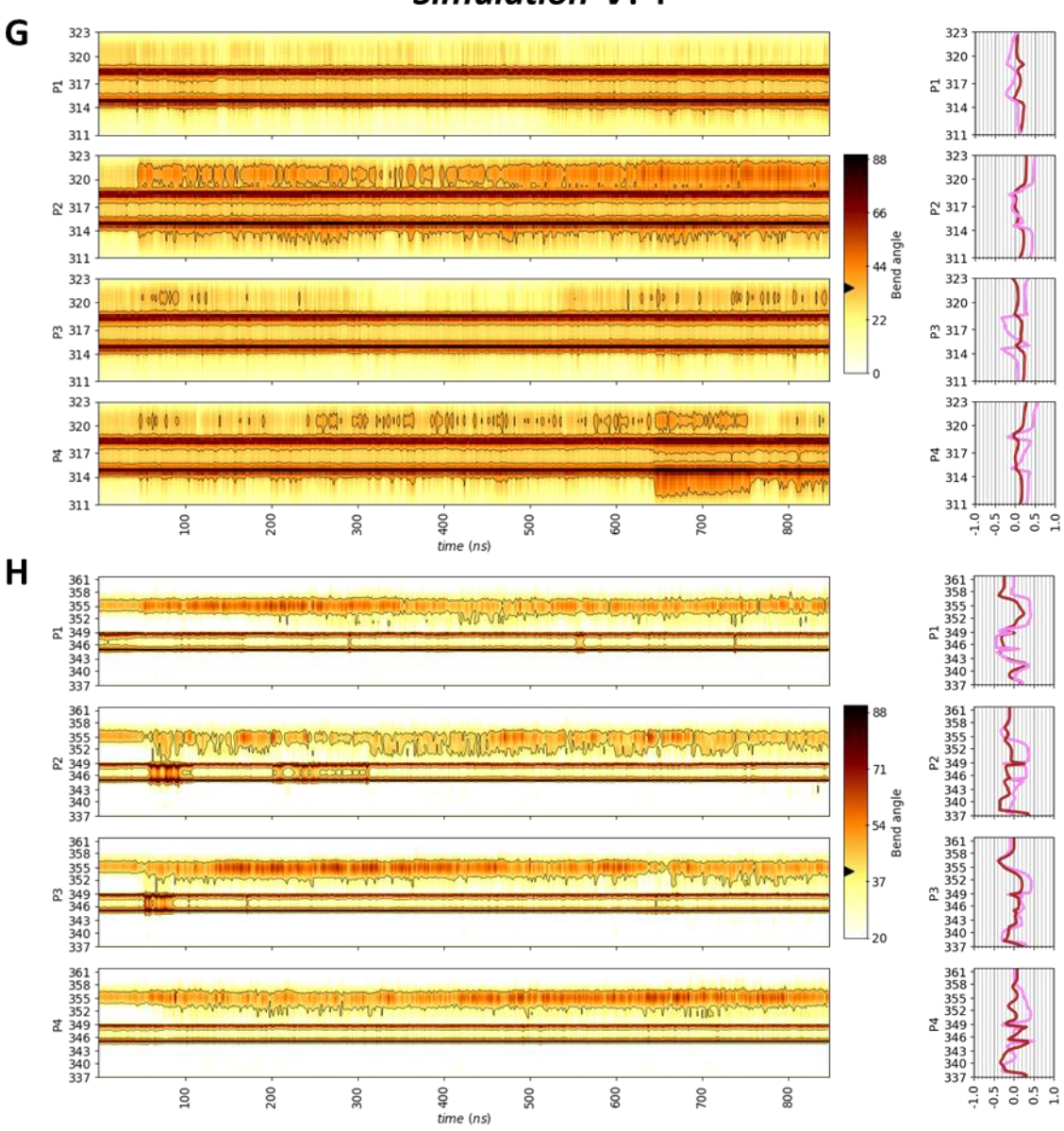
Simulation V: 4
G
H
P1
P2
P3
P4
time (ns)
Bend angle

Simulation V: 9

Norm: #5

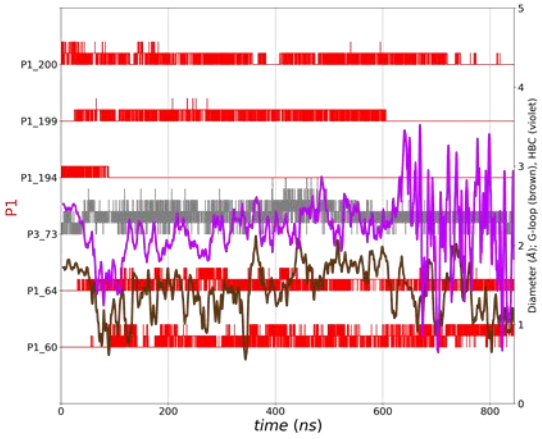

Norm: #5

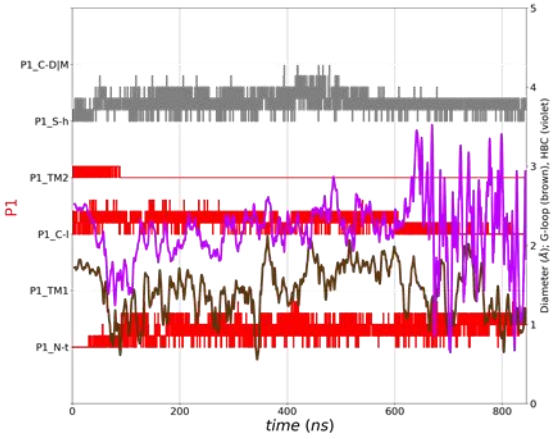

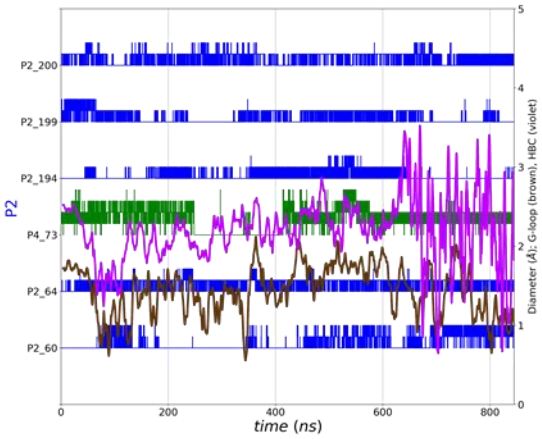

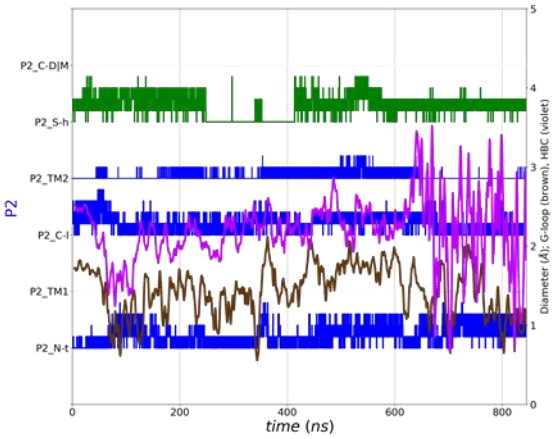

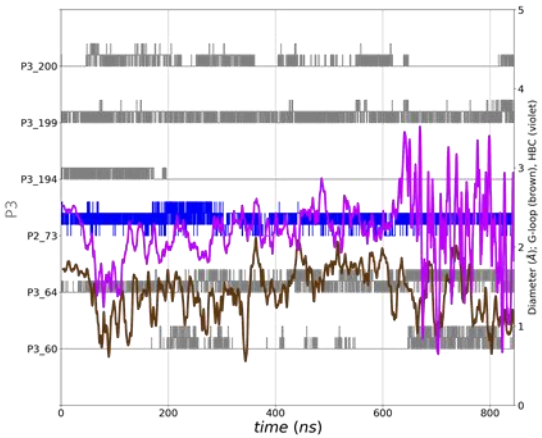

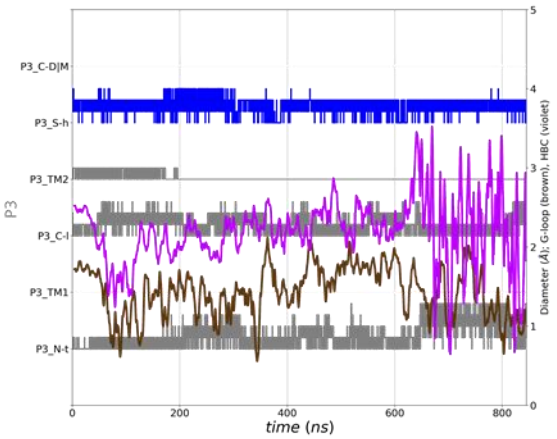

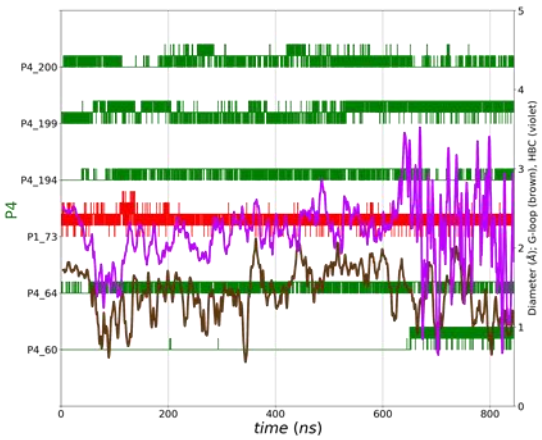

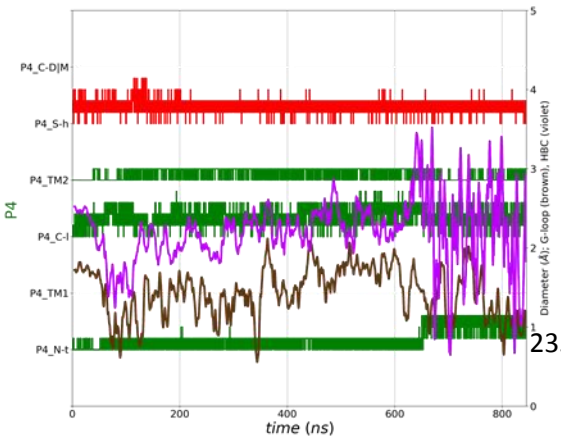

Simulation V: 10

Norm: #5

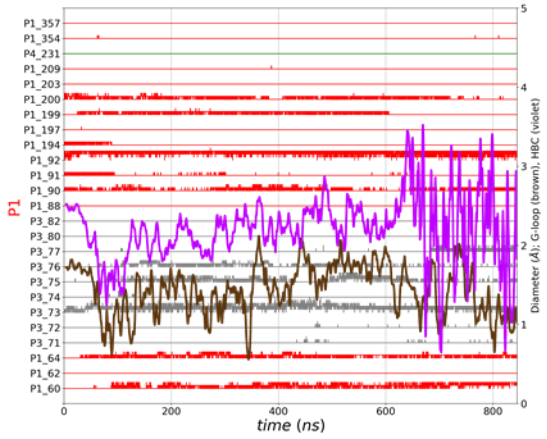

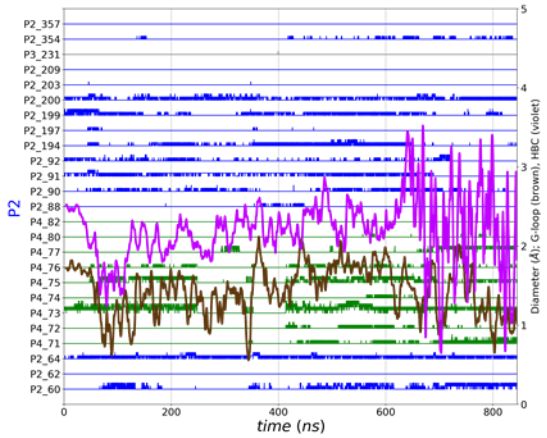

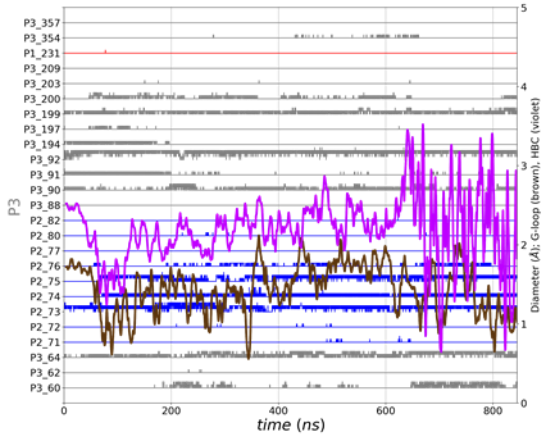

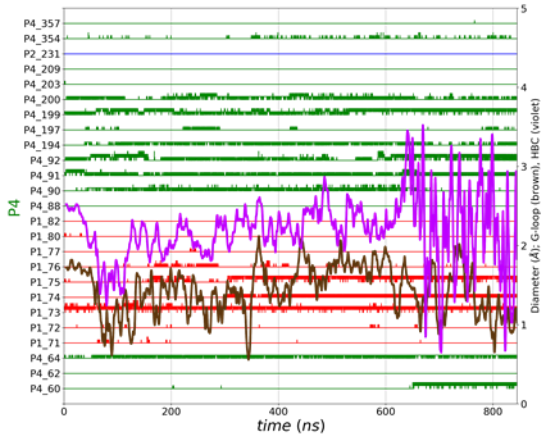

Norm: #9

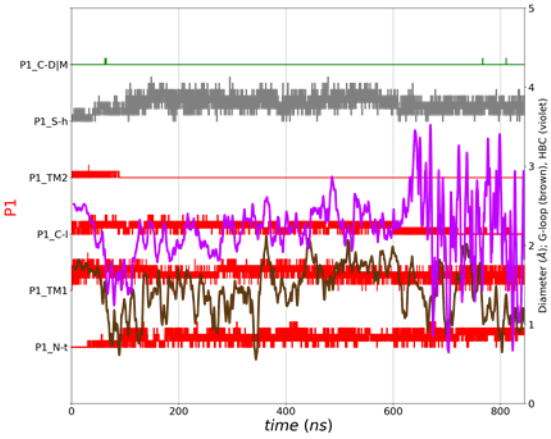

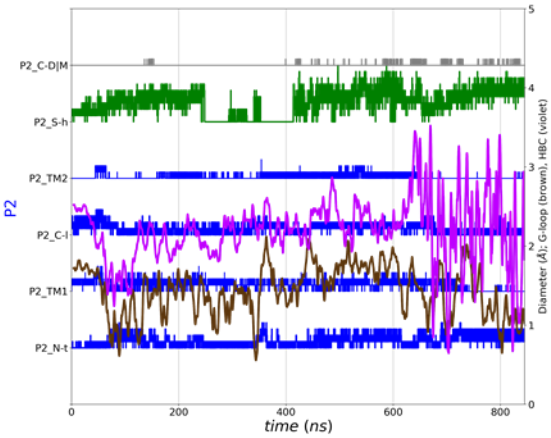

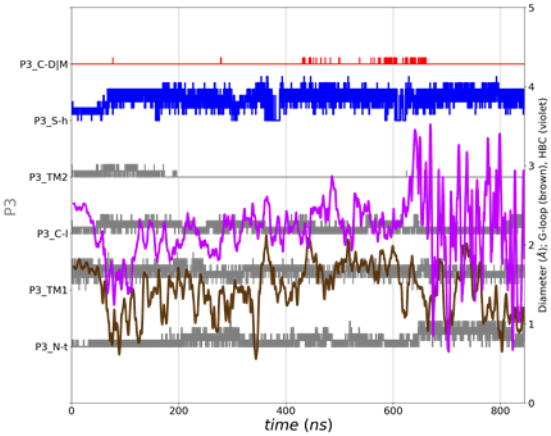

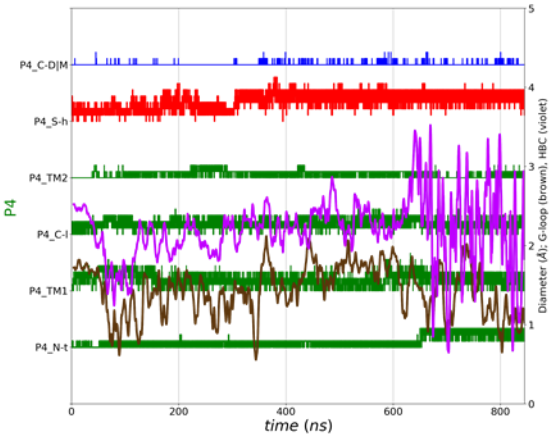

Simulation V: 11

Average electrostatic potential along the pore | **Electrostatic potential in the simulation box *(Y_{axis}= 0)***

A

50 to 70 ns; V_m= -0,07 *(Volts)*

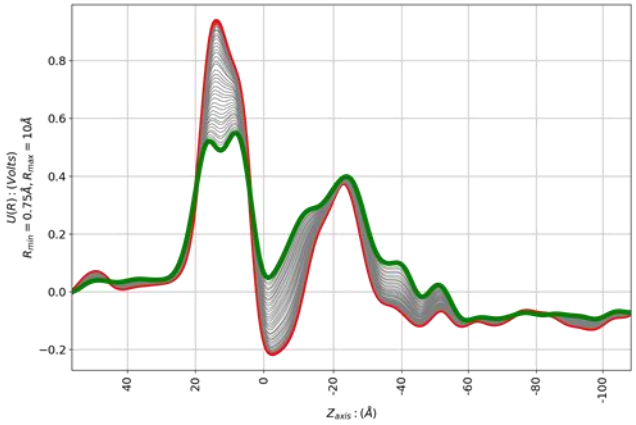

50 to 70 ns; V_m= -0,07 *(Volts)*

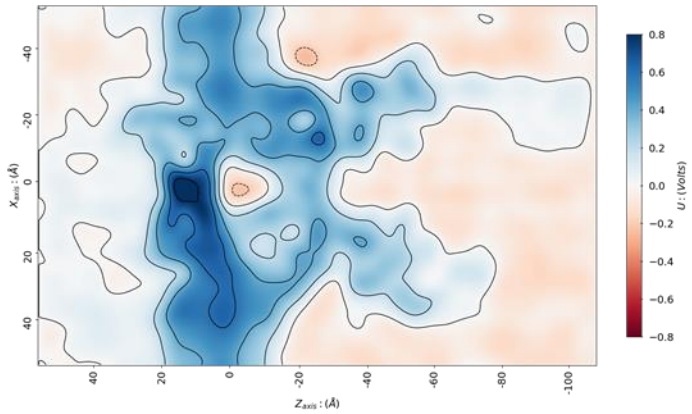

B

420 to 440 ns; V_m= -0,07 *(Volts)*

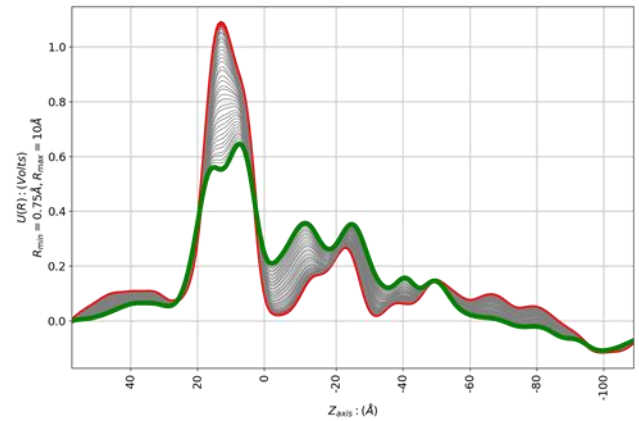

420 to 440 ns; V_m= -0,07 *(Volts)*

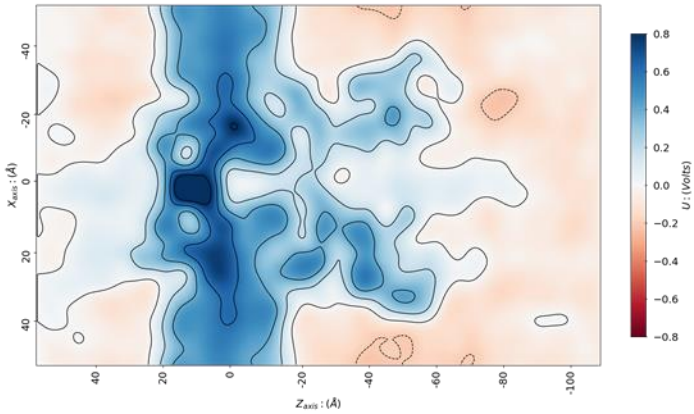

C

620 to 640 ns; V_m= -0,7 *(Volts)*

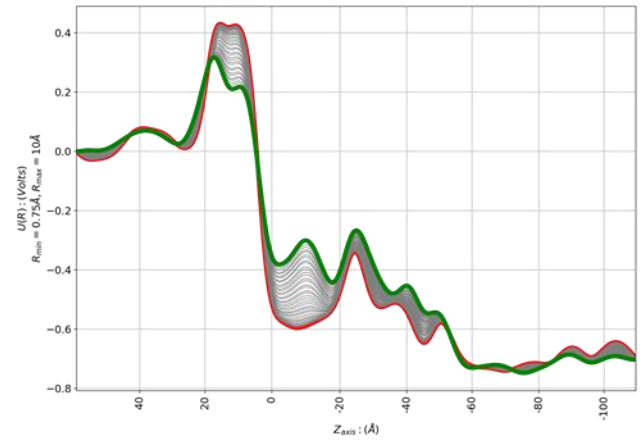

620 to 640 ns; V_m= -0,7 *(Volts)*

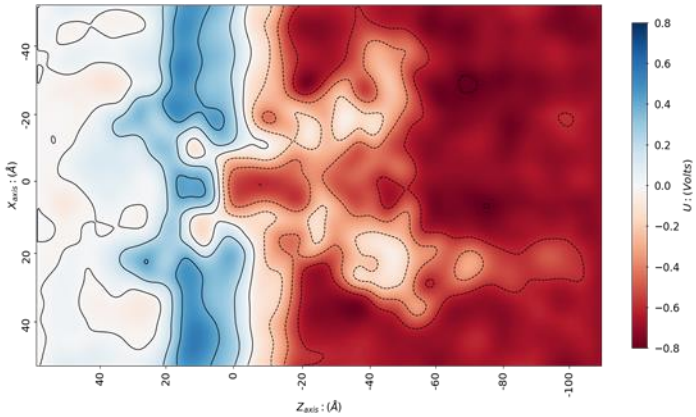

D

820 to 840 ns; V_m= -0,7 *(Volts)*

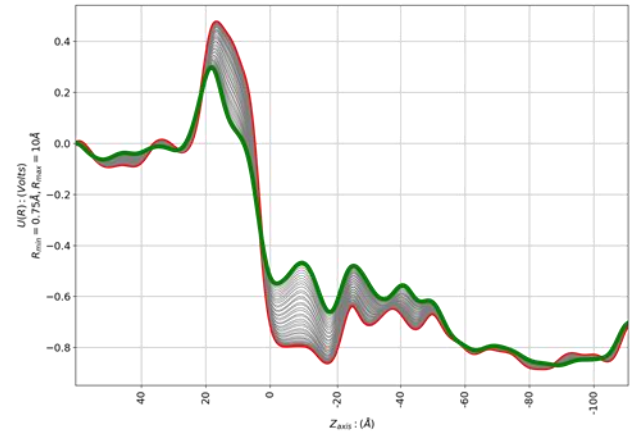

820 to 840 ns; V_m= -0,7 *(Volts)*

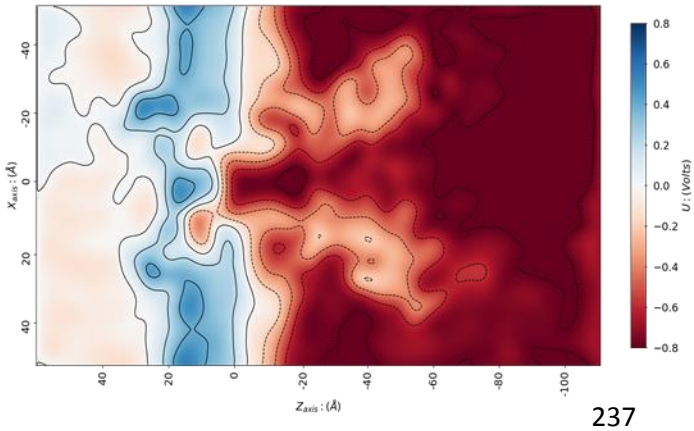

8.8 SIMULATION VI

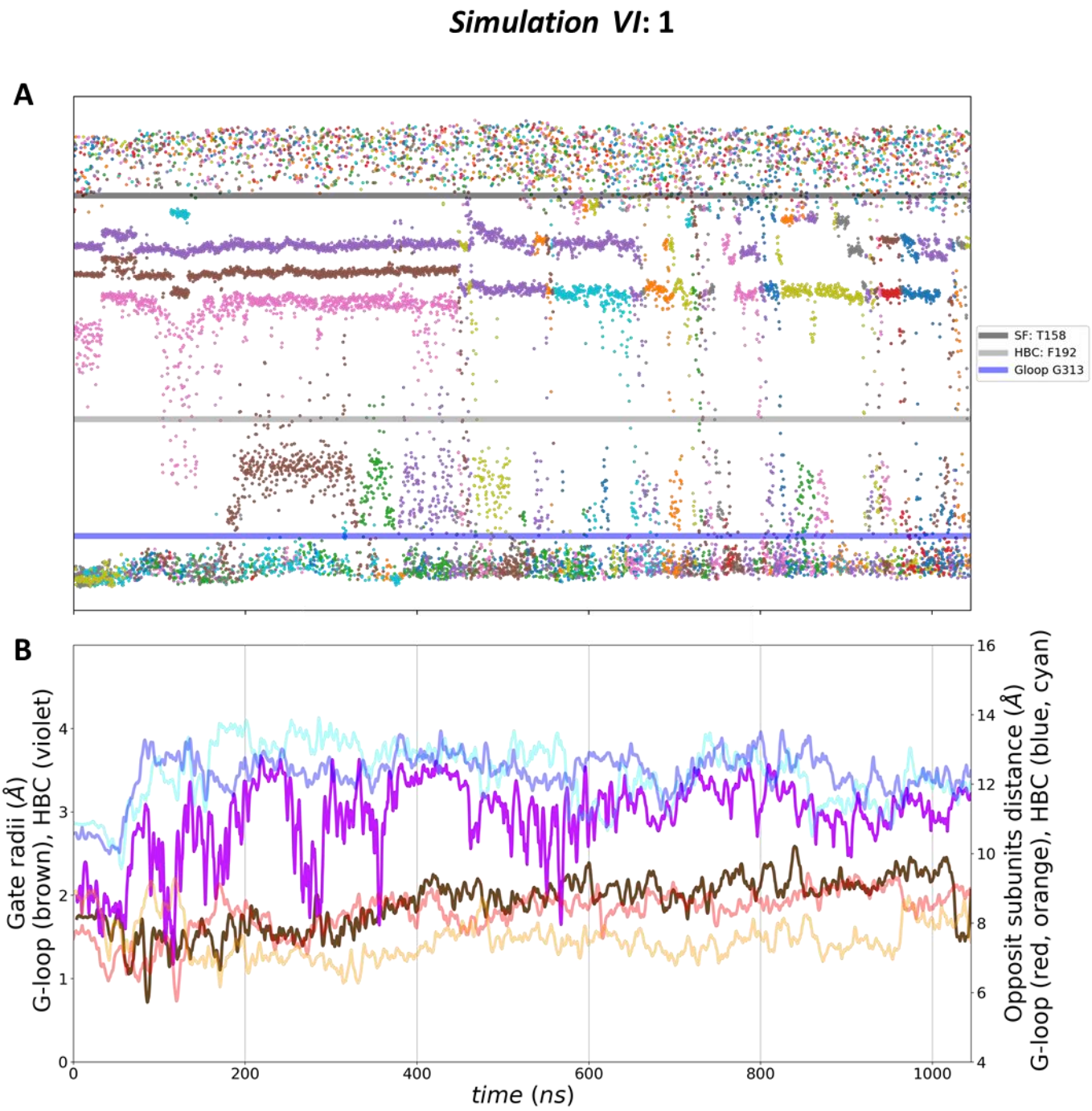

Simulation VI: 2

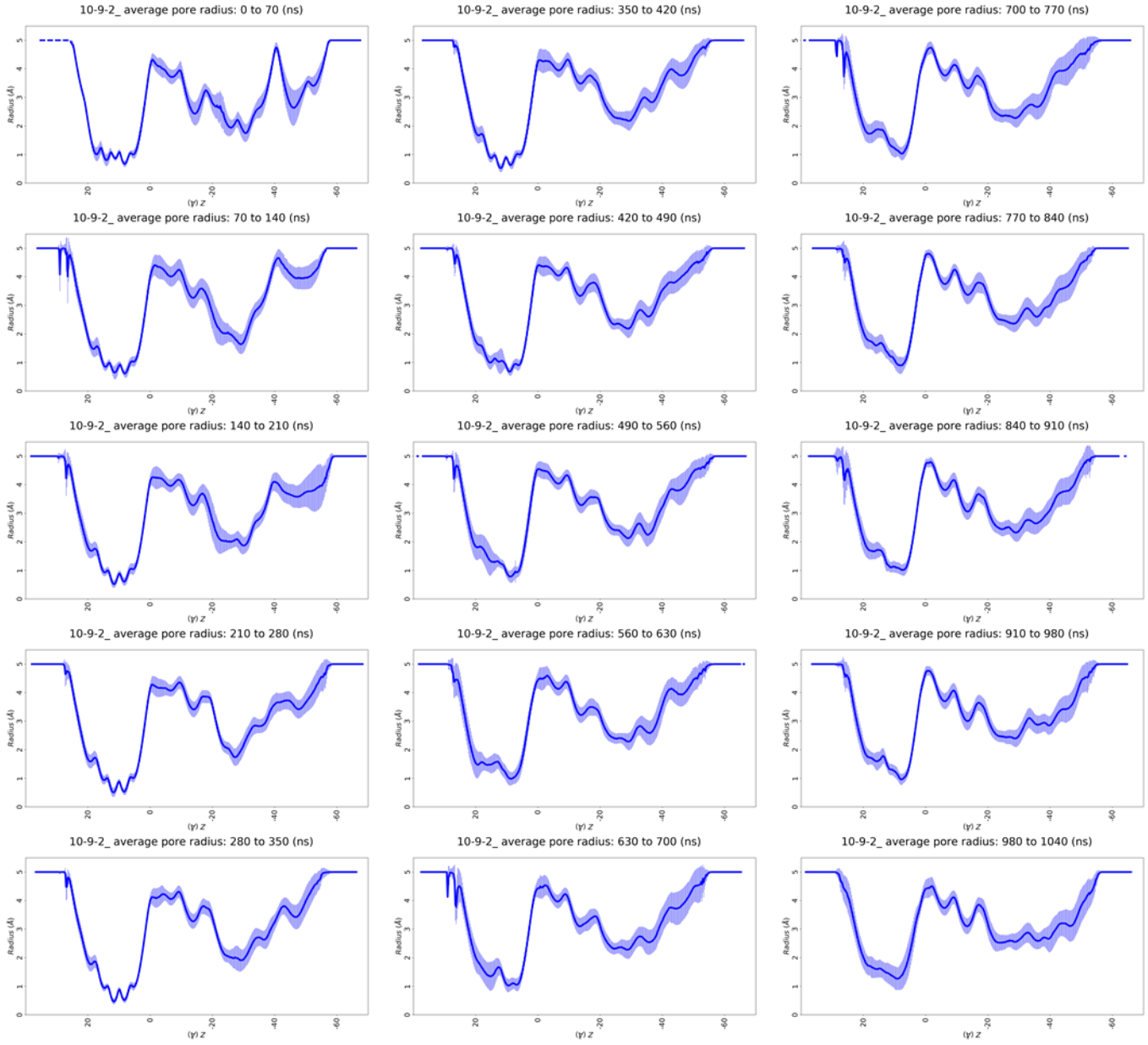

Simulation VI: 3

Bad averaging: signal is 70*0.4 times underestimated

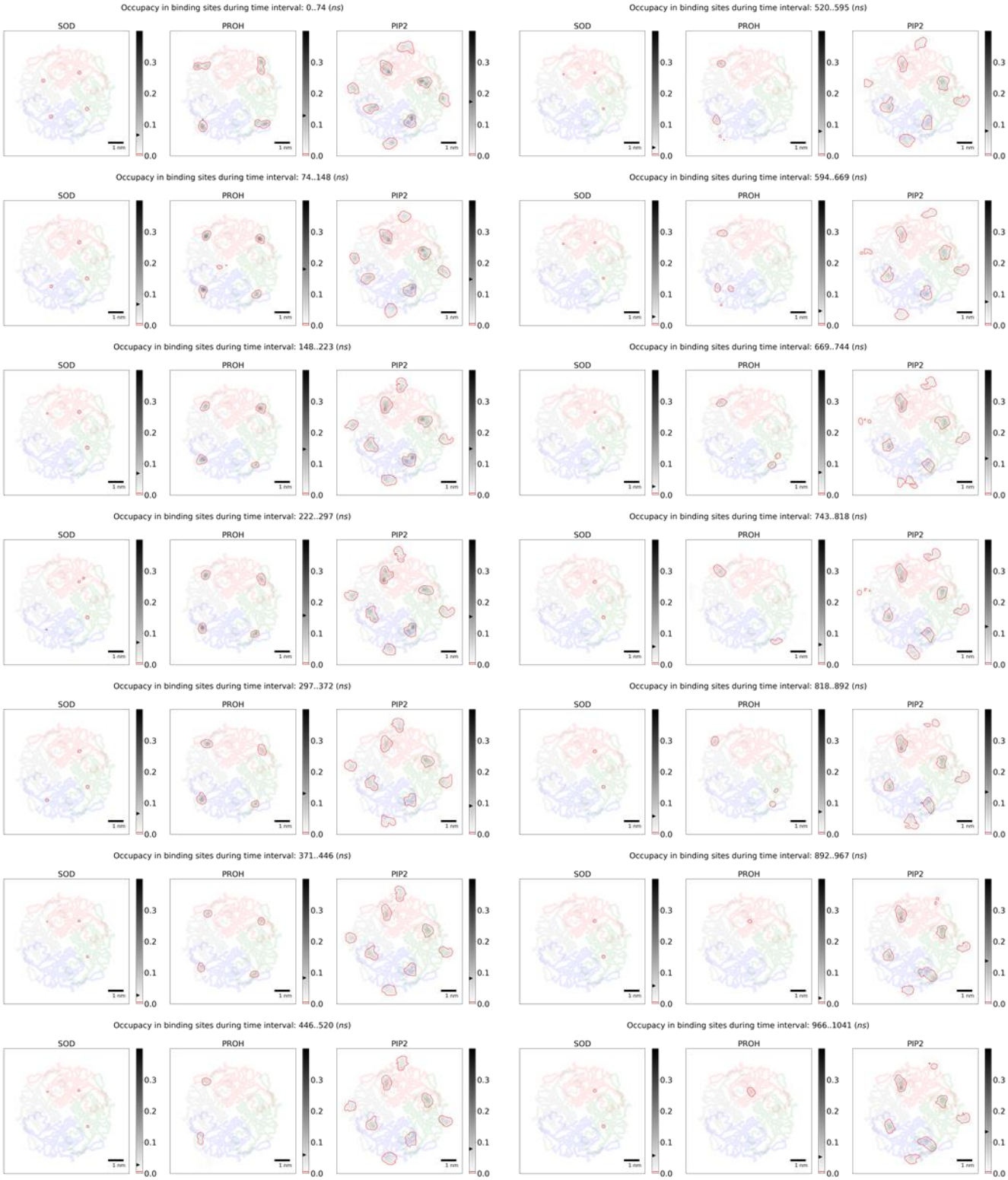

Simulation VI: 4

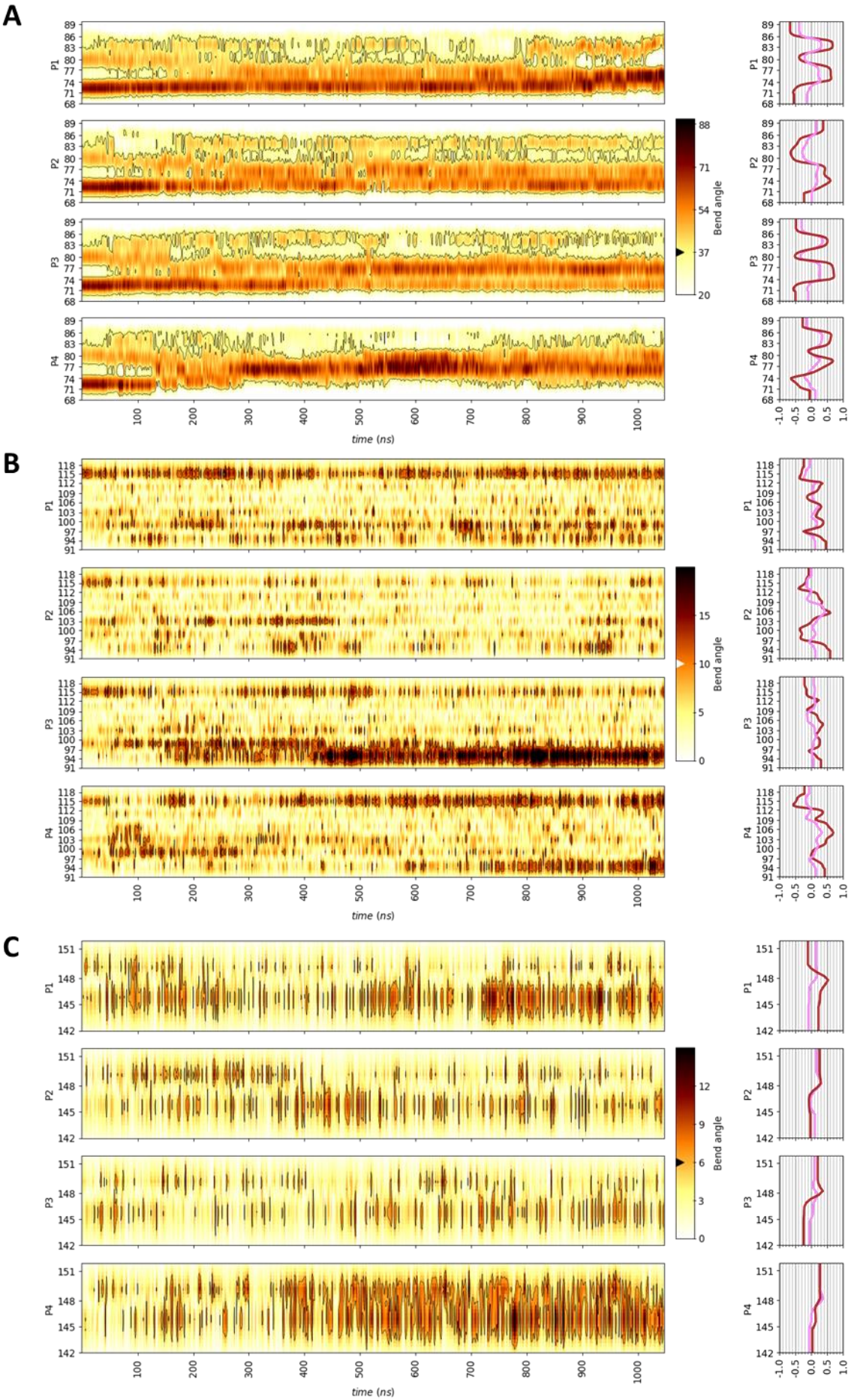

Simulation VI: 4

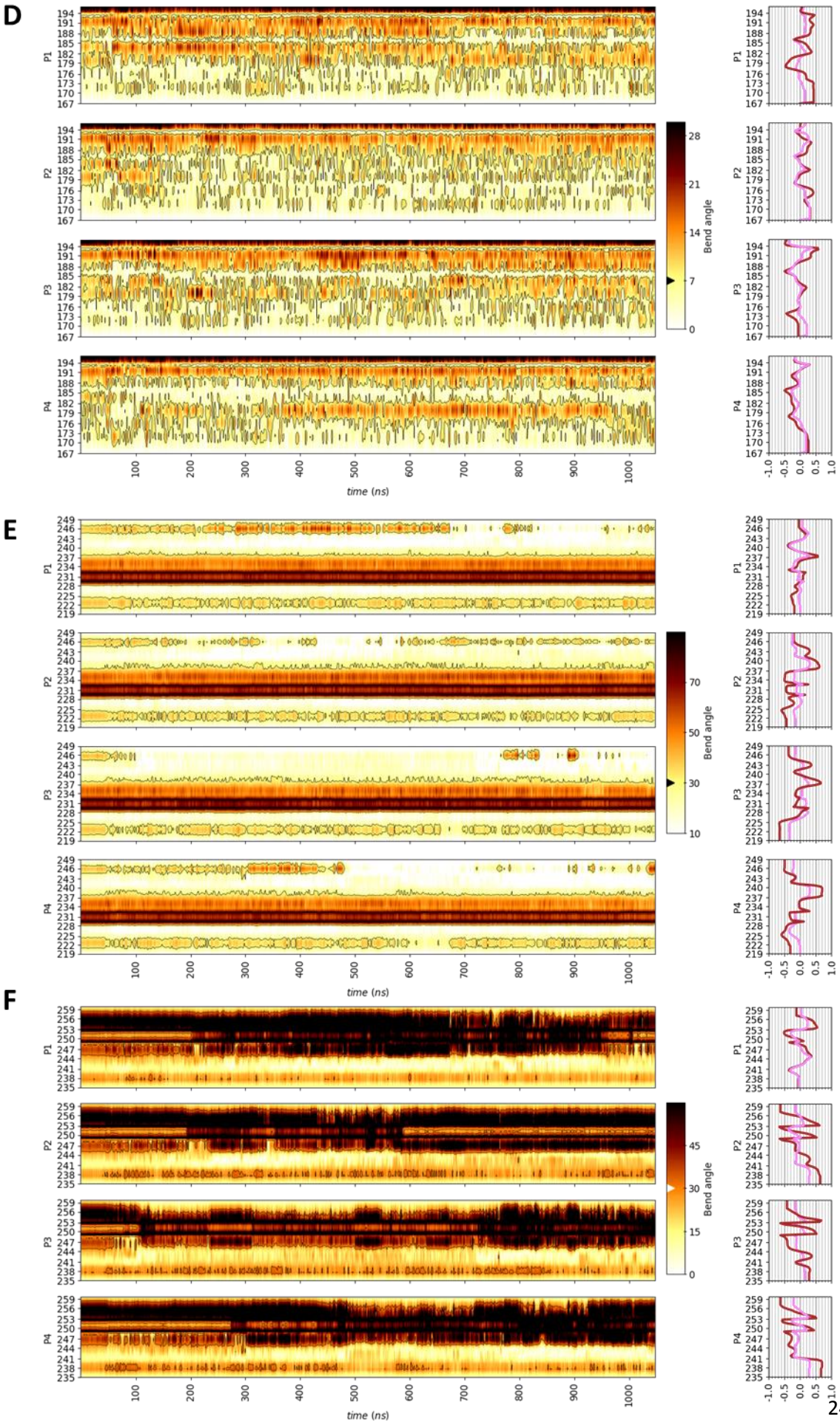

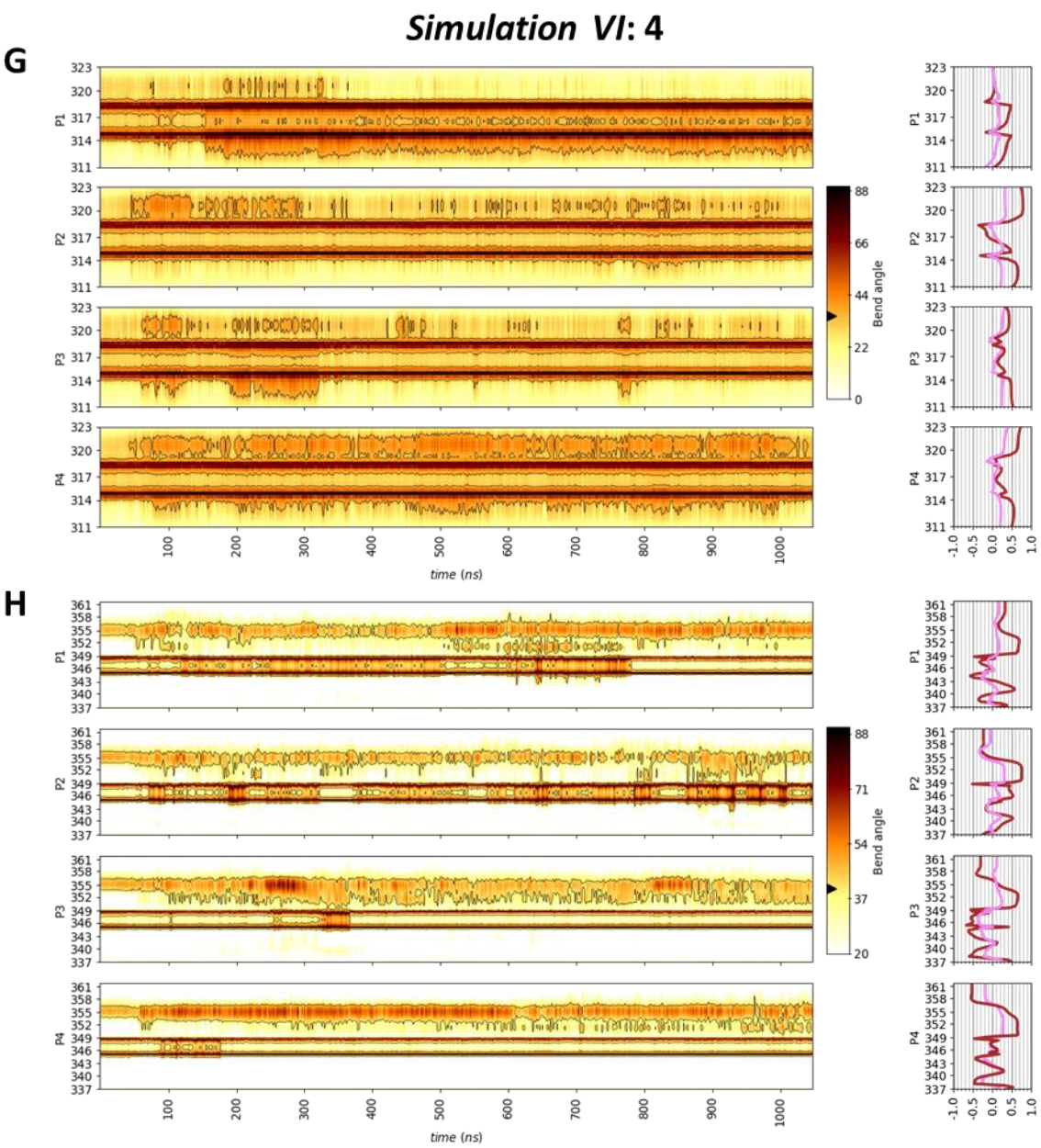
Simulation VI: 4
G
H
P1
P2
P3
P4
Bend angle
time (ns)

Simulation VI: 5

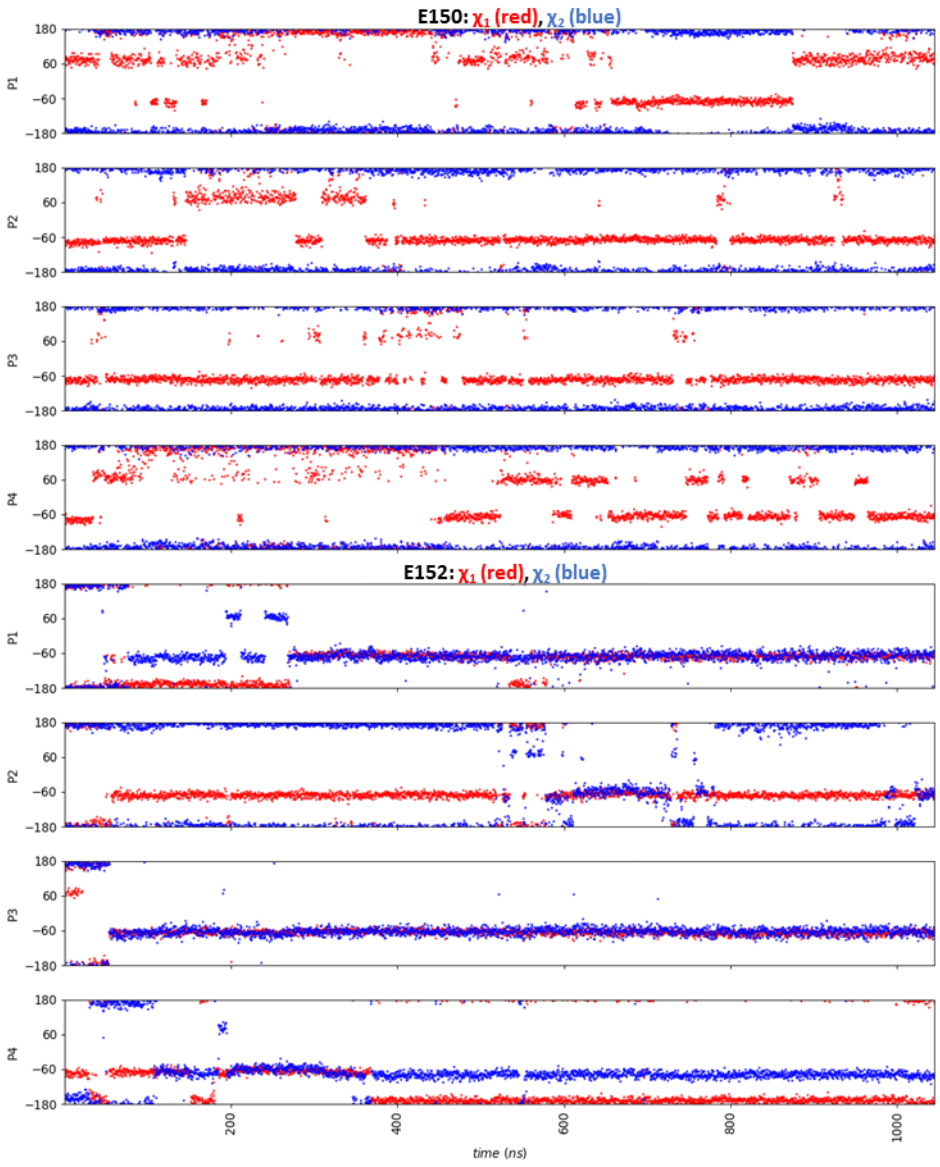

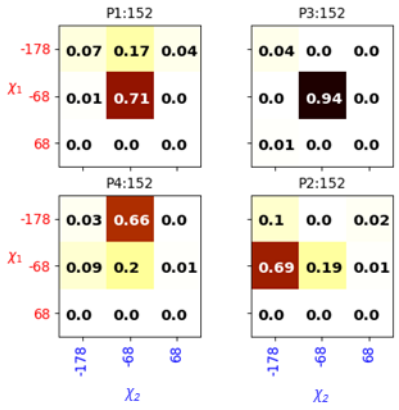

Simulation VI: 6

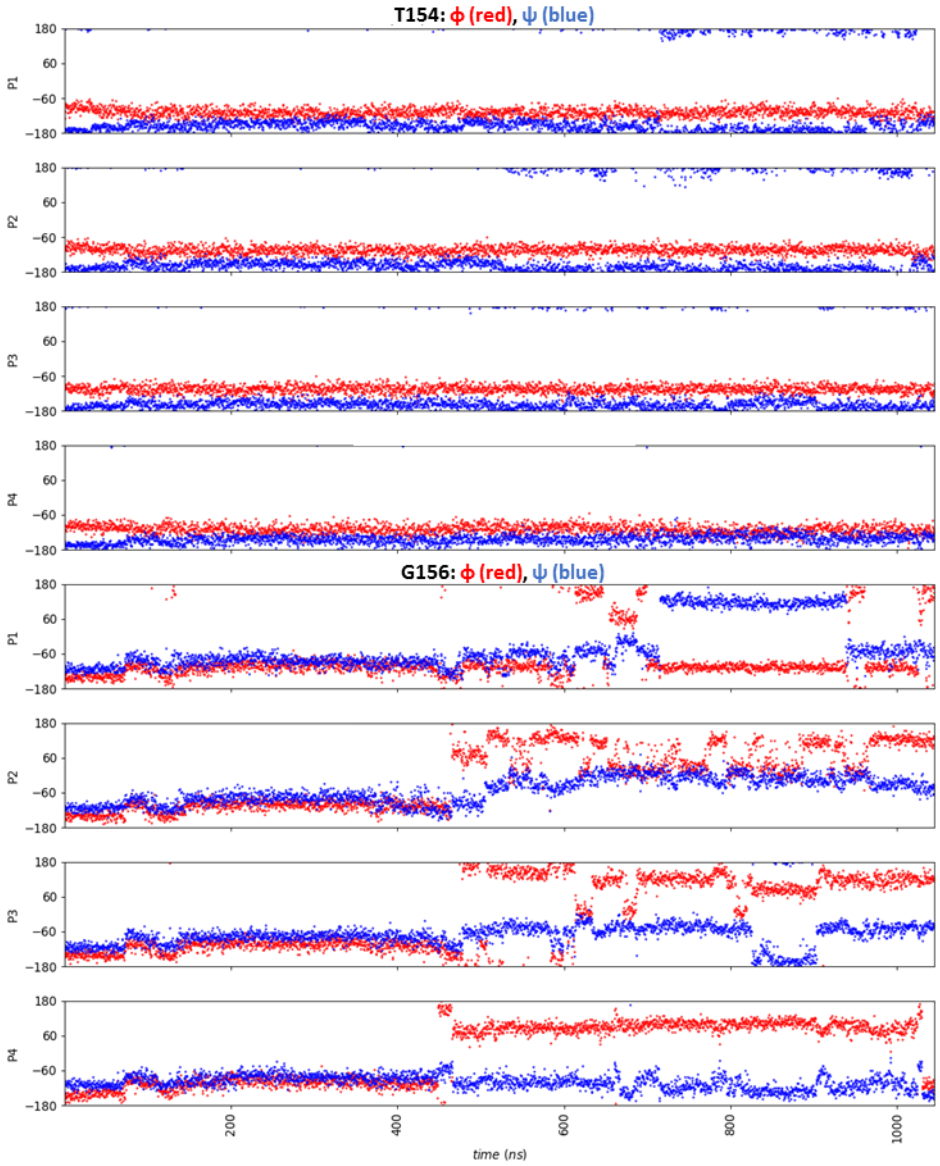

Simulation VI: 6

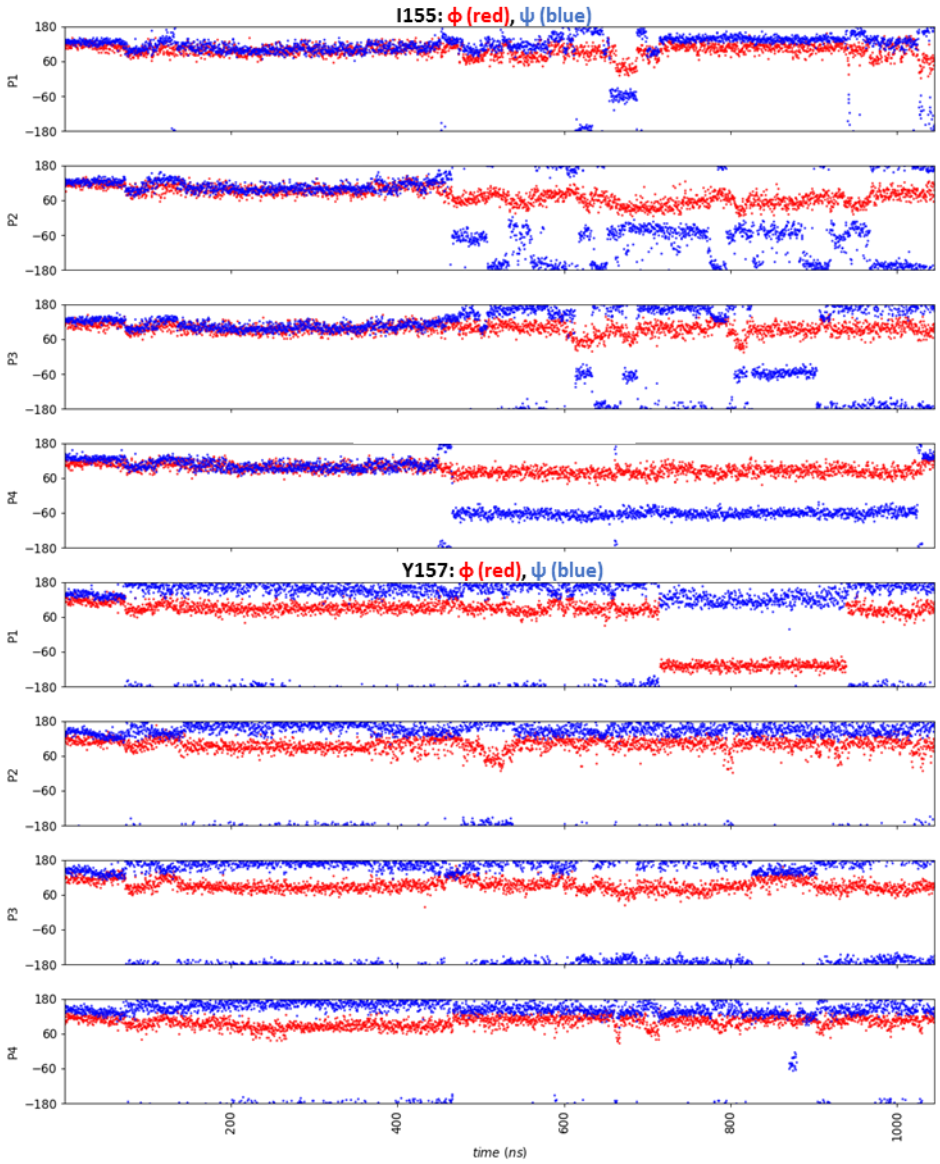

Simulation VI: 6

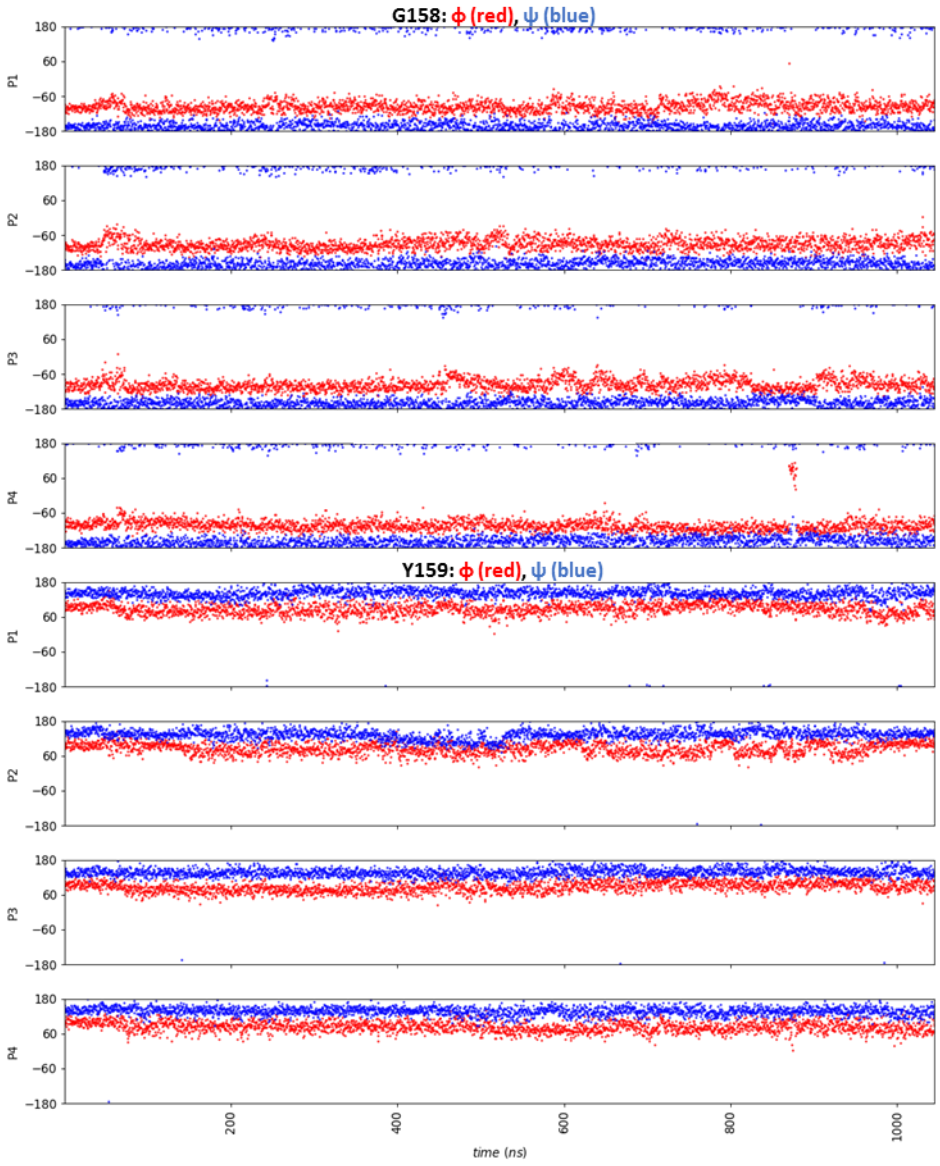

Simulation VI: 7

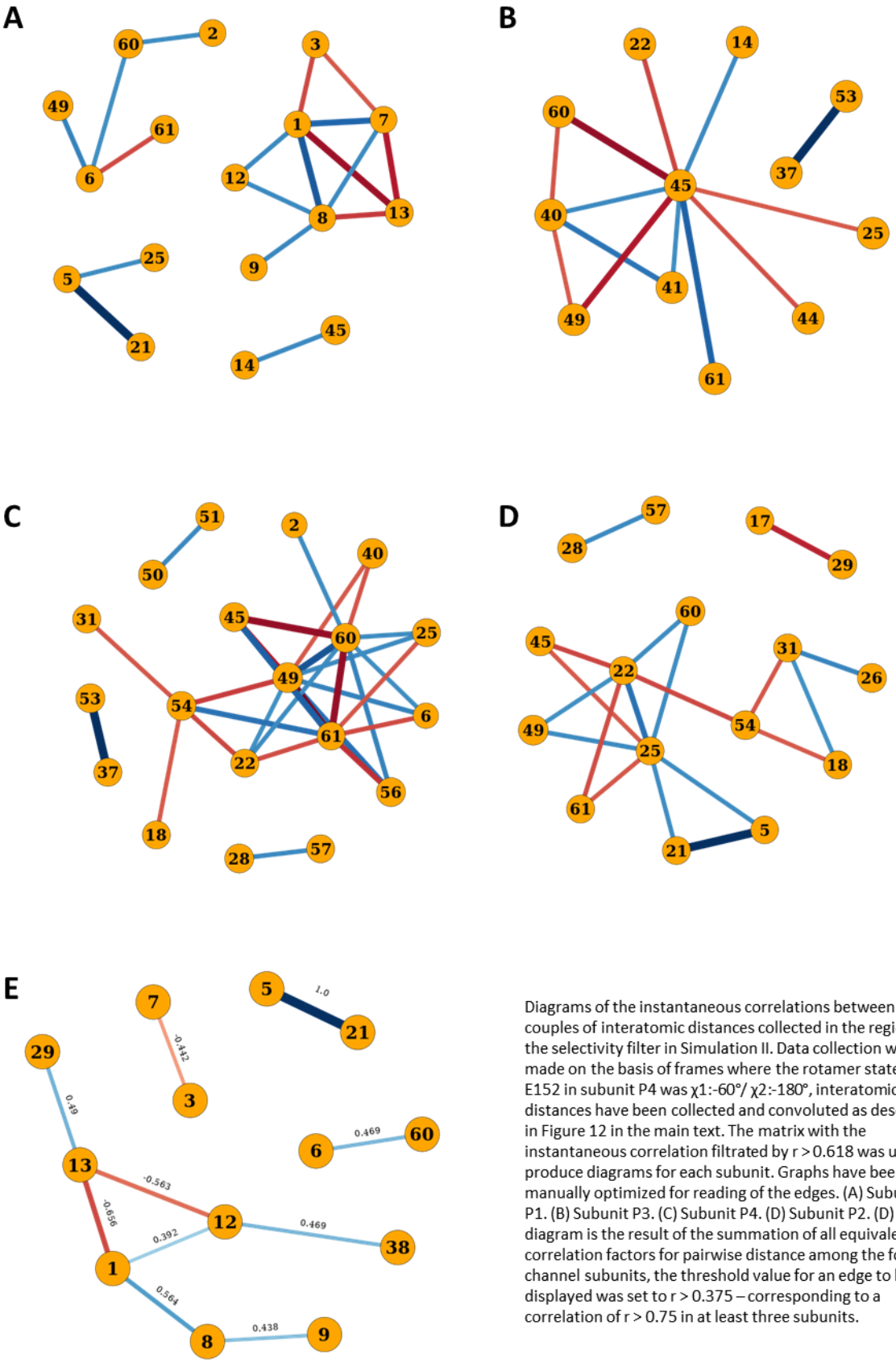

Diagrams of the instantaneous correlations between couples of interatomic distances collected in the region of the selectivity filter in Simulation II. Data collection was made on the basis of frames where the rotamer state of E152 in subunit P4 was χ1:-60°/ χ2:-180°, interatomic distances have been collected and convoluted as described in Figure 12 in the main text. The matrix with the instantaneous correlation filtrated by r > 0.618 was used to produce diagrams for each subunit. Graphs have been manually optimized for reading of the edges. (A) Subunit P1. (B) Subunit P3. (C) Subunit P4. (D) Subunit P2. (D) This diagram is the result of the summation of all equivalent correlation factors for pairwise distance among the four channel subunits, the threshold value for an edge to be displayed was set to r > 0.375 – corresponding to a correlation of r > 0.75 in at least three subunits.

Simulation VI: 8

A

	P1	P3	P2	P4
P1	S	N	O	P
P3	P	S	N	O
P2	O	P	S	N
P4	N	O	P	S

P1	P3	P2	P4	
0	14	7	21	P1:105:CA | P2:105:CA
1	15	8	22	P1:188:CA | P2:188:CA
2	16	9	23	P1:105:OG1 | P1:152:CD
3	17	10	24	P1:155:CA | P3:151:CA
4	18	11	25	P1:155:CA | P3:173:CA
5	19	12	26	P1:155:CD | P3:173:CG
6	20	13	27	P1:155:CA | P2:155:CA

B

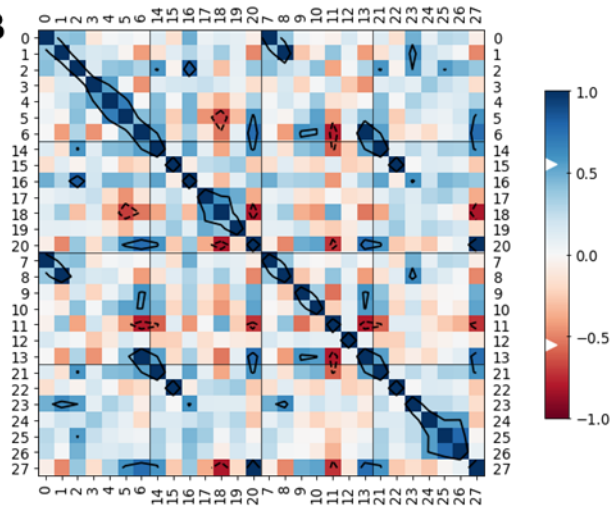

C

Network threshold $r \geq 0.375$

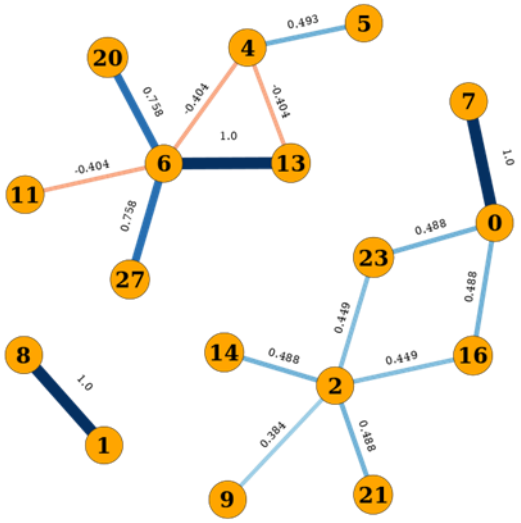

D

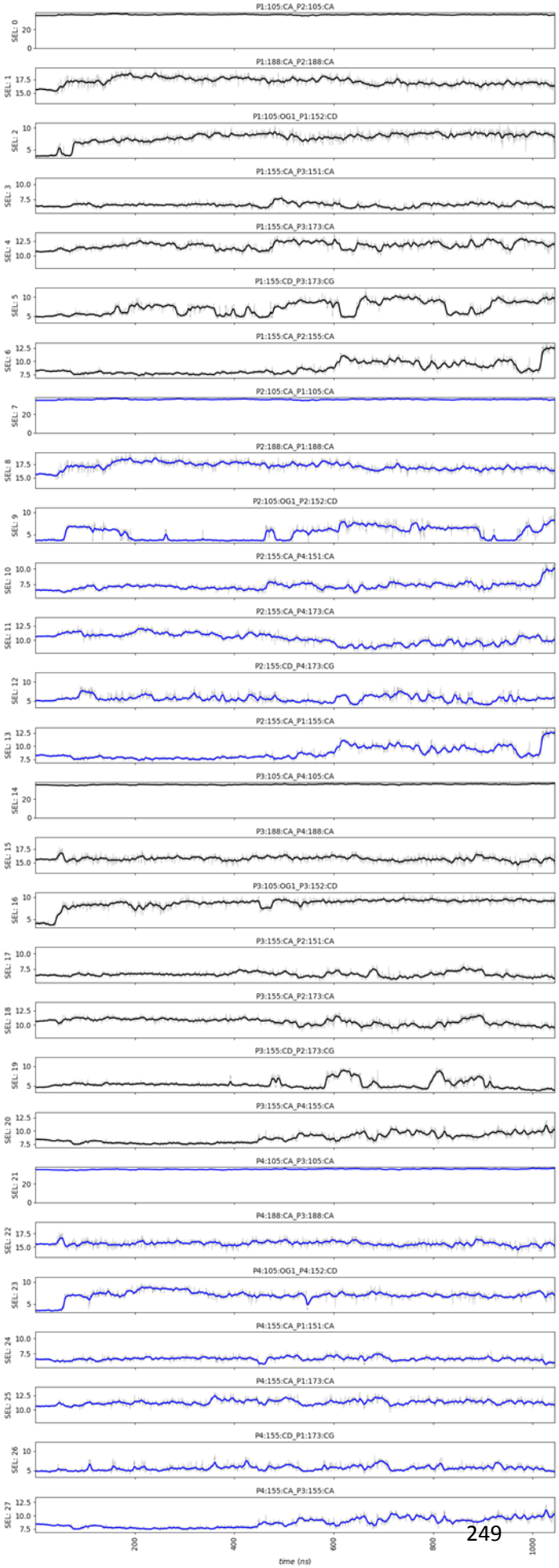

Simulation VI: 9

Norm: #5

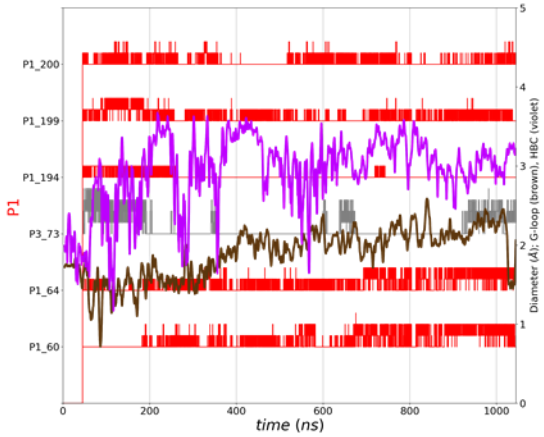

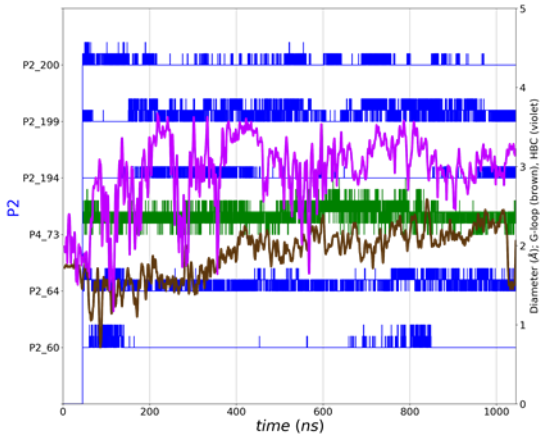

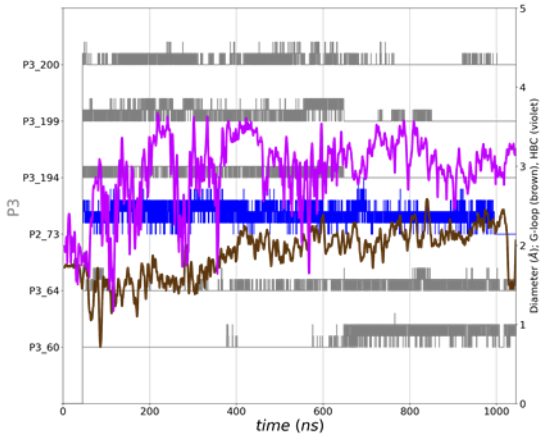

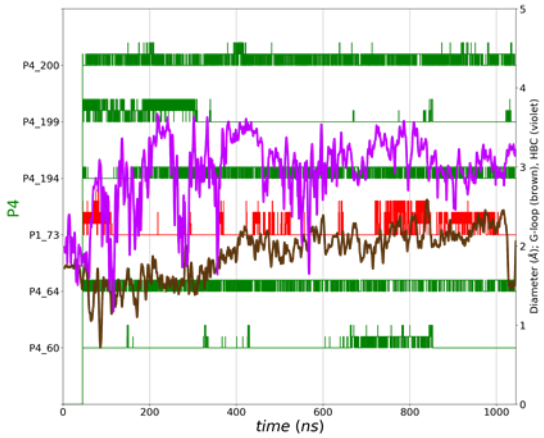

Norm: #5

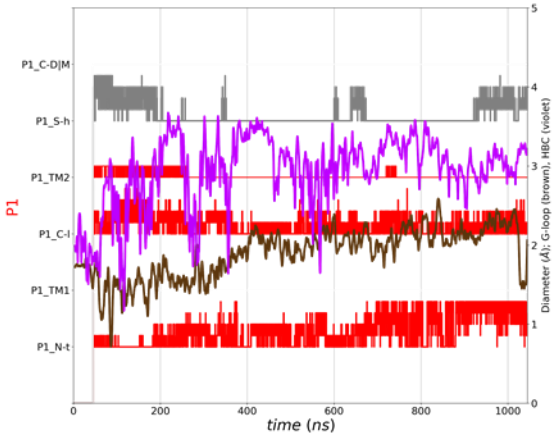

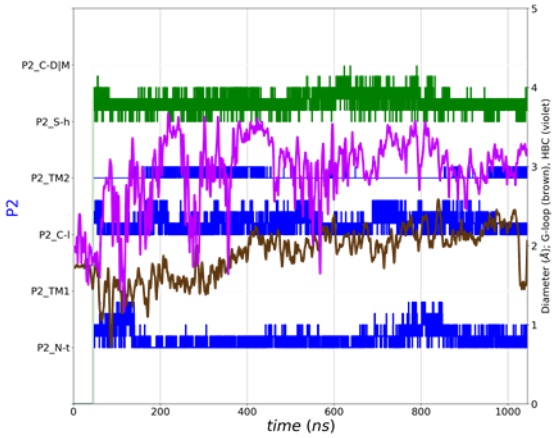

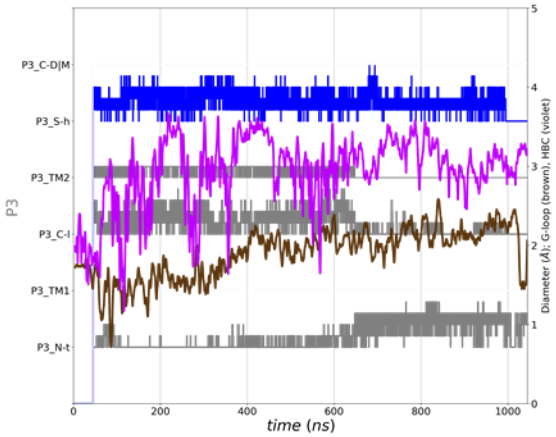

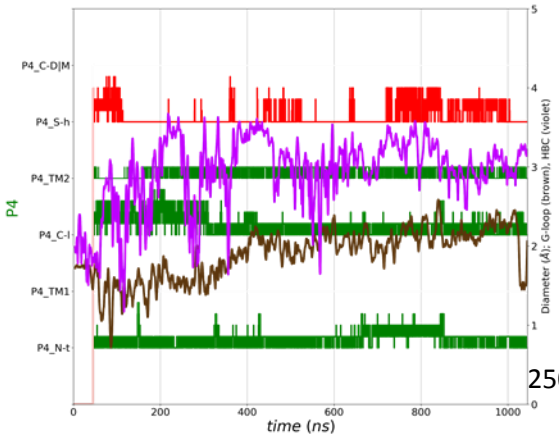

Simulation VI: 10

Norm: #5

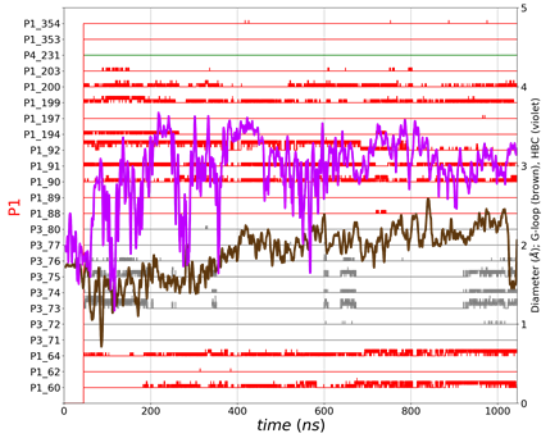

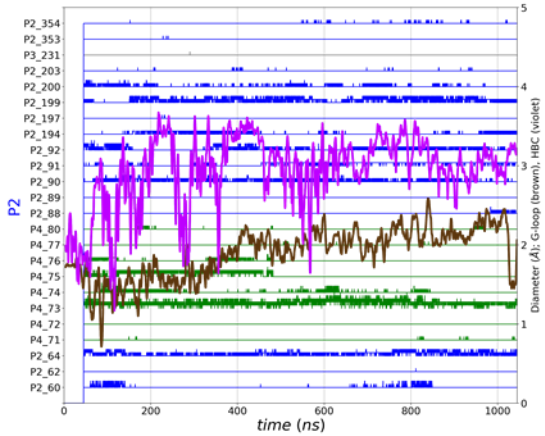

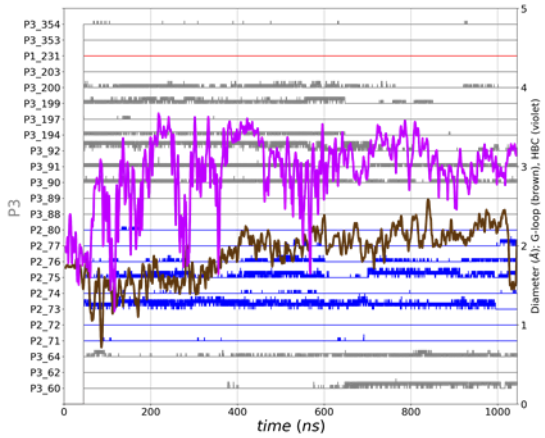

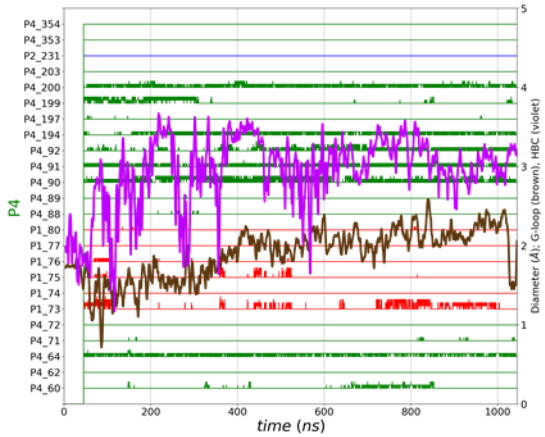

Norm: #8

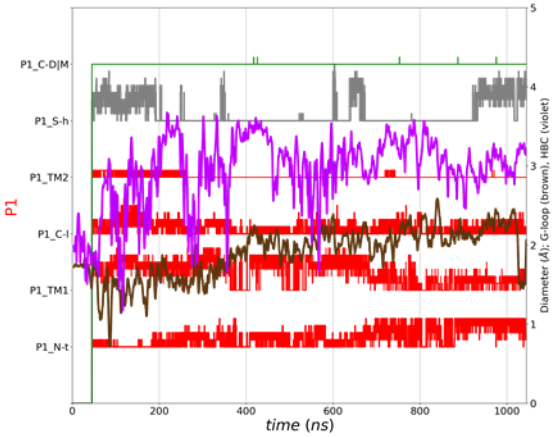

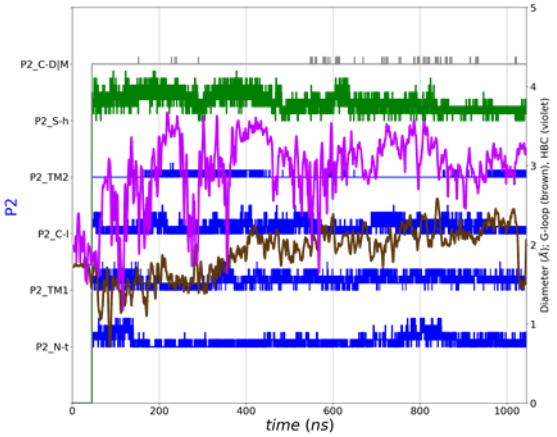

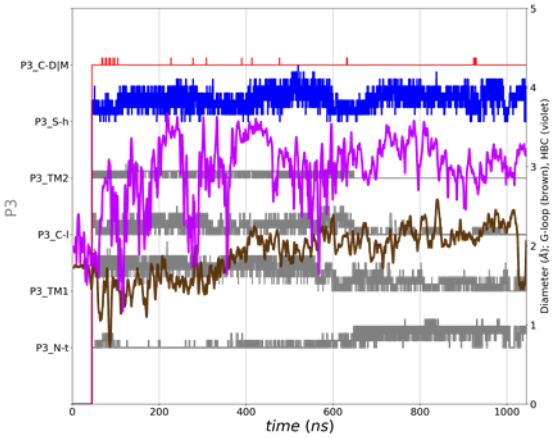

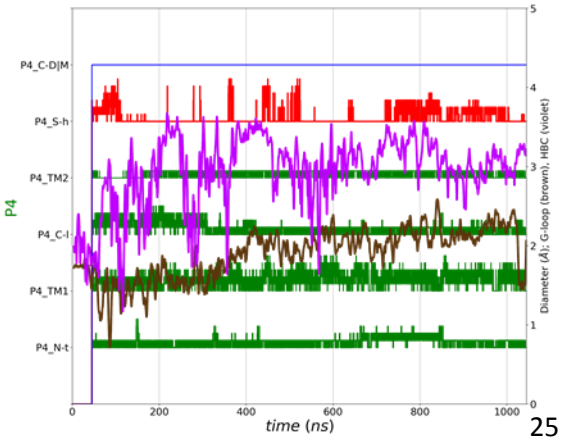

Simulation VI: 10

Average electrostatic potential along the pore

Electrostatic potential in the simulation box *(Y_{axis}= 0)*

A

50 to 70 ns; V_m= -0,07 *(Volts)*

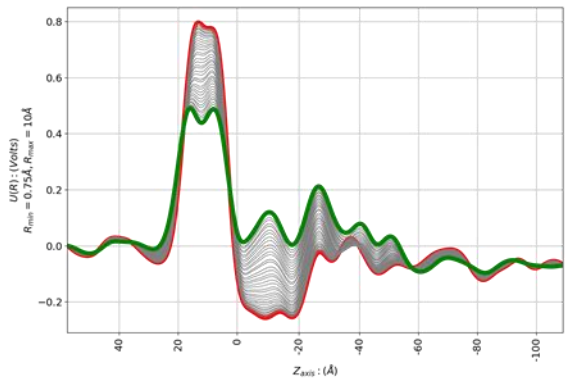

50 to 70 ns; V_m= -0,07 *(Volts)*

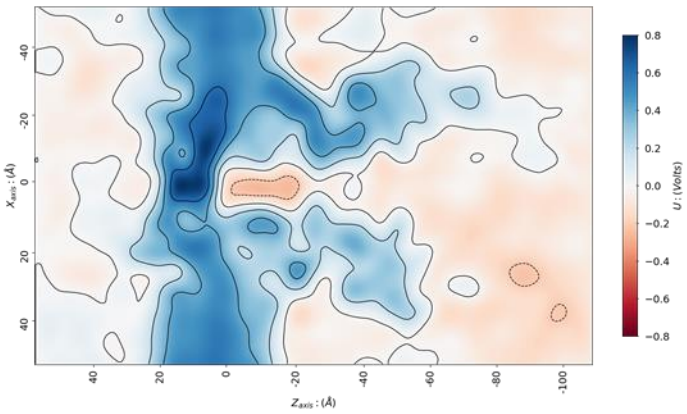

B

420 to 440 ns; V_m= -0,07 *(Volts)*

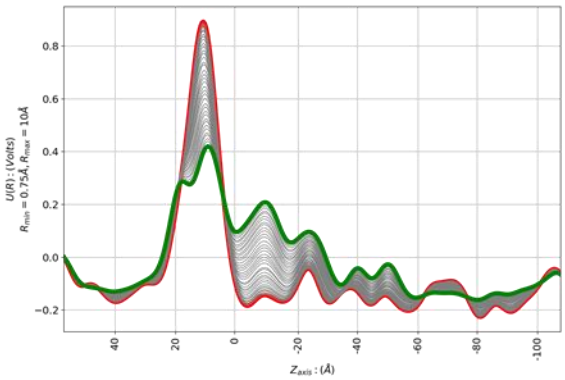

420 to 440 ns; V_m= -0,07 *(Volts)*

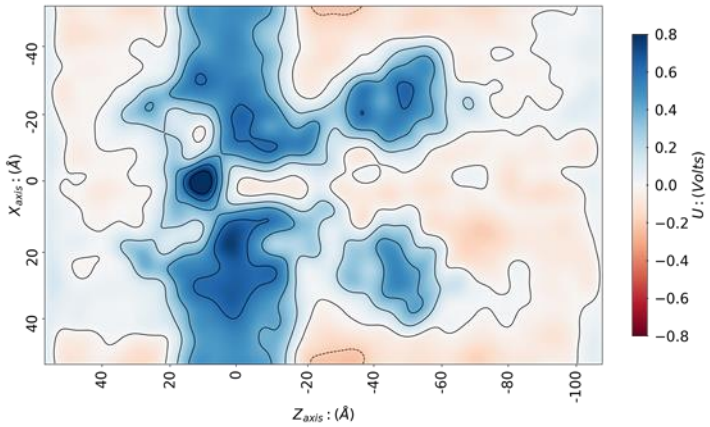

C

620 to 640 ns; V_m= -0,7 *(Volts)*

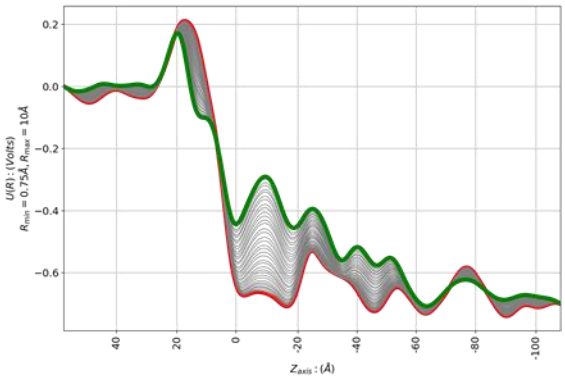

620 to 640 ns; V_m= -0,7 *(Volts)*

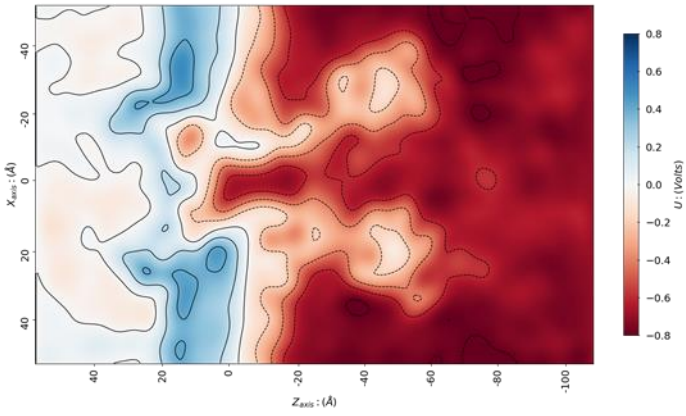

D

1020 to 1040 ns; V_m= -0,7 *(Volts)*

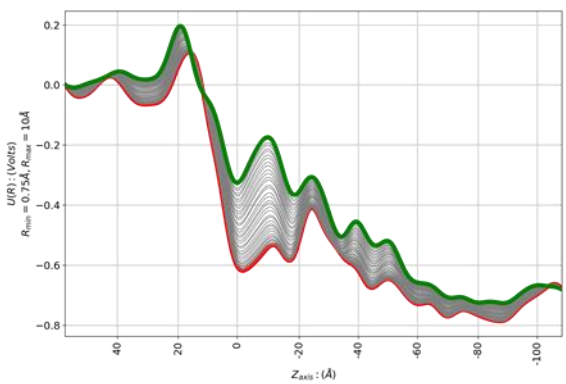

1020 to 1040 ns; V_m= -0,7 *(Volts)*

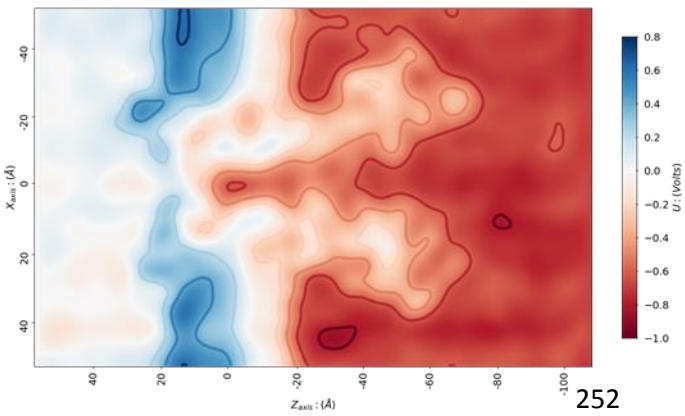

8.9 SIMULATION VII

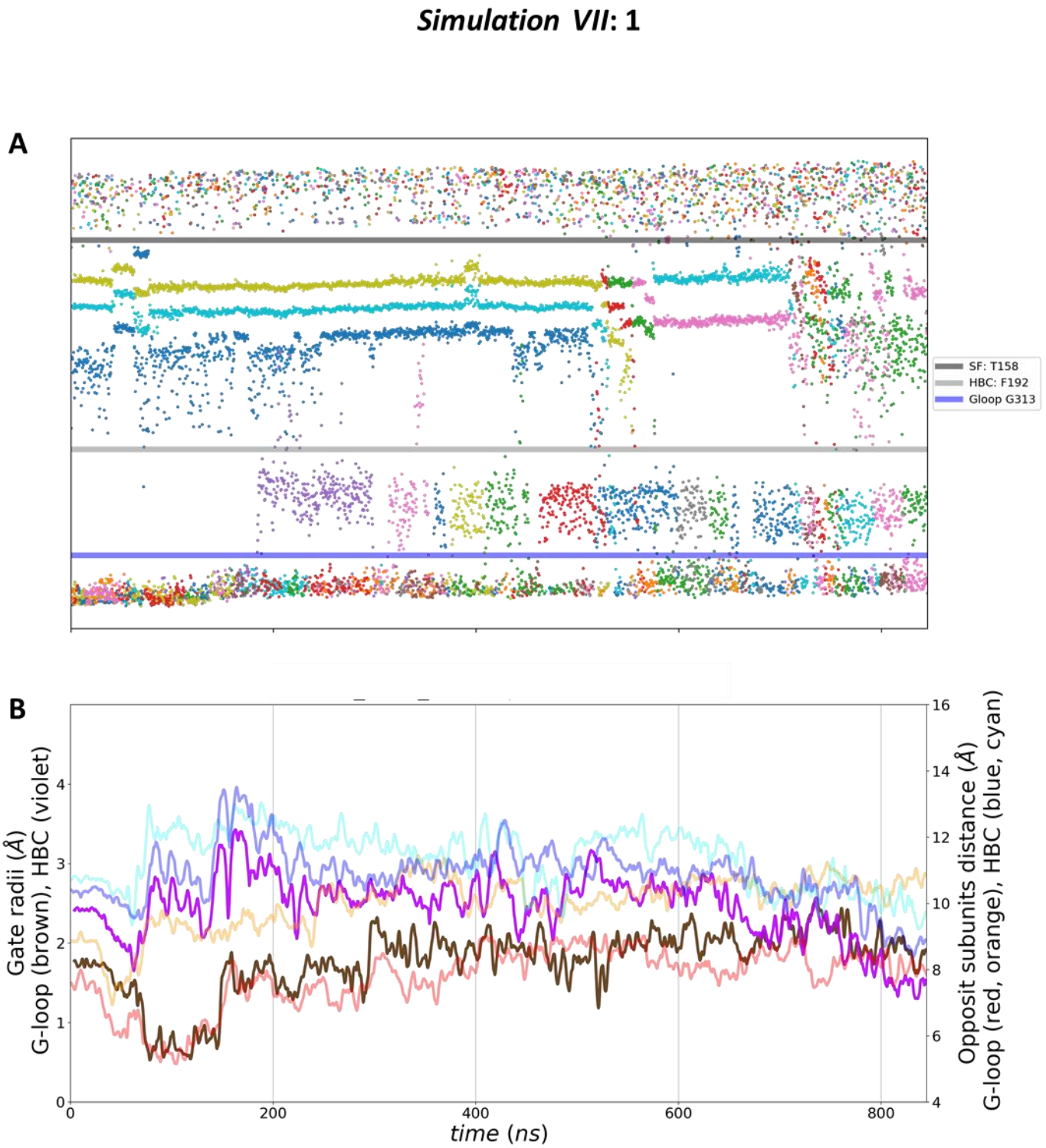

Simulation VII: 2

10-5-1_ average pore radius: 0 to 70 (ns)

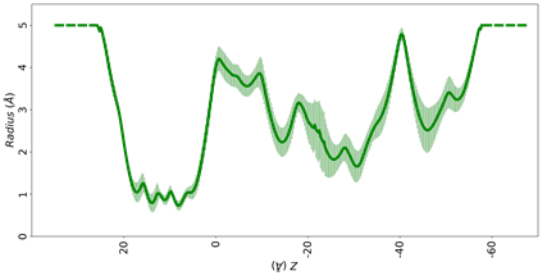

10-5-1_ average pore radius: 420 to 490 (ns)

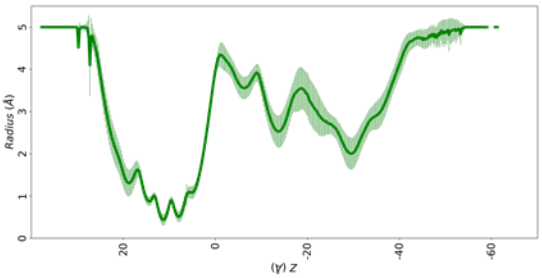

10-5-1_ average pore radius: 70 to 140 (ns)

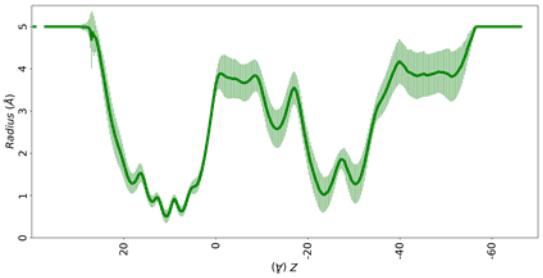

10-5-1_ average pore radius: 490 to 560 (ns)

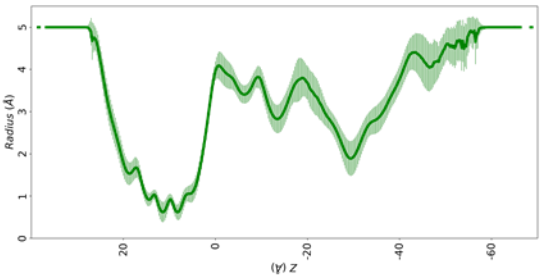

10-5-1_ average pore radius: 140 to 210 (ns)

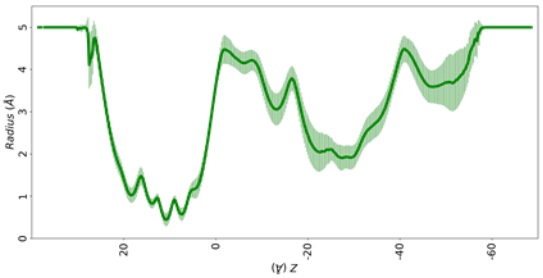

10-5-1_ average pore radius: 560 to 630 (ns)

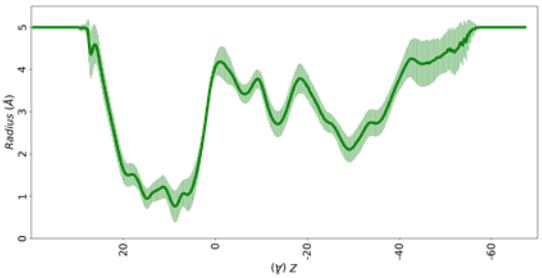

10-5-1_ average pore radius: 210 to 280 (ns)

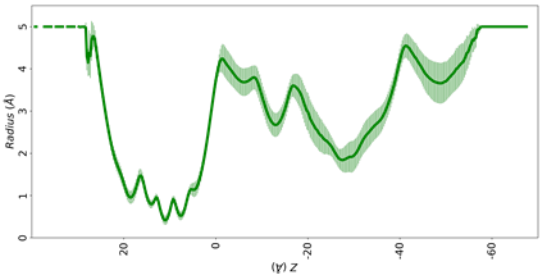

10-5-1_ average pore radius: 630 to 700 (ns)

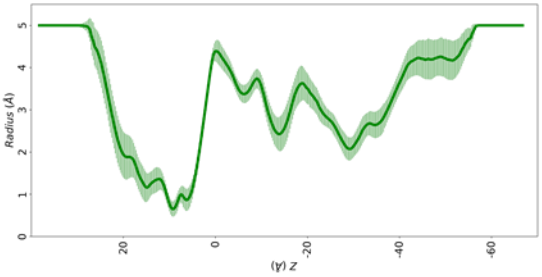

10-5-1_ average pore radius: 280 to 350 (ns)

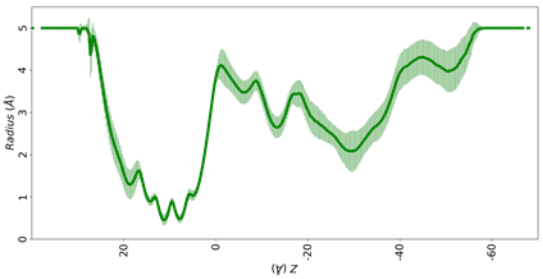

10-5-1_ average pore radius: 700 to 770 (ns)

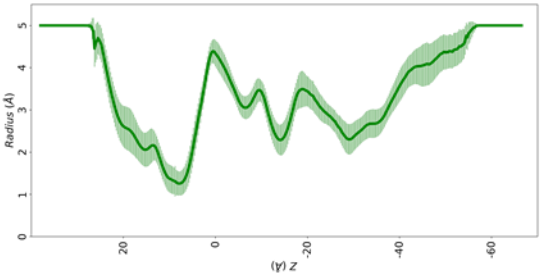

10-5-1_ average pore radius: 350 to 420 (ns)

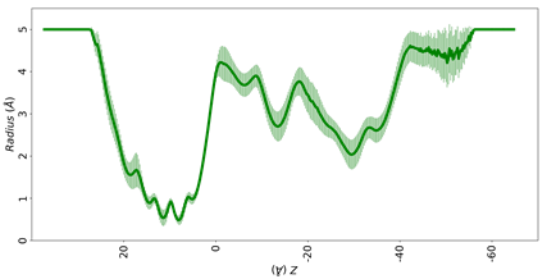

10-5-1_ average pore radius: 770 to 840 (ns)

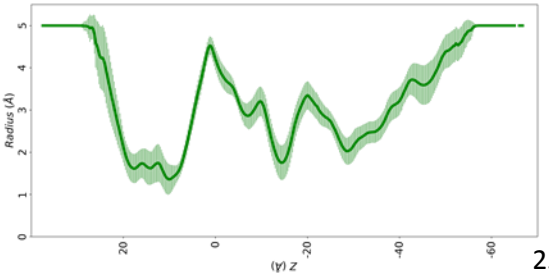

Simulation VII: 3

Occupacy in binding sites during time interval: 0..70 (*ns*)

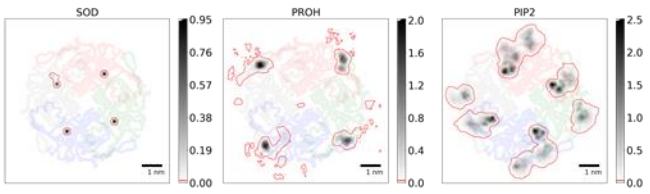

Occupacy in binding sites during time interval: 422..492 (*ns*)

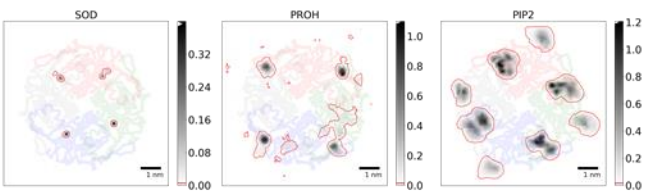

Occupacy in binding sites during time interval: 70..140 (*ns*)

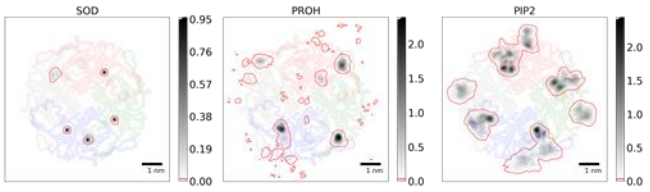

Occupacy in binding sites during time interval: 492..563 (*ns*)

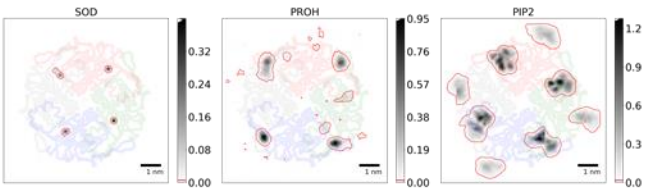

Occupacy in binding sites during time interval: 140..211 (*ns*)

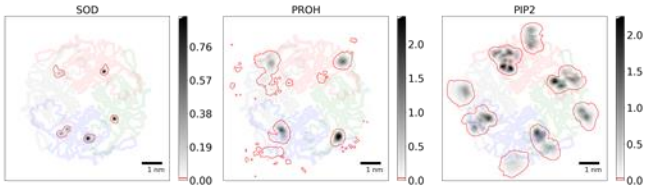

Occupacy in binding sites during time interval: 562..633 (*ns*)

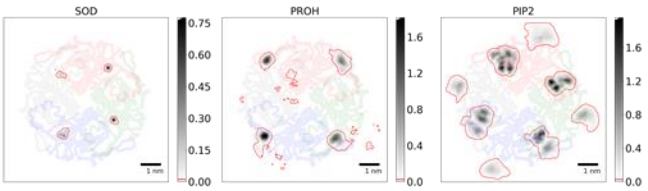

Occupacy in binding sites during time interval: 210..281 (*ns*)

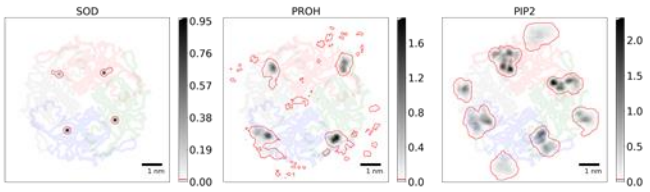

Occupacy in binding sites during time interval: 633..704 (*ns*)

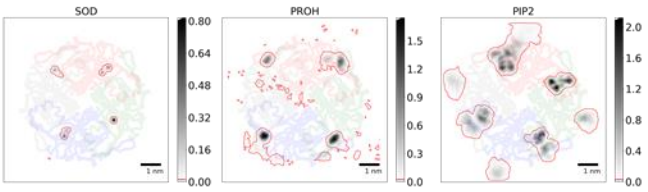

Occupacy in binding sites during time interval: 281..352 (*ns*)

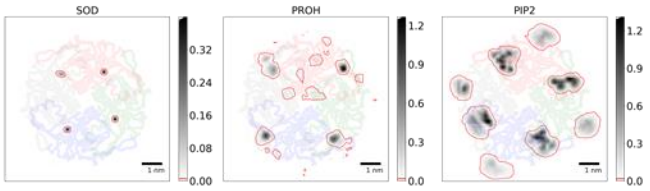

Occupacy in binding sites during time interval: 703..774 (*ns*)

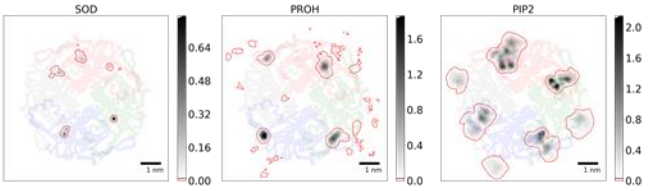

Occupacy in binding sites during time interval: 351..422 (*ns*)

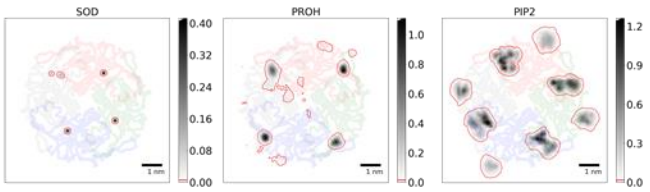

Occupacy in binding sites during time interval: 774..844 (*ns*)

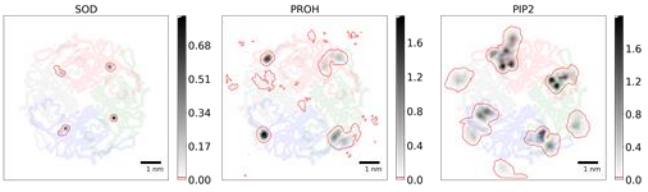

Simulation VII: 4

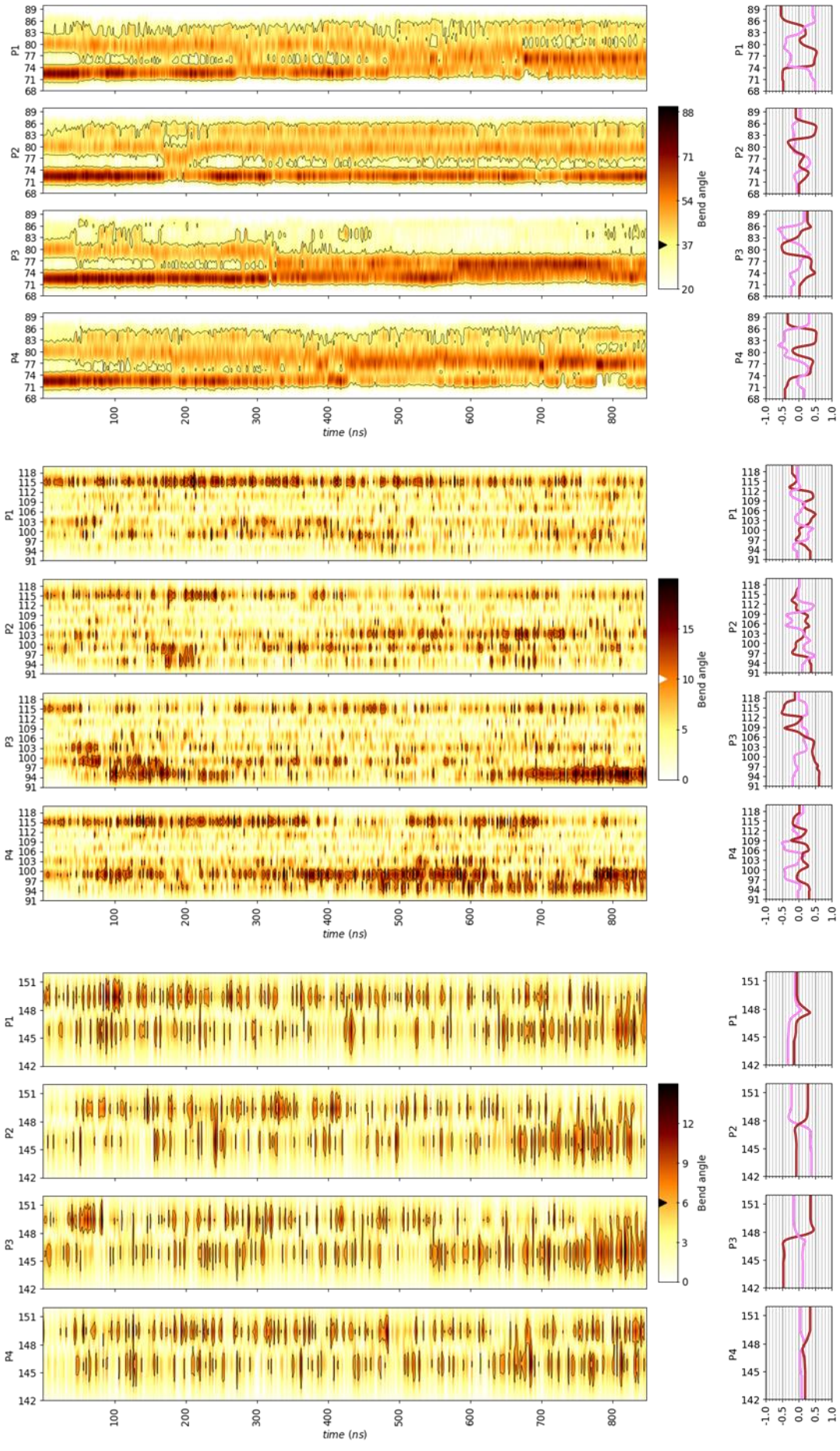

Simulation VII: 4

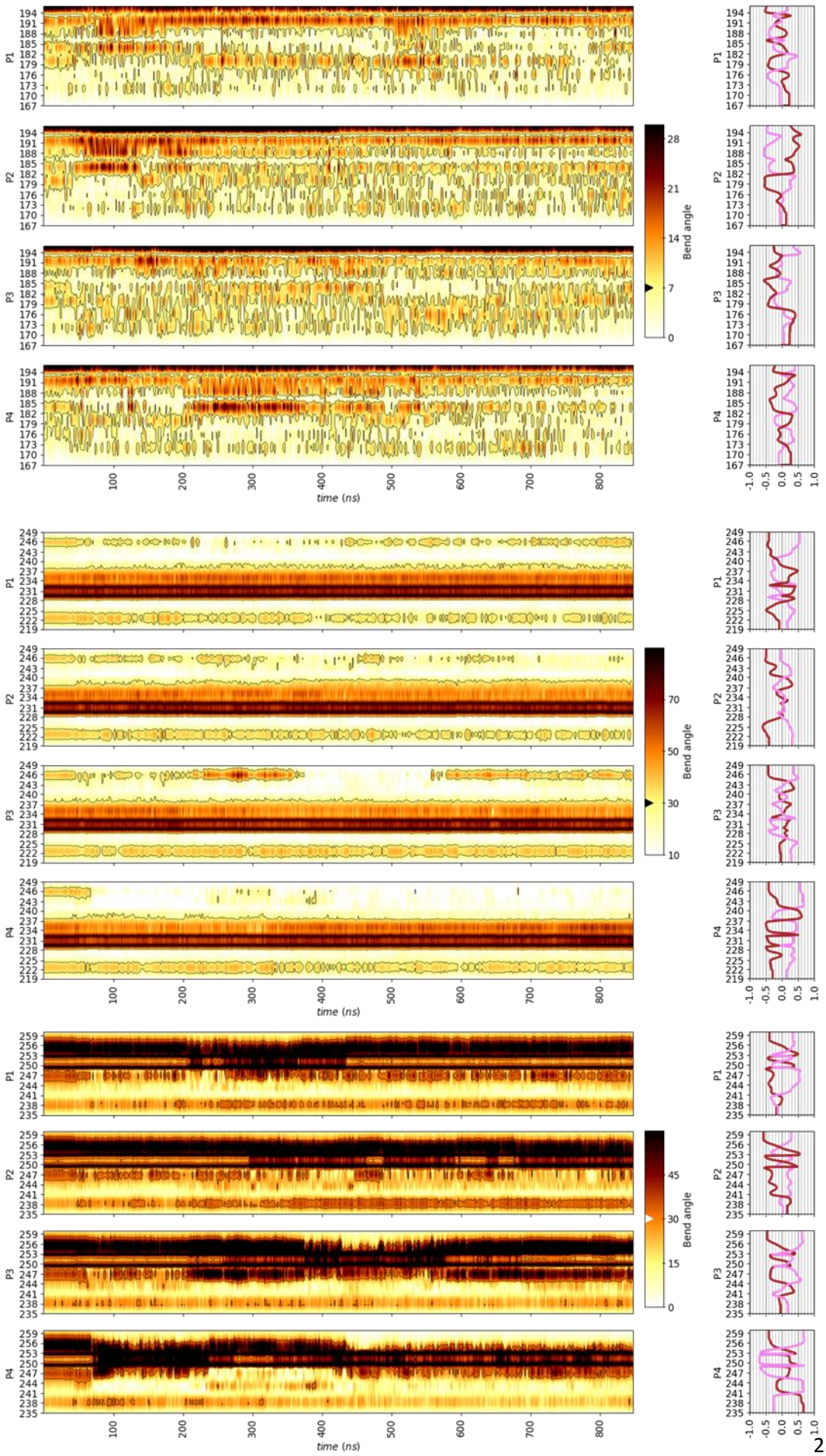

Simulation VII: 4

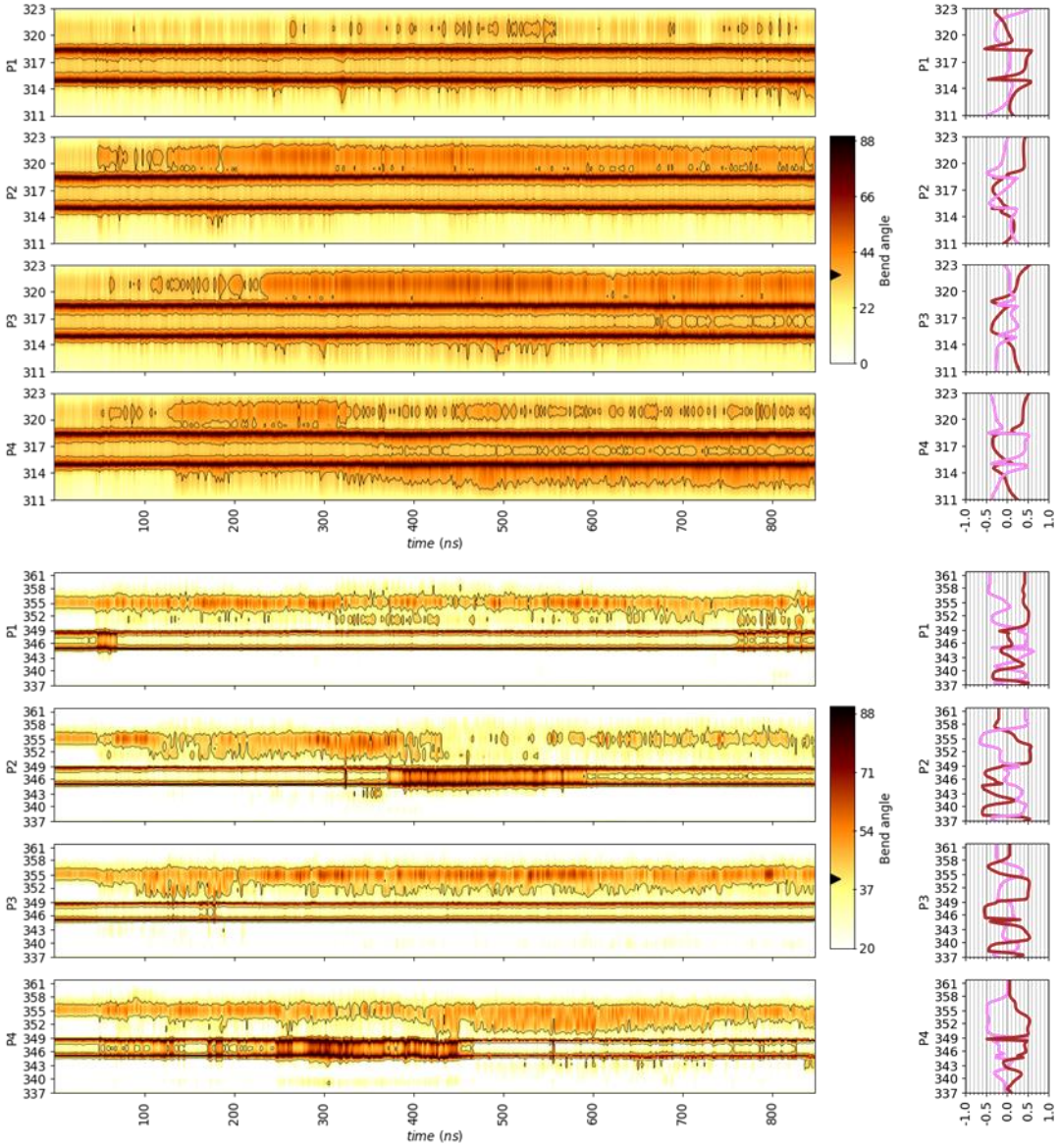

Simulation VII: 5

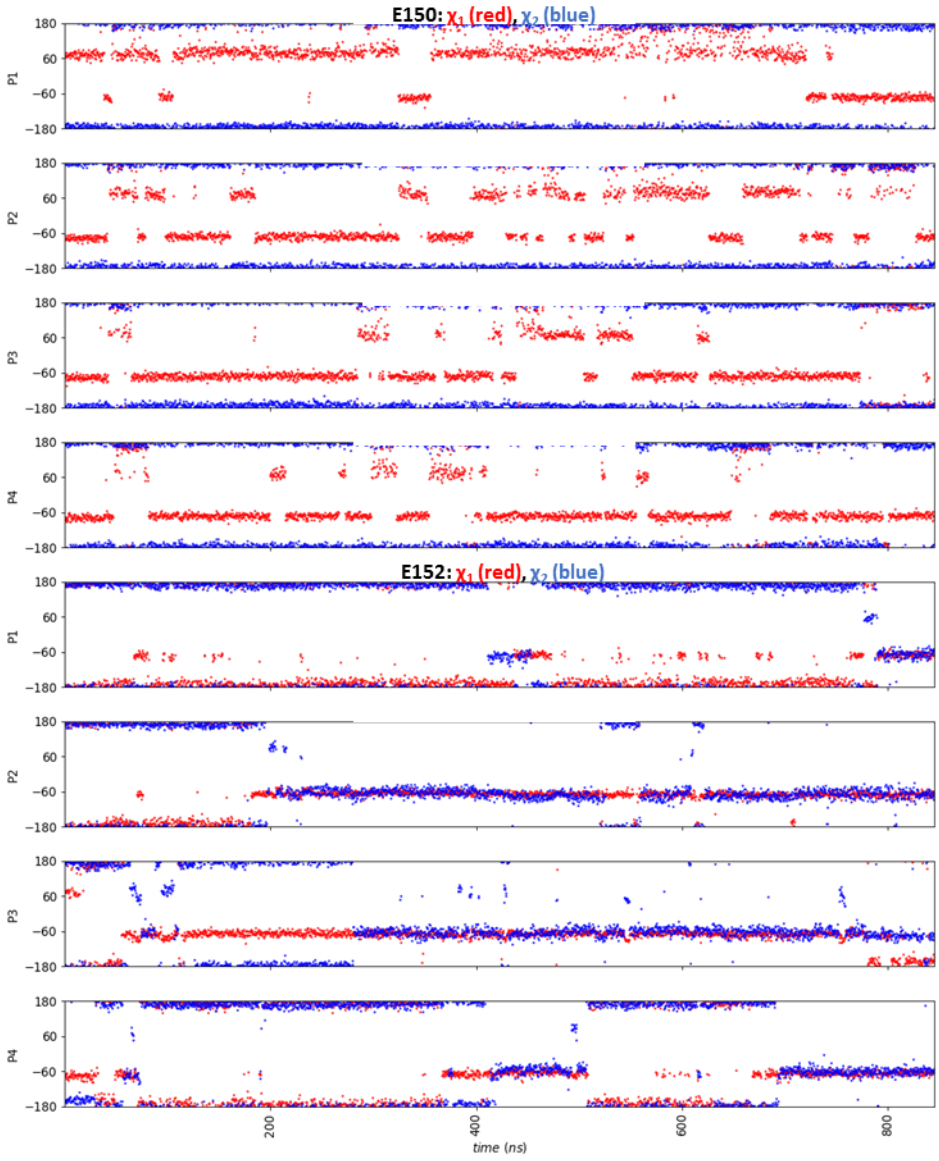

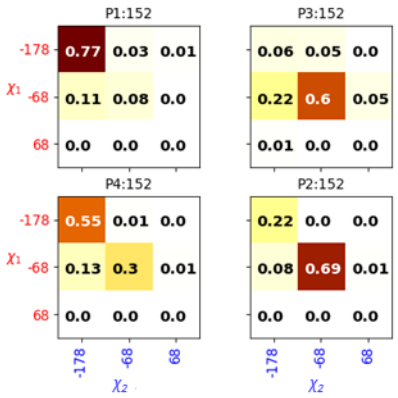

Simulation VII: 6

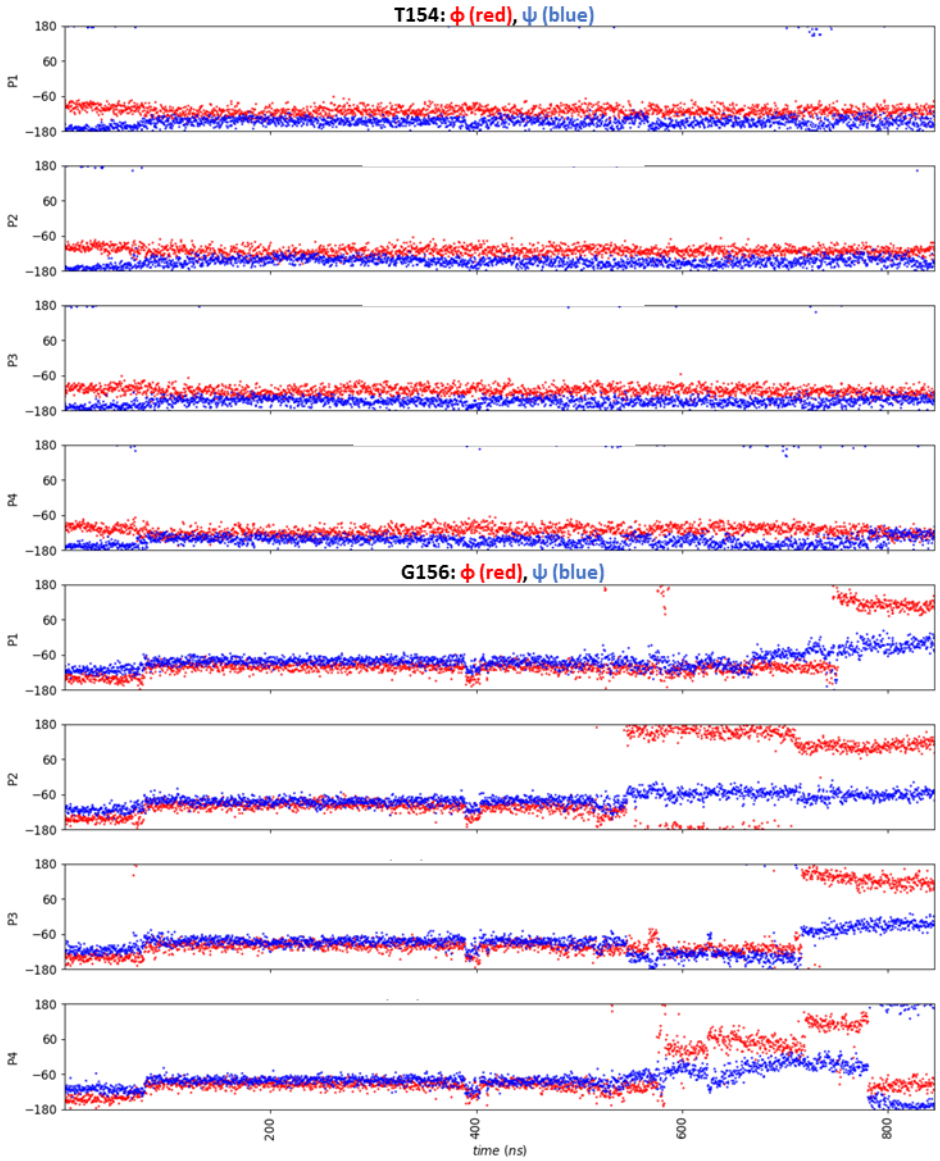

Simulation VII: 6

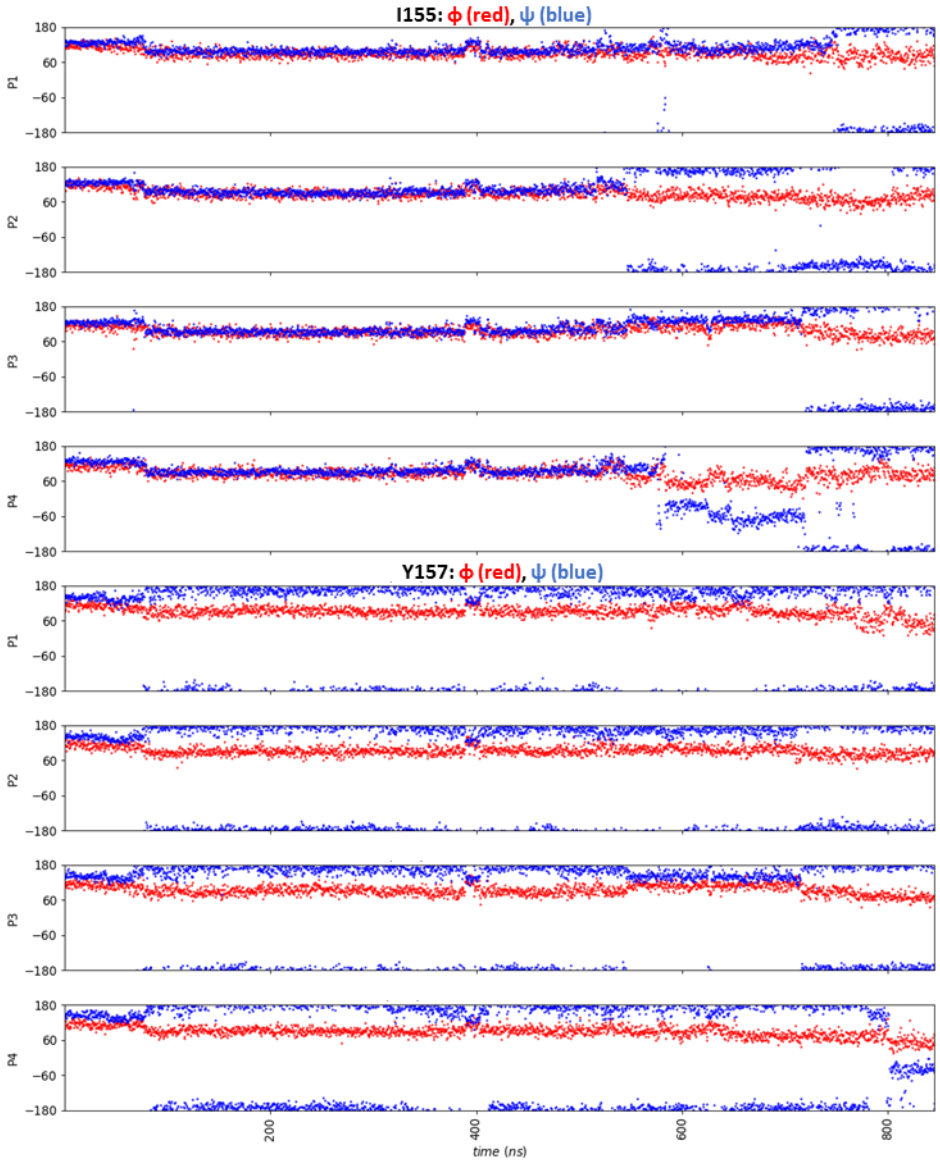

Simulation VII: 6

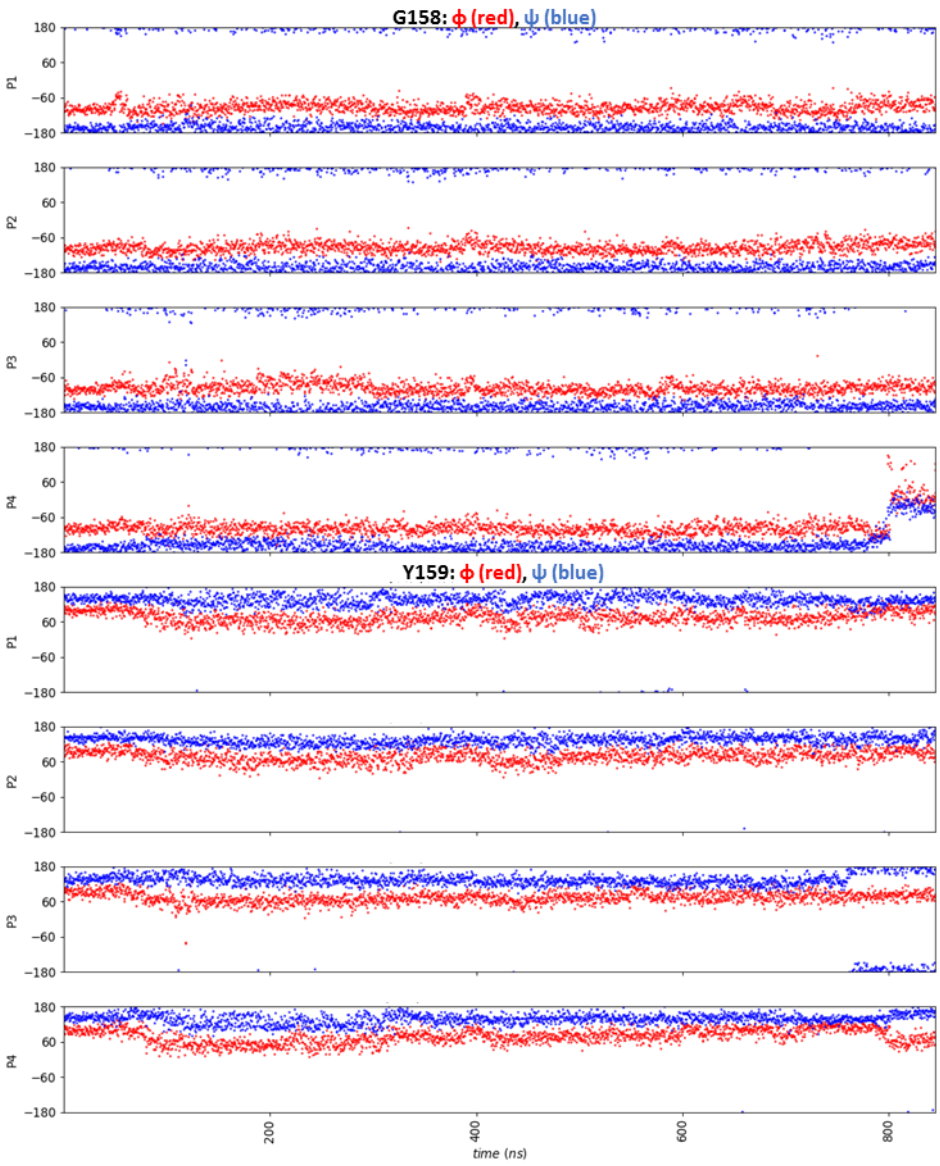

Simulation VII: 7

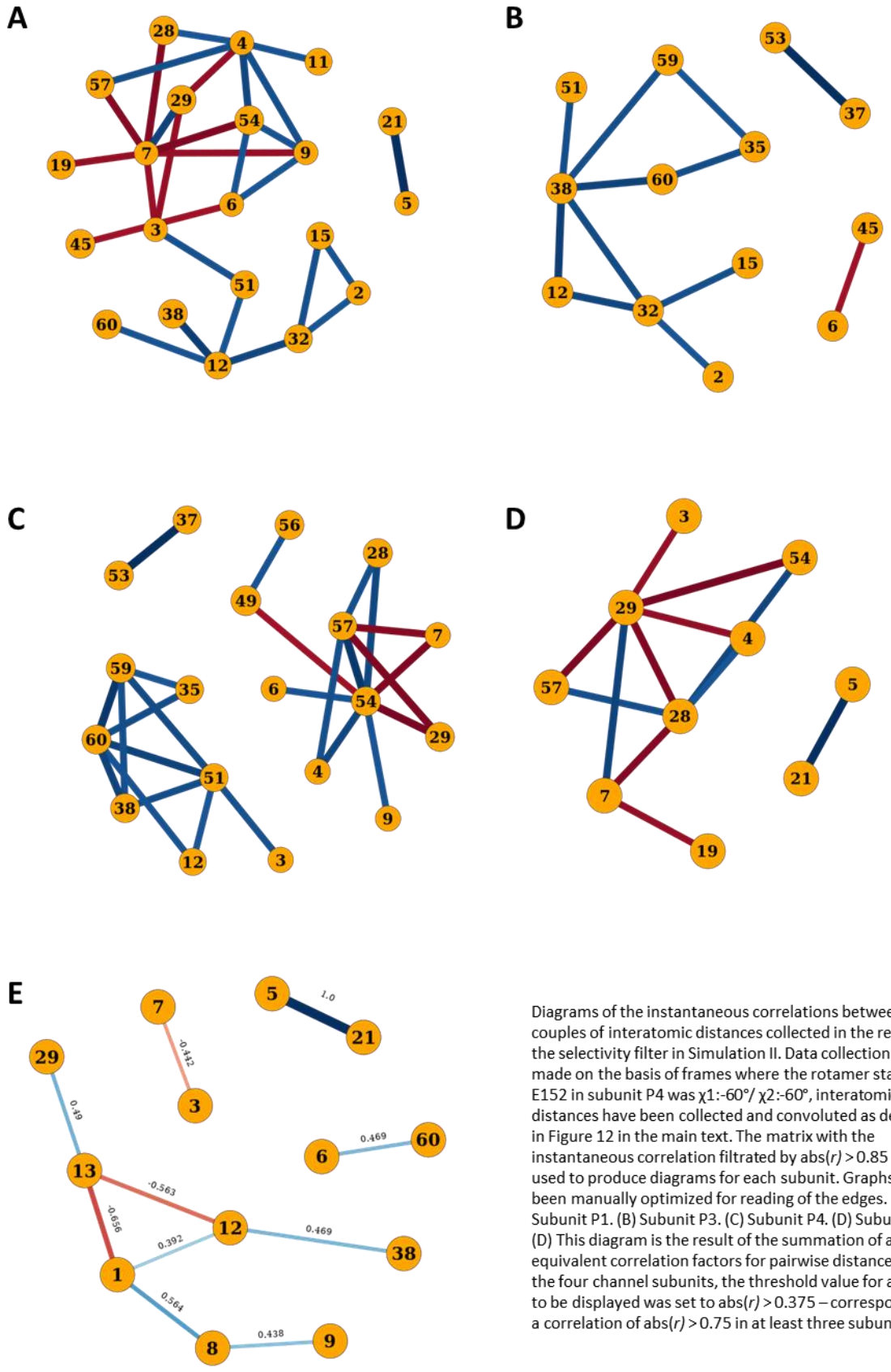

Diagrams of the instantaneous correlations between couples of interatomic distances collected in the region of the selectivity filter in Simulation II. Data collection was made on the basis of frames where the rotamer state of E152 in subunit P4 was χ1:-60°/ χ2:-60°, interatomic distances have been collected and convoluted as described in Figure 12 in the main text. The matrix with the instantaneous correlation filtrated by abs(*r*) > 0.85 was used to produce diagrams for each subunit. Graphs have been manually optimized for reading of the edges. (A) Subunit P1. (B) Subunit P3. (C) Subunit P4. (D) Subunit P2. (D) This diagram is the result of the summation of all equivalent correlation factors for pairwise distance among the four channel subunits, the threshold value for an edge to be displayed was set to abs(*r*) > 0.375 – corresponding to a correlation of abs(*r*) > 0.75 in at least three subunits.

Simulation VII: 8

A

	P1	P3	P2	P4
P1	S	N	O	P
P3	P	S	N	O
P2	O	P	S	N
P4	N	O	P	S

P1	P3	P2	P4	
0	14	7	21	P1:105:CA | P2:105:CA
1	15	8	22	P1:188:CA | P2:188:CA
2	16	9	23	P1:105:OG1 | P1:152:CD
3	17	10	24	P1:155:CA | P3:151:CA
4	18	11	25	P1:155:CA | P3:173:CA
5	19	12	26	P1:155:CD | P3:173:CG
6	20	13	27	P1:155:CA | P2:155:CA

B

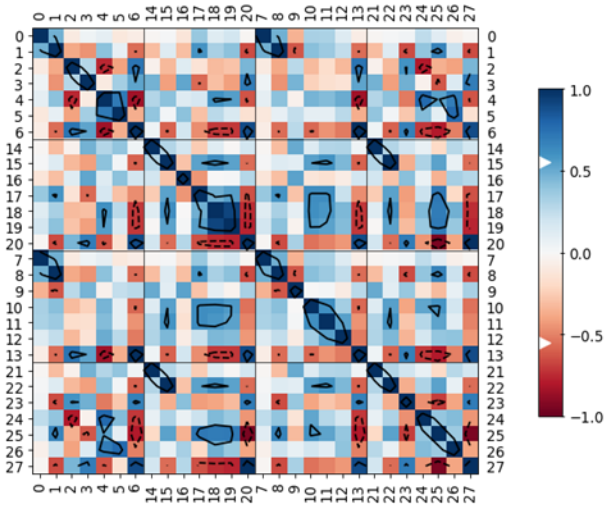

C

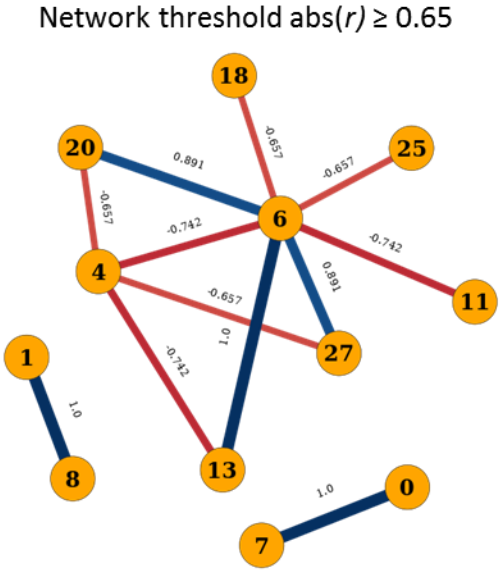

D

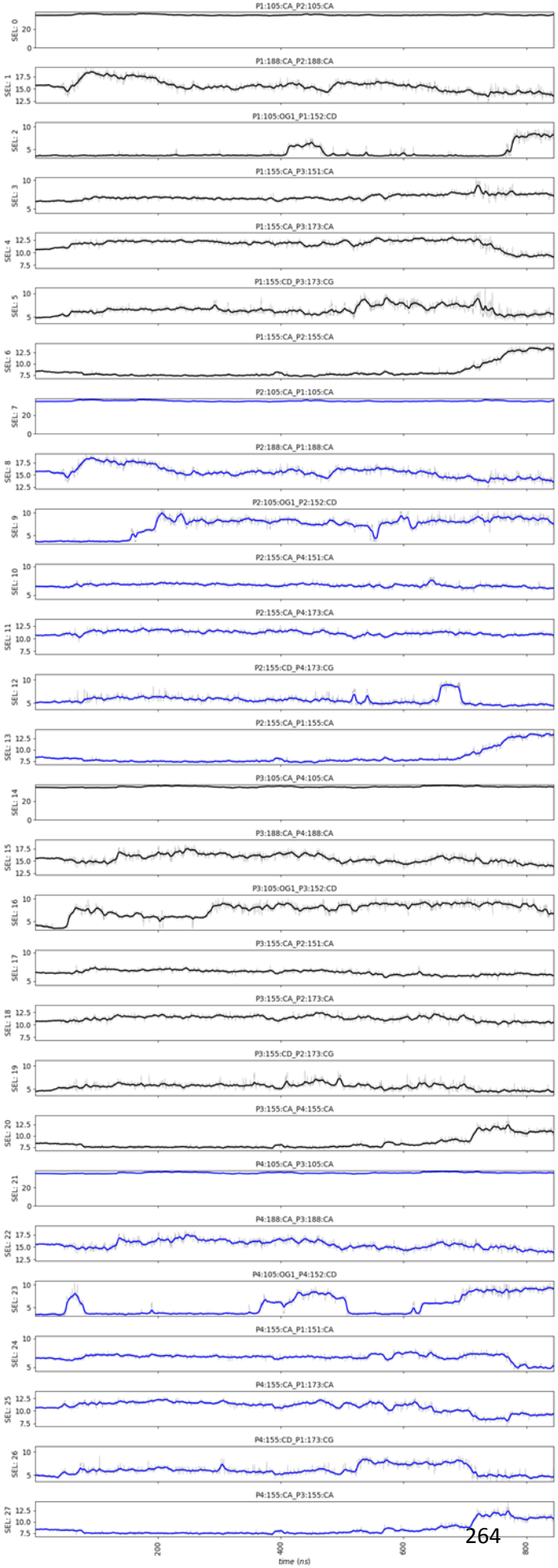

Simulation VII: 9

Norm: #7

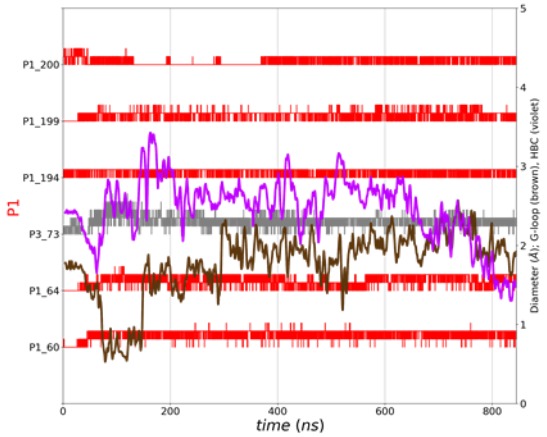

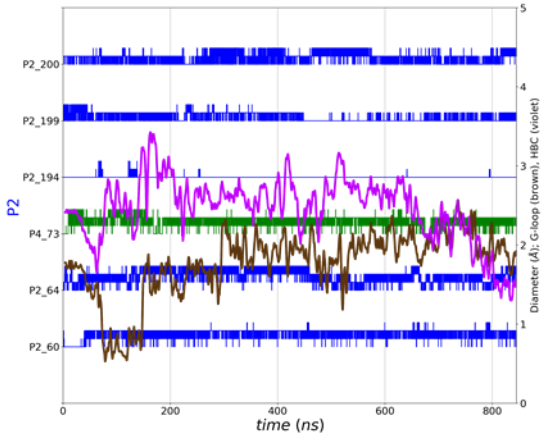

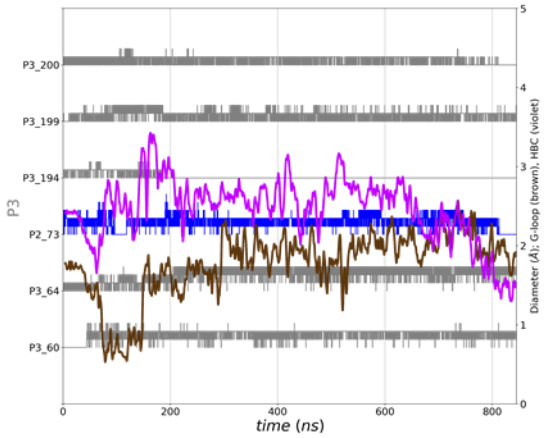

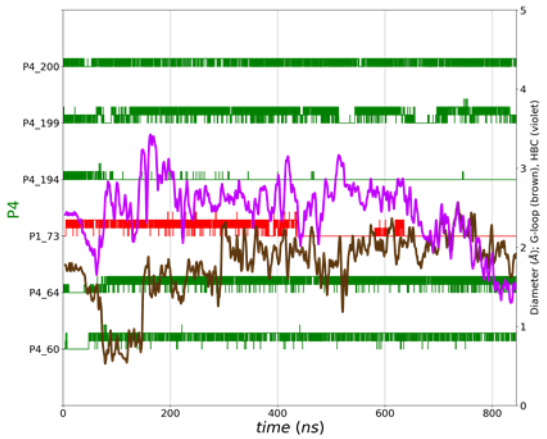

Norm: #6

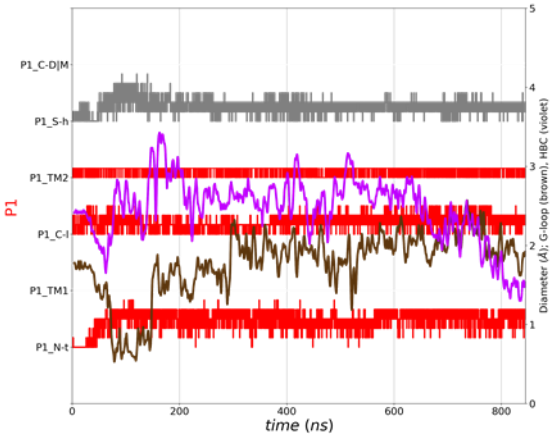

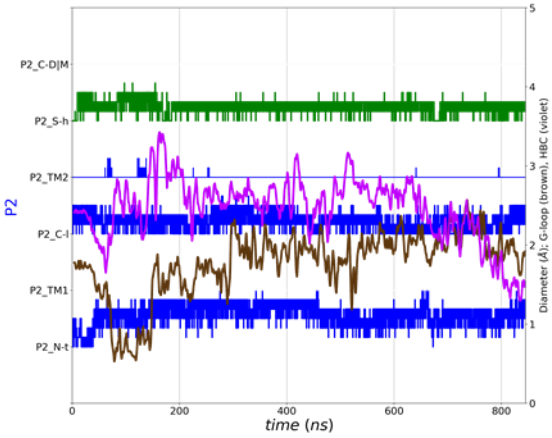

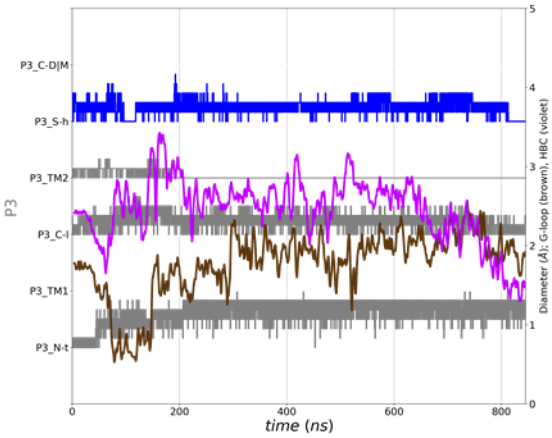

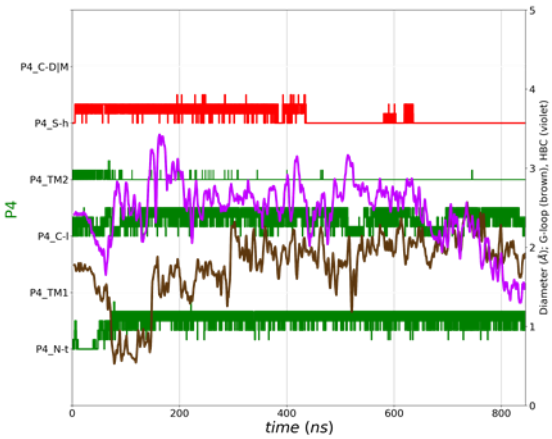

Simulation VII: 10

Norm: #7

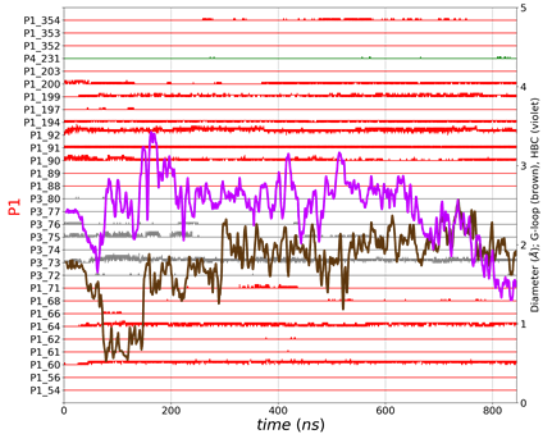

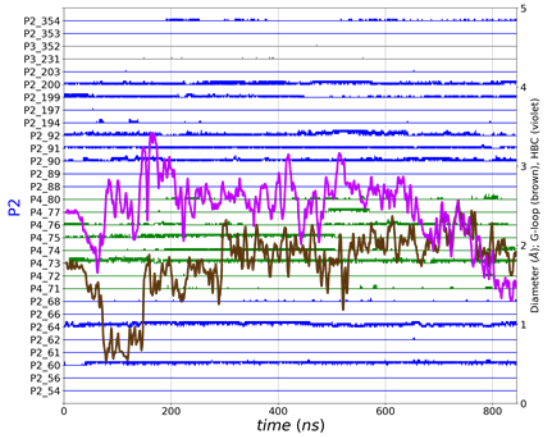

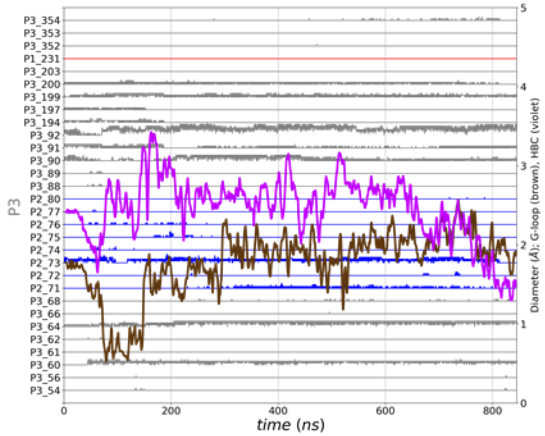

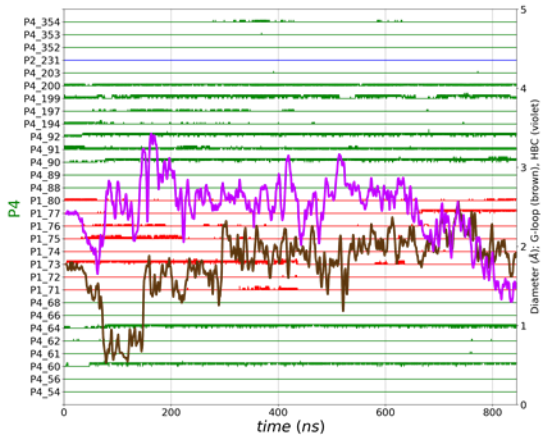

Norm: #10

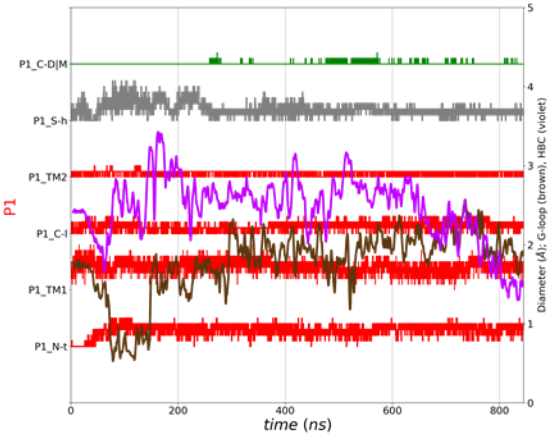

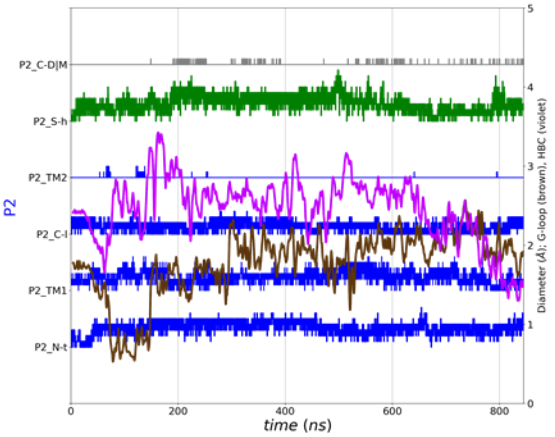

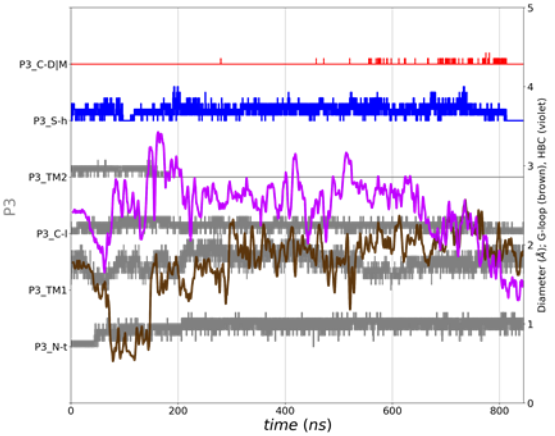

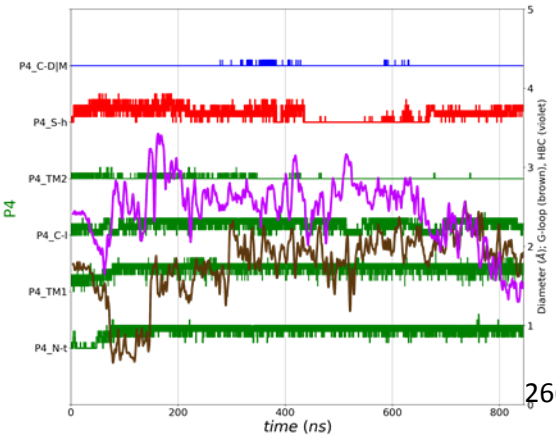

Simulation VII: 11

Average electrostatic potential along the pore | **Electrostatic potential in the simulation box (Y_{axis}= 0)**

A

50 to 70 ns; V_m= -0,07 *(Volts)*

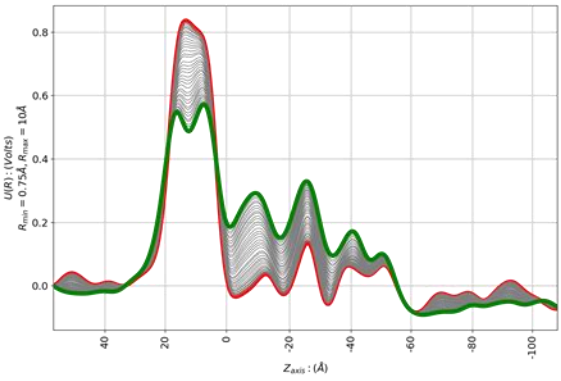

50 to 70 ns; V_m= -0,07 *(Volts)*

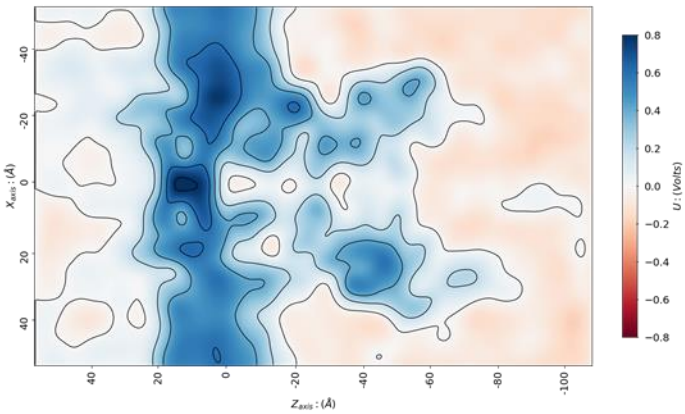

B

420 to 440 ns; V_m= -0,07 *(Volts)*

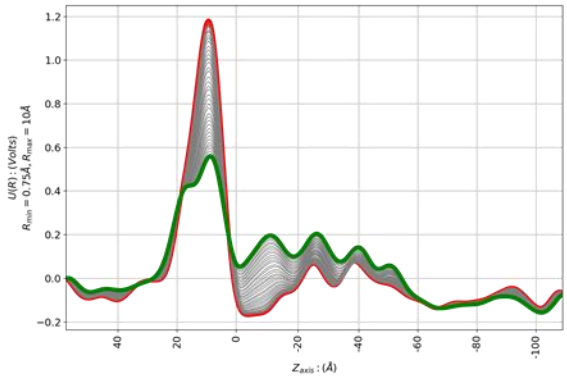

420 to 440 ns; V_m= -0,07 *(Volts)*

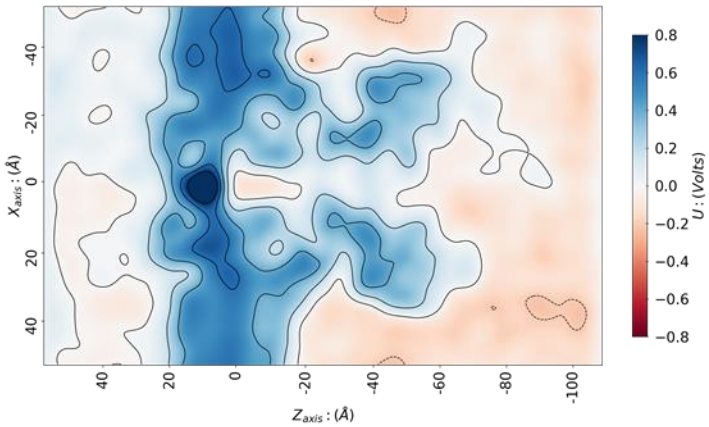

C

620 to 640 ns; V_m= -0,7 *(Volts)*

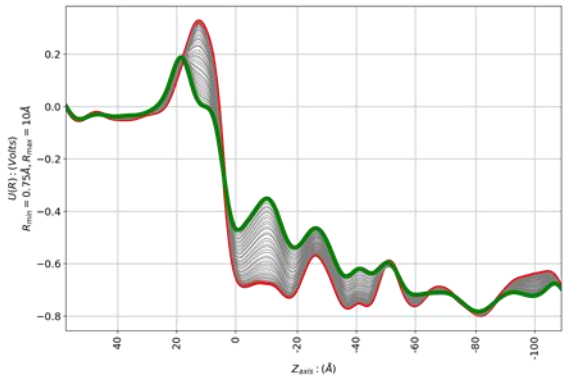

620 to 640 ns; V_m= -0,7 *(Volts)*

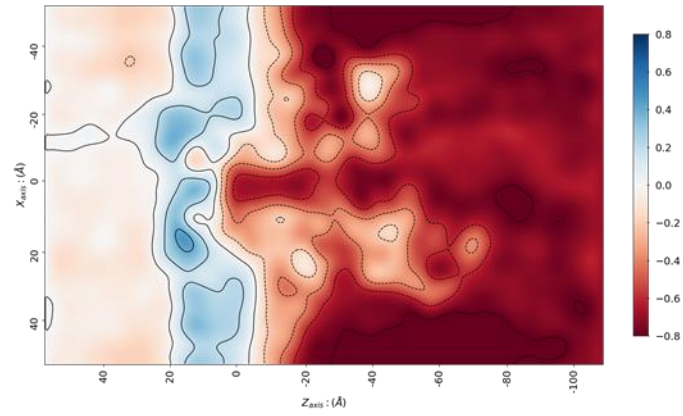

D

820 to 840 ns; V_m= -0,7 *(Volts)*

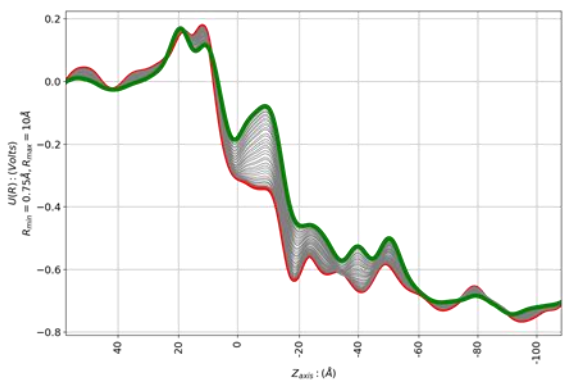

820 to 840 ns; V_m= -0,7 *(Volts)*

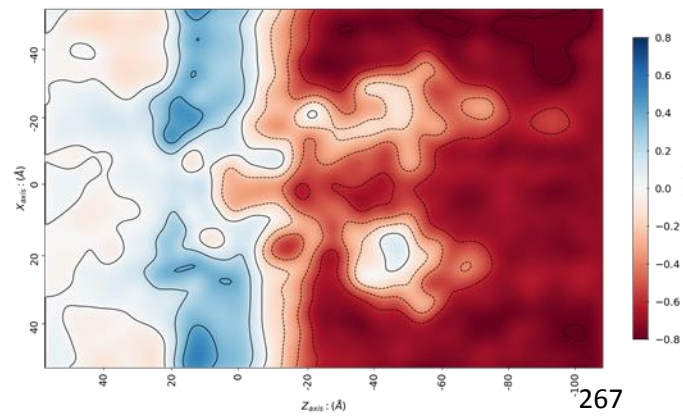

8.10 Simulation VIII

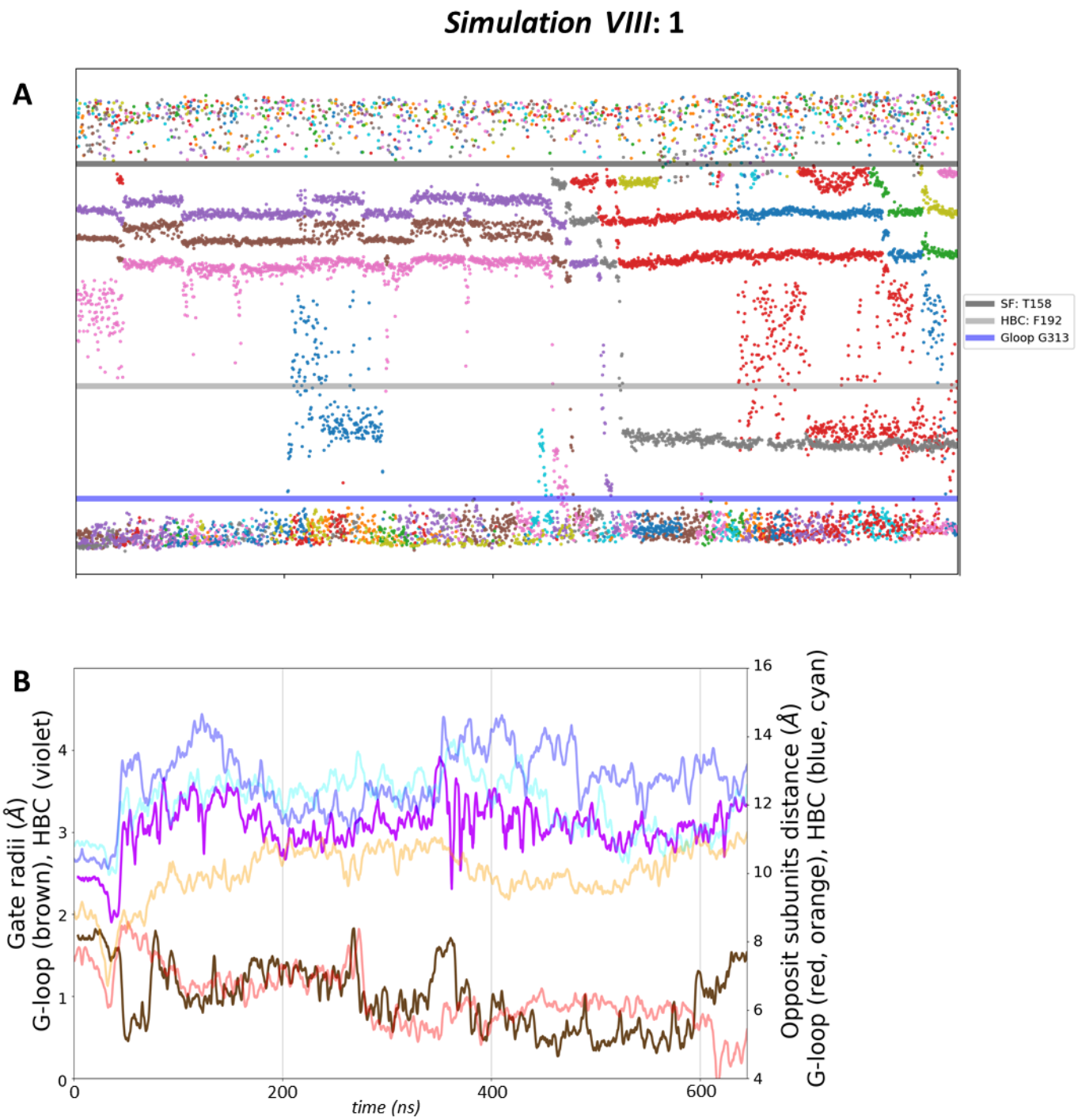

Simulation VIII: 2

10-5-2_ average pore radius: 0 to 70 (ns)

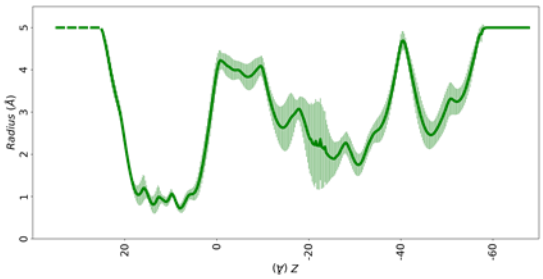

10-5-2_ average pore radius: 420 to 490 (ns)

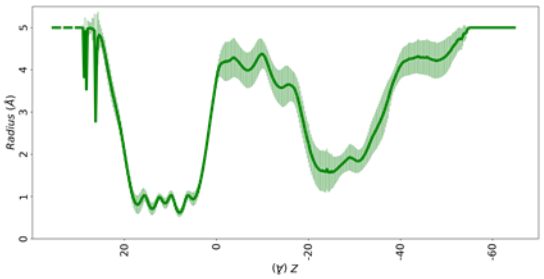

10-5-2_ average pore radius: 70 to 140 (ns)

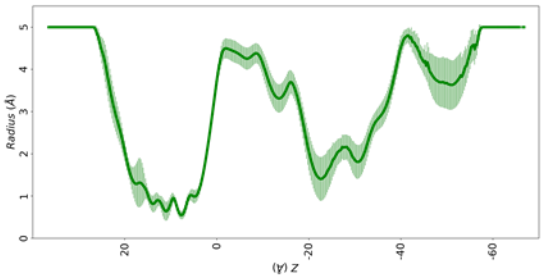

10-5-2_ average pore radius: 490 to 560 (ns)

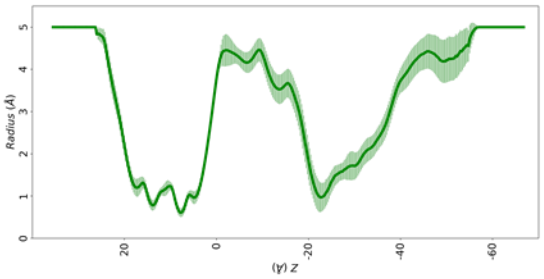

10-5-2_ average pore radius: 140 to 210 (ns)

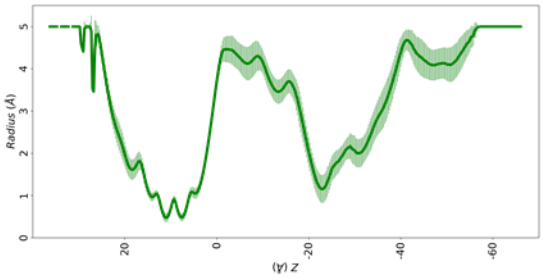

10-5-2_ average pore radius: 560 to 630 (ns)

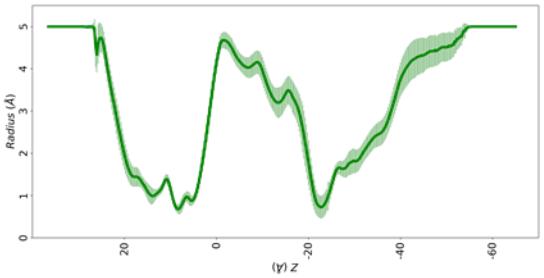

10-5-2_ average pore radius: 210 to 280 (ns)

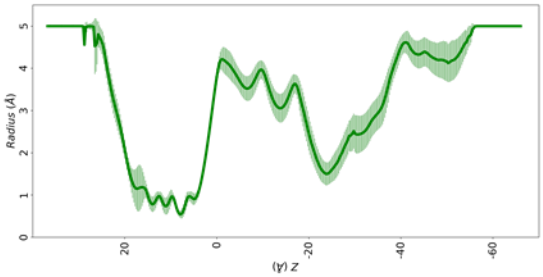

10-5-2_ average pore radius: 630 to 700 (ns)

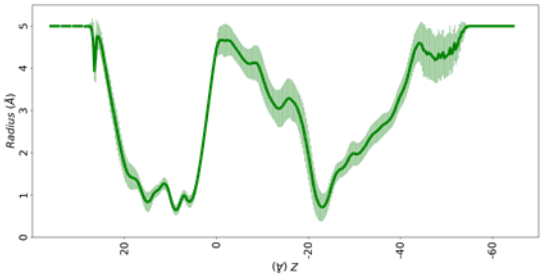

10-5-2_ average pore radius: 280 to 350 (ns)

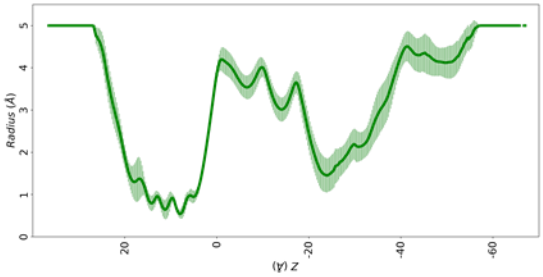

10-5-2_ average pore radius: 700 to 770 (ns)

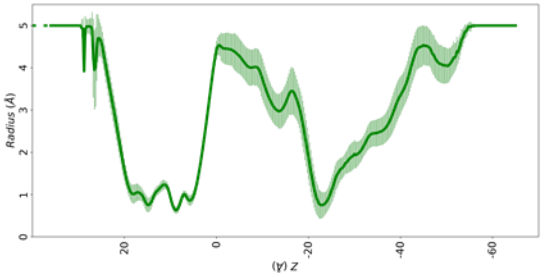

10-5-2_ average pore radius: 350 to 420 (ns)

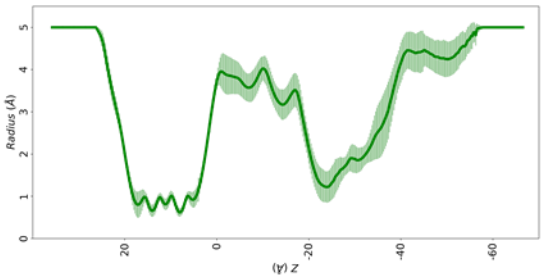

10-5-2_ average pore radius: 770 to 840 (ns)

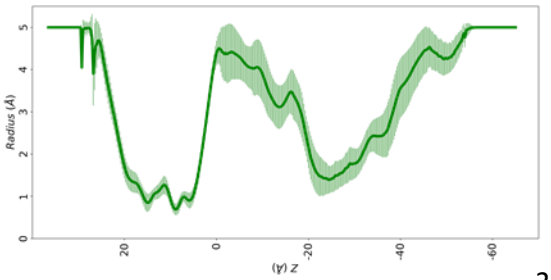

Simulation VIII: 3

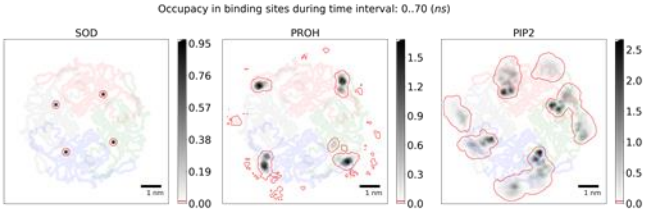

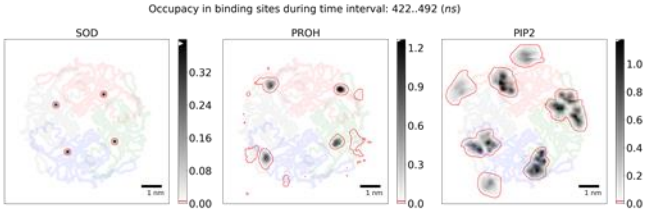

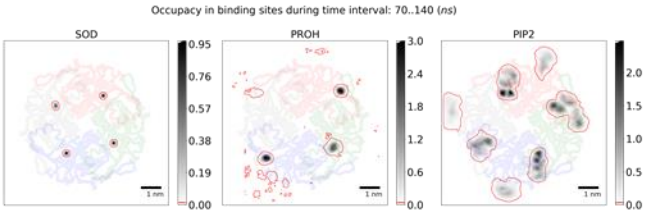

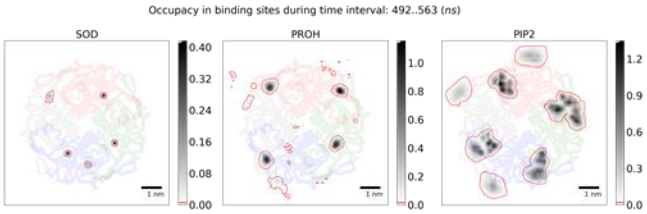

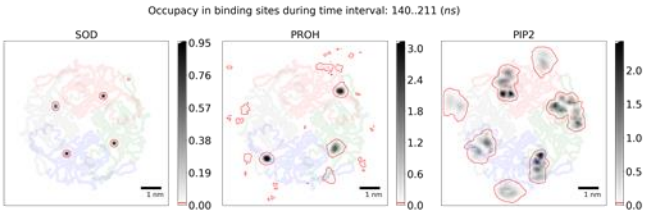

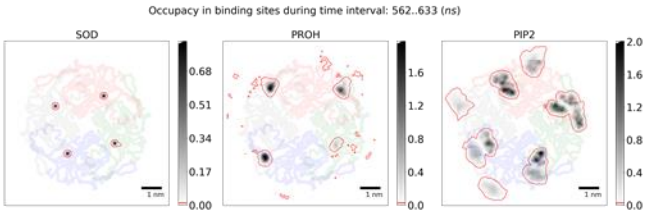

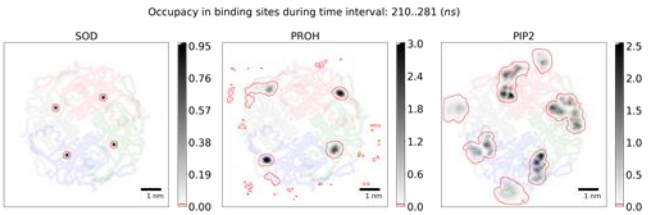

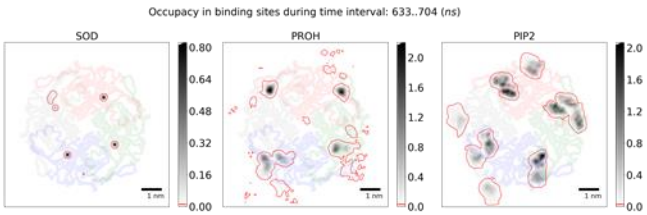

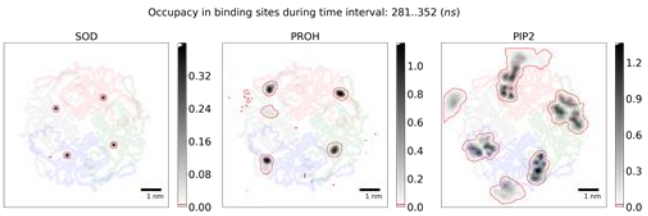

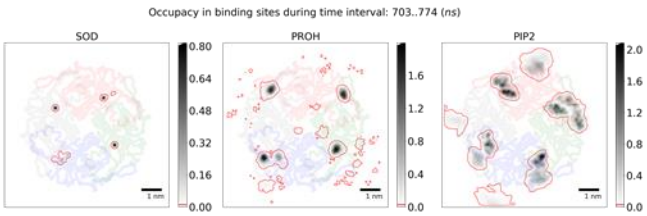

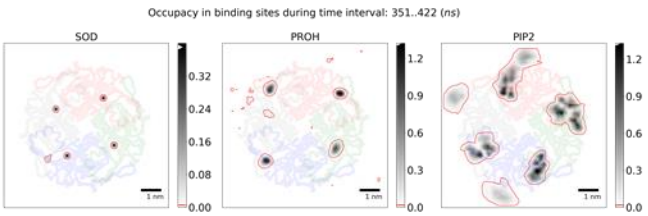

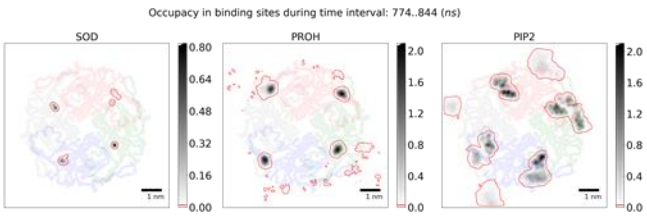

Simulation VIII: 4

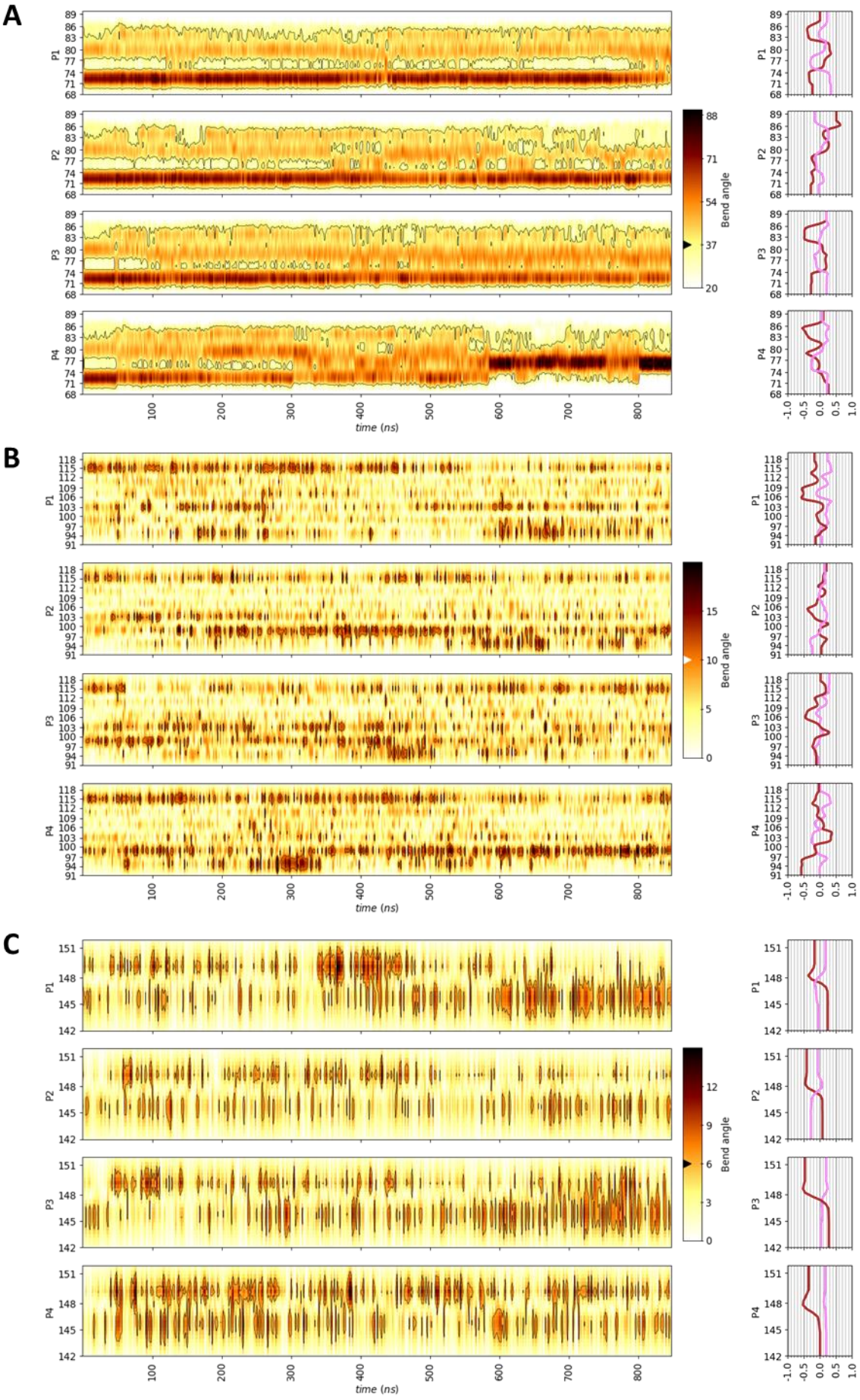

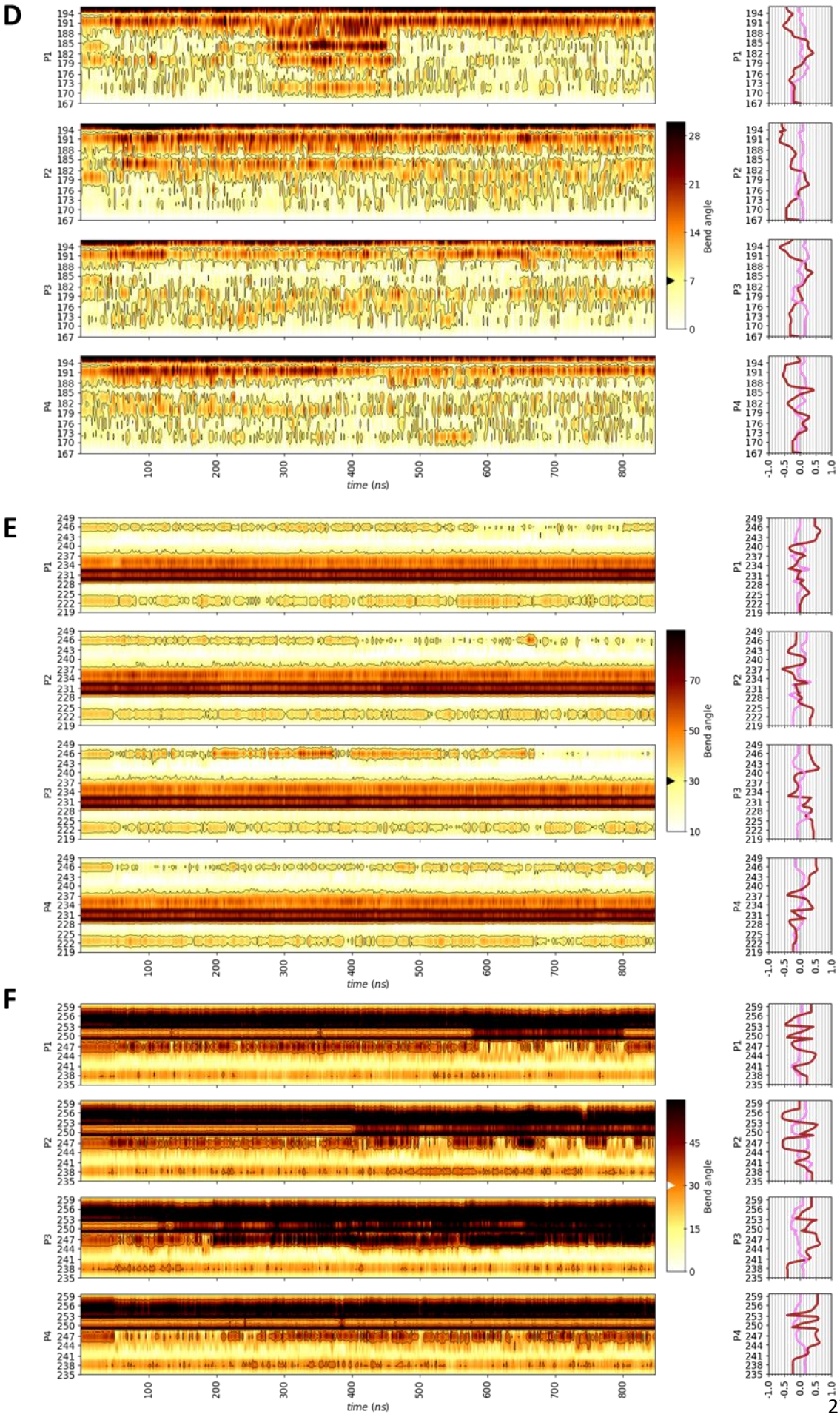
D
E
F
P1
P2
P3
P4
Bend angle
time (ns)

Simulation VIII: 4

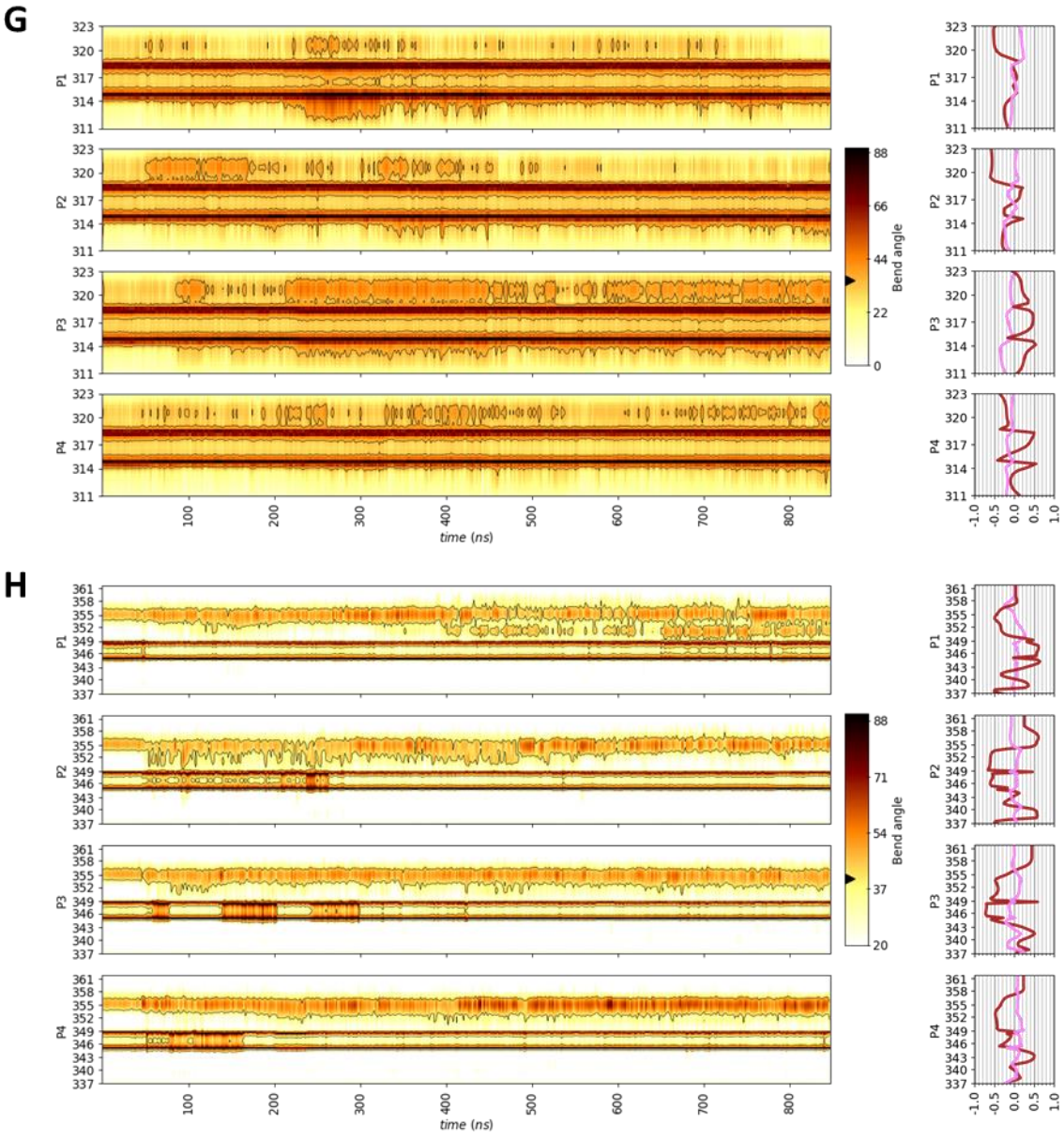

Simulation VIII: 9

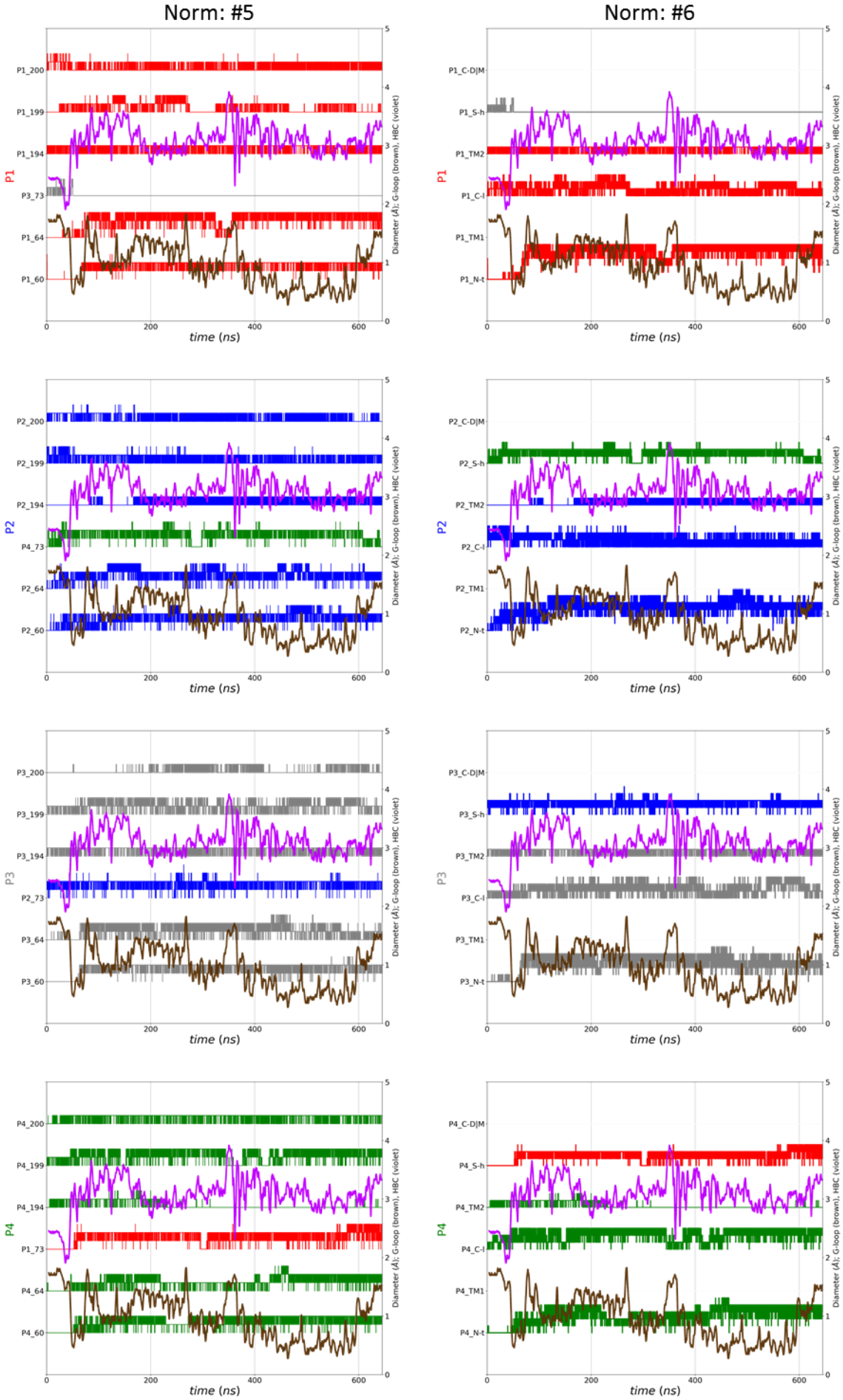

Simulation VIII: 10

Norm: #5

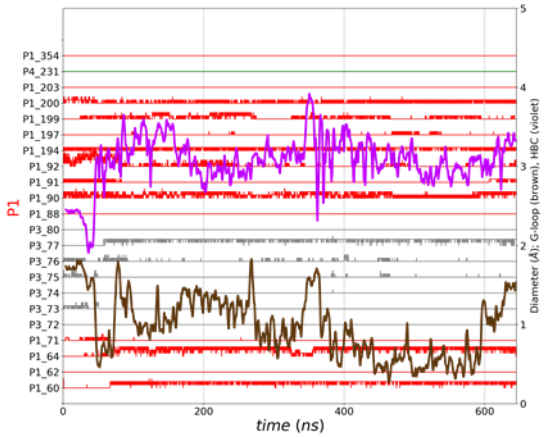

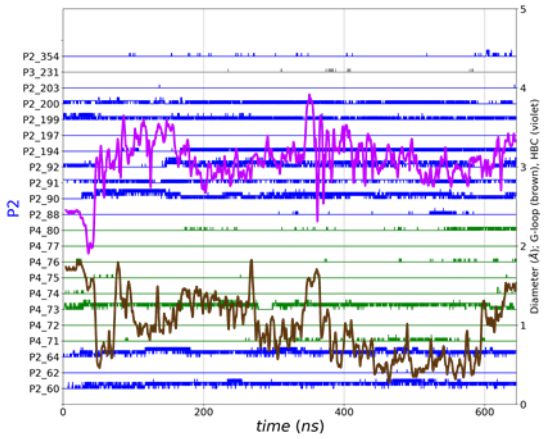

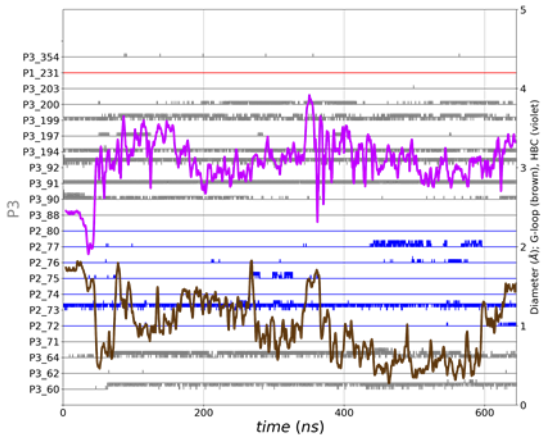

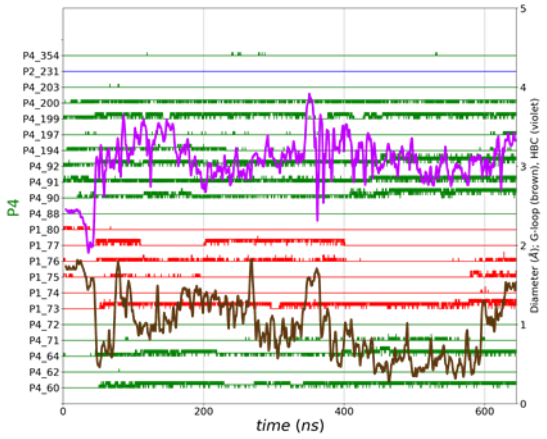

Norm: #6

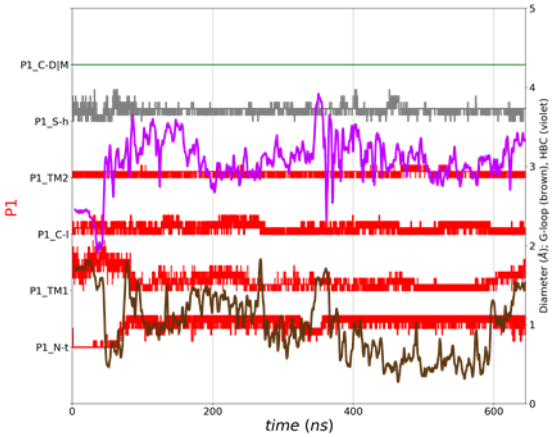

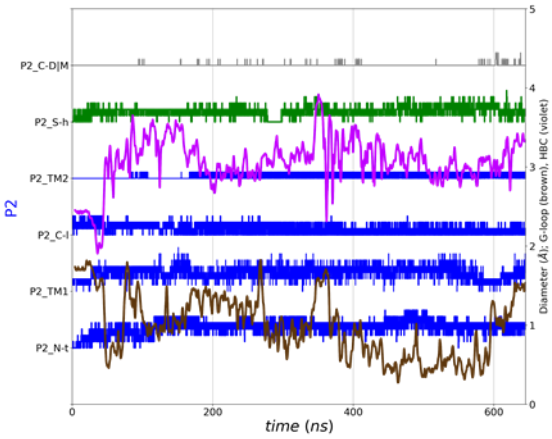

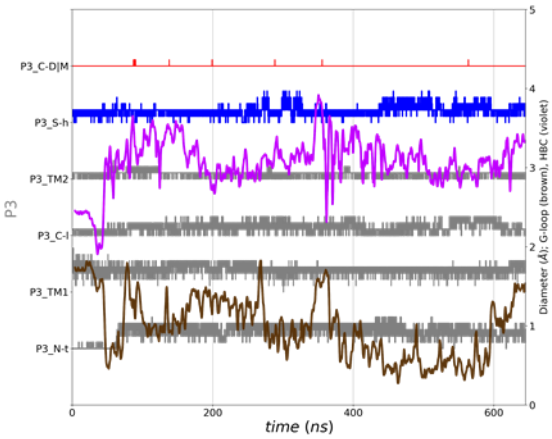

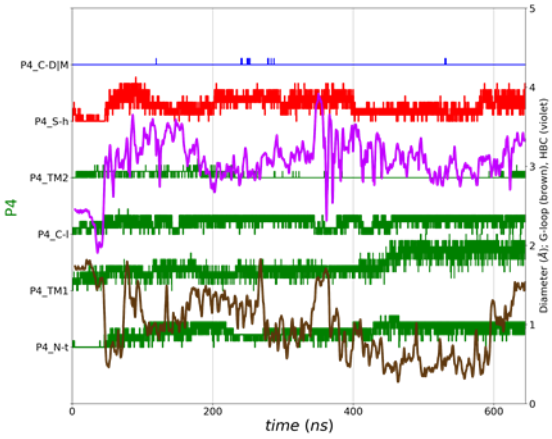

Simulation VIII: 11

Average electrostatic potential along the pore

Electrostatic potential in the simulation box *(Y_{axis}= 0)*

A

50 to 70 ns; V_m= -0,07 *(Volts)*

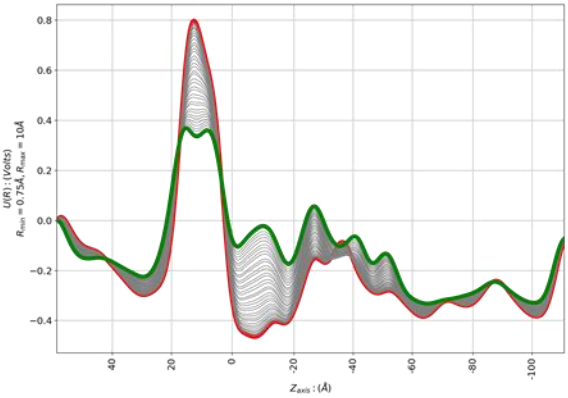

50 to 70 ns; V_m= -0,07 *(Volts)*

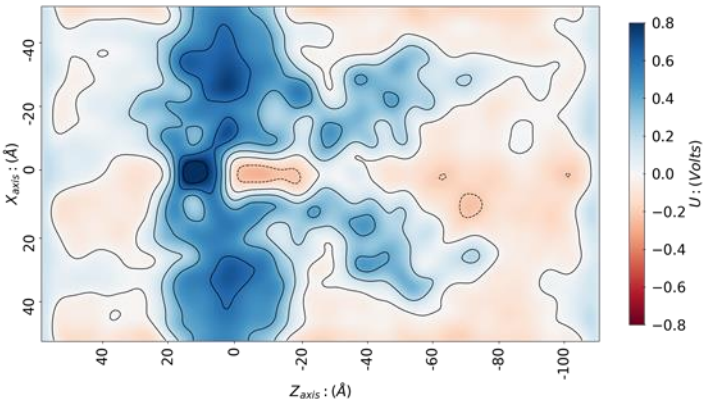

B

420 to 440 ns; V_m= -0,07 *(Volts)*

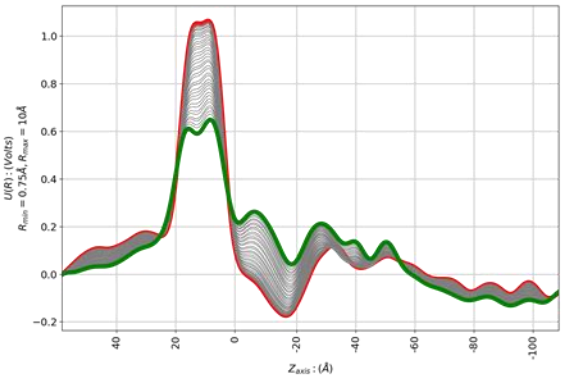

420 to 440 ns; V_m= -0,07 *(Volts)*

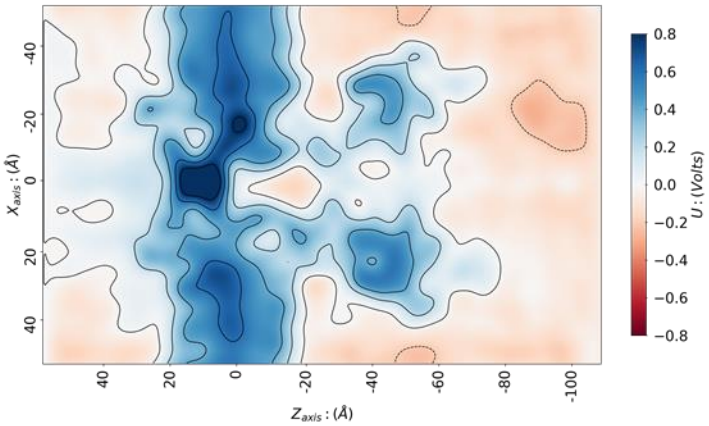

C

620 to 640 ns; V_m= -0,7 *(Volts)*

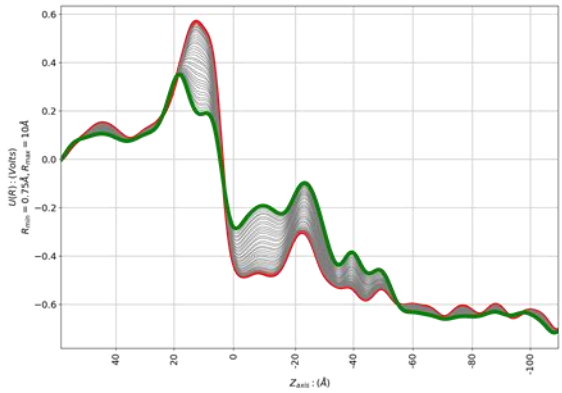

620 to 640 ns; V_m= -0,7 *(Volts)*

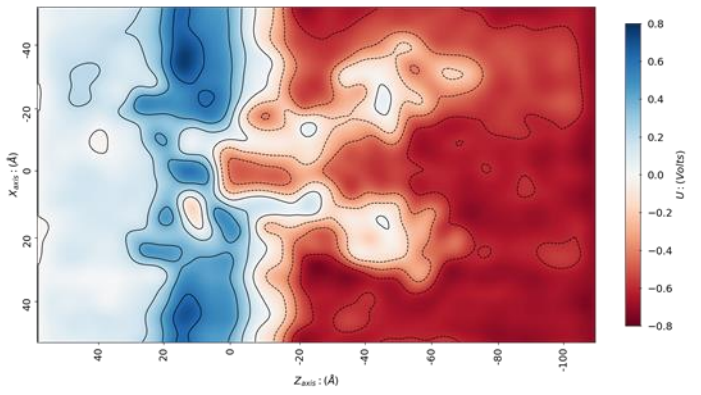

D

820 to 840 ns; V_m= -0,7 *(Volts)*

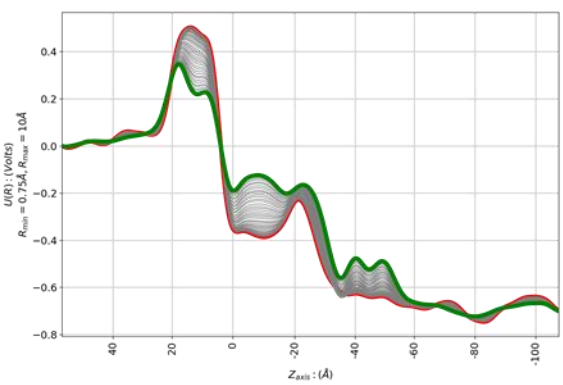

820 to 840 ns; V_m= -0,7 *(Volts)*

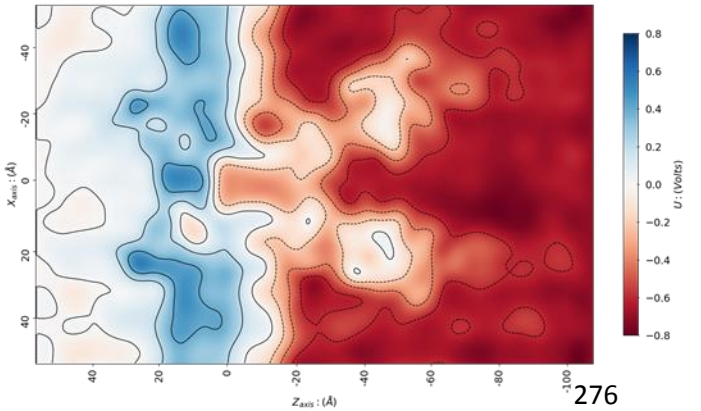

8.11 Simulation IX

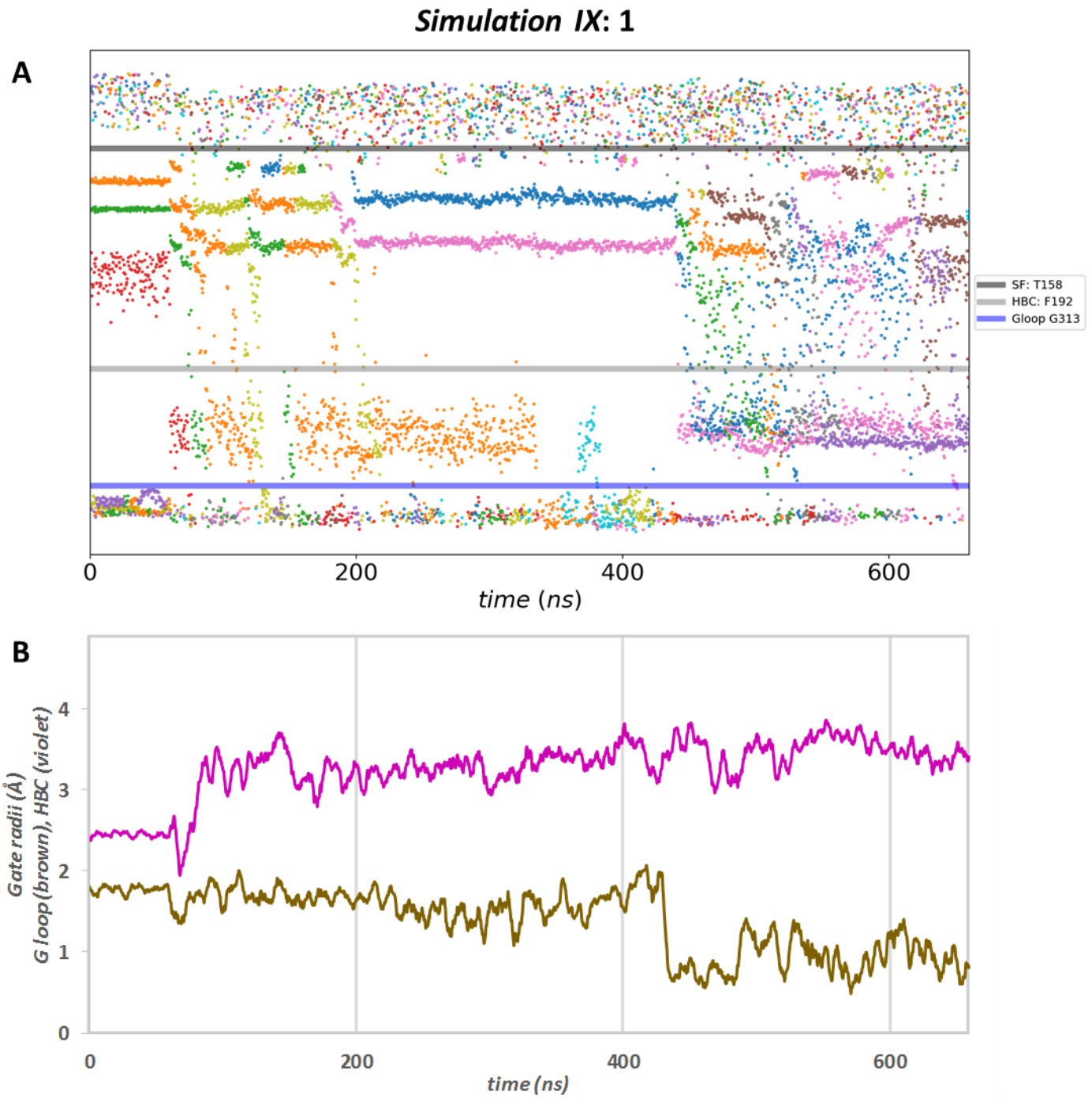

Simulation IX: 2

4KFM_EF-2-neg700mV_ average pore radius: 0 to 70 (ns)

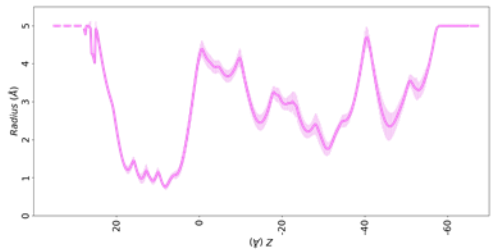

4KFM_EF-2-neg700mV_ average pore radius: 350 to 420 (ns)

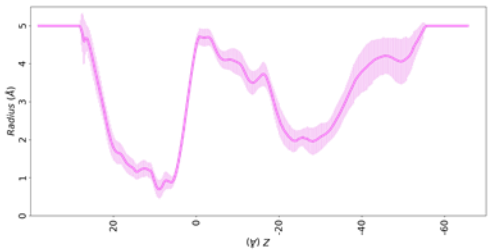

4KFM_EF-2-neg700mV_ average pore radius: 70 to 140 (ns)

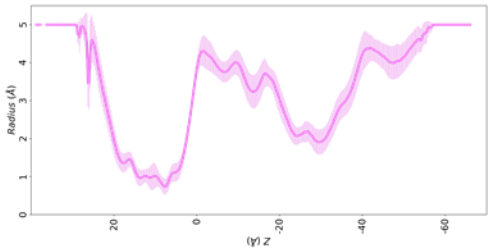

4KFM_EF-2-neg700mV_ average pore radius: 420 to 490 (ns)

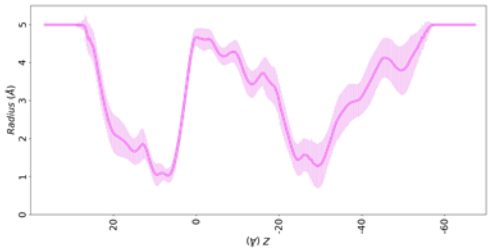

4KFM_EF-2-neg700mV_ average pore radius: 140 to 210 (ns)

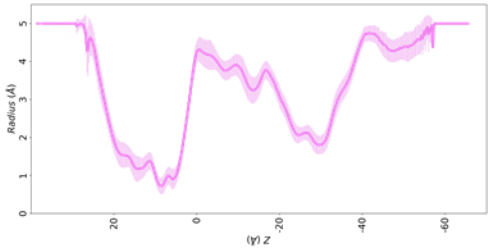

4KFM_EF-2-neg700mV_ average pore radius: 490 to 560 (ns)

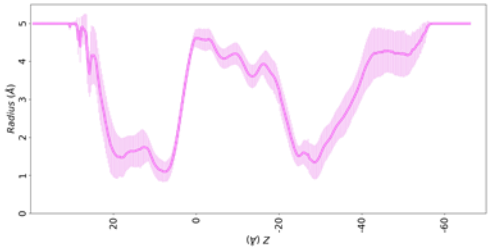

4KFM_EF-2-neg700mV_ average pore radius: 210 to 280 (ns)

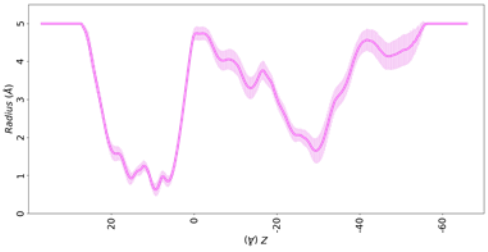

4KFM_EF-2-neg700mV_ average pore radius: 590 to 660 (ns)

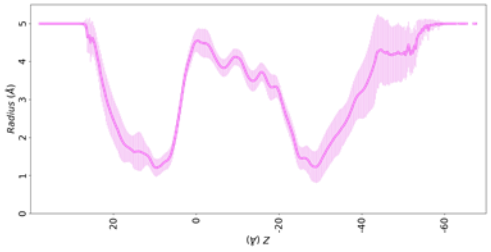

4KFM_EF-2-neg700mV_ average pore radius: 280 to 350 (ns)

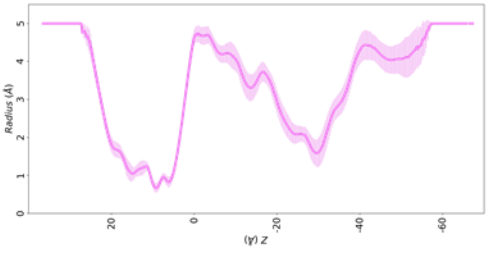

Simulation I: 3

Occupacy in binding sites during time interval: 0..73 (*ns*)

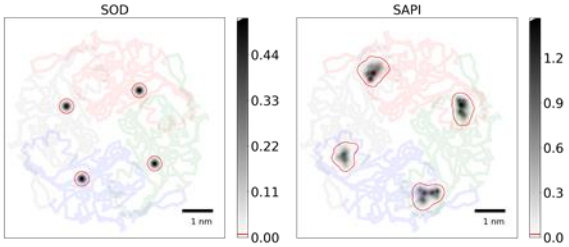

Occupacy in binding sites during time interval: 365..439 (*ns*)

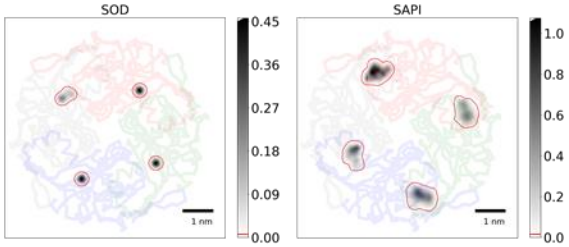

Occupacy in binding sites during time interval: 72..146 (*ns*)

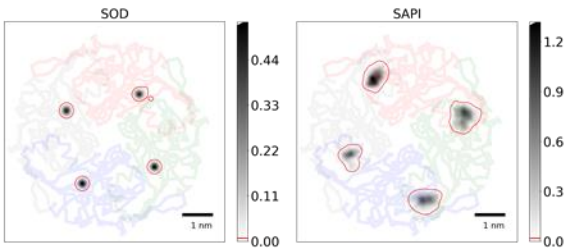

Occupacy in binding sites during time interval: 438..512 (*ns*)

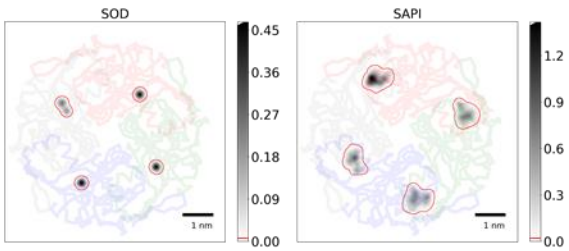

Occupacy in binding sites during time interval: 146..219 (*ns*)

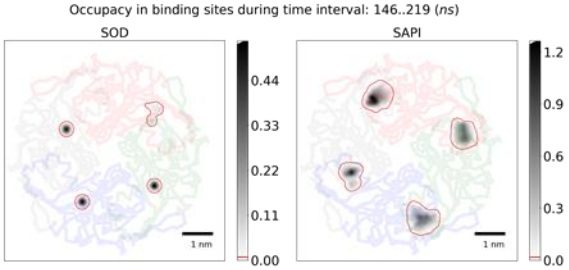

Occupacy in binding sites during time interval: 512..585 (*ns*)

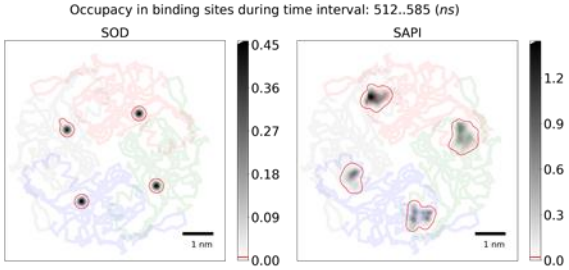

Occupacy in binding sites during time interval: 219..292 (*ns*)

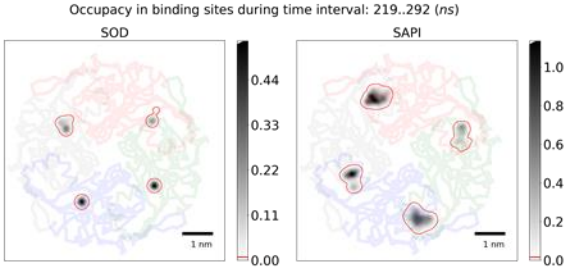

Occupacy in binding sites during time interval: 585..658 (*ns*)

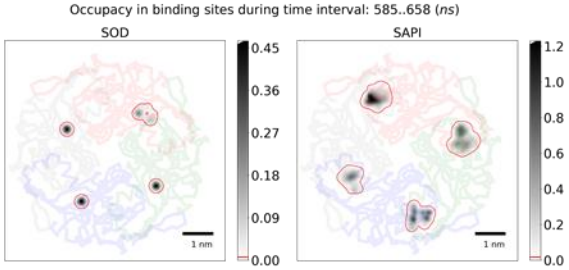

Occupacy in binding sites during time interval: 292..366 (*ns*)

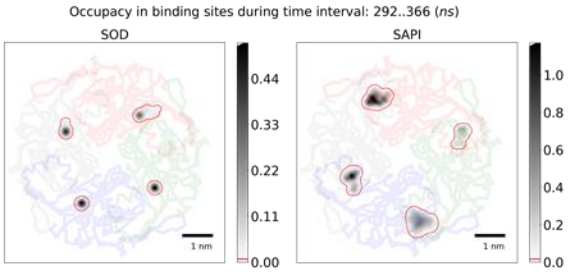

Simulation IX: 5

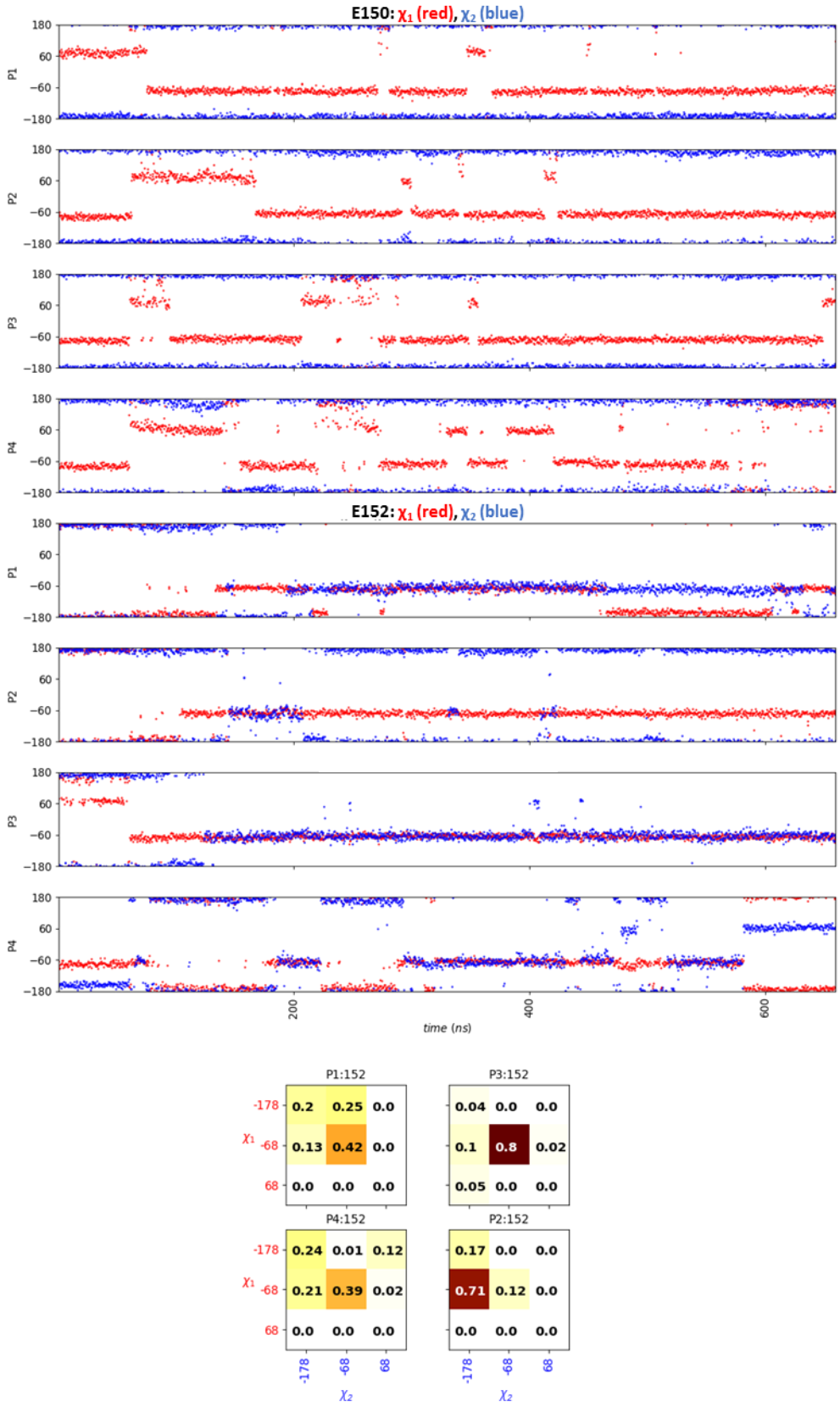

Simulation IX: 6

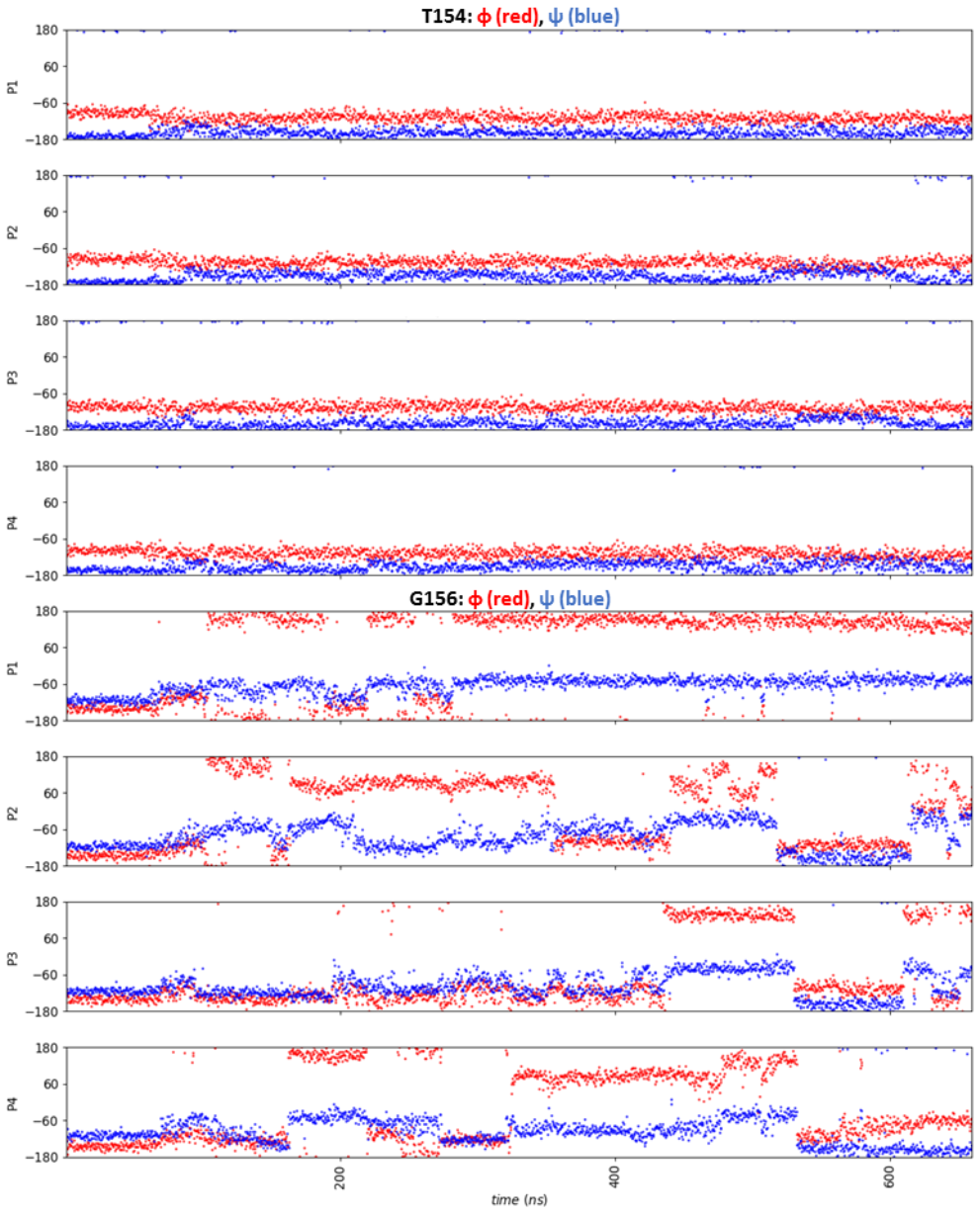

Simulation IX: 6

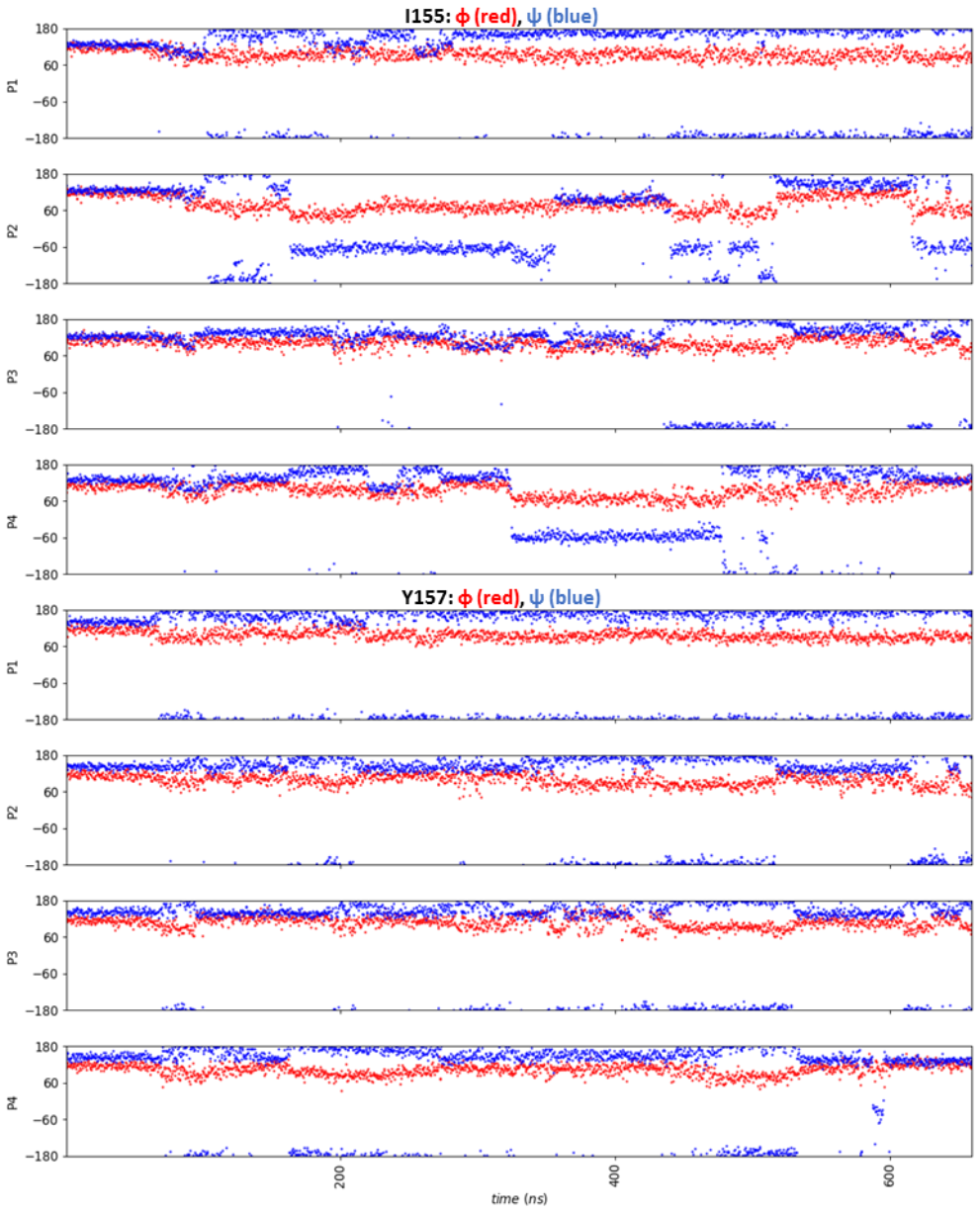

Simulation IX: 6

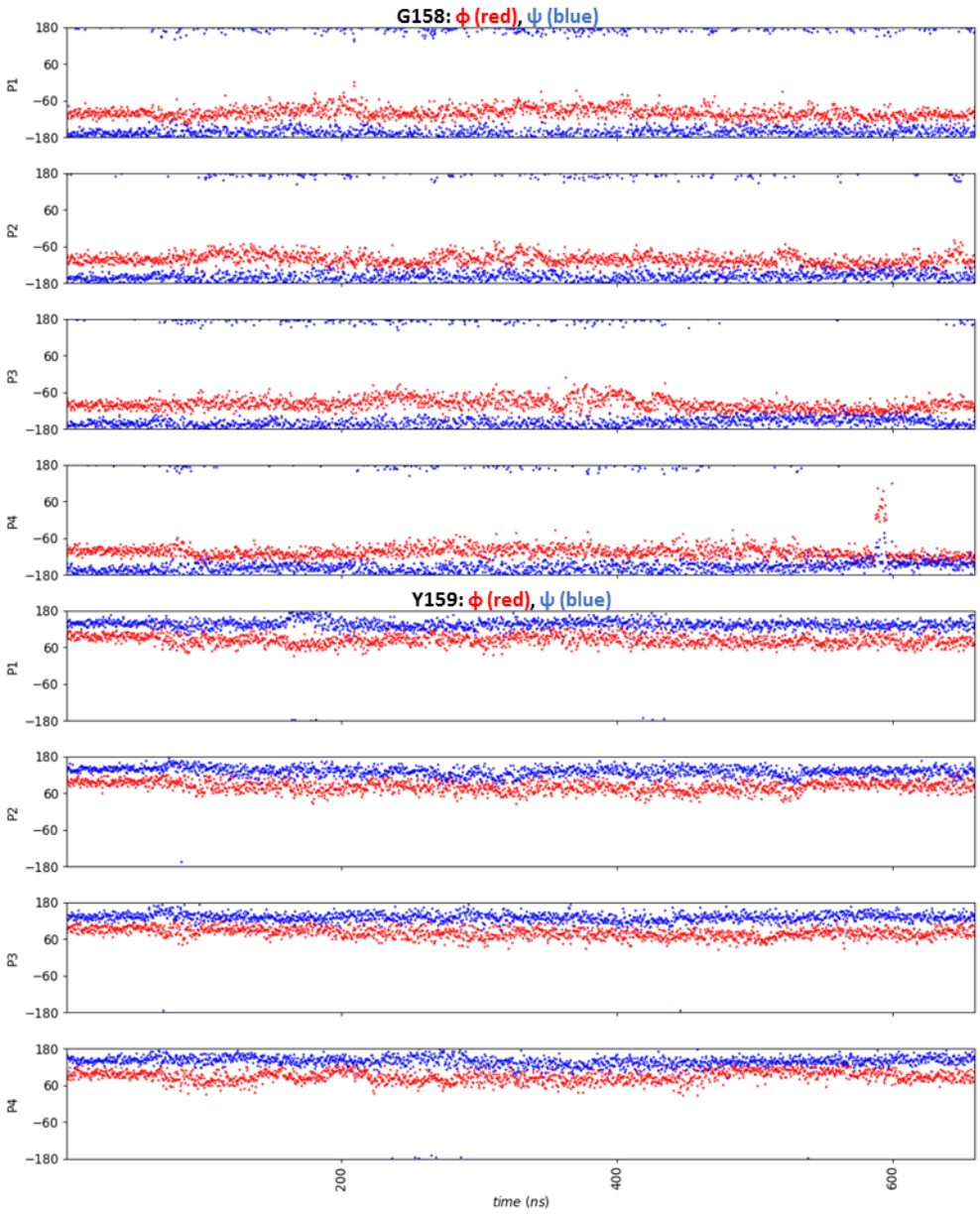

Simulation IX: 7

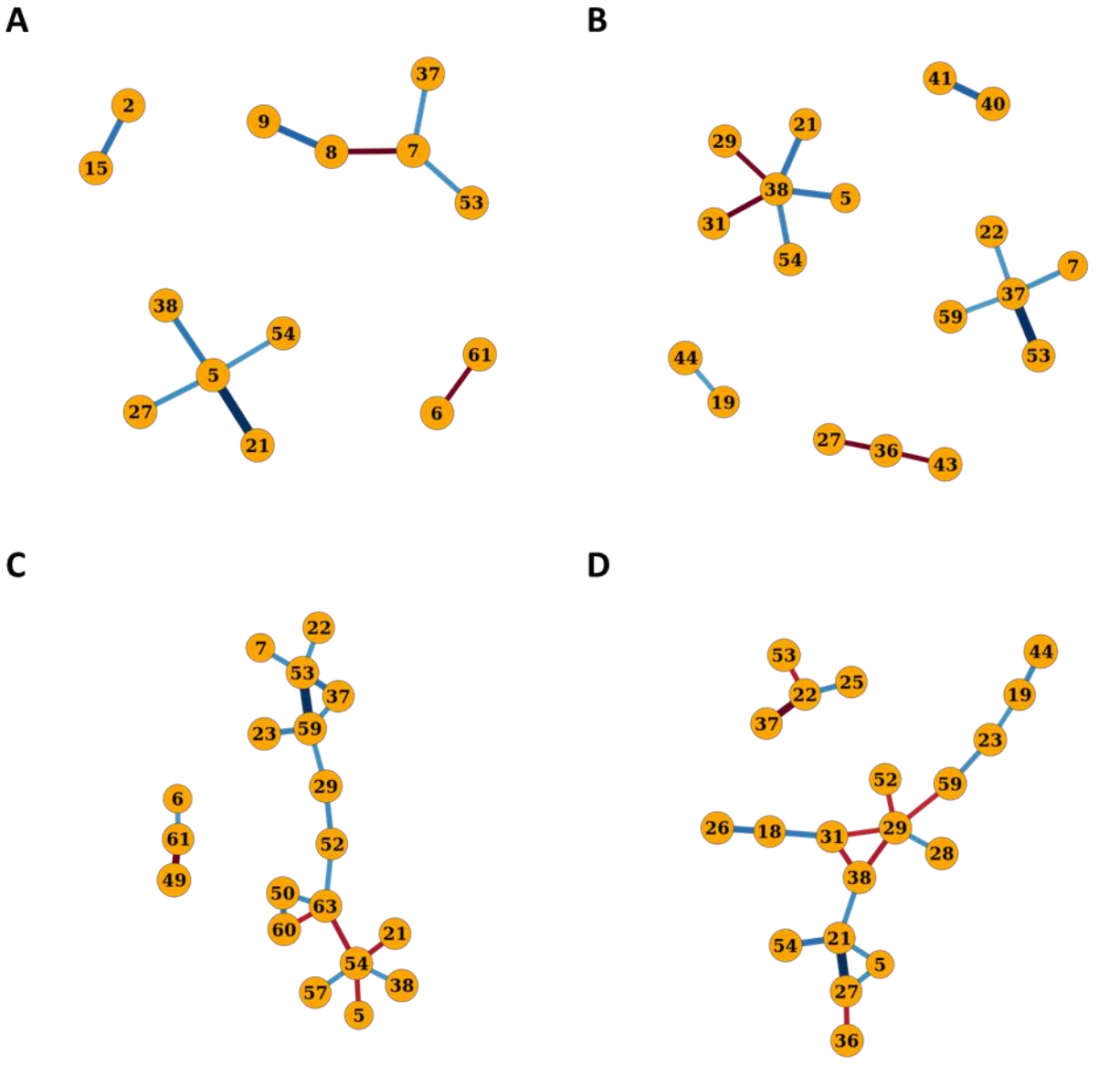

Diagrams of the instantaneous correlations between couples of interatomic distances collected in the region of the selectivity filter in Simulation IX. Data collection was made on the basis of frames where the rotamer state of E152 in subunit P4 was χ1:-180°/ χ2:-180°, interatomic distances have been collected and convoluted as described in Figure 12 in the main text. The matrix with the instantaneous correlation filtrated by abs(r) > 0.5 was used to produce diagrams for each subunit. Graphs have been manually optimized for reading of the edges. (A) Subunit P1. (B) Subunit P3. (C) Subunit P4. (D) Subunit P2. (D) This diagram is the result of the summation of all equivalent correlation factors for pairwise distance among the four channel subunits, the threshold value for an edge to be displayed was set to abs(r) > 0.39 – corresponding to a correlation of abs(r) > 0.73 in at least three subunits.

Simulation IX: 11

Average electrostatic potential along the pore

Electrostatic potential in the simulation box *(Y_{axis}=0)*

A

20 to 40 ns; V_m= -0,7 *(Volts)*

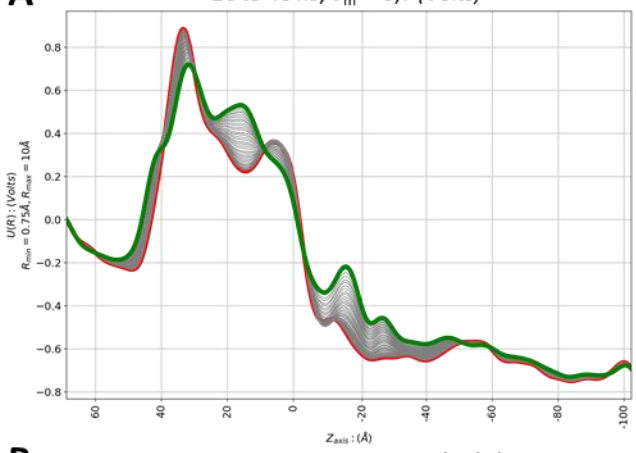

20 to 40 ns; V_m= -0,07 *(Volts)*

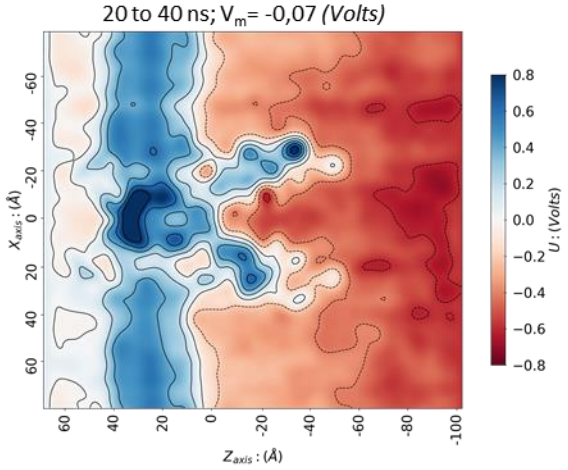

B

220 to 240 ns; V_m= -0, 7 *(Volts)*

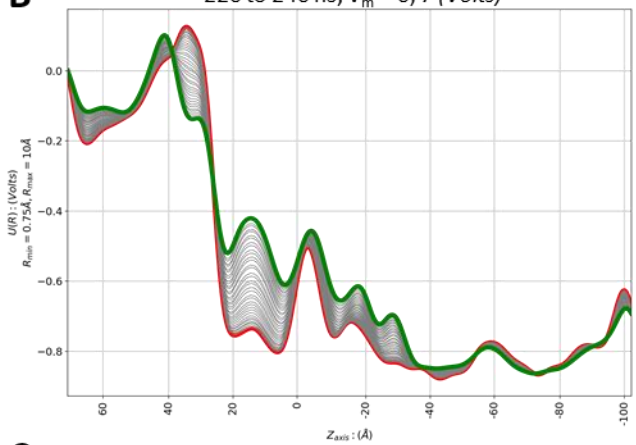

220 to 240 ns; V_m= -0,7 *(Volts)*

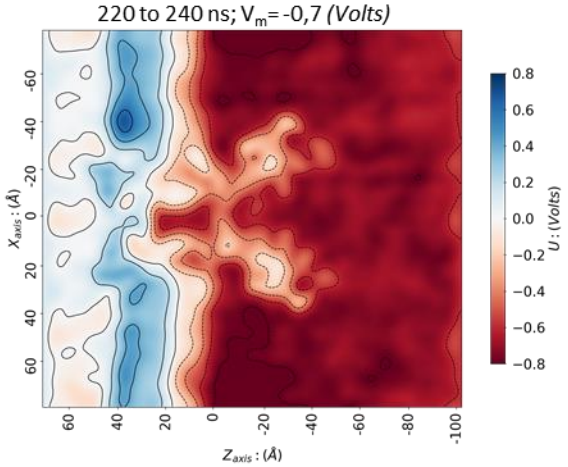

C

420 to 440 ns; V_m= -0,7 *(Volts)*

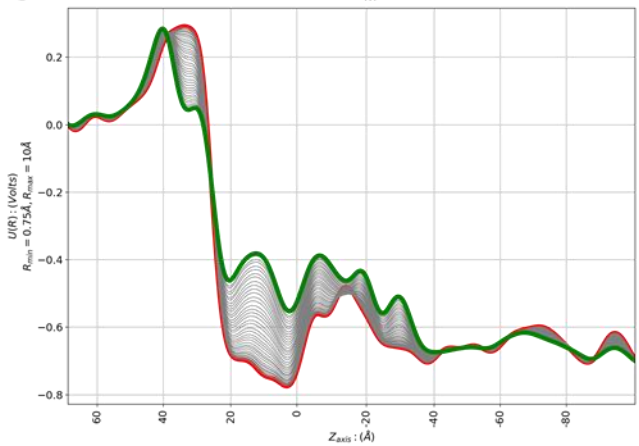

420 to 740 ns; V_m= -0,7 *(Volts)*

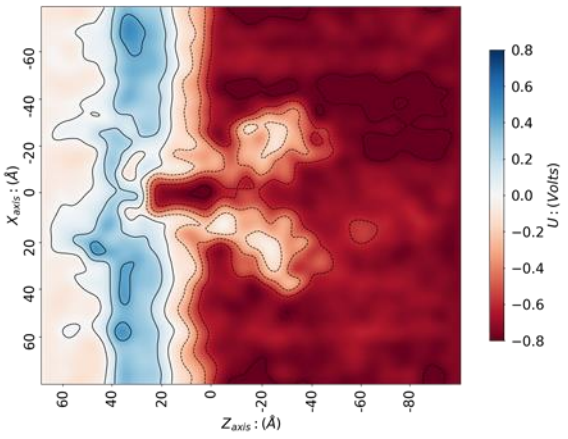

D

620 to 640 ns; V_m= -0,7 *(Volts)*

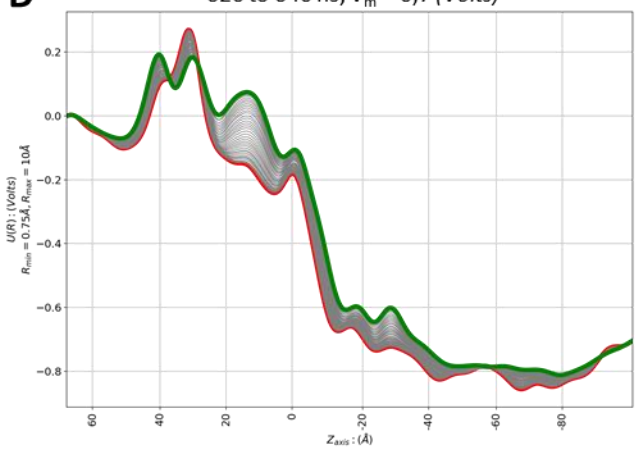

820 to 840 ns; V_m= -0,7 *(Volts)*